PETROLOGY AND GEOCHEMISTRY OF A SUITE OF GRANULITE FACIES ROCK AND ASSOCIATED GRANITOIDS FROM MAKROHAR GRANULITE BELT, CENTRAL INDIA

Thesis submitted to Jadavpur University

for the degree of

Doctor of Philosophy (Science)

By

Arimita Chakrabarty

Department of Geological Sciences

Jadavpur University

2024

যাদবপুর বিশ্ববিদ্যালয়
কলকাতা-৭০০০৩২, ভারত

JADAVPUR UNIVERSITY
KOLKATA-700032, INDIA

FACULTY OF SCIENCE : DEPARTMENT OF GEOLOGICAL SCIENCES

CERTIFICATE FROM THE SUPERVISOR(S)

This is to certify that the thesis entitled "**PETROLOGY AND GEOCHEMISTRY OF A SUITE OF GRANULITE FACIES ROCK AND ASSOCIATED GRANITOIDS FROM MAKROHAR GRANULITE BELT, CENTRAL INDIA**" submitted by Smt. **Arimita Chakrabarty** who got her name registered on **31.01.2018** for the award of Ph. D. (Science) degree of Jadavpur University, is absolutely based upon her own work under the supervision of **Professor Pulak Sengupta and Professor Sanjoy Sanyal** and that neither this thesis nor any part of it has been submitted for either any degree / diploma or any other academic award anywhere before.

Pulak Sengupta 16/1/24

Supervisor

Prof. PULAK SENGUPTA

Department of Geological Sciences

Jadavpur University

Kolkata-700032

Dr. Pulak Sengupta
Professor
Dept. of Geological Sciences
Jadavpur University
Kolkata - 700032, India

Sanjoy Sanyal 16.01.2024

Supervisor

Prof. SANJOY SANYAL

Department of Geological Sciences

Jadavpur University

Kolkata-700032

Dr. Sanjoy Sanyal
Professor
Dept. of Geological Sciences
Jadavpur University
Kolkata - 700032, India

The method of science is tried and true. It is not perfect; it's just the best we have. And to abandon it with its skeptical protocols is the pathway to a dark age.

■ Carl Sagan (1997) "The Demon-Haunted World: Science as a Candle in the Dark"

Dedicated to *my parents*...

Acknowledgements

I want to start by stating that I am grateful to everyone who supported me along the way and helped me achieve my goal.

I am indebted to my supervisors, Professor Pulak Sengupta and Professor Sanjoy Sanyal. I sincerely want to express my gratitude to them for their unwavering patience and for always inspiring me. Their relentless efforts and advice, which have significantly improved my work, have been a constant source of encouragement for me, and for that I am truly grateful.

I am appreciative of the advice of Dr. Shyamal Sengupta during my research.

I express my gratitude to the Department of Science and Technology (DST) for their financial support, which has greatly facilitated my work.

I would want to express my gratitude to all of the faculty members, researchers, and staff of Department of Geological Sciences, Jadavpur University for their assistance and support.

I am grateful to Prof. Dewashish Upadhyay of IIT Kharagpur for his assistance with the analysis of the zircon grains used in this work. In addition, I would like to express my gratitude to Dr. Upama Dutta for her invaluable assistance with the EPMA analysis at IIT-ISM Dhanbad and for her academic support throughout this effort. I like to thank Prof. Biswajit Mishra for his assistance with the EPMA analysis at IIT Kharagpur. I am thankful to Dr. Indra Sekhar Sen for his support in the trace element geochemical analysis at IIT Kanpur.

I would like to express my gratitude to Dr. Shreya Karmakar for her invaluable assistance and advice during my research. I am indebted to Prithwiraj Maiti, Sustava Bhattacharya and Mohai Menul Hasan for their immense help and support during field work.

I am grateful to every member of the Lab who collaborated so well, shared ideas, and on multiple occasions assisted me in overcoming obstacles in my personal and

academic life. My sincere and profound appreciation goes out to Sirina di for her unwavering support, encouragement, and guidance, both academically and beyond. Special thanks to Somdipta Chatterjee, my lab mate as well as classmate for his suggestions in both academic and personal spheres. I would like to express my gratitude to Dr. Anindita Dey, Dr. Enakshi Das, Dr. Satabdi Das and Nivedita Lahiri for being wonderful seniors and constant inspirations throughout my PhD tenure. I would also like to thank Dr. Nandini Chattopadhay for being a supportive senior. I am thankful to Sourav Mitra, Shreyasi Das and Nilanjan Bhowmik as they have been very supportive and wonderful juniors.

I would like to express my honest and heartfelt gratitude to Dr. Subham Mukherjee for being a wonderful companion both in my academic and personal life. He has been my biggest ally throughout the PhD tenure. His patience, utmost belief in me and relentless effort to motivate me to make my dream come true has been a rock-solid foundation for me.

Most importantly, I would like to convey that I am indebted to my parents, without whom I could not be able to pursue my dream in academia and research. Their selflessness and unwavering faith in me have been truly an incentive for my research work. Last but not the least I would like to express my gratitude to my other parents (in-laws) for being wonderful, nurturing and supportive pillars of my academic life and to my brother (in-law) with whom I have had some enlightening conversations.

Arimita Chakrabarty
Department of Geological Sciences
Jadavpur University,
Kolkata

TABLE OF CONTENTS

ABSTRACT 1
CHAPTER 1: INTRODUCTION 5
CHAPTER 2: BACKGROUND GEOLOGY 12
2.1. Geology of different sectors of CITZ 14
2.1.1. South-west (SW) sector 14
2.1.2. North-east (NE) sector 24
2.2. Chotanagpur Granite Gneissic Complex (CGGC) 28
CHAPTER 3: LITHOLOGY AND STRUCTURES OF THE STUDY AREA 31
3.1 Lithological distribution of the study area 31
3.1.1. Basement metagranitoids 33
3.1.2. Felsic orthogneisses 37
3.1.3. Metasedimentary rocks 39
3.1.4. Meta-mafic rocks and pegmatites 42
3.2. Structures in the study area 46
CHAPTER 4: PETROGENESIS OF THE PORPHYRITIC METAGRANITOID. ..... 48.
4.1. Petrography 49
4.2. Mineral compositions 53
4.3. Whole rock geochemistry 64
4.3.1. Choice of samples 64
4.3.2. Geochemical characters of the studied metagranitoids 64
4.4. Zircon saturation thermometry 71
4.5. Tectonic affinity of the protolith magma 72
4.6. Open system phase equilibria modeling 74
4.6.1. Methodology 75
4.6.2. Model for combined crustal assimilation and fractional crystallization of mafic magma 77
4.6.3. Model for post-emplacement crystal fractionation of felsic magma 83
4.7. U-Pb zircon geochronology 99

CHAPTER 5: SUBSOLIDUS MYRMEKITE FORMATION IN PORPHYRITIC METAGRANITOID 103
5.1. Petrography and feldspar composition in the myrmekite domains 104
5.2. Physical conditions of myrmekite formation 110
5.3. Controls of mobile and immobile species during the formation of myrmekite 110
5.3.1. Mass balance approach 110
5.3.2. Element mobility (immobility) during the myrmekite formation: behavior of Al and Si 111
5.3.3. Element mobility during the formation of the secondary biotite 115
5.3.4. Thermodynamic drive on the formation of myrmekite and secondary biotite: the chemical potential diagram 116
CHAPTER 6: EVOLUTION OF THE FELSIC ORTHOGNEISSES 120
6.1. Petrography of Felsic Orthogneiss 120
6.1.1. Charnockitic Orthogneiss (COG) 121
6.1.2. Garnet Orthogneiss (GOG) 123
6.2. Mineral chemistry 125
6.3. Whole rock geochemistry 132
6.3.1. Major element characteristics 133
6.3.2. Trace element characteristics 135
6.3.3. Temperature of magma from zircon saturation thermometry 138
6.3.4. Tectonic affinity of the protolith magma 139
6.4. Physical conditions of metamorphism 141
6.4.1. Conventional geothermobarometry 142
6.4.2. Phase equilibria study (pseudo-section analysis) 145
Methodology 145
Results 148
6.5. Geochronology 151
6.5.1. U-Pb zircon geochronology (in-situ LA-ICPMS) 152
6.5.2. Th-U-total Pb monazite geochronology (in-situ, EPMA) 156
CHAPTER 7: EVOLUTION OF THE METAPELITES 160
7.1. Banded psammopelite 160
7.1.1. Petrography 160

7.1.2. Mineral chemistry 162
7.1.3. Physical condition of metamorphism 165
7.2. Garnet-cordierite-biotite rock (GCB) 169
7.2.1. Petrography of Association 1 169
7.2.2. Petrography of Association-2 171
7.2.3. Petrography of Type I and Type II veins 173
7.2.4. Mineral paragenesis in both the association of GCB 177
Association-1 177
Association-2 178
7.2.5. Mineral chemistry 179
7.2.6. Reaction modeling 192
7.2.7. Physical conditions of metamorphism 194
Conventional thermobarometry 194
Temperature constrained from the T-X_{MgO} diagrams 195
Phase compatibilities in the Al_2O_3-FeO-MgO (AFM) diagram 197
P-T constrains from the microbulk of Association 1 199
CHAPTER 8: EVOLUTION OF THE META-MAFIC ROCKS 201
8.1. Petrography of meta-mafic rocks 201
8.1.1. Type-I 203
Type-IA 203
Type-IB: 207
8.1.2. Type-II 212
Type-IIA 212
Type-IIB 217
8.1.3. Mineral paragenesis and multiple coronae in the meta-mafic rocks 218
8.2. Mineral chemistry 219
8.3. Physical condition of metamorphism 237
8.3.1. Conventional geothermobarometry 237
8.3.2. Pseudosection analysis 239
8.3.3. Emplacement depth and subsequent metamorphism 241
CHAPTER 9: DISCUSSION 243

9.1. Magmatic history of the MKGB 243
9.1.1. Paleoproterozoic magmatism in MKGB 243
Chemical variation in the Paleoproterozoic granitic magma of MKGB..... 244
9.1.2. Mesoproterozoic magmatism in MKGB 250
Chemical variation in the Mesoproterozoic granitic magma of MKGB..... 250
9.2. Metamorphic history of the MKGB 256
9.2.1. Metamorphic evolution of the felsic orthogneisses..... 256
9.2.2. Metamorphic evolution of the metasedimentary and meta-mafic rocks 257
9.2.3. Tectonic implication of the Neoproterozoic metamorphic imprint in MKGB 258
9.2.4. Retrograde metamorphism and fluid-induced structures in the lithounits of MKGB..... 260
Extensive myrmekitisation within porphyritic metagranitoid 260
Vein formation within metapelites (GCB) and aluminium mobility 265
9.3. Proterozoic evolution of MKGB in the context of the CITZ..... 267
I. Late Paleoproterozoic (Statherian period):..... 267
II. Early Mesoproterozoic (early Calymmian period): 270
III. Mesoproterozoic (late Calymmian and Ectasian period):..... 271
IV. Early Neoproterozoic (Tonian period): 272
9.4. Linking the Proterozoic scenario of CITZ with India..... 274
9.4.1. Late Paleoproterozoic magmatic and metamorphic events in India..... 274
9.4.2. Mesoproterozoic magmatic events in India..... 279
9.4.3. Neoproterozoic high grade metamorphic event in India 280
9.5. CITZ in the context of Proterozoic supercontinental cycle 282
CHAPTER 10: CONCLUSIONS 288
PUBLICATIONS..... 291
APPENDIX..... 293
REFERENCES 297

ABSTRACT

Thermotectonic evolution of the rocks of Central Indian Tectonic Zone (CITZ) is crucial to understand the growth of the Indian shield and its response to the supercontinental cycles of the Earth. In this study detail petrology and robust geochronological data from a suite of metaigneous (porphyritic metagranitoid, felsic orthogneiss and meta-mafic rocks) and metasedimentary rocks (metapelite and garnet-cordierite biotite rock) from the least studied Makrohar Granulite Belt (MKGB) that is situated in the NE part of the CITZ are presented and analyzed.

The porphyritic metagranitoid suite develops megacrystic K-feldspar and plagioclase phenocrysts, embedded in medium to fine-grained matrix of biotite ± amphibole + quartz + K-feldspar + plagioclase + ilmenite ± garnet with widely variable phenocryst (variably deformed) to matrix ratio. The bulk compositions of the rocks overlap with the compositions of the I-type granitoid, emplaced in a continental arc setting. Systematic geochemical trends combined with the variation in modal mineralogy suggest crystal fractionation to be the dominant process during the evolution of this arc magma. Phase equilibrium modeling in Na_2O-CaO-K_2O-FeO-MgO-Al_2O_3-SiO_2-H_2O-TiO_2 system under various physicochemical conditions suggests that both post-emplacement fractionation of a felsic magma and combined fractionation-crustal assimilation of a mafic magma at shallow depths (≤5 kbar) likely to produce the observed chemical variation in the arc granites. The in-situ U-Pb zircon age of the zircon with oscillatory zoning constrains the timing of magmatism at 1750 Ma.

Petrology and geochemical data of the felsic orthogneisses identify two rock groups: charnockitic orthogneiss (COG) and garnet orthogneiss (GOG). Geochemical fingerprints suggest that the magmatic protoliths of the gneisses are S-type granitoids, formed in a continental arc setting. In situ U-Pb zircon dates yield the time of the arc magmatism at ca. 1400-1350 Ma. This is the first report of mid-Mesoproterozoic arc magmatism in the CITZ. These arc granites were subsequently metamorphosed at granulite facies condition that culminated at ~800-850°C, 7-7.5 kbar and then followed

sequentially by a steeply and mildly decompressive retrograde P-T path that can be traced upto 4 kbar and 500ºC. The geometry of the P-T paths (‘clock wise’) combined with secondary planar structures in the outcrop of these rocks are consistent with reworking of the Mesoproterozoic arc rocks and the adjoining metapelites and metabasic rocks in a continent-continent collisional setting. In-situ Th-U-total Pb monazite and in-situ U-Pb ages of zircon overgrowth date the deformation and metamorphism in the span of ca. 974-913 Ma.

Combined field relations, and phase equilibria modeling study on the banded psammopelites identify an early granulite facies metamorphism (garnet + plagioclase + K-feldspar + quartz + ilmenite without any feldspar and muscovite); manifested by the garnetiferous leucosomes that define a regional planar fabric formed at ~800°C, 7 kbar which is corroborated well with the P-T conditions reported from the adjoining felsic orthogneisses. The garnet-cordierite-biotite rock occurs as patches in the strike continuity of the psammopelite and develops two mineralogically exclusive domains (with and without anthophyllite). Both the domains form high variance mineral assemblage presumably results from infiltration driven metamorphism. The garnet-aluminosilicate veins that dissect the garnet-cordierite-biotite rock are interpreted by infiltration-driven metasomatism where the infiltrated fluid interacted with aluminous host rock, caused hydrofractures and deposited prismatic sillimanite, coarse vein quartz and garnet (crack-seal mechanism). Formation of fibrolite in places supports that unlike the aluminosilicate veins where Al was mobile, Al was also locally immobile. Variation of chemical potentials of chemical species at nearly constant P-T was responsible for the stability of anthophyllite.

Field study and petrographic observations identify two groups of meta-mafic rocks among which the coarse grained ones have a magmatic mineral association of olivine + clinopyroxene + orthopyroxene + plagioclase + ilmenite + magnetite ± apatite. In the subsolidus stage diffusion controlled reactions between primary olivine and plagioclase formed the double coronae (inner corona: orthopyroxene and outer corona: amphibole + spinel). Olivine in few cases is extensively replaced and pseudomorphed by symplectic association of orthopyroxene + magnetite pointing towards a mechanism governed by oxidation. Phase equilibrium modeling of the garnetiferous meta-mafic

rocks suggest that metamorphism culminated at 750-800 °C and 7-9 kbar stabilizing the peak metamorphic mineralogy of garnet + clinopyroxene + orthopyroxene + plagioclase + ilmenite + quartz. Combining the physical conditions of the formation of amphibole + biotite during retrogression the depicted metamorphic P-T path is well matched with the felsic orthogneisses and metapelites of the MKGB.

The K-feldspar megacryst in the porphyritic metagranitoid develops extensive myrmekite all along the periphery of the alkali feldspar megacryst. Myrmekite shows two different morphologies: (1) vermicular intergrowth of plagioclase (An_{38-39}) and quartz (Myr1) and (2) polygonal aggregates of coarse plagioclase (An_{45-46}) and quartz (Myr2). Petrographic features suggest that (1) myrmekite nucleates on alkali feldspar and plagioclase porphyroclast and the myrmekite front moved into the alkali-feldspar by replacing it and (2) the myrmekite and the secondary biotite that replaces plagioclase porphyroclasts and garnet form together. Whereas deformation had a decisive role in forming the polygonal aggregates in Myr2, field and microtextural features do not support any significant control of deformation during the formation of Myr1. Reaction modeling and mass balance calculation suggest that Ca and Na are added to and K is removed from the alkali-feldspar during synergic formation of the myrmekite and the secondary biotite. Interpretation of the reaction textures in different isothermal-isobaric sections of μK_2O-μCaO in the KCFASH system suggest a feedback mechanism that operated between the two reaction sites (at myrmekite and at the site of secondary biotite) during infiltration of brine rich fluid in the metagranitoid at c. 550^{o}-600^{o}C and 5-6 kbar). Integrating the analyses of this study with the published information following inferences are drawn:

1. MKGB experienced a protracted period of magmatism, both felsic and mafic compositions, sedimentation (protoliths of metasedimentary rocks) and deformation that can be tracked from ca.1750 Ma to 913 Ma.

2. The ca. 1750 Ma old arc magmatism in the MKGB is consistent with the view that both MKGB and Mahakoshal Supracrustal Belt, now separated by the Son Narmada South Fault formed a coherent block till 1750 Ma. A southward

progression of the arc front in the Indian shield from ca. 1900 Ma to ca. 1600 Ma is envisaged during the growth of the Columbia supercontinent.

3. The ca. 1400-1350 Ma arc magmatism is presumably linked to collapse or closure of a basin (either north or south of the MKGB) in the CITZ in response to the prolonged accretionary phase of the Columbia supercontinent and preponderance of ca. 1000-950 Ma tectonometamorphic event superposed on the older continental basement in the CITZ, Chotanagpur Granite Gneiss Complex, the Eastern Ghats mobile belt and in many other parts raises the possibility that major part of the Indian Shield behaved as a coherent block during this tectonothermal event during the assembly of the Rodinia supercontinent.

CHAPTER 1
INTRODUCTION

Studies in the past several decades have suggested that the birth, maturity and demise of the large continental mass known as supercontinental cycle occurred several times and are perceived to be the consequence of the secular changes of the Earth's internal and external processes (reviewed in Condie, 2013; Li et al., 2008; Meert and Santosh, 2017; Nance and Murphy, 2013; Rogers and Santosh, 2002a; Zhao et al., 2011, 2004, Bose et al. 2023, Dora et al.2023). Extensive studies have identified three major supercontinental cycles, Columbia, Rodinia and Gondwana in order of decreasing age, across the Proterozoic and Phanerozoic Eon. Owing to inadequate and robust petrological, geochronological, paleomagnetic data from several parts of the Precambrian crust, exact configuration of the supercontinents remains poorly understood (reviewed in Bhowmik, 2019; Chattopadhyay et al., 2020; Dasgupta et al., 2017; Meert and Santosh, 2017; Zhao and Cawood, 2012). Being the most abundant lithology with large variation in geochemistry and mineral assemblages granitic rocks serve as proxies to trace source heterogeneity and various other petrogenetic processes including magma mixing, assimilation-fractional crystallization, depth of magma emplacement and the tectonic setting in which the felsic magmas are generated (reviewed in Castro, 2014; Deering and Bachmann, 2010; Farina et al., 2020; Garcia-Arias and Stevens, 2017; Jagoutz, 2010; Nandedkar et al., 2014, Bose et al.2023). Furthermore, the mineralogy of the granitic rocks (amphibole–biotite-feldspars and quartz with variable zircon and monazite) are susceptible to the variation of the ambient

to physicochemical conditions during metamorphism and can serve as proxies to reconstruct the P-T-t path of metamorphism and put constraints on the process of migmatite formation (Brown, 2013). The NNE/SSW trending orogenic belt known as the Central Indian Tectonic Zone (CITZ) dissects the Indian shield and is perceived to have sutured a North Indian Block (Bundelkhand craton) and a South Indian Block (Bastar, Singhbhum and Dharwar craton) to form what is known as Greater Indian Landmass (Acharyya, 2003; Jain et al., 1991; Roy and Prasad, 2003; Yedekar et al., 1990). A thorough understanding of the geological history of the rocks in the CITZ has the paramount importance not only to trace the growth of the Greater Indian Landmass but also to understand the formation and disintegration of the Proterozoic supercontinents, especially the Columbia and Rodinia supercontinent (reviewed in Bhowmik, 2019; Chattopadhyay et al., 2020; Dasgupta et al., 2017; Meert and Santosh, 2017; Zhao and Cawood, 2012). Existing information from a few scattered areas suggests that the ENE-WSW trending CITZ can be broadly divided into two longitudinal units or sectors with distinct geological history. From north to south, the sectors are as follows: (1) Mahakoshal Supracrustal Belt (MSB) + (Son-Narmada Fault system) + Makrohar Granulite Belt (MKGB) and (2) Betul Supracrustal Belt (BSB) + Gavilgarh-Tan Shear Zone + Ramakona-Katangi Granulite Belt (RKGB) + Sausar Supracrustal Belt (SSB) + Balaghat-Bhandara Granulite Belt (BBGB).

In the northern sector, MSB exposes andalusite type low pressure-high temperature metasupracrustal rocks, metamorphosed during a major tectonothermal event at ca. 1800-1600 Ma, which is intruded by syn- to post-collisional granitoid (Bora et al., 2013; Deshmukh et al., 2017; Yadav et al., 2020). In southern sector, Betul belt (BSB), a volcano-sedimentary terrain is characterized as a continental magmatic arc on the orogenic front in the periphery of the North Indian Block (Chattopadhyay et al., 2017). Petrology, structural and geochronological studies from the Gavilgarh-Tan Shear Zone, a Neoproterozoic shear zone that got reactivated repeatedly during Phanerozoic, indicate that the final stitching of the North and South Indian Blocks occurred during global Grenvillian orogeny (Chattopadhyay et al., 2017). To the south of BSB, this sector exposes granulites and gneisses [RKGB, BBGB] and a suite of Barrovian type metasupracrustal rocks [SSB]. Evidence of an

accretionary orogeny at ca. 1600 Ma [emplacement of the protolith of the Tirodi Biotite Gneiss and ultra-high temperature metamorphism in the BBGB] signifies the subduction of the South Indian Block underneath the North Indian Block at the end of Paleoproterozoic (Bhowmik, 2019). Different lithounits of the RKGB and SSB experienced a clockwise metamorphic P-T path, attesting continent-continent collision during ca. 1000-950 Ma (reviewed in Bhowmik, 2019). The Chotanagpur Granite Gneissic Complex (CGGC) and the Shillong-Meghalaya Gneissic Complex are presumed as the eastern extension of the CITZ (Acharyya, 2003).

Lack of exposure of lithounits in a large portion of the CITZ and proper correlation between different units pose several questions including (a) the relation of the Paleoproterozoic MSB with the younger units lying to the south, (b) does ca. 1000-950 Ma old Grenvillian event, so dominant in the SSB continues further north? (c) Did the crust of the CITZ remain tectonically undisturbed during the interlude period between ca. 1500-1000 Ma? and (d) does the southern part of MSB in CITZ preserve any evidence of Paleoproterozoic tectonomagmatic event(s) that are recorded in the MSB (reviewed in Chattopadhyay et al., 2020) and the Chotanagpur Granite Gneiss Complex (CGGC) (Mukherjee et al., 2019). The latter one is considered to be the eastern extension of the CITZ (Banerjee et al., 2021). Such information is crucial to support (or reject) the ideas of Zhao et al. (2004) and Rogers and Santosh (2002) that the Indian shield including the CITZ formed a part of the Columbia supercontinent.

Origin of the delicate intergrowth of quartz rods with plagioclase after alkali feldspar known as ‘vermicular quartz’ (Fouqué and Lévy, 1879) and 'myrmekite' (Sederholm, 1899) is one of the unresolved phenomena in deformed rock. A range of models including (a) Ca- and Na metasomatism (Becke, 1908) (b) exsolution of plagioclase and quartz from the immediate alkali feldspar (Schwantke, 1909), (c) combination of replacement and exsolution (Ashworth, 1972) are proposed (reviewed in Phillips, 1980). Formation of myrmekite preferentially on the alkali feldspar has been reported from variably deformed rocks of diverse bulk compositions(Abart et al., 2014; Ceccato et al., 2018; Cesare et al., 2002; Lazaro and Baumgartner, 2019; Tsurumi et al., 2002; Vernon et al., 1983). Whereas the replacement theory, originally proposed by Becke (1908), is considered to be the dominant chemical process in the

myrmekite formation, the relative importance between stress and chemical replacement remains to be a debated topic (Abart et al., 2014; Lazaro and Baumgartner, 2019; Menegon et al., 2006; Vernon, 2004). Vernon et al. (1991), argued that the ambient stress only helps the access of Ca, Na bearing fluid to alkali feldspar. The argument of Vernon (1991) has been subsequently supported by (Abart et al., 2014; Cesare et al., 2002; Menegon et al., 2006). Whether or not stress is the dominant factor for the formation of myrmekite, the fact remains that the formation of myrmekite requires chemical alteration of alkali feldspar in an open system, at least in the scale of myrmekite. In any heterogeneous system, chemical species move along its chemical potential gradient. This requires that for significant progress of the myrmekite low chemical potentials for Ca and Na (high chemical potential for K) have to be maintained at the alkali feldspar site to be replaced by myrmekite. No detailed study to date has been published that explains how the chemical potential gradients that bring Ca and Na toward and remove K away from the myrmekite could be created and maintained during the formation of myrmekite. This then follows that the assumption of constancy of Al and Si in myrmekite forming process as invoked in several studies needs to be studied on case to case basis. The behavior of Al in the fluid-assisted crustal process is a contentious issue (Newton and Manning, 2000). Whereas in most of the geological conditions, Al remains immobile even in the grain scale, a much larger scale (several cm to meters) of fluid-mediated transport of Al has been recorded in the aluminosilicate veins (reviewed in Philpotts and Ague, 2009). Study of aluminosilicate veins and their causative factors provides invaluable information on the conditions and the composition that allow significant transport of Al during the geological process (Ague, 1995; Sepahi et al., 2004; Whitney and Dilek, 2000).

The geological history of the rocks of the MKGB, located at the immediate contact of the MSB may hold the key to unveiling the Mesoproterozoic tectonothermal history of the CITZ. Unfortunately, no robust petrological and geochronological study has been attempted in the granulites of the MKGB. The MKGB also exposes exotic garnet-cordierite-biotite rock without feldspar and muscovite and the rock is dissected randomly by veins rich in sillimanite and garnet (my preliminary personal

information). In this study, I present detailed petrological and robust geochronological data to achieve the following objectives.

Objective of the study

1. To identify the mutual relations among the different lithounits in parts of the Makrohar Granulite Belt (MKGB) and the deformational fabrics preserved within. To trace the probable source, petrogenetic processes and tectonic settings in which the protoliths of the meta felsic rocks (both charnockitic and non-charnockitic rocks) were formed.
2. To study the internal morphology of the zircon and determination of the U-Pb isotopes of zircon to put constraints on the time of emplacement of the felsic magmas and the metamorphic overgrowth on the magmatic zircon. To decipher the metamorphic history of the different rocks, both metasedimentary and meta-igneous, of the studied area combining the field relations, textural and thermodynamic modeling of the metamorphic mineral assemblages. Combining the petrological attributes with Th-U-total Pb electron microprobe dating of monazite grains and the U-Pb ages of metamorphic overgrowth of zircon P-T-t evolutionary path and the plausible tectonic setting will be discerned.
3. To understand the length scale of transport of nominally soluble (Al) and significantly soluble chemical species (K, Ca, Na, Fe, Mg, Si etc) during fluid-rock interaction during regional metamorphism integrating the textural modeling study and interpretation of reaction textures in the chemical potential diagrams. This study will also explore a viable mechanism and examine relative controls of stress and chemical potential drive during for the development of myrmekite after alkali feldspar.
4. To decipher the physicochemical control on the formation of the garnet-cordierite-biotite rock and the aluminosilicate-garnet rich veins within.
5. To trace the magmatic and metamorphic evolution of the meta mafic rocks that commonly occur in the form of dyke.

6. Integrating all the petrological and geochronological inputs, attempts will be made to (a) identify the episodes of magmatism and metamorphism and the corresponding tectonic setting that shaped the rocks of the MKGB, (b) compare the magmato-metamorphic events of the MKGB with the extant information from other parts of the CITZ and its eastern extension (CGGC) for better understanding on the time of formation of the Greater Indian Land (GIL) mass (c) understand the significance of the magmato-metamorphic impress in the MKGB in the context of the Proterozoic supercontinental cycles.

Thesis layout

Chapter 2 presents the background geology of the study area that encompasses updated published geological information from the Central Indian Tectonic Zone along with its eastern extension (Chotanagpur Granite Gneissic Complex).

Chapter 3 presents a detailed description of all the lithounits incorporating their interrelationship and depicted secondary structures in the outcrop scale.

Chapter 4 comprises detailed petrography, representative mineral chemistry, geochemistry and U-Pb in-situ zircon geochronological study of the porphyritic metagranitoids. This chapter also describes the post-emplacement fractional crystallization scenario in the protolith granitic magma that shaped their significant chemical variation using the program Rcrust.

The contents of this chapter have been published as:

Chakrabarty Arimita, Mukherjee Subham, Karmakar Shreya, Sanyal Sanjoy, Sengupta Pulak (2023). Petrogenesis and in situ U-Pb zircon dates of a suite of granitoid in the northern part of the Central Indian tectonic Zone: Implications for prolonged arc magmatism during the formation of the Columbia supercontinent. Precambrian Research, 387, https://doi.org/10.1016/j.precamres.2023.106990

Chapter 5 encompasses the genesis of myrmekite, a widely studied microtexture in the porphyritic metagraniotoids from the study area.

Observation made from this chapter is accepted to be published to:

Chakrabarty Arimita, Karmakar Shreya, Dutta Upama, Sanyal Sanjoy, Sengupta Pulak. Evidence of fluid-induced myrmekite formation after K-feldspar megacryst: example from metaporphyritic granite in Makrohar, Madhya Pradesh, India. Mineralogical Magazine, DOI: https://doi.org/10.1180/mgm.2023.90

Chapter 6 contains petrography, representative mineral chemistry, geochemistry, quantitative thermobarometry, U-Pb in-situ zircon and Th-U-total Pb monazite EPMA dating of the felsic orthogneisses in the study area.

The contents of this chapter have been published to:

Chakrabarty Arimita, Karmakar Shreya, Mukherjee Subham, Roy Choudhury, Sirina, Maiti Prithwiraj, Sanyal Sanjoy, Sengupta Pulak (2022). Neoproterozoic reworking of a Mesoproterozoic magmatic arc from the north-eastern part of the Central Indian Tectonic Zone: Implication for the growth and disintegration of the Indian shield in the Proterozoic supercontinental cycles. Precambrian Research, 378, 1-22. https://doi.org/10.1016/j.precamres.2022.106758

Chapter 7 comprises petrography, representative mineral chemistry, reaction modeling and quantitative thermobarometry of the metapelites in the study area. This chapter also describes an exotic highly metasomatised garnet-cordierite-biotite rock comprising high variance mineral assemblage and proliferous veins *(Manuscript under preparation).*

Chapter 8 deals with the petrography, representative mineral chemistry and quantitative geothermobarometry from varieties of meta-mafic rocks in the study area.

Chapter 9 integrates all the petrological, geochemical and geochronological outcomes of the current study to decipher the tectonic evolution of the Makrohar Granulite Belt. This chapter also correlates the tectonothermal events of the entire CITZ to understand the accretion of the Archean crustal blocks of India, the formation of the Greater Indian Landmass and their relation with the global supercontinental cycle.

CHAPTER 2

BACKGROUND GEOLOGY

The Greater Indian Landmass (GIL) comprises of the Archean cratons and Proterozoic orogenic belts where the orogenic belts are inferred to be the paleosuture zones that encircles stable cratonic nuclei of the continental crust ((Naqvi and Rogers, 1987). The Greater India Proterozoic Fold Belt (GIPFB) is the accreted boundary that divides the GIL into two major crustal blocks/provinces, Bundelkhand-Marwar craton in the north and Bastar, Singhbhum and Dharwar craton in the south (Radhakrishna and Naqvi, 1986). The GIPFB is arguably

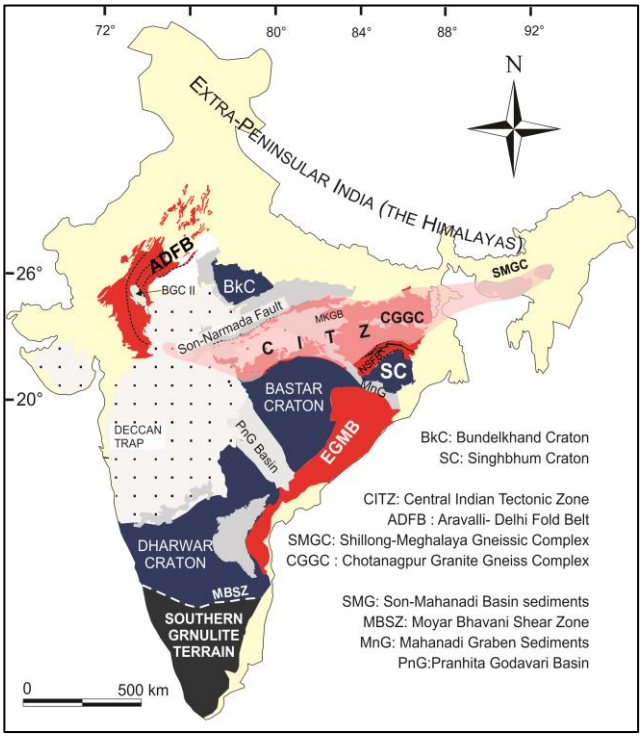

Figure 2.1. Geological map of Indian subcontinent comprising of Archean cratons and Proterozoic mobile belts (modified after Mukherjee et al., 2019). Zone marked in light pink comprises of Central Indian Tectonic Zone (CITZ), Chotanagpur Granite Gneissic Complex (CGGC) and Shillong Meghalaya Gneissic Complex (SMGC).

made up of several crustal domains or components which are Aravalli Delhi Fold Belt (ADFB), Central Indian Tectonic Zone (CITZ), Chotanagpur Granite Gneissic Complex (CGGC) and Shillong Meghalaya Gneissic Complex (SMGC) (Chatterjee and Ghose, 2011). CGGC and SMGC are considered to be the eastern extension of the CITZ and together these three blocks represent a NE-SW trending transcontinental suture zone (Banerjee et al. 2021 and references therein) (Fig. 2.1).

The North Indian Block (NIB) and South Indian Block (SIB) are believed to be amalgamated along the CITZ during Proterozoic era and formed the Greater Indian Landmass (GIL) (Bhowmik et al., 2012). This transcontinental suture zone is further inferred to be extended up to Madagascar to the west and up to Western Australia to the east via Pinjara craton and Albani-Fraser orogen (Harris, 1993; Katz and Premoli, 1979). Albeit substantially covered by Permo-Carboniferous Gondwana sediments, Mesozoic Deccan volcanics and Neogene Gangetic alluvium, CITZ contains several components that experienced repeated tectonothermal events owing to the formation and fragmentation of two Proterozoic supercontinents named Columbia and Rodinia (Chattopadhyay et al., 2020).

Location of Gondwana sedimentary cover and Deccan Trap divides the CITZ into north-east (NE) sector and south-west (SW) sector (Fig. 2.2). NE sector comprises of Mahakoshal Supracrustal Belt (MSB) and Makrohar Granulite Belt (MKGB) along with Son-Narmada Fault system (Son Narmada North Fault and Son Narmada South Fault). SW sector consists of Betul Supracrustal Belt (BSB) and Gavilgarh-Tan Shear Zone (GTSZ), Ramakona-Katangi Granulite Belt (RKGB), Sausar Supracrustal Belt (SSB), Balaghat-Bhandara Granulite Belt (BBGB) and Central Indian Suture (CIS) (Fig. 2.2).

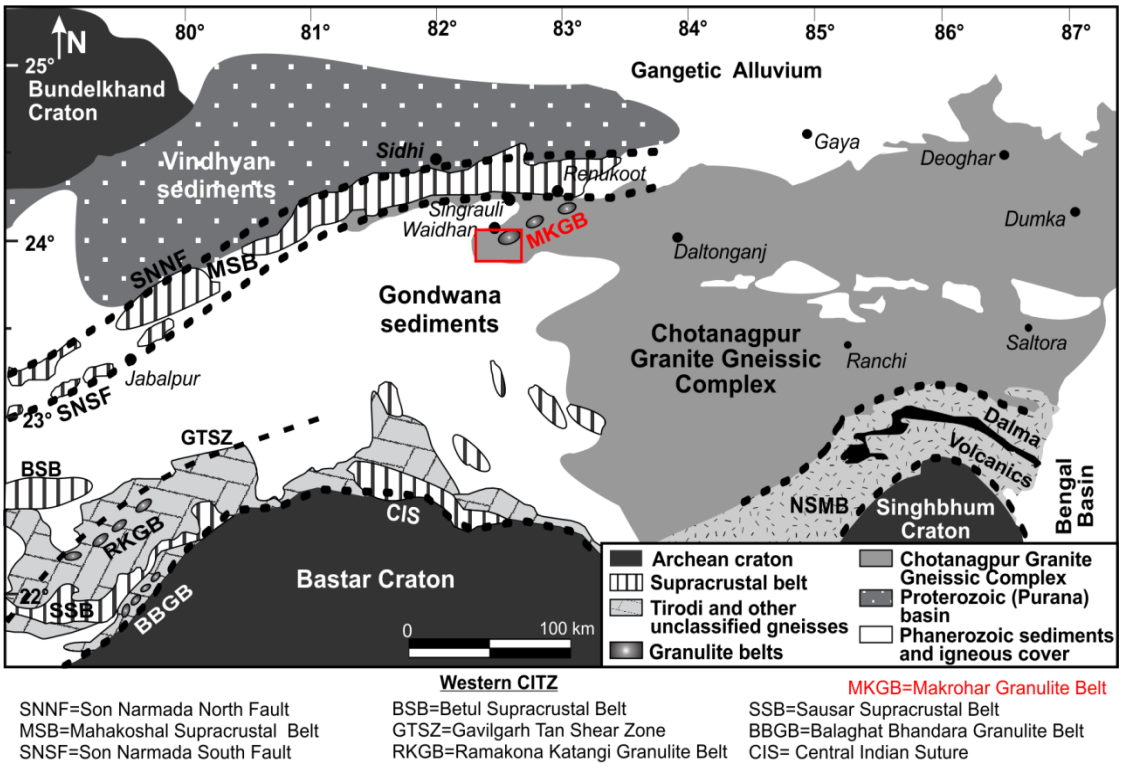

Figure 2.2. Geological map of Central India showing parts of the Bundelkhand-Bastar-Singhbhum craton and different components of the CITZ along with the Chotanagpur Granite Gneissic Complex (CGGC) as extended CITZ; compiled after (Bhowmik et al., 2012). The red rectangular area is current study area.

2.1. Geology of different sectors of CITZ

2.1.1. South-west (SW) sector

The south-western domain of the CITZ is bounded by Gondwana Supergroup in the north and Amgaon gneiss and Dongargarh/ Malanjkhand granitoids (components of Bastar craton) in the south. This sector consists of: a) elliptical rafts and lenses of two granulite belts (RKGB and BBGB), b) two metasedimentary sequences (SSB and BSB) and c) two fault/shear zones (GTSZ and CIS). Aside from BSB and GTSZ, rests of the aforementioned components are collectively termed as Sausar Mobile Belt (SMB) (Fig. 2.3) (Bhowmik, 2019). All the published geochronological data from RKGB and SSB are presented in Table-2.1a. Data reported from the BBGB are given in Table-2.1b and those from the BSB are presented in Table-2.1c.

The lithological units of the RKGB are composed of pods and lenses of mafic, pelitic granulite, garnetiferous amphibolites and porphyritic charnockite embedded

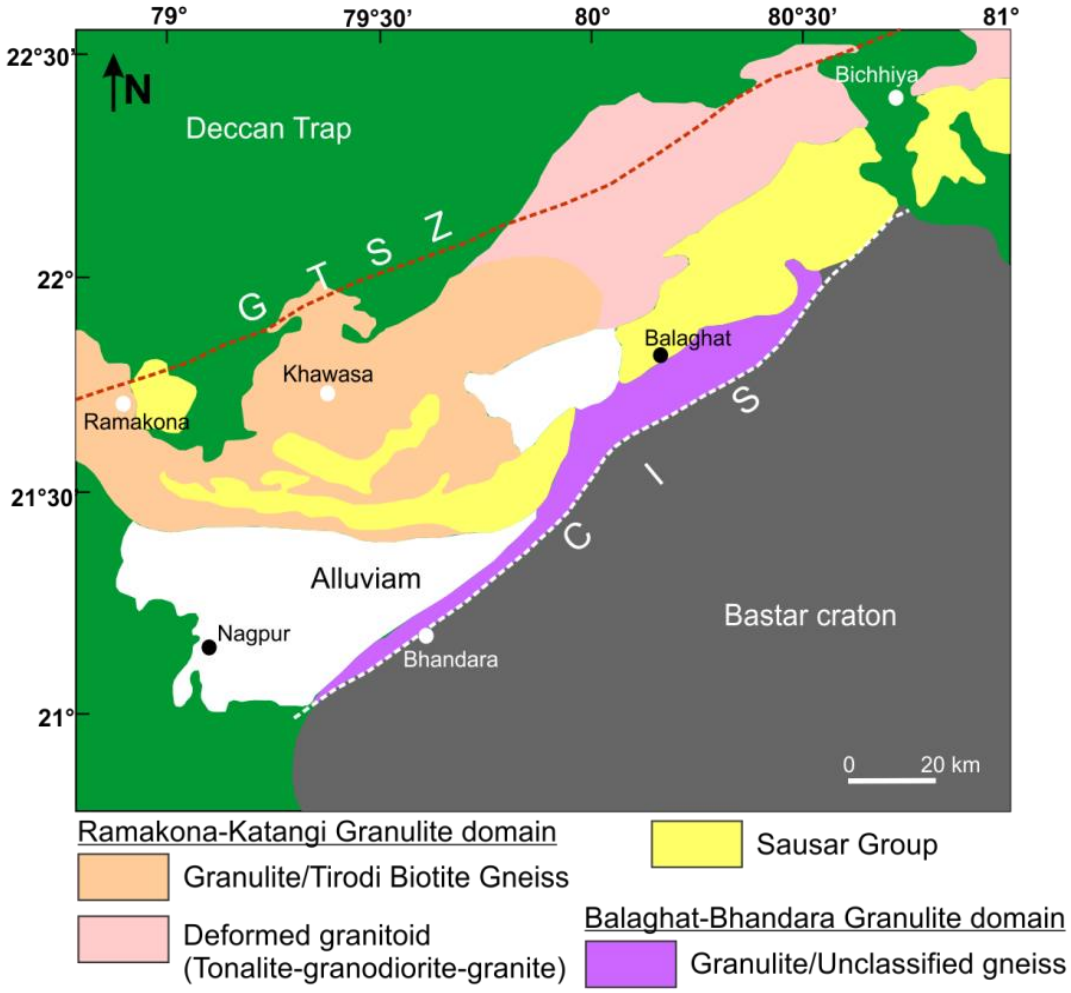

Figure 2.3. Simplified geological map of Sausar Mobile Belt (SMB), comprising of RKGB, SSB and BBGB bounded by Deccan volcanics and Amgaon gneiss and Dongargarh/Malanjkhand granitoid (components of Bastar craton) (modified after Bhowmik, 2019).GTSZ: Gavilgarh-Tan Shear Zone; CIS: Central Indian Suture (Yedekar et al. 1990)

within migmatitic felsic gneiss (Tirodi Biotite Gneiss) (Bhowmik and Roy, 2003). Gneissic mafic granulite and garnetiferous amphibolites from the central Katangi-Khawasa area record peak metamorphism at 750-800 °C and 9-10 kbar and 675 °C-8 kbar respectively (Bhowmik and Roy, 2003). An overall clockwise P-T path can be illustrated from prograde inclusion mineral assemblage, peak metamorphic condition,

subsequent decompression (750 °C-7 kbar for mafic granulite and 700 °C-6.4 kbar for garnetiferous amphibolite) and near-isobaric cooling (650 °C-6 kbar) in this domain (Bhowmik and Roy, 2003). An equivalent high grade metamorphism and P-T path is reported from the metapelitic granulite in the western Ramakona sector of this domain (Bhowmik and Spiering, 2004). Sm-Nd mineral-whole rock isochron ages from garnetiferous metadolerite dykes (1112±77 Ma) and amphibolites (847-830 Ma) were interpreted as post-decompressional metamorphic event in RKGB (Roy et al., 2006). Th-U-total Pb monazite electron probe microanalyzer dating of a metapelitic granulite and U-Pb SHRIMP zircon dating of a charnockite yield 1043±18 to 955±11

Table-2.1a. Published geochronological information from the RKGB and SSB of the Central Indian Tectonic Zone

Area	Rock type	Age (Ma)	Event	Method of Dating	Reference
Dongri Buzurg area	Tirodi Biotite Gneiss	1525±70	Main phase of regional Amphibolite facies metamorphism in SSB	Rb-Sr whole rock	Sarkar et al. (1986)
Tirodi Biotite Gneiss	Tirodi Biotite Gneiss	860	Terminal thermal overprint on SSB	K-Ar mineral isochron	Sarkar et al. (1986)
Sitapar, RKGB	Manganese deposit	950	K-introducing alteration process subsequent to amphibolite facies	40Ar/39Ar (cryptomelane)	Lippolt and Hautmann, 1995
Tirodi Biotite Gneiss	Amphibolite	847±65	-	Sm-Nd whole rock isochron	Roy et al. (2006)
Tirodi Biotite Gneiss	Amphibolite	929±85	-	Rb-Sr whole rock	Roy et al. (2006)
Western part of SSB	Garnet-staurolite-kyanite schist	1062±13	Peak metamorphism of SSB	EMP monazite	Bhowmik et al. (2012)
Eastern part of SSB, near Khara	Garnet-biotite-muscovite-quartz schist	993±19	Retrograde metamorphism of SSB	EMP monazite	Bhowmik et al. (2012)
Wesetrn part of SSB	Foliated granite	944±5	Symmetamorphic granite emplacement	EMP monazite	Chattopadhyay et al. (2015)
	Massive granite	928±4	Post-tectonic granite emplacement	EMP monazite	Chattopadhyay et al. (2015)
Tirodi Biotite Gneiss	Tirodi Biotite Gneiss	948±4	Peak amphibolite facies metamorphism in the central domain of SSB	EMP monazite	Chattopadhyay et al. (2015)

Ma and 938±3 Ma ages respectively. 1043 and 955 Ma are interpreted as the ages of the peak and retrograde metamorphism of the RKGB whereas ca. 938 Ma is the timing

Table-2.1a (continued). Published geochronological information from the RKGB and SSB of the Central Indian Tectonic Zone

Area	Rock type	Age (Ma)	Event	Method of Dating	Reference
Umri village, SSB	Calc-silicate gneiss	2450-2410	Minimum deposition age of Sausar sediements	Re-Os molybdenite	Stein et al. (2014)
Seoni Ghats section, N of Katangi (TBG)	Migmatitic gneiss	1618±8	Magmatic crystallisation of protolith	U-Pb zircon	Bhowmik et al. (2011)
Seoni Ghats section, N of Katangi (TBG)	Migmatitic gneiss	2523-2093 (mean value: 2379)	Source/Reservoir of magma	Lu-Hf zircon (model age)	Bhowmik et al. (2011)
Tirodi Biotite Gneiss	Migmatitic gneiss	1534±13	Magmatic crystallisation of protolith	U-Pb zircon	Ahmad et al. (2009)
Tirodi Biotite Gneiss	Migmatitic gneiss	1454±5	later thermal overprint	U-Pb zircon	Ahmad et al. (2009)
Mansar, Hiura, Potgowari, Ghuksi and Maudi villages	Intrusive granitoids	1322±3	Magmatic crystallisation	U-Pb zircon (core)	Bose et al. (2023)
		1000-950 Ma	Metamorphic imprint	U-Pb zircon (core)	
Bichhiya (eastern part of RKGB)	Charnockite	2064	Source/Reservoir of magma	Lu-Hf zircon (model age)	Bhowmik et al. (2012)
Nainpur-Lalbara, RKGB	Tourmaline bearing granites, intrusive within SG	1147±16	Emplacement (granite magmatism in sausar belt)	Rb-Sr whole rock	Pandey et al. (1998)
RKGB	Metadolerite	1112±77	Cooling event of (CW) metamorphism	Sm-Nd whole rock isochron	Roy et al. (2006)
Ramakona area	Pelitic migmatitic gneiss (granulite)	1043±18	Peak metamorphism	EMP Monazite (core)	Bhowmik et al. (2012)
Ramakona area	Pelitic migmatitic gneiss (granulite)	955±11	Low Pressure decompression metamorphism	EMP Monazite (rim)	Bhowmik et al. (2012)
Bichhiya (eastern part of RKGB)	Charnockite	938±3	Magmatic crystallisation	U-Pb zircon	Bhowmik et al. (2012)
RKGB	Metadolerite	834±21	Main Sausar metamorphism event	Rb-Sr whole rock	Roy et al. (2006)

of post-peak decompression and syn-metamorphic felsic (charnockitic) magma emplacement in this domain (Bhowmik et al., 2012). Tirodi Biotite Gneiss (TBG) is a composite of tonalite-granodiorite-granite gneiss, intrusive granitoids and migmatites which is regarded as basement of Sausar sediments. This is evident from a conglomerate unit containing pebbles of gneissic rocks, quartz between SSB and granulite, gneisses in Balaghat area Bhowmik et al. (2011) and Ahmad et al. (2009) constrained the emplacement or magmatic crystallization age of TBG using U-Pb zircon dating at 1618±8 Ma and 1534±13Ma (with a late thermal imprint at 1454±5Ma) respectively. Lu-Hf isotope analyses of these zircon grains stipulate a model age of 2523-2093 (average 2379 Ma) of its protolith which is dominantly juvenile material with minor crustal component (Bhowmik et al., 2011). The lithounits of RKGB record four phases of secondary structures or deformational events producing folds with variable geometry and often TBG is co-folded with SSB units at many places (Chattopadhyay et al., 2020).

The southernmost metasedimentary unit (SSB), 300 km in length and 70 km in width represents platformal association of quartzite-pelite-carbonate which hosts stratabound manganese ore deposits (Bhowmik, 2019 and references therein). Barring a contact between deformed and metamorphosed basal conglomerate-sandstone unit of the SSB and Malanjkhand granitoid (part of Bastar craton) at the eastern side of this belt, the basement-cover relationships are highly tectonised (Pal and Bhowmik, 1998). This litho-succesion experienced four phases of deformation and regional Barrovian-type metamorphism at low greenschist (towards the southern boundary with the BBGB) to middle-upper amphibolite facies (at the contact with the RKGB in the north) conditions (Pal and Bhowmik, 1998). The peak metamorphism is constrained at 675 °C-7 kbar from the northern domain of SSB and medium P/T conditions (garnet+ kyanite zone) from Khara, eastern part of SSB (Bhowmik et al., 2012, 1999). An overall clockwise P-T trajectory is established from this metasedimentary lithounits which implies a continent-continent collisional set up during sausar orogeny (Bhowmik et al., 2012, 2011). Rb-Sr whole rock isochron age (1525±70 Ma) and mineral-whole rock isochron age (ca. 860 Ma) by Sarkar et al. (1986) from TBG were interpreted as timing of the amphibolite-facies metamorphism in SSB and

Table-2.1b. Published geochronological information from the BBGB of the Central Indian Tectonic Zone

Area	Rock type	Age (Ma)	Event	Method of Dating	Reference
Dongargaon, Waiganga river bed near Pipariya (BBG)	Granite gneiss	3630-3051	Source/Reservoir of magma	Lu-Hf zircon (model age)	Bhowmik et al. (2011)
Dongariya, BBGB	Charnockite	2672±54	Peak high Temperature (Anticlockwise) metamorphism	Sm-Nd whole rock isochron age	Roy et al. (2006)
Dongargaon,BBGB	Garnet cordierite granulite	1600	UHT metamorphism	EMP monazite chemical age	Bhandari et al. (2011)
Dongargaon, Waiganga river bed near Pipariya (BBG)	Granite gneiss	1600	Magmatic crystallisation of protolith	U-Pb zircon + Monazite chemical age	Bhowmik et al. (2011)
Dongargaon, Waiganga river bed near Pipariya (BBG)	Polyphase metamorphosed psammopelitic granulite, undeformed garnetiferous granite, deformed granite gneiss	3584±3 to 2530±3	Detrital or inherited zircon cores	U-Pb zircon + Monazite chemical age	Bhowmik et al. (2011, 2014)
		1572±7	Metamorphic recrystallisation		
		1658 ± 12	High grade UHT metamorphic event		
		1595 ± 5 to 1590 ± 6	High-T anatectic event corresponding to the peak UHT metamorphism and synchronous granite magmatism		
		1574 ± 9	Crystallization of anatectic melt		
		1539 ± 24	Terminal hydration event		
BBGB	-	1415±23	Terminal metamorphic event	Monazite chemical age	Bhowmik et al. (2011)
BBGB	Mafic Granulite	1403±99	Cooling event (retrograde metamorphism in sialic component/ mafic body empacement?)	Sm-Nd whole rock isochron age	Roy et al. (2006)
BBGB	Mafic granulite	967±72	Main Sausar metamorphism event	Rb-Sr whole rock	Roy et al. (2006)
Northern sheared parts of BBGB	Charnockite and mafic granulite	970-800	Final overprint of Sausar orogeny	Rb-Sr whole rock	Roy et al. (2006)
Dongariya, BBGB	Charnockite	800±171	Main Sausar metamorphism event	Rb-Sr whole rock	Roy et al. (2006)
Larsara area, BBGB	Psammopelitic granulite	2089 ± 14 to 2040 ± 17	Peak UHT metamorphism	Monazite chemical age	Bhowmik et al. (2005)
		1525 ± 13 to 1450 ± 9	Reworking of UHT granulites (subsequent cycles of metamorphism		

migmatisation of the metasediments to produce TBG. Peak and retrograde

metamorphic events of the SSB are constrained at 1062±13 and 993±19 Ma from pelitic schists (Th-U-total Pb monazite dating) (Bhowmik et al., 2012). ~945 Ma age of granite magmatism, syntectonic to second phase of deformation in SSB and ~928 Ma age of the post-tectonic granite magmatism (Electron microprobe monazite dating by Chattopadhyay et al., 2015) advocate for a younger and short-lived sausar orogeny.

500-1000 meter long and 50-200 meter wide granulite rock association between SSB and CIS exposes lenses or slivers of two pyroxene (gabbro-norite suite) granulite-charnockite-metapelite-metamorphosed BIF within country rock of felsic gneisses (Bhowmik, 2019; Chattopadhyay et al., 2020). Pioneer workers described BBGB as exhumed oceanic crust i.e. leading front of the Bundelkhand craton from its rock association (Jain et al., 1991). Detailed mineral assemblage of all the granulite facies rocks is given in Bhowmik (2019). Conventional thermobarometry and pseudosection approach constrain UHT granulite facies polyphase metamorphism from the central segments and non-UHT medium pressure-temperature granulite metamorphism from east and northeast parts of the BBGB (Bhowmik, 2019; Bhowmik et al., 2014; Bhowmik and Chakraborty, 2017). Among three distinct cycles of UHT metamorphism the peak condition of the earliest one (M_1) is constrained at 900-1000 °C and 8-9.5 kbar and retrograde condition is fixed at 670 °C-9 kbar which give an overall counterclockwise (CCW) P-T path (Bhowmik, 2006; Bhowmik et al., 2005). These granulites were subsequently metamorphosed along a clockwise P-T trajectory (peak: 725 °C-6 kbar, retrograde: 600-680 °C-3-4 kbar) and then a counterclockwise path (peak: 735-760 °C-7.3-9.4 kbar and final cooling either via an isobaric path or accompanied by decompression) (Bhowmik and Chakraborty, 2017; Sarbadhikari and Bhowmik, 2008). Previously, electron microprobe monazite dating measured two age populations from the UHT metamorphosed psammopelitic granulites: 2089 ± 14 Ma to 2040 ± 17 Ma and 1525 ± 13 Ma to 1450 ± 9 Ma (Bhowmik et al., 2005) whereas Bhandari et al., (2011) reported ca. 1600 Ma for the same event. To resolve this controversy, combined U-Pb SHRIMP zircon dating and Th-U-total Pb monazite chemical dating using several samples from the BBGB terrain constrained a ~50 million years long (1600-1540 Ma) metamorphic cycle in

this domain and a mature crustal protolith of Paleoarchean (3630-3051 Ma) ancestry from the anatectic granites (Bhowmik et al., 2014, 2011).

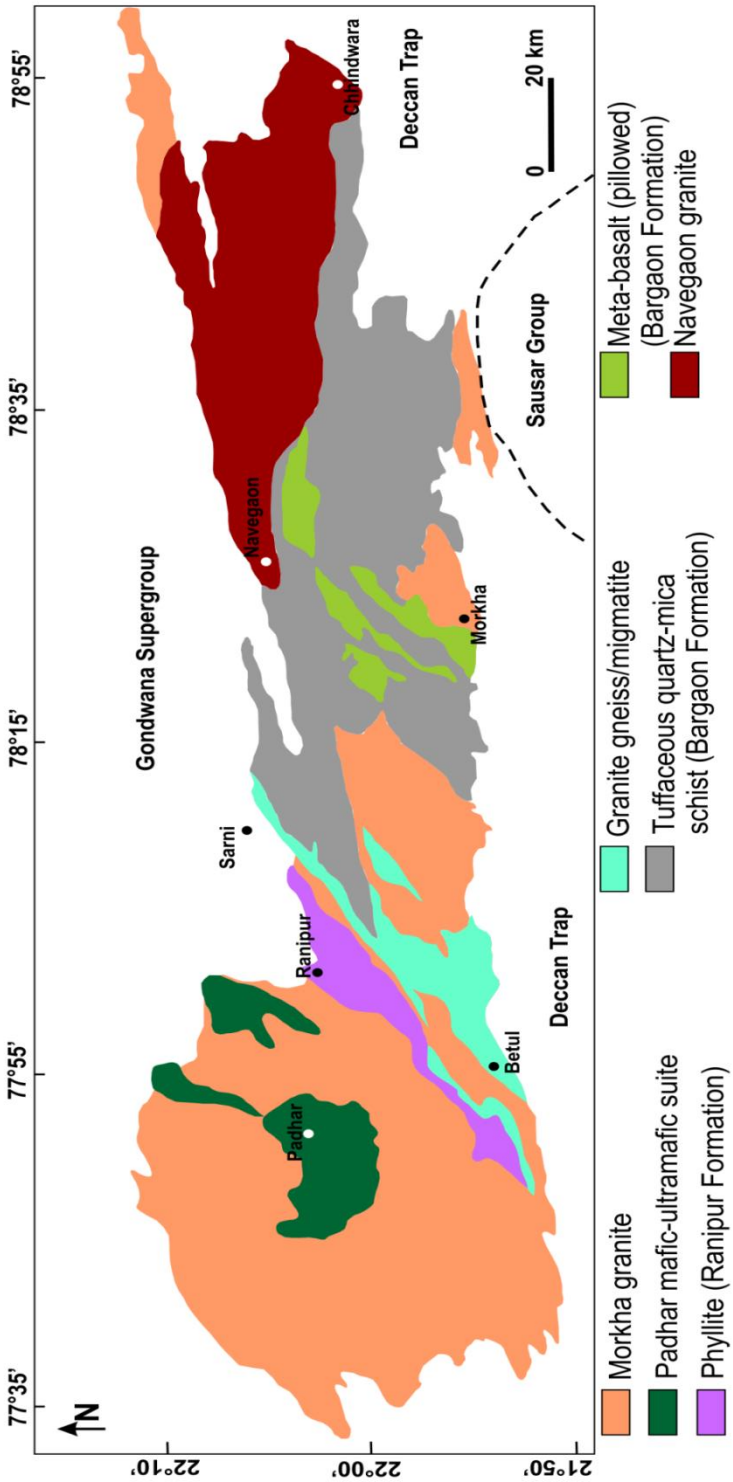

Figure 2.4. Simplified geological map of Betul Supracrustal Belt (BSB) comprising of different lithounits (modified after Dora et al., 2023).

Betul Supracrustal Belt (BSB), a volcano-sedimentary unit consists of basement granite gneisses, low to medium grade metamorphosed supracrustal sediments and bimodal intrusive volcanic rocks. 135 km long, 20-30km wide this supracrustal association, bound by Phanerozoic Gondwana Supergroup and Deccan Trap in the north and Gavilgarh-Tan Shear Zone (GTSZ) in the south (Dora et al., 2023). Major lithounits of this volcanosedimentary sequence comprises of biotite gneisses, metapelites, quartzites, rhyolites, pillow basalts, calc-silicates which are intruded by granites, syenites and mafic-ultramafic rocks (Dora et al., 2023; Raut and Mahakud, 2004). Petrochemical study from the Padhar Mafic-Ultramafic complex, in the western part of BSB indicates the presence of a continental arc near the boundary of the Bundelkhand craton during an inferred Mesoproterozoic time period

Table-2.1c. Published geochronological information from the BSB of the Central Indian Tectonic Zone

Area	Rock type	Age (Ma)	Event	Method of Dating	Reference
Betul Supracrustal Belt	Granite gneiss (Betul Gneiss)	2167±11	Magmatic (I-S type granite) crystallization	TIMS U-Pb zircon	Dora et al. (2023)
	Rhyolite	1715±10	Magmatic (A-type granite) crystallization	TIMS U-Pb zircon	Dora et al. (2023)
	Morkha Granite	1671±29	Magmatic (A-type granite) crystallization	TIMS U-Pb zircon	Dora et al. (2023)
		1040±55	Metamorphism	TIMS U-Pb zircon	Dora et al. (2023)
	Navegaon Granite	1079	Emplacement?	TIMS U-Pb zircon	Dora et al. (2023)
		954	Metamorphic overprint?	TIMS U-Pb zircon	Dora et al. (2023)
	Alkali gabbro	1326±75	Metamorphism	Th-U-total Pb monazite	Dora et al. (2023)
	Hornblende gabbro	1026	Metamorphism	Th-U-total Pb monazite	Dora et al. (2023)
	Deformed intrusive granite	1550±15	Syn-orogenic magmatism	Rb-Sr whole rock	Raut and Mahakud (2002)
	Intrusive granite	850±50	Magmatism	Rb-Sr whole rock	Roy and Prasad (2003)
Gavilgarh-Tan Shear Zone	Sheared granites and gneisses	1050-950	Transpression and granite magmatism	U-Pb zircon, Th-U-total Pb monazite	Chattopadhyay et al. (2017)

(Roy et al., 2004; Yousuf et al., 2019). Rocks of the BSB experienced three phases of deformation and upper amphibolite facies peak metamorphism and late greenschist metamorphic event (Mahakud et al., 2001). Peak metamorphism is constrained at 580-650 °C-5.8-7 kbar by Praveen et al. (2021) and Baswani et al. (2022) reported a retrograde metamorphism at 450-550 °C from Ti-in biotite geothermometer. Geochemistry of the Betul gneiss suggest significant continental crustal contribution in their protolith that emplaced in an arc setting at ca. 2167±11 Ma. Detrital zircon ages (Meso-archean) from the Betul gneiss corroborate well with the Bundelkhand granitoids (Dora et al., 2023). Sr and Nd isotope composition of pillowed basalt, hornblende gabbro and alkali gabbro yields an isochron with 2051±80 Ma age which imply that a subduction-accretion tectonic setup was developed during 2050-1800 Ma in this domain of the CITZ (Dora et al., 2023; Khanna et al., 2020). Extensional granite emplacement in the BSB between 1800-1715 Ma and ca. 1671 Ma signifies a back arc/ rift system during the end of late Paleoproterozoic (Dora et al., 2023). Post-collisional mafic-ultramafic magmatism, synchronous with the reported Th-U-total Pb monazite dates from metapelite indicates Mesoproterozoic closure and metamorphism of the Betul basin (Dora et al., 2023). Final accretion event (1079-954 Ma), evident from U-Pb zircon date of younger intrusive granite and Th-U-total Pb monazite date of a hornblende gabbro from the BSB corroborates well with the Neoproterozoic Sausar orogeny and granite magmatism and transpression in the GTSZ (Bhowmik, 2019; Chattopadhyay et al., 2020; Dora et al., 2023).

GTSZ, the 300 km long and 2-3 km wide crustal-scale shear zone between the BSB and SSB presents a long history of tectonic activation from Neoproterozoic to Quaternary (Chattopadhyay et al., 2020). It exposes sheared granites and gneisses in the eastern part and faults affecting the Phanerozoic sedimentary rocks and Deccan basalt in the western part (Chattopadhyay et al., 2020). Geochemical characterization of the sheared granite gneisses reveal that these peraluminous, calc-alkaline granite - granodiorite and quartz monzonites got emplaced in a continental collisional setting (Chattopadhyay et al., 2020). U-Pb zircon and Th-U-total Pb monazite dates provide the timing of transpression and extensive syn-tectonic granite magmatism at 1050-950 Ma in the GTSZ (Chattopadhyay et al., 2017).

2.1.2. North-east (NE) sector

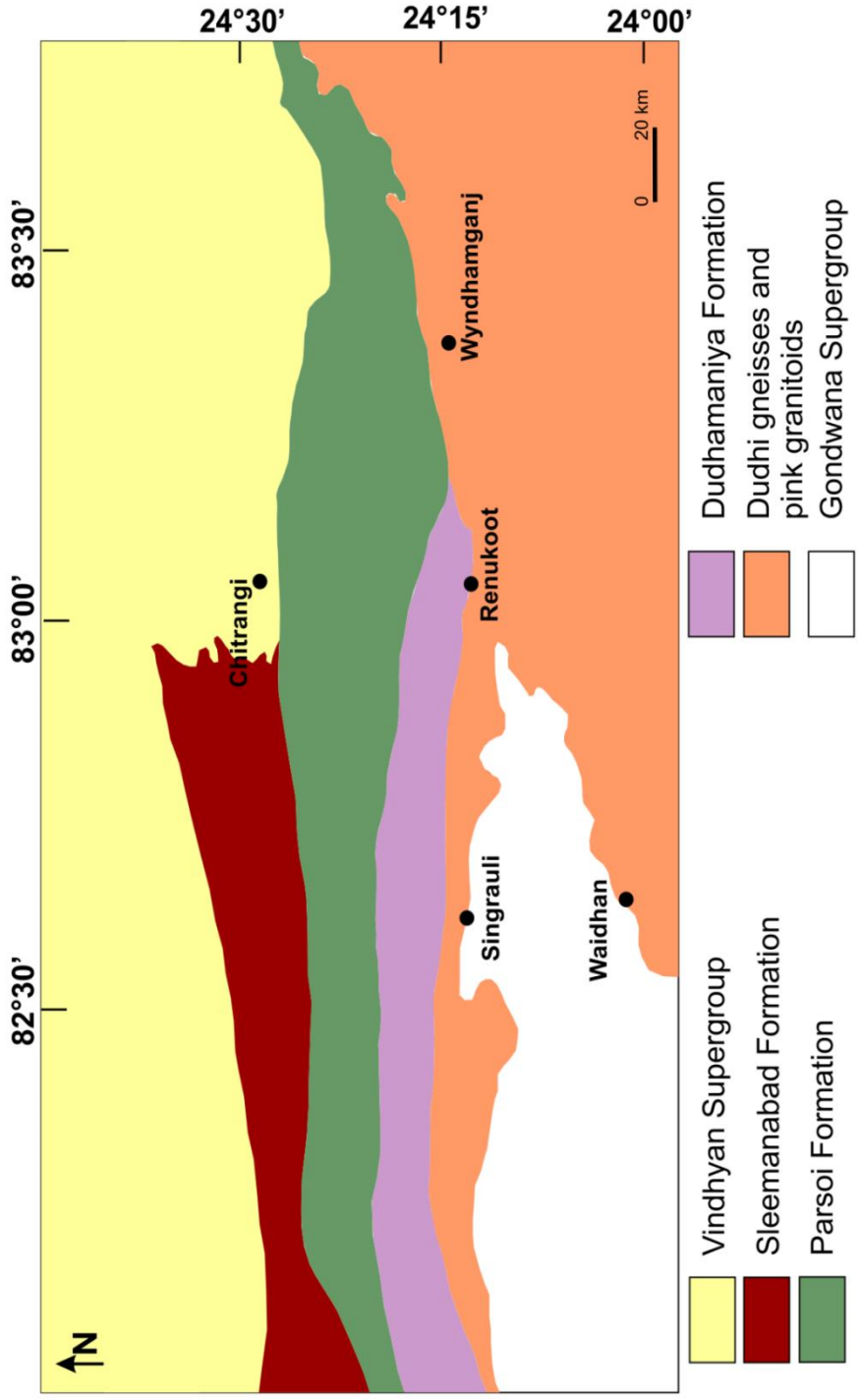

Figure 2.5. Simplified geological map of Mahakoshal Supracrustal Belt (MSB) and parts of Makrohar Granulite Belt (MKGB) (modified after Deshmukh et al., 2017)

Published geochronological information and corresponding references from the north-eastern sector the CITZ are presented in Table-2.1d.

Around 500 km long and 20 km wide, ENE-WSW to E-W trending MSB is separated from the Meso-Neoproterozoic Vindhyan Supergroup by Son-Narmada North Fault (SNNF) in the north and from the Proterozoic granitic intrusives or Gondwana Supergroup by Son-Narmada South Fault (SNSF) (Chattopadhyay et al., 2020; Sharma et al., 2022). The litho-succesion of Mahakoshal is dominated by metasedimentary rocks (quartzite, phyllites, pelitic schists, carbonate, greywacke and BIF) with minor amount of metabasalt, ultramafics and intrusive syn-tectonic granitoids (Chattopadhyay et al., 2020; Sharma et al., 2022). Argillaceous-calcareous Sleemanabad Formation, conglomerate, metasediments and volcanics bearing Lower Parsoi and meta-argillite and thin siltstone bearing Upper Parsoi Formation and BIF-argillite sequence of Dudhmania Formation are major components of Mahakoshal Group of rocks (Roy and Devarajan, 2000). Several workers have proposed shallow marine intertidal to marine shelf-slope depositional setting for the succession of Mahakoshal sedimentary rocks (Ramachandra et al., 2020; Roy and Devarajan, 2000). The MSB experienced polyphase (M_1, M_2, M_3) metamorphic and deformational (D_1, D_2, D_3) event which resulted in the greenschist-amphibolite facies (clockwise P-T trajectory) rocks and E-W trend of this supracrustal belt in the CITZ (Chattopadhyay et al., 2020; Deshmukh et al., 2017). D_1 folds are upright to gently inclined with prominently developed axial planar schistosity whereas D_2 folds are superposed and reclined folds coeval with granite emplacement (Deshmukh et al., 2017). Deshmukh et al. (2017) has reported that andalusite schist and garnet-staurolite schists of the southern margin of the MSB has recorded prograde (M_1), peak (M_2) (~520 °C-8 kbar) and retrograde metamorphism (~2-3 kbar) from 1900-1500 Ma (late Paleoproterozoic to early Mesoproterozoic). Rb-Sr dates from the intrusive granitoids in the south-eastern parts of the MSB yield 1576±76 Ma, 1708±36 Ma, 1731±36 Ma, 1813±65 Ma, 1850±40 Ma, 1856±68 Ma (Sarkar et al., 1998). U-Pb SHRIMP zircon dates from the syn-tectonic Jhirgadandi granitoids and mafic microgranular enclaves in that study area yield similar age (1753±9 Ma) (Bora et al., 2013). Petrology and geochemical studies show that protoliths of granitoid plutons within the MSB are I-S type in nature and emplaced in a continental arc setting and got reworked more or less contemporaneously during the late Paleoproterozoic period

Table-2.1d. Published geochronological information from the MSB and MKGB of the Central Indian Tectonic Zone

Area	Rock type	Age (Ma)	Event	Method of Dating	Reference
Mahakoshal Supracrustal Belt	Andalusite schists/phyllites	1850, 1720, 1600	Prograde metamorphism:1900-1800 Ma; Peak metamorphism:1750-1650 Ma; Retrograde metamorphism:1600-1500 Ma	Th-U-total Pb monazite	Deshmukh et al. (2017)
	Grey intrusive granite	1850, 1720	Emplacement	Th-U-total Pb monazite	Deshmukh et al. (2017)
	Intrusive granitoids	1576±76, 1708±36, 1731±36, 1813±65, 1850±40, 1856±68	-	Rb-Sr whole rock	Sarkar et al., (1998)
	Madanmahal Granite	1695±9	Emplacement (A-type granite)	ID-TIMS U-Pb zircon	Yadav et al. (2020)
	Sidhi porphyritic grey Granite	1796±17	Emplacement (A-type granite)	ID-TIMS U-Pb zircon	Yadav et al. (2020)
	Sidhi pink Granite	1645±25	Emplacement (A-type granite)	ID-TIMS U-Pb zircon	Yadav et al. (2020)
	Jhirgadandi granitoid	1753±9	Emplacement (I-S type granite)	SHRIMP U-Pb zircon	Bora et al. (2013)
	Mafic microgranular enclave	1758±19	Magmatic crystallization	SHRIMP U-Pb zircon	Bora et al. (2013)
Makrohar Granulite Belt	Parsoi Formation-pyroclastic unit	1894±9	Magmatic crystallization	LA-ICPMS U-Pb zircon	Sharma et al. (2022)
	Dudhi gneiss and associated hornblende granites	1720, 1600, 1250, 850	-	Th-U-total Pb monazite	Deshmukh et al. (2017)
	Intrusive granite gneiss	1498±38	Emplacement (A-type granite)	U-Pb zircon	Yadav et al. (2022)
	Porphyritic granitoid	1750	Emplacement (I-S type granite)	LA-ICPMS U-Pb zircon	Chakrabarty et al. (2023)
	Felsic orthogneiss	1377-1352	Emplacement (I-S type granite)	LA-ICPMS U-Pb zircon	Chakrabarty et al. (2022)
	Deformed granite	1731±36, 1709±102	-	Rb-Sr whole rock	Sarkar et al., (1998)

(Bora et al., 2013). Throughout the Paleoproterozoic (ca. 1880-1640 Ma; Bora et al., 2013; Yadav et al., 2020), intrusive granitic magmatism is ubiquitous and occurs in several phases as stocks and concordant sheet-like plutons. These granitoids are

spanning a range of tectonic environments, from continental-arc to collisional to post-collisional, and from I-type to A-type (Yadav et al., 2020, 2015). A recent geochemical study and U-Pb zircon dating from a pyroclastic deposit of the MSB reveal the earliest acidic magmatism (within a proposed volcanic arc to syn-collisional tectonic setting) in the MSB and the entire CITZ occurred in 1894±9 Ma (Sharma et al., 2022). Dudhi anatectic gneiss, adjacent to the Son-Narmada South Fault (located immediately north-east of the study area) records four monazite populations among which the 1720 and 1600 Ma dates overlap with the tectonothermal events of the MSB, but the Meso- to Neoproterozoic (1250 and 850 Ma) thermal imprints remain unclassified (Deshmukh et al., 2017).

Makrohar Granulite Belt (MKGB) is ENE-WSW trending narrow isolated sliver of granulite facies rocks within the vast country rock comprising of porphyritic granitoid of the Chotanagpur Granite Gneissic Complex (CGGC). This scarcely studied zone, located at the south of the Son Narmada South Fault exposes the following major rock groups which are: felsic granulite and their retrograded counterparts, vast country rock of porphyritic metagranites and gneisses, supracrustal rocks involving calc-silicates and metapelites, a suite of metamorphosed olivine norite and younger intrusives (pegmatite and dolerite dykes). Petrography and thermobarometric study from a suite of garnet-cordierite bearing granulites in the MKGB constrain peak metamorphic condition at 800 °C-9 kbar followed by post-peak near-isothermal decompression to 740 °C-6.5 kbar and final isobaric cooling to 685C/6–6.5 kbar (Solanki et al., 2003). The authors have inferred a clockwise P-T path indicating a continental collisional set-up though the timing of this orogenic cycle was not clear (Solanki et al., 2003). The calc-silicates and mafic intrusives experienced a late-stage hydration event (5-6 kbar, 650-700 °C) (Karmakar, 2021). A suite of deformed intrusive granitoids with enclaves of metapelites yielded Rb-Sr date of 1731±36 and 1709±102 Ma (Sarkar et al., 1998), which is broadly coeval with the metamorphism and syn-tectonic granite emplacement within the MSB. Detailed petrology, geochemistry and geochronological study from the augen gneisses (described as intrusive porphyritic granite gneiss) in and around Sidhi Khurd and Makrohar villages, reveal that these are metaluminous to peralkaline ferroan granitoids

derived from a mixed mantle and crustal source likely Bundelkhand craton (Model age from Sm-Nd isotopic data: 3677-2338 Ma) and emplaced at 1498±38 Ma (U-Pb zircon dating) (Yadav et al., 2023).

2.2. Chotanagpur Granite Gneissic Complex (CGGC): Eastern extension of the CITZ

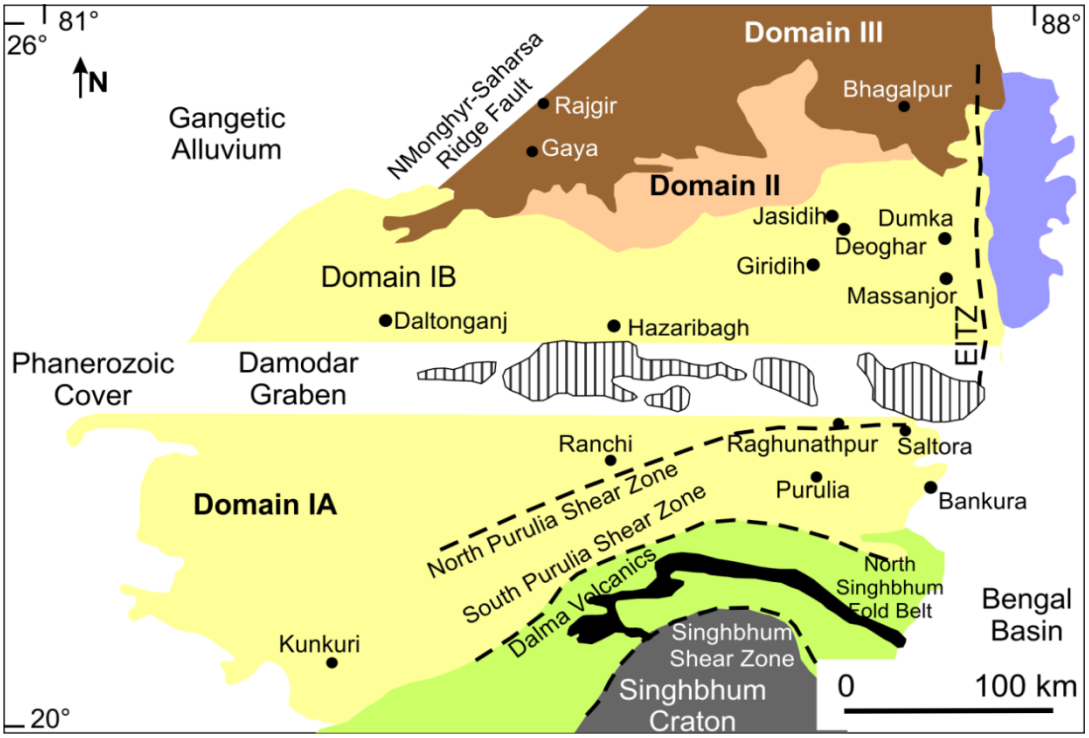

Figure 2.6. General geological map of the Chotanagpur Granite Gneissic Complex (CGGC) showing all the domains (modified after Mukherjee et al., 2019). EITZ: Eastern Indian Tectonic Zone.

Chotanagpur Granite Gneissic Complex (CGGC) is located towards the eastern parts of the CITZ and very close to the studied MKGB (Fig. 2.2). Similarity of the tectonothermal events and lack of any distinct boundary between the CITZ and CGGC lend the notion that CGGC represent the eastern extension of the CITZ. CGGC is bounded by South Purulia Shear Zone in the south, Monghyr- Saharsa Ridge Fault in the north and Rajmahal trap and Phanerozoic sediments in the east. CGGC is divided into three domains (from north to south, Domain-III, II and I; Mukherjee et al., 2019b)

where the Great Boundary Fault and Gondwana sediments bisect the Domain-I in two halves further (Domain IA and IB) (Fig. 2.6).

Domain I is the largest domain in the CGGC and is dominated by migmatitic felsic orthogneiss with enclaves of metasedimentary and meta-mafic rocks and younger intrusives such as mafic dyes, syenites and pegmatites. For Domain IA deformed migmatitic felsic orthogneiss is the country rock which contains lenses of mafic granulite and calc silicate gneisses, intruded by Bengal anorthosite (Chatterjee and Ghose, 2011; Maji et al., 2008). In the area around Bero, Saltora, three phases of deformation accompanied by four metamorphic events varying from granulite to amphibolite grade are recorded by the lithounits of this domain and the last and most pervasive metamorphic event is marked during early Neoproterozoic time (Maji et al., 2008). In the Raghunathpur, Adra area, three phases of deformational events are accompanied by two distinct metamorphic imprints around ca. 990-940 Ma with the peak condition culminated at 800-870 °C at 11 kbar pressure (Karmakar et al., 2011) or at lower pressure (6.5-7.5 kbar; Goswami and Bhattacharyya, 2010).

For Domain IB, in the area around Massanjor and Dumka, three phases of deformational events are retrieved from the lithological association of the host migmatitic felsic gneisses with Khondalite. Mg-Al granulite, calc silicate and mafic granulite enclaves (Sanyal and Sengupta, 2012). In the area between Dumka and Deoghar, metapelite enclaves record medium pressure ultrahigh temperature metamorphism followed by second phase of metamorphism with peak condition at 770±50°C and 9±1kbar which affected the host felsic orthogneisses along with the enclaves (Dey et al., 2019). Overall the earliest foliation S_1 is developed within the pelitic enclaves, S_2 grows within the host felsic orthogneisses and finally S_2 and dykes get folded and N-S closing S_3 develops. From the geochronological studies in different areas of Domain I it is perceived that the sedimentation occurred at ca. 1750-1650 Ma on an older (>1750 Ma) basement (Chatterjee et al., 2010; Dey et al., 2019; Mukherjee et al., 2019a) and earliest metamorphism (UHT) and deformational event affected the metasedimentary units at ca. 1650 Ma which is contemporaneous with a felsic magmatism. The ca. 1750 Ma arc magmatism (Mukherjee et al., 2019a) is followed by a prolonged phase of extension marked by anorthosite magmatism (ca. 1550±12 Ma;

Chatterjee et al., 2008), intrusion of a syenite body (ca. 1457±63 Ma; Ray Barman and Bishui, 1994) and ferroan A-type granite emplacement (ca. 1450 Ma; Mukherjee et al., 2018, 2017) which is the protolith of the host migmatitic felsic gneisses in the eastern part of Domain I. Next phase of pervasive metamorphic event with coeval felsic magmatism is recorded at ca. 1025-921 Ma, retrieved by U-Pb zircon and Th-U-total Pb monazite dating by several authors (Chatterjee et al., 2010, 2008; Karmakar et al., 2011; Rekha et al., 2011). An even younger phase (ca. 900-750 Ma) of metamorphism and deformation was accompanied by felsic magmatism (Chatterjee et al., 2010).

Domain II, mainly comprising of Bihar Mica Belt, consists of muscovite-biotite schist with micaceous quartzites, conglomerates, calc-silicate rocks and hornblende schists. Metapelites show the earliest foliation S_1 which is folded and E-W trending S_2 develops which is showing a weak folding at some places (Mahadevan, 2002). No robust geochronological studies are published from this domain. Domain III comprises of migmatitic felsic gneisses, intruded by dolerite dykes and younger supracrustals and three phases of deformational and thermal imprints are recorded by these lithoassociation. Chatterjee and Ghose (2011) reported U-Pb monazite, xenotime and uraninite ages of 1697±17 Ma of magmatic and ca. 1583±50, 929 and 768±11 Ma of metamorphic and thermal imprints and Wanjari et al. (2012) published ca. 1044±35 Ma magmatic event from this domain.

CHAPTER 3

LITHOLOGY AND STRUCTURES OF THE STUDY AREA

The study area belongs to the north-eastern sector of the CITZ, the Makrohar Granulite Belt, between Waidhan in the north (24.06° N, 82.62° E) and Makrohar (23.90° N, 82.63° E) in the south, Singrauli district, Madhya Pradesh (Fig. 2.2).

3.1 Lithological distribution of the study area

The area is dominated by different types of metagranitoids (dominantly porphyritic ones) within which a suite of felsic granulites, metasedimentary rocks and meta-mafic bodies are intruded as younger lithounits (Fig. 3.1). In the following section the lithology and structures of the study area are described in four major groups of rocks: **A.** Porphyritic metagranitoids occurring as the country rock with minor pink and grey metagranites; **B.** Felsic granulite [Charnockitic (Orthopyroxene-bearing felsic granulite) and non-charnockitic (Orthopyroxene-absent felsic granulite)]; **C.** Metasedimentary rocks (marble-calc silicate interlayered unit, banded psammopelite, garnet-cordierite-biotite bearing rock) and **D.** Pegmatites (deformed and undeformed ones) and meta-mafic rocks (garnetiferous fine-grained variety and non-garnetiferous coarse grained ones).

Among these major lithounits, felsic granulites and banded psammopelites contain distinct gneissic banding with alternating leucosome- melanosome inferred to be the evidence of partial melting during granulite grade metamorphism

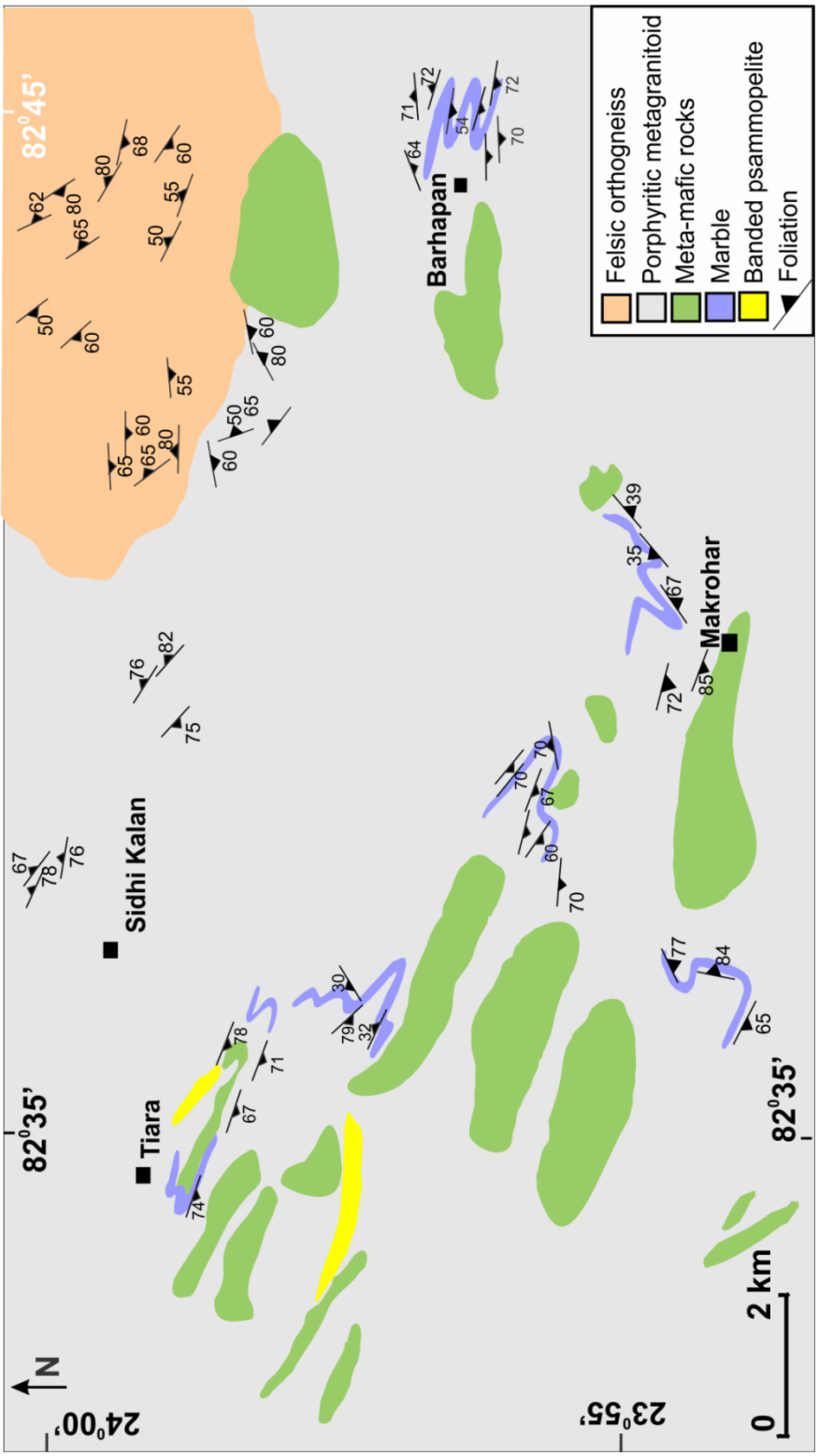

Figure 3.1. Lithological distribution and structures of the study area (part of the Makrohar Granulite Belt)

experienced by these rocks. Due to the presence of distinctive gneissic banding and inferred magmatic origin of their protolith, felsic granulites are, hereafter, named and discussed as ***'felsic orthogneisses'***. The orthopyroxene-bearing felsic granulites are termed as ***'charnockitic orthogneiss (COG)'*** and the non-charnockitic orthogneisses which contain garnet porphyroblasts but do not preserve orthopyroxene are named as ***'garnet orthogneiss (GOG)'*** (Chakrabarty et al., 2022). The mineral abbreviations used in the following sections are taken from Whitney and Evans (2010).

3.1.1. Basement metagranitoids

A suite of metagranitoids comprising of dominant porphyritic metagranitoids, minor pink and grey metagranites constitutes the country rock of the study area (Fig. 3.1). Among these the dominant porphyritic metagranitoids occur as isolated small hillocks and flat ground-level outcrops. The disposition of the lithounits portrayed in the lithological map indicates that the protolith of the felsic orthogneisses intruded the porphyritic metagranitoids. This interpretation is also consistent with the fact that the porphyritic metagranitoids, having magmatic protolith, never occurs as vein/patch within the felsic orthogneisses. The magmatic protoliths of the porphyritic metagranitoid do not intrude the metasupracrustal rocks anywhere in the study area. The field features are consistent with the view that the sedimentary protolith of the metasupracrustal rocks (stable shelf association of limestone-shale-sandstone) were deposited on the porphyritic metagranitoid basement.

Tabular idiomorphic phenocrysts are haphazardly oriented in a fine biotite ± amphibole rich matrix which does not develop any fabric (Fig. 3.1.1a). At places where the porphyritic metagranitoids are deformed, stretched K-feldspar porphyroclasts (augen) and thin layers of biotite ± amphibole define the foliation (Fig. 3.1.1b). In the outcrop, large (5-8 cm) K-feldspar and plagioclase (1-2 cm) grains are present as phenocrysts that are set in a distinctly fine-grained (<1 mm) matrix, made up of biotite + quartz + K-feldspar + plagioclase ± garnet ± amphibole (Fig. 3.1.1a, b). The porphyritic metagranitoids show considerable variation in terms of mineralogy, phenocryst-matrix ratio and shape of the phenocryst and presence of deformational features. Variation in K-feldspar and plagioclase ratio is also noted among the phenocrysts. Commonly the phenocrysts show euhedral to subhedral outline and are

randomly oriented in the matrix minerals (Fig. 3.1.1a). The phenocryst-matrix ratio varies from 1:2 to 4:1 in different outcrops. K-feldspar is the dominant phenocryst in the rock with low phenocryst matrix ratio.

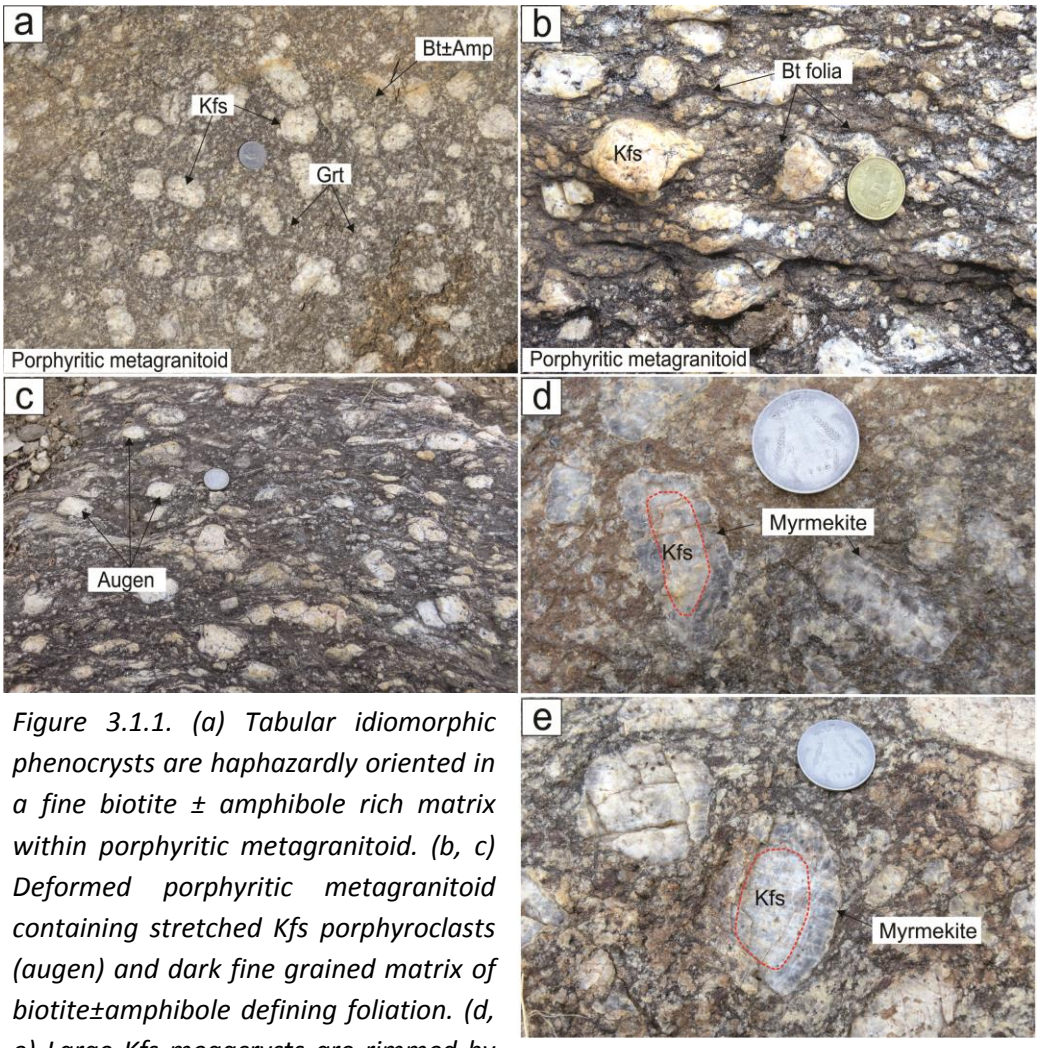

Figure 3.1.1. (a) Tabular idiomorphic phenocrysts are haphazardly oriented in a fine biotite ± amphibole rich matrix within porphyritic metagranitoid. (b, c) Deformed porphyritic metagranitoid containing stretched Kfs porphyroclasts (augen) and dark fine grained matrix of biotite±amphibole defining foliation. (d, e) Large Kfs megacrysts are rimmed by dark translucent coronae identified as myrmekite under microscope.

In the relatively deformed part, feldspar porphyroclasts show elliptical to sub-elliptical shape (feldspar augen) that are swerved by thin and laterally continuous to discontinuous folia of biotite (Fig. 3.1.1b, c). The feldspar augen do not show any deflection of the tapered end (i.e. form σ- or δ- objects) neither defines any distinct lineation. Combining these features, presence of abundant euhedral grains

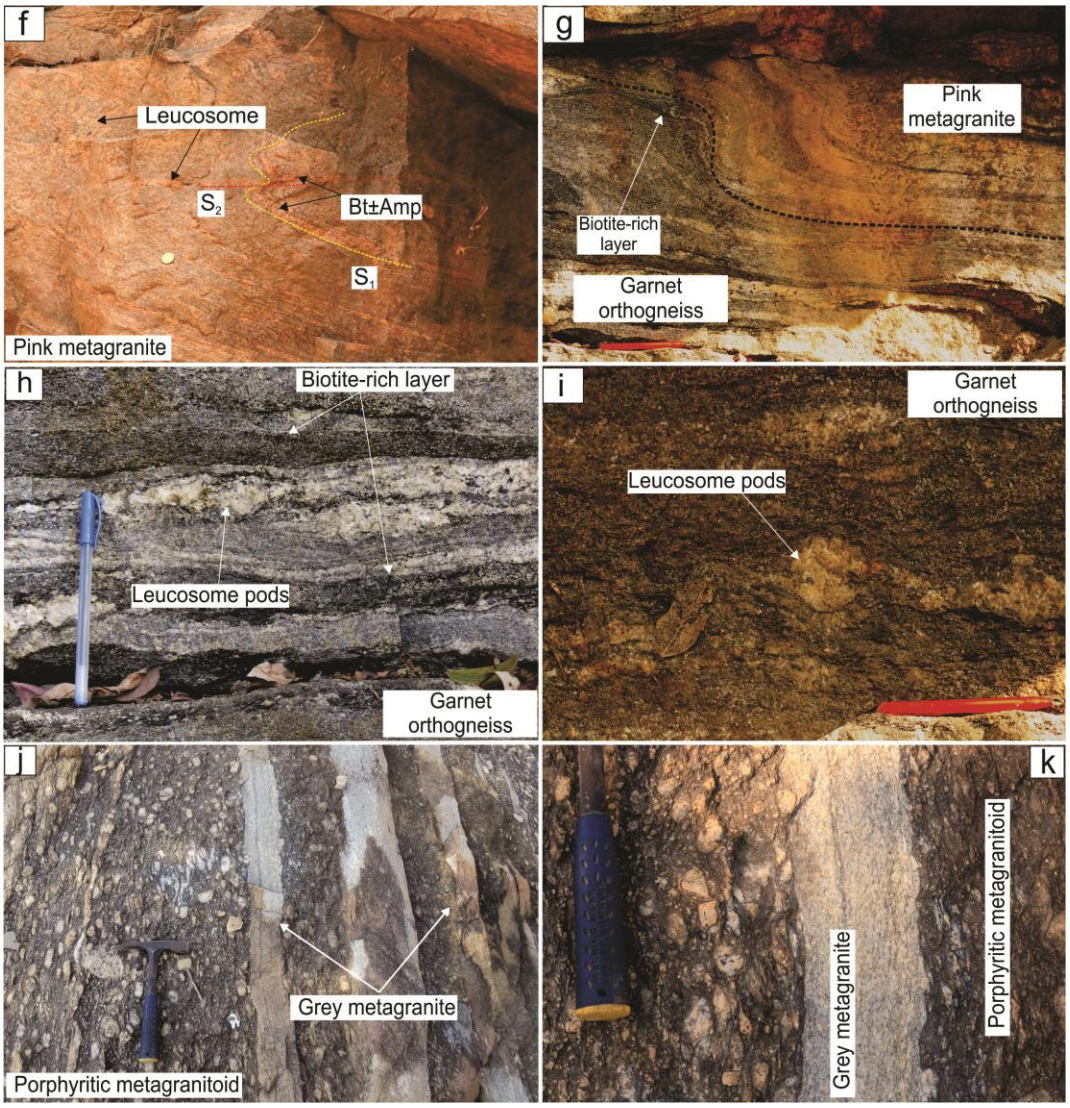

Figure 3.1.1 contd. (f) Pink metagranite develops non-garnetiferous leucosomes, defining S_1 which got folded during D_2 (second) regional deformation event. Second set of leucosome is present along the F_1 axis and biotite clots are present along leucosomes. (g) Garnet orthogneiss intrudes within pink metagranite and at their shared thrusted contact both the lithounits get folded with asymmetric limbs. (h, i) At the contact, garnet orthogneiss contains asymmetric leucosomal pods and biotite-rich melanosome. (j) Grey metagranite intrudes within deformed porphyritic metagranitoid. (k) Foliation, defined by biotite within grey metagranites is parallel to the foliation within deformed porphyritic metagranitoids.

of feldspar megacryst and the absence of intense grain size reduction in laterally persistent zones, it can be stated that the studied metagranitoids has not been subjected

to intense shearing (Vernon 2004). The laterally discontinuous biotite folia are sparsely developed in the less deformed part of the metagranitoid rocks. Randomly oriented K-feldspar megacrysts with both euhedral to elliptical outlines are completely surrounded by a grey, translucent rim (Fig. 3.1.1d, e). Optical and scanning electron microscopy conform that the grey, translucent rim is an intergrowth of quartz–plagioclase (myrmekite). The thickness of the myrmekite rim is not constant and varies along the periphery of a single grain as well as one grain to the other.

Field disposition and contact relationships with porphyritic metagranitoids suggest that the protolith of grey metagranites (not to scale in the lithological map) intruded as dykes within porphyritic ones. Direct contact between porphyritic metagranitoids and pink metagranites are not observed anywhere in the study area but felsic orthogneisses appear to be thrusted within pink metagranites and their contact show some evidences of shearing or intense deformation.

The pink metagranite (not in map scale) develops leucosomes that are completely devoid of garnet (Fig. 3.1.1f). Leucosomes defining the folia in pink metagranites are folded during the second regional deformation that affected all the lithounits of study area. A lineation defined by amphibole and biotite clots has developed along the F_2 fold axis. A second generation of leucosome is observed along the axial plane of these folds (Fig. 3.1.1f) which implies syntectonic melting in pink metagranites. At the thrusted contact between felsic orthogneiss and pink metagranite both the lithounits are deformed into asymmetric folds (Fig. 3.1.1g). At the lithocontact, felsic orthogneiss contains biotite-rich melanosome layer and asymmetric pods of leucosomes (Fig. 3.1.1h, i).

Migmatitic banding is not developed in the grey metagranite of the study area. In the outcrop, the grey metagranite is seen to intrude within the porphyritic metagranites as dykes (Fig. 3.1.1j). Weak foliation, defined by biotite within this unit is parallel to the biotite ± amphibole foliation of the porphyritic metagranitoids (Fig. 3.1.1k).

3.1.2. Felsic orthogneisses [charnockitic orthogneiss (COG) and garnet orthogneiss (GOG)]

Isolated small hillock type outcrops of felsic orthogneisses are exposed in road cut and railway cutting sections in the north-eastern part of the study area, near Waidhan, Singrauli district and immediate south of the Rihand-Renusagar dam. They are concentrated around E-W trending Bijpur road and continue up to around 2 km north of the Barhapan village (Fig. 3.1). Depending on the difference in field appearance and mineralogy two types of felsic orthogneisses are identified in the study area: charnockitic orthogneiss (COG) and garnet orthogneiss (GOG). Magmatic protolith of the felsic orthogneisses were intruded the porphyritic metagranitoid. Extensive tropical weathering obliterates the contact relation between the host metagranitoid and the felsic orthogneisses but overall lithological disposition point towards that fact that the latter is the younger unit. Felsic orthogneisses share a thrusted contact with the foliated pink metagranite where the former one intrudes the latter. No direct field contact between the metasedimentary units and felsic orthogneisses is observed. Garnetiferous meta-mafic dyke is observed to intrude the felsic orthogneiss (Fig. 3.1.2a).

The COG shows a prominent gneissic banding defined by dark melanosome (biotite + amphibole + garnet ± orthopyroxene ± plagioclase ± quartz) that are interleaved with 3-5 cm thick, relatively coarse grained and laterally continuous to streaky leucosome (quartz + K-feldspar + plagioclase + garnet) (Fig. 3.1.2b). Commonly, the proportion of leucosome in the COG is <10 vol% (rarely up to 15 vol%). Garnet in the leucosome is distinctly coarser than in the melanosome. Where orthopyroxene is present, the COG imparts a greasy appearance (Fig. 3.1.2b, c). The gneissic banding of the GOG, the dominant felsic orthogneiss of the area is defined by alternating garnet + biotite rich melanosome and laterally continuous leucosome (quartz + K-feldspar + plagioclase + garnet) (Fig. 3.1.2d). Compared to the COG, the GOG has distinctly thicker and higher proportion of leucosome (15-20 vol%).

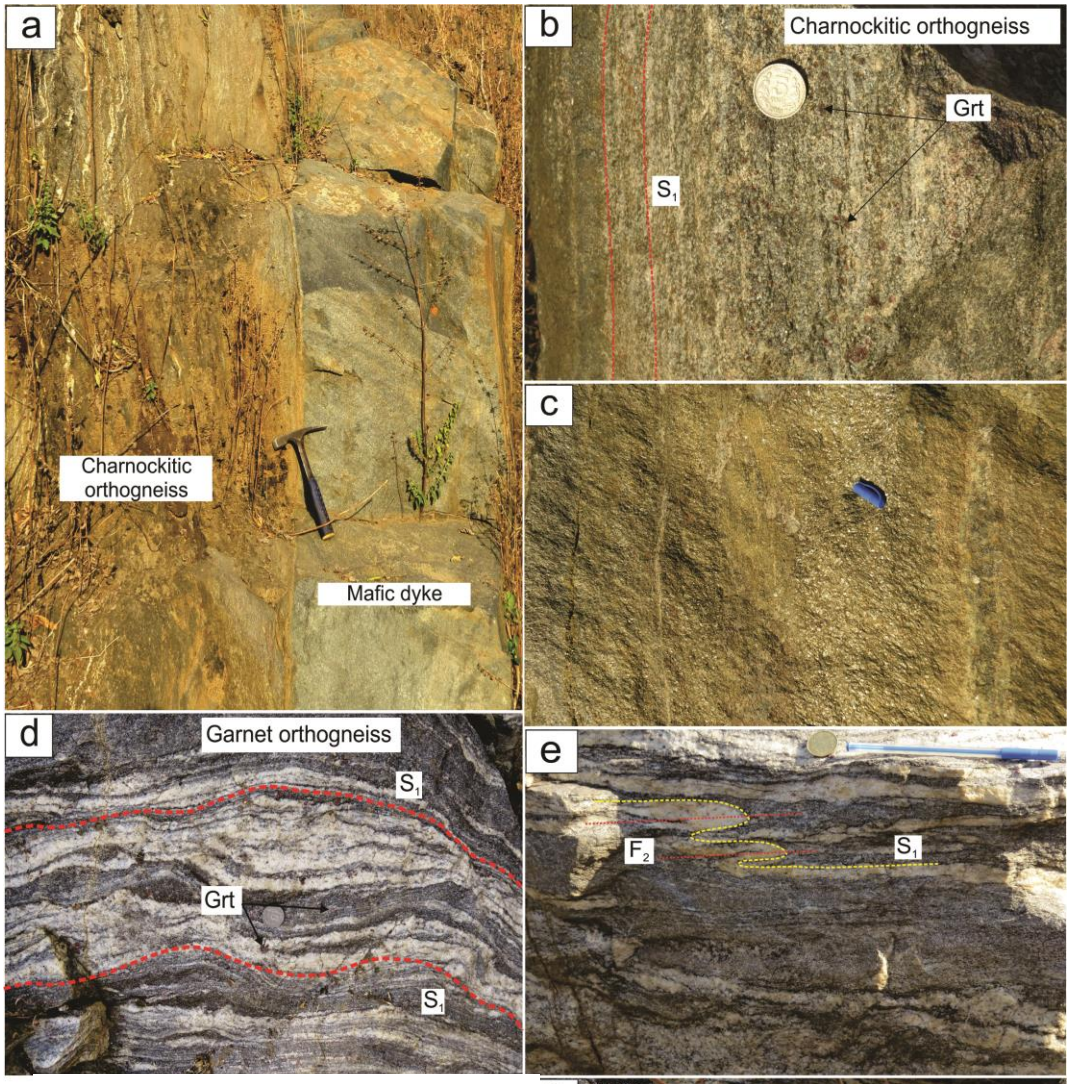

Figure 3.1.2. (a) Garnetiferous meta-mafic rock intrudes as dyke within the COG. (b) COG consisting of fine leucosome and melanosomes that define S_1 foliation. (c) Greasy field appearance of COG. (d) GOG containing 15–20 vol% of leucosome (quartz + K-feldspar + plagioclase + garnet) which defines S_1 foliation and biotite + garnet rich melanosome. Garnet in the leucosome is coarser than that within the melanosome. Leucosomes show pinch and swell structure due to stretching as an effect of second deformation. (e, f) Garnetiferous leucosomes in GOG, defining S_1 fabric have been folded tightly in the second event of deformation (D_2) such that S_1 and S_2 appear parallel to each other. Attitude of F_2 is variable.

3.1.3. Metasedimentary rocks

The study area exposes patches of metasupracrustal rocks including marble (with thin calc-silicate compositional banding), metapelite (garnet-cordierite-biotite-sillimanite-quartz) (not to map scale), banded psammopelite (garnet-biotite-quartz ± sillimanite) and rare quartzite. The metasupracrustal rocks rest on the porphyritic metagranitoid with a sharp contact.

Marble-calc silicate interlayered units are scattered in and around Sidhi Kalan, Tiara, Barhapan and Makrohar villages in the study area (Fig. 3.1). They occur as isolated boulder type outcrops which show strong deformational signatures in the field. The calcitic marble in the study area is a white colored, coarse grained, saccharoidal rock with very small amount of silicate. At places, calcitic marble show direct contact with porphyritic metagranitoid (Fig. 3.1.3a). The diopside + spinel + olivine bearing calc-silicate layers within marble is the earliest compositional banding that define a set of tight to isoclinal folds (F_1 folds during D_1 deformation) (Fig. 3.1.3b). The marble shows foliation which is parallel to the regional S_1 fabric and runs along the axial plane of the F_1 fold (Fig. 3.1.3b). Extensive channelized hydration develops clinohumite-rich bands along the interface of calc-silicate rocks and the marble (Fig. 3.1.3c). The clinohumite-rich bands are mostly parallel to and locally cut the S_1 fabric of the marble at low angle (Karmakar, 2021). Superposed folding of the calc-silicate bands within marble during second regional deformation event resulted in hook-shaped interference pattern in the outcrop (Fig. 3.1.3b). These structural patterns in the interlayered marble-calc-silicate rocks suggest that the F_1 and F_2 folds were formed in one progressive deformation.

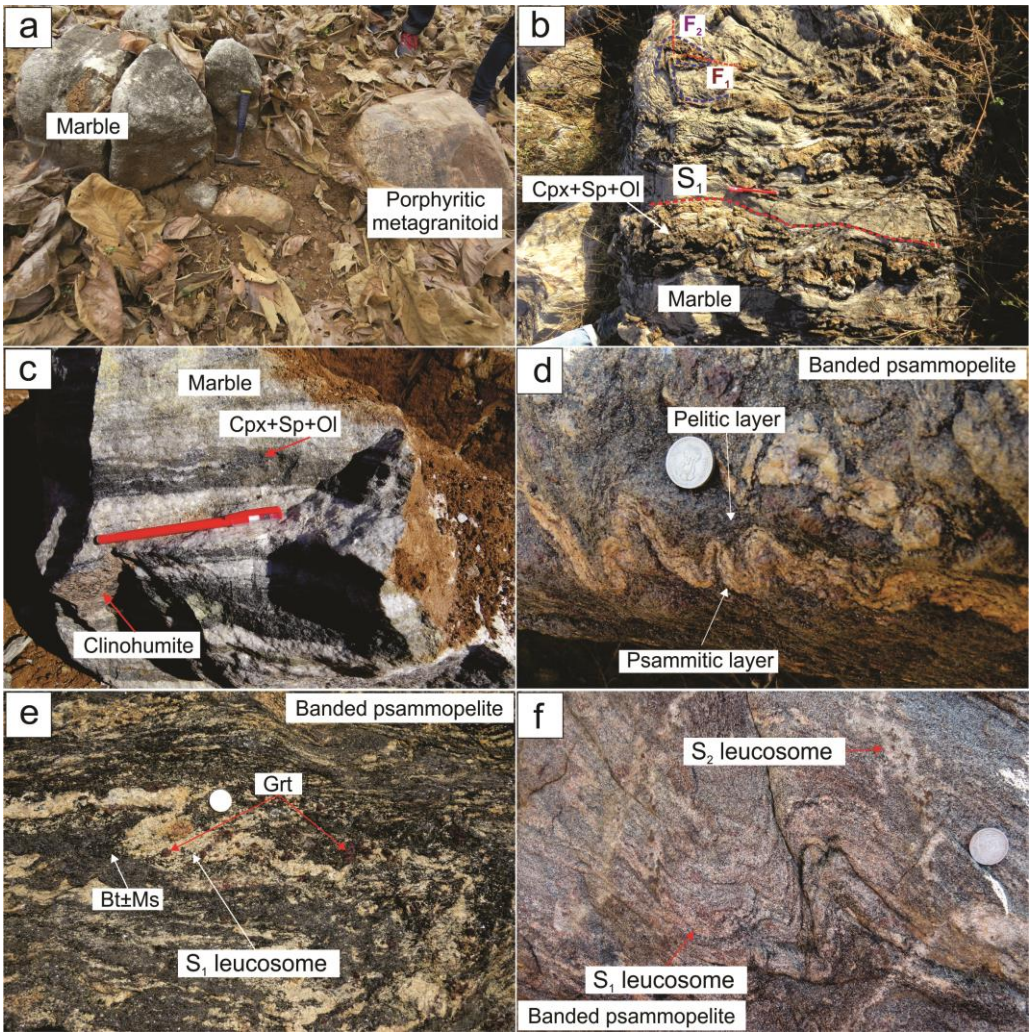

Figure 3.1.3. (a) Field contact between calcitic marble and deformed porphyritic metagranitoid. (b) Spinel+Clinopyroxene+Olivine layers within marble define a set of tight to isoclinals folds (F_1). Host marble shows strong foliation which runs parallel to the F_1 axial plane. Folding of F_1 folds of the calc silicate bands in marble by F_2 folds develop hook-shaped interference pattern. (c) Spinel+Clinopyroxene+Olivine rich bands within marble. Clinohumite develops at the contact of marble and calc-silicate layers. (d) Banded psammopelitic unit with distinct pelitic and psammitic part. Compositional banding shows congruous S-M-Z folds. (e) Garnetiferous leucosomes are showing recumbent folds in the metapelitic part. Oriented biotite grains cut the hinge of this recumbent fold. (f) Leucosomes, defining S_1 are showing upright folds due to second deformation event in the study area. Leucosomal segregates along the F_2 axial plane.

Banded psammopelites occur as isolated, flat, ground-level and elongated band-like outcrops in the study area (Fig. 3.1). Compositional banding comprising of alternate mica-rich (pelitic) and quartz-rich (psammitic) layers defines the earliest secondary planar structure similar to the felsic orthogneisses (Fig. 3.1.3d). This S_1 fabric of the banded psammopelite defined by compositional banding as well as garnetiferous leucosomes is parallel with the gneissic banding in the felsic orthogneisses and the foliation as well as compositional banding (calc-silicate layers) within marble. Though psammitic portion also contains garnet, it is more concentrated in the biotite-rich pelitic part. The banded psammopelites contain leucosomal segregates (15-20 vol% in the outcrop) which are showing early recumbent folds (Fig. 3.1.3e). The S_1 fabric (compositional banding as well as leucosome in the metapelitic portions) shows congruous folding and locally axial planar foliation is developed parallel to F_2 in the banded psammopelites (Fig. 3.1.3d, e, f). Dimensional orientation of biotite (and rare muscovite) define a pervasive foliation (S_2) cuts the hinge of the F_1 recumbent folds defined by the leucosomes in the metapelitic part (Fig. 3.1.3e). Stringers of the garnet bearing leucosomes are also developed along the axial plane of the F_2 fold (S_2 fabric) (Fig. 3.1.3f).

The metapelite (garnet-cordierite-biotite rock) occurs as small isolated hillock in the study area and it is grouped with the banded psammopelitic unit in the lithological map because of its scarcity and strike continuity combined with similar chemical composition with the psammopelitic unit. Garnet-cordierite-biotite (GCB) rock is melanocratic and very tough rock. In this rock rounded garnet grains/aggregates of garnet grains are sprinkled within cordierite-dominated matrix, showing a dark bluish hue (Fig. 3.1.3g). Fine acicular sillimanite and rare quartz are also present in the rock. Two sets of cross cutting, translucent white colored veins rich in blades of sillimanite, quartz and variable amount of garnet form network within the host rock (Fig. 3.1.3h). Both the outcrop and polished hand specimen show that biotite and garnet are concentrated along the margin of the veins (Fig. 3.1.3i, j). Kinking of the sillimanite-quartz veins and the biotite segregates at the margin are noted (Fig. 3.1.3i, j). Thin and continuous and discontinuous laminae of biotite are also present away from the sillimanite-quartz veins (not visible in outcrop scale).

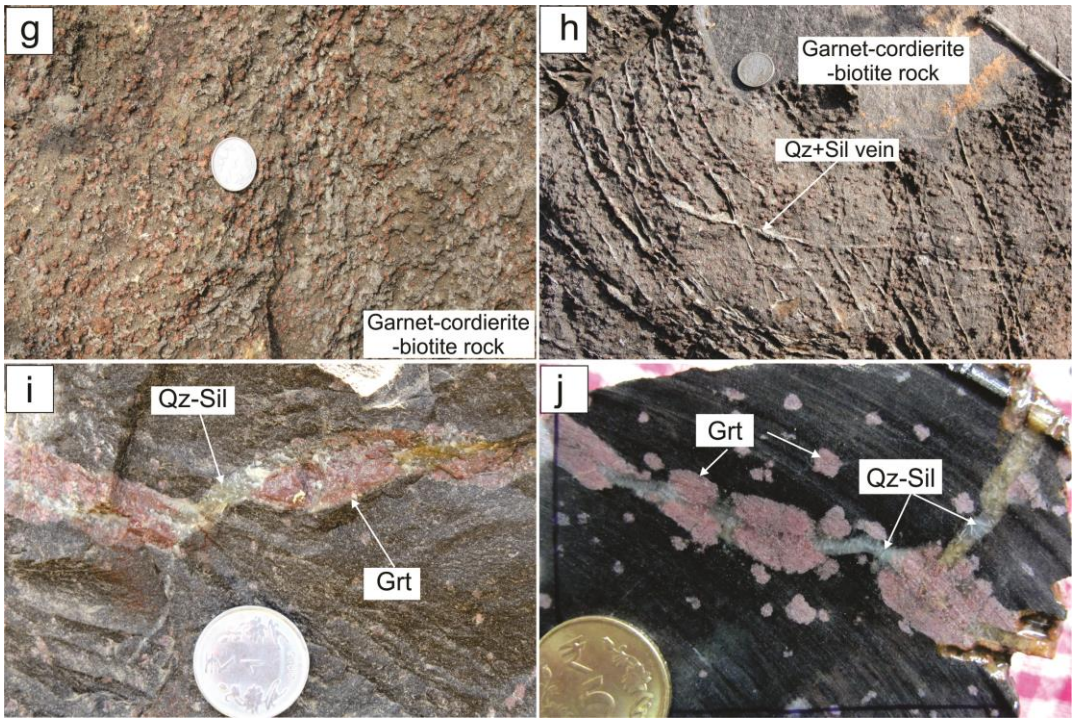

Figure 3.1.3 contd. (g) Dark bluish field appearance of the garnet-cordierite-biotite rock where garnet grains are sprinkled within cordierite-dominated matrix. (b) Numerous cross-cutting translucent white colored veins form network within the garnet-cordierite-biotite rock. (i, j) Vein consists of coarse quartz and sillimanite blades and garnet is noted to be accumulated at the boundary of veins.

3.1.4. Meta-mafic rocks and pegmatites

Meta-mafic rocks in the study area either occur as isolates boulder type outcrops occupying a vast field (Fig. 3.1; 3.1.4a) or intrude the porphyritic metagranitoids, felsic orthogneisses, metasedimentary units and porphyritic metadiorite (not to map scale) as dykes (Fig. 3.1.4b-e). The interface between the meta-mafic rocks and

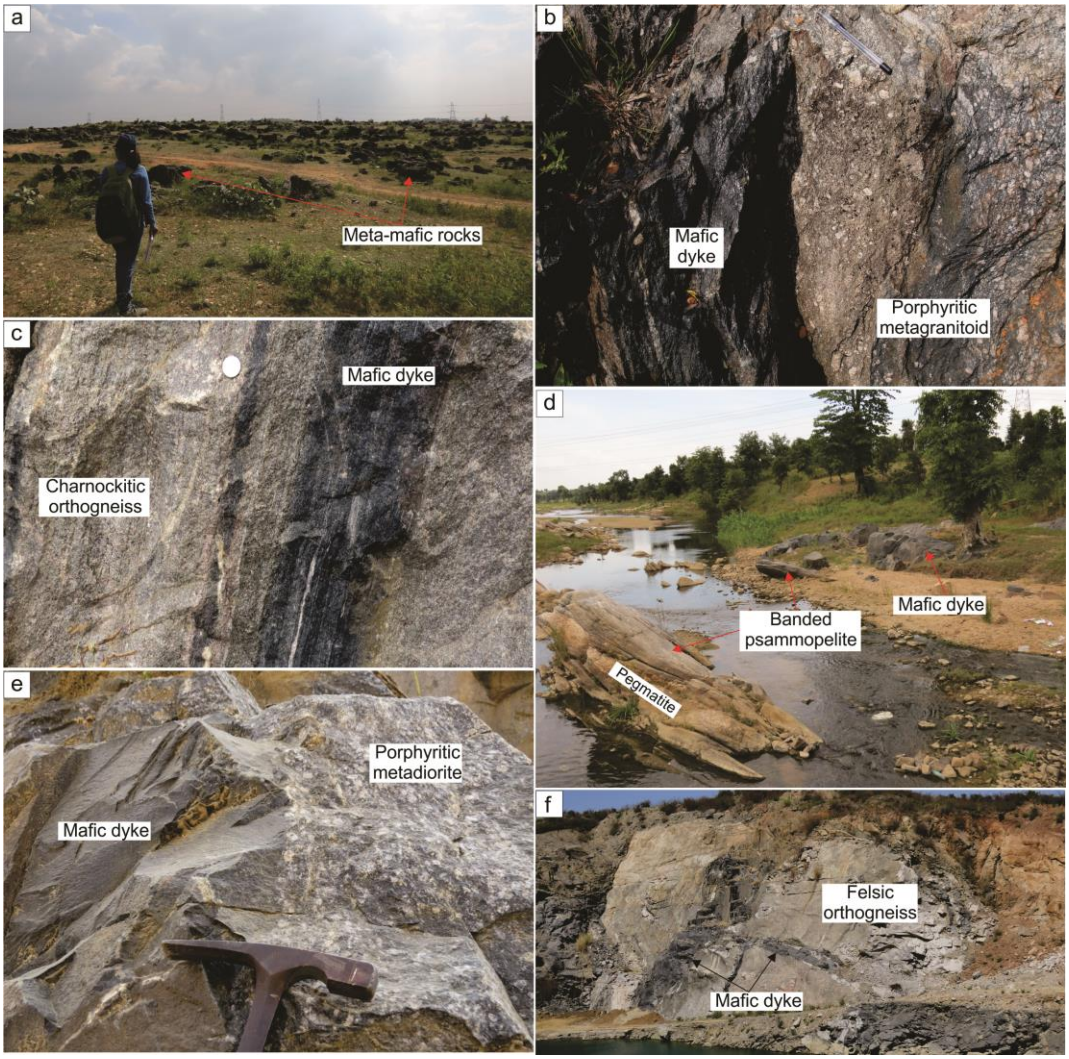

Figure 3.1.4. (a) Meta-mafic rocks occurring as isolated boulders at few locations in the field. (b) Mafic dyke intrudes as dyke within porphyritic metagranitoid. (c) Garnetiferous mafic dyke intruding charnockitic orthogneiss (COG). Weak foliation, defined by bt+amp within meta-mafic rock is parallel to the foliation S_2 within the COG. (d) Mafic dyke intrudes within banded psammopelite in a nala section. (e) Meta-mafic rock intruding porphyritic metadiorite. (f) Bifurcation of the mafic dyke within felsic orthogneiss.

host lithounits is sharp and the elongated mafic bodies are roughly parallel with foliation that developed parallel to the limbs of the tight folds defined by the calc-silicate rocks as illustrated in the lithological map of the study area (Fig. 3.1). The field features of the mafic rocks are consistent with the view that the magmatic protoliths of the mafic rocks were intruded as dykes within their host rock. Local

bifurcations of the mafic bodies also support the intrusive relation of the rock in the host felsic rocks (porphyritic metagranitoids and felsic orthogneisses, Fig. 3.1.4f). Weak foliation, defined by amphibole + biotite within the meta-mafic dykes is parallel to the F_2 axial plane within the felsic orthogneiss (Fig. 3.1.4c). The detached outcrops of the meta-mafic dykes in the lithological map are showing an overall NW-SE trends (parallel to regional F_2 axial plane and S_2 fabric) (Fig. 3.1).

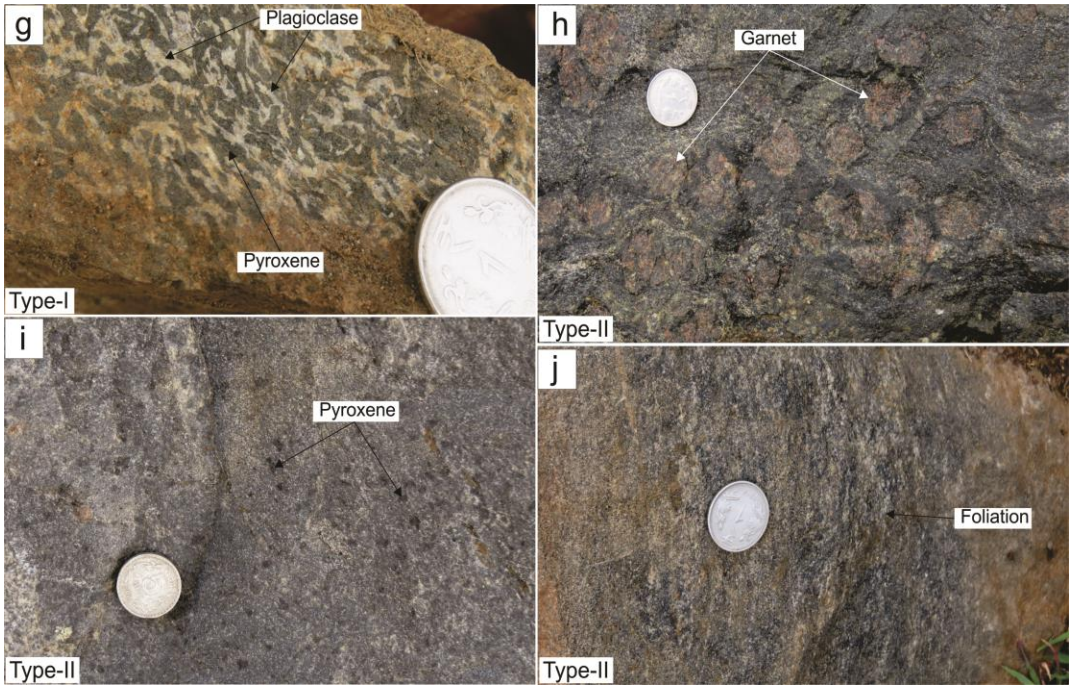

Figure 3.1.4 contd. (g) Coarse grained meta-mafic rock with plagioclase and pyroxene showing intergranular texture in hand specimen. (h-j) Fine grained meta-mafic rocks (Type-II) with occasional presence of garnet and weak foliation.

Though less abundant, few mafic rocks are relatively coarse grained showing plagioclase laths that are oriented haphazardly around the larger pyroxene and olivine crystals (Fig. 3.1.4g). These coarse grained samples show distinct magmatic intergranular texture and devoid of garnet and any foliation in the outcrop (Fig. 3.1.4g). In most places the meta-mafic rocks are fine grained (Fig. 3.1.4ih-j). Rarely, garnet occurs as scattered grains within the finer grained mafic rocks (Fig. 3.1.4h). Locally, amphibole and biotite grains define a feeble foliation (Fig. 3.1.4c, j) which is parallel with the regional S_2 fabric that formed during D_2 deformation. Depending on

the grain size, presence of feeble foliation and primary texture in the outcrop the meta-mafic rocks in the study area are divided as Type-I (coarse grained, dominance of magmatic mineralogy and texture and lacking foliation) and Type-II (dominantly fine grained, deformed and metamorphosed).

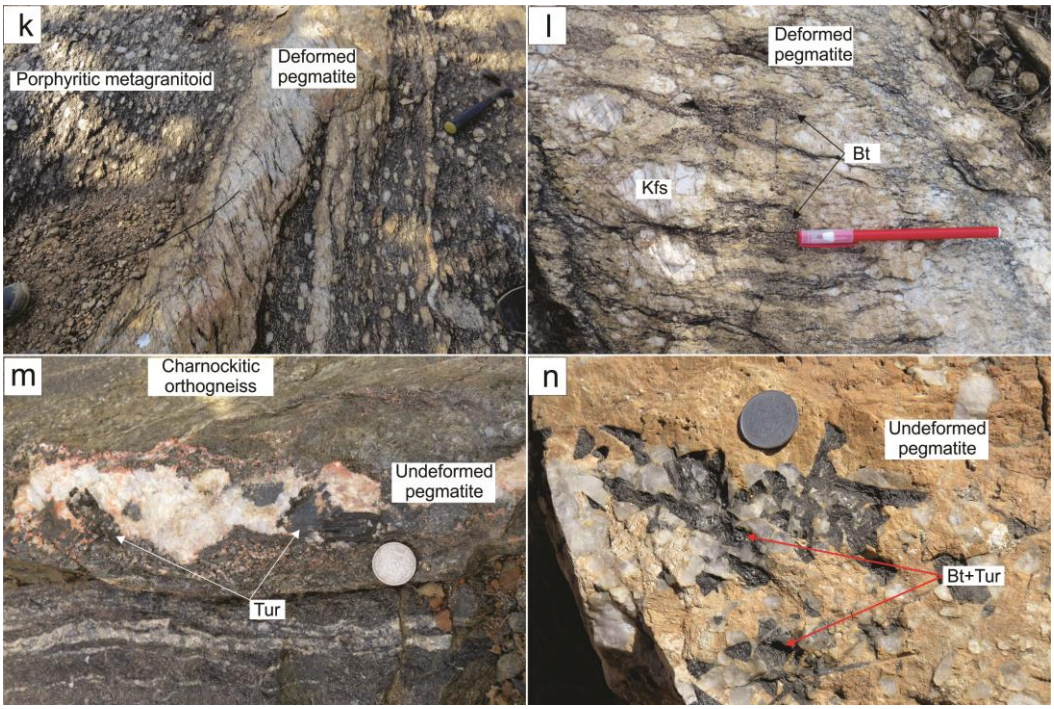

Figure 3.1.4 contd. (k, l) Biotite-rich deformed pegmatite intruding the porphyritic metagranitoid and devoid of tourmaline. (m, n) Tourmaline-rich undeformed pegmatite intrudes within charnockitic orthogneiss (COG).

Two types of pegmatites intrude the porphyritic metagranitoids and felsic orthogneisses in the study area. The first ones are biotite-rich pegmatites devoid of tourmaline and these pegmatites are folded and develop fabric (Fig. 3.1.4k, l). The second ones are undeformed pegmatites with haphazardly oriented large tourmaline grains which form pods along with biotite at some places (Fig. 3.1.4m, n).

3.2. Structures in the study area

Field observations suggest that all the major lithounits are intensely deformed in multiple tectonothermal events but prominent structures are mainly preserved within felsic orthogneisses and metasedimentary rocks in the study area. The most conspicuous planar structures in the outcrops of the study area are manifested by garnetiferous leucosomes in felsic orthogneisses; compositional banding as well as garnetiferous leucosomes in banded psammopelites, calc-silicate layers within marble, foliation defined by oriented biotite ± amphibole and stretched quartz and feldspar porphyroclasts in porphyritic metagranitoids and migmatitic banding in foliated pink metagranite. Migmatitic banding within felsic orthogneisses, compositional banding within marble-calc silicate interlayered units, compositional banding as well as garnetiferous leucosomes within banded psammopelites define the earliest secondary planar structure (S_1) in the study area. Pre-S_1 (S_0) deformation fabric, if there was any, are obliterated due to subsequent deformation. The early fold along the axial plane of which the S_1 planar fabric might have developed, is not preserved in the study area. S_1 in all the aforementioned lithounits show a strike amount towards NE-SW in the outcrops. F_1 folds, geometry varies from recumbent to upright have variable attitudes probably due to superposed deformation. S_1 fabric in the felsic orthogneisses has been subsequently folded into tight isoclinal recumbent to asymmetric inclined folds with NW-SE trending fold axis (F_2) presumably in a second event of deformation (D_2). Pinch and swell structure often observed in many leucosomes presumably occurred due to stretching as an effect of second deformation. Refolding of the limbs of F_1 folds and the S_1 defined superposed patterns in the lithounits of the study area. Compositional banding within psammopelitic unit shows buckle folding with S-M-Z congruous folds (F_2) and shallow plunging puckers. The calc silicate layers within marbles show hook shaped outcrops. S_1 fabric within metagranitoids show asymmetric folds with steep (>70° ➔ N) short limb and long limb with variable dip (20-60° ➔ S). The lithocontact or boundary between felsic orthogneiss and pink metagranite also show asymmetric folds. The geometry of F_2 folds are variable but mostly low plunging. Rarely a crude fabric (S_2) is developed locally along F_2, best preserved in the

metasupracrustal rocks. Occasional second generation of leucosomal banding developed within pink metagranites and banded psammopelitic units also runs parallel to S_2. Dimensional orientation of biotite ± amphibole define foliation within porphyritic metagranitoid, grey metagranite and type-II meta-mafic dykes and this foliation is parallel to the axial plane of F_2 (S_2 fabric). Tightness of the D_2 folds made S_1, S_2 and the lithocontacts to be virtually parallel except the hinge zone of the D_2 fold. Hence most of the planar structures are subparallel or transposed in the study area. The planar structures variably show N-S closing nearly neutral open fold with sub-vertical axial plane (F_3) in the lithological map of the study area.

CHAPTER 4

PETROGENESIS OF THE PORPHYRITIC METAGRANITOID

Geochemical variations in magmas serve as proxies to trace the source heterogeneity and various other petrogenetic processes including magma mixing, assimilation-fractional crystallization and depth of magma emplacement (Castro, 2014; Deering and Bachmann, 2010; Farina et al., 2020; Garcia-Arias and Stevens, 2017; Jagoutz, 2010; Nandedkar et al., 2014). In the parlance of the supercontinental cycle, felsic magmatism is considered to be one of the dominant processes of supercontinent growth (Condie and Kröner, 2013; Hinchey, 2021; Zhao et al., 2004).

A vast body of metagranitoid occurs as the country rock i.e. basement of felsic orthogneisses and metasedimentary rocks of the MKGB. Extensive tropical weathering obliterates the continuity between the outcrops and their direct field contact with the felsic orthogneisses. The abundant and dominant member of this metagranitoid suite contains feldspar megacrysts, embedded within fine dark matrix which imparts their porphyritic nature. In the outcrop, porphyritic metagranitoids show a large spectrum of feldspar shapes: varying from rectangular feldspar porphyroclasts in undeformed matrix to stretched feldspar augen in foliated matrix.

4.1. Petrography

A total of 17 samples, dispersed in the study area are studied in detail. Their field locations and modal proportions of the phenocryst and matrix minerals in each of the studied samples are presented in the Table-4.1. Mineral abbreviations in the figures and the tables in following sections are taken from Whitney and Evans (2010).

Even in the thin section scale, the porphyritic metagranitoids show polymodal grain size distribution, observed in the outcrops. Alkali feldspar megacrysts are ~1 cm in length and 5-10 mm in width, plagioclase and garnet grains are ≤5 mm in length and width whereas the matrix phases (biotite ± amphibole + ilmenite + quartz + alkali feldspar + plagioclase) are <200 μm in size. Optical microscopy backed up by BSE images shows that alkali feldspar and plagioclase are present in the megacryst as well as in the matrix. In the least deformed

Table 4.1: Comparative modal abundance of the studied porphyritic metagranitoids. Mineral abbreviations are after Whitney and Evans (2010).

Sample no	Major minerals										Location of the sample	Phenocryst		Matrix (Felsic)		
	Qz	*Pl*	*Kfs*	*Grt*	*Amp*	*Bt*	*Ttn*	*Ilm*	*Zrn*	*Mnz*		*Kfs*	*Pl*	*Qz*	*Kfs*	*Pl*
SR35D	30	15	28	10	-	15	-	P	P	-	N23°58.27'E82°38.28'	80	20	30	60	10
SR36	30	15	30	-	-	20	P	P	P	-	N23°57.09'E82°38.65'	100	-	35	55	10
SR38A	25	20	25	5	10	15	P	P	P	-	N23°58.78'E82°38.65'	100	-	30	60	10
SR50C	30	15	25	10	-	20	-	P	-	-	N23°56.41'E82°43.40'	80	20	30	50	20
SR54A	20	20	30	5	8	15	P	P	P	-						
SR54B	20	25	30	5	8	10	-	P	-	-	N23°56.60'E82°43.38'	100	-	30	55	15
SR82A	30	20	28	-	-	20	P	-	-	-	N23°58.67'E82°37.06'	80	20	40	40	20
SR111	25	18	30	-	15	10	P	-	P	-	N24°1.50'E83°1.54'	90	10	40	40	20
SR89B	15	30	20	10	-	20	-	P	P	-	N23°53.81'E82°34.70'	40	60	50	30	20
SR91	15	25	20	10	5	25	-	P	P	-	N23°54.17'E82°34.20'	40	60	50	30	20
SR92	20	25	18	10	5	20	-	P	P	-		40	60	50	30	20
SR92A	20	30	25	-	-	25	-	-	P	-	N23°54.64'E82°34.14'	40	60	50	30	20
SR142	15	25	20	10	10	20	P	P	P	-	N23°54.39'E82°39.34'	50	50	40	30	30
SR145	15	20	25	10	15	15	P	P	P	-	N23°54.97'E82°39.98'	50	50	40	30	30
SR146	15	25	25	-	10	20	-	P	P	-	N23°54.87'E82°40.30'	45	55	40	30	30
SR149	30	20	30	-	-	20	-	-	-	-	N23°56.33'E82°40.17'	50	50	40	30	30
SR150B	15	20	30		10	20	P	P	-	-	N24°1.20'E83°3.08'	75	25	30	50	20

P= Present in minor content

variety of porphyritic metagranitoids, idiomorphic alkali feldspar megacrysts contain relict tartan twinning and inclusions of plagioclase, quartz and locally developed very fine plagioclase lamellae (Fig. 4.1a-e). Alkali feldspar grains are rimmed by quartz-plagioclase aggregate (both as myrmekite and granular recrystallized type; Fig. 4.1f). Based on morphology two types of myrmekite, namely Myr1 and Myr2 are identified. The quartz grains in Myr1 show vermicular intergrowth in the base of plagioclase whereas Myr2 shows polygonal aggregates, commonly showing triple point junction and the size of the quartz grains is distinctly coarser than the quartz in Myr1 (Fig. 4.1f). Plagioclase phenocrysts contain complex twinning and oscillatory zoning (Fig. 4.1g-j). Commonly, the magmatic feldspars show impress of deformation and the intensity of deformation significantly varies from weakly deformed to relatively more deformed samples. This is manifested by the bending of lamellar twin planes of plagioclase, undulose extinction, grain boundary recrystallization and formation of polygonal aggregates along the margin of feldspar grains (Fig. 4.1i-k). Recrystallization is more pronounced in the alkali feldspar than the plagioclase grains. The deformed feldspar grains, megacrysts as well as those in the matrix, will be referred to as feldspar porphyroclasts. In the relatively deformed samples, quartz grains in the matrix either form polygonal grain aggregates or form elongate aggregates of coarsely recrystallized grains with planar contacts (Fig. 4.1j, k). Grain boundary bulging of recrystallized quartz grains are also noted (Fig. 4.1j). Locally, elongated quartz grains separate the porphyroclasts of plagioclase from alkali-feldspar and also form veins within the porphyroclasts of feldspars (Fig. 4.1l). Garnet grains with subhedral to euhedral outlines and containing inclusions of tiny ilmenite, quartz, plagioclase and biotite are highly fractured (Fig. 4.1m). Extensive replacement of garnet by biotite makes estimation of the garnet mode difficult. The preserved garnet portion occupies about 5-10 volume percent of the rock. Biotite grains occur at least in four distinct modes. The biotite inclusions in garnet form the earliest mode. The second mode of biotite that shows undulose extinction and bending defines the biotite folia that swerve around and replace the garnet, and porphyroclasts of feldspar (Fig. 4.1n). Commonly, the biotite grains, in the third mode, in the folia show random

orientation and are free from any internal deformation (Fig. 4.1o). This biotite extensively replaces plagioclase (less commonly the alkali feldspar) and garnet

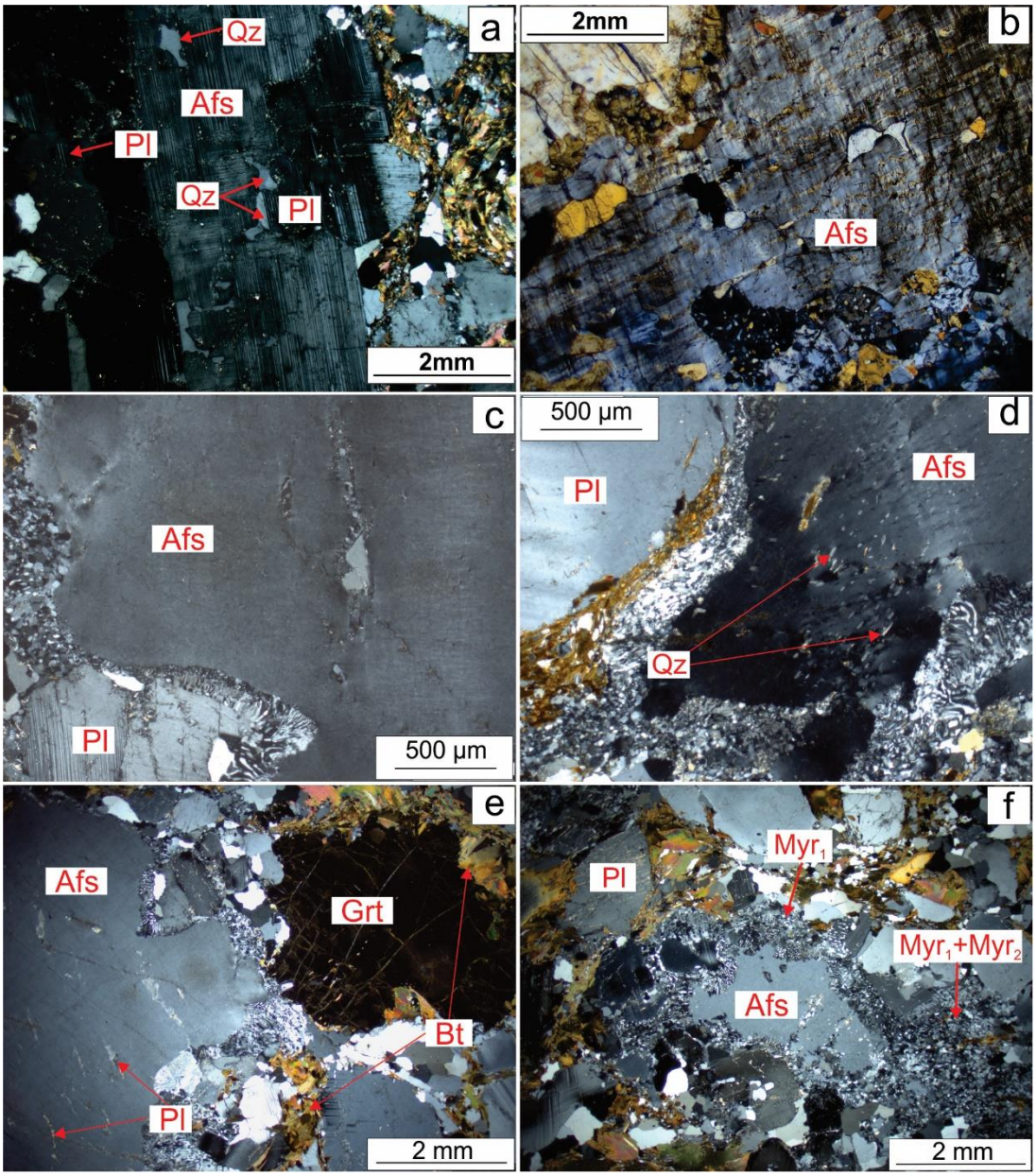

Figure 4.1. a) Alkali feldspar megacryst containing plagioclase and quartz inclusions. b, c) Alkali feldspar megacrysts show relict tartan twinning. d, e) Alkali feldspar with relict tartan twinning contain quartz inclusions, plagioclase lamellae and is replaced by myrmekite. Both garnet and plagioclase porphyroclasts are replaced by secondary biotite. f) Alkali feldspar extensively replaced and rimmed by myrmekite. Both vermicular (Myr1) and granular (Myr2) quartz intergrowths are present in the myrmekite coronae.

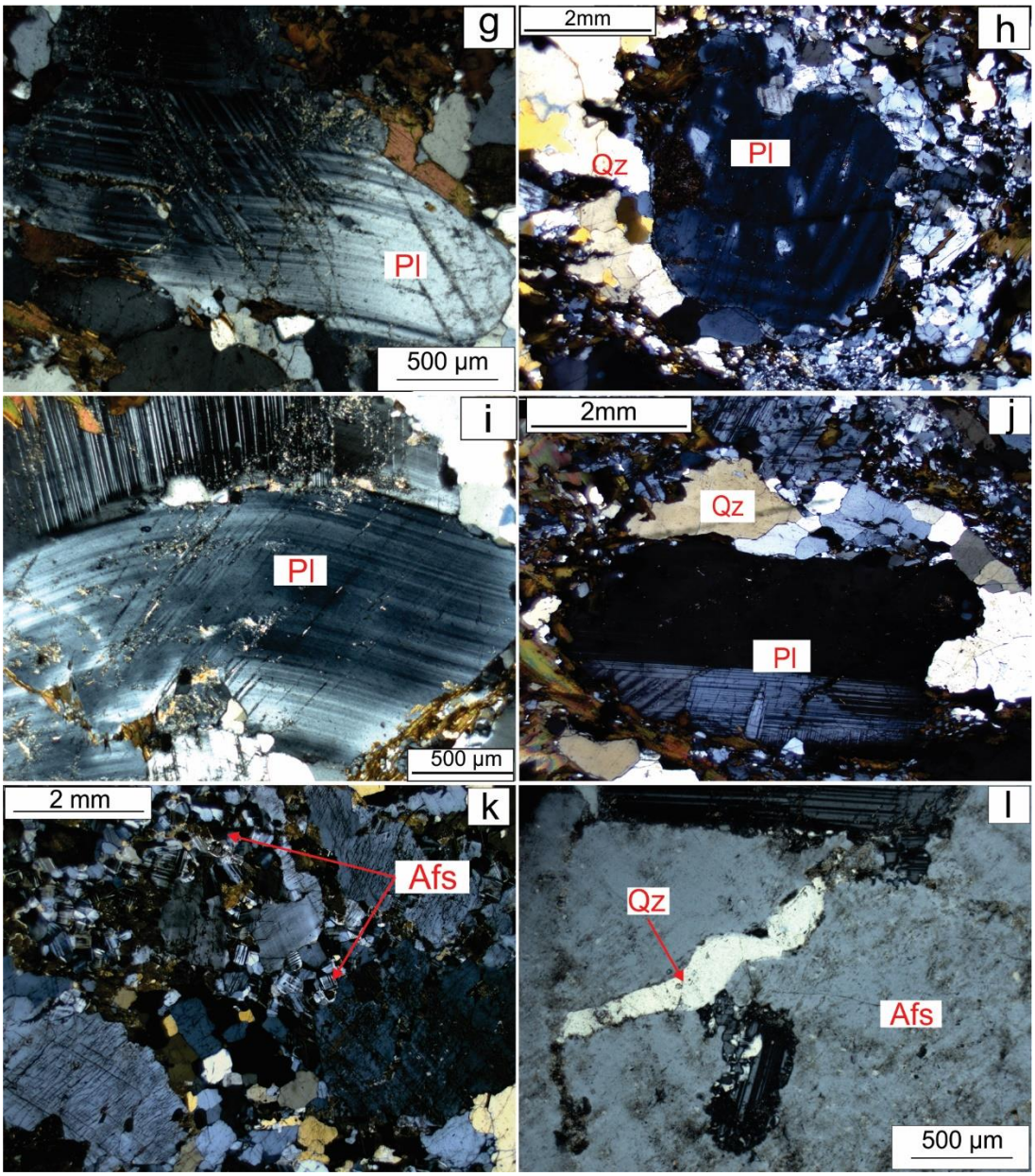

Figure 4.1 contd. g) Complex twinning within plagioclase porphyroclasts are bent in deformed porphyritic metagranitoids. h) Plagioclase porphyroclasts preserve oscillatory zoning. i) In some cases, plagioclase grains get bent along with their lamellar twinning. j) Complex twinning in plagioclase. Recrystallized quartz grains are present along diffused grain boundary of plagioclase porphyroclasts. Grain boundary bulging is noted in quartz grains. k) Polygonal aggregate of alkali feldspar and quartz in the matrix. l) Elongated quartz grains form vein within alkali feldspar megacryst.

along the grain boundaries as well as along the fractures. The biotite-quartz intergrowth, in the fourth mode occurs randomly and replaces feldspars as well as polygonal aggregates of quartz and plagioclase (Fig. 4.1p). Based on petrographic features, the second to fourth modes of biotite will be referred to as 'secondary' biotite as the grains replace deformed feldspar and garnet grains. On the contrary, amphiboles are only present in one mode, always associated with biotite in the matrix and replace the garnet (Fig. 4.1q, r). The textural/microstructural features also suggest that second to fourth generation of biotite grew during and outlasted the deformation that affected the porphyritic metagranitoid rock. Commonly, the plagioclase grains proximal to the secondary biotite show normal zoning (thickness of the albitic rim is highly variable). Rarely the plagioclase grains with oscillatory zoning also undergo recrystallization (Fig. 4.1s).

4.2. Mineral compositions

Representative mineral compositions of the studied samples have been analyzed with Electron Probe Microanalyzer at the Department of Geology and Geophysics, Indian Institute of Technology, Kharagpur and the Department of Applied Geology, Indian Institute of Technology (IIT-ISM), Dhandbad. Detailed analytical technique is discussed in Appendix. The analytical results are given in Table-4.2. The relevant phase compositions are described below.

Feldspars: The alkali feldspar porphyroclasts are essentially microcline ($Or_{87.3-89.4}Ab_{10.5-12.9}An_{<1}Cs_{1.3-1.8}$) (Table-4.2a). 'Or' stands for $KAlSi_3O_8$ molecule without any reference of Al-Si ordering. Presence of significant albite molecule in alkali-feldspar does not rule out the possibility that very fine perthitic lamellae can be resolved compositionally. The composition of the recrystallized alkali-feldspar is marginally impoverished in albite molecule $Or_{89-92}Ab_{7.8-10.7}An_{<1}Cs_{1.5-1.9}$ (Table-4.2a). The small patches of alkali feldspar in the myrmekite are distinctly rich in BaO (1.36-1.75 wt%) relative to the alkali-feldspar porphyroclasts (0.70-1.08 wt%, Table-4.2a). The composition of these fine remnants of alkali feldspar within myrmekite rim is $Or_{89.1-92.4}Ab_{7.5-10.4}An_{<1}Cs_{2.5-3.2}$. No significant compositional zoning in the alkali-

feldspar has been noted close to the myrmekite (Table-4.2a; Core: $Or_{89.4}Ab_{10.5}An_{<1}Cs_{1.3}$ and Rim immediate to myrmekite: $Or_{87.5}Ab_{12.4}An_{<1}Cs_{1.7}$).

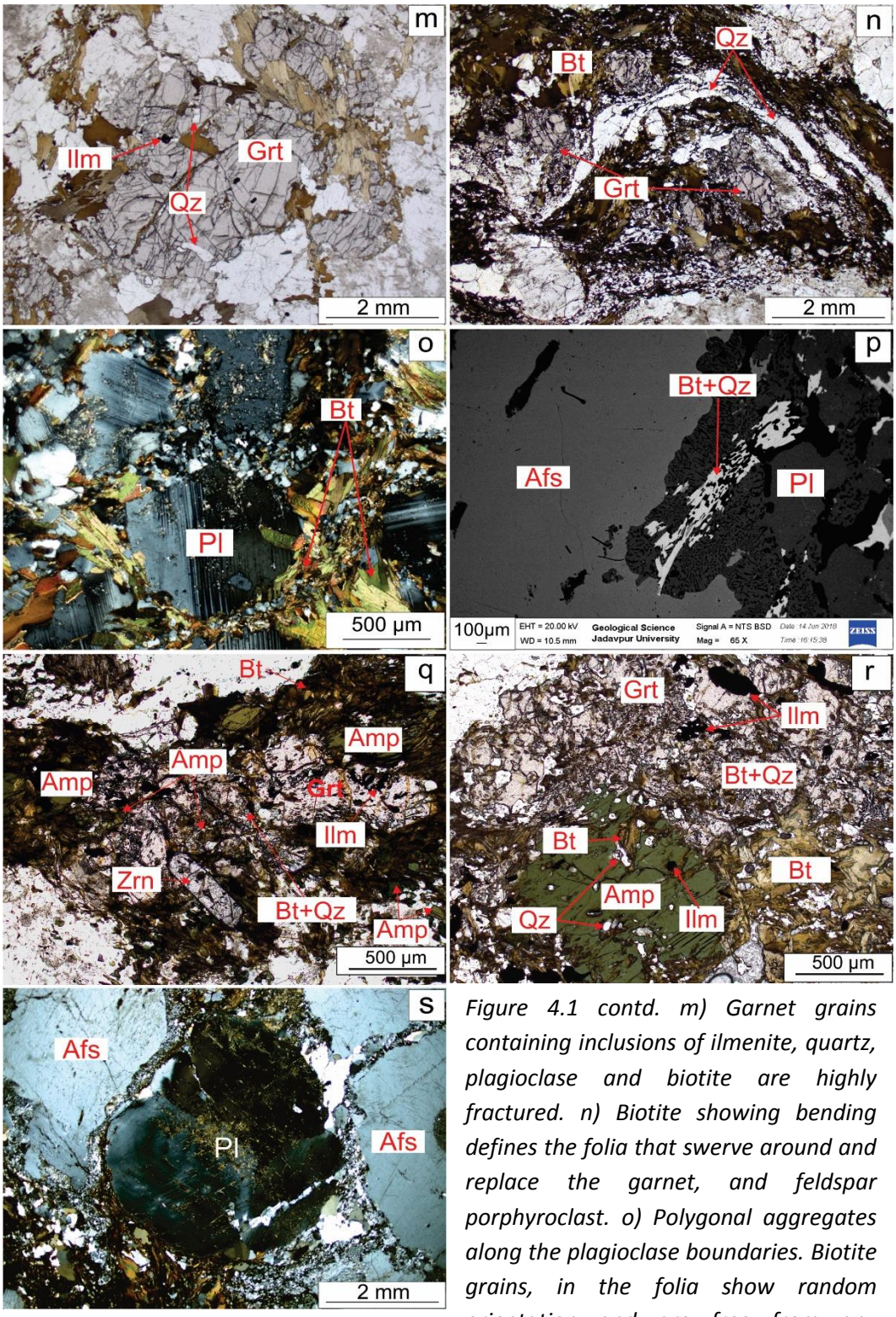

Figure 4.1 contd. m) Garnet grains containing inclusions of ilmenite, quartz, plagioclase and biotite are highly fractured. n) Biotite showing bending defines the folia that swerve around and replace the garnet, and feldspar porphyroclast. o) Polygonal aggregates along the plagioclase boundaries. Biotite grains, in the folia show random orientation and are free from any internal deformation.

Figure 4.1 contd. p) Biotite-quartz intergrowth replaces plagioclase porphyroclast as well as polygonal aggregates of quartz and plagioclase. q) Garnet porphyroblasts containing numerous inclusions are replaced secondary amphibole along corroded grain margins. r) Large amphibole grain containing quartz + ilmenite inclusions replaces garnet along with biotite. s) Partial recrystallization in oscillatory zoned plagioclase porphyroclast.

Table 4.2a: Representative chemical analyses for alkali-feldspar (representative oxygen basis is given). Mineral abbreviation is used after Whitney and Evans (2010). Cation calculations have been done following the procedure of Grew (1984).

Sample no	**SR89**	**SR89**	**SR89**	**SR89**	**SR89**	**SR89**	**SR89**	**SR89**	**SR89**	**SR89**	**SR89**	**SR89**	**SR89**	**SR89**	**SR89**	**SR89**	**SR89**	**SR89**	**SR89**	**SR89**	**SR89**
Mineral	*Afs*	*Afs*	*Afs*	*Afs*	*Afs*	*Afs*	*Afs*	*Afs*	*Afs*	*Afs*	*Afs*	*Afs*	*Afs*	*Afs*	*Afs*	*Afs*	*Afs*	*Afs*	*Afs*	*Afs*	*Afs*
Textural setting	*Phenocryst profile (Rim to Core)*																				
SiO_2	62.78	63.60	63.56	64.11	63.55	63.63	63.88	63.59	63.62	63.35	63.12	63.86	63.63	63.45	63.59	63.75	63.17	63.60	63.07	64.04	
TiO_2	0.21	0.05	0.01	0.03	0.01	0.03	0.02	0.02	0.02	0.01	0.02	0.00	0.02	0.03	0.03	0.03	0.03	-0.01	0.02	0.02	
Al_2O_3	18.72	18.94	18.66	18.77	18.75	18.74	19.01	18.71	18.82	19.02	18.91	18.89	18.91	18.89	19.02	18.86	19.03	18.84	18.69	18.82	
Cr_2O_3	-0.01	-0.01	-0.01	-0.01	0.01	-0.01	-0.02	0.00	-0.02	-0.03	0.00	-0.02	-0.02	-0.02	-0.03	-0.03	0.00	-0.02	-0.03	-0.02	
FeO	0.28	0.05	0.03	0.06	-0.13	-0.08	0.08	-0.03	-0.11	0.10	0.09	-0.10	0.01	0.09	0.04	0.07	-0.05	-0.14	0.04	0.15	
MnO	0.08	0.02	0.04	0.03	0.00	-0.12	-0.04	-0.07	0.03	-0.08	-0.02	-0.09	0.02	0.00	0.02	0.00	0.01	-0.02	0.02	-0.08	
MgO	0.00	0.00	0.02	0.00	0.01	-0.01	-0.01	0.00	0.01	0.01	0.00	0.02	0.00	0.01	0.01	0.00	0.01	-0.01	-0.01	0.01	
CaO	0.01	0.01	0.04	-0.03	0.02	0.00	-0.02	0.02	-0.01	0.02	0.04	0.02	0.21	0.04	0.02	0.07	0.05	0.04	0.04	0.03	
Na_2O	1.36	1.33	1.27	1.21	1.32	1.18	1.31	1.15	1.29	1.18	1.19	1.32	1.27	1.33	1.27	1.43	1.29	1.17	1.32	1.13	
K_2O	14.55	14.68	14.94	14.64	14.54	14.48	14.40	14.56	14.61	14.64	14.73	14.52	14.49	14.44	14.70	14.62	14.69	14.60	14.65	14.65	
BaO	0.95	0.94	0.85	0.80	0.84	0.99	0.97	0.92	0.90	0.94	0.89	0.86	0.81	0.79	0.75	0.73	0.74	0.80	0.70	0.70	
Sum	97.98	98.67	98.56	98.81	98.08	97.84	98.61	97.95	98.26	98.22	98.08	98.42	98.54	98.26	98.67	98.80	98.23	98.05	97.81	98.75	
Oxygen basis	**8**	**8**	**8**	**8**	**8**	**8**	**8**	**8**	**8**	**8**	**8**	**8**	**8**	**8**	**8**	**8**	**8**	**8**	**8**	**8**	
Si	2.96	2.97	2.97	2.98	2.98	2.98	2.97	2.98	2.98	2.97	2.96	2.98	2.97	2.97	2.97	2.97	2.96	2.98	2.97	2.98	
Ti	0.01	0.00	0.00	0.00	0.00	0.00	0.00	0.00	0.00	0.00	0.00	0.00	0.00	0.00	0.00	0.00	0.00	0.00	0.00	0.00	
Al-tot	1.04	1.04	1.03	1.03	1.04	1.04	1.04	1.03	1.04	1.05	1.05	1.04	1.04	1.04	1.05	1.04	1.05	1.04	1.04	1.03	
Cr	0.00	0.00	0.00	0.00	0.00	0.00	0.00	0.00	0.00	0.00	0.00	0.00	0.00	0.00	0.00	0.00	0.00	0.00	0.00	0.00	
Fe+2	0.01	0.00	0.00	0.00	-0.01	0.00	0.00	0.00	0.00	0.00	0.00	0.00	0.00	0.00	0.00	0.00	0.00	-0.01	0.00	0.01	
Mn	0.00	0.00	0.00	0.00	0.00	0.00	0.00	0.00	0.00	0.00	0.00	0.00	0.00	0.00	0.00	0.00	0.00	0.00	0.00	0.00	
Mg	0.00	0.00	0.00	0.00	0.00	0.00	0.00	0.00	0.00	0.00	0.00	0.00	0.00	0.00	0.00	0.00	0.00	0.00	0.00	0.00	
Ca	0.00	0.00	0.00	0.00	0.00	0.00	0.00	0.00	0.00	0.00	0.00	0.00	0.01	0.00	0.00	0.00	0.00	0.00	0.00	0.00	
Na	0.12	0.12	0.12	0.11	0.12	0.11	0.12	0.10	0.12	0.11	0.11	0.12	0.11	0.12	0.11	0.13	0.12	0.11	0.12	0.10	
K	0.87	0.87	0.89	0.87	0.87	0.87	0.86	0.87	0.87	0.87	0.88	0.86	0.86	0.86	0.87	0.87	0.88	0.87	0.88	0.87	
Ba	0.02	0.02	0.02	0.01	0.02	0.02	0.02	0.02	0.02	0.02	0.02	0.02	0.01	0.01	0.01	0.01	0.01	0.01	0.01	0.01	
Sum	5.02	5.01	5.02	4.99	5.00	4.98	4.99	4.99	5.00	5.00	5.01	4.99	5.00	5.00	5.01	5.01	5.01	4.99	5.01	4.99	
Or - KAlSi3O8	*0.88*	*0.88*	*0.88*	*0.89*	*0.88*	*0.89*	*0.88*	*0.89*	*0.88*	*0.89*	*0.89*	*0.88*	*0.87*	*0.88*	*0.88*	*0.87*	*0.88*	*0.89*	*0.88*	*0.89*	
Ab - NaAlSi3O8	*0.12*	*0.12*	*0.11*	*0.11*	*0.12*	*0.11*	*0.12*	*0.11*	*0.12*	*0.11*	*0.11*	*0.12*	*0.12*	*0.12*	*0.12*	*0.13*	*0.12*	*0.11*	*0.12*	*0.10*	
An - CaAl2Si2O8	*0.00*	*0.00*	*0.00*	*0.00*	*0.00*	*0.00*	*0.00*	*0.00*	*0.00*	*0.00*	*0.00*	*0.00*	*0.01*	*0.00*	*0.00*	*0.00*	*0.00*	*0.00*	*0.00*	*0.00*	
Celsian X-Ba	*1.72*	*1.70*	*1.52*	*1.47*	*1.53*	*1.83*	*1.79*	*1.70*	*1.64*	*1.72*	*1.62*	*1.57*	*1.48*	*1.45*	*1.37*	*1.31*	*1.34*	*1.48*	*1.27*	*1.29*	

Table 4.2a (continued): Representative chemical analyses for alkali-feldspar (representative oxygen basis is given). Mineral abbreviation is used after Whitney and Evans (2010). Cation calculations have been done following the procedure of Grew (1984).

Sample no	**SR89**	**SR89**	**SR89**	**SR89**	**SR89**	**SR89**	**SR89**	**SR91**	**SR91**	**SR91**	**SR145**	**SR145**
Mineral	*Afs*	*Afs*	*Afs*	*Afs*	*Afs*	*Afs*	*Afs*	*Afs*	*Afs*	*Afs*	*Afs*	*Afs*
Textural setting	*Fine remnants within the Myr1*			*Matrix*				*Pheno cryst*	*Pheno cryst*	*Matrix*	*Matrix*	*Matrix*
SiO_2	62.76	63.56	64.13	64.09	63.61	64.87	65.26	65.35	65.41	65.22	64.65	64.84
TiO_2	0.01	0.01	0.00	0.01	0.02	0.00	0.00	0.00	0.00	0.00	0.00	0.01
Al_2O_3	19.21	20.26	18.63	18.38	18.98	18.22	18.22	18.22	18.06	18.37	18.19	18.27
Cr_2O_3	0.00	0.00	0.01	0.00	0.00	0.04	0.05	0.08	0.00	0.14	0.23	0.07
FeO	0.00	0.02	0.00	0.00	0.00	0.26	0.00	0.00	0.03	0.00	0.00	0.00
MnO	0.00	0.00	0.02	0.00	0.00	0.01	0.04	0.00	0.00	0.00	0.00	0.00
MgO	0.01	0.00	0.00	0.00	0.00	0.00	0.00	0.00	0.00	0.00	0.00	0.00
CaO	0.04	0.00	0.05	0.00	0.04	0.00	0.00	0.00	0.00	0.00	0.00	0.00
Na_2O	0.83	1.13	0.90	1.02	1.18	0.94	0.85	0.87	0.98	0.97	0.59	0.75
K_2O	15.02	14.51	14.97	14.92	14.94	15.09	15.15	15.47	15.43	15.18	15.66	15.52
BaO	1.75	1.53	1.36	0.84	1.08	0.88	0.91	-	-	-	-	-
Sum	99.63	101.02	100.08	99.26	99.85	99.44	99.57	99.99	99.90	99.88	99.42	99.47
Oxygen basis	**8**	**8**	**8**	**8**	**8**	**8**	**8**	**8**	**8**	**8**	**8**	**8**
Si	2.95	2.94	3.00	3.00	2.97	3.00	3.01	3.02	3.02	3.01	3.01	3.01
Ti	0.00	0.00	0.00	0.00	0.00	0.00	0.00	0.00	0.00	0.00	0.00	0.00
Al-tot	1.07	1.10	1.03	1.01	1.04	0.99	0.99	0.99	0.98	1.00	1.00	1.00
Cr	0.00	0.00	0.00	0.00	0.00	0.00	0.00	0.04	0.01	0.05	0.04	0.04
Fe+2	0.00	0.00	0.00	0.00	0.00	0.01	0.00	0.00	0.00	0.00	0.00	0.00
Mn	0.00	0.00	0.00	0.00	0.00	0.00	0.00	0.00	0.00	0.00	0.00	0.00
Mg	0.00	0.00	0.00	0.00	0.00	0.00	0.00	0.00	0.00	0.00	0.00	0.00
Ca	0.00	0.00	0.00	0.00	0.00	0.00	0.00	0.00	0.00	0.00	0.00	0.00
Na	0.08	0.10	0.08	0.09	0.11	0.08	0.08	0.08	0.09	0.09	0.05	0.07
K	0.90	0.86	0.89	0.89	0.89	0.89	0.89	0.91	0.91	0.89	0.93	0.92
Ba	0.03	0.03	0.02	0.02	0.02	0.02	0.02	-	-	-	-	-
Sum	5.00	5.01	4.98	4.99	5.01	4.99	4.97	5.00	5.00	5.00	5.00	5.00
Or - KAlSi3O8	*0.89*	*0.89*	*0.91*	*0.91*	*0.89*	*0.91*	*0.92*	*0.92*	*0.91*	*0.91*	*0.95*	*0.93*
Ab - NaAlSi3O8	*0.07*	*0.11*	*0.08*	*0.09*	*0.11*	*0.09*	*0.08*	*0.08*	*0.09*	*0.09*	*0.05*	*0.07*
An - CaAl2Si2O8	*0.00*	*0.00*	*0.00*	*0.00*	*0.00*	*0.00*	*0.00*	*0.00*	*0.00*	*0.00*	*0.00*	*0.00*
Celsian X-Ba	*3.19*	*2.70*	*2.52*	*1.55*	*1.94*	*1.57*	*1.66*	-	-	-	-	-

The oscillatory zoned plagioclase, presumably inherited magmatic characters, show alternation of relatively anorthite poor ($Ab_{59-61}An_{38-41}Or_{<1}$) and anorthite rich ($Ab_{47-50}An_{49-52}Or_{<1}$) compositions (Table-4.2b). Proximal to secondary biotite and myrmekite, the plagioclase porphyroclasts show normal compositional zoning with anorthite-rich core ($Ab_{50}An_{49}Or_1$) and anorthite poor rim ($Ab_{57}An_{42.5}Or_{0.5}$, Table-4.2b). The plagioclase base of myrmekite shows systematic chemical zoning. Plagioclase in Myr1 from the fine variety in contact with alkali feldspar to relatively thick vermicular quartz away from myrmekite front shows a very small decrease in albite component ($Ab_{61.6}An_{37.9}Or_{0.5\text{-}0.9}$ to $Ab_{60.6}An_{38.9}Or_{0.5}$) (Table-4.2b). A sharp

change is noted across Myr1 and Myr2 where polygonal plagioclase in Myr2 is distinctly anorthite rich ($Ab_{58}An_{41}Or_1$ to $Ab_{53}An_{46}Or_1$; Table-4.2b).

Table 4.2b: Representative chemical analyses for plagioclase (representative oxygen basis is given). Mineral abbreviation is used after Whitney and Evans (2010). Cation calculations have been done following the procedure of Grew (1984).

Sample no	**SR89**	**SR89**	**SR89**	**SR89**	**SR91**	**SR91**	**SR91**	**SR91**	**SR91**	**SR91**
Mineral	***Pl#***	*Pl*	*Pl*	*Pl*	*Pl*	*Pl*	*Pl*	*Pl*	*Pl*	*Pl*
Textural setting	*Porphyroclast (Rim)*		*Porphyroclast (Core)*		*Oscillatory zoned plagioclase porphyroclast (Rim to Core)*					
SiO_2	57.62	57.00	54.79	56.44	59.46	56.87	59.65	56.27	58.63	55.13
TiO_2	0.00	0.00	0.01	0.00	0.00	0.00	0.02	0.00	0.00	0.00
Al_2O_3	26.60	27.05	27.22	28.03	25.88	27.56	24.57	28.05	26.54	27.83
Cr_2O_3	0.00	0.00	0.00	0.00	0.01	0.00	0.03	0.03	0.10	0.00
FeO	0.00	0.00	0.12	0.03	0.06	0.05	0.12	0.04	0.16	0.02
MnO	0.00	0.04	0.00	0.03	0.00	0.01	0.01	0.05	0.00	0.00
MgO	0.00	0.00	0.00	0.00	0.00	0.00	0.00	0.00	0.00	0.00
CaO	8.99	8.44	10.09	10.22	8.06	10.12	6.76	10.50	8.61	10.82
Na_2O	6.62	6.23	5.78	5.77	7.14	5.76	6.92	5.70	6.90	5.38
K_2O	0.09	0.22	0.12	0.16	0.14	0.19	1.47	0.18	0.12	0.17
BaO	0.00	0.02	0.03	0.00	0.00	0.00	0.00	0.00	0.00	0.00
Sum	99.92	100.07	98.15	100.72	100.75	100.56	99.55	100.82	101.09	99.35
Oxygen basis	**8**	**8**	**8**	**8**	**8**	**8**	**8**	**8**	**8**	**8**
Si	2.58	2.58	2.51	2.52	2.64	2.54	2.68	2.51	2.60	2.50
Ti	0.00	0.00	0.00	0.00	0.00	0.00	0.00	0.00	0.00	0.00
Al-tot	1.41	1.44	1.47	1.48	1.35	1.45	1.30	1.48	1.39	1.49
Cr	0.00	0.00	0.00	0.00	0.00	0.00	0.00	0.00	0.00	0.00
Fe+2	0.00	0.00	0.00	0.00	0.00	0.00	0.00	0.00	0.01	0.00
Mn	0.00	0.00	0.00	0.00	0.00	0.00	0.00	0.00	0.00	0.00
Mg	0.00	0.00	0.00	0.00	0.00	0.00	0.00	0.00	0.00	0.00
Ca	0.43	0.41	0.50	0.49	0.38	0.48	0.33	0.50	0.41	0.53
Na	0.58	0.55	0.51	0.50	0.61	0.50	0.60	0.49	0.59	0.47
K	0.01	0.01	0.01	0.01	0.01	0.01	0.08	0.01	0.01	0.01
Ba	0.00	0.00	0.00	0.00	0.00	0.00	0.00	0.00	0.00	0.00
Sum	5.00	4.98	5.01	5.00	5.00	4.99	5.01	5.00	5.01	5.00
Or - KAlSi3O8	*0.01*	*0.01*	*0.01*	*0.01*	*0.01*	*0.01*	*0.08*	*0.01*	*0.01*	*0.01*
Ab - NaAlSi3O8	*0.57*	*0.56*	*0.51*	*0.50*	*0.61*	*0.50*	*0.60*	*0.49*	*0.59*	*0.47*
An - CaAl2Si2O8	*0.43*	*0.42*	*0.49*	*0.49*	*0.38*	*0.49*	*0.32*	*0.50*	*0.41*	*0.52*
Celsian X-Ba	*0.00*	*0.04*	*0.06*	*0.00*	*0.00*	*0.00*	*0.00*	*0.00*	*0.00*	*0.00*

#' denotes the mineral compositions used for C-space textural modeling

Table 4.2b (continued): Representative chemical analyses for plagioclase (representative oxygen basis is given). Mineral abbreviation is used after Whitney and Evans (2010). Cation calculations have been done following the procedure of Grew (1984).

Sample no	**SR89**	**SR89**	**SR89**	**SR89**	**SR89**	**SR89**	**SR89**	**SR89**	**SR89**	**SR89**	**SR89**
Mineral	***Pl#***	*Pl*	*Pl*	*Pl*	*Pl*	*Pl*	*Pl*	***Pl#***	*Pl*	*Pl*	*Pl*
Textural setting	*Myr1 (profile from Afs boundary towards Pl porphyroclast*					*(towards Pl porphyroclast)*			*Myr2 (direct contact of Afs)*		
SiO_2	58.34	57.81	57.94	57.63	58.08	58.47	56.03	55.50	58.57	58.45	57.47
TiO_2	-0.01	0.02	0.00	0.03	0.00	-0.02	0.02	0.00	0.02	0.00	0.00
Al_2O_3	26.41	26.95	26.78	26.54	27.06	26.71	27.71	27.96	26.22	26.65	27.17
Cr_2O_3	0.01	0.00	0.00	-0.01	0.01	0.01	0.01	0.00	0.00	0.00	0.00
FeO	-0.04	0.06	0.07	0.12	0.11	0.12	0.18	0.17	0.21	0.00	0.07
MnO	-0.07	-0.05	0.07	0.06	-0.02	0.01	0.02	0.04	0.00	0.08	0.00
MgO	0.01	0.00	0.00	-0.01	0.00	0.00	-0.01	0.00	0.00	0.00	0.02
CaO	8.14	8.12	8.22	8.25	8.36	8.59	9.63	9.75	9.77	9.43	9.37
Na_2O	7.31	7.18	7.22	7.21	7.21	6.86	6.33	6.19	6.52	5.89	6.18
K_2O	0.09	0.09	0.11	0.17	0.10	0.28	0.18	0.15	0.16	0.06	0.22
BaO	-0.01	0.00	0.01	-0.04	0.00	-0.01	0.00	0.00	0.00	0.02	0.01
Sum	100.19	100.18	100.41	99.99	100.91	101.03	100.10	99.76	101.47	100.66	100.50
Oxygen basis	**8**	**8**	**8**	**8**	**8**	**8**	**8**	**8**	**8**	**8**	**8**
Si	2.61	2.58	2.59	2.59	2.58	2.59	2.52	2.51	2.59	2.60	2.57
Ti	0.00	0.00	0.00	0.00	0.00	0.00	0.00	0.00	0.00	0.00	0.00
Al-tot	1.39	1.42	1.41	1.40	1.42	1.40	1.47	1.49	1.37	1.40	1.43
Cr	0.00	0.00	0.00	0.00	0.00	0.00	0.00	0.00	0.00	0.00	0.00
Fe+2	0.00	0.00	0.00	0.00	0.00	0.00	0.01	0.01	0.01	0.00	0.00
Mn	0.00	0.00	0.00	0.00	0.00	0.00	0.00	0.00	0.00	0.00	0.00
Mg	0.00	0.00	0.00	0.00	0.00	0.00	0.00	0.00	0.00	0.00	0.00
Ca	0.39	0.39	0.39	0.40	0.40	0.41	0.46	0.47	0.46	0.45	0.45
Na	0.63	0.62	0.62	0.63	0.62	0.59	0.55	0.54	0.56	0.51	0.54
K	0.01	0.01	0.01	0.01	0.01	0.02	0.01	0.01	0.01	0.00	0.01
Ba	0.00	0.00	0.00	0.00	0.00	0.00	0.00	0.00	0.00	0.00	0.00
Sum	5.02	5.02	5.02	5.03	5.02	5.01	5.02	5.02	5.00	4.96	4.99
Or - KAlSi3O8	*0.00*	*0.01*	*0.01*	*0.01*	*0.01*	*0.02*	*0.01*	*0.01*	*0.01*	*0.00*	*0.01*
Ab - NaAlSi3O8	*0.62*	*0.61*	*0.61*	*0.61*	*0.61*	*0.58*	*0.54*	*0.53*	*0.54*	*0.53*	*0.54*
An - CaAl2Si2O8	*0.38*	*0.38*	*0.38*	*0.38*	*0.39*	*0.40*	*0.45*	*0.46*	*0.45*	*0.47*	*0.45*
Celsian X-Ba	*-0.02*	*0.00*	*0.02*	*-0.07*	*0.00*	*-0.02*	*0.00*	*0.00*	*0.00*	*0.04*	*0.01*

#' denotes the mineral compositions used for C-space textural modeling

Table 4.2b (continued): Representative chemical analyses for plagioclase (representative oxygen basis is given). Mineral abbreviation is used after Whitney and Evans (2010). Cation calculations have been done following the procedure of Grew (1984).

Sample no	**SR89**	**SR89**	**SR89**	**SR89**	**SR89**	**SR91**	**SR91**	**SR145**	**SR145**	**SR145**
Mineral	*Pl*	*Pl*	*Pl*	*Pl*	*Pl*	**Pl**	**Pl**	**Pl**	**Pl**	**Pl**
Textural setting	*Myr1 (at veins/apophyges*			*Matrix*		*Matrix ^Grt, Bt*	*Matrix ^Grt, Amp*	*Matrix ^Grt, Amp*	*Matrix ^Grt, Amp*	*Inclusion ^Grt*
SiO_2	57.62	59.73	55.94	55.98	58.22	59.36	59.07	63.19	62.72	63.01
TiO_2	0.00	0.00	-0.01	-0.01	0.00	0.00	0.00	0.01	0.00	0.00
Al_2O_3	26.80	25.53	27.60	28.20	26.76	25.71	25.67	22.81	22.16	23.11
Cr_2O_3	-0.01	0.00	0.01	0.01	0.00	0.05	0.21	0.40	0.27	0.15
FeO	0.02	0.00	-0.01	0.06	0.12	0.02	0.00	0.00	0.00	0.02
MnO	0.06	0.00	-0.06	-0.01	0.05	0.00	0.00	0.00	0.00	0.00
MgO	-0.01	0.00	0.01	-0.01	0.00	0.00	0.00	0.00	0.00	0.00
CaO	8.31	7.36	9.56	9.77	8.79	7.89	7.91	4.79	4.15	4.78
Na_2O	7.24	6.63	6.43	6.03	6.73	7.02	7.24	8.95	8.92	9.05
K_2O	0.14	0.07	0.19	0.17	0.15	0.14	0.11	0.12	0.27	0.13
BaO	-0.02	0.00	0.00	0.02	0.00	0.00	0.00	0.00	0.00	0.00
Sum	100.17	100.39	99.66	100.19	100.97	100.19	100.20	100.27	98.49	100.25
Oxygen basis	**8**	**8**	**8**	**8**	**8**	**8**	**8**	**8**	**8**	**8**
Si	2.58	2.67	2.53	2.51	2.59	2.65	2.63	2.80	2.82	2.78
Ti	0.00	0.00	0.00	0.00	0.00	0.00	0.00	0.00	0.00	0.00
Al-tot	1.41	1.35	1.47	1.49	1.40	1.35	1.35	1.19	1.18	1.20
Cr	0.00	0.00	0.00	0.00	0.00	0.04	0.00	0.02	0.03	0.00
Fe+2	0.00	0.00	0.00	0.00	0.00	0.00	0.00	0.00	0.00	0.00
Mn	0.00	0.00	0.00	0.00	0.00	0.00	0.00	0.00	0.00	0.00
Mg	0.00	0.00	0.00	0.00	0.00	0.00	0.00	0.00	0.00	0.00
Ca	0.40	0.35	0.46	0.47	0.42	0.38	0.38	0.23	0.20	0.23
Na	0.63	0.57	0.56	0.52	0.58	0.61	0.63	0.77	0.78	0.77
K	0.01	0.00	0.01	0.01	0.01	0.01	0.01	0.01	0.02	0.01
Ba	0.00	0.00	0.00	0.00	0.00	0.00	0.00	0.00	0.00	0.00
Sum	5.03	4.95	5.03	5.01	5.00	5.00	5.00	5.00	5.00	5.00
Or - KAlSi3O8	*0.01*	*0.00*	*0.01*	*0.01*	*0.01*	*0.01*	*0.01*	*0.01*	*0.02*	*0.01*
Ab - NaAlSi3O8	*0.61*	*0.62*	*0.54*	*0.52*	*0.58*	*0.61*	*0.62*	*0.77*	*0.78*	*0.77*
An - CaAl2Si2O8	*0.39*	*0.38*	*0.45*	*0.47*	*0.42*	*0.38*	*0.37*	*0.23*	*0.20*	*0.22*
Celsian X-Ba	*-0.03*	*0.00*	*0.00*	*0.04*	*0.00*	*0.00*	*0.00*	*0.00*	*0.00*	*0.00*

Garnet: In the porphyritic metagranitoid where biotite is the only hydrous ferromagnesian phase garnet is chiefly constituted of almandine and pyrope ($X_{Alm}+X_{Prp} \geq$ 85 mol%) with minor grossular and spessartine component (Table-4.2c). Garnet is compositionally homogeneous from core to rim portion of the grain ($Alm_{77-80}Prp_{8-9}Grs_7Sps_{5-7}$) (Table-4.2c). In amphibole-present samples, grossular component [$X_{Grs}=Ca/(Fe^{2+}+Mg+Ca+Mn)$] is relatively high (core: X_{Grs}=0.21-0.23 and rim: X_{Grs}=0.16-0.17; Table-4.2c) than the amphibole-absent ones (X_{Grs}=0.07-0.09). In these

Table 4.2c: Representative chemical analyses for garnet (representative oxygen basis is given). Mineral abbreviation is used after Whitney and Evans (2010). Cation calculations have been done following the procedure of Grew (1984).

Sample no	**SR89**	**SR89**	**SR89**	**SR89**	**SR89**	**SR89**	**SR89**	**SR89**	**SR89**	**SR89**	**SR91**	**SR91**	**SR91**	**SR91**	**SR145**	**SR145**	**SR145**	**SR145**	**SR145**	**SR145**	**SR145**
Mineral	*Grt*	*Grt*	*Grt*	***Grt#***	*Grt*	*Grt*	*Grt*	*Grt*	*Grt*	*Grt*	*Grt*	*Grt*	*Grt*	*Grt*	*Grt*	*Grt*	*Grt*	*Grt*	*Grt*	*Grt*	*Grt*
Textural setting	*Porphyroblast (Rim to Core)*										*Rim*	*Rim*	*Core*	*Core*		*Core*			*Rim*		
SiO_2	37.02	36.6	36.52	36.43	36.46	36.60	36.69	36.55	36.31	36.39	37.43	38.08	37.54	38.18	37.09	37.46	37.43	37.05	36.95	37.32	37.14
TiO_2	0.04	0.05	0.03	0.04	0.05	0.03	0.05	0.05	0.03	0.05	0.00	0.01	0.00	0.00	0.07	0.08	0.08	0.04	0.04	0.05	0.02
Al_2O_3	20.47	20.72	20.94	20.71	20.79	20.76	20.90	21.01	20.99	20.92	21.20	22.37	21.16	21.27	20.34	20.56	20.43	20.63	20.39	20.58	20.87
Cr_2O_3	0.02	0	0.01	0.00	-0.01	0.02	0.01	0.00	0.03	0.07	0.02										
FeO	34.98	36.25	36.98	36.10	35.84	35.95	36.32	35.34	34.52	34.56	28.28	26.23	27.11	27.10	32.35	31.70	33.32	32.31	34.39	33.61	34.40
MnO	2.11	2.47	2.23	2.63	2.60	2.59	2.86	2.34	2.80	2.88	4.17	4.93	5.29	4.80	0.61	0.76	0.76	0.67	0.76	0.72	0.70
MgO	1.53	1.97	2.18	2.25	2.20	2.06	2.07	2.17	2.37	2.29	0.85	0.90	1.44	1.79	2.48	1.65	1.88	2.70	2.16	2.54	2.37
CaO	2.45	2.41	2.47	2.49	2.47	2.51	2.48	3.52	2.53	2.42	8.01	7.46	7.94	8.35	7.14	7.69	7.68	7.25	5.77	5.45	6.02
Na_2O	0.00	0.00	0.01	0.01	-0.02	0.02	0.01	0.02	0.01	0.06	0.00	0.02	0.01	0.01	0.00	0.04	0.02	0.01	0.00	0.00	0.00
K_2O	0.01	0.00	0.00	0.00	0.02	-0.01	0.00	0.01	-0.02	0.00	0.02	0.00	0.00	0.00	0.01	0.00	0.01	0.02	0.00	0.01	0.00
Sum	98.63	100.47	101.37	100.66	100.40	100.53	101.39	101.01	99.57	99.64	99.96	100.00	100.50	101.51	100.11	99.96	101.61	100.67	100.47	100.28	101.61
Oxygen basis	**12**	**12**	**12**	**12**	**12**	**12**	**12**	**12**	**12**	**12**	**12**	**12**	**12**	**12**	**12**	**12**	**12**	**12**	**12**	**12**	**12**
Si	3.02	2.96	2.92	2.95	2.96	2.97	2.96	2.95	2.96	2.96	3.01	3.05	2.99	3.01	2.97	3.01	2.96	2.94	2.96	2.99	2.94
Ti	0.00	0.00	0.00	0.00	0.00	0.00	0.00	0.00	0.00	0.00	0.00	0.00	0.00	0.00	0.00	0.01	0.00	0.00	0.00	0.00	0.00
Al	1.97	1.97	1.98	1.98	1.99	1.98	1.98	2.00	2.02	2.01	2.01	2.11	1.99	1.97	1.92	1.94	1.90	1.93	1.93	1.94	1.95
Cr	0.00	0.00	0.00	0.00	0.00	0.00	0.00	0.00	0.00	0.00	0.00	0.00	0.00	0.00	0.00	0.00	0.00	0.00	0.00	0.00	0.00
Fe+2	2.41	2.35	2.30	2.45	2.43	2.44	2.45	2.38	2.35	2.35	1.93	1.96	1.78	1.77	2.02	2.09	2.03	1.96	2.16	2.17	2.10
Fe+3	0.22	0.17	0.15	0.00	0.00	0.00	0.00	0.00	0.00	0.00	0.00	0.00	0.00	0.00	0.00	0.00	0.00	0.00	0.00	0.00	0.00
Mn	0.19	0.24	0.26	0.18	0.18	0.18	0.20	0.16	0.19	0.20	0.28	0.33	0.36	0.32	0.04	0.05	0.05	0.05	0.05	0.05	0.05
Mg	0.21	0.21	0.21	0.27	0.27	0.25	0.25	0.26	0.29	0.28	0.10	0.11	0.17	0.21	0.30	0.20	0.22	0.32	0.26	0.30	0.28
Ca	0.00	0.00	0.00	0.22	0.21	0.22	0.21	0.30	0.22	0.21	0.69	0.64	0.68	0.70	0.61	0.66	0.65	0.62	0.50	0.47	0.51
Na	0.00	0.00	0.00	0.00	0.00	0.00	0.00	0.00	0.00	0.01	0.00	0.00	0.00	0.00	0.00	0.01	0.00	0.00	0.00	0.00	0.00
K	0.00	0.00	0.00	0.00	0.00	0.00	0.00	0.00	0.00	0.00	0.00	0.00	0.00	0.00	0.00	0.00	0.00	0.00	0.00	0.00	0.00
Sum	8.00	8.00	8.00	8.05	8.04	8.04	8.05	8.06	8.03	8.03	8.00	8.00	8.00	8.00	8.00	8.00	8.00	8.00	8.00	8.00	8.00
Alm- Fe3Al2	*0.80*	*0.79*	*0.78*	*0.79*	*0.79*	*0.79*	*0.79*	*0.77*	*0.77*	*0.77*	*0.64*	*0.64*	*0.60*	*0.59*	*0.68*	*0.68*	*0.68*	*0.67*	*0.73*	*0.73*	*0.72*
Sps- Mn3Al2	*0.05*	*0.06*	*0.06*	*0.06*	*0.06*	*0.06*	*0.06*	*0.05*	*0.06*	*0.07*	*0.09*	*0.10*	*0.12*	*0.12*	*0.01*	*0.02*	*0.02*	*0.02*	*0.02*	*0.02*	*0.02*
Prp- Mg3Al2	*0.08*	*0.08*	*0.08*	*0.09*	*0.09*	*0.08*	*0.08*	*0.08*	*0.09*	*0.09*	*0.03*	*0.04*	*0.06*	*0.07*	*0.10*	*0.08*	*0.08*	*0.10*	*0.09*	*0.10*	*0.10*
Grs- Ca3Al2	*0.07*	*0.07*	*0.07*	*0.07*	*0.07*	*0.07*	*0.07*	*0.10*	*0.07*	*0.07*	*0.23*	*0.22*	*0.23*	*0.23*	*0.21*	*0.23*	*0.22*	*0.22*	*0.17*	*0.16*	*0.17*

#' denotes the mineral compositions used for C-space textural modeling

samples, core of the garnet porphyroblasts are mildly impoverished in almandine component than their rim parts. This weak compositional zoning is present at the contact of amphibole and biotite and the compositional range varies in different samples (SR91: core: $Alm_{59}Prp_{7}Grs_{23}Sps_{12}$ and rim: $Alm_{64}Prp_{3}Grs_{23}Sps_{9}$; SR145: core: $Alm_{67}Prp_{10}Grs_{22}Sps_{2}$ and rim: $Alm_{73}Prp_{10}Grs_{16}Sps_{2}$) (Table-4.2c).

Amphibole: According to the classification of Leake et al.(2004), the amphibole in porphyritic metagranitoid is dominantly ferropargasite in composition with X_{Mg} vary in a restricted range of 0.15-0.29. TiO_2 content of the amphibole ranges between 0.36-1.77 wt% (Table-4.2d).

Biotite: In all the analyzed samples, biotite (both inclusion and secondary) are Fe-rich with X_{Mg} in the range of 0.15-0.32 (Table-4.2e). TiO_2 of the biotite is distinctly high (1.98-4.27 wt%). X_{Mg} value show minor variation in different samples (SR145: 0.15-0.21; SR91: 0.25-0.27; SR89: 0.30-0.32; Table-4.2e).

Ilmenite: Ilmenite, associated with the matrix and included within porphyroblastic garnet is pure in composition with a very minor Fe^{3+} content (0.03 apfu).

Table 4.2d: Representative chemical analyses for amphibole (representative oxygen basis is given). Mineral abbreviation is used after Whitney and Evans (2010). Cation calculations have been done following the procedure of Leake et al. (2004).

Sample no	**SR91**	**SR91**	**SR91**	**SR91**	**SR145**	**SR145**	**SR145**	**SR145**	**SR145**	**SR145**	**SR145**	**SR145**	**SR145**	**SR145**
Mineral	**Amp**	**Amp**	**Amp**	**Amp**	**Amp**	**Amp**	**Amp**	**Amp**	**Amp**	**Amp**	**Amp**	**Amp**	**Amp**	**Amp**
Textural setting	*^Grt*	*^Grt*	*Matrix ^Pl*	*Matrix ^Pl*		*Porphyroblast (rim to core)*				*Inclusion ^Grt*	*^Grt,Pl*	*^Grt,Pl*	*Matrix ^Pl*	*Matrix ^Pl*
SiO_2	40.67	40.04	41.15	40.51	39.50	40.87	39.81	40.17	40.34	39.31	39.34	39.42	39.58	39.92
TiO_2	0.84	0.80	0.36	0.40	1.62	1.50	1.58	1.65	1.57	1.64	1.57	1.77	1.46	1.05
Al_2O_3	11.88	12.41	11.94	12.23	11.31	10.99	11.16	11.38	10.76	11.70	11.40	11.56	11.43	11.39
FeO	25.30	25.12	24.91	26.05	27.38	26.96	27.70	27.78	28.26	26.96	27.83	27.56	27.96	27.89
MnO	0.26	0.38	0.17	0.44	0.16	0.20	0.25	0.25	0.16	0.26	0.07	0.25	0.10	0.19
MgO	4.31	4.45	4.97	4.59	2.75	3.05	2.76	2.93	2.90	3.02	2.79	2.71	2.87	3.11
CaO	11.47	11.19	11.58	11.44	11.05	10.85	10.81	10.90	10.87	11.20	11.09	11.01	11.22	11.25
Na_2O	1.07	1.07	1.01	1.09	1.28	1.19	1.41	1.44	1.25	1.41	1.35	1.47	1.15	1.22
K_2O	1.49	1.54	1.38	1.42	1.60	1.38	1.56	1.63	1.47	1.57	1.61	1.69	1.55	1.40
Total	97.34	97.01	97.47	98.18	96.67	97.04	97.03	98.15	97.58	97.06	97.10	97.45	97.37	97.47
Oxygen basis	**23**	**23**	**23**	**23**	**23**	**23**	**23**	**23**	**23**	**23**	**23**	**23**	**23**	**23**
Si	6.38	6.28	6.39	6.27	6.34	6.48	6.37	6.35	6.41	6.28	6.30	6.29	6.30	6.33
Al (IV)	1.62	1.72	1.61	1.73	1.66	1.52	1.63	1.65	1.59	1.72	1.70	1.71	1.70	1.67
Ti	0.00	0.00	0.00	0.00	0.00	0.00	0.00	0.00	0.00	0.00	0.00	0.00	0.00	0.00
Sum T	8.00	8.00	8.00	8.00	8.00	8.00	8.00	8.00	8.00	8.00	8.00	8.00	8.00	8.00
Al (VI)	0.58	0.57	0.58	0.51	0.49	0.54	0.47	0.47	0.42	0.49	0.45	0.47	0.44	0.45
Ti	0.10	0.09	0.04	0.05	0.20	0.18	0.19	0.20	0.19	0.20	0.19	0.21	0.17	0.13
Fe+3	0.30	0.45	0.44	0.62	0.15	0.18	0.20	0.21	0.27	0.17	0.23	0.15	0.32	0.40
Mg	1.01	1.04	1.15	1.06	0.66	0.72	0.66	0.69	0.69	0.72	0.67	0.64	0.68	0.73
Fe+2	3.01	2.84	2.79	2.75	3.50	3.38	3.48	3.44	3.43	3.43	3.46	3.52	3.37	3.28
Mn	0.00	0.00	0.00	0.01	0.00	0.00	0.00	0.00	0.00	0.00	0.00	0.00	0.00	0.00
Li	0.00	0.00	0.00	0.00	0.00	0.00	0.00	0.00	0.00	0.00	0.00	0.00	0.00	0.00
Sum C	5.00	5.00	5.00	5.00	5.00	5.00	5.00	5.00	5.00	5.00	5.00	5.00	5.00	5.00
Mg	0.00	0.00	0.00	0.00	0.00	0.00	0.00	0.00	0.00	0.00	0.00	0.00	0.00	0.00
Fe+2	0.00	0.01	0.01	0.00	0.02	0.02	0.02	0.03	0.05	0.00	0.04	0.01	0.03	0.02
Mn	0.03	0.05	0.02	0.05	0.02	0.03	0.03	0.03	0.02	0.03	0.01	0.03	0.01	0.03
Li	0.00	0.00	0.00	0.00	0.00	0.00	0.00	0.00	0.00	0.00	0.00	0.00	0.00	0.00
Ca	1.93	1.88	1.93	1.90	1.90	1.85	1.85	1.85	1.85	1.92	1.90	1.88	1.91	1.91
Na	0.04	0.06	0.04	0.05	0.05	0.10	0.09	0.09	0.08	0.04	0.05	0.07	0.05	0.05
Sum B	2.00	2.00	2.00	2.00	2.00	2.00	2.00	2.00	2.00	2.00	2.00	2.00	2.00	2.00
Ca	0.00	0.00	0.00	0.00	0.00	0.00	0.00	0.00	0.00	0.00	0.00	0.00	0.00	0.00
Na	0.29	0.26	0.27	0.27	0.35	0.26	0.35	0.35	0.31	0.39	0.37	0.38	0.31	0.33
K	0.30	0.31	0.27	0.28	0.33	0.28	0.32	0.33	0.30	0.32	0.33	0.34	0.31	0.28
Sum A	0.58	0.57	0.54	0.55	0.67	0.54	0.66	0.68	0.60	0.71	0.70	0.73	0.62	0.61
TOTAL	15.58	15.57	15.54	15.55	15.67	15.54	15.66	15.68	15.60	15.71	15.70	15.73	15.62	15.61
Classification	*Calcic Ferropargasite*			*Calcic Hastingsite*	*Calcic Ferropargasite*									
X_{Mg}	*0.25*	*0.27*	*0.29*	*0.28*	*0.16*	*0.17*	*0.16*	*0.17*	*0.16*	*0.17*	*0.16*	*0.15*	*0.17*	*0.18*

Table 4.2e: Representative chemical analyses for biotite and ilmenite (representative oxygen basis is given). Mineral abbreviation is used after Whitney and Evans (2010). Cation calculations have been done following the procedure of Grew (1984).

Sample no	**SR89**	**SR89**	**SR89**	**SR89**	**SR89**	**SR89**	**SR89**	**SR89**	**SR91**	**SR91**	**SR91**	**SR91**	**SR145**	**SR145**	**SR145**	**SR145**	**SR145**	**SR145**	**SR89**
Mineral	*Bt*	*Bt*	*Bt*	***Bt#***	*Bt*	*Bt*	*Bt*	*Bt*	*Bt*	*Bt*	*Bt*	*Bt*	*Bt*	*Bt*	*Bt*	*Bt*	*Bt*	*Bt*	*Ilm*
Textural setting	*^Grt*	*^Grt*	*^Grt,Pl*		*^Grt,Pl*			*Inclusion ^ Grt*	*Inclusion^ Grt*	*^Grt*	*^Grt,Pl*	*^Grt,Pl*	*Matrix*	*Matrix*	*^Grt*	*^Grt*	*Inclusion ^Grt*	*Inclusion ^Grt*	
SiO_2	34.56	34.42	34.54	34.25	34.91	34.12	34.67	34.94	34.97	34.29	34.30	35.76	34.30	33.26	33.00	34.37	33.67	34.48	0.00
TiO_2	4.14	4.11	4.27	4.32	4.30	4.04	4.17	4.53	4.27	3.97	3.27	3.51	3.61	3.23	3.41	3.61	1.98	3.56	50.98
Al_2O_3	15.23	15.31	15.45	15.25	15.35	15.58	15.44	15.28	14.57	14.32	14.91	15.03	14.15	13.97	15.04	15.44	15.36	16.15	0.00
FeO	25.26	26.50	27.50	26.82	25.56	25.55	25.61	25.46	28.62	27.54	27.39	26.80	30.63	29.50	31.48	30.69	33.85	32.48	43.53
MnO	0.00	0.14	0.15	0.16	0.08	0.05	0.00	0.12	0.09	0.09	0.14	0.32	0.17	0.19	0.08	0.09	0.12	0.32	3.37
MgO	6.72	6.72	6.76	6.79	6.93	6.67	6.83	6.50	5.44	5.30	5.46	5.69	4.36	4.46	3.94	3.84	3.42	3.94	0.00
CaO	0.00	0.00	0.07	0.02	0.00	-0.02	-0.02	0.02	0.00	0.00	0.06	0.00	0.02	0.14	0.11	0.11	0.39	0.35	0.00
Na_2O	0.10	0.08	0.09	0.07	0.05	0.02	0.06	0.05	0.04	0.07	0.04	0.03	0.05	0.13	0.07	0.12	0.01	0.14	0.04
K_2O	9.15	9.23	8.93	9.26	9.34	8.70	9.25	9.17	9.03	9.25	8.97	9.26	8.46	7.54	6.95	7.74	7.11	5.32	0.00
Total	95.12	96.55	97.75	96.95	96.56	94.72	96.03	96.12	97.04	94.91	94.61	96.40	95.77	92.42	94.08	96.06	94.90	96.78	98.07
Oxygen basis	**11**	**11**	**11**	**11**	**11**	**11**	**11**	**11**	**11**	**11**	**11**	**11**	**11**	**11**	**11**	**11**	**11**	**11**	**3**
Si	2.73	2.70	2.68	2.68	2.72	2.70	2.72	2.73	2.75	2.76	2.77	2.80	2.76	2.76	2.70	2.74	2.73	2.71	0.00
Ti	0.25	0.24	0.25	0.25	0.25	0.24	0.25	0.27	0.25	0.24	0.20	0.21	0.22	0.20	0.21	0.22	0.12	0.21	0.99
Al	1.42	1.41	1.41	1.41	1.41	1.46	1.43	1.41	1.35	1.36	1.42	1.39	1.34	1.37	1.45	1.45	1.46	1.49	0.00
Fe+2	1.67	1.74	1.78	1.75	1.67	1.69	1.68	1.66	1.88	1.85	1.85	1.76	2.06	2.05	2.15	2.04	2.29	2.13	0.91
Mn	0.00	0.01	0.01	0.00	0.00	0.00	0.00	0.00	0.01	0.01	0.01	0.02	0.01	0.01	0.01	0.01	0.01	0.02	0.03
Mg	0.79	0.79	0.78	0.79	0.80	0.79	0.80	0.76	0.64	0.64	0.66	0.66	0.52	0.55	0.48	0.46	0.41	0.46	0.07
Ca	0.00	0.00	0.01	0.00	0.00	0.00	0.00	0.00	0.00	0.00	0.00	0.00	0.00	0.01	0.01	0.01	0.03	0.03	0.00
Na	0.02	0.01	0.01	0.01	0.01	0.00	0.01	0.01	0.01	0.01	0.01	0.00	0.01	0.02	0.01	0.02	0.00	0.02	0.00
K	0.92	0.92	0.88	0.92	0.93	0.88	0.92	0.91	0.91	0.95	0.82	0.93	0.87	0.80	0.72	0.79	0.73	0.53	0.00
Sum	7.78	7.82	7.82	7.83	7.79	7.77	7.79	7.76	7.78	7.80	7.74	7.76	7.79	7.77	7.74	7.72	7.79	7.61	2.00
X_{Mg}	*0.32*	*0.31*	*0.30*	*0.31*	*0.33*	*0.32*	*0.32*	*0.31*	*0.25*	*0.26*	*0.26*	*0.27*	*0.20*	*0.21*	*0.18*	*0.18*	*0.15*	*0.18*	

#' denotes the mineral compositions used for C-space textural modeling

4.3. Whole rock geochemistry

The representative bulk compositions of the studied rocks are presented in Table-4.3. The samples are analyzed from the National Centre for Earth Sciences Studies (NCESS), Thiruvananthapuram, Kerala and ICPMS facility of Indian Institute of Technology, Kanpur. Details of the analytical procedure are discussed in the Appendix.

4.3.1. Choice of samples

It has been described in the previous section that the studied rocks are metamorphosed and locally deformed. To avoid significant alteration effect, we chose comparatively large chunk of samples where the volume of the secondary hydrous phases are minimum (<30 volume %), feldspars grains show euhedral outline and the plagioclase shows oscillatory zoning and complex twining. These features suggest that magmatic characters are retained in the studied rocks. To test the effect of post-magmatic chemical alteration, we calculated the representative weathering indices, using molecular proportions of major oxides from the bulk chemical analysis (Ohta and Arai, 2007 and references therein). The values of Chemical Index of Alteration (48-54), Plagioclase Index of Alteration (46-58), and Weathering Index of Parker (>85) further support the view that the chosen rock samples are minimally altered (cf. Ohta and Arai, 2007). The ternary MFW (M=fresh mafic rocks, F=fresh felsic rocks, W=weathered rocks) plot of the studied metagranitoids shows a trend from felsic to mafic source with no data plotted towards the weathered/altered materials (Fig. 4.2a) (Ohta and Arai, 2007).

4.3.2. Geochemical characters of the studied metagranitoids

Normative calculation of the studied samples using whole-rock chemistry shows that the studied rocks can be classified as monzogranite to quartz-monzonite in the QAP (quartz-alkali feldspar-plagioclase; Le Maitre et al., 2002) diagram (Fig. 4.2b). Studied porphyritic metagranitoids show significant compositional variations in terms of SiO_2 (60 to 76 wt. %), total ferromagnesian content (FeO_t+ MgO ≈ 1.51 to 8.18 wt. %), CaO content (0.41-4.44 wt. %) and K_2O/Na_2O (1.70-3.40) (Table-4.3). TAS

diagram (Middlemost, 1994) categorizes the metagranitoids (barring 2 samples) as granite to monzonite (Fig. 4.2c). Studied rocks are ferroan [$FeO_t/(FeO_t+MgO)$ = 0.80-0.95] (Fig. 4.2d), alkali-calcic to alkalic (Fig. 4.2e) and mildly peraluminous [Alumina Saturation Index (ASI) = 0.92-1.19] (Fig. 4.2f). In the MALI (Na_2O+K_2O-CaO) versus SiO_2 diagram, the studied porphyritic metagranitoids are plotted in the calc-alkalic to alkalic zone and show a weak positive trend (Fig. 4.2e).

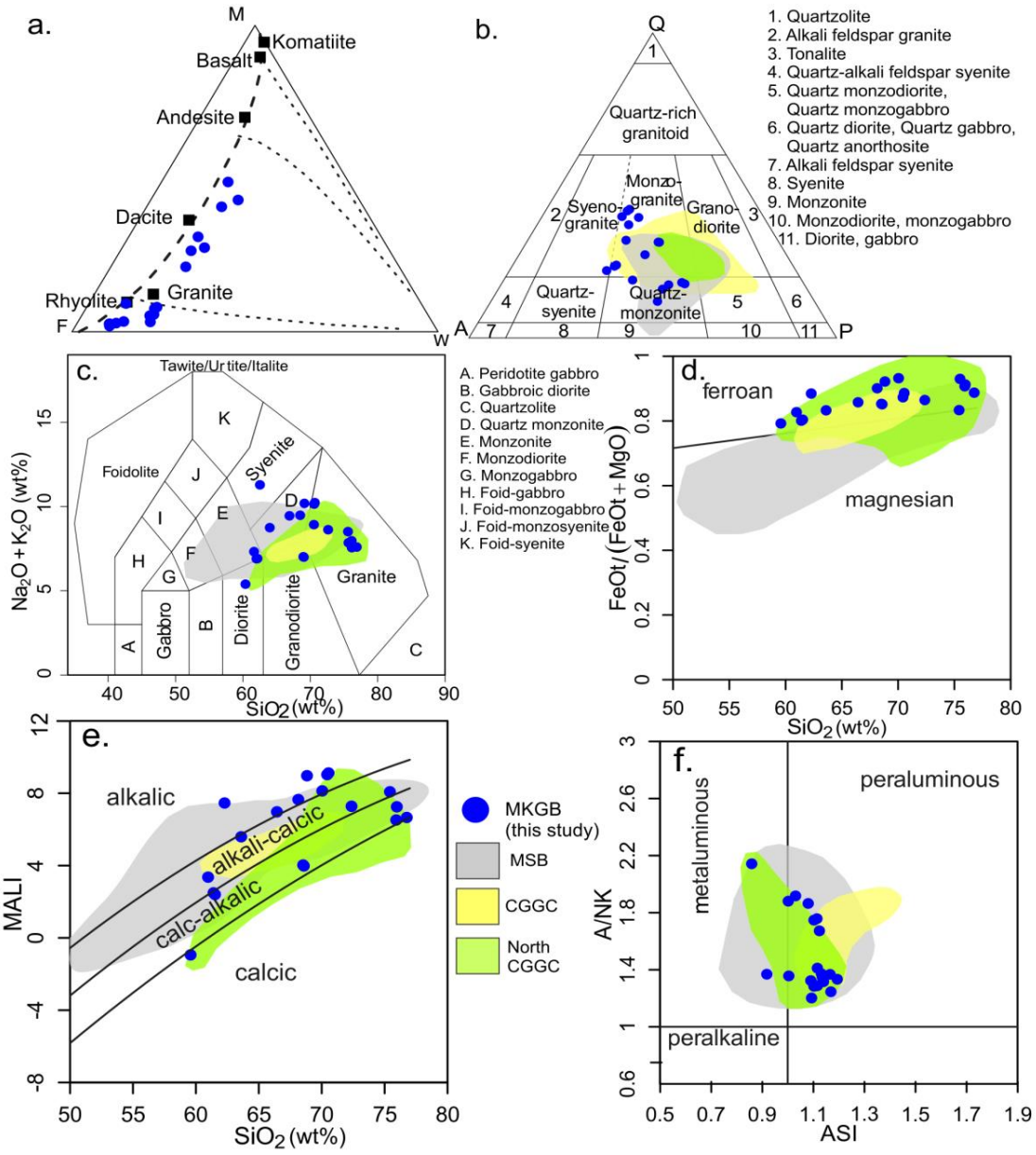

Figure 4.2. Geochemical characteristics of the studied porphyritic granitoids are presented and they are compared with the coeval arc granitoids from Mahakoshal Supracrustal Belt (Bora et al. 2013), CGGC (Domain-I of the Chotanagpur Granite Gneissic Complex in Mukherjee et al. 2019), north CGGC (Domain-III in Mukherjee et al. 2019) (Saikia et al. 2017) (a) MFW (M=fresh Mafic source), F-fresh Felsic source, W=weathered rocks) triangular plot (Ohta and Arai, 2007) of the studied metagranitoids. (b-c) The studied porphyritic granitoids are classified as Monzogranite to Quartz-monzonite in the modal QAP diagram (Le Maitre et al., 2002). Nomenclature of the studied rocks is similar in the TAS diagram (Middlemost, 1984). (d-f) Granitoid classification scheme (Frost et al., 2001) showing mostly ferroan, calc-alkalic to alkali and metaluminous to slightly peraluminous nature of the granitoids. MALI= modified Alkali Lime Index (Na_2O+K_2O-CaO) A/NK = molar $Al_2O_3/(Na_2O+K_2O)$ and ASI= molar $Al_2O_3/(CaO+Na_2O+K_2O)$.

Primitive mantle normalized (N) (McDonough and Sun, 1995) spider diagram for trace elements shows enrichment of Rb, Th, U, Pb, P and depletion of Ba, Sr, Nb and Ti (Fig. 4.2g). Enrichment of incompatible trace elements over compatible ones [$(Pb/Ta)_N$=2.99-22.3, $(Pb/Nb)_N$=1.65-57.4, $(Th/Nb)_N$=3.74-105, $(Y/Nb)_N$=0.11-0.98, $(Nb/Ta)_N$=0.19-1.51, $(Ce/Pb)_N$=0.14-1.48] in the studied metagranitoids, signify dominant crustal contribution in the genesis of the protolith magma. Chondrite-normalized (CN, McDonough and Sun, 1995) REE patterns of the studied samples show a narrow range of LREE enrichment [$(La/Lu)_{CN}$=14.0-42.6] and variable Eu anomaly [Eu/Eu*= 0.5-1.8] (Fig. 4.2h).

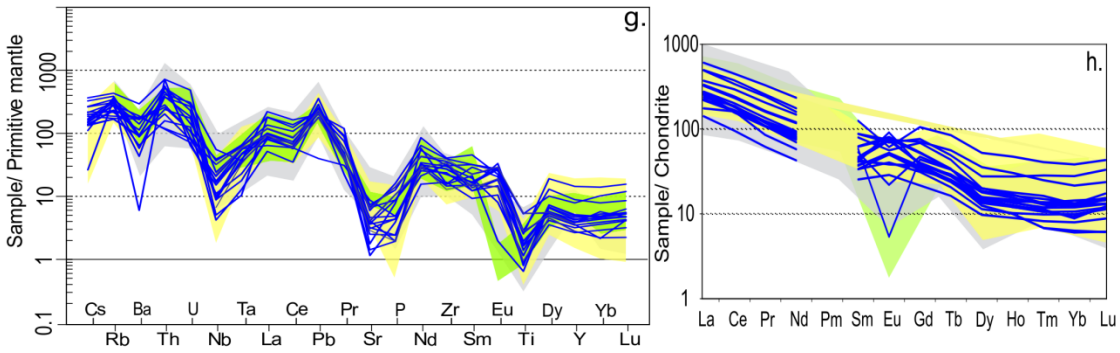

Figure 4.2 contd. (g) Primitive mantle normalized trace element spider diagram. (h) Chondrite-normalised REE spider diagram. Normalization data are after McDonough & Sun (1995).

Table 4.3: Major and trace element chemistry of the studied porphyritic metagranitoids; Major element concentrations are in weight% and trace element concentrations are in ppm.

Sample	SR 35 D	SR 38 A	SR 54 A	SR 82 A	SR 54 B	SR 50 C	SR 36 X	SR 36	SR 111	SR 145	SR 149	SR 142	SR 146	SR 89 B	SR 91	SR 92 A	SR 91 A	SR 150 B	SR 89 C
SiO_2	75.50	76.76	68.14	75.92	62.28	75.42	70.54	70.43	72.37	68.83	75.97	60.97	70.04	61.40	68.58	64.60	68.52	66.44	61.52
TiO_2	0.18	0.16	0.35	0.28	0.39	0.23	0.19	0.18	0.33	0.34	0.13	1.06	0.51	1.08	0.56	0.53	0.56	0.57	1.08
Al_2O_3	13.04	12.81	16.10	12.47	18.83	13.25	16.15	16.34	14.00	15.75	13.44	17.10	13.74	16.81	15.35	18.57	15.47	15.73	16.57
FeO_t	1.86	1.34	3.10	2.15	2.61	1.60	1.40	1.38	2.49	2.95	1.36	6.80	4.82	6.55	3.96	3.89	3.94	3.80	6.56
MnO	0.04	0.04	0.07	0.02	0.04	0.01	0.02	0.01	0.04	0.05	0.02	0.11	0.09	0.08	0.05	0.06	0.05	0.08	0.08
MgO	0.14	0.17	0.34	0.22	0.34	0.32	0.18	0.20	0.39	0.25	0.13	1.42	0.35	1.63	0.69	0.78	0.68	0.63	1.60
CaO	1.14	0.92	1.78	1.01	3.78	0.41	1.09	1.09	1.31	1.17	0.70	3.88	0.73	4.34	2.97	3.10	2.94	2.41	4.44
Na_2O	1.83	2.06	2.13	1.96	2.83	2.57	2.64	2.59	2.27	2.29	2.62	2.37	3.27	2.44	2.24	3.01	2.23	2.56	2.50
K_2O	6.00	5.52	7.30	5.57	8.41	5.92	7.57	7.53	6.32	7.85	5.33	4.87	5.59	4.39	4.71	5.68	4.74	6.82	4.34
P_2O_5	0.05	0.04	0.18	0.09	0.10	0.04	0.04	0.05	0.10	0.09	0.08	0.33	0.16	0.29	0.22	0.18	0.22	0.26	0.29
Sc	1.12	1.43	6.28	6.55	7.93	2.07	1.76	1.77	3.47	5.96	3.02	17.74	12.56	12.82	7.94	7.62	7.88	11.65	13.06
V	5.94	4.91	9.18	9.13	21.12	4.56	5.56	5.49	11.73	6.43	1.14	49.89	4.26	47.77	21.34	26.50	20.62	20.01	46.40
Cr	2.14	1.19	0.99	2.14	2.04	bdl	3.25	3.18	2.23	1.98	0.08	30.33	bdl	21.77	7.13	9.39	5.82	bdl	19.48
Ni	2.70	3.15	4.15	4.10	6.57	2.78	2.65	2.66	3.69	2.99	2.02	14.50	2.08	14.18	7.26	8.75	7.44	4.16	13.82
Cu	3.96	1.59	7.19	7.12	33.87	2.03	16.47	16.35	2.99	3.66	14.98	25.96	4.18	16.27	8.92	7.08	8.82	7.26	15.83
Zn	30.38	15.09	50.29	48.94	18.09	20.32	20.19	20.26	36.11	48.11	134.36	98.07	123.71	95.57	55.28	59.75	53.27	56.87	89.81
Ga	12.82	12.09	15.18	14.96	15.10	13.09	13.75	13.73	12.72	16.04	15.55	22.54	19.35	19.26	15.09	15.69	14.44	14.77	18.14
Rb	139.00	129.21	139.74	135.93	204.37	165.28	202.11	185.52	181.00	170.75	220.81	134.54	206.41	112.28	100.87	169.30	100.71	156.39	103.55
Sr	63.61	82.21	73.21	72.02	173.57	28.21	57.28	49.86	91.82	61.27	13.41	118.65	35.04	134.03	80.48	131.97	82.75	146.08	126.53
Cs	4.14	4.58	2.94	2.87	0.55	3.21	3.57	3.40	4.49	3.10	2.33	5.53	15.30	4.21	2.87	7.66	2.79	5.59	3.91
Ba	423.82	747.22	1124.46	1085.99	380.20	285.21	581.82	581.13	607.89	1245.30	39.68	927.62	613.13	1184.19	607.29	1940.78	593.42	1099.88	1114.03
Ta	0.48	0.39	1.75	2.04	2.10	1.76	1.21	1.28	1.45	0.84	0.66	2.42	1.36	2.32	2.11	1.70	2.16	2.28	2.20
Pb	36.21	34.91	38.31	37.65	5.98	31.29	34.88	30.97	32.91	35.73	53.69	33.24	29.83	33.58	26.97	43.16	26.18	31.55	31.27
Hf	4.69	4.86	6.94	7.15	8.43	8.19	3.69	4.09	6.33	5.74	5.92	9.82	11.03	8.95	8.97	5.62	8.80	8.08	9.34
Zr	176.28	166.27	286.37	283.65	333.58	313.63	135.39	153.14	248.86	233.95	163.20	414.59	425.10	376.03	357.34	235.68	358.30	321.68	407.29
Nb	2.77	3.33	10.90	11.46	15.88	6.03	4.39	6.60	5.76	7.29	5.82	24.16	36.46	21.14	13.65	9.97	14.72	25.64	21.33
Y	11.43	21.21	16.53	16.41	18.13	22.04	11.75	11.98	13.67	18.66	20.00	33.85	62.01	15.42	15.04	16.96	15.60	38.24	15.61
Th	12.67	42.26	22.63	40.19	29.99	41.95	19.19	19.17	30.55	9.33	57.49	36.72	33.07	9.56	16.25	15.09	-	20.62	10.11
U	2.52	4.60	2.14	1.71	5.34	5.80	2.59	3.48	3.70	1.43	9.70	2.85	6.17	1.65	1.59	1.28	-	2.17	2.01

Table 4.3 (continued): Major and trace element chemistry of the studied porphyritic metagranitoids; Major element concentrations are in weight% and trace element concentrations are in ppm.

Sample	SR 35 D	SR 38 A	SR 54 A	SR 82 A	SR 54 B	SR 50 C	SR 36 X	SR 36	SR 111	SR 145	SR 149	SR 142	SR 146	SR 89 B	SR 91	SR 92 A	SR 91 A	SR 150 B	SR 89 C
La	33.48	116.37	63.54	64.04	41.59	65.43	61.37	56.28	64.08	51.61	53.44	117.51	143.15	76.59	59.28	52.35	60.60	87.84	78.85
Ce	58.33	207.58	113.44	112.27	98.91	123.14	110.76	115.06	111.10	98.48	100.97	229.16	274.22	141.97	95.57	102.55	98.61	180.38	147.93
Pr	5.70	22.46	11.44	11.38	7.89	12.52	11.43	10.91	10.04	10.08	11.49	23.64	30.34	14.77	9.90	10.06	10.02	18.99	15.12
Nd	19.50	72.66	39.94	39.52	26.40	42.85	37.65	36.33	31.84	37.19	41.69	80.07	106.70	53.57	34.25	35.50	34.63	67.60	54.74
Sm	3.77	11.78	6.61	6.56	4.99	7.87	6.32	6.15	4.98	6.90	8.62	12.96	18.51	9.15	5.58	6.06	5.47	12.97	9.25
Eu	1.62	3.16	4.08	4.13	2.81	1.24	2.15	2.18	2.27	4.34	0.30	3.91	3.44	4.29	2.81	5.12	2.95	4.20	4.53
Gd	4.30	13.67	7.99	7.75	6.49	9.37	7.37	7.14	6.22	7.61	8.73	15.18	20.95	10.33	6.91	7.52	7.27	14.12	10.57
Tb	0.59	1.56	1.03	1.00	0.91	1.22	0.91	0.91	0.74	1.05	1.20	1.77	3.05	1.22	0.85	0.89	0.90	2.03	1.23
Dy	2.39	4.93	3.85	3.88	3.88	4.91	3.09	3.07	2.79	4.40	4.57	6.81	12.85	3.66	3.30	3.64	3.48	8.75	3.79
Ho	0.49	0.92	0.74	0.73	0.80	0.97	0.55	0.55	0.56	0.85	0.90	1.50	2.59	0.65	0.66	0.76	0.69	1.66	0.68
Tm	0.20	0.33	0.29	0.30	0.33	0.40	0.17	0.17	0.24	0.32	0.37	0.70	1.01	0.27	0.26	0.34	0.27	0.61	0.28
Yb	1.28	2.05	1.92	2.52	2.31	2.11	1.02	0.97	1.59	1.96	2.15	4.49	6.16	0.95	1.71	2.09	-	3.47	0.93
Lu	0.22	0.36	0.32	0.32	0.37	0.43	0.15	0.15	0.28	0.33	0.38	0.81	1.06	0.29	0.29	0.36	0.31	0.58	0.30
$(Pb/Ta)_N$	18.7	22.3	5.4	4.6	0.7	4.4	7.1	5.9	5.6	10.4	20.1	3.4	5.4	3.6	3.2	6.2	3.0	3.4	3.5
$(Pb/Nb)_N$	57.4	46.0	15.4	14.4	1.7	22.8	34.8	20.6	25.1	21.5	40.4	6.0	3.6	7.0	8.7	19.0	7.8	5.4	6.4
$(Th/Nb)_N$	37.9	105.2	17.2	29.0	15.6	57.5	36.1	24.0	43.9	10.6	81.7	12.6	7.5	3.7	9.9	12.5	-	6.7	3.9
$(Th/Ta)_N$	12.4	50.8	6.0	9.2	6.6	11.1	7.4	6.9	9.8	5.1	40.6	7.1	11.3	1.9	3.6	4.1	-	4.2	2.1
$(Y/Nb)_N$	0.6	1.0	0.2	0.2	0.2	0.6	0.4	0.3	0.4	0.4	0.5	0.2	0.3	0.1	0.2	0.3	0.2	0.2	0.1
$(Nb/Ta)_N$	0.3	0.5	0.4	0.3	0.4	0.2	0.2	0.3	0.2	0.5	0.5	0.6	1.5	0.5	0.4	0.3	0.4	0.6	0.5
$(La/Nb)_N$	12.3	35.5	5.9	5.7	2.7	11.0	14.2	8.7	11.3	7.2	9.3	4.9	4.0	3.7	4.4	5.3	4.2	3.5	3.8
$(Ce/Pb)_N$	0.1	0.5	0.3	0.3	1.5	0.4	0.3	0.3	0.3	0.2	0.2	0.6	0.8	0.4	0.3	0.2	0.3	0.5	0.4
$(La/Lu)_N$	16.1	33.9	20.6	20.9	11.8	16.0	42.6	38.6	24.0	16.5	14.7	15.1	14.1	27.9	21.2	15.2	20.3	15.7	27.3
Eu/Eu*	1.23	0.76	1.71	1.76	1.51	0.44	0.96	1.00	1.24	1.83	0.11	0.85	0.53	1.34	1.38	2.31	1.43	0.95	1.40
$T_{Zr}(^0C)(W\&H)$	777	826	818	855	-	827	739	750	750	776	798	-	739	-	730	781	779	828	-
$T_{Zr}(^0C)(B)$	720	776	753	710	-	772	671	684	684	720	736	-	671	-	678	716	714	775	-
CIA	53	54	52	53	48	54	53	53	52	52	54	51	52	50	52	53	52	50	50
PIA	56	57	55	56	46	58	56	57	54	55	58	52	53	50	53	54	53	49	49
WIP	86	87	124	92	145	111	111	113	121	119	86	231	118	252	145	171	144	158	249

N=Primitive mantle normalized (Sun and McDonough, 1995)

$Eu/Eu^* = (Eu)_{CN}/[(Sm)_{CN} \times (Gd)_{CN}]^{0.5}$; CN=Chondrite normalized (Sun and McDonough, 1995)

$T_{Zr}(^0C)$(W&H)= Zircon saturation temperature (Watson and Harrison, 1984); (B)=Boehnke et al., 2013.

CIA=Chemical Index of Alteration (Nesbitt and Young, 1982)

PIA=Plagioclase Index of Alteration (Fedo et al., 1995)

WIP=Weathering Index of Parker (Parker. 1970)

In the Harker diagram, porphyritic metagranitoids show a negative correlation of FeO_t, MgO, CaO, TiO_2 and P_2O_5 with respect to SiO_2 content (Fig. 4.2i-o). Positive correlations of Sr with CaO (Fig. 4.2p) and Nb with TiO_2 (Fig. 4.2q) are noted. TiO_2,

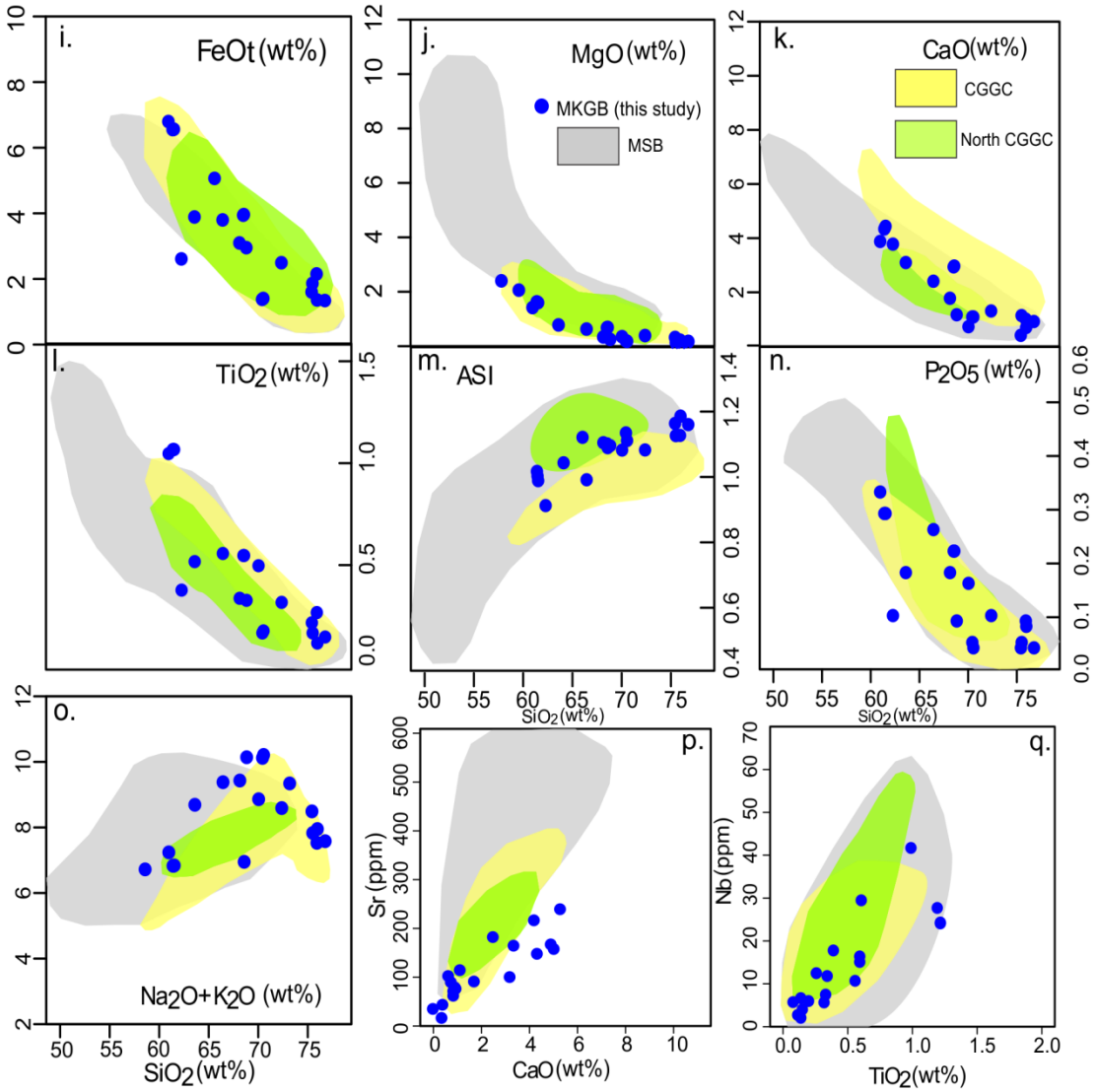

Figure 4.2 contd. (i-o) Harker diagram or bivariate plots of the major oxides with respect to SiO_2 content (wt. %) of the studied rocks showing differentiation trends, quite similar to other Paleoproterozoic arc granites of Central India. (p-q) Sr content shows positive trend with respect to CaO (wt. %) and Nb versus TiO_2 plot of the studied rocks shows positive pattern.

CaO and P_2O_5 show a positive correlation with maficity (FeO_t+MgO) (Fig. 4.2r-t) whereas SiO_2, ASI illustrates a negative trend with increasing maficity (Fig. 4.2u, v). The total alkali amount ($Na_2O + K_2O$) shows an initial strong positive and subsequent

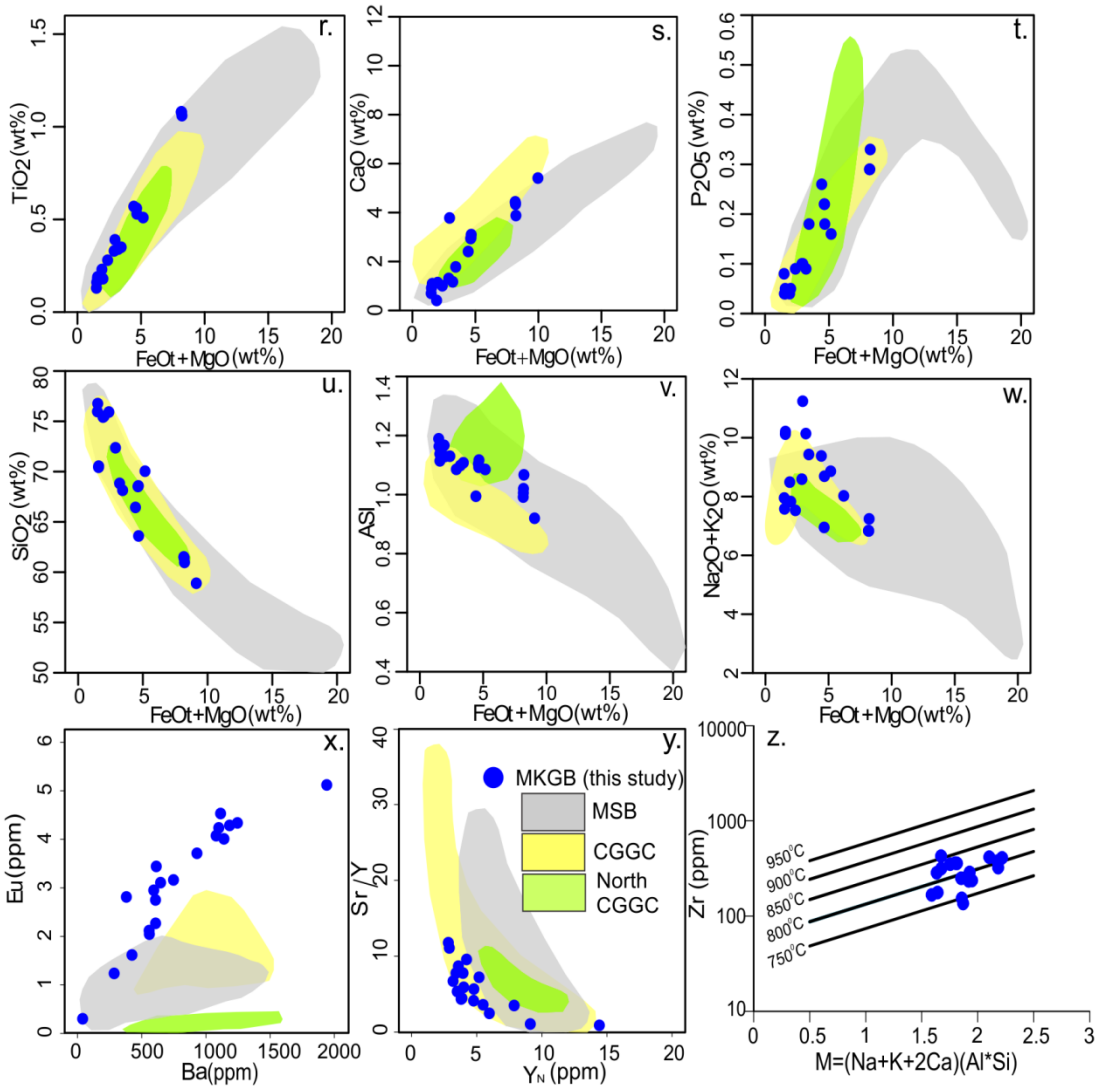

Figure 4.2 contd. (r-w) Bivariate plots showing evidence of differentiation with the trends of major oxides with respect to maficity (FeO_t + MgO) in the studied porphyritic metagranitoids. (x-y) Europium content show positive trend with increasing Ba content in the studied samples and Sr/Y value show negative trend with increasing Y_N value (N=Normalized by the concentration within Primitive Mantle). (z) Zircon Saturation temperature calculated using the calibration of Watson and Harrison (1983).

negative pattern against maficity (Fig. 4.2w). Eu shows a crude positive trend with increasing Ba content (Fig. 4.2x) and the ratio of Sr/Y decreases with increasing Y_N (N=Primitive Mantle normalization) in the studied metagranitoids (Fig. 4.2y).

4.4. Zircon saturation thermometry

Zircon solubility in silicate melts depends on the composition and temperature of the magma which leads several authors to develop a relationship between the Zr contents, composition of the rock and zircon saturation temperatures (Boehnke et al., 2013; Watson and Harrison, 1983). However, considering the complex geological contexts, Siégel et al. (2018) argued that this thermometry should be applied to xenocryst-absent silicic (>64 wt% SiO_2) granites with $0.9 < M = (K + Na + 2Ca) / (Al*Si) < 1.9$ (Watson and Harrison, 1983) and unmodified trace element contents. Kirkland et al.(2015) demonstrated that at temperature <800ºC, zircon saturation thermometry may overestimate the temperature by more than 200ºC at which melt was in equilibrium with zircon grains. Kirkland et al. (2015) have postulated a mathematical equation using Th and U content within zircon and whole-rock [$Th_{(Zircon/Rock)}/U_{(Zircon/Rock)}$] to understand the degree of chemical differentiation in a crystallizing magma (Kirkland et al., 2015). Following the equation, the apparent temperature, calculated from Th and U content in the analyzed zircons and whole-rock chemistry, broadly corroborates with the estimated zircon saturation temperature from the bulk of the studied samples. Therefore a good match exists between zircon saturation temperature from the whole rock and the temperature at which the melt and the zircon were in equilibrium. Hence the calculated temperature from the whole-rock geochemistry data provides a reliable estimate of the temperature of the granitic magma. Zircon grains in the studied samples show simple oscillatory zoning and are devoid of any xenocryst. Following the calibration of Watson and Harrison (1983) and Boehnke et al. (2013) the temperatures calculated from the zircon saturation thermometry vary from 730 to 855 °C (average 785 °C) and 671 to776 ºC (average 719 °C) respectively [Table-4.3; Fig. 4.2z showing isotherms and results using calculations by Watson and Harrison (1983)].

4.5. Tectonic affinity of the protolith magma

Highly potassic and metaluminous to peraluminous (ASI=0.92-1.19) character of the porphyritic metagranitoids coupled with the enriched Pb, Rb, Th, U, pronounced Nb-Ta depletion [$(Nb/La)_N$ = 0.03–0.29, average 0.17; $(Ta/La)_N$ = 0.6–0.62, average 0.41] advocate for significant crustal contributions in their protolith magma. Plotting the chemical composition of the studied metagranitoids in the source diagram of Moyen et al. (2017) also suggests the possibility that they were derived via partial melting of older felsic or basic igneous rocks (Fig. 4.3a). Diagram to discriminate A-type with the orogenic granites [Whalen et al. (1987)] suggest that the metagranitoids have arc affinity (I- type/S-type in granitoids (Fig. 4.3b-e). Plots of the studied rocks in several tectonic discriminant diagrams with HFSEs and High $(Th/Nb)_N$ (28.65) and $(Th/Ta)_N$ (11.13) ratios also confirm the tectonic setting (Pearce et al., 1984; Schandl and Gorton, 2002). These geochemical signatures can also be attained by fractionation of a mantle-derived mafic magma undergoing assimilation/contamination with the upper continental crust (Castro, 2014). The geochemical characteristics of the Paleoproterozoic granitic magmas from CGGC (Mukherjee et al., 2019; Saikia et al., 2017) and MSB (Bora et al., 2013) show similar arc affinity in all these discrimination diagrams (Fig. 4.3). Majority of the studied metagranitoids show either positive or no Eu anomaly (average Eu/Eu*=1.2). However, moderate LREE enrichment [$(La/Lu)_N$=14.0 to 42.6; avg. 22.7], absence of HREE depletion and low Sr/Y (0.5-8.6) coupled with moderate Y_N (2.7-8.9) suggest that garnet did not play a significant role during the formation of melt. Experimental studies have postulated that during the anatexis of amphibole-dominated mafic to intermediate rocks, garnet becomes stable between 8-10 kbar depending on the iron content of the source (Patiño Douce and Beard, 1995; Watkins et al., 2007). During fractionation from mafic magma, garnet disappears below 8 kbar pressure at 800°C in water-undersaturated melts as amphibole takes over as the major ferromagnesian phase (Alonso-perez et al., 2009). Therefore, absence of garnet in the source, inferred from low Sr/Y and absence of HREE depletion in the studied rock, suggest the

protolith of the porphyritic metagranitoids were likely to have formed in the depth range not exceeding 25-35 km (corresponding to 8-10 kbar pressure).

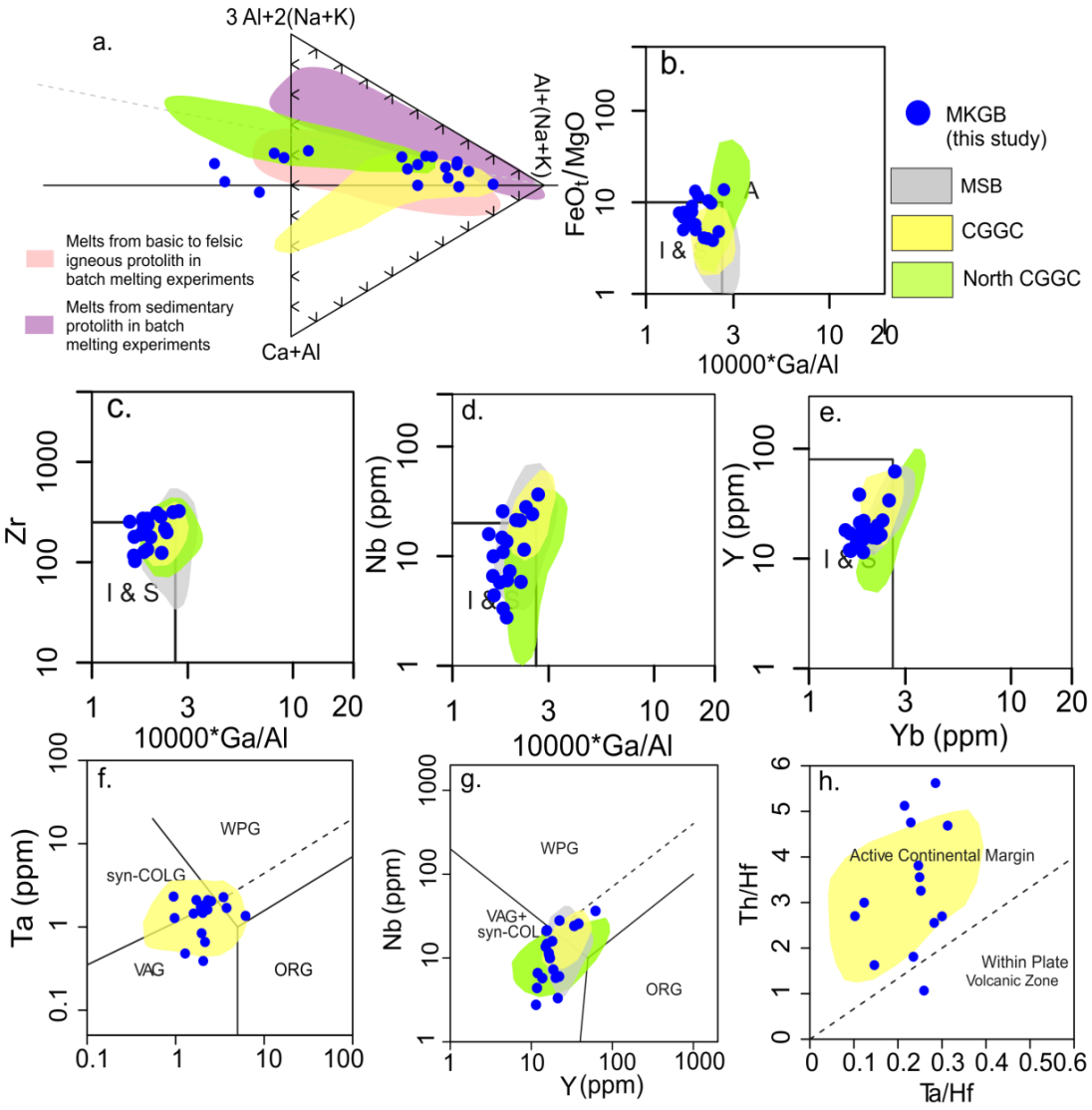

Figure 4.3. (a)Probable source rock of the studied metagranitoids after Moyen et al. (2017) show that the whole rock compositions mostly overlap with that of the experimental batch melts from basic to felsic igneous protolith. (b-e) Plots classifying the studied rocks as arc granites (fields for I- & S-type granitic magmas in the diagram after Whalen et al. 1987). (f-g) Trace element discrimination diagrams show that studied the studied granitoids plot within syn-collisional granites (syn-COLG) and volcanic arc granites (VAG) in the diagrams (Pearce et al. 1984). (h) Tectonic discrimination diagram using HFSE (Schandl and Gorton, 2002) shows the arc affinity of the protolith magma of studied metagranitoids.

4.6. Open system phase equilibria modeling

Trends observed in the variation diagrams of felsic igneous rocks are commonly inferred to be the consequences of one or more of the following petrogenetic processes:

a) Magma mixing/mingling i.e., mechanical and chemical mixing of mafic and felsic magmas in a magma chamber (Baxter, 2003; Baxter and Feely, 2002; Chappell, 1996; Gogoi et al., 2021)

b) Crustal assimilation of a mafic magma followed by fractionation (Castro, 2014; Guo and Zou, 2022; Shafaii Moghadam et al., 2015)

c) Fractional crystallization of a felsic magma (Farina et al., 2020; Garcia-Arias and Stevens, 2017; Mukherjee et al., 2022)

In porphyritic metagranitoids, megacrystic K-feldspar phenocrysts are proposed to be formed via magma mixing and crystal fractionation (Vernon and Paterson, 2008). Several porphyritic granitoids from the adjacent terrains [e.g., Mahakoshal belt (MSB) and Bathani Volcanic Suite or north CGGC] are associated with mafic microgranular enclaves (MME), which is interpreted as evidence of magma mixing (Bora, 2015; Gogoi et al., 2021). The presence of quartz xenocrysts, rapakivi or anti-rapakivi texture, resorbed and embayed crystals, amphibole-rich mafic clots, veins carrying mineral components from mafic to felsic zones in hybrid rocks, viscous folding of these veins and wide compositional variation (SiO_2 ranging from 48 wt. % to 75 wt. % in mafic microgranular enclaves and granites are deemed to support the magma mixing model (Bora, 2015; Gogoi et al., 2021). Absence of the aforesaid distinctive field and petrographic features (cf. Baxter and Feely, 2002) in the studied granitoids suggest that magma mixing is not a viable option.

Crustal assimilation combined with fractional crystallization of mafic magma is considered to be one of the significant processes in producing compositional variation, especially for the felsic magmas generated in the arc settings (Castro, 2014; Guo and Zou, 2022; Nebel et al., 2007). Geochemical features of the studied rocks e.g., high ratios of Th/Nb, Th/Ta, Pb/Nb, Pb/Ta point to significant crustal contribution in the genesis of the protolith magma. Systematic patterns in the bivariate plots for the

studied porphyritic metagranitoids are also very much compatible with the possibility (c) i.e., post-emplacement fractional crystallization of an initial felsic magma itself. Given these observations, we have performed a modeling study to trace the magmatic evolution of the studied rocks for the two scenarios: 1) fractional crystallization of mafic magma, followed by assimilation with crustal material during its ascent and continued crystal fractionation and 2) post-emplacement crystal fractionation of a granitic magma using open-system phase equilibrium modeling. Similar approaches were also carried by different workers (Farina et al., 2020; Gao et al., 2021; Garcia-Arias and Stevens, 2017; Mayne et al., 2020; Mukherjee et al., 2022; Zheng and Gao, 2021).

4.6.1. Methodology

To model an open-system scenario in the NCKFMASHTO (Na_2O-CaO-K_2O-FeO-MgO-Al_2O_3-SiO_2-H_2O-TiO_2-O_2) system, we have used the program Rcrust (version 2022-03-09; Mayne et al., 2020, 2016) which is interfaced with the program Perple_X (version 6.8.6; Connolly, 2009). Mn is not considered in the system for calculation as MnO content in the studied granitoids is very low (<0.1 wt. %). The activity-composition relations to model crustal assimilation process are as follows: biotite, garnet, muscovite, ilmenite and orthopyroxene are from White et al. (2014); clinopyroxene from Augite from Green et al. (2016); ternary feldspar from Holland and Powell (2003); magnetite-spinel from White et al. (2002), epidote from Holland and Powell (2011), clino-amphibole from Green et al. (2016). Considering the mafic composition of the starting melt, the melt model is taken from Green et al. (2016). Pure endmembers of "ab" (albite) and "mic" (microcline) were excluded from consideration. The fO_2 condition during the fractionation of the mafic magma is constrained at fayalite-magnetite-quartz (FMQ) oxygen buffer.

Castro (2014) argued that fractionation of hydrous basalt may lead to an andesitic melt which undergoes further fractionation and crustal assimilation to produce granite-granodiorite magma. Therefore, in the current model we perform fractionation of mafic magma followed by crustal assimilation and fractionation along an isobaric cooling path. In order to comprehend the effects of combined crustal assimilation and crystal fractionation of a mantle-derived magma, composition of a

mafic xenolith from the vicinity is used as starting composition (Bora and Kumar, 2015). The mafic magma is modeled to cool and crystallize from 1000 to 650 °C and during the fractionation the fractionating melt becomes gradually silicic and eventually andesitic at approximately 880°C. Following the model proposed by Castro (2014), at this point certain proportion (20 wt. % and 40 wt.%) of the material of upper continental crust (Rudnick and Gao, 2003) got contaminated with the magma and continues to fractionate up to the solidus. As the mafic magma is less viscous and more prone to gravitational settling i.e., complete separation of crystal from the restitic melt system, 100% of the crystallized material is separated from the magma system once the 10 wt% critical crystal fraction (CCF) is achieved. We have used 10% CCF for this model because unlike the felsic magma, mafic magmas commonly inferred to undergo gravitative settling crystallization with low CCF (Garcia-Arias and Stevens, 2017).

The activity-composition relations for post emplacement crystal fractionation modeling for biotite, garnet, muscovite, ilmenite, orthopyroxene and melt are taken from White et al. (2014); clinopyroxene from Augite from Green et al. (2016); ternary feldspar from Holland and Powell (2003); magnetite-spinel from White et al. (2002), epidote from Holland and Powell (2011) , clino-amphibole from Green et al. (2016). Pure endmembers of “ab” (albite) and “mic” (microcline) were excluded from consideration.

In an attempt to understand the role of the batch crystallization in making significant chemical variation in granitic magma, the studied granitoid compositions need to be compared with the modeled crystallized fractions of the protolith magma. Hence the average whole-rock composition of the porphyritic granitoids is used as the starting composition. Zircon saturation thermometry recorded mean temperature of 719-785 ºC which represents the minimum magmatic temperatures. Therefore, the modeling has been done between 900-650 °C. The geochemical characteristics of the porphyritic granitoids combined with their moderate to low LREE/HREE (14.0-42.6) and low Sr/Y (0.5-8.6) suggest that the parental melt of the granitoids were formed at shallow crustal depths not conducive for development of large amount of garnet, in the residue. Hence though the post-emplacement crystallization along isobaric cooling

paths has been modeled within a range of 8-3 kbar pressure with 1 kbar intervals, the results presented hereby are in the range of 5-3 kbar pressure. Following the approach of Farina et al. (2020), H_2O content of the emplaced magma has been considered 1-4 wt% [results are shown for 2 and 4 wt%]. The fO_2 condition during the fractionation of these granitoids is constrained at fayalite-magnetite-quartz (FMQ) oxygen buffer.

Though fractional crystallization in a magma chamber can occur either by gravitative settling or filter-pressing mechanism in highly viscous felsic magmas filter pressing is more viable process (Deering and Bachmann, 2010). As the critical crystal fraction (CCF), at which point the melt is squeezed out of the crystalline mush is not unequivocally established yet, current study considers 35 wt%, 45 wt% and 55 wt% as the threshold for CCF (following the previous works of Farina et al., 2020; Lake, 2013; Mayne et al., 2020; Rosenberg and Handy, 2005). Feldspar phenocrysts are inferred to be early crystallizing phases while the matrix represents late crystallization from melt and among the studied samples highest phenocrysts: matrix ratio is around 4:1. Therefore, the modeling is done in such a way that for all three modeled CCF scenario, once the threshold is achieved, 20 wt% melt is retained with 80% of the crystallized material at each and every step of fractionation process. So that the 20% melt portion designates the matrix part of the porphyritic granitoids and 80% of the solid phase demarcates the phenocryst portion. The modeled crystal-laden mush evolves as two different bulks [reactive bulk and extracted bulk] along the liquid line of descent. The solidus temperature and temperature at which H_2O is exsolved as a free phase are more or less same (670-660 °C) for all the stipulated conditions in the current study.

4.6.2. Model for combined crustal assimilation and fractional crystallization of mafic magma

The bulk composition and modal abundance (volume %) of extracted mineral phases in the modeled solid/crystal system of the evolving mafic magma, undergoing gravitational settling fractional crystallization and contamination with upper continental crust are presented in Table-4.4a, b and Fig. 4.4. As the separated phases, their modal abundance and temperatures of extraction points are grossly similar in the

models with added 40 and 20 wt. % assimilant, only the results for the latter are illustrated in Fig. 4.4. The results reveal that the extracted rocks contain a wide compositional range (45-76 wt. % SiO_2) encompassing the broad range of mafic, intermediate and felsic compositions (Table-4.4a). Maficity (FeO_t + MgO) of these modeled extracted crystal fraction or bulk varies from <1 wt. % to 25 wt. % and they also have variable alkali (Na_2O + K_2O) and CaO contents. The phase abundance study from the model shows that the mafic magma first crystallizes plagioclase + clinopyroxene + amphibole + biotite + ilmenite at 995 °C under all stipulated conditions. Subsequent crystallization phases are dominated by plagioclase, orthopyroxene, clinopyroxene and biotite which results in an andesitic melt (SiO_2 ~ 59 wt. %). At this point (approximate around 880°C) crustal materials are assimilated which leads to crystallization of K-feldspar and quartz along with plagioclase biotite. At all the pressure conditions, amphibole is absent in the solid system after 935 °C whereas biotite is present upto 675 °C along with its absence in a temperature interval of 880-750 °C in the extracted mineral assemblage. At all simulated pressure conditions in the current model, plagioclase crystallizes throughout the entire temperature range and each extraction point below the solidus (995-660 °C). At 5 kbar pressure, K-feldspar gets separated from the melt at 890 °C whereas at lower pressure this mineral phase crystallizes at 40-50°C lower temperature. At the lowest pressure (3 kbar) scenario, quartz crystallizes and is extracted from the liquid system only at 660 °C, just below the solidus. Considering the three simulated pressure conditions, extraction and separation of crystals occur from the restitic melt at the most gradual temperature interval for 4 to 5 kbar. While initial fractionation is dominated by plagioclase, after the assimilation, extracted plagioclase: K-feldspar ratio varies from 1:5 to 5:1 at both 4 and 5 kbar pressure conditions (Table- 4.4b).

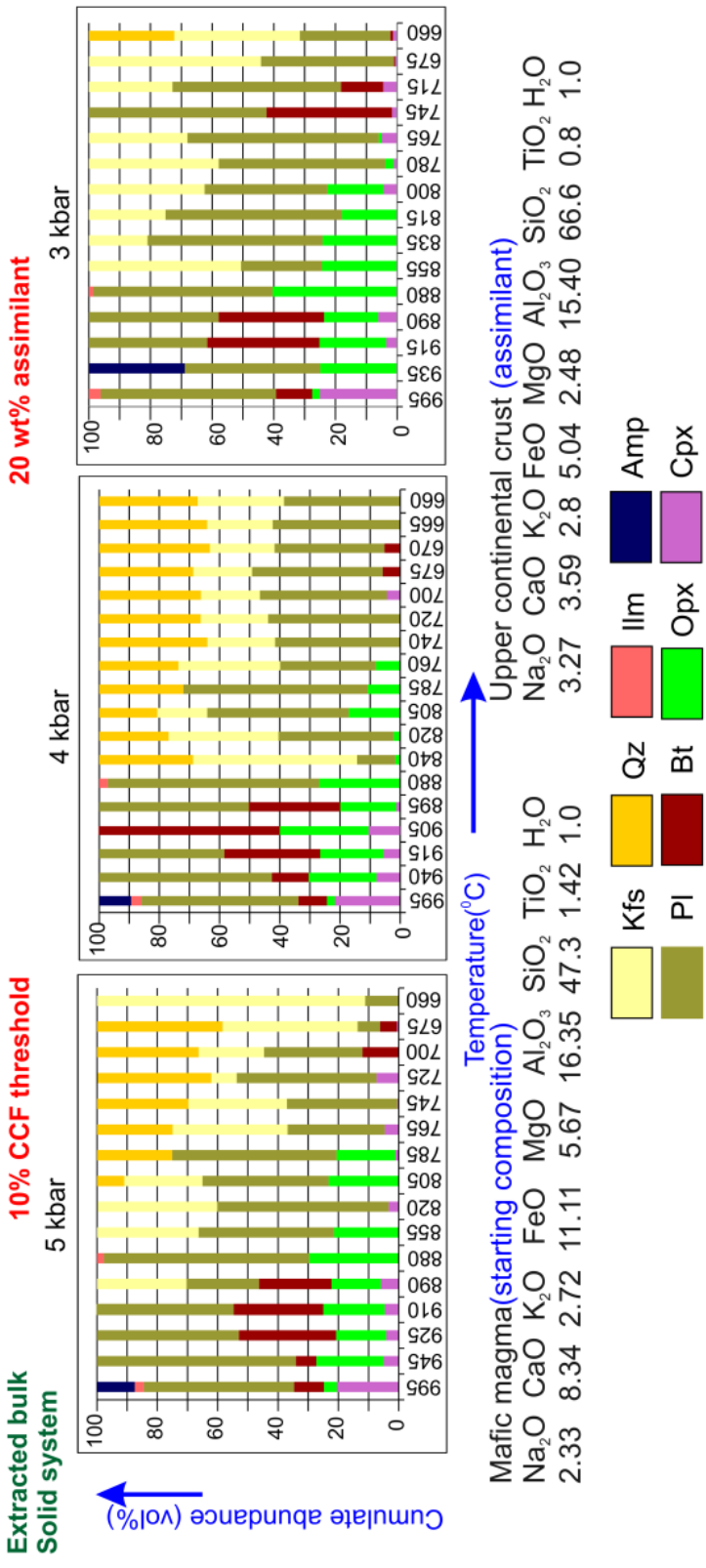

Figure 4.4. T-X diagrams showing the extracted bulk i.e., solid system, separated from an evolving mafic magma (starting composition) along the course of fractional crystallization and assimilation with upper continental crust (20 wt%) at a certain temperature point. Composition of the mafic magma is taken from Bora et al., 2015 and upper continental crust from Rudnick and Gao, 2003.

Table 4.4a: Major element composition of modeled solid (extracted bulk i.e. eb) system of a crystallizing mafic magma, contaminated with 20 (AFC20) wt% upper continental crustal material along isobaic cooling path

Process_Assimilant	Na_2O	MgO	Al_2O_3	SiO_2	K_2O	CaO	TiO_2	FeO_t
AFC20	1.67	7.50	18.80	45.63	1.35	13.71	2.93	8.40
AFC20	2.88	7.81	19.15	52.69	1.29	8.10	0.00	8.07
AFC20	2.05	9.39	17.82	48.66	3.90	6.10	0.00	12.08
AFC20	3.78	3.64	14.58	54.67	4.50	2.59	0.00	16.24
AFC20	2.17	5.70	15.44	51.93	5.53	4.45	0.00	14.79
AFC20	3.98	4.87	16.44	53.22	0.71	4.82	1.30	14.66
AFC20	3.60	2.95	15.67	59.78	5.72	1.96	0.00	10.33
AFC20	4.20	0.28	19.50	60.97	7.15	2.77	0.00	5.13
AFC20	2.74	1.86	13.64	61.62	5.17	2.02	0.00	12.95
AFC20	1.49	0.98	9.99	68.30	6.30	0.75	0.00	12.19
AFC20	2.90	0.00	15.88	69.36	4.64	4.53	0.00	2.69
AFC20	2.01	0.00	12.19	67.70	4.91	2.06	0.00	11.13
AFC20	1.33	0.00	12.81	69.18	6.16	3.38	0.00	7.15
AFC20	1.88	0.00	13.49	70.75	5.96	2.05	0.00	5.87
AFC20	0.64	0.00	11.81	75.71	7.09	1.77	0.00	2.99
AFC20	1.52	7.13	19.38	45.09	1.27	14.48	3.16	7.97
AFC20	2.01	9.37	18.37	50.68	1.63	8.89	0.00	9.05
AFC20	1.81	10.84	16.00	48.85	3.75	5.63	0.00	13.12
AFC20	3.82	3.43	14.42	55.01	4.69	2.37	0.00	16.27
AFC20	2.47	7.50	17.23	49.55	3.99	4.68	0.00	14.58
AFC20	4.12	5.38	17.28	53.16	0.55	5.20	1.54	12.78
AFC20	4.22	0.29	15.08	73.91	3.01	2.68	0.00	0.81
AFC20	3.55	0.28	16.39	70.65	5.26	2.68	0.00	1.19
AFC20	2.28	1.51	12.69	66.72	5.85	1.43	0.00	9.52
AFC20	1.87	0.98	11.52	71.95	7.09	0.42	0.00	6.17
AFC20	2.62	0.52	14.79	69.44	4.54	3.04	0.00	5.06
AFC20	1.90	0.00	13.47	73.28	5.74	2.27	0.00	3.33
AFC20	1.69	0.00	13.17	69.89	5.78	2.27	0.00	7.19
AFC20	1.55	0.00	12.55	70.83	5.77	3.17	0.00	6.13
AFC20	1.73	0.00	14.30	72.00	7.06	2.03	0.00	2.88
AFC20	1.77	0.00	13.52	73.92	5.95	2.23	0.00	2.61
AFC20	1.17	6.54	19.80	44.81	1.42	15.25	3.36	7.66
AFC20	2.00	10.86	18.44	48.48	0.43	9.79	0.00	10.00
AFC20	1.68	12.05	15.89	48.39	4.23	4.89	0.00	12.87
AFC20	2.22	9.59	15.56	49.30	4.08	5.36	0.00	13.87
AFC20	3.14	6.68	14.10	52.26	0.44	4.62	0.98	17.77
AFC20	4.15	3.72	16.02	58.35	3.33	3.19	0.00	11.24
AFC20	3.35	2.93	14.45	59.74	5.99	1.59	0.00	11.96
AFC20	3.88	1.64	15.91	60.70	6.31	1.70	0.00	9.85
AFC20	3.12	1.58	12.35	54.67	4.34	2.68	0.00	21.26
AFC20	3.75	0.24	15.20	55.99	5.84	1.83	0.00	17.15
AFC20	3.12	0.24	13.13	54.54	6.16	2.09	0.00	20.72
AFC20	4.77	2.62	16.90	52.44	5.30	2.16	0.00	15.82
AFC20	4.45	0.45	17.45	60.03	7.67	2.28	0.00	7.66
AFC20	6.91	0.00	19.68	65.74	6.01	1.18	0.00	0.48
AFC20	4.65	0.00	13.67	75.02	4.93	0.76	0.00	0.97

Table 4.4a (continued): Major element composition of modeled solid (extracted bulk i.e. eb) system of a crystallizing mafic magma, contaminated with 40 (AFC40) wt% upper continental crustal material along isobaic cooling path

Process_Assimilant	Na_2O	MgO	Al_2O_3	SiO_2	K_2O	CaO	TiO_2	FeO_t
AFC40	1.17	6.54	19.80	44.81	1.42	15.25	3.36	7.66
AFC40	2.00	10.86	18.44	48.48	0.43	9.79	0.00	10.00
AFC40	1.68	12.05	15.89	48.39	4.23	4.89	0.00	12.87
AFC40	2.22	9.59	15.56	49.30	4.08	5.36	0.00	13.87
AFC40	3.53	6.04	15.08	52.61	0.48	4.69	1.18	16.40
AFC40	5.22	2.77	17.15	59.85	3.07	2.93	0.00	9.01
AFC40	3.64	3.13	14.76	58.90	4.77	2.04	0.00	12.76
AFC40	4.10	0.26	18.27	61.77	8.12	1.52	0.00	5.96
AFC40	3.59	1.49	14.65	58.59	5.02	2.15	0.00	14.51
AFC40	3.10	1.42	13.41	58.64	5.81	2.44	0.00	15.18
AFC40	3.86	0.00	15.95	58.77	6.81	2.49	0.00	12.11
AFC40	3.53	0.00	14.40	74.06	5.27	1.78	0.00	0.97
AFC40	1.95	0.00	10.56	72.39	6.02	1.87	0.00	7.21
AFC40	3.66	0.00	13.38	75.68	5.28	1.08	0.00	0.92
AFC40	1.52	7.13	19.38	45.09	1.27	14.48	3.16	7.97
AFC40	2.01	9.37	18.37	50.68	1.63	8.89	0.00	9.05
AFC40	1.81	10.84	16.00	48.85	3.75	5.63	0.00	13.12
AFC40	3.82	3.43	14.42	55.01	4.69	2.37	0.00	16.27
AFC40	2.47	7.50	17.23	49.55	3.99	4.68	0.00	14.58
AFC40	4.16	5.07	17.24	55.50	0.51	5.21	1.59	10.72
AFC40	4.04	0.30	13.67	76.67	1.75	2.81	0.00	0.76
AFC40	3.25	0.29	14.76	73.71	4.33	2.58	0.00	1.06
AFC40	2.52	0.38	13.82	72.97	6.50	1.41	0.00	2.40
AFC40	1.98	1.05	12.13	71.61	7.31	0.43	0.00	5.49
AFC40	1.48	1.70	11.64	66.75	5.69	1.55	0.00	11.20
AFC40	3.56	0.00	17.28	71.84	2.56	4.76	0.00	0.00
AFC40	1.65	0.00	14.75	71.55	6.09	2.82	0.00	3.15
AFC40	1.45	0.00	13.55	69.54	5.85	2.36	0.00	7.25
AFC40	1.75	0.00	14.16	74.63	6.92	2.05	0.00	0.49
AFC40	1.62	0.00	13.12	74.30	6.03	1.96	0.00	2.97
AFC40	1.67	7.50	18.80	45.63	1.35	13.71	2.93	8.40
AFC40	2.88	7.81	19.15	52.69	1.29	8.10	0.00	8.07
AFC40	2.05	9.39	17.82	48.66	3.90	6.10	0.00	12.08
AFC40	3.78	3.64	14.58	54.67	4.50	2.59	0.00	16.24
AFC40	2.17	5.70	15.44	51.93	5.53	4.45	0.00	14.79
AFC40	4.27	5.06	17.02	53.62	0.65	4.90	1.43	13.04
AFC40	3.66	0.28	14.21	74.85	4.11	2.06	0.00	0.83
AFC40	3.36	0.67	15.85	69.23	5.56	2.37	0.00	2.96
AFC40	1.82	0.47	11.65	75.11	7.35	0.37	0.00	3.23
AFC40	2.71	1.25	13.77	64.24	3.61	2.98	0.00	11.45
AFC40	1.25	0.47	13.02	69.01	7.23	1.51	0.00	7.52
AFC40	2.12	0.00	14.57	71.86	5.19	3.90	0.00	2.36
AFC40	1.22	0.00	12.94	67.71	5.75	2.58	0.00	9.80
AFC40	1.69	0.00	14.67	73.95	6.47	2.69	0.00	0.52
AFC40	1.67	0.00	12.89	69.60	6.42	1.76	0.00	7.65

Table 4.4b: Relative abundance of mineral phases in extracted bulk (solid system) of a crystallizing mafic magma, contaminated with 20 wt% continental crustal material. Mineral abbreviations are after Whitney and Evans (2010).

10% critical crystal fraction; 5 kbar								
Temperature °C	*Cpx_eb*	*Opx_eb*	*Bt_eb*	*Pl_eb*	*Ilm_eb*	*Amp_eb*	*Kfs_eb*	*Qz_eb*
995	20.48	4.27	9.94	49.81	2.97	12.53	0.00	0.00
945	5.05	22.22	6.79	65.94	0.00	0.00	0.00	0.00
925	4.19	16.57	32.17	47.07	0.00	0.00	0.00	0.00
910	4.44	20.36	29.74	45.46	0.00	0.00	0.00	0.00
890	5.93	16.32	24.07	24.01	0.00	0.00	29.66	0.00
880	0.00	29.68	0.00	68.02	2.29	0.00	0.00	0.00
855	0.00	21.42	0.00	44.88	0.00	0.00	33.69	0.00
820	3.44	0.00	0.00	58.46	0.00	0.00	38.10	0.00
805	0.00	23.22	0.00	41.80	0.00	0.00	25.95	9.03
785	1.15	19.52	0.00	54.41	0.00	0.00	0.00	24.93
765	4.68	0.00	0.00	32.37	0.00	0.00	37.74	25.21
745	0.44	0.00	0.00	40.72	0.00	0.00	25.18	33.65
725	7.98	0.00	0.00	50.51	0.00	0.00	9.16	32.35
700	0.05	0.00	11.97	32.63	0.00	0.00	21.66	33.69
675	0.59	0.00	5.57	7.51	0.00	0.00	44.72	41.61
660	0.00	0.00	0.00	11.11	0.00	0.00	88.89	0.00
10% critical crystal fraction; 4 kbar								
Temperature °C	*Cpx_eb*	*Opx_eb*	*Bt_eb*	*Pl_eb*	*Ilm_eb*	*Amp_eb*	*Kfs_eb*	*Qz_eb*
995	21.67	2.66	9.47	52.16	3.41	10.63	0.00	0.00
940	7.87	22.59	12.14	57.41	0.00	0.00	0.00	0.00
915	5.56	21.00	31.80	41.64	0.00	0.00	0.00	0.00
905	10.50	29.51	59.99	0.00	0.00	0.00	0.00	0.00
895	1.32	18.58	30.30	49.80	0.00	0.00	0.00	0.00
880	0.00	26.84	0.00	70.32	2.83	0.00	0.00	0.00
840	0.00	1.65	0.00	12.64	0.00	0.00	54.51	31.20
820	0.00	2.19	0.00	38.25	0.00	0.00	36.47	23.09
805	0.00	17.03	0.00	47.12	0.00	0.00	16.54	19.31
785	0.00	10.84	0.00	61.18	0.00	0.00	0.00	27.98
760	0.00	8.11	0.00	31.77	0.00	0.00	33.84	26.28
740	0.00	0.00	0.00	41.61	0.00	0.00	22.44	35.95
720	0.00	0.00	0.00	43.90	0.00	0.00	22.39	33.72
700	4.36	0.00	0.00	42.31	0.00	0.00	19.52	33.81
675	0.00	0.00	5.84	43.40	0.00	0.00	19.51	31.24
670	0.00	0.00	5.27	36.45	0.00	0.00	21.55	36.72
665	0.00	0.00	0.00	42.41	0.00	0.00	21.74	35.85
660	0.00	0.00	0.00	38.65	0.00	0.00	28.65	32.69
10% critical crystal fraction; 3 kbar								
Temperature °C	*Cpx_eb*	*Opx_eb*	*Bt_eb*	*Pl_eb*	*Ilm_eb*	*Amp_eb*	*Kfs_eb*	*Qz_eb*
995	25.05	2.50	11.77	56.85	3.83	0.00	0.00	0.00
935	0.00	24.94	0.00	43.96	0.00	31.09	0.00	0.00
915	3.63	21.54	36.41	38.42	0.00	0.00	0.00	0.00
890	6.18	17.53	34.19	42.09	0.00	0.00	0.00	0.00
880	0.00	40.39	0.00	58.23	1.38	0.00	0.00	0.00
855	0.00	24.42	0.00	26.19	0.00	0.00	49.40	0.00
835	0.00	24.14	0.00	56.84	0.00	0.00	19.02	0.00
815	0.22	17.73	0.00	57.18	0.00	0.00	24.86	0.00
800	4.91	20.21	0.00	44.48	0.00	0.00	30.40	0.00
780	1.37	3.14	0.00	63.17	0.00	0.00	32.32	0.00
765	6.19	1.13	0.00	75.86	0.00	0.00	16.81	0.00
745	1.73	0.00	40.61	57.66	0.00	0.00	0.00	0.00
715	4.59	0.00	13.61	54.69	0.00	0.00	27.11	0.00
675	0.66	0.00	0.40	43.14	0.00	0.00	55.80	0.00
660	1.36	0.00	0.81	29.43	0.00	0.00	40.67	27.73

4.6.3. Model for post-emplacement crystal fractionation of felsic magma

The modeled system yields different mineral phases in the reactive and extracted bulk depending on the physical conditions and H_2O contents (Table-4.4c-e). Under all the simulated conditions only the relative proportion of melt increases with the increasing water content and lower pressure conditions (Fig. 4.5, 4.6). As a result at higher pressures, first crystal fractionation occurs at 5-20 °C higher temperatures compared to the lower pressure conditions (Fig. 4.5, 4.6). Irrespective of the water content and pressure, the crystallization begins at 900 °C dominantly with plagioclase and a small amount of K-feldspar, quartz and orthopyroxene (Fig 4.5 & 4.6). With decreasing temperature, the amount of K-feldspar and quartz increases significantly. Subsequently, biotite

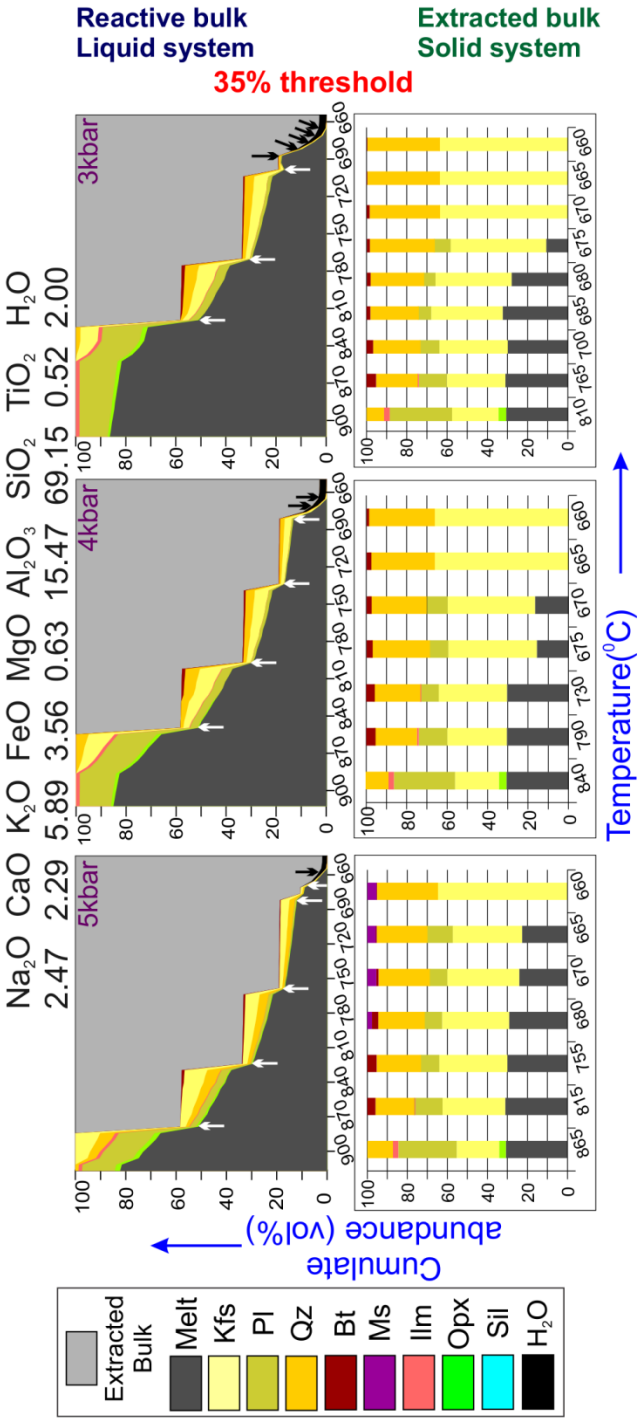

Figure 4.5. a) T-X diagrams, illustrating reactive bulk i.e., the liquid system and extracted bulk i.e., the solid system are presented. The white and black arrows in the reactive bulks mark the extraction temperatures at which crystal-melt separation occurs after attaining the threshold (35% critical crystal fraction).

crystallization begins between 850-820 °C (depending on pressure and H_2O) contents and orthopyroxene disappears (Fig. 4.5, 4.6).

With 2 wt.% H_2O, first crystal separation occurs between 865 °C to 815 °C (5 to 3 kbar) for 35% CCF value, between 840 °C to 795 °C (5 to 3 kbar) for 45% CCF value and between 815 °C to 765 °C (5 to 3 kbar) for 55% CCF value (Table-4.4c). With 4 wt. % H_2O, first crystal separation occur approximately 120 °C below compared to those that resulted from 2 wt. % H_2O (Table- 4.4d). Regardless of the difference in CCF, pressure condition and water content plagioclase + K-feldspar + quartz + ilmenite + melt represents the first crystal-dominated assemblage to be separated from the magma (Fig. 4.5, 4.6). A Small amount of orthopyroxene (<5 wt. %) also occurs in the first crystal-dominated assemblage for 2 wt. % H_2O content and only at a low CCF threshold. Under all other CCF threshold conditions, biotite (~10 wt. %) appears to be

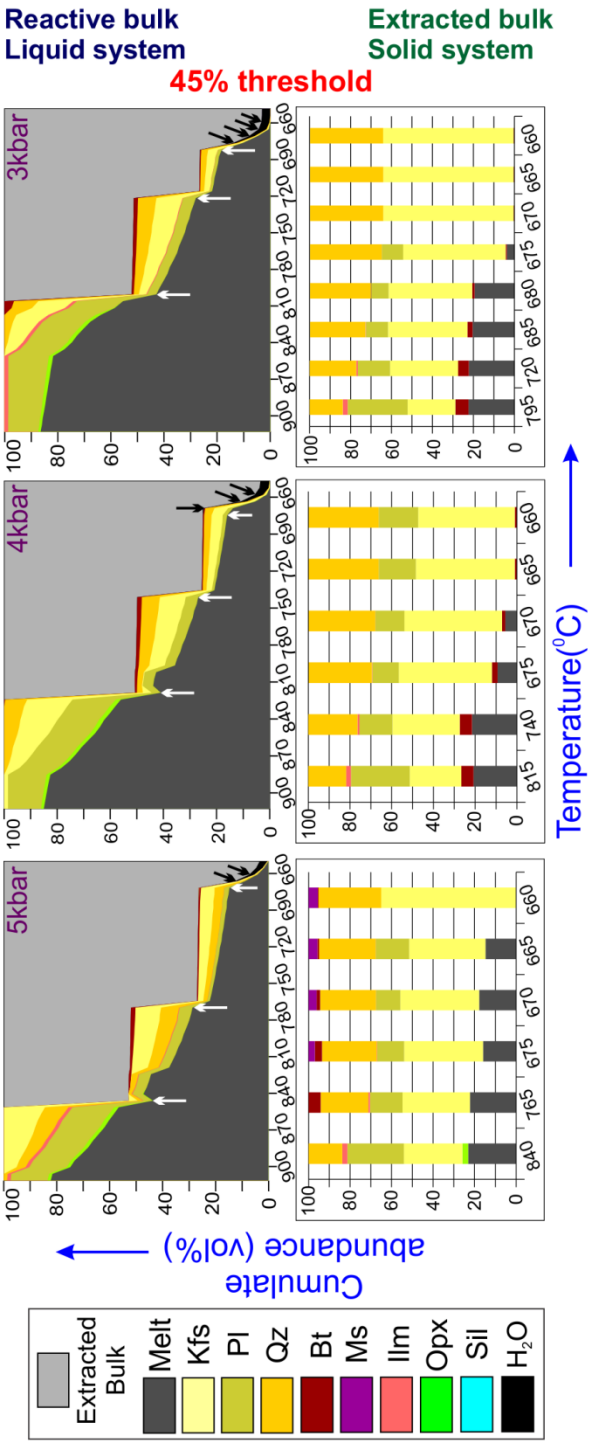

Figure 4.5. b) T-X diagrams, illustrating reactive bulk i.e., the liquid system and extracted bulk i.e., the solid system are presented. The white and black arrows in the reactive bulks mark the extraction temperatures at which crystal-melt separation occurs after attaining the threshold (45% critical crystal fraction).

the dominant ferromagnesian phase in the first crystal-dominated assemblage at lower pressures (4 and 3 kbar). However, for 4 wt. % H_2O, biotite is the only ferromagnesian phase at all pressure under all crystal threshold conditions. In subsequent crystal-dominated assemblages K-feldspar and plagioclase ratio increases whereas and amount of quartz (25-30 wt. %) remains almost the same under all the stipulated conditions (Table-4.4e). In some cases, plagioclase is absent within crystallized assemblage at low CCF threshold and low temperature (670-660 °C). At ~680-660 °C and 5 kbar mica (muscovite) crystallizes with the extracted bulk of granitic (K-feldspar + quartz + plagioclase + biotite) composition (Fig. 4.5, 4.6). In the modeled extracted bulk, plagioclase: K-feldspar ratio varies from 1:1.6 to 1:6 (Table-4.4e).

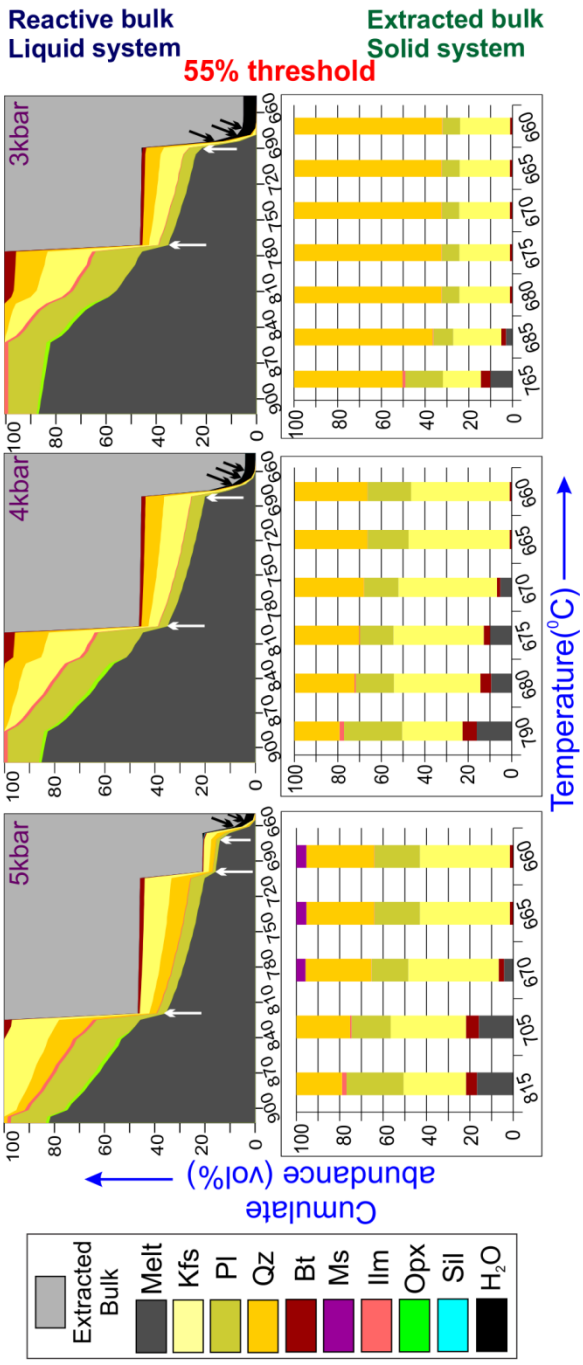

Figure 4.5. c) T-X diagrams, illustrating reactive bulk i.e., the liquid system and extracted bulk i.e., the solid system are presented. The white and black arrows in the reactive bulks mark the extraction temperatures at which crystal-melt separation occurs after attaining the threshold (55% critical crystal fraction).

Considering all the modeled crystal fractionation events, the solid system (extracted bulk) contains 63-77 wt. % SiO_2 whereas the liquid system (reactive bulk) has a narrow range of SiO_2 content (72-76 wt. %) (Table-4.4c, d). In all the stipulated

conditions at variable CCF, pressure and water content the crystallizing magma creates large chemical variations in the extracted bulk or solid system for the first crystal fraction/fractionation episode. These bulks are relatively more mafic (FeO + MgO=3.03-7.22 wt. %) and less siliceous (SiO_2=62.96-71.32 wt. %).

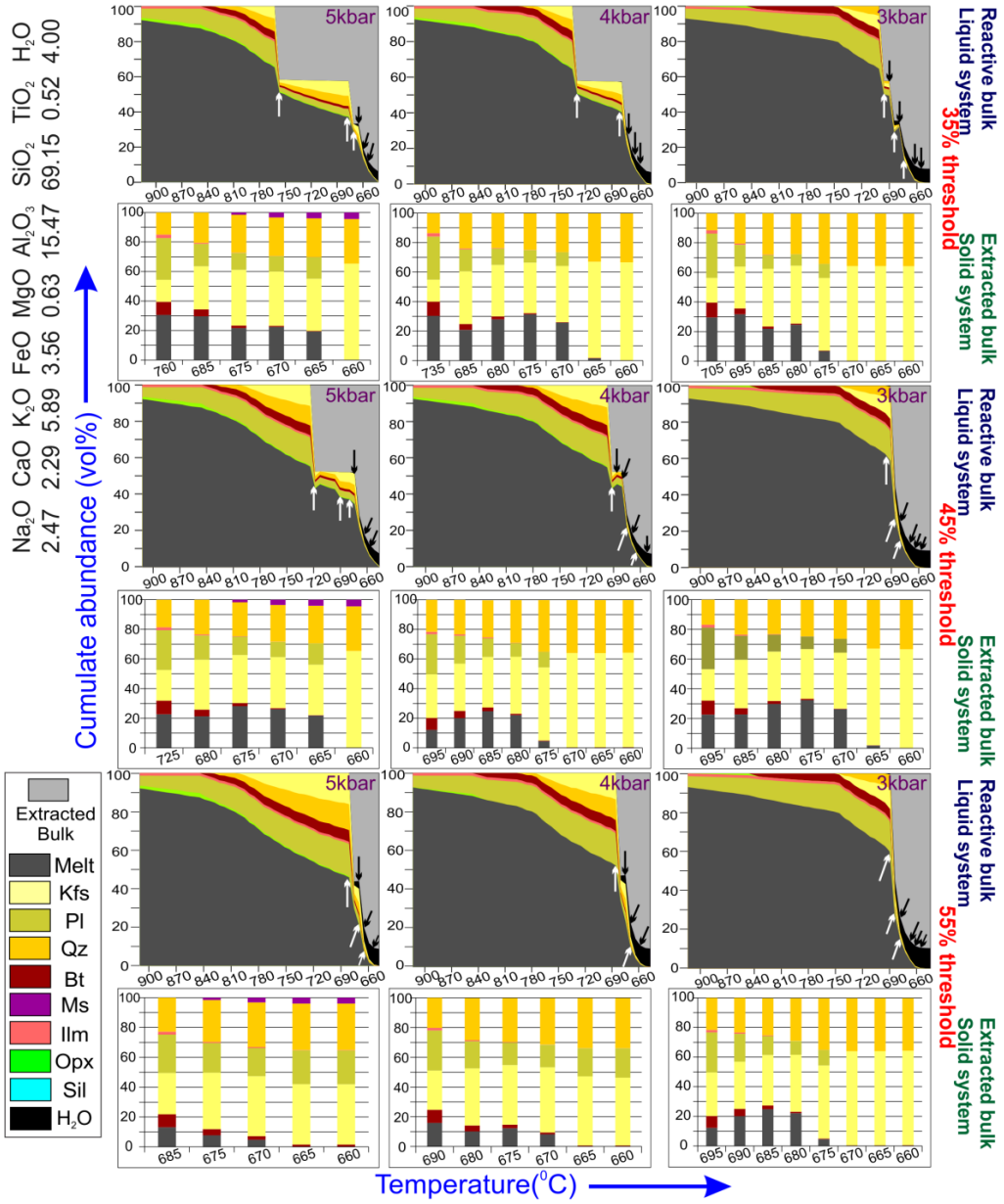

Figure 4.6. T-X diagrams, illustrating reactive bulk i.e., the liquid system and extracted bulk (EB) i.e., the solid system are presented starting with the average whole-rock composition of the studied rocks added with 4 wt% H_2O and varying crystallinity threshold (CCF) and pressure. The white and black arrows in the reactive bulks indicate the extraction points at which crystal-melt separation occurs.Mineral abbreviations are used after Whitney and Evans (2010).

Table 4.4c: Major element composition of modelled melt-dominated (reactive bulk i.e. rb) and crystal-dominated (extracted bulk i.e. eb) system of a crystallizing granitic magma along isobaic cooling path

H_2O (wt%)	Threshold	Pressure (kbar)	Temperature (°C)	Na_2O	MgO	Al_2O_3	SiO_2	K_2O	CaO	TiO_2	FeO_t
2	35-eb	5	865	2.59	0.93	16.69	64.92	4.91	3.56	0.94	5.47
2	35-eb	5	815	2.18	0.57	14.88	70.70	6.52	1.81	0.34	2.98
2	35-eb	5	755	2.18	0.40	14.07	73.08	7.07	1.12	0.12	1.97
2	35-eb	5	680	2.32	0.20	14.28	74.08	7.03	0.84	0.04	1.21
2	35-eb	5	670	2.66	0.07	14.34	75.13	6.69	0.62	0.01	0.46
2	35-eb	5	665	3.30	0.03	14.35	75.49	6.13	0.47	0.01	0.22
2	35-eb	5	660	4.18	0.02	14.40	75.64	5.37	0.26	0.00	0.14
2	35-eb	4	840	2.64	0.97	16.95	64.27	4.96	3.63	0.93	5.65
2	35-eb	4	790	2.17	0.57	14.60	71.19	6.51	1.78	0.34	2.86
2	35-eb	4	730	2.11	0.33	13.86	73.66	7.05	1.04	0.12	1.83
2	35-eb	4	675	2.42	0.12	14.08	75.16	6.83	0.66	0.03	0.71
2	35-eb	4	670	2.89	0.06	14.24	75.57	6.35	0.50	0.02	0.38
2	35-eb	4	665	3.63	0.03	14.34	75.85	5.68	0.29	0.01	0.17
2	35-eb	3	810	2.67	1.00	17.38	63.46	5.06	3.72	0.93	5.79
2	35-eb	3	765	2.16	0.55	14.39	71.50	6.48	1.71	0.34	2.86
2	35-eb	3	700	2.17	0.27	13.50	74.59	6.93	0.93	0.12	1.49
2	35-eb	3	685	2.27	0.12	13.35	76.11	6.85	0.63	0.04	0.63
2	35-eb	3	680	2.54	0.04	13.63	76.69	6.37	0.45	0.01	0.26
2	35-eb	3	675	3.04	0.02	13.91	76.66	5.95	0.30	0.00	0.12
2	35-eb	3	670	3.52	0.01	14.09	76.53	5.54	0.20	0.00	0.11
2	35-rb	5	855	2.37	0.39	14.50	72.56	6.68	1.28	0.19	2.03
2	35-rb	5	810	2.52	0.24	14.21	74.02	6.80	0.86	0.07	1.28
2	35-rb	5	750	2.80	0.12	14.32	74.78	6.59	0.65	0.02	0.72
2	35-rb	5	680	3.20	0.05	14.36	75.35	6.22	0.49	0.01	0.32
2	35-rb	5	670	3.73	0.02	14.37	75.56	5.75	0.37	0.00	0.18
2	35-rb	5	665	4.18	0.02	14.40	75.64	5.37	0.26	0.00	0.14
2	35-rb	5	860	2.37	0.39	14.50	72.56	6.68	1.28	0.19	2.03
2	35-rb	4	840	2.34	0.36	14.28	73.09	6.64	1.22	0.19	1.89
2	35-rb	4	790	2.47	0.20	14.03	74.62	6.75	0.77	0.07	1.11
2	35-rb	4	725	2.76	0.08	14.17	75.39	6.50	0.55	0.02	0.52
2	35-rb	4	675	3.21	0.04	14.28	75.69	6.06	0.41	0.01	0.29
2	35-rb	4	670	3.63	0.03	14.35	75.86	5.68	0.29	0.01	0.17
2	35-rb	3	805	2.31	0.33	13.93	73.80	6.57	1.13	0.19	1.74
2	35-rb	3	760	2.42	0.16	13.56	75.60	6.64	0.68	0.07	0.88
2	35-rb	3	695	2.63	0.07	13.61	76.41	6.40	0.47	0.03	0.38
2	35-rb	3	680	3.22	0.02	13.98	76.62	5.80	0.26	0.00	0.11
2	35-rb	3	675	3.52	0.01	14.09	76.54	5.54	0.20	0.00	0.10

Table 4.4c (continued): Major element composition of modelled melt-dominated (reactive bulk i.e. rb) and crystal-dominated (extracted bulk i.e. eb) system of a crystallizing granitic magma along isobaic cooling path

H_2O (wt%)	Threshold	Pressure (kbar)	Temperature (°C)	Na_2O	MgO	Al_2O_3	SiO_2	K_2O	CaO	TiO_2	FeO_t
2	45-eb	5	840	2.50	0.86	16.34	65.97	5.24	3.23	0.82	5.04
2	45-eb	5	765	2.21	0.58	14.71	70.86	6.52	1.78	0.33	3.01
2	45-eb	5	675	2.35	0.26	14.55	73.30	6.88	1.07	0.12	1.47
2	45-eb	5	670	2.70	0.13	14.34	74.68	6.58	0.76	0.06	0.75
2	45-eb	5	665	3.35	0.06	14.37	75.27	6.05	0.52	0.02	0.35
2	45-eb	5	660	4.09	0.03	14.38	75.60	5.45	0.30	0.01	0.16
2	45-eb	4	815	2.50	0.87	16.46	65.83	5.37	3.22	0.80	4.95
2	45-eb	4	740	2.21	0.56	14.56	71.10	6.44	1.74	0.34	3.04
2	45-eb	4	675	2.47	0.21	14.18	74.28	6.66	0.90	0.11	1.19
2	45-eb	4	670	2.96	0.11	14.27	75.08	6.24	0.62	0.06	0.66
2	45-eb	4	665	3.37	0.07	14.33	75.44	5.88	0.45	0.03	0.42
2	45-eb	3	795	2.55	0.92	16.77	65.04	5.33	3.35	0.82	5.22
2	45-eb	3	720	2.21	0.51	14.53	71.37	6.54	1.69	0.33	2.81
2	45-eb	3	685	2.32	0.22	13.62	74.88	6.68	0.91	0.13	1.23
2	45-eb	3	680	2.57	0.10	13.72	76.09	6.33	0.58	0.06	0.56
2	45-eb	3	675	3.10	0.04	13.95	76.46	5.89	0.33	0.02	0.22
2	45-eb	3	670	3.34	0.03	14.03	76.46	5.69	0.27	0.01	0.17
2	45-eb	3	660	3.35	0.03	14.09	76.42	5.69	0.27	0.01	0.15
2	45-rb	5	840	2.44	0.39	14.59	72.42	6.56	1.34	0.21	2.06
2	45-rb	5	765	2.68	0.19	14.46	74.03	6.60	0.87	0.09	1.08
2	45-rb	5	675	3.13	0.09	14.35	75.00	6.23	0.61	0.04	0.54
2	45-rb	5	670	3.66	0.05	14.37	75.40	5.80	0.43	0.02	0.28
2	45-rb	4	815	2.44	0.37	14.39	72.80	6.46	1.28	0.22	2.04
2	45-rb	4	740	2.69	0.17	14.22	74.60	6.48	0.78	0.09	0.98
2	45-rb	4	675	3.08	0.10	14.29	75.19	6.13	0.57	0.05	0.59
2	45-rb	4	670	3.38	0.07	14.32	75.45	5.88	0.45	0.03	0.42
2	45-rb	3	795	2.39	0.33	14.14	73.42	6.47	1.20	0.21	1.84
2	45-rb	3	720	2.57	0.15	13.73	75.54	6.40	0.69	0.09	0.83
2	45-rb	3	685	2.85	0.07	13.84	76.26	6.10	0.46	0.04	0.39
2	45-rb	3	680	3.17	0.03	13.97	76.45	5.84	0.32	0.02	0.21

Table 4.4c (continued): Major element composition of modelled melt-dominated (reactive bulk i.e. rb) and crystal-dominated (extracted bulk i.e. eb) system of a crystallizing granitic magma along isobaic cooling path

H_2O (wt%)	Threshold	Pressure (kbar)	Temperature (°C)	Na_2O	MgO	Al_2O_3	SiO_2	K_2O	CaO	TiO_2	FeO_t
2	55-eb	5	815	2.41	0.83	16.09	66.75	5.47	3.00	0.74	4.71
2	55-eb	5	705	2.31	0.52	14.76	70.95	6.48	1.75	0.33	2.90
2	55-eb	5	670	2.73	0.20	14.59	73.80	6.45	0.97	0.12	1.14
2	55-eb	5	665	3.19	0.14	14.52	74.46	6.10	0.73	0.08	0.77
2	55-eb	4	790	2.43	0.85	16.15	66.54	5.51	3.02	0.73	4.78
2	55-eb	4	680	2.35	0.43	14.68	71.75	6.50	1.57	0.30	2.42
2	55-eb	4	675	2.63	0.25	14.43	73.72	6.32	1.07	0.17	1.40
2	55-eb	4	670	3.07	0.13	14.41	74.84	6.04	0.69	0.09	0.73
2	55-eb	4	665	3.43	0.08	14.41	75.31	5.77	0.49	0.05	0.45
2	55-eb	4	650	3.46	0.07	14.51	75.34	5.81	0.50	0.01	0.31
2	55-eb	3	765	2.46	0.86	16.35	66.09	5.57	3.06	0.73	4.88
2	55-eb	3	685	2.40	0.37	14.39	72.68	6.38	1.43	0.27	2.08
2	55-eb	3	680	2.67	0.22	14.19	74.40	6.17	0.95	0.16	1.23
2	55-eb	3	660	2.66	0.20	14.18	74.54	6.15	0.94	0.21	1.12
2	55-rb	5	815	2.54	0.38	14.68	72.25	6.43	1.39	0.24	2.10
2	55-rb	5	705	2.86	0.18	14.57	73.98	6.35	0.90	0.11	1.04
2	55-rb	5	670	3.19	0.14	14.52	74.47	6.10	0.73	0.08	0.77
2	55-rb	4	790	2.52	0.35	14.59	72.61	6.39	1.34	0.24	1.97
2	55-rb	4	680	2.83	0.20	14.42	74.17	6.19	0.91	0.14	1.14
2	55-rb	4	675	3.18	0.12	14.41	74.97	5.96	0.63	0.08	0.65
2	55-rb	3	765	2.48	0.32	14.33	73.19	6.32	1.29	0.24	1.83
2	55-rb	3	685	2.67	0.22	14.20	74.40	6.17	0.95	0.16	1.24

Table 4.4d: Major element composition of modelled melt-dominated (reactive bulk i.e. rb) and crystal-dominated (extracted bulk i.e. eb) system of a crystallizing magma along isobaic cooling path

H_2O (wt%)	Threshold	Pressure (kbar)	Temperature (°C)	Na_2O	MgO	Al_2O_3	SiO_2	K_2O	CaO	TiO_2	FeO_t
4	35-eb	5	685	2.20	0.46	14.71	71.32	6.63	1.77	0.33	2.57
4	35-eb	5	675	2.41	0.15	14.01	74.56	6.84	0.99	0.11	0.91
4	35-eb	5	670	2.74	0.07	14.08	75.39	6.56	0.69	0.05	0.41
4	35-eb	5	665	3.37	0.03	14.27	75.58	6.04	0.49	0.02	0.20
4	35-eb	5	660	4.16	0.02	14.35	75.72	5.39	0.27	0.00	0.09
4	35-eb	4	735	2.44	1.09	17.06	63.60	5.12	3.64	0.92	6.13
4	35-eb	4	685	2.24	0.38	14.35	72.37	6.69	1.56	0.29	2.13
4	35-eb	4	680	2.47	0.18	13.74	74.77	6.67	0.99	0.14	1.05
4	35-eb	4	675	2.62	0.08	13.87	75.85	6.43	0.66	0.05	0.44
4	35-eb	4	670	3.05	0.03	14.22	75.92	6.12	0.46	0.02	0.17
4	35-eb	4	665	3.74	0.01	14.36	75.98	5.56	0.27	0.00	0.07
4	35-eb	4	660	3.85	0.01	14.37	76.01	5.46	0.24	0.00	0.07
4	35-eb	3	705	2.49	1.08	17.45	62.96	5.32	3.68	0.90	6.12
4	35-eb	3	695	2.25	0.43	14.33	72.14	6.38	1.71	0.35	2.42
4	35-eb	3	685	2.31	0.15	13.02	76.10	6.66	0.82	0.11	0.83
4	35-eb	3	680	2.63	0.07	13.48	76.46	6.38	0.55	0.04	0.39
4	35-eb	3	675	3.11	0.02	13.89	76.59	5.91	0.32	0.01	0.14
4	35-eb	3	670	3.45	0.02	14.04	76.53	5.61	0.23	0.01	0.11
4	35-rb	5	760	2.53	0.27	14.38	73.33	6.57	1.23	0.19	1.50
4	35-rb	5	685	2.80	0.10	14.10	75.02	6.52	0.78	0.07	0.61
4	35-rb	5	675	3.22	0.05	14.19	75.52	6.16	0.55	0.03	0.28
4	35-rb	5	670	3.73	0.03	14.31	75.63	5.74	0.39	0.01	0.16
4	35-rb	4	735	2.50	0.25	14.15	73.80	6.53	1.16	0.19	1.42
4	35-rb	4	685	2.79	0.11	13.93	75.37	6.36	0.72	0.08	0.63
4	35-rb	4	680	3.07	0.05	14.10	75.91	6.09	0.49	0.03	0.27
4	35-rb	4	675	3.42	0.02	14.29	75.96	5.82	0.36	0.01	0.12
4	35-rb	3	700	2.45	0.24	13.79	74.46	6.38	1.10	0.19	1.38
4	35-rb	3	695	2.61	0.10	13.36	76.30	6.39	0.63	0.07	0.55
4	35-rb	3	685	2.93	0.04	13.71	76.51	6.09	0.42	0.03	0.26
4	35-rb	3	680	3.22	0.02	13.93	76.58	5.82	0.29	0.01	0.13

Table 4.4d (continued): Major element composition of modelled melt-dominated (reactive bulk i.e. rb) and crystal-dominated (extracted bulk i.e. eb) system of a crystallizing magma along isobaic cooling path

H_2O (wt%)	Threshold	Pressure (kbar)	Temperature (°C)	Na_2O	MgO	Al_2O_3	SiO_2	K_2O	CaO	TiO_2	FeO_t
4	45-eb	5	725	2.31	0.97	16.40	65.41	5.40	3.25	0.81	5.46
4	45-eb	5	680	2.33	0.41	14.66	71.67	6.52	1.72	0.33	2.36
4	45-eb	5	675	2.60	0.20	14.36	73.92	6.55	1.10	0.15	1.12
4	45-eb	5	670	2.82	0.08	14.21	75.25	6.44	0.70	0.06	0.44
4	45-eb	5	665	3.41	0.03	14.33	75.53	5.99	0.49	0.02	0.19
4	45-eb	5	660	4.20	0.01	14.37	75.72	5.35	0.26	0.00	0.08
4	45-eb	4	700	2.38	0.97	16.72	64.86	5.46	3.31	0.81	5.49
4	45-eb	4	685	2.32	0.42	14.41	72.09	6.40	1.69	0.33	2.35
4	45-eb	4	680	2.50	0.20	13.70	74.76	6.55	1.01	0.16	1.13
4	45-eb	4	675	2.64	0.08	13.78	75.92	6.40	0.66	0.06	0.46
4	45-eb	4	670	3.06	0.03	14.19	75.95	6.11	0.46	0.02	0.18
4	45-eb	4	665	3.74	0.01	14.35	76.00	5.56	0.27	0.00	0.07
4	45-eb	4	660	3.86	0.01	14.36	76.03	5.45	0.23	0.00	0.06
4	45-eb	3	695	2.41	0.81	16.16	66.73	5.75	2.86	0.67	4.59
4	45-eb	3	690	2.43	0.50	14.77	71.08	6.11	1.89	0.41	2.81
4	45-eb	3	685	2.51	0.24	13.89	74.43	6.31	1.08	0.19	1.36
4	45-eb	3	680	2.65	0.10	13.83	76.03	6.17	0.63	0.07	0.53
4	45-eb	3	675	3.13	0.03	13.99	76.47	5.84	0.34	0.02	0.18
4	45-eb	3	670	3.40	0.02	14.07	76.45	5.62	0.26	0.02	0.15
4	45-rb	5	725	2.64	0.27	14.50	73.12	6.41	1.28	0.21	1.56
4	45-rb	5	680	2.98	0.12	14.32	74.72	6.28	0.80	0.09	0.68
4	45-rb	5	675	3.32	0.05	14.28	75.44	6.05	0.54	0.03	0.29
4	45-rb	5	670	3.79	0.02	14.35	75.62	5.68	0.38	0.01	0.14
4	45-rb	4	700	2.56	0.27	14.16	73.72	6.34	1.21	0.21	1.52
4	45-rb	4	685	2.82	0.12	13.90	75.41	6.28	0.72	0.09	0.66
4	45-rb	4	680	3.09	0.05	14.06	75.95	6.06	0.49	0.03	0.27
4	45-rb	4	675	3.43	0.02	14.27	75.97	5.81	0.35	0.01	0.13
4	45-rb	3	695	2.56	0.34	14.37	73.08	6.13	1.37	0.27	1.89
4	45-rb	3	690	2.72	0.15	13.90	75.35	6.14	0.77	0.12	0.85
4	45-rb	3	685	2.92	0.06	13.92	76.23	5.98	0.48	0.05	0.36

Table 4.4d (continued): Major element composition of modelled melt-dominated (reactive bulk i.e. rb) and crystal-dominated (extracted bulk i.e. eb) system of a crystallizing magma along isobaic cooling path

H_2O (wt%)	Threshold	Pressure (kbar)	Temperature (°C)	Na_2O	MgO	Al_2O_3	SiO_2	K_2O	CaO	TiO_2	FeO_t
4	55-eb	5	685	2.31	0.83	15.98	66.97	5.70	2.86	0.68	4.66
4	55-eb	5	675	2.56	0.38	14.76	71.95	6.24	1.60	0.32	2.18
4	55-eb	5	670	2.91	0.23	14.53	73.63	6.15	1.10	0.18	1.28
4	55-eb	5	665	3.33	0.15	14.48	74.40	5.90	0.80	0.11	0.82
4	55-eb	5	650	3.31	0.15	14.37	74.84	5.89	0.79	0.03	0.60
4	55-eb	4	690	2.37	0.87	16.31	66.14	5.66	3.01	0.72	4.91
4	55-eb	4	680	2.45	0.37	14.35	72.56	6.27	1.55	0.31	2.14
4	55-eb	4	675	2.66	0.22	14.24	74.17	6.21	1.07	0.18	1.26
4	55-eb	4	670	3.09	0.11	14.32	75.11	5.99	0.67	0.09	0.63
4	55-eb	4	665	3.53	0.06	14.36	75.54	5.67	0.44	0.04	0.35
4	55-eb	4	650	3.58	0.01	14.03	76.37	5.53	0.44	0.00	0.04
4	55-eb	3	695	2.41	0.81	16.16	66.73	5.75	2.86	0.67	4.59
4	55-eb	3	690	2.43	0.50	14.77	71.08	6.11	1.89	0.41	2.81
4	55-eb	3	685	2.51	0.24	13.89	74.43	6.31	1.08	0.19	1.36
4	55-eb	3	680	2.65	0.10	13.83	76.03	6.17	0.63	0.07	0.53
4	55-eb	3	675	3.13	0.03	13.99	76.47	5.84	0.34	0.02	0.18
4	55-eb	3	670	3.40	0.02	14.07	76.45	5.62	0.26	0.02	0.15
4	55-eb	3	660	3.41	0.04	14.09	76.39	5.64	0.27	0.01	0.16
4	55-rb	5	685	2.72	0.33	14.68	72.57	6.19	1.41	0.26	1.84
4	55-rb	5	675	3.03	0.20	14.52	73.84	6.08	1.01	0.16	1.16
4	55-rb	4	685	2.61	0.30	14.32	73.28	6.20	1.31	0.25	1.72
4	55-rb	4	680	2.89	0.17	14.27	74.59	6.08	0.89	0.14	0.98
4	55-rb	4	675	3.24	0.09	14.33	75.26	5.88	0.60	0.07	0.53
4	55-rb	3	695	2.56	0.34	14.37	73.08	6.13	1.37	0.27	1.89
4	55-rb	3	690	2.72	0.15	13.90	75.35	6.14	0.77	0.12	0.85
4	55-rb	3	685	2.92	0.06	13.92	76.23	5.98	0.48	0.05	0.36

Table 4.4e: Relative abundance of mineral phases in reactive and extracted bulk (liquid and solid system) of a crystallizing felsic magma with 4wt% of added H_2O at melt extraction points/temperatures after attaining 35% CCF threshold. Mineral abbreviations are after Whitney and Evans (2010).

Temperature	**35% critical crystal fraction: 4 wt% H_2O; 5 kbar**																	
(°C)	*Melt_rb*	*Opx_rb*	*Pl_rb*	*Spl_rb*	*Ilm_rb*	*Bt_rb*	*Qz_rb*	*Kfs_rb*	*H2O_rb*	*Ms_rb*	*Ilm_rb*	*Melt_eb*	*Bt_eb*	*Kfs_eb*	*Pl_eb*	*Ilm_eb*	*Qz_eb*	*Ms_eb*
760	44.41	0.00	3.05	0.25	0.20	1.09	1.55	7.66	0.00	0.00	0.00	11.10	4.36	6.13	12.21	0.80	6.20	0.00
685	41.73	0.00	1.59	0.03	0.09	0.56	2.06	14.52	0.04	0.00	0.00	10.43	2.24	11.62	6.35	0.37	8.24	0.00
675	31.98	0.00	1.26	0.01	0.03	0.22	2.69	19.69	2.67	0.18	0.00	8.00	0.86	15.75	5.02	0.13	10.76	0.72
670	31.34	0.00	1.07	0.00	0.01	0.08	2.59	18.25	7.37	0.36	0.00	7.83	0.33	14.60	4.28	0.05	10.36	1.46
665	25.73	0.00	1.45	0.00	0.00	0.04	2.47	16.60	16.12	0.41	0.00	6.43	0.15	13.28	5.79	0.01	9.87	1.65
660	0.00	0.00	0.00	0.00	0.00	0.02	3.28	20.51	32.33	0.52	0.00	0.00	0.07	28.08	0.00	0.00	13.10	2.10

	35% critical crystal fraction: 4 wt% H_2O; 4 kbar															
	Melt_rb	*Opx_rb*	*Pl_rb*	*Spl_rb*	*Ilm_rb*	*Bt_rb*	*Qz_rb*	*Kfs_rb*	*H2O_rb*	*Sil_rb*	*Ms_rb*	*Melt_eb*	*Bt_eb*	*Kfs_eb*	*Pl_eb*	*Ilm_eb*	*Qz_eb*
735	47.12	0.00	3.39	0.25	0.22	1.23	1.51	1.63	0.00	0.00	0.00	11.78	4.90	6.53	13.55	0.87	6.03
685	37.50	0.00	1.99	0.05	0.10	0.58	3.07	4.53	1.54	0.00	0.00	9.38	2.31	18.10	7.96	0.40	12.30
680	43.79	0.00	1.30	0.02	0.04	0.25	2.64	3.85	4.75	0.01	0.00	10.95	1.01	15.40	5.20	0.16	10.55
675	44.18	0.00	0.89	0.01	0.01	0.10	2.41	3.41	10.04	0.13	0.00	11.04	0.38	13.62	3.57	0.06	9.63
670	35.61	0.00	0.96	0.00	0.00	0.04	2.45	3.71	18.63	0.20	0.00	8.90	0.16	14.84	3.85	0.02	9.82
665	2.79	0.00	0.00	0.00	0.00	0.03	3.88	8.12	34.68	0.33	0.00	0.70	0.12	32.49	0.00	0.00	15.53
660	0.00	0.00	0.00	0.00	0.00	0.01	1.87	3.94	70.05	0.16	0.00	0.00	0.06	15.77	0.00	0.00	7.49

	35% critical crystal fraction: 4 wt% H_2O; 3 kbar													
	Melt_rb	*Pl_rb*	*Spl_rb*	*Ilm_rb*	*Opx_rb*	*Bt_rb*	*Kfs_rb*	*Qz_rb*	*H2O_rb*	*Sil_rb*	*Melt_eb*	*Bt_eb*	*Kfs_eb*	*Pl_eb*	*Qz_eb*
705	46.35	3.53	0.23	0.23	0.00	1.28	1.85	1.29	0.00	0.00	11.59	5.13	7.41	14.13	5.16
695	48.32	1.70	0.07	0.09	0.00	0.50	3.06	2.24	1.33	0.00	12.08	2.00	12.23	6.78	8.95
685	37.68	1.21	0.02	0.03	0.00	0.21	4.74	3.43	4.65	0.00	9.42	0.86	18.98	4.85	13.70
680	38.09	0.90	0.01	0.01	0.00	0.09	4.27	2.95	10.57	0.13	9.52	0.38	17.10	3.58	11.80
675	12.62	1.32	0.00	0.00	0.00	0.05	6.45	4.26	22.04	0.35	3.16	0.19	25.81	5.29	17.05
670	0.00	0.00	0.00	0.00	0.00	0.03	6.50	3.43	48.69	0.30	0.00	0.13	26.00	0.00	13.71
665	0.00	0.00	0.00	0.00	0.00	0.01	2.20	1.16	82.61	0.10	0.00	0.04	8.82	0.00	4.65
660	0.00	0.00	0.00	0.00	0.00	0.00	0.51	0.27	95.96	0.02	0.00	0.01	2.05	0.00	1.08

Table 4.4e (continued): Relative abundance of mineral phases in reactive and extracted bulk (liquid and solid system) of a crystallizing felsic magma with 2wt% of added H_2O at melt extraction points/temperatures after attaining 35% CCF threshold. Mineral abbreviations are after Whitney and Evans (2010).

Temperature	**35% critical crystal fraction: 2 wt% H_2O; 5 kbar**																	
(°C)	*Melt_rb*	*Opx_rb*	*Pl_rb*	*Spl_rb*	*Ilm_rb*	*Qz_rb*	*Kfs_rb*	*Gt_rb*	*Bt_rb*	*Sil_rb*	*Ms_rb*	*H2O_rb*	*Melt_eb*	*Opx_eb*	*Kfs_eb*	*Pl_eb*	*Ilm_eb*	*Qz_eb*
865	48.00	0.50	3.27	0.28	0.28	1.38	2.28	0.00	0.00	0.00	0.00	0.00	12.00	1.98	9.14	13.10	1.13	5.51
815	48.92	0.00	1.52	0.11	0.07	2.10	3.39	0.27	0.32	0.00	0.00	0.00	12.23	0.00	13.54	6.08	0.27	8.39
755	48.25	0.00	1.07	0.03	0.00	2.45	3.78	0.00	0.61	0.00	0.00	0.00	12.06	0.00	15.10	4.27	0.00	9.79
680	47.52	0.00	1.06	0.00	0.00	2.60	3.76	0.00	0.41	0.00	0.29	0.00	11.88	0.00	15.03	4.22	0.00	10.40
670	41.34	0.00	1.10	0.00	0.00	3.03	4.26	0.00	0.15	0.00	0.59	2.67	10.34	0.00	17.05	4.40	0.00	12.12
665	37.74	0.00	1.54	0.00	0.00	2.90	3.96	0.00	0.06	0.00	0.54	7.78	9.44	0.00	15.86	6.18	0.00	11.61
660	0.00	0.00	0.00	0.00	0.00	4.78	10.24	0.00	0.04	0.00	0.80	20.67	0.00	0.00	40.96	0.00	0.00	19.13
	35% critical crystal fraction: 2 wt% H_2O; 4 kbar																	
	Melt_rb	*Opx_rb*	*Pl_rb*	*Spl_rb*	*Ilm_rb*	*Kfs_rb*	*Qz_rb*	*Gt_rb*	*Bt_rb*	*Sil_rb*	*H2O_rb*	*Melt_eb*	*Opx_eb*	*Kfs_eb*	*Pl_eb*	*Ilm_eb*	*Qz_eb*	*Bt_eb*
840	47.80	0.54	3.41	0.32	0.26	2.34	1.18	0.00	0.00	0.00	0.00	11.95	2.18	9.34	13.63	1.05	4.74	0.00
790	48.40	0.00	1.61	0.15	0.03	3.24	2.27	0.00	0.60	0.00	0.00	12.10	0.00	12.94	6.45	0.12	9.07	2.42
730	48.54	0.00	1.04	0.04	0.00	3.72	2.51	0.00	0.56	0.00	0.00	12.14	0.00	14.89	4.14	0.00	10.04	2.23
675	31.08	0.00	1.34	0.01	0.00	6.01	3.90	0.00	0.30	0.24	2.20	7.77	0.00	24.03	5.34	0.00	15.60	1.19
670	30.62	0.00	1.35	0.00	0.00	5.54	3.56	0.00	0.15	0.28	7.34	7.66	0.00	22.16	5.38	0.00	14.25	0.60
665	0.06	0.00	0.00	0.00	0.00	10.44	5.01	0.00	0.09	0.42	20.16	0.01	0.00	41.74	0.00	0.00	20.06	0.34
660	0.00	0.00	0.00	0.00	0.00	5.79	2.78	0.00	0.05	0.23	55.75	0.00	0.00	23.15	0.00	0.00	11.13	0.19
	35% critical crystal fraction: 2 wt% H_2O; 3 kbar																	
	Melt_rb	*Opx_rb*	*Pl_rb*	*Spl_rb*	*Ilm_rb*	*Kfs_rb*	*Qz_rb*	*Bt_rb*	*Sil_rb*	*H2O_rb*	*Melt_eb*	*Opx_eb*	*Kfs_eb*	*Pl_eb*	*Ilm_eb*	*Qz_eb*	*Bt_eb*	
810	47.65	0.56	3.51	0.35	0.24	2.49	0.93	0.00	0.00	0.00	11.91	2.25	9.94	14.06	0.95	3.74	0.00	
765	48.79	0.00	1.59	0.15	0.03	3.18	2.24	0.61	0.00	0.00	12.20	0.00	12.71	6.35	0.13	8.97	2.45	
700	48.00	0.00	1.11	0.04	0.01	3.79	2.62	0.43	0.00	0.00	12.00	0.00	15.17	4.43	0.04	10.48	1.74	
685	49.74	0.00	0.72	0.01	0.00	3.79	2.56	0.19	0.05	1.22	12.44	0.00	15.15	2.88	0.01	10.23	0.75	
680	44.54	0.00	0.69	0.00	0.00	4.16	2.93	0.08	0.20	4.01	11.13	0.00	16.66	2.76	0.00	11.70	0.31	
675	21.45	0.00	1.20	0.00	0.00	6.55	4.34	0.05	0.38	10.62	5.36	0.00	26.20	4.79	0.00	17.36	0.19	
670	0.00	0.00	0.00	0.00	0.00	9.21	4.85	0.05	0.44	27.23	0.00	0.00	36.84	0.00	0.00	19.41	0.19	
665	0.00	0.00	0.00	0.00	0.00	4.41	2.32	0.02	0.21	65.17	0.00	0.00	17.64	0.00	0.00	9.29	0.09	

Table 4.4e (continued): Relative abundance of mineral phases in reactive and extracted bulk (liquid and solid system) of a crystallizing felsic magma with 4wt% of added H_2O at melt extraction points/temperatures after attaining 45% CCF threshold. Mineral abbreviations are after Whitney and Evans (2010).

Temperature	**45% critical crystal fraction: 4 wt% H_2O; 5 kbar**																
(°C)	*Melt_rb*	*Opx_rb*	*Pl_rb*	*Spl_rb*	*Ilm_rb*	*Bt_rb*	*Qz_rb*	*Kfs_rb*	*H2O_rb*	*Ms_rb*	*Melt_eb*	*Bt_eb*	*Kfs_eb*	*Pl_eb*	*Ilm_eb*	*Qz_eb*	*Ms_eb*
725	39.57	0.00	3.49	0.19	0.26	1.31	2.31	2.55	0.00	0.00	9.89	5.23	10.19	13.98	1.02	9.26	0.00
680	38.04	0.00	2.18	0.03	0.13	0.65	2.96	4.22	1.57	0.00	9.51	2.60	16.89	8.74	0.51	11.86	0.00
675	43.84	0.00	1.45	0.01	0.05	0.26	2.52	3.55	4.93	0.21	10.96	1.06	14.20	5.79	0.21	10.08	0.85
670	39.28	0.00	1.16	0.00	0.02	0.09	2.65	3.64	11.04	0.41	9.82	0.37	14.57	4.63	0.07	10.58	1.66
665	30.96	0.00	1.52	0.00	0.01	0.03	2.55	3.40	21.52	0.45	7.74	0.13	13.58	6.09	0.02	10.20	1.80
660	0.00	0.00	0.00	0.00	0.00	0.02	3.60	7.73	40.36	0.58	0.00	0.06	30.92	0.00	0.00	14.39	2.34
	45% critical crystal fraction: 4 wt% H_2O; 4 kbar																
	Melt_rb	*Opx_rb*	*Pl_rb*	*Spl_rb*	*Ilm_rb*	*Bt_rb*	*Qz_rb*	*Kfs_rb*	*H2O_rb*	*Sil_rb*	*Ms_rb*	*Melt_eb*	*Bt_eb*	*Kfs_eb*	*Pl_eb*	*Ilm_eb*	*Qz_eb*
700	39.50	0.00	3.65	0.16	0.27	1.35	2.10	2.60	0.00	0.00	0.00	9.87	5.40	10.38	14.59	1.07	8.40
685	39.51	0.00	2.09	0.05	0.11	0.60	2.91	3.98	1.92	0.00	0.00	9.88	2.38	15.93	8.34	0.46	11.63
680	45.17	0.00	1.28	0.02	0.05	0.25	2.50	3.54	5.35	0.00	0.00	11.29	1.01	14.15	5.13	0.18	10.01
675	44.62	0.00	0.87	0.01	0.02	0.09	2.33	3.25	10.85	0.11	0.00	11.16	0.38	13.00	3.48	0.06	9.32
670	35.64	0.00	0.94	0.00	0.00	0.04	2.39	3.60	19.63	0.19	0.00	8.91	0.16	14.39	3.75	0.02	9.56
665	3.14	0.00	0.00	0.00	0.00	0.03	3.79	7.92	35.80	0.32	0.00	0.79	0.11	31.68	0.00	0.00	15.15
660	0.00	0.00	0.00	0.00	0.00	0.01	1.83	3.86	70.72	0.16	0.00	0.00	0.05	15.43	0.00	0.00	7.32
	45% critical crystal fraction: 4 wt% H_2O; 3 kbar																
	Melt_rb	*Pl_rb*	*Spl_rb*	*Ilm_rb*	*Opx_rb*	*Bt_rb*	*Kfs_rb*	*Qz_rb*	*H2O_rb*	*Sil_rb*	*Melt_eb*	*Bt_eb*	*Kfs_eb*	*Pl_eb*	*Ilm_eb*	*Qz_eb*	
695	25.10	4.14	0.20	0.24	0.00	1.35	4.31	3.17	1.56	0.00	6.28	5.38	17.26	16.55	0.97	12.68	
690	35.13	2.46	0.09	0.13	0.00	0.70	3.93	2.90	5.05	0.00	8.78	2.79	15.71	9.85	0.51	11.61	
685	37.75	1.46	0.03	0.05	0.00	0.30	3.67	2.70	11.49	0.05	9.44	1.22	14.67	5.83	0.20	10.80	
680	31.10	0.97	0.01	0.02	0.00	0.11	3.82	2.76	21.73	0.18	7.77	0.45	15.29	3.89	0.06	11.05	
675	7.03	1.20	0.00	0.00	0.00	0.05	5.34	3.59	38.72	0.31	1.76	0.19	21.37	4.82	0.02	14.34	
670	0.00	0.00	0.00	0.00	0.00	0.02	3.82	2.03	69.71	0.18	0.00	0.09	15.28	0.00	0.01	8.12	
665	0.00	0.00	0.00	0.00	0.00	0.01	1.01	0.54	92.01	0.05	0.00	0.02	4.03	0.00	0.00	2.14	

Table 4.4e (continued): Relative abundance of mineral phases in reactive and extracted bulk (liquid and solid system) of a crystallizing felsic magma with 2wt% of added H_2O at melt extraction points/temperatures after attaining 45% CCF threshold. Mineral abbreviations are after Whitney and Evans (2010).

Temperature	**45% critical crystal fraction: 2 wt% H_2O; 5 kbar**																	
(°C)	*Melt_rb*	*Opx_rb*	*Pl_rb*	*Spl_rb*	*Ilm_rb*	*Qz_rb*	*Kfs_rb*	*Gt_rb*	*Bt_rb*	*Sil_rb*	*Ms_rb*	*H2O_rb*	*Ilm_rb*	*Melt_eb*	*Opx_eb*	*Kfs_eb*	*Pl_eb*	*Bt_eb*
840	40.17	0.47	3.43	0.28	0.28	1.97	3.38	0.15	0.00	0.00	0.00	0.00	0.00	10.04	1.87	13.52	13.71	0.00
765	39.97	0.00	2.05	0.13	0.05	2.89	4.04	0.00	0.86	0.00	0.00	0.00	0.00	9.99	0.00	16.15	8.18	3.42
675	31.74	0.00	1.88	0.02	0.03	3.68	5.24	0.00	0.56	0.00	0.46	1.02	0.00	7.94	0.00	20.97	7.51	2.24
670	33.12	0.00	1.57	0.01	0.01	3.49	4.87	0.00	0.26	0.00	0.55	4.82	0.00	8.28	0.00	19.49	6.30	1.02
665	26.52	0.00	2.10	0.00	0.00	3.41	4.55	0.00	0.11	0.00	0.59	13.04	0.00	6.63	0.00	18.22	8.38	0.46
660	0.00	0.00	0.00	0.00	0.00	4.19	8.92	0.00	0.05	0.00	0.68	30.80	0.00	0.00	0.00	35.69	0.00	0.21

	45% critical crystal fraction: 2 wt% H_2O; 4 kbar															
	Melt_rb	*Opx_rb*	*Pl_rb*	*Spl_rb*	*Ilm_rb*	*Kfs_rb*	*Qz_rb*	*Bt_rb*	*Sil_rb*	*H2O_rb*	*Ms_rb*	*Melt_eb*	*Bt_eb*	*Kfs_eb*	*Pl_eb*	*Ilm_eb*	*Qz_eb*
815	37.86	0.00	3.71	0.41	0.15	3.11	2.30	0.86	0.00	0.00	0.00	9.46	3.45	12.43	14.83	0.59	9.21
740	39.15	0.00	2.11	0.13	0.05	4.05	3.00	0.87	0.00	0.00	0.00	9.79	3.49	16.21	8.42	0.21	11.99
675	20.66	0.00	2.06	0.03	0.03	6.90	4.59	0.49	0.21	2.62	0.00	5.17	1.98	27.58	8.24	0.13	18.36
670	12.38	0.00	2.24	0.01	0.02	7.24	4.76	0.28	0.32	10.16	0.00	3.10	1.12	28.97	8.98	0.06	19.02
665	0.00	0.00	2.57	0.01	0.01	6.52	4.42	0.16	0.33	29.86	0.00	0.00	0.66	26.10	10.27	0.03	17.68
660	0.00	0.00	1.24	0.00	0.00	2.90	2.01	0.08	0.15	68.03	0.00	0.00	0.30	11.61	4.97	0.02	8.06

	45% critical crystal fraction: 2 wt% H_2O; 3 kbar															
	Melt_rb	*Opx_rb*	*Pl_rb*	*Spl_rb*	*Ilm_rb*	*Kfs_rb*	*Qz_rb*	*Bt_rb*	*H2O_rb*	*Sil_rb*	*and_rb*	*Melt_eb*	*Bt_eb*	*Kfs_eb*	*Pl_eb*	*Ilm_eb*
795	39.58	0.00	3.76	0.42	0.13	2.85	2.00	0.93	0.00	0.00	0.00	9.90	3.73	11.41	15.03	0.53
720	40.04	0.00	2.05	0.12	0.06	4.13	2.86	0.77	0.00	0.00	0.00	10.01	3.08	16.53	8.18	0.23
685	37.55	0.00	1.44	0.03	0.03	4.94	3.45	0.38	1.37	0.06	0.00	9.39	1.54	19.76	5.76	0.12
680	35.13	0.00	1.13	0.01	0.01	5.10	3.59	0.17	4.89	0.22	0.00	8.78	0.68	20.39	4.51	0.05
675	8.30	0.00	1.67	0.01	0.00	7.77	5.18	0.09	13.83	0.44	0.00	2.07	0.38	31.07	6.70	0.01
670	0.00	0.00	0.00	0.00	0.00	7.72	4.12	0.06	38.67	0.36	0.00	0.00	0.24	30.88	0.00	0.00
665	0.00	0.00	0.00	0.00	0.00	3.03	1.62	0.02	75.91	0.14	0.00	0.00	0.10	12.13	0.00	0.00

Table 4.4e (continued): Relative abundance of mineral phases in reactive and extracted bulk (liquid and solid system) of a crystallizing felsic magma with 4wt% of added H_2O at melt extraction points/temperatures after attaining 55% CCF threshold. Mineral abbreviations are after Whitney and Evans (2010).

Temperature	**55% critical crystal fraction: 4 wt% H_2O; 5 kbar**																	
(°C)	*Melt_rb*	*Opx_rb*	*Pl_rb*	*Spl_rb*	*Ilm_rb*	*Gt_rb*	*Qz_rb*	*Bt_rb*	*Kfs_rb*	*Ms_rb*	*H2O_rb*	*Melt_eb*	*Bt_eb*	*Kfs_eb*	*Pl_eb*	*Ilm_eb*	*Qz_eb*	*Ms_eb*
695	30.83	0.00	3.74	0.07	0.33	0.00	3.15	1.45	3.56	0.00	0.00	7.71	5.82	14.23	14.95	1.30	12.59	0.00
675	23.00	0.00	3.04	0.01	0.17	0.00	3.96	0.71	5.30	0.33	3.68	5.75	2.84	21.18	12.17	0.66	15.83	1.34
670	25.27	0.00	2.42	0.00	0.08	0.00	3.39	0.36	4.74	0.36	11.68	6.32	1.42	18.96	9.68	0.33	13.57	1.42
665	19.99	0.00	2.30	0.00	0.03	0.00	2.85	0.15	3.98	0.31	26.87	5.00	0.60	15.91	9.19	0.14	11.41	1.26
660	0.00	0.00	2.76	0.00	0.01	0.00	2.81	0.06	3.82	0.30	51.22	0.00	0.24	15.29	11.02	0.04	11.23	1.20

	55% critical crystal fraction: 4 wt% H_2O; 4 kbar															
	Melt_rb	*Opx_rb*	*Pl_rb*	*Spl_rb*	*Ilm_rb*	*Bt_rb*	*Qz_rb*	*Kfs_rb*	*H2O_rb*	*Sil_rb*	*Ms_rb*	*Melt_eb*	*Bt_eb*	*Kfs_eb*	*Pl_eb*	*Ilm_eb*	*Qz_eb*
690	30.95	0.00	3.91	0.14	0.28	1.39	2.80	3.61	0.64	0.00	0.00	7.74	5.56	14.45	15.65	1.12	11.18
680	21.39	0.00	2.87	0.05	0.14	0.69	4.22	5.69	4.76	0.04	0.00	5.35	2.77	22.75	11.48	0.54	16.90
675	22.54	0.00	2.07	0.02	0.07	0.36	3.74	5.17	13.92	0.16	0.00	5.63	1.42	20.66	8.29	0.28	14.94
670	12.99	0.00	1.78	0.01	0.03	0.16	3.36	4.90	31.45	0.23	0.00	3.25	0.63	19.58	7.13	0.11	13.43
665	0.00	0.00	1.60	0.00	0.01	0.07	2.57	3.71	59.22	0.20	0.00	0.00	0.26	14.85	6.39	0.04	10.26
660	0.00	0.00	0.49	0.00	0.00	0.02	0.76	1.08	87.88	0.06	0.00	0.00	0.08	4.33	1.98	0.02	3.05

	55% critical crystal fraction: 4 wt% H_2O; 3 kbar														
	Melt_rb	*Pl_rb*	*Spl_rb*	*Ilm_rb*	*Opx_rb*	*Bt_rb*	*Kfs_rb*	*Qz_rb*	*H2O_rb*	*Sil_rb*	*Melt_eb*	*Bt_eb*	*Kfs_eb*	*Pl_eb*	*Ilm_eb*	*Qz_eb*
695	25.10	4.14	0.20	0.24	0.00	1.35	4.31	3.17	1.56	0.00	6.28	5.38	17.26	16.55	0.97	12.68
690	35.13	2.46	0.09	0.13	0.00	0.70	3.93	2.90	5.05	0.00	8.78	2.79	15.71	9.85	0.51	11.61
685	37.75	1.46	0.03	0.05	0.00	0.30	3.67	2.70	11.49	0.05	9.44	1.22	14.67	5.83	0.20	10.80
680	31.10	0.97	0.01	0.02	0.00	0.11	3.82	2.76	21.73	0.18	7.77	0.45	15.29	3.89	0.06	11.05
675	7.03	1.20	0.00	0.00	0.00	0.05	5.34	3.59	38.72	0.31	1.76	0.19	21.37	4.82	0.02	14.34
670	0.00	0.00	0.00	0.00	0.00	0.02	3.82	2.03	69.71	0.18	0.00	0.09	15.28	0.00	0.01	8.12
665	0.00	0.00	0.00	0.00	0.00	0.01	1.01	0.54	92.01	0.05	0.00	0.02	4.03	0.00	0.00	2.14

Table 4.4e (continued): Relative abundance of mineral phases in reactive and extracted bulk (liquid and solid system) of a crystallizing felsic magma with 2wt% of added H_2O at melt extraction points/temperatures after attaining 55% CCF threshold. Mineral abbreviations are after Whitney and Evans (2010).

Temperature	**55% critical crystal fraction: 2 wt% H_2O; 5 kbar**																	
(°C)	*Melt_rb*	*Opx_rb*	*Pl_rb*	*Spl_rb*	*Ilm_rb*	*Qz_rb*	*Kfs_rb*	*Gt_rb*	*Bt_rb*	*Ms_rb*	*H2O_rb*	*Melt_eb*	*Bt_eb*	*Kfs_eb*	*Pl_eb*	*Ilm_eb*	*Qz_eb*	*Ms_eb*
815	32.53	0.00	3.67	0.35	0.19	2.84	3.85	0.16	0.81	0.00	0.00	8.13	3.22	15.40	14.69	0.76	11.37	0.00
705	31.94	0.00	2.61	0.08	0.10	3.46	4.80	0.00	0.97	0.00	0.00	7.99	3.88	19.18	10.43	0.41	13.85	0.00
670	10.53	0.00	2.97	0.01	0.05	5.15	7.02	0.00	0.48	0.79	4.39	2.63	1.94	28.09	11.88	0.22	20.61	3.18
665	0.00	0.00	3.55	0.01	0.03	5.13	6.73	0.00	0.31	0.83	17.05	0.00	1.23	26.92	14.21	0.14	20.52	3.30
660	0.00	0.00	2.11	0.00	0.02	3.05	4.00	0.00	0.18	0.49	50.69	0.00	0.74	16.00	8.45	0.08	12.20	1.97

	55% critical crystal fraction: 2 wt% H_2O; 4 kbar															
	Melt_rb	*Opx_rb*	*Pl_rb*	*Spl_rb*	*Ilm_rb*	*Kfs_rb*	*Qz_rb*	*Bt_rb*	*Sil_rb*	*H2O_rb*	*Ms_rb*	*Melt_eb*	*Bt_eb*	*Kfs_eb*	*Pl_eb*	*Ilm_eb*	*Qz_eb*
790	31.73	0.00	3.83	0.38	0.16	3.79	2.86	1.06	0.00	0.00	0.00	7.93	4.23	15.14	15.31	0.62	11.45
680	21.29	0.00	2.86	0.06	0.12	6.17	4.28	0.90	0.07	1.08	0.00	5.32	3.62	24.68	11.42	0.49	17.12
675	21.33	0.00	2.39	0.03	0.07	6.13	4.28	0.50	0.21	5.36	0.00	5.33	2.01	24.50	9.54	0.26	17.11
670	11.07	0.00	2.38	0.01	0.03	6.52	4.41	0.26	0.31	16.47	0.00	2.77	1.05	26.10	9.53	0.13	17.65
665	0.00	0.00	2.25	0.01	0.01	5.29	3.64	0.14	0.28	41.90	0.00	0.00	0.54	21.16	9.01	0.06	14.57
660	0.00	0.00	0.89	0.00	0.01	1.93	1.36	0.05	0.10	78.28	0.00	0.00	0.21	7.71	3.56	0.02	5.45

	55% critical crystal fraction: 2 wt% H_2O; 3 kbar															
	Melt_rb	*Opx_rb*	*Pl_rb*	*Spl_rb*	*Ilm_rb*	*Kfs_rb*	*Qz_rb*	*Bt_rb*	*H2O_rb*	*Sil_rb*	*Melt_eb*	*Bt_eb*	*Kfs_eb*	*Pl_eb*	*Ilm_eb*	*Qz_eb*
765	31.85	0.00	3.94	0.37	0.15	3.76	2.69	1.13	0.00	0.00	7.96	4.50	15.03	15.76	0.61	10.75
685	13.81	0.00	3.04	0.09	0.11	7.01	5.00	0.78	2.02	0.12	3.45	3.14	28.05	12.15	0.43	19.99
680	0.00	0.00	3.03	0.05	0.07	8.24	5.93	0.51	9.24	0.33	0.00	2.02	32.97	12.10	0.27	23.70
675	0.00	0.00	2.21	0.04	0.05	6.02	4.33	0.37	33.73	0.24	0.00	1.49	24.07	8.84	0.20	17.31
670	0.00	0.00	0.94	0.01	0.02	2.57	1.84	0.16	71.79	0.10	0.00	0.64	10.26	3.74	0.09	7.37
665	0.00	0.00	0.25	0.00	0.01	0.66	0.48	0.04	92.71	0.03	0.00	0.17	2.63	0.98	0.02	1.90

4.7. U-Pb zircon geochronology

The section discusses the results of in-situ U-Pb zircon geochronology that were carried out at the Department of Geology and Geophysics, Indian Institute of Technology, Kharagpur. Details of the analytical techniques are described in Appendix. The results are presented in Table-4.5 and Fig. 4.7.

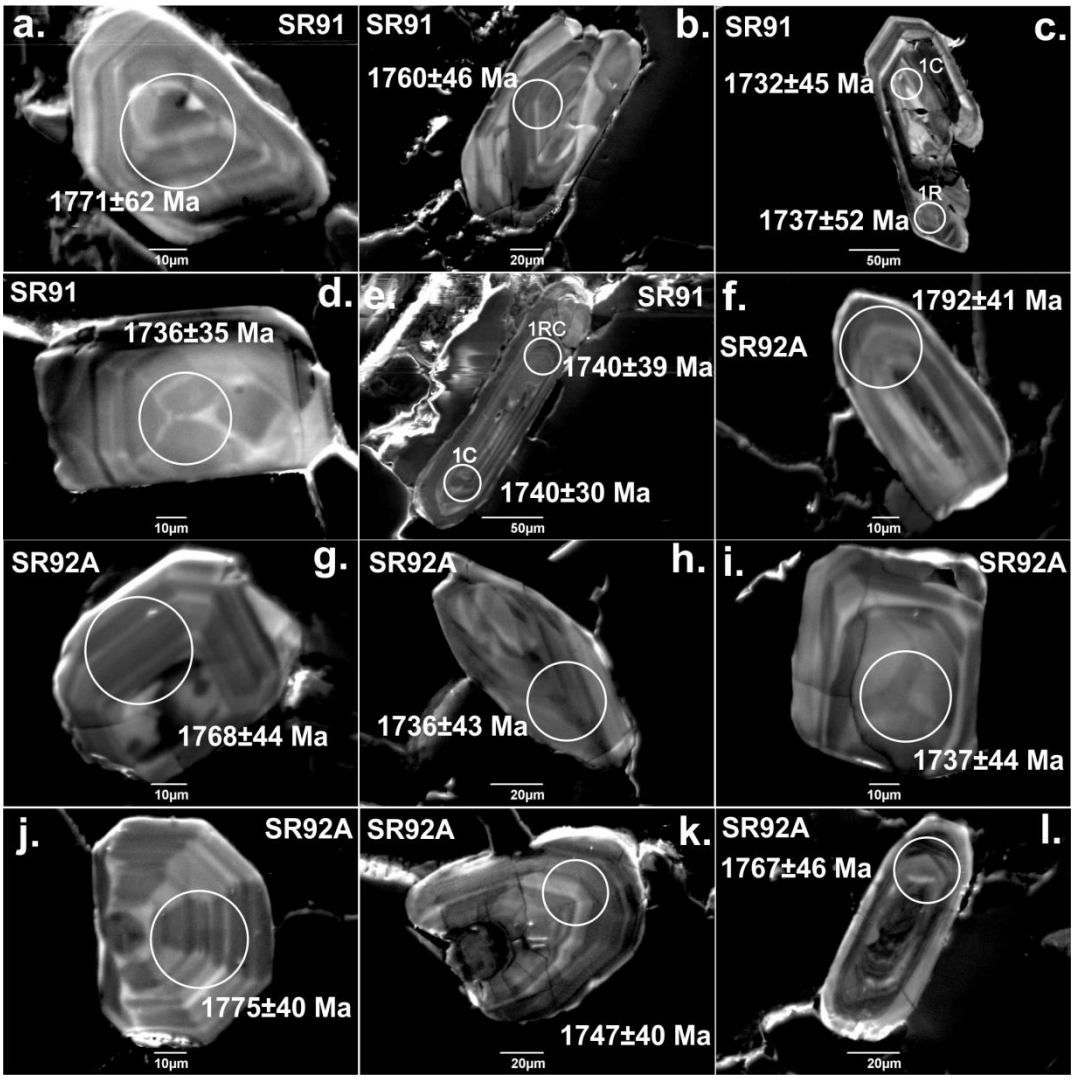

Figure 4.7. (a-l) CL images of few representatives euhedral to subhedral zircon grains in the studied porphyritic metagranitoid (SR91, SR92A) that are selected for LA-ICPMS analysis. Analysed concordant spots (25-35µm diameter) and respective $^{207}Pb/^{206}Pb$ spot dates (Ma) within the oscillatory zones are presented in the figure.

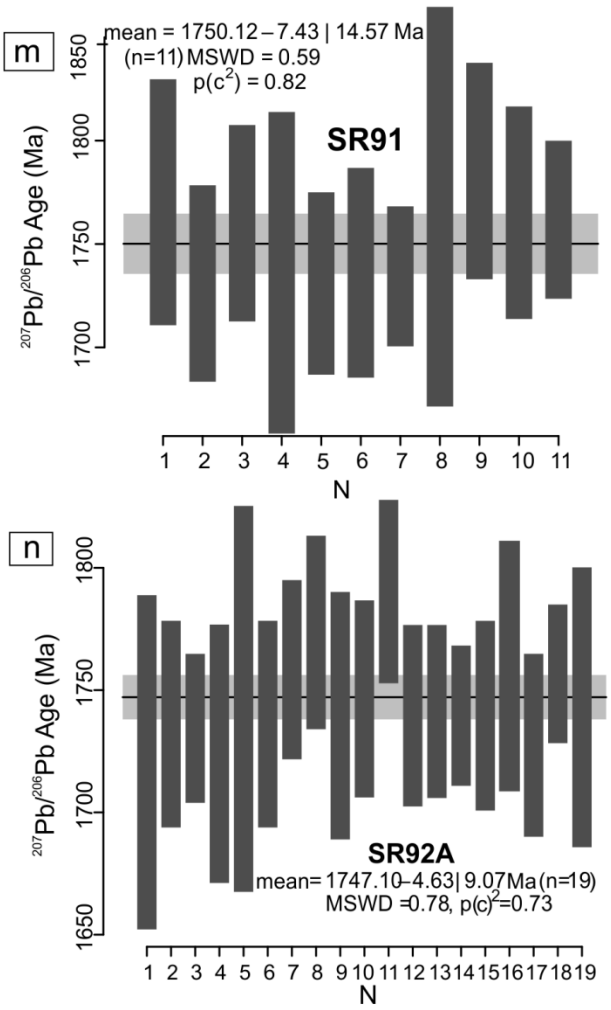

Figure 4.7 contd. (m-n) Results of $^{207}Pb/^{206}Pb$ weighted mean age of the two representative samples yield the magmatic emplacement age of the porphyritic metagranitoid of the study area.

Both the optical and scanning electron microscopic study reveals that the studied porphyritic metagranitoids have large (50 to 200 µm) elongated to tabular, stumpy or rounded zircon grains with aspect ratios varying from 3:1 to 1:1 which are frequently associated with biotite, amphibole, quartz and feldspars in the matrix and rarely in association with garnet porphyroblasts. Cathode-luminescence (CL) images show that most of the zircons have oscillatory zoning whereas occasional patchy zoning is also observed in a few grains (Fig. 4.7a-l). Oscillatory zoning is present within zircons crystallized from a high temperature melt and yields the timing of magmatic event (Corfu et al., 2003). Lack of conspicuous leucosome evident from petrographic study and field features suggests that studied metagranitoids were not metamorphosed under high temperature conditions. Hence, oscillatory zoning in the studied zircon grains reflects crystallization from magma.

U-Pb concentrations from two representative samples of porphyritic metagranitoids (11 grains from SR91 and 20 grains from SR92A) are presented in table-4.5. Considering the concordant (>90% concordance) dates from both the oscillatory and patchy zones of the zircons from the SR91 yield a weighted mean $^{207}Pb/^{206}Pb$ age of 1750±15 Ma (n=11; MSWD = 0.59, ρ (x^2) = 0.82) whereas zircons

Table 4.5: U-Pb isotopic dating of in-situ zircon grains from two representative porphyritic granitoids of the studied area

Sample no	Analysis name	Spot size (μm)	U (ppm)	Pb (ppm)	Th/U	Ratios						rho	Date (Ma)						Degree of concordance(%)
						$^{206}Pb/^{238}U$	±2σ (abs.)	$^{207}Pb/^{235}U$	±2σ (abs.)	$^{207}Pb/^{206}Pb$	±2σ (abs.)		$^{206}Pb/^{238}U$	±2σ	$^{207}Pb/^{235}U$	±2σ	$^{207}Pb/^{206}Pb$	±2σ	
	21-1C	30	653.16	158.89	0.99	0.32	0.0114	4.74	0.2335	0.11	0.0036	0.73	1778	56	1775	41	1771	62	100
	17-1C	30	314.22	83.97	0.62	0.31	0.0077	4.51	0.1648	0.11	0.0028	0.68	1733	38	1732	30	1732	49	100
	13-1C	30	372.07	99.09	0.44	0.30	0.0080	4.42	0.1622	0.11	0.0027	0.73	1682	40	1717	30	1760	46	96
	12-1C	30	398.78	99.91	0.61	0.30	0.0145	4.35	0.2827	0.11	0.0046	0.75	1677	72	1704	54	1737	79	97
	2-1C	25	336.15	95.00	0.77	0.31	0.0087	4.51	0.1685	0.11	0.0026	0.76	1734	43	1733	31	1732	45	100
SR91	2-1R	30	452.90	120.67	0.30	0.29	0.0076	4.21	0.1638	0.11	0.0030	0.68	1627	38	1676	32	1737	52	94
	2-2C	30	300.43	84.46	0.47	0.30	0.0076	4.45	0.1394	0.11	0.0020	0.79	1709	37	1721	26	1736	35	98
	2-3C	30	355.62	92.74	0.73	0.32	0.0141	4.74	0.3186	0.11	0.0055	0.66	1774	69	1775	56	1775	92	100
	4-1C	30	618.76	137.37	0.54	0.32	0.0100	4.79	0.2053	0.11	0.0032	0.73	1779	49	1783	36	1787	53	100
	6-1C	30	497.03	139.94	0.19	0.29	0.0117	4.29	0.2132	0.11	0.0031	0.82	1633	59	1692	41	1766	52	92
	10-1C	30	237.06	65.82	0.70	0.30	0.0064	4.46	0.1334	0.11	0.0023	0.71	1692	32	1724	25	1763	38	96
	13-1C	30	524.61	152.09	0.30	0.30	0.0093	4.43	0.2145	0.11	0.0040	0.63	1716	46	1718	40	1721	69	100
	10-1C	30	664.70	174.04	0.75	0.31	0.0077	4.53	0.1538	0.11	0.0025	0.73	1736	38	1736	28	1736	43	100
	2-1C	30	511.28	144.36	0.21	0.31	0.0041	4.53	0.0983	0.11	0.0018	0.62	1736	20	1736	18	1735	31	100
	2-2C	30	444.91	114.10	0.27	0.29	0.0101	4.19	0.1917	0.11	0.0031	0.77	1630	51	1672	38	1726	54	94
	8-1C	30	192.46	50.18	0.73	0.29	0.0063	4.28	0.1371	0.11	0.0025	0.67	1652	31	1690	26	1737	44	95
	11-1C	30	553.06	149.44	0.74	0.31	0.0087	4.67	0.1604	0.11	0.0022	0.81	1762	43	1761	29	1760	37	100
	22-1C	30	250.93	72.21	0.51	0.32	0.0091	4.74	0.1715	0.11	0.0024	0.80	1773	45	1774	30	1775	40	100
	20-1C	30	583.00	159.51	0.30	0.31	0.0098	4.56	0.1940	0.11	0.0030	0.74	1743	48	1742	35	1741	52	100
	16-1C	30	262.82	71.69	0.60	0.31	0.0059	4.56	0.1290	0.11	0.0022	0.68	1742	29	1742	24	1741	38	100
SR92A	13-1RC	30	856.19	239.93	0.27	0.28	0.0071	4.05	0.1364	0.11	0.0023	0.77	1570	36	1644	27	1740	39	90
	17-1C	30	517.71	138.14	0.41	0.28	0.0078	4.01	0.1396	0.11	0.0022	0.81	1566	39	1636	28	1728	37	91
	17-2C	30	500.60	140.49	0.43	0.31	0.0053	4.63	0.1065	0.11	0.0017	0.74	1754	26	1755	19	1757	28	100
	3-1C	26	438.58	103.27	0.49	0.28	0.0073	4.06	0.1687	0.11	0.0034	0.63	1569	37	1646	34	1744	59	90
	1-1C	30	393.28	104.29	0.39	0.27	0.0171	3.93	0.3060	0.11	0.0047	0.82	1525	87	1621	63	1747	81	97
	17-1C	30	574.63	164.36	0.21	0.26	0.0061	3.88	0.1237	0.11	0.0024	0.72	1507	31	1610	26	1747	40	96
	18-1C	30	627.09	153.70	0.87	0.26	0.0064	3.94	0.1283	0.11	0.0023	0.75	1495	33	1622	26	1791	39	93
	10-1C	30	777.16	175.21	0.91	0.26	0.0079	3.78	0.1386	0.11	0.0021	0.84	1577	40	1589	29	1741	37	95
	13-1C	30	1054.34	283.07	0.56	0.27	0.0052	3.96	0.0997	0.11	0.0017	0.77	1538	26	1625	20	1740	30	98
	19-1C	25	802.72	202.81	0.43	0.25	0.0083	3.80	0.1597	0.11	0.0029	0.78	1552	43	1592	34	1782	48	91

from SR92A yield a weighted mean $^{207}Pb/^{206}Pb$ age of 1747±9 Ma (n=19; MSWD = 0.78, ρ (x^2) = 0.73) (Fig. 4.7m, n). Spencer et al. (2016) proposed a criterion between MSWD and the number of analyses to understand the reliability of the mean age. The results of the current study are compared with these analytical criteria which suggest that current results provide robust and reliable estimates for the magmatic emplacement age of the protolith of metagranitoids.

CHAPTER 5

SUBSOLIDUS MYRMEKITE FORMATION IN PORPHYRITIC METAGRANITOID

Myrmekite, the delicate intergrowth of quartz rods with plagioclase develops extensively on all sides of alkali feldspar in some of the weakly deformed porphyritic metagranitoids. Becke (1908) considered that myrmekite forms by replacement of the immediate alkali feldspar due to fluid induced Ca- and Na alteration of the latter ("replacement" theory). Whereas Schwantke (1909) proposed that plagioclase and quartz in the myrmekite were derived from the immediate alkali-feldspar ("exsolution" theory). Detail study by Ashworth (1972) argued that both the earlier processes, i.e. replacement and exsolution, can operate simultaneously at constant Al and Si during the formation of myrmekite on alkali feldspar. Irrespective of the role of deformation, the fact remains that the formation of myrmekite requires chemical alteration of alkali feldspar in an open system, at least in the scale of myrmekite. No detailed study has been published that explains how the chemical potential gradients that drive the transport of Ca and Na toward and K away from the myrmekite front were created and maintained during the formation of myrmekite. Influence of pressure, temperature and deformation on the myrmekite forming process in the porphyritic metagranites is discussed.

General petrographic descriptions of the porphyritic metagranitoids (17 samples dispersed in the entire study area) are presented in section 4.1 in the previous chapter. The dark translucent rims surrounding the alkali-feldspar phenocrysts, as observed in the field, are microscopic intergrowth of vermicular and/or polygonal aggregates of quartz + plagioclase (the myrmekite). The detailed features and microstructural ambiance of the myrmekite are described below. Mineral abbreviations in the following sections are taken from Whitney and Evans (2010).

5.1. Petrography and feldspar composition in the myrmekite domains

'Myrmekite' is an intimate intergrowth between quartz and plagioclase. The boundary between the myrmekite and the alkali feldspar will be referred to as "myrmekite front". Based on morphology two types of myrmekite, namely Myr1 and Myr2 are identified. The quartz grains in Myr1 show vermicular intergrowth in the base of plagioclase (Fig. 5.1a-c). The thickness and the interlamellar distance of quartz show systematic variation. At the immediate contact with the alkali feldspar, quartz vermiculae in the Myr1 are thin (20 microns length and 5 microns width), have small interlamellar distance (10 microns) and are parallel to each other (Fig. 5.1a, c). The interface between the small quartz vermiculae and the base plagioclase is mildly curved. The thickness and the interlamellar distance of the quartz vermiculae increase, commonly quite abruptly, away from the myrmekite front (Fig. 5.1a-c). The shapes of these quartz vermiculae are irregular and resemble the "garben structure" of quartz vermiculae as described by Remmert et al. (2018). The myrmekite front has bulbous shape that is convex toward the alkali feldspar (Fig. 5.1a, c). The smaller quartz vermiculae are always nearly normal to the myrmekite interface (Fig. 5.1a-c). Like the myrmekite around the alkali feldspar megacrysts, the shape of the myrmekite front is highly irregular and develops all along the periphery of the smaller alkali feldspar grains (Fig. 5.1d, e). In most places, the myrmekite front dissects the alkali feldspar grains. Rafts of alkali feldspar, with highly irregular grain boundaries, occur in the Myr1 (Fig. 5.1f). Myr1 also develops at the interface of plagioclase inclusion within

alkali-feldspar (Fig. 5.1g). The proportion of quartz in Myr1 varies between 20-25 vol%, and quartz proportion increases away from the alkali feldspar.

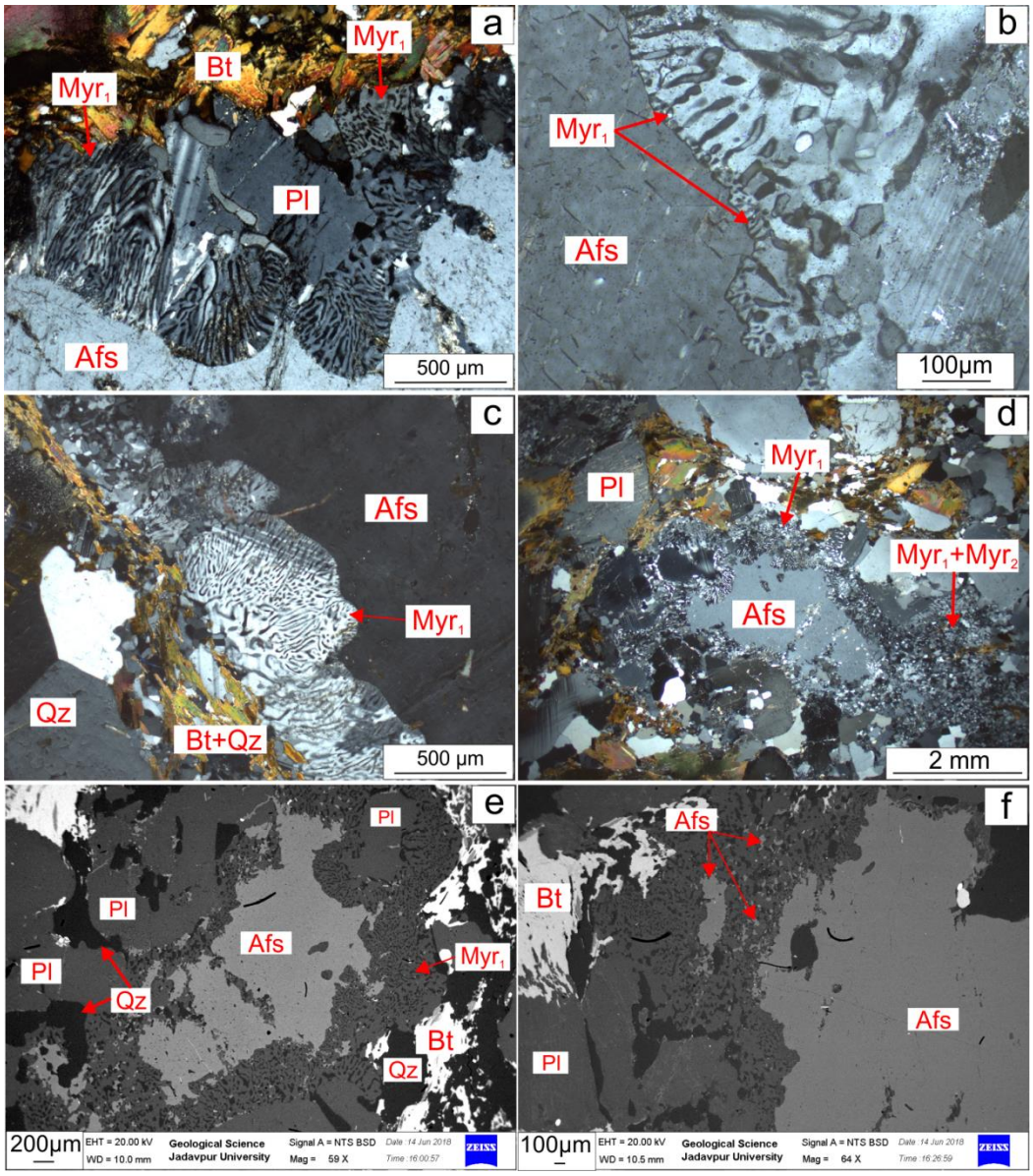

Figure 5.1. (a-c) Characteristics of Myr1 domains and microtextures of quartz vermicules. The myrmekite front is bulbous and convex towards alkali feldspar megacrysts. (d-e) Myrmekite develops all along the periphery of the alkali feldspar grains. Myrmekite grows on alkali feldspar and plagioclase porphyroclasts. (f) Rafts of alkali feldspar, with highly irregular grain boundaries, occur in the Myr1.

In contrast to Myr1, the Myr2 shows polygonal aggregates, commonly showing triple point junction and the size of the quartz grains is distinctly coarser (20-40 microns in length and width) than the quartz in Myr1 (Fig. 5.1h). Commonly,

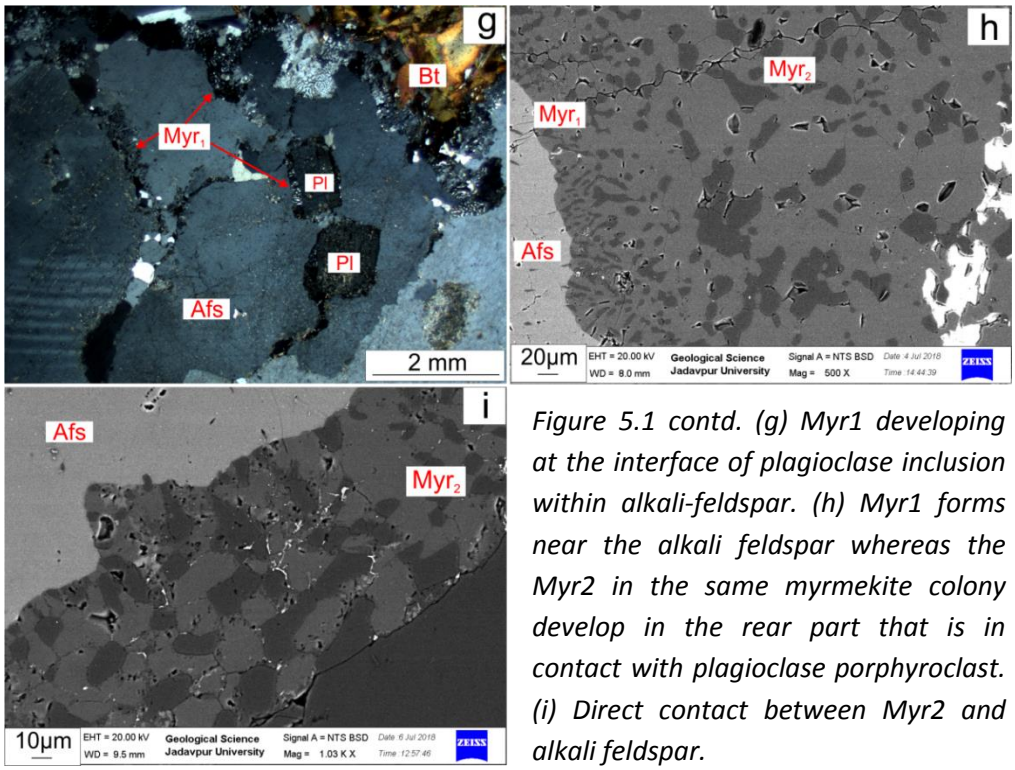

Figure 5.1 contd. (g) Myr1 developing at the interface of plagioclase inclusion within alkali-feldspar. (h) Myr1 forms near the alkali feldspar whereas the Myr2 in the same myrmekite colony develop in the rear part that is in contact with plagioclase porphyroclast. (i) Direct contact between Myr2 and alkali feldspar.

Myr1 forms near the alkali feldspar whereas Myr2 in the same myrmekite colony develops in the distal part that is in contact with plagioclase (Fig. 5.1h). Direct contact between Myr2 and alkali feldspar is also noted (Fig. 5.1i). The polygonal Myr2, locally grades into the recrystallized plagioclase along the border of plagioclase porphyroclasts. Myr2 never develops at the interface of the plagioclase inclusion within the alkali-feldspar. Myrmekite always develops at the contact between plagioclase and alkali feldspar. In many places, a layer of quartz separates the myrmekite from and is oriented parallel to the grain boundary of plagioclase porphyroclast (Fig. 5.1j, k). Where the direct contact between Myr1 and plagioclase porphyroclast exists, the twining in the latter can be traced within the plagioclase base of the myrmekite (Fig. 5.1l). These features can be best explained by nucleation of the myrmekite on the plagioclase porphyroclasts

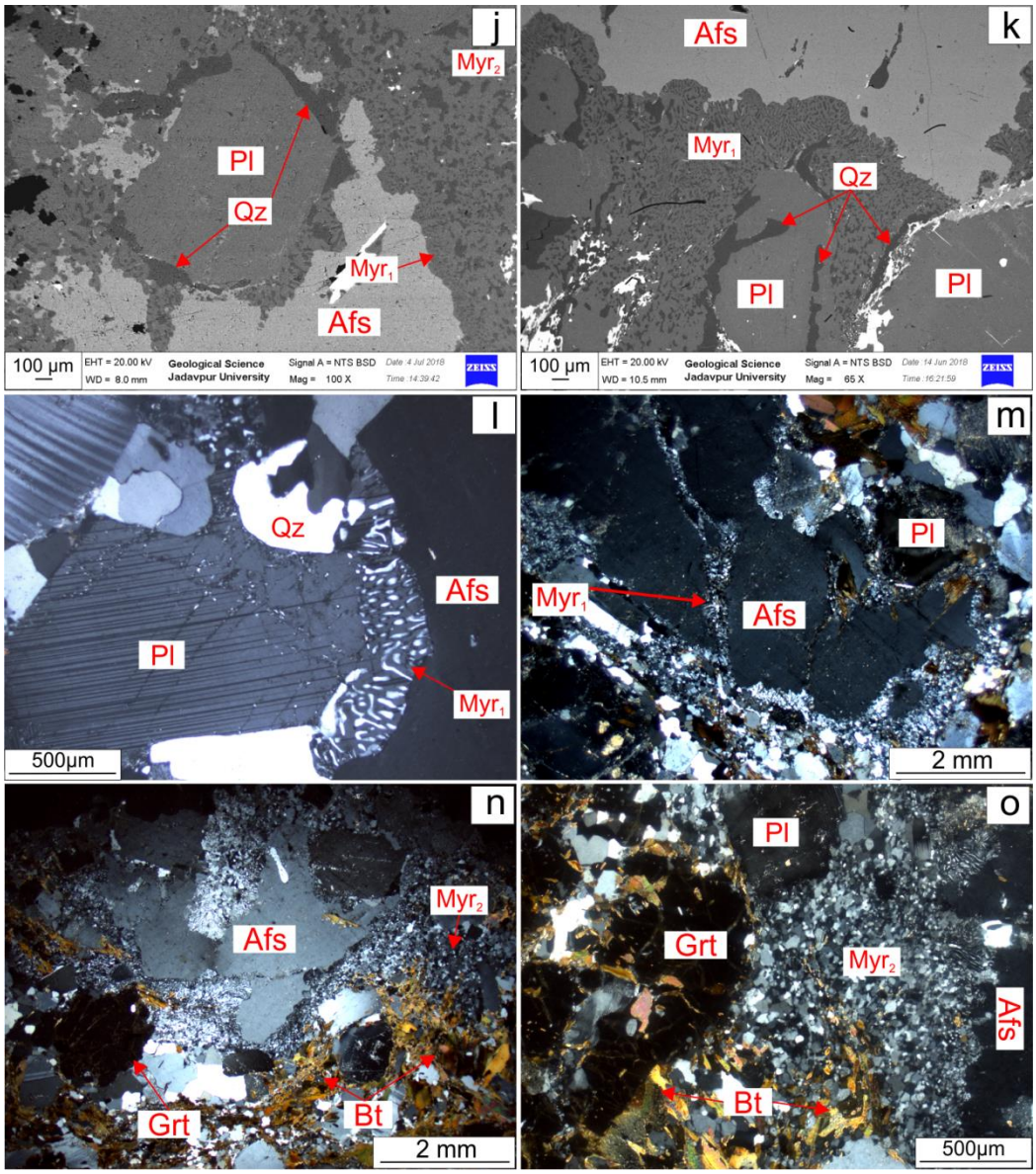

Figure 5.1 contd. (j-k) A layer of quartz separates the myrmekite from and oriented parallel to the grain boundary of plagioclase porphyroclast. (l) The twining in plagioclase porphyroclast can be traced within the plagioclase base of the myrmekite. (m) Myrmekite forms random veins/apophyges within the alkali feldspar. (n-o) Intimate association of myrmekite and secondary biotite. Secondary biotite replaces garnet and plagioclase porphyroclasts as well as Myr2.

(Abart et al., 2014, 2012; Cisneros-Lazaro et al., 2019; Vernon, 2004, 1991). The myrmekite forms random veins/apophyges within the alkali feldspar (Fig. 5.1m). There is an intimate relation between the myrmekite and the secondary biotite. The

plagioclase porphyroclast, commonly with normal zoning, on which Myr1 and 2 grow are extensively replaced by the secondary biotite. The garnet in the vicinity is also replaced by the secondary biotite. Locally the secondary biotite (with or without quartz intergrowth) replaces the polygonal aggregates of Myr2 but the immediate Myr1 remains virtually unaffected and shows sharp planar contact (Fig. 5.1n, o). Rarely, Myr1 is seen to be replaced by biotite. These textural features support the view that the bulk of Myr1 was either contemporaneous or formed after the major part of hydration. Textural features are equivocal on the relation between Myr2 and secondary biotite. Secondary biotite can form during or outlast the deformation that produced the polygonal aggregates of quartz and plagioclase. Textural features are also inconclusive regarding the original shape of the Myr2 prior to the recrystallization. Nevertheless, the polygonal fabric of Myr2 indicates a reduction of surface energy relative to the vermicular internal texture of Myr1(Cisneros-Lazaro et al., 2019; Vernon, 2004).

Detail mineralogical composition of the metagranitoid in this area is presented in the previous chapter. In the following section, feldspar compositions of the myrmekite rich samples are presented. The analytical details and results/data are presented in the previous chapter (Table-4.2a-e).

Feldspar: The alkali feldspar porphyroclasts are essentially microcline ($Or_{87.3-89.4}Ab_{10.5-12.9}An_{<1}Cs_{1.3-1.8}$) (Fig. 5.2a). The composition of the recrystallized alkali-feldspar is marginally impoverished in albite molecule $Or_{89-92}Ab_{7.8-10.7}An_{<1}Cs_{1.5-1.9}$. The small patches of alkali feldspar in the myrmekite are distinctly rich in BaO (1.36-1.75 wt%) relative to the alkali-feldspar porphyroclasts (0.70-1.08 wt%). The composition of these fine remnants of alkali feldspar within Myr1 is $Or_{89.1-92.4}Ab_{7.5-10.4}An_{<1}Cs_{2.5-3.2}$. No significant compositional zoning in the alkali-feldspar has been noted close to the myrmekite (Fig. 5.2a; Core: $Or_{89.4}Ab_{10.5}An_{<1}Cs_{1.3}$ and Rim immediate to Myr1: $Or_{87.5}Ab_{12.4}An_{<1}Cs_{1.7}$).

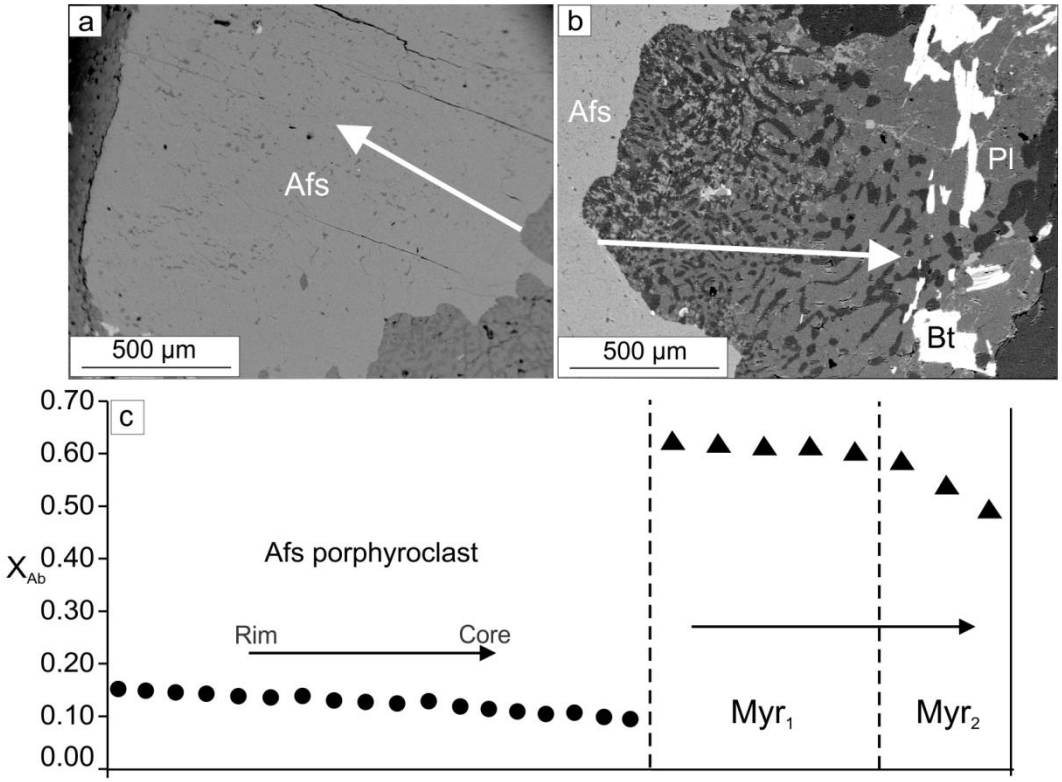

Figure 5.2. (a) BSE image of the analyzed alkali-feldspar porphyroclast. White arrow represents the direction of the compositional profile from rim to core of the porphyroclast. (b) BSE image of the analyzed plagioclase base of myrmekite. (c) Compositional profile of alkali feldspar porphyroclast and plagioclase base of myrmekite. Black arrows correspond with the white arrows of the BSE images. Composition of alkali-feldspar (in terms of X_{Ab}) is homogeneous and plagioclase base in myrmekite show chemical zoning.

Proximal to secondary biotite and myrmekite, the plagioclase porphyroclasts show normal compositional zoning with anorthite-rich core ($Ab_{50}An_{49}Or_1$) and anorthite poor rim ($Ab_{57}An_{42.5}Or_{0.5}$). The plagioclase base of myrmekite shows systematic chemical zoning which is presented in the compositional profile in Fig. 5.2b, c. Plagioclase in Myr1 from the fine variety in contact with alkali feldspar to relatively thick vermicular quartz away from myrmekite front shows a very small decrease in albite component ($Ab_{61.6}An_{37.9}Or_{0.5\text{-}0.9}$ to $Ab_{60.6}An_{38.9}Or_{0.5}$) (Fig. 5.2c). A sharp change is noted across Myr1 and Myr2 where polygonal plagioclase in Myr2 is distinctly anorthite rich ($Ab_{58}An_{41}Or_1$ to $Ab_{53}An_{46}Or_1$; Fig. 5.2c).

5.2. Physical conditions of myrmekite formation

The studied rock (c.1750 Ma emplacement age) shared the tectonothermal events at c 950 Ma with the younger felsic intrusive (now partially retrogressed charnockite with emplacement age of c.1400 Ma, Chakrabarty et al. 2022, 2023). Chakrabarty et al. (2022) demonstrated that at the terminal phase of 950 Ma tectonothermal event the rocks of the studied area underwent cooling (at nearly constant pressure) and extensive hydration in the range of ~500-600°C and ~4-5 kbar. It is, therefore, likely that the secondary biotite and the adjoining myrmekite in the studied rock should equilibrate under similar physical conditions. Lack of compositional zoning in alkali feldspar at the immediate contact with the myrmekite suggests that myrmekitic plagioclase is not in equilibrium with the alkali feldspar. Garnet-biotite thermometry cannot be used as garnet and secondary biotite is not in equilibrium and that does not show compositional zoning against the latter. Nevertheless, recrystallization of alkali feldspar requires temperature ≥ 500°C (Harlov and Wirth, 2000; Menegon et al., 2006; Vernon, 2004). Temperature ≥ 500°C is considered to be suitable for the myrmekite formation (with oligoclase and more calcic plagioclase, Harlov and Wirth 2000). Pressure below 5.5 kbar at ≥500°C is consistent with the absence of epidote/clinozoisite in the studied rock. Taken together, all the information supports that myrmekite and the secondary biotite were formed in the terminal phase of 950 Ma tectonothermal event (500°-600°C and 4-5 kbar).

5.3. Controls of mobile and immobile species during the formation of myrmekite

5.3.1. Mass balance approach

Composition of the alkali feldspar is grossly different from the composition of the myrmekite colony that replaces the alkali feldspar. This then follows that a number of chemical species should be mobile during the myrmekitisation of the alkali feldspar (Abart et al., 2014, 2012; Cisneros-Lazaro et al., 2019; Simpson and Wintsch, 1989; Vernon, 2004, 1991). Fluid mediated, interface-controlled, solution-reprecipitation

process (Putnis, 2002) is consistent with a number of textural features presented in this study including (a) the bulbous outlines of the myrmekite colony that are convex towards the precursor alkali feldspar and (b) presence of relict patches of alkali feldspar within the myrmekite colony. Intimate association of myrmekite with the secondary biotite that replaces the garnet and plagioclase porphyroclast with albitic rim suggests a genetic connection between the two processes. The nature and extent of the element mobility (or immobility) across the myrmekite-alkali feldspar boundary will be assessed first. This will be followed by evaluation of the genetic connection between the myrmekite formation on the alkali feldspar and the hydration of the garnet and plagioclase in the immediate vicinity.

5.3.2. Element mobility (immobility) during the myrmekite formation: behavior of Al and Si

Quantification of the extent of element mobility across the myrmekite-alkali feldspar boundary requires a reference frame. Concentration of at least one immobile element can serve as a good reference frame against which enrichment/depletion of mobile elements can be quantified (Ague, 2003; Philpotts and Ague, 2009). A number of studies have documented that Al and Si remain virtually immobile during the myrmekitisation of alkali feldspar (Cisneros-Lazaro et al. 2019, Abart et al. 2014, Cesare et al. 2002). However, studies have demonstrated that Al and Si can be mobile in different length scale during a metasomatic process (Chakrabarty et al., 2022; Roy Choudhury et al., 2023). Behavior of Al (and Si) should be evaluated in each individual case before using Al as a reference frame for quantification of the extent of mobile elements.

In this study, we have adopted two approaches to understand the behavior of Al and Si during the formation of myrmekite after alkali feldspar.

Approach 1

It has been demonstrated in a number of studies (reviewed in Philpotts and Ague, 2009) that any immobile element during metasomatism should follow the relation:

$$C_i^o M_i^o = C_i' M_i' \qquad (1a)$$

Where C_i^o and C_i' represent the concentrations (in ppm, wt%) of any immobile species 'i' and M_i^o and M_i' are the masses of precursor and altered rocks.

Equation 1a, leads to the relation that all the immobile elements will have the same C_i'/C_i^o ratio in a given metasomatic environment. For a given set of C_i' and C_i^o, the amount of enrichment and depletion of the mobile elements can be quantified by the relation (cf. Phillpotts and Ague, 2009):

$$\Delta n_j\ \% = [(C_i^o/C_i')*(C_j'/C_j^o) - 1]\% \qquad (1b)$$

C_j^o and C_j' are the concentrations of the mobile species 'j' in the precursor and metasomatic rocks. Δn_j is the % change of the species j (negative and positive signs of Δn_j indicate depletion and enrichment of the species j in the metasomatic zone respectively).

Table 5.1: Concentration ratios and enrichment/depletion of chemical species involved in myrmekitization

Elements in Myr formation	C_x'/C_x^0-Myr1	C_x'/C_x^0-Myr2	Δn-Myr1 (%)	Δn-Myr2 (%)
SiO_2	1.017	1.058	2	6
Al_2O_3	1.031	0.977	3	-2
CaO	165.000	188.889	16400	18789
Na_2O	7.141	5.399	614	440
K_2O	0.005	0.008	-100	-99
BaO	0.005	0.017	-100	-98

C_x^o and C_x' represent the concentration of a given species x in alkali feldspar and myrmekite

Δn represents depletion and enrichment of a species in the metasomatic zone

In this study, the phase composition of alkali feldspar and the bulk composition of the myrmekite colony are considered as the M_i^o and M_i' for the alkali feldspar-myrmekite system. Leaving out the trace elements, the composition of myrmekite-alkali feldspar can be represented in the six component system (K_2O-Na_2O-BaO-CaO-Al_2O_3-SiO_2). The bulk composition of the myrmekite has been computed by combining the volume proportion of the quartz and plagioclase from the BSE image and their measured compositions ("microbulk"; Evans, 2004; Stüwe, 1997). Table- 5.1

and Fig. 5.3a represent the $C_x^{'}/C_x^{o}$ (C_x^{o} and C_x' represent the concentration of a given species x in alkali feldspar and myrmekite). The ratios $C^{'}_{Al2O3}/C^{o}_{Al2O3}$ and $C^{'}_{SiO2}/C^{o}_{SiO2}$ in the alkali feldspar-myrmekite pair perfectly match within the uncertainties of measurement of mineral composition and 'microbulk' composition of myrmekite (both Myr1 and Myr2, Table-5.1 and Fig. 5.3a). The match between the two parameters is the best for alkali feldspar-Myr1 pair. This observation supports the view that SiO_2 and Al_2O_3 remained virtually constant during the formation of myrmekite after alkali feldspar. The ratios of $C_x^{'}/C_x^{o}$ for CaO, Na_2O, K_2O and BaO deviate significantly from the $C^{'}_{Al2O3}/C^{o}_{Al2O3}$ (or $C^{'}_{SiO2}/C^{o}_{SiO2}$, Table-5.1, Fig. 5.3a) and are, therefore, considered as mobile components during the myrmekite formation after alkali feldspar (Philpotts and Ague 2009).

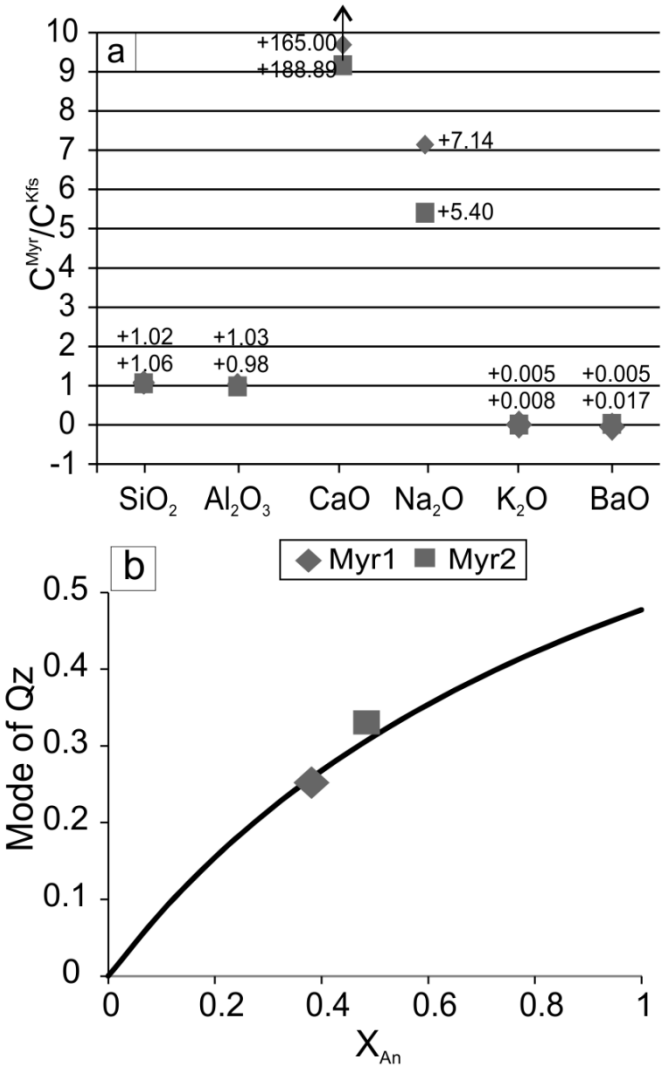

Figure 5.3. a) Change in concentration of mobile and immobile species, involved in myrmekitisation ($C_x^{'}/C_x^{o}$ where C_x^{o} and C_x' represent the concentration of a given species x in alkali feldspar and myrmekite), calculated for both Myr1 and Myr2. b) The curvilinear relation between m_{qtz} and X_{An} as defined by the equation by Abart et al. (2014). The modal volumes of quartz, estimated from the BSE images, are plotted against the measured compositions of the corresponding matrix plagioclase in Myr1 and Myr2.

Approach 2

For Al and Si being conserved, the modal volume of quartz in the myrmekite follows a curvilinear relation with the anorthite content (X_{An}) of the matrix plagioclase (Abart et al., 2014; Ashworth, 1972). This relation is expressed by the equation (Abart et al. 2014):

$$m_{qtz} = 4X_{An}*V_{qtz}/(4X_{An}*V_{qtz}+V_{plg}) \quad (1c)$$

m_{qtz}, V_{qtz} and V_{plg} are the modal quartz, volume of quartz and volume of plagioclase respectively.

In Fig. 5.3b the curvilinear relation between m_{qtz} and X_{An} as defined by equation 1c is shown. The V_{qtz} and V_{plg} are calculated at 550°C and 5 kbar pressure, the likely physical condition of myrmekite formation in the studied rock.

The modal volumes of quartz, estimated from the BSE images, are plotted against the measured compositions of the corresponding matrix plagioclase in Myr1 and Myr2 (Fig. 5.3b). Both Myr1 and Myr2 are plotted close to the theoretical line (equation 1c) for their corresponding X_{An}. The close correspondence of the theoretical and observed modal quartz for a given X_{An} of plagioclase corroborate the observation of Approach 1 that Al and Si were effectively conserved during the myrmekite formation after alkali feldspar. Similar to Approach 1, better correspondence between theoretical and observed modal quartz value at a given X_{An} was noted for Myr1.

Using Al as reference frame, application of equation 1b shows a whopping loss of K_2O (Myr1=100%, Myr2=99%) and BaO (Myr1=100% And Myr2=98%) and gain in Na_2O (Myr1=614% And Myr2=440%) and CaO (Myr1=16400% And Myr2=18789% during the formation of myrmekite after alkali feldspar (Table-5.1).

For conserved Si and Al, the balanced metasomatic reaction that presumably operated across the myrmekite-alkali-feldspar interface is modeled. The measured compositions of alkali feldspar and plagioclase matrix of myrmekite (quartz is considered pure SiO_2) are used as input parameters. The details of textural modeling study with C-Space are discussed in a number of publications (Roy Choudhury et al. 2023). In view of the variation in the compositions of matrix plagioclase, the balanced reactions are obtained for Myr1 and Myr2 separately.

Balanced chemical reaction for Myr1:

3.43 **[**$K_{0.87}Na_{0.12}Ca_{0.01}Al_{1.04}Si_3O_8$] + 1.00$Ca^{2+}$ + 1.14Na^+

=2.50 [$Na_{0.63}Ca_{0.39}Al_{1.39}Si_{2.61}O_8$] + 3.72$SiO_2$ + 2.98K^+

3.43**Kfs** + 1.00Ca^{2+} + 1.14Na^+=2.50$\mathbf{Pl_{Myr1}}$ + 3.72**Qz** + 2.98K^+ (2a)

ΔV_S = -9.5%; V_{Pl}:V_{Qz} = 3:1

Balanced chemical reaction for Myr2:

4.06 [$K_{0.87}Na_{0.12}Ca_{0.01}Al_{1.04}Si_3O_8$] + 1.38$Ca^{2+}$ + 1.00Na^+

=2.81 [$Na_{0.54}Ca_{0.47}Al_{1.49}Si_{2.51}O_8$]+ 5.04$SiO_2$ + 3.51K^+

4.06**Kfs** + 1.38Ca^{2+} + 1.00Na^+=2.81$\mathbf{Pl_{Myr2}}$+ 5.04**Qz** + 3.51K^+ (2b)

ΔV_S = -10%; V_{Pl}:V_{Qz} = 2.2:1

The ΔV_S represents the volume change of the solid phases (product –reactant phases) expressed in %. A negative value of ΔV_S suggests a negative volume change in the tune of 9.5-10% during the formation across the myrmekite-alkali-feldspar interface. The estimated volume reduction during the formation of myrmekite in this work compares well with the volume reduction reported by Simpson and Wintsch (1989, -10%) during myrmekite formation. The modal ratios of quartz and matrix plagioclase calculated from the balanced reactions 2 a and b (expressed as V_{Pl}:V_{Qz}) matches well with the observed ratio of quartz and plagioclase in Myr1 (Calculated=1:3, Observed=1:3) and Myr2 (Calculated=1:2.2, Observed=1:2). The balanced chemical reactions (2 a, b) are consistent with the results of mass balance calculation and suggest addition of Ca and Na to and removal of K during replacement of alkali feldspar by myrmekite.

5.3.3. Element mobility during the formation of the secondary biotite

Textural features suggest intimates relation between myrmekite (both Myr1 and Myr2) secondary biotite that replaces plagioclase and garnet porphyroclasts. Textural modeling was done with C-Space program using the measured compositions of secondary biotite, compositions of garnet and plagioclase porphyroclasts (calcic core and albitic rim as separate entity) as input parameters. The textural modeling returns the following mass balanced metasomatic reaction:

15.30{($Fe_{2.45}Mg_{0.27}Ca_{0.22}$)$Al_{1.98}Si_3O_{12}$}+20.57$SiO_2$+1.00$Na^+$+19.78$K^+$+19.94$H_2O$

=19.60{$K_{0.92}$($Fe_{1.75}Mg_{0.79}$)$Al_{1.41}Si_{2.68}O_{10}(OH)_2$}+1.64{$Na_{0.58}Ca_{0.43}Al_{1.41}Si_{2.58}O_8$}+3.20 Ca^{2+}

$15.30\mathbf{Grt}+20.57\mathbf{Qz}+1.00Na^{+}+19.78K^{+}+19.94H_2O=19.60\mathbf{Bt}+1.64\mathbf{Pl_{Rim}}+3.20Ca^{2+}$ (2c)

ΔV_S = +46.5%

The modeled reaction explains the replacement of secondary biotite after garnet and plagioclase porphyroclast and normal zoning in the latter phase at the contact of secondary biotite. The release of Ca^{2+} and consumption of K^{+} as seen in the modeled reaction 2c are likely to facilitate the growth of myrmekite in the adjoining alkali feldspar. Reactions 2a-c requires addition of Na^{+} to progress to the right. This then follows that while local redistribution of Ca^{2+} and K^{+} could explain feedback mechanism between the formation of myrmekite and secondary biotite. However, Na^{+} is to be transported at larger length scale as the secondary biotite and albitic rims on plagioclase porphyroclasts develop throughout the rock irrespective of the occurrence of the alkali feldspar and myrmekite.

5.3.4. Thermodynamic drive on the formation of myrmekite and secondary biotite: the chemical potential diagram

The balanced chemical reactions (equation 2a-c) that are obtained from textural modeling study suggest that Ca, Na and K behaved as mobile elements during formation of secondary biotite. Reactions 2a-c also suggest that behavior of Ca and K are opposite in myrmekite and biotite forming reaction. Both the reactions, however, consume Na in variable proportions. H_2O was consumed in reaction 2c. It is well known that chemical mass transfer is primarily controlled by chemical potential differences of the transporting chemical species (e.g Ca, Na and K, reviewed in Philpotts and Ague, 2009).

In order to demonstrate the directions of the chemical gradients of the mobile species during the formation of myrmekite and secondary biotite, isothermal-isobaric μ_{CaO}-μ_{K2O} diagrams are constructed at different pressure temperature conditions (Fig. 5.4). The system K_2O-CaO-FeO-Al_2O_3-SiO_2-H_2O (KCFASH) has been chosen with garnet, biotite, chlorite, muscovite, plagioclase, K-feldspar and quartz. In view of the pervasive occurrence of biotite in the studied rock, H_2O has been considered an excess phase. Three invariant points are considered. These are I1 [Muscovite, K-feldspar], I2 [Chlorite, K-feldspar] and a degenerate invariant point [Garnet, Biotite, Chlorite]. 550°C and 5 kbar, the likely P-T condition of formation of myrmekite and secondary biotite (discussed early), are used to calculate the μ_{CaO}-μ_{K2O} diagram in the system KCFASH (Fig. 5.4). To account for the

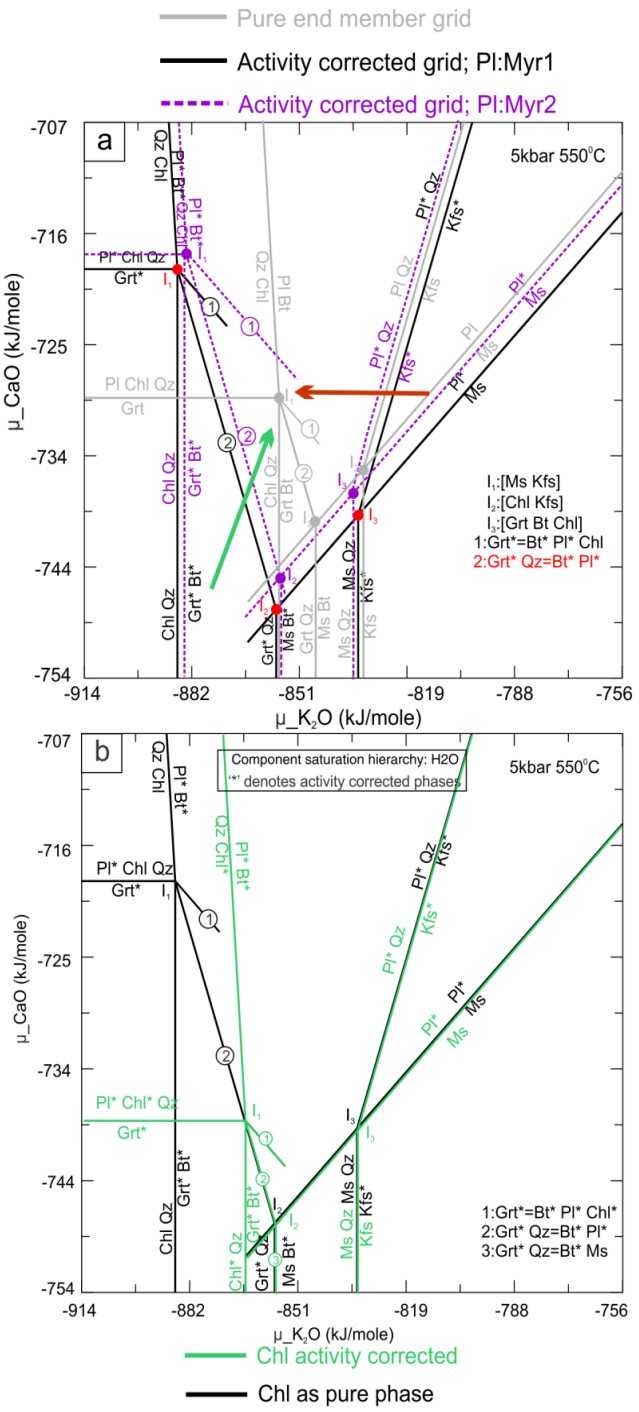

Figure 5.4. The μ_{CaO}-μ_{K2O} diagrams in the system KCFASH. (a) Isothermal-isobaric (iT-iP) chemical potential (μ) diagrams have been computed in NCKFASH system at 550 °C-5 kbar.

Figure 5.4 contd. Grey colored grid represents the reactions and invariant points calculated with pure end members of the minerals. Black grid represents reactions with activity corrected compositions of minerals (except chlorite, muscovite) and plagioclase with the composition of Myr1. Purple grid denotes reactions with plagioclase composition of Myr2. (b) Topology of the chemical potential diagrams does not change significantly other than the invariant points coming closer to each other for chlorite pure and activity corrected compositions.

Na_2O and MgO, the activities of phases of the μ_{CaO}-μ_{K2O} diagrams are calculated from the measured compositions of the solid solution phases. The activity adjusted chemical potential diagram is presented. In view of two distinct compositions the chemical potential diagrams are calculated in two plagioclase compositions (Myr1 and Myr2) (Fig. 5.4a). In the absence of chlorite, the activity of chlorite is set as unity (Fig. 5.4a, c, d). However, the topology of the chemical potential diagrams does not change significantly other than the invariant points coming closer to each other in the chemical potential diagram (Fig. 5.4b). To demonstrate the effects of pressure and

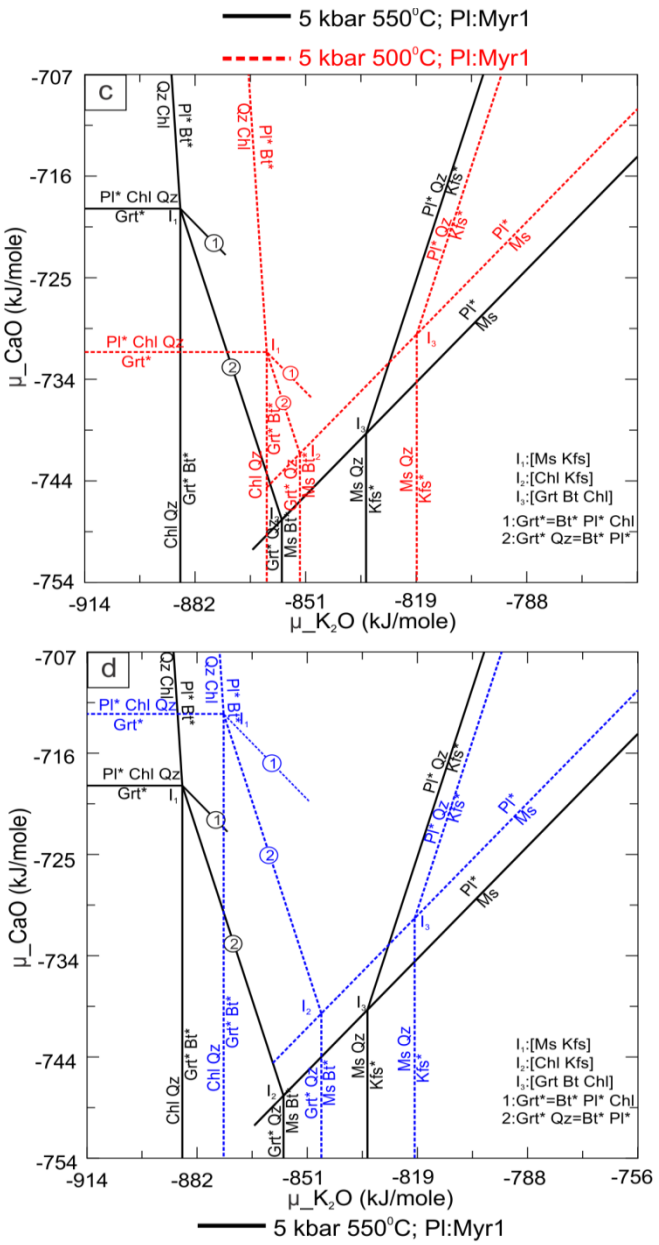

Figure 5.4 contd. (c-d) Effects of pressure and temperature change in the topology with a specific plagioclase composition (Myr1).

temperature topology with a specific plagioclase composition (Myr1) at 550°C and 5 kbar are chosen for reference (Fig. 5.4c, d).

The following observations can be made from the different μ_{CaO}-μ_{K2O} diagrams. These are:

1. The isothermal-isobaric univariant reaction that connects I_1 and I_2, explains the formation of secondary biotite after garnet and has lower μ_{K2O} than the myrmekite forming reaction that emanates from I_3 (Fig. 5.4). Similarly, the reaction at the sites of secondary biotite and myrmekite front creates a gradient of μ_{CaO} towards the latter (Fig. 5.4a).

2. Pressure temperature being constant, Myr2 with more calcic plagioclase forms at lower μ_{K2O} and μ_{CaO} than Myr1 (less calcic, Fig. 5.4a).

3. Pressure and temperature have significant effect on the phase relations of myrmekite stability. Other factors being constant, higher pressure, and lower temperature expand the stability field of plagioclase +quartz (relative to alkali-feldspar) and promote myrmekite formation (Fig. 5.4c, d). In the opposite scenario, heating and decompression impede the growth of myrmekite unless composition of fluid overpowers the effect of these parameters.

CHAPTER 6
EVOLUTION OF THE FELSIC ORTHOGNEISSES

Metamorphic rocks especially granulites document burial and exhumation in the specific thermal environment in which a specific mineral assemblage is equilibrated (Brown, 2001). This evidence is typically expressed as a P-T-t path, which shows how the pressure (P) and temperature (T) of the crust changed over time (t) (Brown, 2008). Two components of felsic granulites (named as ‘felsic orthogneiss owing to the presence of distinctive gneissic banding and inferred magmatic origin of their protolith; Charnockitic orthogneiss and garnet orthogneiss) are present in the study area within the country rock metagranitoids. Though weathering makes it difficult to trace direct field contact between metagranitoids and felsic orthogneisses, their lithological disposition in the map (Fig. 3.1) indicates that protolith of the felsic orthogneisses intruded within porphyritic metagranitoids.

6.1. Petrography of Felsic Orthogneiss

The modal proportions of the observed minerals in the studied felsic orthogneisses are presented in Table-6.1. Depending upon field appearance and mineralogy two varieties of felsic orthogneisses are identified and their salient textural

features are described below. Mineral abbreviations in the following sections are taken from Whitney and Evans (2010).

Table 6.1: Comparative modal abundance of the felsic orthogneisses of the study area. Mineral abbreviations are after Whitney & Evans (2010).

Rock type	Sample	Major minerals								Accessory minerals					Location of the sample
		Qz	Pl	Kfs	Cpx	Opx	Grt	Amp	Bt	Rt	Ttn	Ilm	Zrn	Mnz	
GOG	SR94-3	30	15	25	-	-	10	-	20	-	-	P	-	P	N24^{0}1' E82^{0}40.85'
	SR98	30	25	20	-	-	-	-	25	-	-	-	P	-	N24^{0}1.44' E82^{0}46.7'
	SR95	35	15	30	-	-	-	-	20	-	-	-	-	P	N23^{0}59.95' E82^{0}41.12'
	SR94-4A	35	10	30	-	-	10	-	15	-	-	-	-	-	N23^{0}59.87' E82^{0}40.79'
	SR94-5A	35	15	25	-	-	10	-	15	-	-	P	-	P	N23^{0}59.80' E82^{0}40.75'
	SR94-1	30	20	30	-	-	5	-	15	-	-	-	-	P	N24^0 E82^{0}40.91'
	SR94-6	35	15	25	-	-	10	-	15	-	-	P	-	P	N23^{0}59.87' E82^{0}40.68'
	SR69C	30	20	25	-	-	5	-	20	-	-	-	P	-	N23^{0}59.89' E82^{0}45.97'
	SR69L1	30	10	30	-	-	8	-	20	-	-	P	-	P	N23^{0}59.87' E82^{0}46'
COG	SR94-9	30	15	25	-	-	10	P	20	-	-	-	-	-	N23^{0}59.87' E82^{0}40.62'
	SR69X	30	20	15	-	-	10	P	25	-	-	P	P	P	N23^{0}59.90' E82^{0}45.96'
	SR 115	30	25	20	-	-	15	P	10	-	-	-	P	-	N24^{0}0.26' E82^{0}57.3'
	SR64Y	20	15	10	-	15	12	8	15	P	-	P	P	-	N23^{0}59.62' E82^{0}42.82'
	SR 123	25	20	15	-	-	-	15	20	-	P	P	P	-	N23^{0}55.45' E82^{0}43.85'
	SR64U	20	25	10	-	-	-	20	25	-	P	P	P	P	N23^{0}59.64' E82^{0}42.85'
	SR64W	25	20	15	-	-	-	15	20	-	P	P	-	-	N23^{0}59.63' E82^{0}42.9'
	SR 69 N	30	15	20	-	-	-	20	10	-	P	P	P	-	N24^{0}10' E82^{0}46.68'

P= Present in minor content

6.1.1. Charnockitic Orthogneiss (COG)

The leucosomes of the charnockitic orthogneiss (COG) contain the mineral association quartz + K-feldspar + plagioclase + garnet ± ilmenite whereas the melanosomes are represented by the mineral association plagioclase + quartz + garnet ± orthopyroxene + amphibole + biotite + ilmenite (Fig. 6.1a). Orthopyroxene is preserved only locally. Where garnet and orthopyroxene occur together, they show straight and non-interfering contact (Fig. 6.1b). Inclusions of one or more of the minerals biotite, amphibole, quartz, plagioclase, and ilmenite were found in garnet and orthopyroxene (Fig. 6.1b, c). Zircon, monazite, titanite, ilmenite and rare rutile occur as accessory minerals, scattered in the matrix of melanosome and less commonly in leucosome. Rutile was not observed in the garnet bearing domains. In most places,

orthopyroxene and garnet are variably replaced by amphibole and biotite (Fig. 6.1b-e). The secondary amphibole partially to completely pseudomorphs orthopyroxene (Fig. 6.1b-e). Textural features suggest that biotite was developed in the COG before (as prograde biotite inclusion in garnet) and after (secondary phases) the stabilization of

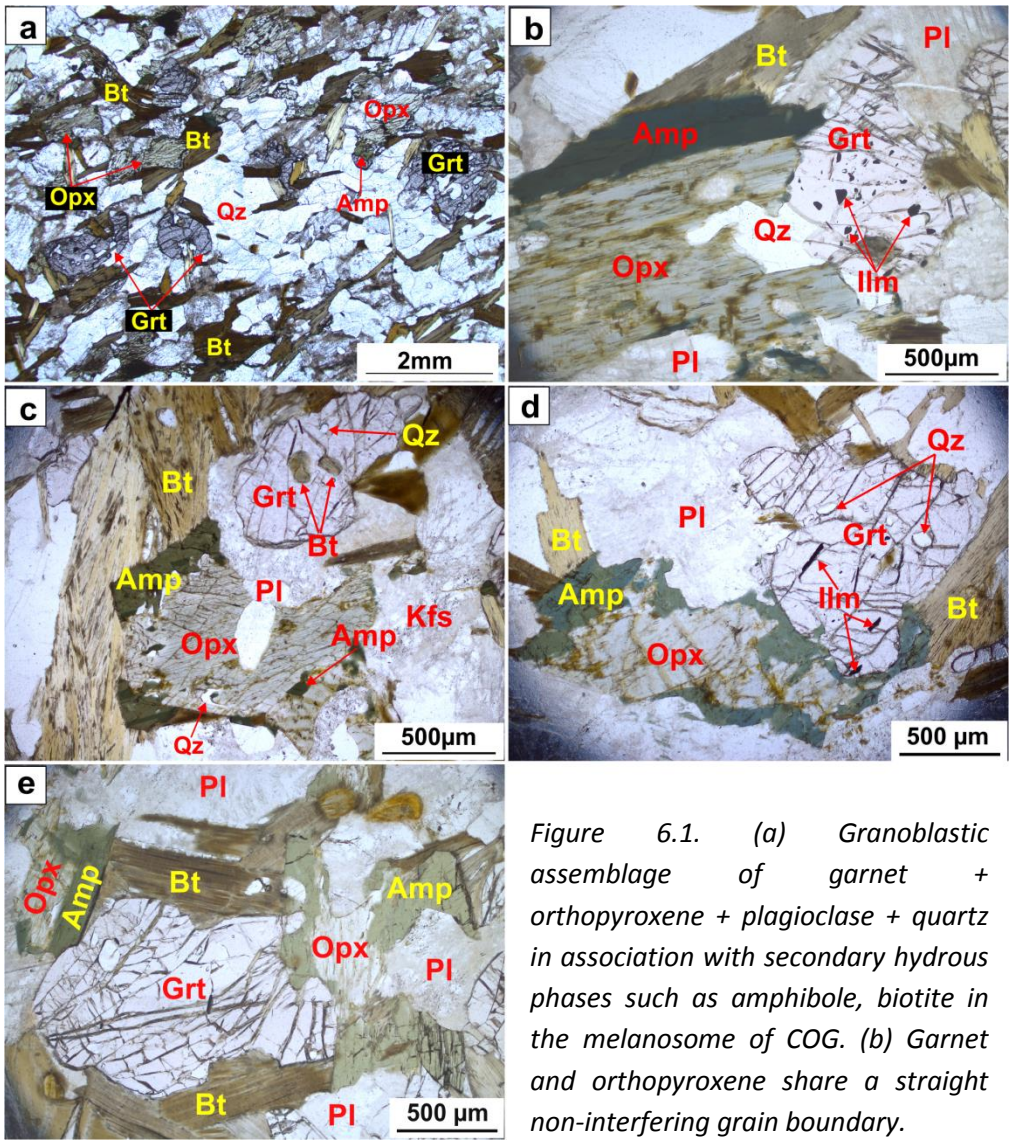

Figure 6.1. (a) Granoblastic assemblage of garnet + orthopyroxene + plagioclase + quartz in association with secondary hydrous phases such as amphibole, biotite in the melanosome of COG. (b) Garnet and orthopyroxene share a straight non-interfering grain boundary. (c) Garnet and orthopyroxene contain quartz + biotite and quartz + amphibole inclusions respectively. Amphibole partially pseudomorphs orthopyroxene and successively replaced by biotite. (d-e) At their immediate contact, garnet and orthopyroxene are separated by amphibole as amphibole partially pseudomorphs orthopyroxene. Garnet is replaced mostly by biotite.

garnet and orthopyroxene. COG contains higher proportion of ferromagnesian (garnet, biotite, amphibole), accessory minerals and plagioclase/K-feldspar ratios than garnet orthogneiss (GOG). In the domains of intense deformation, feldspars and quartz grains are flattened and along the foliation. Recrystallization of the deformed quartz and feldspar is common (manifested by fracture), and orthopyroxene (undulatory extinction and bent cleavage trace) seems to be less. The secondary amphibole and biotite do not show any internal deformation. This feature and random orientation of amphibole and biotite (Fig. 6.1a) suggest that the secondary minerals formed after or outlasted the intense deformation.

6.1.2. Garnet Orthogneiss (GOG)

Compared to the COG, samples of GOG have lower plagioclase/K-feldspar ratio, low amount of accessory phases and do not contain orthopyroxene or amphibole. Owing to the higher proportion of leucosomes, the proportion of quartz and feldspars is also higher in the GOG relative to the COG. The leucosomes in the GOG comprise quartz + K-feldspar + garnet ± plagioclase, whereas melanosomes are composed chiefly of garnet + biotite ± quartz ± plagioclase (Fig. 6.1f). Ilmenite along with a few zircons (<20 μm) and monazite are occasionally present as accessory phases in the matrix. The highly fractured garnet grains in the leucosome are sub- to euhedral and surrounded by a quartzo-feldspathic matrix (Fig. 6.1g). In a few samples, fibrolites are clustered within garnet and K-feldspar grains (Fig. 6.1h, i). Fibrolite is also present in the quartzofeldspathic matrix, particularly along the contacts of quartz, feldspars and biotite (Fig. 6.1j). Owing to large proportion of quartz and feldspar, the GOG shows more prominent deformation microtextures including stretched grains of quartz with undulatory extinctions along with variable proportion of recrystallization (Fig. 6.1k). Garnet grains are highly fractured. Both the feldspars in GOG exhibit recrystallization with polygonal grains and elongated quartz grains with undulose extinction form ribbon structure (Fig. 6.1k). Two generations of biotite are noted. Commonly, the early generation (prograde) of biotite (with or without quartz) occurs as inclusions within garnet porphyroblast in the melanosome (Fig. 6.1l). The younger generation of biotite variably replaces garnet along its margins as well as along the fractures (Fig. 6.1l). The secondary biotite grains do not show any internal deformation and are

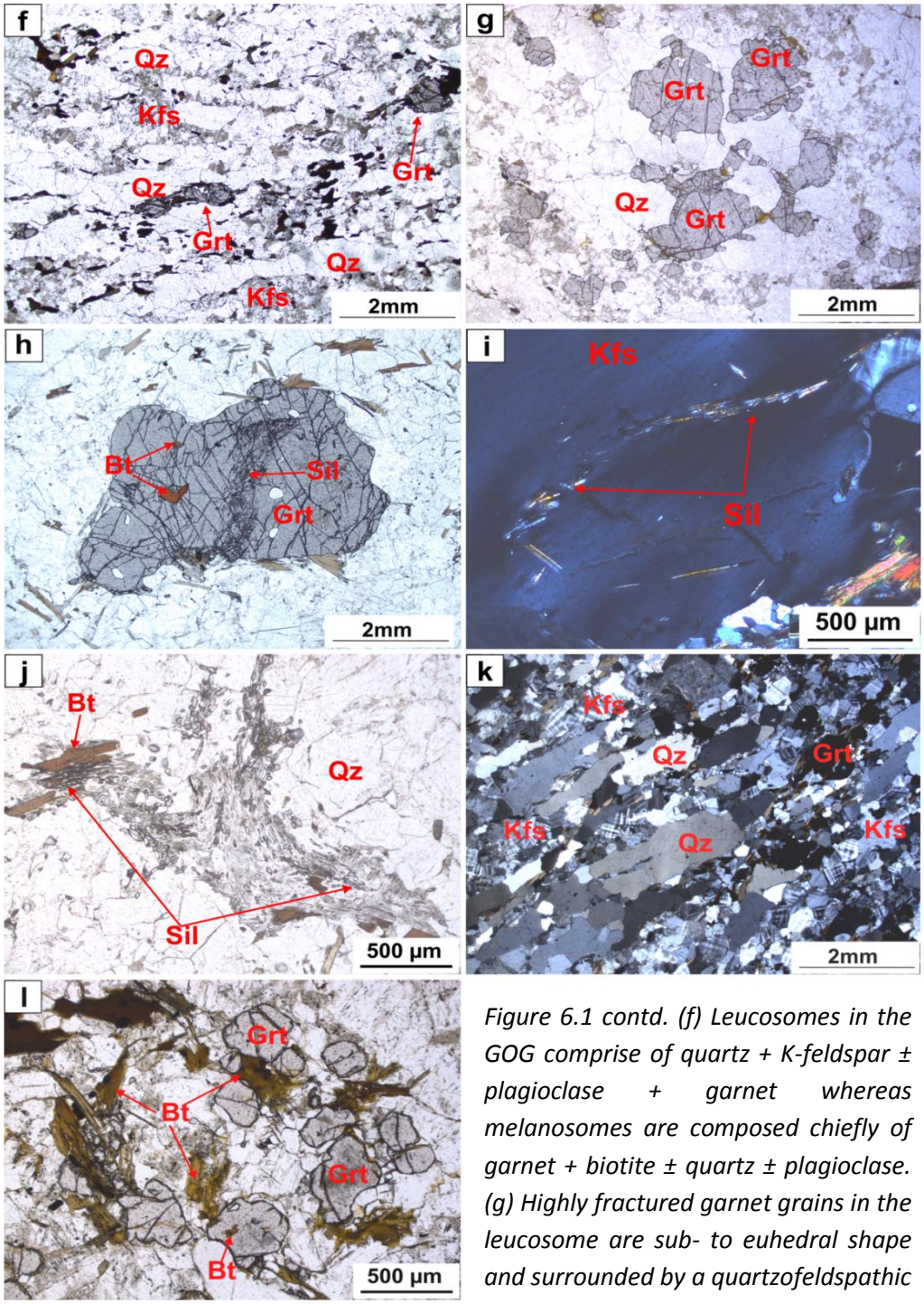

Figure 6.1 contd. (f) Leucosomes in the GOG comprise of quartz + K-feldspar ± plagioclase + garnet whereas melanosomes are composed chiefly of garnet + biotite ± quartz ± plagioclase. (g) Highly fractured garnet grains in the leucosome are sub- to euhedral shape and surrounded by a quartzofeldspathic matrix. (h-i) Small prismatic sillimanite occurred as inclusions within garnet and K-feldspar. (j) Clusters of sillimanite within the quartzofeldspathic matrix, particularly along grain boundaries. (k) Deformation microtextures such as quartz ribbons, variably recrystallized feldspars (mostly K-feldspar with tartan twinning) in garnet orthogneiss (GOG). (l) Quartz + biotite is present as inclusion within rounded garnet grains and they are variably replaced by biotite.

randomly oriented. These features suggest that the growth of secondary biotite outlasted the deformation.

6.2. Mineral chemistry

Mineral chemistry of the studied felsic orthogneisses has been analyzed with an Electron Probe Micro-analyser (EPMA) at the Department of Geology and Geophysics, Indian Institute of Technology (IIT), Kharagpur, West Bengal. The analytical procedures are given in the Appendix. Mineral compositions in COG and GOG vary with rock types, sample locations and textural relations. Representative compositional variations of the samples are presented in Table-6.2. The salient features of the compositional variations of the individual phases are presented below.

Garnet: The garnet is chiefly constituted of almandine and pyrope (together they constitute more than 90 mol%), with grossular content (7-10 mol%). Spessartine component in garnet is low (up to ~5 mol%). The garnet in the GOG is Fe-rich and Ca-poor [X_{Mg} ($Mg/Mg+Fe^{2+}$)=0.09-0.11, X_{Grs}=0.03] relative to its counterpart in the COG (X_{Mg}=0.10-0.18, X_{Grs}=0.07-0.10) (Table-6.2a). No significant compositional difference was noted between the garnet from the melanosome and leucosome in both COG and GOG. Commonly the garnet grains are compositionally homogeneous in both COG and GOG. Rarely garnet shows compositional zoning when it is in physical contact with retrograde biotite. The core part of the garnet is compositionally flat, distinctly rich in Mg (X_{Mg}= $Mg/Mg+Fe^{2+}$ =0.17-0.18, Mg/Fe^{2+}=0.22) that gradually decreases towards the rim of the garnet (Fig. 6.2a, b). At the contact with biotite, the rim of garnet shows the lowest X_{Mg} (0.12), and Mg/Fe^{2+} ratio (0.13) (Table-6.2a). Though the Mn content of garnet is low, an increase in Mn content towards the rim of the garner is apparent. Grossular content of garnet remains virtually constant from core to rim. The observed compositional variation from core to rim of the garnet porphyroblasts is consistent with the diffusional Fe^{2+}-Mg exchange between garnet and biotite at lower temperatures (Spear, 1993). Further, the increase in Mn at the rim could also be related to a retrograde net-transfer reaction that consumed Mn (Kohn and Spear, 2000).

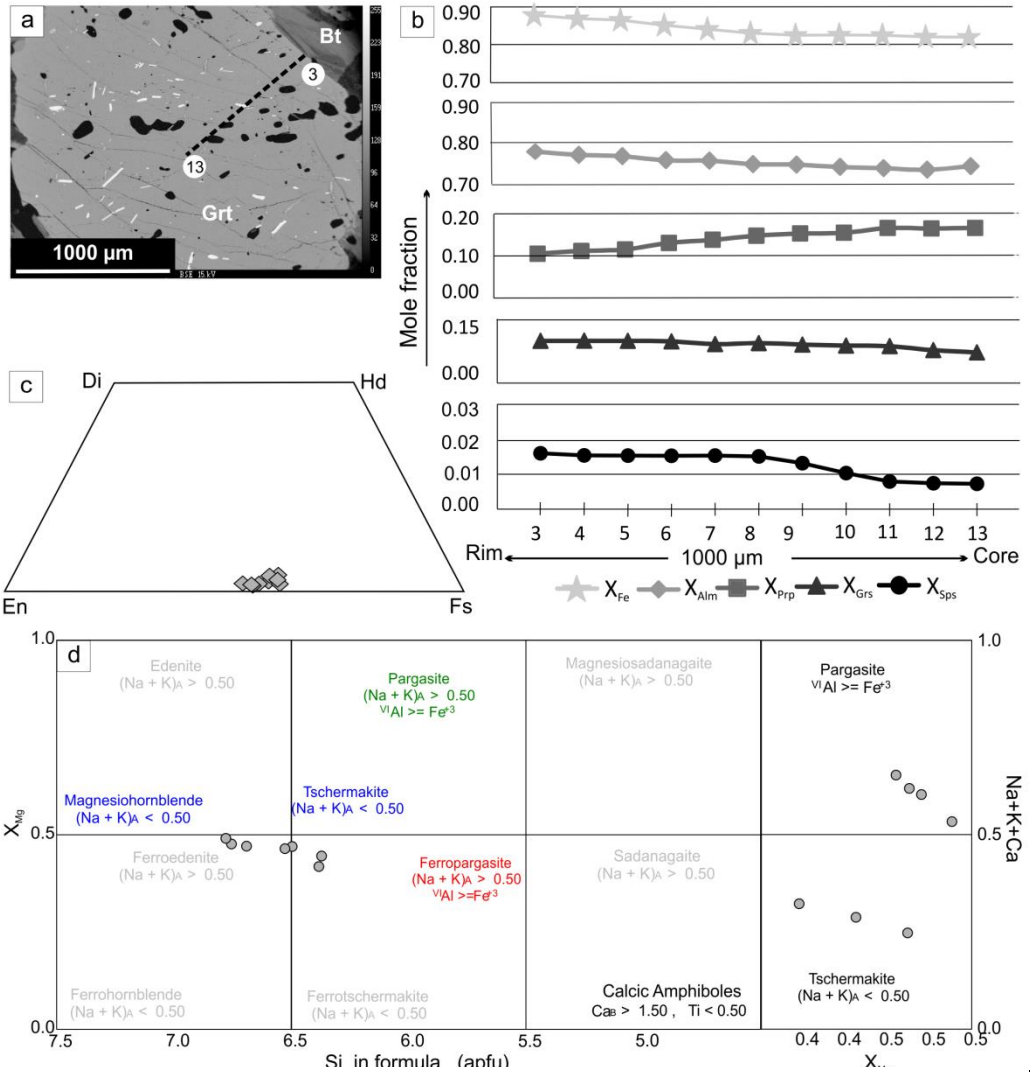

Figure 6.2. (a, b) BSE image of a garnet porphyroblast in contact of secondary ferromagnesian mineral phase (biotite) has been shown. Rim to core compositional profile of the garnet grain along the black dotted line transect (3) to (13). (c) Pyroxene quadrilateral showing the composition of orthopyroxene within COG. (d) Classification of amphibole after Leake et al., (2004).

Orthopyroxene: The orthopyroxene (only in the COG) is Fe-rich (X_{Mg}=Mg/Mg+Fe^{2+}=0.42-0.45) (Table-6.2b; Fig. 6.2c). Individual orthopyroxene grains, irrespective of their textural type, show nearly uniform X_{Mg}. Al_2O_3 content of orthopyroxene varies within 0.93-3.54 wt%. There is a drop of Al_2O_3 content (>1 wt%) from the core to the rim of the orthopyroxene grains.

Feldspar: The plagioclase is albite-rich (X_{Ab} ~0.58-0.76). Individual plagioclase grains do not show any significant compositional zoning. Generally, the plagioclase in the COG is more calcic (X_{An}=0.38-0.42) relative to its counterpart in the GOG (X_{An}=0.23-0.24). Though individual grains of plagioclase do not show any significant compositional variation, plagioclase at the contact of biotite and garnet shows up to 4 mol% higher anorthite molecules than the plagioclase composition in the anhydrous assemblage (Table-6.2c). One garnet and orthopyroxene free sample of COG (SR64U), which contains abundant amphibole shows distinctly albite-rich plagioclase (by ~10 mol%) relative to its orthopyroxene bearing counterpart. Generally, the composition of the K-feldspar varies within a restricted range $Or_{91-94}Ab_{6-9}$. A few grains have higher albite content ($Or_{81-83}Ab_{16-19}$). K-feldspar has very low anorthite (X_{An} up to 2 mol%) (Table-6.2c).

Amphibole: According to the classification of Leake et al.(2004), the amphibole in COG varies between calcic ferro-tschermakite to ferro-edenite in composition with X_{Mg} vary in a restricted range of 0.44-0.49. TiO_2 content of the amphibole ranges between 0.5-1.2 wt% (Table-6.2d; Fig. 6.2d).

Biotite: Biotite in both COG and GOG is Fe rich with X_{Mg} in the range of 0.31-0.51. TiO_2 of the biotite is distinctly high (0.8-2.6 wt%). Biotite in the COG (X_{Mg}=0.43-0.51), are comparatively Fe-rich than those in the GOG (X_{Mg}=0.31-0.36) (Table-6.2d).

Ilmenite: Ilmenite, associated with the matrix and included within porphyroblastic garnet has Fe^{3+} content in the range of 0.06-0.12 apfu in both COG and GOG (Table-6.2d).

Titanite: Titanite, associated with amphibole and biotite has fluorine content in the range of 0.8-1.1 wt% of F (Table-6.2d)

Table 6.2a: Representative chemical analyses for garnet (representative oxygen basis are given). Mineral abbreviations are used after Whitney and Evans (2010). Cation calculation havs been done following the procedure of Grew (1984).

Rock type	**COG**	**COG**	**COG**	**COG**	**COG**	**GOG**	**GOG**	**GOG**	**GOG**	**GOG**	**GOG**	**COG**	**COG**	**COG**	**COG**	**COG**	**COG**	**COG**	**COG**	**COG**	**COG**	**COG**
Sample no	**SR64Y**	**SR64Y**	**SR64Y**	**SR64Y**	**SR64Y**	**SR69L1**	**SR69L1**	**SR69L1**	**SR69L1**	**SR69C**	**SR69C**	**SR64Y**	**SR64Y**	**SR64Y**	**SR64Y**	**SR64Y**	**SR64Y**	**SR64Y**	**SR64Y**	**SR64Y**	**SR64Y**	**SR64Y**
Mineral	*Grt*	*Grt*	*Grt*	*Grt*	*Grt*	*Grt*	*Grt*	*Grt*	*Grt*	*Grt*	*Grt*	*Grt*	*Grt*	*Grt*	*Grt*	*Grt*	*Grt*	*Grt*	*Grt*	*Grt*	*Grt*	*Grt*
Textural setting	*^Bt1, Pl1*	*^Bt2, Pl2*	*Core*	*^Bt27, Pl27, Am27*	*^Bt28, Pl28*	*^Bt37, Pl37*	*rim*	*Core*	*^Bt37, Pl37*	*Core*	*^Bt1, Pl1*	*Profile (rim)*										*Profile (Core)*
Point no.	1#*	2#*	14#*	27#	28#	37#			50#	1	1#	3	4	5	6	7	8	9	10#	11#	12#*	13#*
SiO2	37.25	38.18	38.38	38.12	38.21	37.85	36.85	37.28	37.17	36.99	37.25	37.98	38.04	37.94	38.23	38.10	38.24	38.30	38.36	38.38	38.20	38.38
TiO2	0.02	0.01	0.02	0.05	0.07	0.02	0.02	0.00	0.03	0.01	0.00	0.02	0.00	0.02	0.03	0.02	0.03	0.02	0.01	0.00	0.01	0.02
Al2O3	21.33	21.18	21.10	20.80	20.92	20.95	20.50	20.71	20.66	20.58	21.72	20.94	21.17	21.32	20.80	20.94	21.04	20.83	21.39	20.78	21.06	21.10
FeO	36.11	35.10	34.87	36.06	35.92	37.53	37.20	37.33	36.89	36.73	36.04	35.32	35.41	34.86	34.37	35.11	33.47	33.72	34.39	33.42	34.73	34.87
MnO	2.28	2.86	4.31	2.74	2.51	2.35	2.30	2.31	2.20	2.47	2.44	0.66	0.70	0.70	0.66	0.51	0.40	0.51	0.26	0.27	0.46	0.27
MgO	0.86	0.70	0.27	0.77	0.52	2.03	2.13	2.18	1.93	2.24	1.40	2.65	2.86	2.92	3.33	3.58	3.71	3.89	3.91	4.21	4.31	4.31
CaO	3.64	3.28	2.65	3.41	3.51	1.12	1.12	1.19	1.09	1.14	1.02	3.59	3.64	3.59	3.56	3.39	3.36	3.28	3.17	3.02	2.89	2.65
Na2O	0.04	0.00	0.01	0.01	0.03	0.01	0.01	0.00	0.03	0.03	0.03	0.00	0.00	0.00	0.00	0.01	0.03	0.00	0.00	0.03	0.04	0.01
K2O	0.00	0.00	0.01	0.00	0.00	0.00	0.00	0.00	0.00	0.00	0.00	0.01	0.00	0.00	0.00	0.00	0.00	0.02	0.00	0.00	0.00	0.01
Total	101.53	101.31	101.65	101.98	101.69	101.87	100.13	101.00	100.00	100.19	99.90	101.17	101.82	101.35	100.98	101.66	100.28	100.57	101.49	100.11	101.7	101.65
Oxygen basis	**12**	**12**	**12**	**12**	**12**	**12**	**12**	**12**	**12**	**12**	**12**	**12**	**12**	**12**	**12**	**12**	**12**	**12**	**12**	**12**	**12**	**12**
Si	2.97	3.02	3.01	3.02	3.03	3.02	3.00	3.01	3.02	3.01	3.00	3.02	3.01	3.00	3.03	3.01	3.03	3.04	3.02	3.04	3.00	3.01
Ti	0.00	0.00	0.00	0.00	0.00	0.00	0.00	0.00	0.00	0.00	0.00	0.00	0.00	0.00	0.00	0.00	0.00	0.00	0.00	0.00	0.00	0.00
Al	2.00	1.98	1.95	1.94	1.95	1.97	1.97	1.97	1.98	1.96	2.06	1.96	1.97	1.99	1.94	1.95	1.97	1.95	1.99	1.94	1.95	1.95
Fe^{+2}	2.41	2.32	2.29	2.39	2.38	2.50	2.53	2.52	2.50	2.50	2.43	2.35	2.34	2.31	2.28	2.32	2.22	2.23	2.23	2.22	2.28	2.29
Mg	0.27	0.34	0.50	0.32	0.30	0.28	0.28	0.26	0.27	0.27	0.29	0.31	0.34	0.34	0.39	0.42	0.44	0.46	0.46	0.50	0.51	0.50
Mn	0.06	0.05	0.02	0.05	0.03	0.14	0.15	0.16	0.13	0.17	0.10	0.04	0.05	0.05	0.04	0.03	0.03	0.03	0.02	0.02	0.03	0.02
Ca	0.32	0.28	0.22	0.29	0.30	0.10	0.10	0.10	0.09	0.10	0.09	0.31	0.31	0.30	0.30	0.29	0.29	0.28	0.27	0.27	0.24	0.22
Na	0.01	0.00	0.00	0.00	0.00	0.00	0.00	0.00	0.00	0.00	0.00	0.00	0.00	0.00	0.00	0.00	0.00	0.00	0.00	0.00	0.01	0.00
K	0.00	0.00	0.00	0.00	0.00	0.00	0.00	0.00	0.00	0.00	0.00	0.00	0.00	0.00	0.00	0.00	0.00	0.00	0.00	0.00	0.00	0.00
Total	8.03	7.99	8.01	8.01	8.00	8.00	8.02	8.01	8.00	8.01	7.97	8.00	8.01	8.00	7.99	8.02	7.98	7.99	7.98	7.99	8.00	8.01
X_{Alm}	0.79	0.78	0.75	0.78	0.79	0.83	0.83	0.83	0.84	0.83	0.84	0.78	0.77	0.77	0.76	0.76	0.75	0.75	0.75	0.74	0.74	0.74
X_{Sps}	0.02	0.02	0.01	0.02	0.01	0.05	0.05	0.05	0.04	0.05	0.03	0.02	0.02	0.02	0.01	0.01	0.01	0.01	0.01	0.01	0.01	0.01
X_{Py}	0.09	0.11	0.17	0.11	0.10	0.09	0.09	0.09	0.09	0.09	0.10	0.10	0.11	0.11	0.13	0.14	0.15	0.15	0.15	0.17	0.17	0.17
X_{Grs}	0.10	0.09	0.07	0.09	0.10	0.03	0.03	0.03	0.03	0.03	0.03	0.10	0.10	0.10	0.10	0.09	0.10	0.09	0.09	0.09	0.08	0.07

 # used for conventional geothermobarometry

*** used for phase equillibria study**

Table 6.2b: Representative chemical analyses for orthopyroxene (representative oxygen basis are given). Cation calculation havs been done following the procedure of Grew (1984).

Rock type	**COG**	**COG**	**COG**	**COG**	**COG**	**COG**	**COG**	**COG**	**COG**
Sample no	**SR64Y**	**SR64Y**	**SR64Y**	**SR64Y**	**SR64Y**	**SR64Y**	**SR64Y**	**SR64Y**	**SR64Y**
Mineral	*Opx*	*Opx*	*Opx*	*Opx*	*Opx*	*Opx*	*Opx*	*Opx*	*Opx*
Textural setting	*Core*	*Core*	*Core*	*Core*	*Core*	*Rim*	*Rim*	*Rim*	*Rim*
Point no.	10#	11#	12#	13#	14#				
SiO_2	51.88	51.83	51.06	51.69	51.06	53.55	53.83	54.02	53.68
TiO_2	0.12	0.13	0.23	0.13	0.21	0.04	0.05	0.08	0.05
Al_2O_3	2.95	3.21	3.54	2.67	3.24	0.93	1.21	1.00	0.90
FeO	29.85	31.06	30.26	30.46	30.84	31.59	30.19	29.76	30.47
MgO	12.63	12.50	12.17	12.75	12.46	13.72	13.50	13.93	13.75
MnO	0.17	0.20	0.12	0.07	0.07	0.14	0.16	0.20	0.25
CaO	1.43	1.31	1.80	1.79	1.55	0.41	0.28	0.41	0.35
Na_2O	0.35	0.35	0.46	0.26	0.48	0.07	0.10	0.09	0.06
K_2O	0.02	0.00	0.03	0.04	0.03	0.00	0.00	0.00	0.01
Total	99.41	100.61	99.67	99.86	99.96	100.47	99.33	99.48	99.52
Oxygen basis	**6**	**6**	**6**	**6**	**6**	**6**	**6**	**6**	**6**
Si	2.01	1.99	1.99	2.01	1.99	2.06	2.06	2.07	2.06
Ti	0.00	0.00	0.01	0.00	0.01	0.00	0.00	0.00	0.00
Al	0.13	0.15	0.16	0.12	0.15	0.04	0.06	0.05	0.04
Fe^{+2}	0.97	1.00	0.95	0.96	0.97	1.01	0.98	0.96	0.99
Mg	0.73	0.72	0.71	0.74	0.72	0.79	0.79	0.80	0.80
Mn	0.01	0.01	0.00	0.00	0.00	0.00	0.01	0.01	0.01
Ca	0.06	0.05	0.08	0.07	0.06	0.02	0.01	0.02	0.01
Na	0.03	0.03	0.03	0.02	0.04	0.01	0.01	0.01	0.00
K	0.00	0.00	0.00	0.00	0.00	0.00	0.00	0.00	0.00
Total	3.93	3.94	3.94	3.93	3.95	3.92	3.91	3.90	3.92
X_{Mg}	*0.43*	*0.42*	*0.43*	*0.44*	*0.43*	*0.44*	*0.45*	*0.45*	*0.45*

 # used for conventional geothermobarometry

Table 6.2c: Representative chemical analyses for feldspar (representative oxygen basis are given). Cation calculation havs been done following the procedure of Grew (1984).

Sample no	**SR64Y**	**SR64U**	**SR64U**	**SR69L1**	**SR69L1**
Rock type	**COG**	**COG**	**COG**	**GOG**	**GOG**
Mineral	*Kfs*	*Kfs*	*Kfs*	*Kfs*	*Kfs*
Textural setting	*matrix*	*matrix*	*matrix*	*matrix*	*matrix*
SiO_2	58.41	64.63	64.26	64.74	65.38
TiO_2	0.02	0.00	0.03	0.00	0.01
Al_2O_3	26.33	18.04	18.25	18.25	18.56
FeO	0.24	0.00	0.07	0.00	0.03
MgO	0.08	0.03	0.01	0.01	0.00
MnO	0.02	0.00	0.08	0.07	0.00
CaO	0.40	0.01	0.00	0.00	0.06
Na_2O	2.72	0.72	0.69	0.94	1.85
K_2O	9.93	15.27	15.29	15.13	14.39
Total	98.12	98.51	98.68	99.04	100.26
Oxygen basis	**8**	**8**	**8**	**8**	**8**
Si	2.70	3.01	3.00	3.01	3.00
Ti	0.00	0.00	0.00	0.00	0.00
Al	1.43	0.99	1.00	1.00	1.00
Fe^{+2}	0.01	0.00	0.00	0.00	0.00
Mg	0.01	0.00	0.00	0.00	0.00
Mn	0.00	0.00	0.00	0.00	0.00
Ca	0.02	0.00	0.00	0.00	0.00
Na	0.24	0.07	0.06	0.08	0.16
Total	5.00	4.98	4.98	4.99	5.01
X_{Or}	*0.81*	*0.93*	*0.94*	*0.91*	*0.83*
X_{Ab}	*0.19*	*0.07*	*0.06*	*0.09*	*0.16*
X_{An}	*0.02*	*0.00*	*0.00*	*0.00*	*0.00*

Table 6.2c (continued): Representative chemical analyses for feldspar (representative oxygen basis are given). Cation calculation havs been done following the procedure of Grew (1984).

Rock type	**COG**	**COG**	**COG**	**COG**	**COG**	**COG**	**COG**	**COG**	**COG**	**COG**	**COG**	**COG**	**COG**	**GOG**	**GOG**	**GOG**	**GOG**	**GOG**	**GOG**	**GOG**
Sample no	**SR64Y**	**SR64Y**	**SR64Y**	**SR64Y**	**SR64Y**	**SR64Y**	**SR64Y**	**SR64Y**	**SR64Y**	**SR64U**	**SR64U**	**SR64U**	**SR64U**	**SR69L1**	**SR69L1**	**SR69L1**	**SR69L1**	**SR69C**	**SR69C**	**SR69C**
Mineral	*Pl*	*Pl*	*Pl*	*Pl*	*Pl*	*Pl*	*Pl*	*Pl*	*Pl*	*Pl*	*Pl*	*Pl*	*Pl*	*Pl*	*Pl*	*Pl*	*Pl*	*Pl*	*Pl*	*Pl*
Textural setting	*^Grt 1, Bt 1*	*^Grt 1, Bt 1*	*^Grt 3, Bt 3*	*core*	*core*	*core*	*core*	*^Grt27, Bt27*	*^Grt28, Bt28*	*matrix*	*rim*	*rim*	*core*	*matrix*	*^Grt37, Bt37*	*^Grt38, Bt38*	*^Grt50, Bt50*	*^Grt1, Bt1*	*rim*	*matrix*
Point no.	1#	2#	3#	10#	11#	13#	14#	27#	28#	30	31	99	101	30	37#	38#	50#	1#	11	12
SiO_2	58.79	59.36	58.57	58.87	59.57	59.41	58.82	59.19	58.33	61.94	61.47	62.80	62.40	63.23	62.39	62.22	62.84	62.21	62.13	62.56
TiO_2	0.00	0.02	0.01	0.00	0.00	0.00	0.02	0.01	0.02	0.01	0.02	0.00	0.00	0.01	0.00	0.01	0.00	0.02	0.01	0.01
Al_2O_3	26.93	26.34	27.00	26.97	26.44	26.06	26.70	26.78	26.69	23.61	24.14	24.21	23.54	23.63	23.49	23.11	23.73	23.17	23.15	23.17
FeO	0.00	0.00	0.11	0.14	0.09	0.00	0.01	0.18	0.16	0.07	0.06	0.26	0.15	0.00	0.11	0.00	0.00	0.02	0.00	0.00
MgO	0.01	0.02	0.00	0.00	0.00	0.00	0.01	0.01	0.01	0.01	0.00	0.00	0.00	0.00	0.00	0.00	0.00	0.00	0.00	0.01
MnO	0.00	0.00	0.00	0.04	0.00	0.00	0.08	0.01	0.00	0.04	0.00	0.00	0.02	0.01	0.00	0.00	0.00	0.12	0.03	0.00
CaO	8.76	8.31	8.82	8.36	8.04	8.05	8.51	8.32	8.72	5.45	5.74	5.95	5.28	4.94	4.89	5.00	5.04	4.98	5.01	4.87
Na_2O	6.67	6.94	6.92	7.10	7.28	7.29	7.06	7.06	6.85	8.41	8.49	8.84	8.36	9.07	8.61	8.98	8.83	8.58	9.09	8.70
K_2O	0.05	0.08	0.11	0.04	0.07	0.05	0.05	0.04	0.03	0.17	0.13	0.08	0.11	0.15	0.13	0.23	0.25	0.15	0.15	0.20
Total	101.08	100.94	101.47	101.51	101.49	100.83	101.26	101.62	100.80	99.91	99.99	102.14	100.06	100.97	99.62	99.55	100.56	99.54	99.57	99.43
Oxygen basis	**8**	**8**	**8**	**8**	**8**	**8**	**8**	**8**	**8**	**8**	**8**	**8**	**8**	**8**	**8**	**8**	**8**	**8**	**8**	**8**
Si	2.60	2.62	2.59	2.60	2.62	2.63	2.60	2.61	2.59	2.75	2.73	2.74	2.77	2.77	2.77	2.77	2.77	2.78	2.78	2.78
Ti	0.00	0.00	0.00	0.00	0.00	0.00	0.00	0.00	0.00	0.00	0.00	0.00	0.00	0.00	0.00	0.00	0.00	0.00	0.00	0.00
Al	1.40	1.37	1.41	1.40	1.37	1.36	1.39	1.39	1.40	1.24	1.26	1.24	1.23	1.22	1.23	1.21	1.23	1.22	1.21	1.21
Fe^{+2}	0.00	0.00	0.00	0.01	0.00	0.00	0.00	0.01	0.01	0.00	0.00	0.00	0.00	0.00	0.00	0.00	0.00	0.00	0.00	0.00
Mg	0.00	0.00	0.00	0.00	0.00	0.00	0.00	0.00	0.00	0.00	0.00	0.00	0.00	0.00	0.00	0.00	0.00	0.00	0.00	0.00
Mn	0.00	0.00	0.00	0.00	0.00	0.00	0.00	0.00	0.00	0.00	0.00	0.01	0.01	0.00	0.00	0.00	0.00	0.00	0.00	0.00
Ca	0.42	0.39	0.42	0.39	0.38	0.38	0.40	0.39	0.42	0.26	0.27	0.28	0.25	0.23	0.23	0.24	0.24	0.24	0.24	0.23
Na	0.57	0.59	0.59	0.61	0.62	0.63	0.61	0.60	0.59	0.73	0.73	0.75	0.72	0.77	0.74	0.78	0.75	0.74	0.77	0.75
K	0.00	0.00	0.01	0.00	0.00	0.00	0.00	0.00	0.00	0.02	0.01	0.00	0.01	0.01	0.01	0.01	0.01	0.01	0.01	0.01
Total	4.99	4.99	5.01	5.01	5.00	5.00	5.01	5.00	5.00	5.00	5.01	5.02	5.00	5.01	4.99	5.01	5.00	4.99	5.01	4.99
X_{Or}	*0.00*	*0.00*	*0.01*	*0.00*	*0.00*	*0.00*	*0.00*	*0.00*	*0.00*	*0.02*	*0.01*	*0.00*	*0.01*	*0.01*	*0.01*	*0.01*	*0.01*	*0.01*	*0.01*	*0.01*
X_{Ab}	*0.58*	*0.60*	*0.58*	*0.60*	*0.62*	*0.62*	*0.60*	*0.60*	*0.59*	*0.73*	*0.72*	*0.73*	*0.73*	*0.76*	*0.76*	*0.75*	*0.75*	*0.75*	*0.76*	*0.76*
X_{An}	*0.42*	*0.40*	*0.41*	*0.39*	*0.38*	*0.38*	*0.40*	*0.39*	*0.41*	*0.26*	*0.27*	*0.27*	*0.26*	*0.23*	*0.24*	*0.23*	*0.24*	*0.24*	*0.24*	*0.23*

 # used for conventional geothermobarometry

Table 6.2d : Representative chemical analyses for amphibole and biotite (representative oxygen basis are given in tables). Mineral abbreviations are used after Whitney and Evans (2010). Cation calculations for biotite have been done following the procedure of Grew (1984). Cation calculation of amphibole has been done by the procedure of Leake (2004)

Rock type	**COG**	**COG**	**COG**	**COG**	**COG**	**COG**	**COG**	**COG**	**COG**	**COG**	**COG**	**COG**	**COG**	**COG**	**COG**	**COG**
Sample no	**SR64Y**	**SR64Y**	**SR64Y**	**SR64U**	**SR64U**	**SR64U**	**SR64U**	**SR64Y**	**SR64Y**	**SR64Y**	**SR64Y**	**SR64Y**	**SR64Y**	**SR64U**	**SR64U**	**SR64U**
Mineral	*Amp*	*Amp*	*Amp*	*Amp*	*Amp*	*Amp*	*Amp*	*Bt*	*Bt*	*Bt*	*Bt*	*Bt*	*Bt*	*Bt*	*Bt*	*Bt*
Textural setting	*^Opx*	*^Opx*	*^Opx*	*^Opx*	*^Opx*	*^Opx*	*^Opx*	*^Grt 1, Pl 1*	*^Grt 3, Pl 3*	*^Grt27, Pl27*	*^Grt28, Pl28*	*core*	*core*	*core*	*core*	*rim*
Point no.	1	2	27	30	31	129	136	1#	3#	27#	28#	43	66	96	113	114
SiO_2	42.45	43.28	42.46	44.20	45.03	42.83	43.75	36.46	36.05	36.33	36.21	36.39	36.16	37.53	37.46	37.22
TiO_2	0.54	0.56	0.60	0.98	0.78	1.20	1.00	2.22	2.11	2.41	2.38	2.45	2.35	1.74	1.93	2.12
Al_2O_3	14.11	11.79	13.71	9.09	8.74	10.35	9.53	16.52	16.11	16.16	16.29	16.43	16.42	13.52	13.34	13.35
FeO	20.73	22.52	21.14	18.65	19.42	19.48	18.75	22.79	23.89	21.66	22.35	22.69	22.35	20.42	19.91	20.69
MgO	6.98	8.32	7.37	9.15	9.42	8.65	8.95	9.82	10.39	9.79	9.90	9.76	9.70	11.29	11.67	11.15
MnO	0.05	0.13	0.00	0.41	0.65	0.59	0.52	0.00	0.10	0.08	0.00	0.00	0.00	0.03	0.03	0.04
CaO	10.81	9.18	10.28	11.66	11.61	11.63	11.74	0.04	0.07	0.10	0.03	0.03	0.07	0.06	0.12	0.09
Na_2O	1.30	1.21	1.39	1.37	1.24	1.41	1.33	0.36	0.27	0.36	0.33	0.37	0.34	0.35	0.26	0.23
K_2O	0.41	0.35	0.34	1.34	1.24	1.49	1.39	8.34	7.68	8.29	8.21	8.63	8.30	9.24	9.11	9.35
Total	97.45	97.40	97.35	97.57	98.81	98.50	97.80	96.51	96.72	95.26	95.72	96.77	95.69	94.18	93.83	94.24
Oxygen basis	**23**	**23**	**23**	**23**	**23**	**23**	**23**	**11**	**11**	**11**	**11**	**11**	**11**	**11**	**11**	**11**
Si	6.38	6.49	6.37	6.75	6.78	6.53	6.69	2.77	2.74	2.79	2.77	2.76	2.77	2.88	2.86	2.85
Ti	0.00	0.00	0.00	0.00	0.00	0.00	0.00	0.13	0.12	0.14	0.14	0.14	0.14	0.10	0.11	0.12
Al	2.50	2.09	2.42	1.64	1.55	1.86	1.72	1.48	1.44	1.46	1.47	1.47	1.48	1.22	1.20	1.21
Fe^{+2}	2.17	2.10	2.06	2.29	2.19	2.27	2.30	1.45	1.52	1.39	1.43	1.44	1.43	1.31	1.27	1.33
Mg	1.56	1.86	1.65	2.08	2.11	1.96	2.04	1.11	1.18	1.12	1.13	1.10	1.11	1.29	1.33	1.27
Mn	0.01	0.02	0.00	0.05	0.08	0.08	0.07	0.00	0.01	0.01	0.00	0.00	0.00	0.02	0.02	0.01
Ca	1.74	1.48	1.65	1.91	1.87	1.90	1.92	0.00	0.01	0.01	0.00	0.00	0.01	0.00	0.00	0.00
Na	0.38	0.35	0.40	0.41	0.36	0.42	0.39	0.05	0.04	0.05	0.05	0.05	0.05	0.01	0.02	0.01
K	0.08	0.07	0.07	0.26	0.24	0.29	0.27	0.81	0.75	0.81	0.80	0.84	0.81	0.90	0.89	0.91
Total	15.32	15.25	15.29	15.60	15.53	15.65	15.62	7.79	7.81	7.78	7.78	7.81	7.79	8.01	8.08	8.05
Classification	**Calcic Ferrotschermakite**			**Calcic Ferroedenite**												
X_{Mg}	*0.44*	*0.47*	*0.44*	*0.48*	*0.49*	*0.46*	*0.47*	*0.43*	*0.44*	*0.45*	*0.44*	*0.43*	*0.44*	*0.50*	*0.51*	*0.49*

Table 6.2d (continued) : Representative chemical analyses for biotite, ilmenite and titanite (representative oxygen basis are given in tables). Mineral abbreviations are used after Whitney and Evans (2010). Cation calculations have been done following the procedure of Grew (1984).

Rock type	**GOG**	**GOG**	**GOG**	**GOG**	**GOG**	**GOG**	**GOG**	**COG**	**COG**	**COG**	**COG**
Sample no	**SR69L1**	**SR69L1**	**SR69L1**	**SR69L1**	**SR69C**	**SR69C**	**SR69C**	**SR64Y**	**SR64Y**	**SR64U**	**SR64U**
Mineral	*Bt*	*Bt*	*Bt*	*Bt*	*Bt*	*Bt*	*Bt*	*Ilm*	*Ilm*	*Ttn*	*Ttn*
Textural setting	*matrix*	*^Grt37, Pl37*	*^Grt38, Pl38*	*^Grt50, Pl50*	*^Grt2, Pl2*	*core*	*core*	*incl Grt*	*incl Grt*		
Point no.	19	37#	38#	50#	2#	5	8	17	18	98	104
SiO_2	34.71	34.97	33.25	31.38	35.59	35.07	34.70	0.05	0.06	29.87	30.55
TiO_2	2.62	0.75	2.33	0.96	2.94	2.42	2.88	51.24	50.33	35.28	34.32
Al_2O_3	18.76	20.48	19.66	19.44	19.16	19.25	18.90	0.00	0.00	3.19	3.45
FeO	23.58	22.15	24.66	26.85	23.03	23.42	23.56	47.21	49.96	0.76	0.67
MgO	5.82	6.95	6.44	6.80	6.46	6.48	6.13	1.59	0.80	0.01	0.04
MnO	0.00	0.00	0.17	0.28	0.19	0.14	0.16	0.02	0.00	0.05	0.00
CaO	0.07	0.05	0.12	0.10	0.04	0.02	0.01	0.03	0.01	27.94	27.30
Na_2O	0.14	0.09	0.07	0.14	0.09	0.09	0.17	0.03	0.01	0.04	0.02
K_2O	9.44	9.50	6.95	6.43	9.18	9.46	9.20	0.00	0.00	0.02	0.00
F										0.84	1.11
Total	95.66	94.94	94.04	92.68	97.16	97.03	96.15	100.15	101.04	97.97	97.36
Oxygen basis	**11**	**11**	**11**	**11**	**11**	**11**	**11**	**3**	**3**	**5**	**5**
Si	2.69	2.69	2.61	2.54	2.70	2.67	2.67	0.00	0.00	1.00	1.03
Ti	0.15	0.04	0.14	0.06	0.17	0.14	0.17	0.97	0.94	0.89	0.87
Al	1.71	1.85	1.82	1.85	1.71	1.73	1.72	0.00	0.00	0.13	0.14
Fe+2	1.53	1.42	1.62	1.81	1.46	1.49	1.52	0.93	0.91	0.00	0.00
Mg	0.67	0.80	0.75	0.82	0.73	0.74	0.70	0.06	0.12	0.02	0.02
Mn	0.00	0.00	0.01	0.02	0.01	0.01	0.01	0.00	0.03	0.00	0.00
Ca	0.01	0.00	0.01	0.01	0.00	0.00	0.00	0.03	0.00	1.00	0.98
Na	0.02	0.01	0.01	0.02	0.01	0.01	0.03	0.00	0.00	0.00	0.00
K	0.93	0.93	0.70	0.66	0.89	0.92	0.90	0.00	0.00	0.00	0.00
Sum	7.84	7.75	7.74	7.85	7.78	7.86	7.81	2.00	2.00	3.05	3.04
X_{Mg}	*0.31*	*0.36*	*0.32*	*0.31*	*0.33*	*0.33*	*0.32*				

 # used for conventional geothermobarometry

6.3. Whole rock geochemistry

The variations in the whole rock major and trace element composition of the two variants of the studied felsic orthogneisses reflect their distinct mineral assemblages in melanosome, composition of minerals, and abundance of leucosome and accessory phases. Since the rocks have been extensively metamorphosed and deformed, it is imperative to address the possibility of melt loss and alteration of the chemical composition. Firstly to avoid alteration we have collected fresh samples and while preparing the powder we have also chosen samples that are least altered. As GOG has

15-20 vol% leucosome banding in the outcrop we have chosen considerably large samples with an approximate dimension of 20cm×15cm to reduce the effect of segregation and obtain a homogenized bulk. The possibility of melt loss in the COG is less owing to the small amount of leucosome (<10 vol%) observed in these rocks. Higher proportion (15-20 vol%) of leucosome in GOG invokes the possibility of melt loss, which would impart considerable chemical heterogeneity. Melt loss during the metamorphic process commonly leads to silica, alkali and LILE-poor residue (Clemens, 1990; Sawyer and Brown, 2008). In the studied GOG, however, (a) high silica and alkali contents (SiO_2>70 wt%, K_2O≥5 wt%); (b) the restricted range of compositional variation and (c) coherent trace element and high LILE contents contradicts the evidences of melt loss as suggested by Sawyer and Brown (2008).

In the following section the major and trace element characteristics of the representative samples are described and bulk composition data are presented in Table-6.3. The details of the analytical techniques for obtaining whole rock compositions are discussed in the Appendix.

6.3.1. Major element characteristics

In the modal quartz-alkali feldspar-plagioclase (QAP) diagram (Le Maitre et al., 2002) the studied rocks plot mainly in the fields of monzogranite (GOG) and granodiorite (COG) with a couple of data straddling the boundary between 'granodiorite' and 'tonalite' (Fig. 6.3a). The GOG samples have restricted SiO_2 content of 70-75% and are alkali-calcic to calc-alkalic (Fig. 6.3b), highly potassic with K_2O/Na_2O>1, highly peraluminous (Alumina Saturation Index: ASI>1.1; Fig. 6.3c). In comparison, the COG samples show a large variation in SiO_2 content (60-76%), are distinctly less potassic (K_2O/Na_2O=0.15-0.85), comparatively more calcic and metaluminous to marginally peraluminous (ASI<1.1; Fig. 6.3b, c). In $FeO_t/(FeO_t+MgO)$ versus SiO_2 plot (Fig. 6.3d) the studied rocks plot across the fields of "Ferroan' to "Magnesian", akin to the Cordilleran granite field. Total FeO_t+MgO and CaO contents are considerably higher in the COG than in the GOG (Fig. 6.3d). Major element contents corroborate well with the mineral assemblage observed in the petrography. High FeO_t+MgO contents of the COG correlate well with the higher

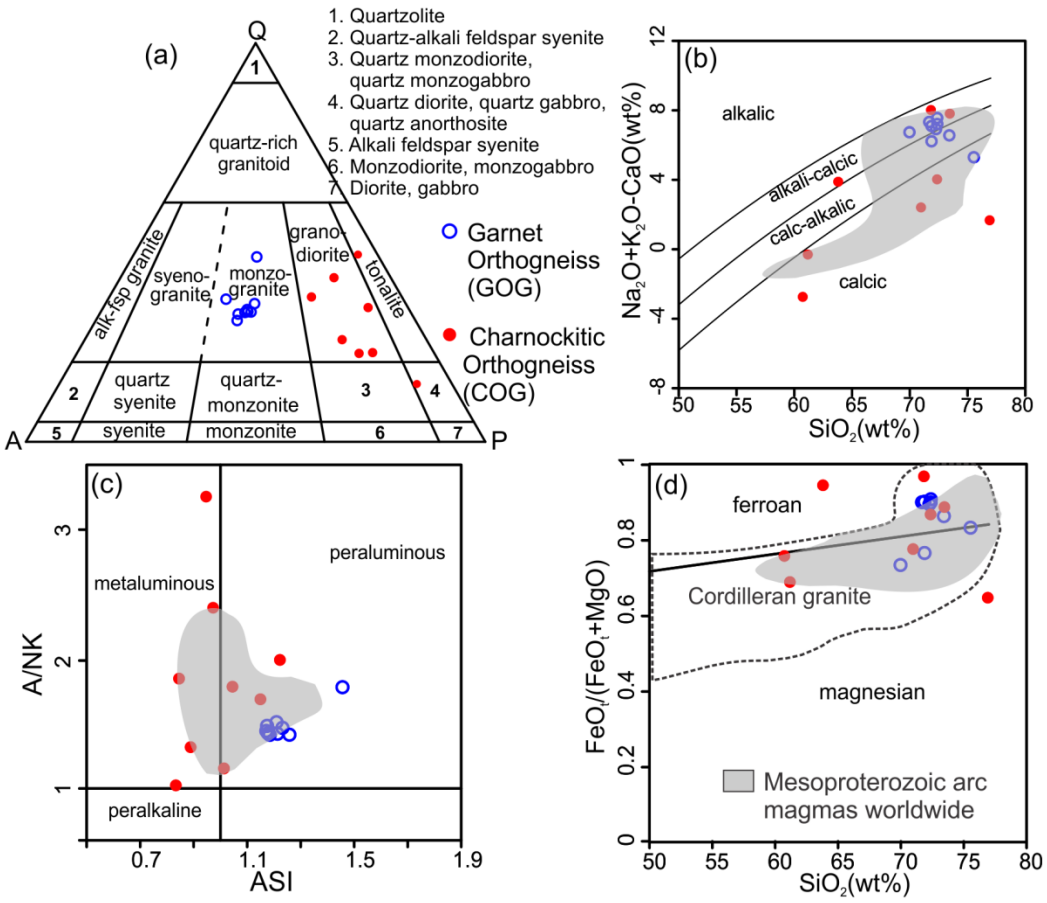

Figure 6.3. (a) Modal QAP diagram (Le Maitre et al., 2002) showing compositional variation within the suite. (b)-(d) Granitoid classification scheme (Frost et al., 2001) showing calcic to alkali-calcic, metaluminous to peraluminous and magnesian to ferroan nature of the protolith of the felsic orthogneisses. Geochemistry of the studied rocks are compared with four other Mesoproterozoic arc granitoids from Musgrave Block, Persimiento Granitoid Complex of Amazonian craton, Tianshan Arc Terrane of Central Asian Orogenic Belt and Mount Brown of East Antarctic (Wade et al. 2006; Matos et al. 2009; He et al. 2015; Liu et al. 2016).

amount of ferromagnesian minerals compared to that of the GOG. On the other hand, higher SiO_2 and K_2O/Na_2O in the GOG corroborate with the higher amount of quartzofeldspathic minerals/leucosome and predominance of K-feldspar. Restricted compositional variation of GOG possibly results in their restricted mineralogy (garnet + biotite + quartz + K-feldspar + plagioclase), developed during metamorphism as compared to COG. In COG not only is the mineralogy more variable (orthopyroxene + amphibole + garnet + biotite + quartz + K-feldspar + plagioclase), but also the relative

abundance of phases varies in different samples. Higher CaO in COG leads to the formation of amphibole during the retrogression. Major element compositions, therefore, are coherent with the observed mineralogical variations.

6.3.2. Trace element characteristics

Primitive mantle normalized (N) (McDonough and Sun, 1995) spider diagram (Fig. 6.3e) for trace elements shows enrichment of Rb, Pb, Nd and depletion of Ba, Nb, Sr, and Ti in both group of samples. Chondrite-normalized (CN) (McDonough and Sun, 1995) REE patterns of the studied samples are shown in Fig. 6.3f. Barring the three samples of COG, the studied rocks show considerable enrichment of LREE over the HREE with $(La/Lu)_{CN}$= ~37-100. Three samples of COG, containing low LREE/HREE ratio [$(La/Lu)_{CN}$ =3-5] show high mafic (FeO_t+MgO) and Y content and contain highest and largest zircon grain concentrations. A prominent negative Eu anomaly is recorded by all the samples.

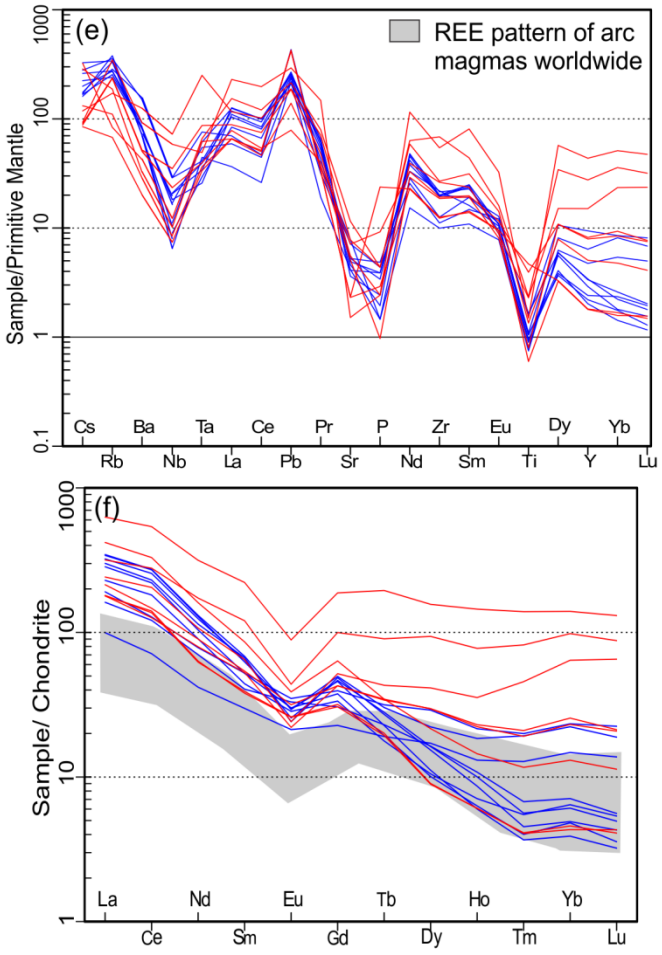

Figure 6.3 contd. (e) Primitive mantle normalized trace element diagram. (f) Chondrite-normalised REE diagram. Normalization data are after McDonough & Sun (1995); grey shaded area shows the REE pattern of some typical arc granites worldwide. Data of arc granites collected from GEOROC (http://georoc.mpch-mainz.gwdg.de/georoc/).

Table 6.3: Major and trace element chemistry of the studied felsic orthogneisses; Major element concentrations are in weight% and trace element concentrations are in ppm.

Sample	SR94-3	SR98	SR95	SR94-4A	SR94-5A	SR94-1	SR94-6	SR69C	SR69L1	SR94-9	SR69X	SR 115	SR64Y	SR 123	SR64U	SR64W	SR 69 N
					GOG								COG				
SiO_2	71.68	71.88	73.42	72.27	72.37	72.38	71.88	69.97	75.54	72.36	70.97	73.46	60.73	63.8	61.17	76.91	71.83
TiO_2	0.19	0.33	0.18	0.21	0.21	0.16	0.22	0.31	0.35	0.27	0.46	0.12	0.5	0.94	0.47	0.16	0.3
Al_2O_3	15.24	14.03	14.81	15.06	15.3	15.15	15.52	15.5	14	15.12	14.39	14.97	12.45	14.47	17.39	12.24	13.68
FeO_t	1.87	2.47	1.44	1.85	1.77	1.46	1.81	2.47	3.00	2.08	4.10	1.09	12.00	7.40	4.76	1.77	2.97
MnO	0.03	0.02	0.02	0.02	0.02	0.02	0.07	0.02	0.03	0.03	0.07	0.01	0.14	0.14	0.15	0.05	0.08
MgO	0.21	0.76	0.23	0.22	0.2	0.15	0.2	0.9	0.5	0.32	1.19	0.14	3.00	0.44	2.16	0.97	0.10
CaO	1.15	1.49	1.42	1.32	0.85	1.21	1.17	1.45	2.5	2.43	2.57	1.08	3.40	3.57	6.26	2.70	1.30
Na_2O	2.72	1.97	2.87	2.91	3.03	2.84	2.87	2.46	2.35	3.48	3.25	5.92	1.72	5.14	5.25	3.77	7.29
K_2O	5.76	5.74	5.11	5.33	5.38	5.58	5.40	5.73	4.00	2.98	1.73	2.97	0.7	2.32	0.71	0.6	2.03
P_2O_5	0.10	0.09	0.08	0.07	0.08	0.05	0.04	0.03	0.03	0.09	0.05	0.06	0.19	0.49	0.09	0.02	0.05
Sc	3.06	6.15	2.47	2.09	2.25	2.54	4.25	5.56	4.44	3.15	9.91	0.38	18.30	0.64	13.61	3.77	3.86
V	5.85	25.48	5.14	6.19	6.27	5.06	5.79	23.51	7.96	7.51	36.06	3.38	91.75	3.36	48.97	3.68	3.81
Cr	0.59	20.45	0.53	0.77	0.66	0.34	0.83	28.66	9.45	1.07	39.68	bdl	66.64	bdl	51.78	0.72	bdl
Mn	239.90	147.89	115.43	126.65	169.18	124.91	484.71	141.46	191.19	175.67	469.55	66.59	954.90	65.93	828.91	288.26	415.53
Co	92.40	101.61	77.03	92.97	83.86	65.55	98.28	77.95	125.55	88.74	89.07	71.38	57.46	72.15	49.13	127.74	68.37
Ni	2.00	11.76	2.00	2.77	3.23	1.97	2.14	9.08	5.04	3.74	14.29	2.05	35.10	2.17	19.95	3.04	2.40
Cu	5.86	11.25	1.11	2.12	1.57	0.90	1.50	2.68	9.38	5.19	4.08	0.84	10.45	0.90	2.34	1.04	3.87
Zn	39.15	23.98	31.69	46.75	43.64	38.35	34.86	55.94	24.02	40.09	84.06	25.04	92.25	25.02	122.13	57.73	109.43
Ga	17.03	12.95	18.40	18.06	17.82	19.10	17.59	18.23	17.81	19.34	18.92	12.08	17.67	12.32	21.93	12.24	22.24
As	1.09	0.36	0.63	0.52	0.65	0.60	0.63	1.04	0.44	0.64	0.67	0.36	0.78	0.42	1.66	0.63	2.26
Se	0.93	1.26	1.26	1.60	0.45	0.86	0.00	1.06	0.79	0.85	0.99	1.14	0.31	1.80	0.44	2.07	10.49
Rb	203.76	171.45	199.21	152.74	165.04	227.38	163.99	213.98	144.21	103.01	112.59	141.10	50.21	142.81	40.59	66.25	208.35
Sr	104.58	142.25	81.57	104.79	97.84	71.84	91.66	155.47	82.91	229.37	110.50	45.94	141.50	46.48	154.62	101.95	30.07
Cs	6.87	3.38	3.67	3.52	5.48	3.58	4.18	5.86	4.71	2.48	6.03	1.85	6.79	1.90	1.78	2.77	1.95
Ba	534.80	1032.46	474.54	561.54	603.19	466.56	553.29	990.24	533.30	825.55	214.38	333.32	279.91	342.49	133.52	189.85	609.98
Cd	0.19	0.15	0.25	0.29	0.28	0.28	0.29	0.14	0.15	0.35	0.52	0.22	0.22	0.22	1.16	0.29	1.16
Ta	1.09	2.02	0.95	2.27	1.45	1.52	1.25	2.80	1.64	2.43	3.22	1.24	1.47	1.35	9.28	2.29	1.82
Pb	37.03	35.46	38.48	31.30	32.41	40.30	38.65	64.81	33.06	32.09	27.92	62.80	11.81	64.01	28.25	20.86	43.99
Bi	0.09	0.02	0.10	0.06	0.06	0.06	0.03	0.20	1.37	0.06	0.18	0.04	0.18	0.04	0.26	0.05	0.12
Hf	6.48	3.32	6.70	7.01	6.35	6.51	6.14	4.10	3.90	8.37	8.61	3.79	5.99	3.83	17.95	6.55	15.70
Zr	229.65	116.81	204.94	225.11	210.12	204.56	210.45	131.92	104.69	281.85	275.12	132.16	201.46	129.07	718.40	195.47	570.50
Nb	5.91	11.13	11.96	7.33	13.73	18.99	13.53	19.06	4.26	8.05	23.06	4.87	15.41	5.63	47.67	6.69	38.52
Mo	1.16	1.33	0.48	0.98	0.73	0.91	0.76	0.16	0.45	1.51	0.22	0.22	0.81	0.19	2.82	0.34	4.25
Sn	3.25	1.86	2.06	3.70	3.94	2.06	3.54	4.31	3.54	1.97	6.18	1.66	8.97	1.67	25.00	4.52	14.55
Sb	0.04	0.03	0.02	0.02	0.01	0.02	0.01	0.06	0.04	0.03	0.02	0.00	0.04	0.00	0.12	0.04	0.00
Y	10.35	14.42	12.51	8.69	9.45	14.64	27.47	40.42	20.38	21.74	64.71	7.70	35.22	7.78	118.56	34.06	187.40

Table 6.3 (continued): Trace element chemistry of the studied felsic orthogneisses; Trace element concentrations are in ppm.

Sample	SR94-3	SR98	SR95	SR94-4A	SR94-5A	SR94-1	SR94-6	SR69C	SR69L1	SR94-9	SR69X	SR 115	SR64Y	SR 123	SR64U	SR64W	SR 69 N
					GOG									COG			
La	54.35	38.33	71.24	80.91	67.51	76.45	81.92	45.27	23.62	99.39	57.34	42.47	50.69	42.77	75.21	42.42	148.86
Ce	111.30	74.36	141.29	166.31	135.08	156.95	167.47	78.49	43.72	202.11	125.61	86.17	90.10	83.91	170.64	77.57	330.62
Pr	10.81	8.07	14.28	15.83	13.25	15.40	16.59	9.25	4.87	20.17	12.17	8.52	10.21	8.48	18.00	9.31	37.52
Nd	41.29	32.05	52.19	58.90	47.53	56.82	59.97	35.86	19.11	73.41	49.04	28.97	41.11	28.46	79.02	36.36	144.22
Sm	6.54	6.00	9.89	9.25	7.71	9.56	10.12	7.75	4.42	12.73	9.61	5.62	8.00	5.79	17.83	7.81	32.80
Eu	1.60	1.86	1.36	1.68	1.69	1.44	1.65	1.97	1.20	2.18	1.36	1.46	1.78	1.47	2.47	1.24	5.00
Gd	6.67	6.08	9.67	9.12	7.49	9.27	9.88	7.87	4.52	12.64	10.32	6.09	8.51	6.32	19.88	8.51	37.38
Tb	0.64	0.83	0.98	0.82	0.70	1.01	1.09	1.14	0.69	1.25	1.56	0.70	1.23	0.73	3.26	1.25	7.04
Dy	2.59	4.02	3.78	2.74	2.48	3.99	5.47	7.14	4.21	5.31	10.17	2.19	7.31	2.22	23.10	7.29	38.51
Ho	0.39	0.59	0.47	0.33	0.34	0.55	1.01	1.18	0.71	0.79	1.94	0.33	1.26	0.33	4.24	1.22	7.91
Er	1.32	1.67	1.33	1.12	1.08	1.61	3.66	3.57	2.25	2.66	7.18	0.00	4.09	0.00	14.16	3.79	0.00
Tm	0.14	0.17	0.11	0.09	0.10	0.14	0.48	0.49	0.32	0.29	1.13	0.10	0.52	0.10	2.02	0.47	3.44
Yb	1.04	1.14	0.79	0.63	0.78	0.98	3.59	3.76	2.38	2.10	10.35	0.70	4.12	0.74	15.80	3.72	22.53
Lu	0.13	0.14	0.11	0.08	0.09	0.12	0.46	0.55	0.34	0.28	1.61	0.11	0.52	0.10	2.16	0.51	3.22
$(La/Lu)_N$	42.85	29.02	70.17	106.41	80.15	65.43	18.39	8.54	7.26	37.16	3.72	41.70	10.10	44.21	3.63	8.65	4.82
Eu/Eu*	0.74	0.94	0.42	0.56	0.68	0.47	0.50	0.77	0.82	0.53	0.42	0.76	0.66	0.74	0.40	0.46	0.43
$T_{Zr}(^0C)$(W&H)	821	749	806	816	817	810	816	758	769	832	829	752	745	720	825	780	865
$T_{Zr}(^0C)$(B)	780	692	760	774	778	768	775	701	727	790	786	692	668	644	742	722	814

N=Primitive mantle normalized (Sun & McDonough, 1995)

$Eu/Eu^* = (Eu)_{CN}/[(Sm)_{CN} \times (Gd)_{CN}]^{0.5}$

$T_{Zr}(^0C)$(W&H)= Zircon saturation temperature (Watson and Harrison, 1984); (B)=Boehnke et al., 2013.

6.3.3. Temperature of magma from zircon saturation thermometry

Zirconium (Zr) being an incompatible element, common rock forming minerals do not contain a significant amount of this element. Zircon, a common accessory mineral in the felsic rock, is the chief sink of Zr (Kirkland et al., 2015; Watson and Harrison, 1983). A number of studies (Boehnke et al., 2013; Miller et al., 2003; Watson and Harrison, 1983) have demonstrated that the minimum temperature of the parental melt of granitoids can be estimated from the Zr concentration of the bulk rock composition (the zircon saturation thermometry; Boehnke et al., 2013; Watson and Harrison, 1983). Two implicit assumptions in the zircon saturation thermometry are:

A) Zircon in the studied rock must be in equilibrium with the melt phase and that the bulk rock composition closely represents the composition of the melt from the zircon grains were crystallized (reviewed in Kirkland et al., 2015; Watson and Harrison, 1983).

B) Subsequent to quenching of the melt, the rock must behave as a close system. If the magmatic rocks undergo metamorphism, Zr concentration of the magmatic protolith must not change (reviewed in Kirkland et al., 2015).

Zr is a High Field Strength Element (HFSE) and hence, the magmatic Zr concentrations are not affected by fluid-rock interaction during metamorphism in most of the geological environment (reviewed in Philpotts and Ague, 2009). So the implicit assumption B remains valid in most of the geological conditions. It is well known that magmatic rocks do inherit materials including zircon grains particularly when the ambient magma temperature is too low to dissolve the xenocrystic zircon (Bea et al., 2007). Even in a given sample population, zircon grains may grow at different times during fractional crystallization (reviewed in Kirkland et al., 2015). All these complex petrological processes lead to a situation in which the implicit assumption A is flouted. This then follows that the zircon saturation temperature as estimated from the bulk rock Zr concentration can overestimate the magmatic temperature if the rock contains inherited/disequilibrium zircon (Kirkland et al., 2015). In their exhausted analyses on a large population of zircon data, Kirkland et al.(2015) demonstrated that at temperature <800ºC, the zircon saturation thermometry may overestimate the temperature by more than 200ºC at which the melt composition was in equilibrium

with the zircon grains. The complex internal morphology of zircon grains, showing dissolution and reprecipitation of zircon, was cited as a corroborative evidence in favor of the inherited/out-of-equilibrium zircon in the rocks having zircon saturation temperature <700ºC. For zircon saturation temperatures at or above 800ºC there exist a good match between zircon saturation temperature and the temperature at which the melt and the zircon were in equilibrium. The zircon grains in the studied samples show simple oscillatory zoning and devoid of that features that might represent dissolution and reprecipitation process (Fig.6.5a-h). This piece of evidence is consistent with in-situ crystallization of the zircon from a melt phase whose composition may be approximated by the bulk rock compositions.

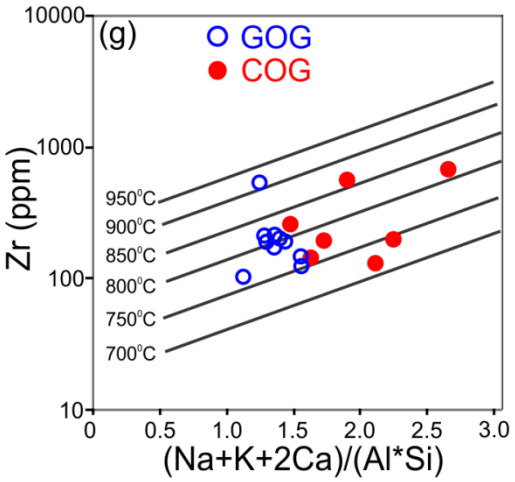

Figure 6.3 contd. (g) Zircon Saturation temperature calculated using the calibration of Boehnke et al. (2013).

In the studied rocks the zircon saturation thermometry of Boehnke et al. (2013) records 700-850ºC (average 740 ± 50ºC) (Fig. 6.3g). Combining the facts (a) the observed morphology of the zircon grains and (b) the fact that this thermometry only registers the minimum temperature of the melt, it seems likely that the magmatic protolith of the studied rocks experienced temperature that is higher than the recorded mean temperature of 740ºC.

6.3.4. Tectonic affinity of the protolith magma

The major element compositions of the studied felsic orthogneisses have remarkable similarity with the compositions of the Cordilleran batholith (after Frost et al. 2001). Most of the samples being plotted in the field stipulated for I-type and S-type granites (after Whalen et al., 1987) corroborate their affinity towards an arc set-up (Fig. 6.3h-j). In the 3Al+2(Na+K)-(Al+Na+K)-Ca+Al ternary plots of Moyen et al. (2017), the compositions of all the GOG overlap with the composition of the

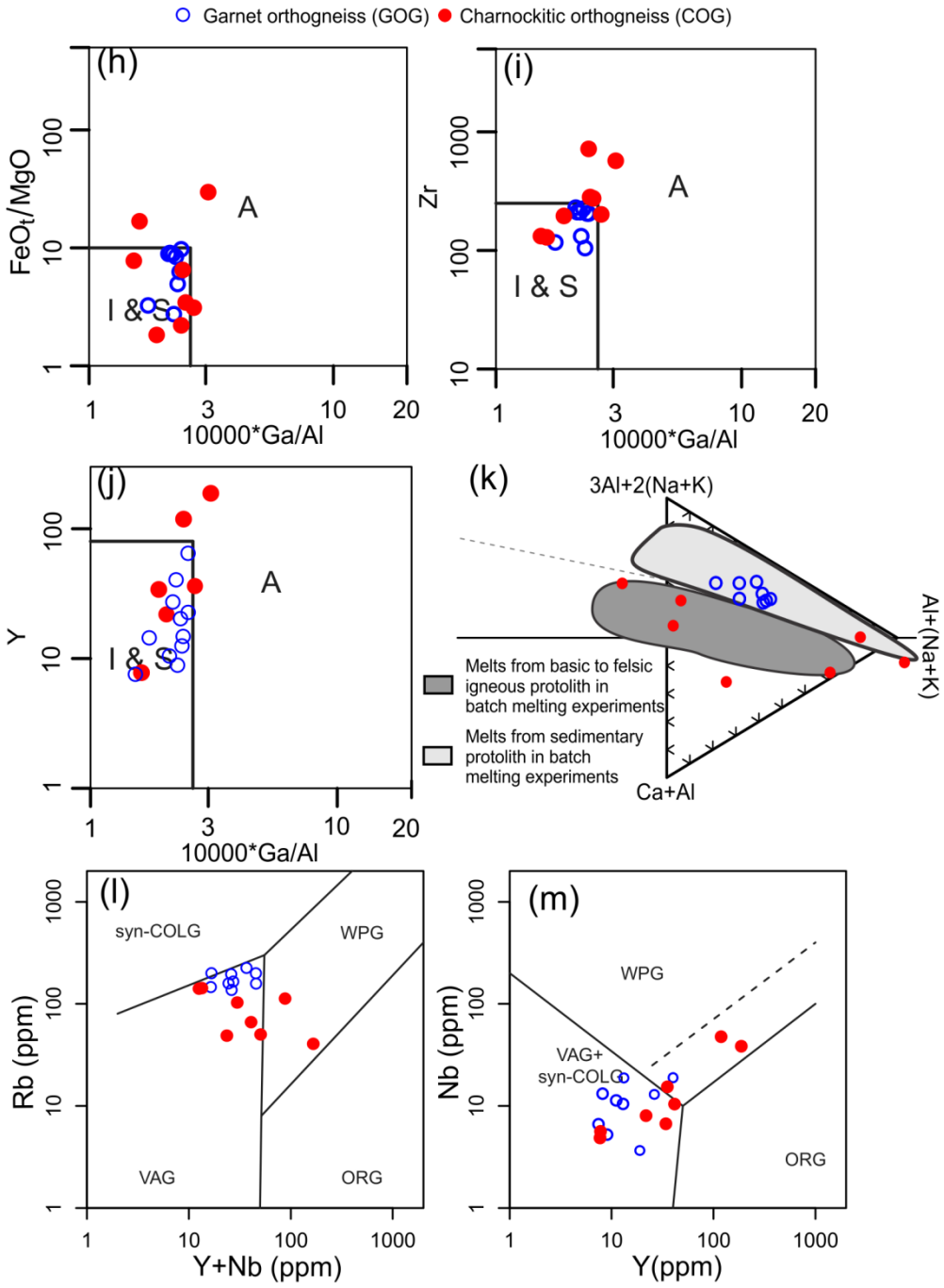

Figure 6.3 contd. (h-j) Plots classifying the studied rocks as arc granites (fields for I & S-type granitic magmas in the diagram after Whalen et al. 1987). (k) Probable source rock of the studied orthogneisses after Moyen et al. (2017). (l, m) Trace element discrimination shows that studied the studied orthogneisses plotted within syn-collisional granites (syn-COLG) and volcanic arc granites (VAG) in the diagrams (Pearce et al. 1984).

experimental melts that are derived from sedimentary precursors and few COG straddle between fields for sedimentary and felsic igneous progenitors (Fig. 6.3k). A number of tectonic discrimination diagrams (after Pearce et al., 1984) suggest that magmatic protolith of the studied felsic orthogneisses are akin to the granitoids that are formed in an arc setting (Fig. 6.3l, m). Enrichment of Cs, Rb and Pb and depletion of Nb and Ti in the Primitive Mantle normalized spidergrams suggest that the magmatic protoliths of the studied rocks were sourced dominantly from the felsic continental crust. High silica, alkali contents and peraluminous nature of the rock further corroborate this view. Moreover, peraluminous (ASI> 1.1) nature of the studied rock, presence of sillimanite in GOG and $K_2O/Na_2O>1$ for most of the samples, points towards a sedimentary (metapelite or metapsammite) source (S-type of Chappell and White, 2001, 1974). Compared to the I-type granites, S-type granites are formed through low temperature ($<800^0$C) melting of clastic sediments, resulting in the strongly peraluminous nature of the melt (Chappell et al., 2004).

6.4. Physical conditions of metamorphism

Textural features of the studied felsic orthogneisses show that a granoblastic assemblage of garnet-orthopyroxene-plagioclase-quartz and garnet-K-feldspar-quartz (±plagioclase) stabilized during peak metamorphic condition in the COG and GOG respectively. Presence of a melt phase with the granoblastic assemblages has been inferred from the quartzofeldspathic leucosomes. Studies have shown that the granulite facies assemblages showing granoblastic fabric attain chemical equilibrium due to faster kinetics of diffusion of elements at high temperature (>700ºC, Chakraborty, 2008) and the presence of a melt phase. Barring the situations where amphibole and biotite are in physical contact with garnet, the porphyroblasts of orthopyroxene, plagioclase and garnet show virtually homogeneous compositions. Hence the textures and compositions of minerals do support that the porphyroblastic phases were in equilibrium during the thermal maxima. The higher diffusivity of the elements might have modified the prograde compositions during crystallization of some or all of the porphyroblastic phases, particularly the garnet that might have formed on the prograde metamorphic path (reviewed in Ganguly and Saxena, 2012;

Spear, 1993). Development and preservation of compositional zoning in garnet grains that are in physical contact with amphibole and/or biotite has been explained by partial resetting of garnet compositions and sluggish kinetics of Fe-Mg diffusion during subsequent cooling/hydration (Ganguly and Saxena, 2012; Indares and Martignole, 1985; Spear, 1993). In view of the observations and following the common practice in petrology, core compositions of the granoblastic assemblage (garnet-orthopyroxene-plagioclase-quartz) are used to constrain the physical condition of the granulite facies metamorphism in the COG. The rim compositions of the garnet that did reset at a lower temperature will be used along with the secondary biotite to constrain the physical conditions of the retrograde metamorphism.

The physical conditions of metamorphisms of the studied rocks at peak granulite facies and subsequent retrogressions are estimated following the two methods: (a) conventional geothermobarometers and (b) intersecting isopleths in the numerically computed phase diagram for a fixed bulk composition of the studied rocks (pseudosection approach).

Lack of orthopyroxene in the GOG renders estimation of physical conditions of granulite facies metamorphism in the GOG difficult. The retrograde biotite will not record the older high grade event and the included biotite in garnet would reset its composition as the rock cooled down. For these reasons, phase equilibrium study has been applied to this rock type rather than using the conventional thermobarometry.

6.4.1. Conventional geothermobarometry

To constrain the physical condition of high grade metamorphism, the geothermobarometers that are calibrated on the assemblage garnet-orthopyroxene-plagioclase-quartz have been applied to the COG samples. We have used (a) the Fe-Mg exchange garnet-orthopyroxene geothermometer of Bhattacharya et al. (1991) and Lee and Ganguly (1988) and (b) P_{Fe} barometer that is based on the net transfer reaction 3ferrosilite + 3anorthite = 2 almandine + grossular + 3 quartz (Bhattacharya et al. 1991). Since the compositions of garnet and orthopyroxene are Fe-rich, the P_{Fe} barometer is used. The results are presented in Table-6.4. Different mineral pairs have been used and the results presented below represent the "average values ± standard deviation" associated with these permutations. For estimation of temperature, an

independent pressure is required. 7 kbar pressure was input based on our observation from the P-T pseudosection study (discussed below). In view of the very steep P-T slope of the Fe-Mg exchange reaction between garnet and orthopyroxene a large error in the input pressure will not affect the results significantly (Ganguly and Saxena, 2012; Spear, 1993). Application of the garnet-orthopyroxene geothermometer yields tightly clustered temperature value of 730±15°C (Bhattacharya et al., 1991) and 750±20ºC (Lee and Ganguly, 1988) (Table-6.4) for peak metamorphism. For the P_{Fe} barometer of garnet-orthopyroxene-plagioclase-quartz, the mean temperature of 740°C was used. The estimated peak pressure clustered within 6.3±0.25 kbar.

The assemblage garnet-biotite-plagioclase-quartz has been used to constrain the physical condition of metamorphism during cooling and retrogression. Compositions of garnet rim and retrograde biotite have been used in the well calibrated garnet-biotite geothermometer (Bhattacharya et al., 1992) and P_{Fe} barometer of GBPS (garnet-biotite-plagioclase-quartz; Hoisch, 1990). These geothermobarometers constrain pressure and temperature in the range of 5.5± 0.12 kbar and 560±20°C respectively for retrogression. Studies have shown that the uncertainties of the P and T estimates with the robust geothermobarometers are better than ±1.5 kbar and ±50ºC respectively (Etzel and Catlos, 2021; Powell and Holland, 2008; Worley and Powell, 2000). The temperature of retrogression might have continued at a temperature that was lower than that recorded by the garnet-biotite geothermometer. Closure temperature of garnet, a complex function of several parameters including the cooling rate, eventually controlled the minimum temperature to be recorded by the garnet-biotite geothermometer (Spear, 1993).

Table 6.4: P–T estimates of COG, obtained using various conventional thermobarometers (T: °C, P: kbar).

Conventional Thermometry							Conventional Barometry					
	Thermometers used	Rock type (Sample No.)	Mineral Assemblages	P_{ref}* (kbar)	Results		Barometers used	Rock type (Sample No.)	Mineral Assemblages	T_{ref}# (°C)	Results	
					T (°C)	Avg					P (kbar)	Avg
Peak	Grt-Opx[a]	COG (SR64Y)	Grt (11) - Opx (11)	7	717	730±15	Grt-Opx-Pl-Qz[c]	COG (SR64Y)	Grt (11) - Opx (11) - Pl (11)	740	6.6	6.3± 0.25
			Grt (14) - Opx (14)		737				Grt (14) - Opx (14) - Pl (14)		6.2	
			Grt (10) - Opx (10)		714				Grt (10) - Opx (10) - Pl (10)		6.3	
			Grt (13) - Opx (13)		744				Grt (13) - Opx (13) - Pl (13)		6.0	
			Grt (12) - Opx (12)		741							
Peak	Grt-Opx[b]	COG (SR64Y)	Grt (11) - Opx (11)	7	731	750±20						
			Grt (14) - Opx (14)		783							
			Grt (10) - Opx (10)		756							
			Grt (13) - Opx (13)		739							
			Grt (12) - Opx (12)		755							
Retrogression	Grt-Bt[d]	COG (SR64Y)	Grt (1) - Bt (1)	5	530	560 ± 20	Grt-Bt-Pl-Qz[e]	COG (SR64Y)	Grt (1) - Bt (1) - Pl (1)	550	5.6	5.5 ± 0.12
			Grt (2) - Bt (2)		577				Grt (2) - Bt (2) - Pl (2)		5.3	
			Grt (3) - Bt (3)		579				Grt (3) - Bt (3) - Pl (3)		5.4	
			Grt (27) - Bt (27)		553				Grt (27) - Bt (27) - Pl (27)		5.3	
			Grt (28) - Bt (28)		545				Grt (28) - Bt (28) - Pl (28)		5.5	

Grt: Garnet, Bt:Biotite, Pl: Plagioclase, Opx: Orthopyroxene, Qz: Quartz

Grt-Opx thermometer: [a] Bhattacharya et al. (1991)

Grt-Opx thermometer: [b] Lee and Ganguly (1988)

Grt-Opx-Pl-Qz barometer: [c] Bhattacharya et al. (1991),

Grt-Bt thermometers: [d] Bhattacharya et al. (1992)

Grt-Bt-Pl-Qz barometer: [e] Hoisch, 1990,

6.4.2. Phase equilibria study (pseudo-section analysis)

Methodology

To constrain the P-T conditions during granulite facies peak metamorphism and subsequent retrogression, P-T pseudosections have been calculated using the representative bulk compositions of COG (SR64Y) and GOG (SR69L1). For this purpose Perple_X 6.9.1 program (Connolly, 2009) has been used along with the internally consistent thermodynamic dataset of Holland and Powell (2011). The activity models of the observed minerals that are used for the calculations in the system NCKFMASTH (Na_2O-CaO-K_2O-FeO-MgO-Al_2O_3-SiO_2-TiO_2-H_2O) are: garnet, orthopyroxene, clinopyroxene, biotite and melt (Holland et al., 2018), plagioclase and K-feldspar as ternary feldspars (Holland and Powell, 2003), amphibole (Green et al., 2016). In the calculations of pseudosection H_2O should be used as input parameters. There is no direct way to infer the amount of H_2O that was locked in the hydrous phases prior to the granulite facies metamorphism. In view of the experimental studies, it is commonly presumed that the significant melting in crustal rocks produce water undersaturated liquid (reviewed in Clemens et al., 2020). This follows that the input H_2O should be such that melt and H_2O do not coexist at high temperature at pressure above 4 kbar (Clemens and Vielzeuf, 1987). Even with these criteria a large variation in the input H_2O is possible. In order to obtain an insight about the reasonable H_2O to be used in input, a T-XH_2O section (Fig. 6.4a, b) has been constructed at 6 kbar (the maximum pressure obtained from conventional geobarometry, Table-6.4).

The input H_2O content (0.2 wt% for COG and 0.5 wt% for GOG) as inferred from the intersecting isopleths of garnet generates H_2O free assemblages under subsolidus conditions (Fig. 6.4a, b). P-T pseudosections at subsolidus conditions are commonly calculated with H_2O as an excess phase. Though this approach is thermodynamically valid, an H_2O excess phase diagram has its limitations. Physically the excess H_2O should stay in the pore spaces. Several studies have shown that in middle to lower crust, metamorphic rocks have very little porosity that can host not more than 0.03 wt% H_2O (Clemens and Vielzeuf, 1987). Increasing pressure

drastically reduces the porosity. It is also likely that these pores may not be interconnected. For this reason, the subsolidus parts of the constructed pseudosections were not made H_2O saturated. For the quartzofeldspathic rocks, an H_2O free subsolidus phase diagram is consistent with the very low porosity of these rocks at pressure >3 kbar.

For the COG (SR64Y), the intersection of the isopleths of garnet core ($Alm_{74-75}Prp_{15-17}Grs_{7-8}$) and the vol% of melt, inferred from the proportion of leucosome (8-10%) occurs in the stability field of the assemblage garnet-orthopyroxene-plagioclase-K-feldspar-quartz(+melt+ilmenite). This is the granoblastic assemblage that is observed in the COG. The intersection defines H_2O=0.2 wt%. Large variations of H_2O and change of ±1 kbar of the input pressure do not modify the T-X(H_2O) diagram significantly. For this reason, H_2O=0.2 wt% has been used for input parameters for the construction of pseudosection of COG. Following the same procedure we have fixed the H_2O content (0.5 wt%) for the GOG (SR69L1). It is a common observation that the melt phase that is generated during partial melting of metamorphic rocks can leave the system (Sawyer and Brown, 2008). The concept of Rheologically Critical Melt Fraction/percentage (RCMF/RCMP 20±10 vol%) as defined by Arzi (1978) for partially molten rock has been challenged in subsequent studies (Plunder et al., 2022; Renner et al., 2000; Rosenberg and Handy, 2005; Yakymchuk and Brown, 2014; Zhang et al., 2019). It is now being recognized that several factors namely permeability, storativity, grain size, fluid viscosity, strain rate, composition of the protoliths etc. may control the length scale of melt segregations. Combining numerical analyses and comprehensive field studies, Zhang et al. (2019) demonstrated that the partially molten rock undergo major rheological change at 7 vol% (Melt Connectivity Transition, MCT), 21 vol% (Frame work Melting Transition, FMT) and 41 vol% (Solid to Liquid Transition, SLT) of melt. For MCT and FMT, the melt is locked by the framework of the rock and thus produces metatexite (discrete or thinly banded migmatite). At SLT the structure of the migmatite is lost and the melt volumes are sufficient to render magmatic flow. The SLT leads to the formation of diatexites. The inference of Zhang et al. (2019) corroborates the view of Takeda and Obata (2003) that the melt viscosity is drastically reduced with melt volume proportion. The volume

and arrangement of leucosomes, the presumed melt phase, in the studied area have a remarkable similarity with the structure of the metatexitic migmatite that is described

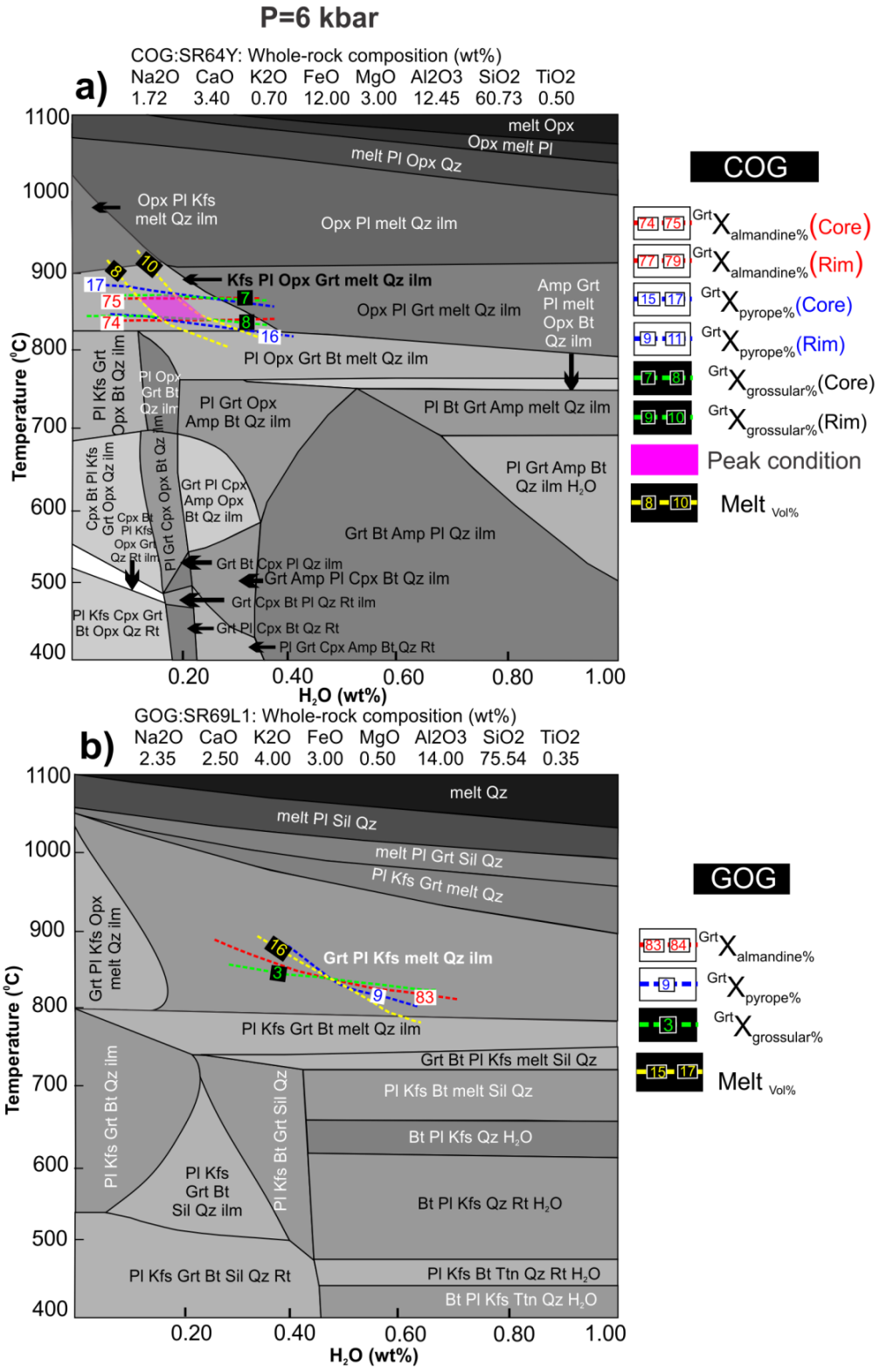

Figure 6.4. (a-b) T-H_2O pseudosection in a NCKFMASTH system at 6 kbar for the representative COG and GOG. The pseudosections are contoured with isopleths of garnet compositions and modes of melt. The intersection define H_2O=0.2 wt% for COG and 0.5 wt% for GOG.

by Zhang et al. (2019). This observation and the absence of a network of leucosomes that dissect the gneissic fabric are consistent with the view that significant melt loss did not occur (beyond a meter or so) during the high grade metamorphism in the studied area. However, melt segregation did occur in a small scale (several cm to a few decimeters), a feature that produced metatexitic migmatites in the studied area. To minimize the effect of such small-scale melt segregation considerably large samples were used for powdering and analyzing the whole rock compositions so that the sample contains both the melanosome and segregated leucosomes.

Results

The numerically computed P-T phase diagrams (pseudosections) for fixed bulk rock compositions of the COG and GOG are shown in Figures 6.4c and d. In COG the melt-in (and amphibole-out) reactions are strongly temperature sensitive and occur at 750ºC. Fig. 6.4c also suggests that biotite-out melting occurs at ~30-50ºC higher temperature than the amphibole-out reactions. The P-T phase diagram for the GOG (Fig. 6.4d) shows that biotite and melt can coexist in a narrow range of temperature ~750-800ºC over a range of pressure before biotite becomes unstable in the zone of melting.

These observations suggest that the maximum temperature that was reached during granulite facies metamorphism exceeded 800ºC. Further insight into the P-T conditions is obtained from the intersections of the garnet isopleths and the inferred volume percent of the melt. The core compositions of garnet in the COG constrain the P-T of high grade metamorphism within ~800-850ºC and ~7-7.5 kbar (Fig. 6.4c). For the GOG, the nearly constant composition of grossular core yield the P-T conditions of granulite facies (800-850^{o}C, ~7 kbar, Fig. 6.4d) that are similar to that estimated for the COG (Fig. 6.4c). The computed vol% of melt at the points of intersection of the

garnet isopleths matches well with the amount of leucosomes in the COG and GOG (Fig. 6.4c, d). This observation further supports that large scale melt loss did not occur (cf. Zhang et al., 2019). The rim compositions of the garnet when plotted on the P-T pseudosections of the COG constrain the P-T conditions of partial retrogressive assemblage within the range of 500-600ºC and 4-5 kbar (Fig. 6.4c). As the analyzed

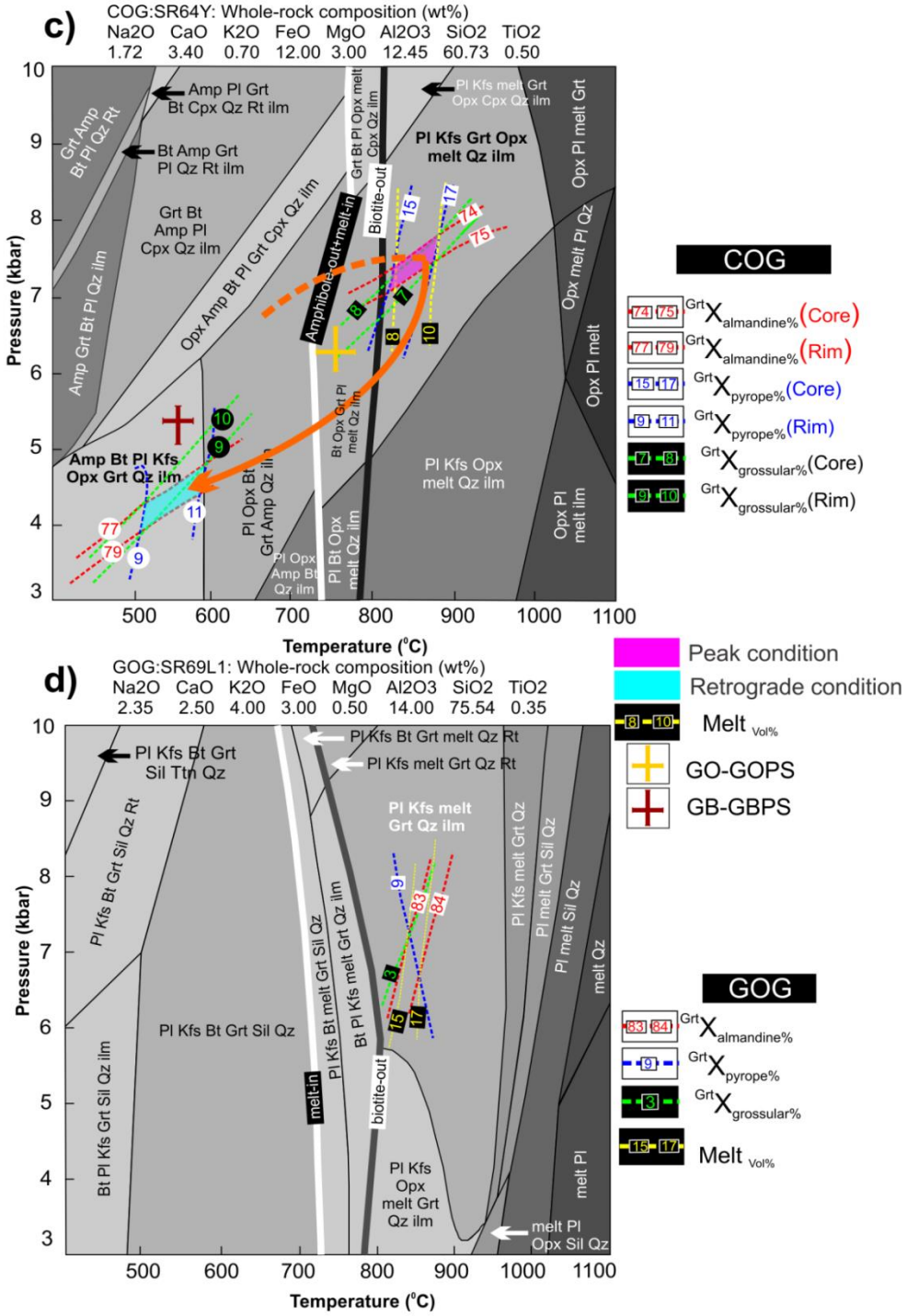

Figure 6.4 contd. P–T pseudosections in a NCKFMASTH system for two representative felsic orthogneisses. The pseudosections are contoured with isopleths of garnet compositions and modes of melt. (c) COG constrains the P-T of high grade metamorphism within ~800-850^{o}C and ~7-7.5 kbar (pink box) and retrograde metamorphism within ~500-600^{o}C and ~4-4.8 kbar (cyan box). Yellow and dark brown crosses represent P–T determined by conventional thermobarometry with abbreviations in the circle suggesting the corresponding thermobarometers: GO: garnet–orthopyroxene; GOPS: garnet–orthopyroxene–plagioclase–quartz and GB: garnet–biotite; GBPS: garnet–biotite–plagioclase–quartz respectively. Arrow indicates the inferred P–T paths. (d) P-T pseudosection in a NCKFMASTH system for representative sample of GOG. The intersections of isopleths of garnet core composition ($Alm_{83-84}Prp_9Grs_3$) and vol% of melt (15-17) constrain an average of 825^{0}C-7 kbar condition for granulite grade metamorphism, experienced by GOG.

garnet in the GOG does not show compositional zoning, and the retrograde P-T conditions could not be estimated.

As evident from the previous section, the P-T estimates from the pseudosection approach record ~50-70ºC higher temperature and ~1 kbar higher pressure (for peak conditions) relative to the conventional geothermobarometry. Considering the uncertainties of Fe-Mg exchange garnet-orthopyroxene geothermometer (±50ºC) is considered, the difference in estimated temperatures between the two methods is likely to be real. A number of studies have demonstrated that Fe-Mg garnet-orthopyroxene thermometry in high to ultra-high temperature granulite facies rocks (T>800ºC) record 50-100ºC lower temperature than the maximum temperature of metamorphism (Aranovich and Berman, 1997; Fitzsimons and Harley, 1994). It seems that the lower temperature recorded in the conventional geothermometry could be related to the limitations of the garnet-orthopyroxene geothermometer. Therefore it seems likely that the Fe-Mg exchange between garnet-orthopyroxene continued at ~50-100ºC lower temperature than the thermal maxima experienced by the studied rocks (Frost and Chacko, 1989; Ganguly and Saxena, 2012).

6.5. Geochronology

Zircon (U-Pb) and monazite (Th-U-total Pb) grains in some representative samples of the studied felsic orthogneisses were analyzed to constrain the timing of emplacement of the protolith granitic magma and its subsequent reworking. Details of analytical technique are described in Appendix and results of the U-Pb zircon and Th-U-total Pb monazite analysis are presented in Table-6.5 and 6.6 respectively. Fig. 6.5a-h and 6.6a-l show the internal morphology of representative zircon (CL images) and monazite (BSE images) grains and obtained dates are presented in Fig. 6.5i-l and 6.6m-o.

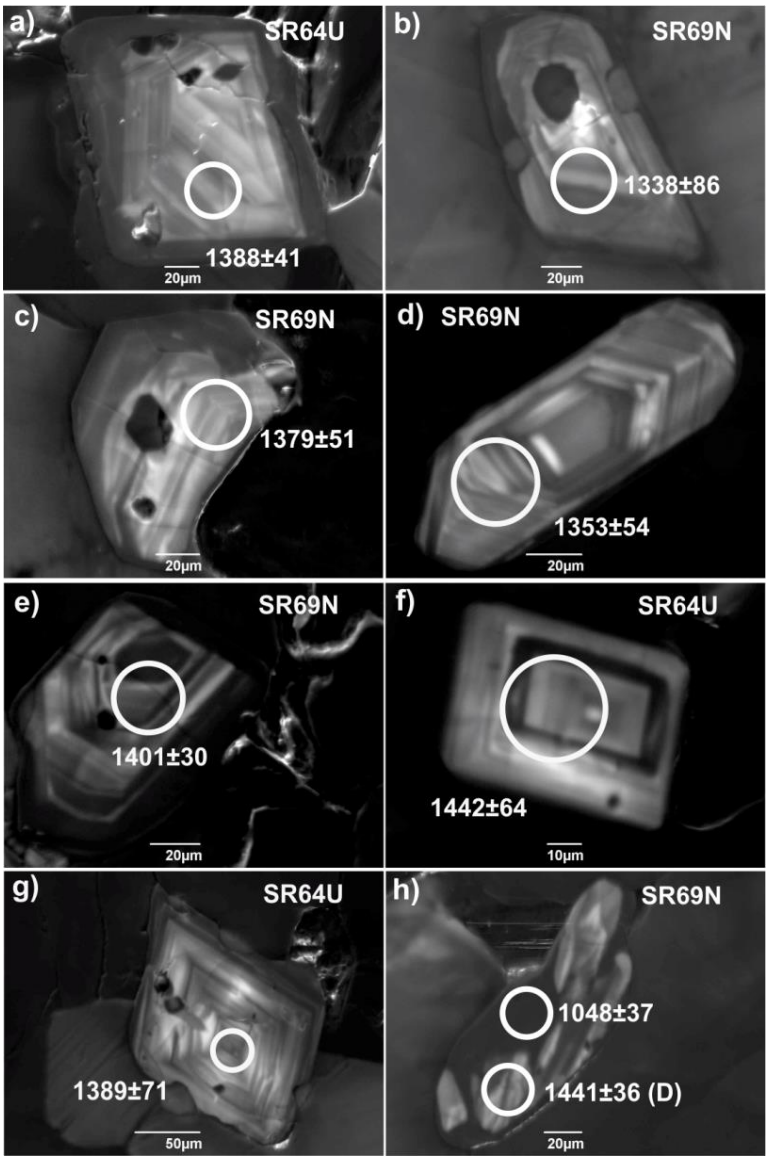

Figure 6.5. (a-h) CL images of few representative euhedral to subhedral zircon grains in COG, selected for LA-ICPMS analysis, showing the analysed concordant spots (25-35µm diameter) and respective $^{206}Pb/^{207}Pb$ spot dates (Ma) within both the oscillatory and homogeneous (and/or patchy) zones.

6.5.1. U-Pb zircon geochronology (in-situ LA-ICPMS)

Both optical and scanning electron microscopic study show that COG contains larger and more number of zircon grains compared to GOG. While a considerable number of zircon grains in the COG is ≥50 μm in length, those in GOG are exclusively <20 μm in length. Since the preferable beam size diameter of the LA-ICPMS is ≥25 μm, zircons of the GOG, being smaller in size, are unsuitable for analysis. U-Pb zircon geochronology, therefore, has been conducted, in-situ, in several thin sections of the COG only (SR69N, SR64U).

Zircon grains occur within the granoblastic quartzofeldspathic mosaic and are frequently associated with biotite, amphibole, titanite and rutile. Cathodo-luminescence images reveal that the zircon grains are euhedral, elongated to tabular stumpy with an aspect ratio of approximately 4:1 to 2:1 (Fig. 6.5a-h). They show distinct oscillatory zoned cores (~40-70 μm wide) and thin homogeneous dark rims (commonly ~10 μm wide; only occasionally up to 25 μm width). Very few zircon grains show either patchy zoning or occur as homogeneous grains (Fig. 6.5h). Oscillatory zoning is typically present within zircons crystallized from a high temperature melt that constrains the timing of the magmatic event or partial melt crystallization during high grade metamorphism, whereas homogeneous and patchy zoned rims constrain the subsequent metamorphic event (Corfu et al., 2003). Th-U ratio in most of the analyzed zircon grains are in the range of 0.4-0.8 which agrees with those of the natural magmatic zircons in granite and granodioritic melt (Kirkland et al., 2015 and references therein). Two spots (>25 μm) within the dark homogeneous rims or overgrowths of zircon gives comparatively lower Th/U value (0.1-0.2) but the data are too few for a statistically robust interpretation. $^{206}Pb/^{238}U$ is more suitable for constraining younger dates whereas $^{207}Pb/^{206}Pb$ dates are suitable for constraining the older ones. However, the cut-off value is highly debated. Following the works of Gehrels et al. (2008) who postulated a cut off value of 1200 Ma, we have calculated the weighted mean using the $^{207}Pb/^{206}Pb$. Spencer (2016) on the other hand sets the cut off value at 1500 Ma. In both the samples of the COG the weighted mean values using $^{206}Pb/^{238}U$ and $^{207}Pb/^{206}Pb$ ratios are consistent within their uncertainty values (Fig. 6.5i-l). Based on a significant number of statistical data Spencer (2016) proposed a

relation between the MSWD and the number of analyses that reveal if the results are reliable or it under/overestimates the uncertainties. Considering the MSWD, calculated for a certain date cluster, number of points (n) and analytical uncertainty (2σ), analysed data plot within the acceptable range in the graph provided by Spencer et al. (2016) and are robust for interpretation.

U-Pb concentrations, obtained from a significant number of zircon grains within COG (20 spots from 19 grains from SR69N, 17 spots from 16 grains from SR64U) are

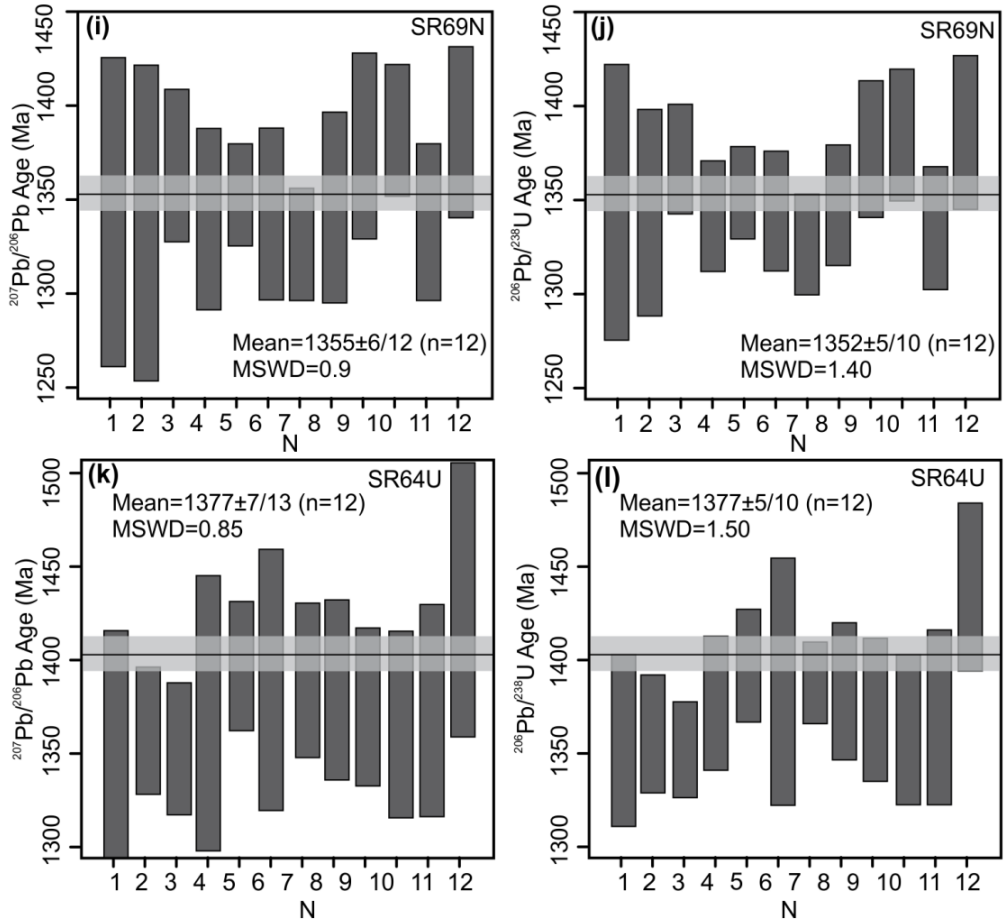

Figure 6.5. contd. Results of $^{207}Pb/^{206}Pb$ weighted mean age [(i) and (k)] and $^{206}Pb/^{238}U$ weighted mean age [(j) and (l)], representing magmatic emplacement age of the two samples (COG) used for U-Pb zircon geochronology are shown in the graphs.

mostly concordant (>90% concordance). Considering the concordant dates (>98% concordance) from prismatic grains with sharp oscillatory zoning and low-luminescent homogeneous grains, SR69N yields a weighted mean $^{207}Pb/^{206}Pb$ date of 1355±6/12

Ma (Fig. 6.5i; n=12; MSWD=0.99; the first digit in the error represents the error of the mean using internal analytical uncertainties and the second digit after '/'includes propagation of the uncertainty owing to the external normalization to a matrix-matched reference material). From the same points $^{206}Pb/^{238}U$ dates yield a weighted mean date of 1352±5/10 Ma (Fig. 6.5j; n=12; MSWD=1.4). From SR64U, elongated, oscillatory zoned zircons cores yield a mean $^{207}Pb/^{206}Pb$ date of 1377±7/13 Ma (Fig. 6.5k; n=12; MSWD=0.85). For the same dates $^{206}Pb/^{238}U$ dates yield a weighted mean age of 1377±5/10 Ma (Fig. 6.5l; n=12; MSWD=1.5).The dark homogeneous rims indicating metamorphic overgrowths are mostly too thin to be dated (spot size 30-35 μm). Spencer (2016) argued that concordia age provides much more precise and reliable estimates for the ages and therefore, to put further constraints we have also calculated concordia dates (1354±7 Ma; MSWD=1.13 for SR69N and 1373±8 Ma; MSWD=0.0049 for SR64U) as well for both the samples which resembles the weighted mean date obtained from the $^{238}U/^{206}Pb$ or $^{207}Pb/^{206}Pb$ methods. On the rare occasions where rims could be analyzed (with a slightly reduced spot size of 25 μm), they yielded $^{207}Pb/^{206}Pb$ concordant dates (>98% concordance) of 1048±37 Ma (SR69N; n=1; Fig. 6.5h) and 962±23 Ma (SR64U; n=1).

Oscillatory zoned zircon grains in the studied rocks could have crystallized (a) from the magmatic protolith (a liquid) and (b) from the anatectic melt during metamorphism (cf. Corfu et al., 2003). The dated zircon grains occur in the melanosome as well as leucosome (presumed melt) with similar internal structure and age. Furthermore, internal morphology of zircon grains does not support the combination of (a) and (b). The protoliths of the COG and GOG were felsic magmas. It is, therefore, likely that zircon did crystalize during the magmatic stage. Studies have demonstrated that once formed it is very difficult to dissolve zircon in natural liquid/fluid completely at temperature below 900^{o}C (Harley et al., 2007). The metamorphic temperatures of the studied rocks were certainly below the ultra-high temperature. It is therefore expected that instead of forming large zircon grains, the anatectic melt would crystallize overgrowth on the magmatic zircon (like oscillatory zoned zircon overgrowth on detrital magmatic zircon; Corfu et al.2003). It is also

unlikely that a felsic rock would not crystallize zircon in its magmatic stage but would crystallize large oscillatory zoned zircon during metamorphism.

Table 6.5: U-Pb isotopic dating of in-situ zircon grains from two representative felsic orthogneisses of the studied area

Sample no	Analysis name	Spot size (µm)	U (ppm)	Pb (ppm)	Th/U	Ratios						rho	Date(Ma)				Degree of concordanc
						$^{206}Pb/^{238}U$	±2σ (abs.)	$^{207}Pb/^{235}U$	±2σ (abs.)	$^{206}Pb/^{207}Pb$	±2σ (abs.)		$^{206}Pb/^{238}U$	±2σ	$^{207}Pb/^{235}U$	±2σ	$^{207}Pb/^{206}Pb$	±2σ	
SR69N	17-1C	30	181.11	38.61	0.47	0.23	0.0138	2.77	0.2034	0.09	0.0037	0.81	1348	72	1346	55	1344	84	100.31
	26-1C	30	102.92	23.59	0.56	0.23	0.0103	2.74	0.1721	0.09	0.0038	0.71	1342	54	1340	47	1338	86	100.27
	33-1C	30	463.00	95.71	0.47	0.23	0.0047	2.85	0.0730	0.09	0.0014	0.78	1349	24	1369	19	1401	30	96.30
	14-1C	30	265.15	52.04	0.49	0.22	0.0102	2.67	0.1871	0.09	0.0046	0.66	1278	54	1319	52	1387	101	92.11
	18-1C	25	436.33	93.27	0.61	0.24	0.0078	2.91	0.1184	0.09	0.0022	0.80	1384	41	1385	31	1387	47	99.73
	10-1C	30	798.24	176.59	0.51	0.24	0.0067	2.91	0.0993	0.09	0.0017	0.82	1383	35	1384	26	1387	37	99.75
	42-1C	30	222.78	47.82	0.35	0.24	0.0068	2.88	0.1124	0.09	0.0023	0.74	1376	36	1377	29	1379	51	99.77
	11-1C	30	423.81	87.23	0.61	0.24	0.0056	2.86	0.0922	0.09	0.0019	0.73	1371	29	1370	24	1369	42	100.18
	29-1R	30	687.66	140.64	0.46	0.23	0.0047	2.79	0.0695	0.09	0.0013	0.81	1354	24	1354	19	1353	28	100.07
	35-1C	30	245.60	51.27	0.43	0.22	0.0068	2.63	0.1096	0.09	0.0024	0.74	1281	36	1308	31	1353	54	94.68
	6-2R	30	624.49	108.43	0.25	0.21	0.0070	2.51	0.1115	0.09	0.0026	0.75	1231	37	1274	32	1348	57	91.30
	3-2C	30	145.31	31.47	0.48	0.23	0.0060	2.77	0.1045	0.09	0.0024	0.69	1346	32	1346	28	1347	53	99.92
	3-1C	30	543.23	100.32	0.48	0.21	0.0045	2.49	0.0754	0.09	0.0018	0.72	1224	24	1268	22	1344	41	91.08
	4-1C	25	236.92	52.07	0.49	0.23	0.0061	2.76	0.0989	0.09	0.0021	0.73	1344	32	1344	27	1343	47	100.04
	27-1C	30	116.92	25.08	0.55	0.23	0.0056	2.75	0.0973	0.09	0.0022	0.68	1342	29	1341	26	1340	50	100.14
	30-1C	30	284.81	62.08	0.77	0.23	0.0060	2.73	0.0941	0.09	0.0019	0.76	1335	32	1336	26	1339	43	99.74
	6-1C	35	936.22	191.33	0.39	0.23	0.0049	2.70	0.0718	0.09	0.0014	0.80	1327	26	1327	20	1327	31	100.00
	29-1C	35	248.53	48.23	0.38	0.21	0.0077	2.42	0.1053	0.08	0.0019	0.85	1217	41	1249	31	1304	44	93.30
	18-2C	25	208.24	40.37	0.34	0.21	0.0085	2.35	0.1280	0.08	0.0030	0.74	1227	45	1227	39	1227	72	99.98
	25-1C	25	944.64	148.08	0.10	0.18	0.0041	1.80	0.0529	0.07	0.0014	0.78	1045	22	1046	19	1048	37	99.73
SR64U	17-1R	30	930.76	187.22	0.34	0.23	0.0061	2.86	0.1010	10.99	0.0021	0.76	1324	32	1372	27	1447	44	91.48
	24-4C	31	123.42	27.18	0.61	0.25	0.0087	3.13	0.1519	11.02	0.0031	0.72	1438	45	1439	37	1442	64	99.69
	6C	30	1468.63	371.00	0.34	0.23	0.0085	2.83	0.1339	11.10	0.0026	0.79	1322	45	1363	36	1428	56	92.62
	5C	30	289.37	39.00	0.20	0.22	0.0085	2.69	0.1308	11.17	0.0026	0.81	1271	45	1326	36	1415	55	89.85
	26-2C	30	524.17	45.77	0.19	0.24	0.0060	2.96	0.0911	11.28	0.0016	0.80	1398	31	1397	23	1397	35	100.02
	19-1C	30	79.57	16.86	0.52	0.24	0.0127	2.93	0.1891	11.32	0.0033	0.82	1389	66	1389	49	1389	71	100.00
	35-1C	31	117.58	25.10	0.39	0.24	0.0043	2.92	0.0811	11.33	0.0019	0.64	1388	22	1388	21	1388	41	100.00
	3-1C	30	699.25	157.90	0.50	0.24	0.0071	2.91	0.1131	11.35	0.0022	0.77	1384	37	1384	29	1384	48	100.00
	34-1C	31	548.30	114.23	0.48	0.24	0.0074	2.87	0.1099	11.41	0.0020	0.81	1374	38	1374	29	1375	43	99.98
	33-1C	35	366.69	70.26	0.34	0.24	0.0090	2.86	0.1384	11.42	0.0026	0.78	1370	47	1371	36	1373	58	99.75
	8-1C	30	42.13	95.32	0.52	0.24	0.0056	2.86	0.1303	11.43	0.0034	0.52	1371	29	1371	34	1371	75	100.03
	14-1C	30	674.43	133.76	0.44	0.24	0.0075	2.83	0.1157	11.47	0.0022	0.78	1363	39	1364	31	1365	50	99.86
	16-1C	30	1073.92	227.80	0.59	0.24	0.0058	2.83	0.0865	11.49	0.0016	0.80	1363	30	1362	23	1362	35	100.05
	17-2R	30	533.18	108.01	0.43	0.23	0.0090	2.81	0.1378	11.52	0.0027	0.78	1358	47	1357	37	1356	60	100.18
	14-2C	30	316.64	63.07	0.44	0.23	0.0047	2.79	0.0765	11.54	0.0016	0.74	1353	25	1353	20	1352	36	100.05
	31-1C	35	231.78	39.0	0.20	0.216	0.007	2.46	0.109	0.0827	0.0026	0.71	1260	36	1261	32	1261	61	99.92
	3R	25	922.00	194.20	0.25	0.16	0.0024	1.58	0.0293	14.05	0.0008	0.80	963	13	962	12	962	23	100.00

Hence, combining the data and the internal texture and using the criterion by Spencer et al. (2016) it can be stated that the calculated $^{207}Pb/^{206}Pb$ mean and concordia dates provide robust and reliable estimates for the magmatic emplacement age (1377-1352 Ma) of the granitoids. The concordant dates obtained from the metamorphic rims, indicate the age of the younger reworking event (metamorphism) from both samples combined.

6.5.2. Th-U-total Pb monazite geochronology (in-situ, EPMA)

Monazite grains are texturally associated with and/or included within feldspar and biotite in an overall granoblastic textural setting (Fig. 6.6a, c, e, g, i, k). Datable monazite grains of significant size were found only in GOG (SR69L). Monazite grains are anhedral to subhedral in shape, highly fractured and varying in size from 50µm to 100µm. Most of the monazite grains are unzoned (Fig. 6.6f, h, j) with few exceptions where weak zoning can be observed under BSE images (Fig. 6.6b, d, l).

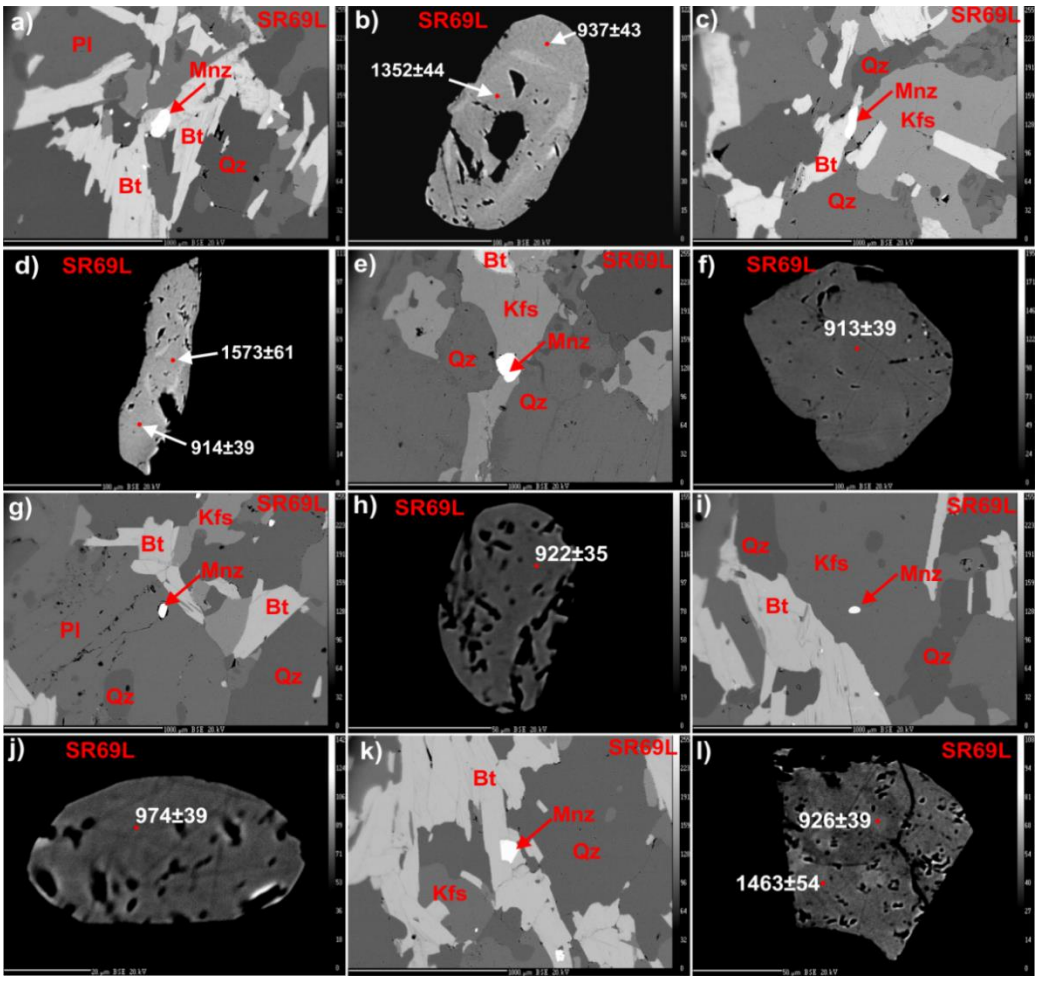

Figure 6.6. (a-l) BSE images of textural settings and their corresponding individual grains of representative monazite in GOG (SR69L), selected for electron microprobe dating. Respective Th-U-total Pb ages of the grains are shown hereby.

The results of the chemical analyses of the monazite grains are presented in Table-6.6. Chemical composition of the monazite grains show a very narrow compositional range of PbO (0.36-0.67 wt%), ThO_2(6-8 wt%) and UO_2 (0.25-1.38 wt%), which corroborates well with the overall unzoned nature of the grains portrayed by the BSE images. However, detailed scrutiny reveals that there is a negative correlation between ThO_2, UO_2, SiO_2, REE and P_2O_5. Fig. 6.6n reveals that the compositional variation dominantly results from cheralitic substitution. The calculated spot dates range from 900 Ma to 1540 Ma, and yield two dominant date clusters at 1421±23 (n=6) and 965±10 Ma (n=16) (Fig. 6.6m). Y_2O_3 and ThO_2 contents are variable (1.7-2.3 wt% and 3.9-6.8 wt% respectively) for the older dates (>1000 Ma). For the younger dates (<1000 Ma), however, Y_2O_3 and ThO_2 content shows a slight increase (2.1-2.9 wt% and 6.4-8.1 wt% respectively). In a few monazite grains, where ages from different clusters occur in the same grain, the older ages are obtained

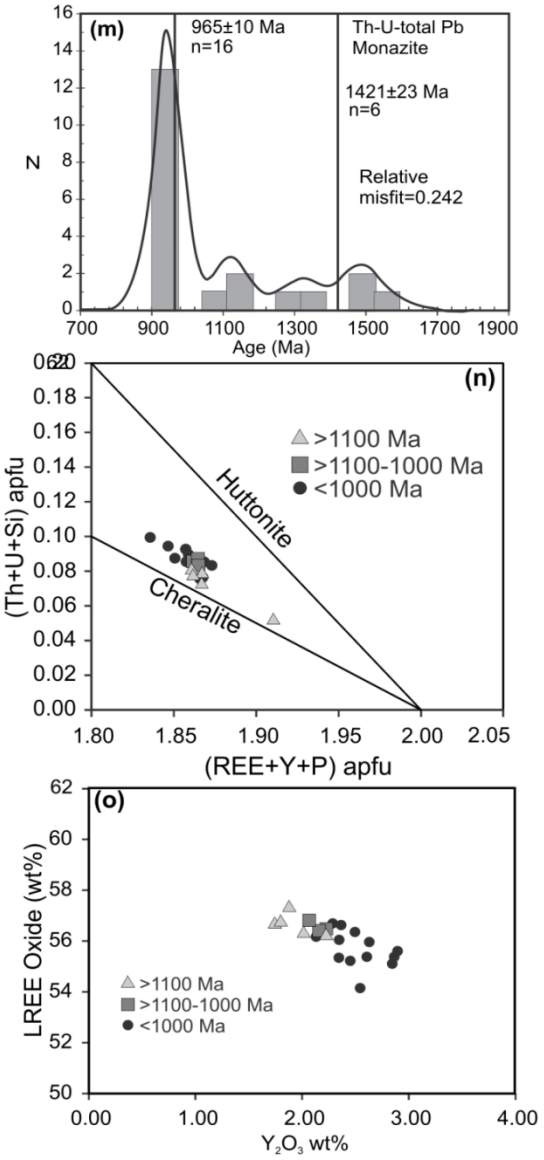

Figure 6.6 contd. (m) Histogram with probable peaks determined from monazite spot dates. (n) The compositional variation resulting from cheralitic substitution which involves incorporation of Th and Ca in the monazite structure. (o) Y_2O_3 content increases between the spots having dates from 974 Ma to 913 Ma.

Table 6.6: Representative analyses of monazite grains from the studied felsic orthogneisses

Sample no	Spot	Textural setting		Zoning and position	SiO2 (wt%)	CaO (wt%)	P2O5 (wt%)	La2O3 (wt%)	Ce2O3 (wt%)	Nd2O3 (wt%)	Sm2O3 (wt%)	Eu2O3 (wt%)	Gd2O3 (wt%)	Dy2O3 (wt%)	Ho2O3 (wt%)	Y2O3 (wt%)	ThO2 (wt%)	UO2 (wt%)	PbO (wt%)	Date (Ma)	Date error (Ma)
SR69L	3 / 1 .	Matrix	Near Biotite	Homogeneous	0.492	1.341	30.425	13.746	26.442	10.062	1.748	0.096	1.475	0.688	0.000	2.50	6.635	0.83	0.381	937	41
	6 / 1 .	Matrix	Included in Or	Homogeneous-core	0.471	1.694	30.296	12.267	25.539	9.916	2.022	0.183	1.406	0.674	0.023	2.55	8.174	1.138	0.477	922	35
	7 / 1 .	Matrix	Near Bt-Or	Homogeneous	0.393	1.557	29.800	13.409	25.821	9.914	1.759	0.155	1.52	0.823	0.068	2.61	6.725	1.219	0.43	922	37
	9 / 1 .	Matrix	Included in Or	Homogeneous	0.457	1.403	29.934	12.871	25.82	10.366	1.922	0.121	1.767	0.784	0.000	2.89	6.556	1.009	0.391	913	39
	10 / 1 .	Matrix	Enclosed in Bt	Core	0.470	1.491	29.872	13.680	27.000	10.430	1.824	0.262	1.306	0.548	0.000	1.88	6.499	0.449	0.558	1573	61
	8 / 1 .	Matrix	Enclosed in Bt	Rim	0.467	1.415	29.967	13.078	26.066	10.263	1.939	0.092	1.687	0.765	0.000	2.63	6.908	0.899	0.391	914	39
	11 / 1 .	Matrix	Near Biotite	Homogeneous-core	0.211	1.207	30.023	15.794	28.528	9.846	1.489	0.141	1.044	0.516	0.000	1.67	3.89	0.651	0.418	1538	71
	12 / 1 .	Matrix	Near Biotite	Homogeneous	0.335	1.565	30.067	14.02	26.663	10.086	1.754	0.162	1.223	0.578	0.000	1.78	6.667	0.833	0.627	1492	51
	13 / 1 .	Matrix	Included in Bt	Core	0.374	1.467	30.419	13.708	26.686	10.235	1.767	0.176	1.32	0.6	0.000	1.75	6.746	0.645	0.576	1463	54
	30 / 1 .	Matrix	Included in Bt	Rim	0.505	1.53	30.293	13.214	25.882	10.026	1.763	0.127	1.547	0.699	0.010	2.35	7.875	0.696	0.407	926	39
	14 / 1 .	Matrix	Included in Bt	Core	0.293	1.528	30.492	13.506	26.055	10.164	1.86	0.11	1.605	0.76	0.000	2.28	5.864	1.382	0.631	1352	44
	29 / 1 .	Matrix	Included in Bt	Rim	0.367	1.378	30.965	13.778	26.678	10.141	1.748	0.063	1.433	0.657	0.000	2.36	6.406	0.742	0.36	937	43
	15 / 1 .	Matrix	Near Bt-Or	Homogeneous-rim	0.281	1.557	30.023	13.992	26.521	9.892	1.664	0.156	1.31	0.581	0.000	2.02	6.111	1.191	0.575	1288	45
	16 / 1 .	Matrix	Near Bt-Or	Homogeneous	0.402	1.409	30.147	14.189	26.73	9.905	1.72	0.144	1.273	0.609	0.107	2.07	6.458	0.854	0.468	1152	46
	17 / 1 .	Matrix	Near Bt-Or	Homogeneous	0.38	1.436	30.678	13.804	26.588	10.028	1.714	0.112	1.29	0.651	0.068	2.17	6.643	0.864	0.466	1121	45
	20 / 1 .	Matrix	Included in Bt	Homogeneous	0.429	1.433	29.606	13.765	26.46	10.11	1.769	0.156	1.412	0.638	0.035	2.23	6.819	0.801	0.452	1094	44
	21 / 1 .	Matrix	Included in Or	Homogeneous	0.409	1.526	30.135	13.57	26.325	9.976	1.734	0.159	1.42	0.699	0.045	2.34	6.801	1.112	0.444	974	39
	22 / 1 .	Matrix	Enclosed in Bt	Homogeneous	0.561	1.376	29.589	13.629	26.308	10.134	1.774	0.116	1.464	0.716	0.000	2.13	7.123	0.865	0.419	967	40
	24 / 1 .	Matrix	Included in Or	Homogeneous	0.41	1.578	30.565	13.362	25.814	9.898	1.788	0.126	1.487	0.781	0.000	2.45	7.103	1.161	0.454	955	37
	25 / 1 .	Matrix	Included in Or	Homogeneous	0.472	1.29	29.674	13.306	26.706	10.228	1.906	0.197	1.386	0.576	0.000	2.30	6.472	0.812	0.379	954	42
	26 / 1 .	Matrix	Near Bt-Or	Homogeneous	0.48	1.463	30.094	12.668	25.725	10.243	1.985	0.121	1.471	0.753	0.050	2.85	6.844	1.203	0.443	944	37
	28 / 1 .	Matrix	Near Bt-Or	Homogeneous	0.447	1.451	30.455	13.22	25.958	9.993	1.835	0.093	1.511	0.822	0.065	2.87	6.629	1.18	0.431	943	38

from the cores, and the younger ages from the rims (Fig. 6.6b, d, l). Amongst the analyzed data points, the preponderance of the younger ages (≤1000 Ma), combined with their occurrence as small, rounded, homogenous grains within leucosomes, constrains the age of metamorphism of the studied felsic orthogneisses between 974 Ma to 913 Ma. This age span is in good agreement with the concordant metamorphic dates revealed by the zircon geochronology.

Lack of monazite inclusions within garnet obscures the precise timing of garnet growth. However, majority of the grains, that yield younger ages, are either partially surrounded or completely included within biotite (Fig. 6.6a, c, k) and rarely by K-feldspar (Fig. 6.6g, i). Amongst these younger age spans, Y_2O_3 content also varies (Fig. 6.6o). Y_2O_3 contents associated with 974-954 Ma age points grossly overlap with that of the older (>1000 Ma) spots. This age span probably indicates the timing of crystallization of leucosome following the peak metamorphic condition. Since ThO_2 enrichment in monazite is frequently linked with fluid mediated processes (Harlov et al., 2011), increasing ThO_2 and Y_2O_3 contents for monazite grains younger than 950 Ma (944-913 Ma) can be correlated with the garnet breakdown and formation of biotite.

CHAPTER 7
EVOLUTION OF THE METAPELITES

A packet of metasedimentary rocks including metapelites (banded psammopelites and garnet-cordierite-biotite rock) and marble with calc silicate bands occurs with basement-cover relationship within porphyritic metagranitoids in the study area (Fig. 3.1). The following sections consist of the description of the metapelitic units of the study area.

7.1. Banded psammopelite

7.1.1. Petrography

Mineral abbreviations in the following sections are taken from Whitney and Evans (2010). The leucosomes in the pelitic part consist of quartz + plagioclase +K-feldspar ± garnet and melanosomes contain biotite ± muscovite ± sillimanite + garnet + quartz + feldspars + ilmenite. Quartz and feldspars show overall granoblastic texture within the leucosomes. Both within the leucosome and melanosome, subhedral to anhedral grains of garnet porphyroblasts contain numerous inclusions of quartz, biotite and ilmenite inclusions (Fig. 7.1a). Biotites in the melanosome, on the other hand, show oriented as well as random grains and replace garnet porphyroblasts (Fig. 7.1a-c). The oriented grains of biotite define a schistosity that swerved around garnet porphyroblasts as well as clusters of quartzofeldspathic aggregates (Fig. 7.1a, b). The

random biotite grains are set in the matrix of polygonal (recrystallized) matrix of quartz and feldspar (both plagioclase and K-feldspar). Volumetrically minor muscovite, relative to biotite, never show oriented grains. Intergrowth of biotite, muscovite, equant sillimanite and ilmenite occurs as patches (Fig. 7.1c, d). The textural features are consistent with the view that (1) micas and sillimanite formed after garnet and polygonal feldspar aggregates, (2) biotite grains formed during and outlasted the deformation, (3) the growth of muscovite outlasted the deformation and (4) biotite grains that might have coexisted with garnet during its formation cannot be recognized in the matrix as the secondary biotite (formed after garnet) are predominant and the recrystallization process might have changed its shape and composition. The primary biotite is only seen in the inclusion within garnet.

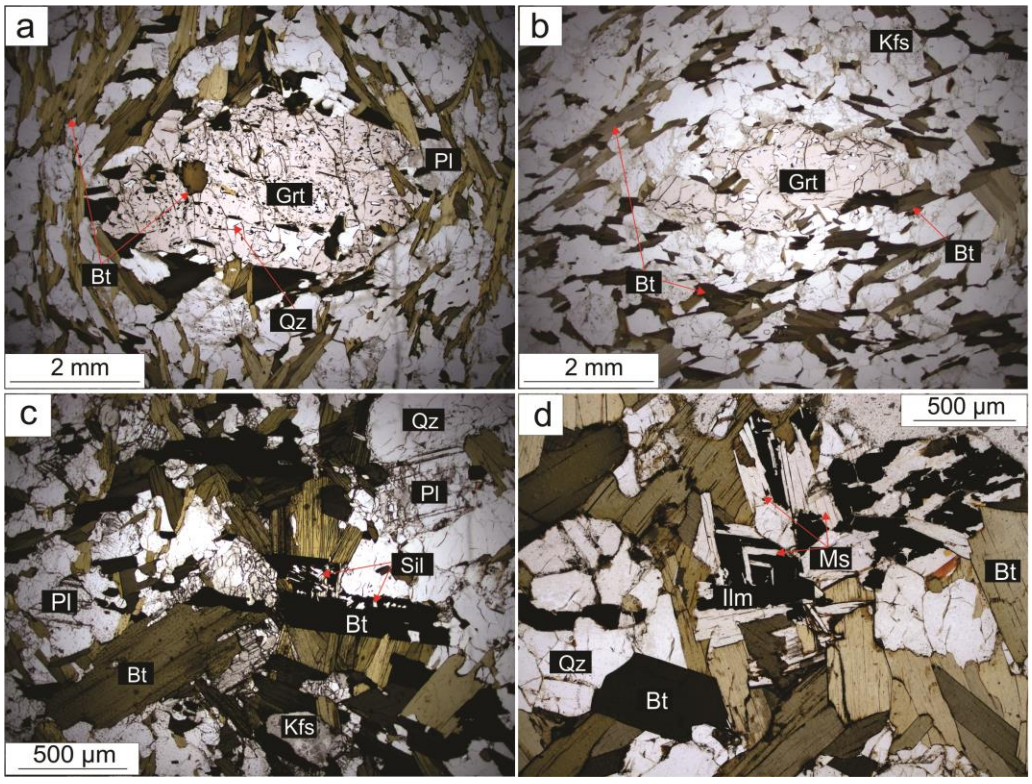

Figure 7.1. (a) Garnet porphyroblast in the melanosome having numerous inclusions of quartz, biotite and ilmenite. Oriented biotite flakes are swerving the garnet. (b) Oriented biotite within melanosome. Biotite replaces garnet. (c) Biotite flakes of various sizes are showing random orientation. Equant sillimanite associated with biotite and ilmenite. (d) Muscovite often associated with ilmenite in the metapelite.

7.1.2. Mineral chemistry

Mineral chemistry of the studied banded psammopelite has been analyzed with an Electron Probe Micro-analyzer (EPMA) at the University of Cologne, Germany. Detailed analytical technique is given in the Appendix. Representative mineral compositions of the banded psammopelite are presented in Table-7.1.

Garnet: The garnet is chiefly constituted of almandine (X_{Alm}=0.70-0.73) and spessartine (X_{Sps}=0.10-0.15) with low grossular (X_{Grs}=0.09-0.10) and pyrope (X_{Prp}=0.05-0.08) components (Table-7.1a). No significant compositional zoning is noted in individual grains. The compositional range of garnet falls within $Alm_{70-73}Py_{5-8}Grs_{9-10}Sps_{10-15}$ (Table-7.1a).

Feldspar: The plagioclase is albite-rich (X_{An}~0.30-0.34). Individual plagioclase grains do not show any significant compositional zoning. Generally, the composition of the K-feldspar varies within a restricted range $Or_{85-89}Ab_{10-14}$. K-feldspar has very low anorthite (X_{An}~0.30-0.60) (Table- 7.1b).

Biotite: The biotite is ferroan (X_{Mg}=0.34-0.39) with 0.14-0.18 apfu titanium (TiO_2=2.32-2.86 wt%; Table-7.1c).

Muscovite: Muscovite associated with biotite and ilmenite are comparatively magnesian in composition (X_{Mg}=0.45-0.49). The analyzed grains are dominant in muscovite component (0.80) with very minor paragonite (0.06-0.07), pyrophyllite (0.04-0.05) and celadonite (0.03-0.05) component in their composition (Table- 7.1c).

Ilmenite: Ilmenites are pure in composition with very minor MnO (2.65 wt%) content (Table- 7.1c).

Table-7.1a: Representative chemical analyses for garnet (representative oxygen basis are given in tables). Mineral abbreviations are used after Whitney and Evans (2010). Cation calculations have been done following the procedure of Grew (1984).

Sample no	SR131	SR131	SR131	SR131	SR131	SR131	SR131	SR131	SR131	SR131
Mineral	Grt	Grt	Grt	Grt	Grt	Grt	Grt	Grt	Grt	Grt
Texture	Core	Rim	Rim	Rim	Rim	Core	Core	Core	Rim	Rim
Point no	1	2	8	9	14	15	23	24	25	26
SiO2	37.23	36.87	36.21	36.80	37.72	36.32	36.48	36.42	35.20	37.21
TiO2	0.02	0.01	0.05	0.03	0.02	0.00	0.33	0.23	0.02	0.00
Al2O3	21.84	21.42	21.30	21.90	22.28	22.20	21.53	21.43	21.13	21.59
Cr2O3	0.02	0.00	0.00	0.03	0.00	0.03	0.00	0.04	0.00	0.01
CaO	3.21	3.29	3.29	3.36	3.37	3.41	3.35	3.31	3.55	3.25
FeO	33.66	32.27	32.81	32.59	32.85	32.19	31.75	31.90	30.88	32.34
MnO	3.53	6.09	5.40	4.75	5.46	5.37	6.68	6.14	6.68	5.77
MgO	2.46	1.43	1.64	2.02	1.58	1.79	1.32	1.57	1.37	1.70
Na2O	0.00	0.00	0.05	0.02	0.00	0.00	0.04	0.05	0.00	0.10
K2O	0.00	0.00	0.00	0.00	0.01	0.01	0.00	0.00	0.01	0.00
Total	101.98	101.38	100.72	101.50	103.27	101.30	101.46	101.11	98.83	101.96
Oxygen basis	**12**	**12**	**12**	**12**	**12**	**12**	**12**	**12**	**12**	**12**
Si	2.94	2.95	2.91	2.93	2.96	2.90	2.92	2.92	2.89	2.95
Ti	0.00	0.00	0.00	0.00	0.00	0.00	0.02	0.01	0.00	0.00
Al	2.03	2.02	2.02	2.05	2.06	2.09	2.03	2.03	2.04	2.02
Fe+2	2.14	2.09	2.05	2.08	2.13	2.03	2.03	2.03	1.94	2.06
Fe+3	0.08	0.07	0.15	0.09	0.03	0.12	0.09	0.11	0.18	0.09
Mg	0.29	0.17	0.20	0.24	0.18	0.21	0.16	0.19	0.17	0.20
Mn	0.24	0.41	0.37	0.32	0.36	0.36	0.45	0.42	0.46	0.39
Ca	0.27	0.28	0.28	0.29	0.28	0.29	0.29	0.28	0.31	0.28
Na	0.00	0.00	0.01	0.00	0.00	0.00	0.01	0.01	0.00	0.02
K	0.00	0.00	0.00	0.00	0.00	0.00	0.00	0.00	0.00	0.00
Total	8.00	8.00	8.00	8.00	8.00	8.00	8.00	8.00	8.00	8.00
X_{Prp}	*0.08*	*0.06*	*0.07*	*0.08*	*0.06*	*0.07*	*0.05*	*0.06*	*0.06*	*0.07*
X_{Alm}	*0.73*	*0.71*	*0.71*	*0.71*	*0.72*	*0.70*	*0.69*	*0.70*	*0.67*	*0.70*
X_{Grs}	*0.09*	*0.10*	*0.10*	*0.10*	*0.10*	*0.10*	*0.10*	*0.10*	*0.11*	*0.09*
X_{Sps}	*0.10*	*0.14*	*0.13*	*0.11*	*0.12*	*0.13*	*0.15*	*0.14*	*0.16*	*0.13*

Table-7.1b: Representative chemical analyses for feldspars (representative oxygen basis are given in tables). Mineral abbreviations are used after Whitney and Evans (2010). Cation calculations have been done following the procedure of Grew (1984).

Sample no	SR131	SR131	SR131	SR131	SR131	SR131	SR131	SR131	SR131	SR131	SR131
Mineral	Pl	Pl	Pl	Pl	Pl	Pl	Pl	Pl	Pl	Kfs	Kfs
Texture	^Grt, Bt (Core)	^Grt, Bt (Rim)	Rim	^Grt, Bt (Core)	Qz-Fls aggregate	Qz-Fls aggregate	^Grt, Bt (Rim)	^Grt, Bt (Rim)	Qz-Fls aggregate	^Ms	^Ms
Point no	4	5	10	12	17	21	27	28	32	78	81
SiO2	58.52	60.28	56.53	58.05	55.78	58.81	57.87	57.85	58.22	64.01	65.09
TiO2	0.00	0.01	0.00	0.00	0.02	0.00	0.00	0.00	0.00	-0.01	0
Al2O3	25.58	25.74	26.01	25.67	25.70	25.39	25.87	25.62	26.01	18.21	18.41
Cr2O3	0.00	0.02	0.00	0.00	0.00	0.00	0.01	0.00	0.00	-0.03	0.04
CaO	7.38	6.91	6.65	6.91	6.90	6.84	6.66	6.87	6.82	0.07	0.02
FeO	0.04	0.16	0.50	0.15	0.07	0.07	0.18	0.04	0.17	0.03	0.09
MnO	0.00	0.01	0.12	0.02	0.00	0.01	0.02	0.00	0.00	0.01	0.01
MgO	0.00	0.00	0.00	0.01	0.00	0.00	0.01	0.00	0.00	0.05	0.12
Na2O	7.78	8.60	8.21	8.31	7.92	7.90	8.36	8.04	8.22	1.1	1.53
K2O	0.09	0.11	0.31	0.07	0.07	0.09	0.26	0.08	0.09	15.08	13.96
Total	99.38	101.84	98.33	99.18	96.45	99.11	99.24	98.50	99.53	98.54	99.29
Oxygen basis	**8**	**8**	**8**	**8**	**8**	**8**	**8**	**8**	**8**	**8**	**8**
Si	2.62	2.62	2.54	2.59	2.56	2.64	2.58	2.60	2.59	2.99	3.00
Ti	0.00	0.00	0.00	0.00	0.00	0.00	0.00	0.00	0.00	0.00	0.00
Al	1.35	1.32	1.38	1.35	1.39	1.34	1.36	1.36	1.36	1.00	1.00
Fe+2	-0.10	-0.16	-0.25	-0.19	-0.20	-0.08	-0.21	-0.14	-0.16	0.00	0.00
Fe+3	0.10	0.17	0.27	0.19	0.20	0.08	0.22	0.14	0.17	0.00	0.00
Mg	0.00	0.00	0.00	0.00	0.00	0.00	0.00	0.00	0.00	0.00	0.00
Mn	0.00	0.00	0.00	0.00	0.00	0.00	0.00	0.00	0.00	0.00	0.00
Ca	0.35	0.32	0.32	0.33	0.34	0.33	0.32	0.33	0.33	0.00	0.01
Na	0.67	0.73	0.72	0.72	0.70	0.69	0.72	0.70	0.71	0.10	0.14
K	0.00	0.01	0.02	0.00	0.00	0.01	0.01	0.00	0.00	0.90	0.82
Total	5.00	5.00	5.00	5.00	5.00	5.00	5.00	5.00	5.00	5.00	4.97
X_{An}	*0.34*	*0.31*	*0.30*	*0.31*	*0.32*	*0.32*	*0.30*	*0.32*	*0.31*	*0.00*	*0.00*
X_{Ab}	*0.65*	*0.69*	*0.68*	*0.68*	*0.67*	*0.67*	*0.68*	*0.68*	*0.68*	*0.10*	*0.14*
X_{Or}	*0.00*	*0.01*	*0.02*	*0.00*	*0.00*	*0.01*	*0.01*	*0.00*	*0.00*	*0.89*	*0.85*

Table-7.1c: Representative chemical analyses for micas and ilmenite (representative oxygen basis are given in tables). Mineral abbreviations are used after Whitney and Evans (2010). Cation calculations have been done following the procedure of Grew (1984).

Sample no	SR131	SR131	SR131	SR131	SR131	SR131	SR131	SR131	SR131	SR131
Mineral	Bt	Bt	Bt	Bt	Bt	Bt	Ms	Ms	Ms	Ilm
Texture	^Grt, Pl	^Grt, Pl	^Grt, Pl	^Grt, Pl	^Grt, Pl		^Bt	^Bt	^Bt	
Point no	3	6	13	29	30	31	55	70	72	18
SiO2	32.25	34.41	34.46	31.66	31.43	34.26	45.73	46.63	47.03	0.00
TiO2	2.86	2.32	2.55	2.74	2.83	2.84	0.08	0.73	0.54	52.28
Al2O3	17.16	16.70	17.12	16.46	16.56	16.87	35.57	35.87	36.09	0.05
Cr2O3	0.05	0.04	0.02	0.06	0.04	0.05	0.04	0.07	0.06	0.05
CaO	0.04	0.20	0.03	0.15	0.13	0.04	0.15	0.06	0.03	0.02
FeO	24.69	23.68	24.90	25.38	24.23	25.05	0.97	1.05	1.22	44.73
MnO	0.24	0.10	0.14	0.14	0.17	0.17	-0.03	-0.01	0.06	2.65
MgO	7.42	8.64	8.07	7.45	7.43	7.64	0.46	0.56	0.55	0.00
Na2O	0.23	0.35	0.24	0.48	0.24	0.24	0.44	0.47	0.52	0.00
K2O	9.36	9.22	9.21	8.39	9.11	9.30	10.65	10.55	10.57	0.00
Total	94.30	95.66	96.74	92.90	92.15	96.45	94.28	96.18	96.87	99.77
Oxygen basis	**11**	**11**	**11**	**11**	**11**	**11**	**11**	**11**	**11**	**3**
Si	2.58	2.68	2.67	2.58	2.58	2.67	3.07	3.07	3.08	0.00
Ti	0.17	0.14	0.15	0.17	0.17	0.17	0.00	0.04	0.03	0.99
Al-tot	1.62	1.54	1.56	1.58	1.60	1.55	2.82	2.78	2.78	0.00
Al-iv	1.24	1.18	1.18	1.25	1.25	1.17	0.92	0.89	0.90	0.00
Al-vi	0.38	0.36	0.38	0.33	0.36	0.38	1.89	1.89	1.88	0.00
Cr	0.00	0.00	0.00	0.00	0.00	0.00	0.00	0.00	0.00	0.94
Ca	0.00	0.02	0.00	0.01	0.01	0.00	0.01	0.00	0.00	0.01
Fe+2	1.65	1.54	1.61	1.73	1.66	1.63	0.05	0.06	0.07	0.00
Mn	0.02	0.01	0.01	0.01	0.01	0.01	0.00	0.00	0.00	0.06
Mg	0.89	1.00	0.93	0.90	0.91	0.89	0.05	0.05	0.05	0.00
total-vi	2.93	2.91	2.93	2.97	2.94	2.91	1.99	2.00	2.01	0.00
Na	0.04	0.05	0.04	0.08	0.04	0.04	0.06	0.06	0.07	0.00
K	0.96	0.92	0.91	0.87	0.95	0.92	0.91	0.89	0.88	0.00
Total	7.93	7.90	7.88	7.94	7.94	7.87	7.02	6.99	7.00	2.00
X_{Mg}	*0.35*	*0.39*	*0.37*	*0.34*	*0.35*	*0.35*	*0.46*	*0.49*	*0.45*	

7.1.3. Physical condition of metamorphism

Textural features revealed from petrographic study show that a granoblastic assemblage of garnet-plagioclase-K-feldspar-quartz stabilized during peak metamorphism of the studied psammopelitic unit. Owing to lack of suitable mineral assemblages, estimation of the physical conditions during the formation of the garnet bearing leucosomes cannot be determined by conventional thermobarometry. The small biotite inclusions within garnet are likely to reset at lower temperature (large

garnet/biotite volume ratio, Ferry and Spear, 1978). The P-T condition at the time of formation of the garnet bearing leucosomes has been inferred from the pseudosection approach. Owing to extreme lithological heterogeneity, effective bulk or microbulk compositions in the system NCKFMASTH (Na_2O-CaO-K_2O-FeO-MgO-Al_2O_3-SiO_2-TiO_2-H_2O) system have been computed from the modal proportion of minerals and the mineral compositions. The activity models of the observed minerals that are used for the calculations are: garnet, orthopyroxene, biotite, muscovite, chlorite and melt (White et al., 2014), plagioclase and K-feldspar as ternary feldspars (Holland and Powell, 2003). The pseudosection is calculated in the temperature and pressure range of 400°-1000°C and 2-9 kbar. The input H_2O content with the effective bulk of the studied psammopelitic rock is considered in such a way that the resulting pseudosection generates H_2O free associations under subsolidus conditions and that liquid and H_2O do not coexist in in the chosen P-T range (Fig. 7.2). The metamorphic association (garnet + plagioclase + K-feldspar + quartz + ilmenite) that developed at the culmination of peak metamorphism in psammopelite has a narrow temperature range of 750°-800°C at ~5.5 to 9 kbar. In this field the volume of melt is 16-20% which is consistent with the mode of leucosome observed in the field. Mineral composition in the psammopelite does not show large compositional variation. Nevertheless the intersecting isopleths for observed compositional range of the solid solution phases converge at ~800 ºC and ~7 kbar in the field of the peak metamorphic association of psammopelite (Fig. 7.2). Absence of significant compositional zoning in garnet and plagioclase the precise P-T condition of the retrograde association garnet + plagioclase+ biotite + muscovite +quartz could not be obtained. However, the calculated pseudosection provides a broad P-T range of 500-600°C in the pressure range of 4-7 kbar. A lower temperature would stabilize chlorite which is not observed in the studied rock.

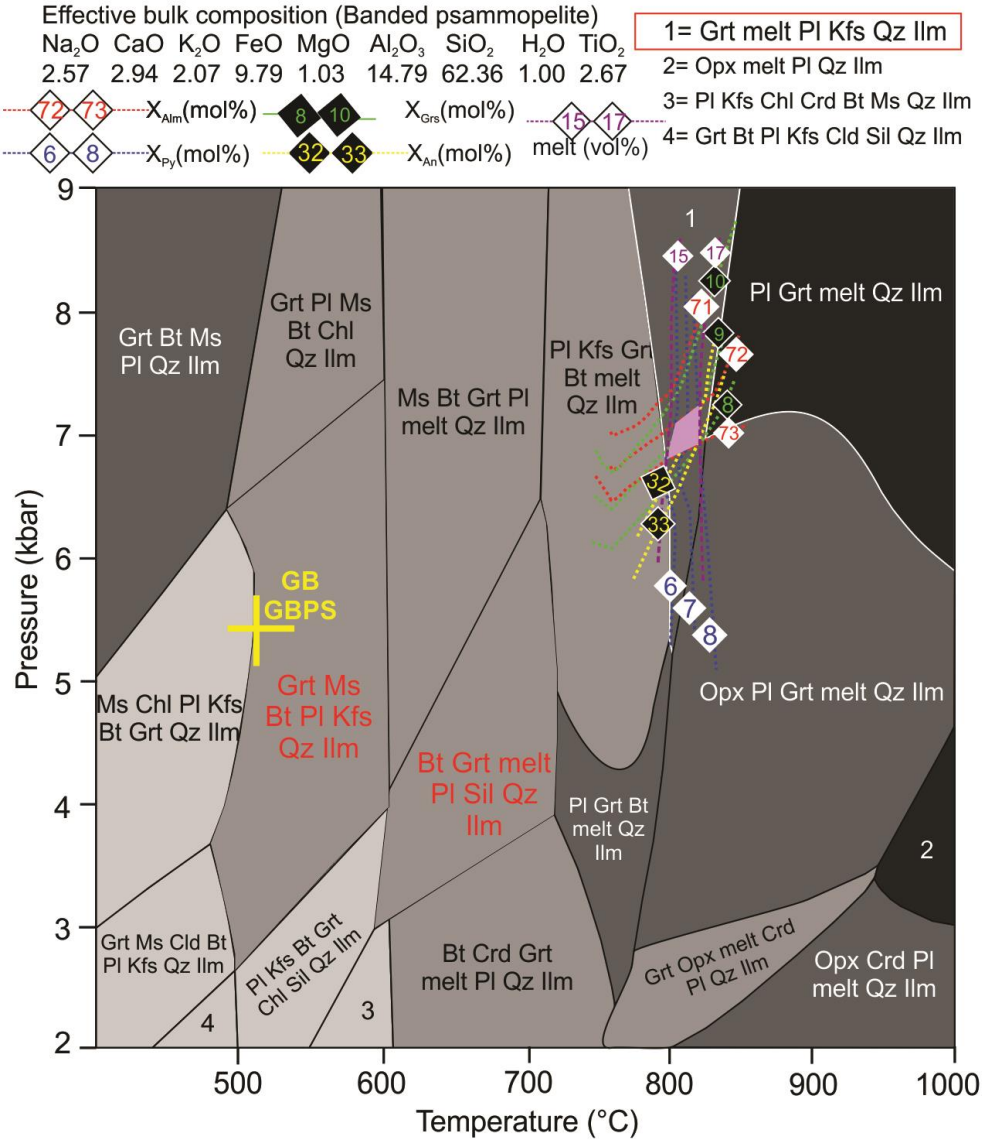

Figure 7.2. P–T pseudosection in a NCKFMASTH system for banded psammopelite. The pseudosection is contoured with isopleths of garnet, plagioclase compositions and modes of melt. Conditions of peak metamorphism are constrained at ~800ºC and ~7 kbar (purple box). Yellow cross represents P–T determined by conventional thermobarometry with abbreviations: GB: garnet–biotite; GBPS: garnet–biotite–plagioclase–quartz respectively. Two bivariant fields with phases marked in red are the anticipated conditions during retrograde metamorphism.

Although the peak metamorphic condition could not be constrained from conventional geothermobarometry due to lack of suitable mineral association, the retrograde condition can be obtained using garnet-biotite (Bhattacharya et al., 1992) thermometry and garnet-biotite-plagioclase-quartz barometry (Hoisch, 1990). Different mineral pairs have been used and the results presented below represent the "average values ± standard deviation" associated with these permutations. Studies have shown that the uncertainties of the P and T estimates with the robust geothermobarometers are better than ±1.5 kbar and ±50ºC respectively (Etzel and Catlos, 2021; Powell and Holland, 2008; Worley and Powell, 2000). Using the garnet-biotite pairs, the retrograde temperature can be constrained at 505±15 °C (Table-7.2). Using garnet rim and adjacent biotite, matrix plagioclase rim composition 5.5±0.5 kbar pressure is obtained at a certain temperature (500 ° C which is constrained from the same garnet-biotite pairs) from P_{Fe} barometer of GBPS (garnet-biotite-plagioclase-quartz; Hoisch, 1990). This retrograde P-T condition obtained from conventional thermobarometry fits well within the range of last P-T record registered in the pseudosection.

Table 7.2: P–T estimates of banded psammopelite, obtained using various conventional thermobarometers (T: °C, P: kbar).

Conventional Thermometry						
	Thermometers used	**Rock type (Sample No.)**	**Mineral Assemblages**	**P_{ref} (kbar)**	**Results**	
Retrogression	**Grt-Bt[a]**	**SR131**	Grt (2) - Bt (3)	5	496	506 ± 15
			Grt (8) - Bt (6)		498	
			Grt (14) - Bt (13)		499	
			Grt (25) - Bt (29)		507	
			Grt (26) - Bt (30)		530	

Conventional Barometry						
	Barometers used	**Rock type (Sample No.)**	**Mineral Assemblages**	**T_{ref} (°C)**	**Results**	
Retrogression	**Grt-Bt-Pl-Qz[b]**	**SR131**	Grt (2) - Bt (3) -Pl (4)	500	5.4	5.5 ± 0.35
			Grt (8) - Bt (6) -Pl (5)		5.8	
			Grt (14) - Bt (13) -Pl (12)		5.7	
			Grt (25) - Bt (29) -Pl (27)		6.0	
			Grt (26) - Bt (30) -Pl (28)		5.1	

7.2. Garnet-cordierite-biotite rock (GCB)

Garnet-cordierite-biotite rock preserves two different mineral associations: garnet + cordierite + sillimanite + biotite + quartz + ilmenite (association 1) and garnet + cordierite + orthoamphibole + biotite + quartz + ilmenite (association 2).). Association 1 is distinguished from Association 2 on the basis of mutual exclusion of orthoamphibole (Association 1) and sillimanite (association 2). In the following section salient petrographic features of the two associations are presented. Mineral abbreviations in all the figures and tables are taken from Whitney and Evans (2010).

7.2.1. Petrography of Association 1

The mineralogy and the modal proportion of different minerals in the Association-1: Sillimanite (30%) + cordierite (30%) + biotite (20%) + garnet (10%) + quartz (5%) + ilmenite (2%) ± chlorite (1%). Overprinting mineralogy is a conspicuous feature in this association. Away from the Type I veins, the earliest granoblastic association in the rock includes garnet porphyroblasts that are embedded within the recrystallized aggregates of cordierite, commonly showing polygonal grain boundaries ($Cordierite_1$, Fig. 7.3a). Garnet porphyroblasts have overall rounded shape and corroded grain margins. A few grains of sillimanite + ilmenite are scattered in the cordierite matrix (Fig. 7.3b, c). Garnet porphyroblasts contain inclusions of one or more of biotite, ilmenite, quartz and cordierite (Fig. 7.3d, e). $Cordierite_1$ is variably replaced with randomly oriented grains of biotite and fine acicular sillimanite (fibrolite; Fig. 7.3b, c). The original polygonal shape of the $cordierite_1$ is retained during replacement by fibrolite and biotite (Fig. 7.3b). In places, network of fibrolite is formed along the polygonal grain boundaries of $cordierite_1$ that forms pods that is swerved around by thin layers of biotite rich zone (Fig. 7.3f). The mineral association (biotite + cordierite + fibrolite) inside and outside of biotite rich zone are same but the ratio of biotite-cordierite is around three times higher within the zone (Fig. 7.3g). Individual biotite grains in the zone are haphazardly oriented and none of the grains have well-developed cleavage plane. The garnet is also replaced variably by fibrolite and sometimes biotite (Fig. 7.3d, e). Commonly the garnet develops two sets of nearly orthogonal fractures that are followed by fibrolite (Fig. 7.3e). The fibrolite grains

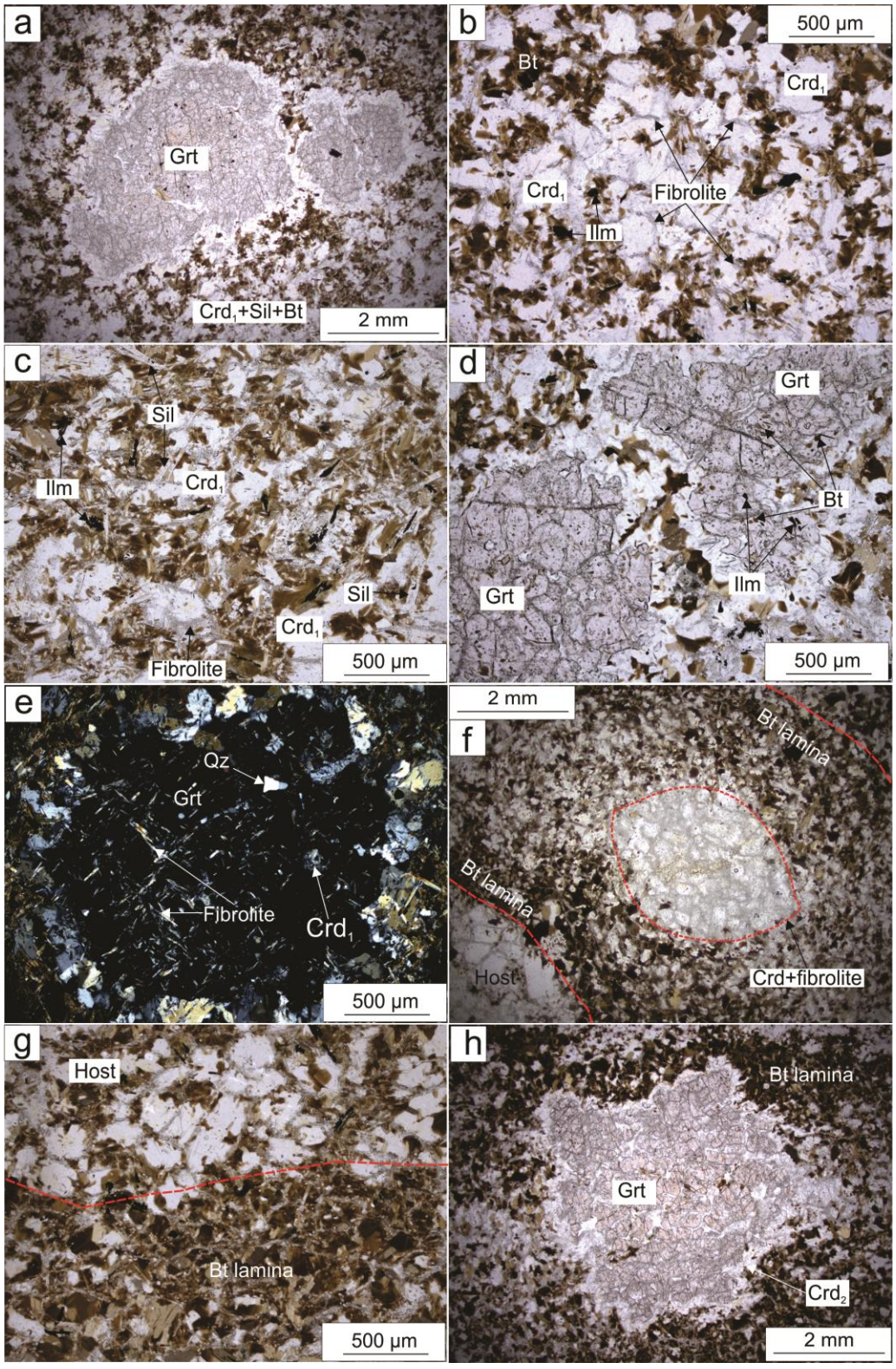
a
Grt
Crd1+Sil+Bt
2 mm
b
500 µm
Bt
Crd1
Crd1
Fibrolite
Ilm
c
Sil
Ilm
Crd1
Sil
Crd1
Fibrolite
500 µm
d
Grt
Bt
Ilm
Grt
500 µm
e
Qz
Grt
Fibrolite
Crd1
500 µm
2 mm
f
Bt lamina
Bt lamina
Host
Crd+fibrolite
g
Host
Bt lamina
500 µm
h
Bt lamina
Grt
Crd2
2 mm

Figure 7.3. Association 1 under microscope. a) Garnet porphyroblasts are embedded within recrystallized aggregates of cordierite, commonly showing polygonal grain boundaries in association 1. b) Groundmass of the GCB comprising of recrystallized polygonal cordierite$_1$ and sillimanite needles. Cordierite$_1$ is replaced by fibrolite and biotite to variable extent. c) Cordierite$_1$ + sillimanite + ilmenite as early association with garnet in association 1. Proportion of biotite varies in the groundmass. Polygonal grain boundaries of cordierite$_1$ become irregular with the replacement by biotite at few places. d) Garnet contains biotite, ilmenite inclusions. They contain nearly orthogonal fractures. Garnet is torn out and the detached portions of the garnet are rimmed by cordierite$_2$. Biotite rich zone is separated from garnet by cordierite$_2$. e) Garnet contains quartz, cordierite$_1$ inclusions. Fibrolite grains protrude the garnet blocks that are bounded by orthogonal fractures. f) Cordierite$_1$ + fibrolite form pod that is swerved around by thin layers of biotite rich zone or biotite lamina. g) Mineral association (biotite + cordierite + fibrolite) inside and outside of biotite lamina are same but the ratio of biotite-cordierite is around three times higher within the lamina. h) Garnet porphyroblast having overall round shape and corroded grain margin and surrounded by rind of cordierite$_2$. Biotite lamina is separated from garnet by rim cordierite$_2$.

protrude the garnet blocks that are bounded by orthogonal fractures (Fig. 7.3d, e). Garnet always develops a moat of cordierite grains (Cordierite$_2$). Cordierite$_2$ separates the garnet from the biotite rich zone (Fig. 7.3h). In domains, grains of the garnet is torn out and the detached portion of the garnet are rimmed by cordierite$_2$ (Fig. 7.3d). All the features suggest that the Cordierite$_2$ was developed during the waning phase/after the cessation of deformation.

7.2.2. Petrography of Association-2

The mineralogy and the modal proportion of different minerals in the Association-2: Cordierite (40%) + biotite (20%) + orthoamphibole (15%) + garnet (10%) + quartz (10%) + ilmenite (5%). The earliest association includes garnet porphyroblasts and cordierite and very fine grained ilmenite which essentially form the matrix of this association. Haphazardly oriented biotite grains replace the recrystallized cordierite in the matrix to variable extent (Fig. 7.4a). Garnet porphyroblasts with mostly straight, angular margins are present within the fine

grained recrystallized matrix of cordierite + biotite + ilmenite (Fig. 7.4b). Garnet contains inclusions of one or more of the following minerals: cordierite, biotite, ilmenite (Fig. 7.4c). Partially corroded grain boundaries of euhedral

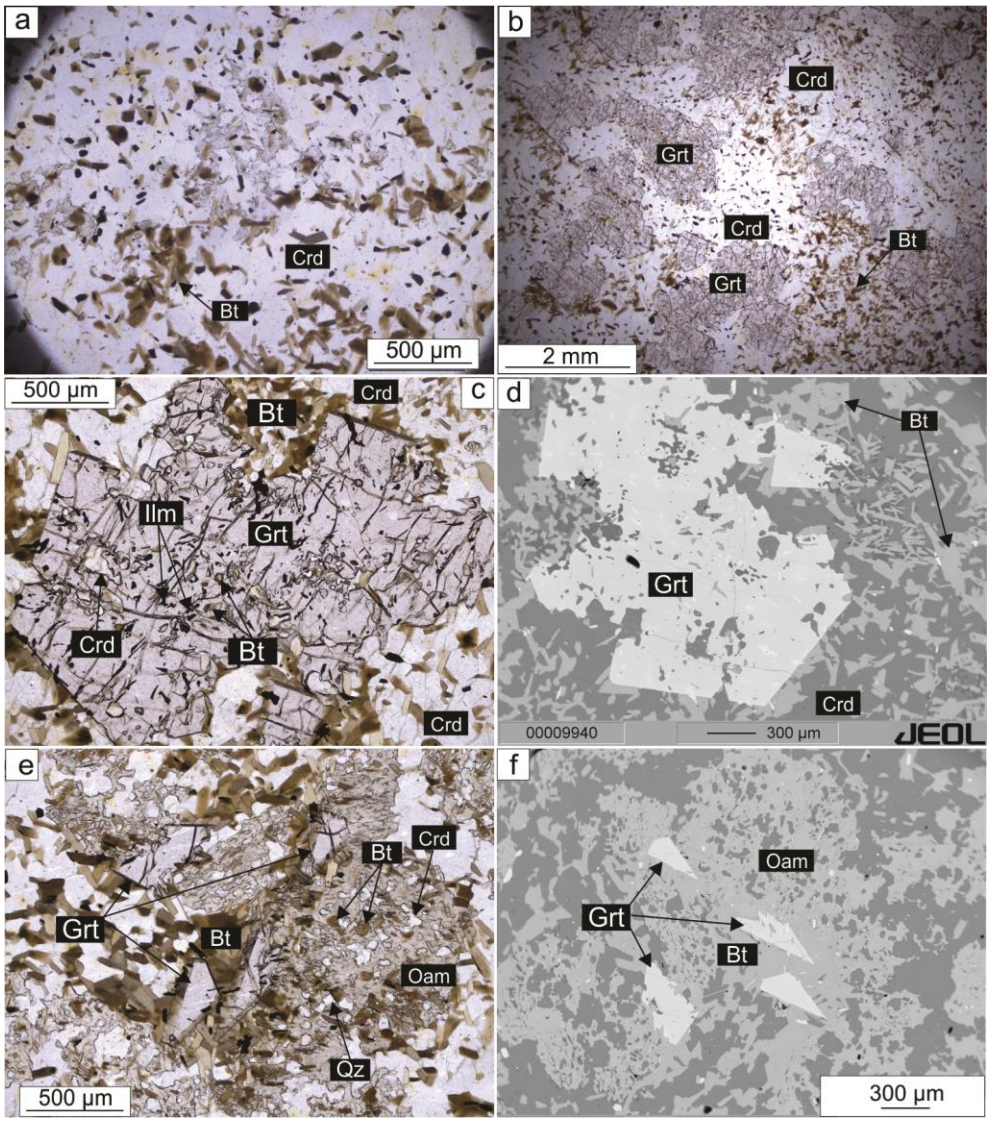

Figure 7.4. Association 2 under microscope. a) Recrystallized cordierite variably replaced by biotite and scattered orthoamphibole in the groundmass of association 2. b) Garnet porphyroblasts embedded within the groundmass of association 2. (c) Garnet porphyroblasts have partially straight grain margins and contain biotite, ilmenite, cordierite and quartz inclusions. d) Biotite replaces garnet along the portions of corroded grain margins. e & f) Orthoamphiboles intergrown with biotite contain numerous cordierite inclusions which give them sieve-like textures. Garnet grains present as relics within orthoamphibole grains.

garnet porphyroblasts share contact with cordierite and biotite of the matrix (Fig. 7.4d). Few triangular small garnet grains are present as relics within orthoamphibole (Fig. 7.4e, f). Grain size of the orthoamphibole varies in the association. Anhedral fine grained ortho- amphiboles are associated with cordierite + biotite + ilmenite in the matrix (Fig. 7.4g). Orthoamphibole containing numerous inclusions of cordierite shows sieve texture in this association (Fig. 7.4h). Both the anhedral fine grained and poikiloblastic orthoamphibole are intergrown with biotite.

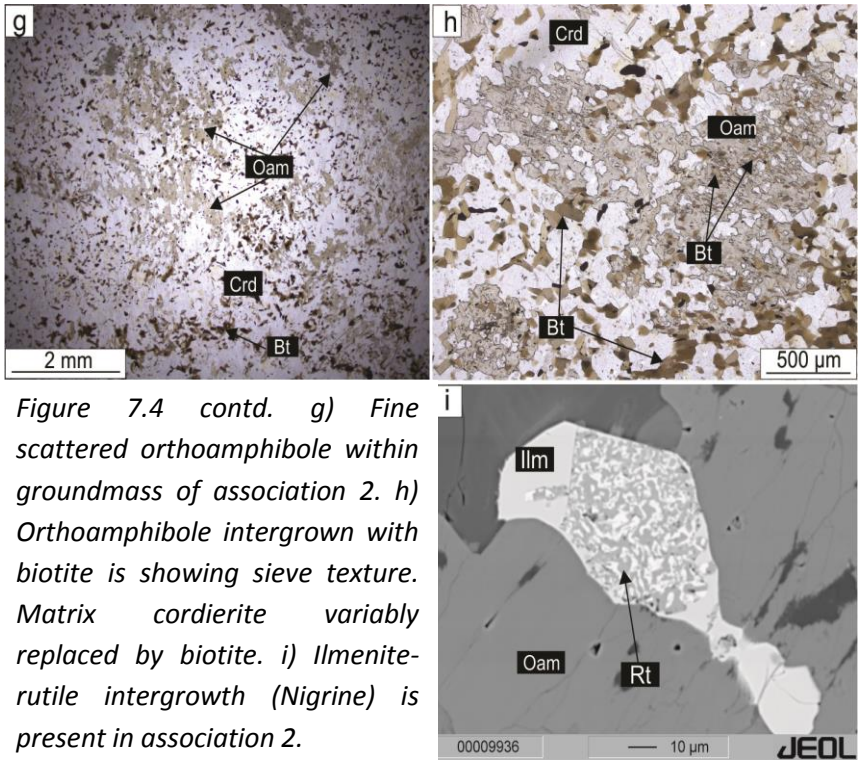

Figure 7.4 contd. g) Fine scattered orthoamphibole within groundmass of association 2. h) Orthoamphibole intergrown with biotite is showing sieve texture. Matrix cordierite variably replaced by biotite. i) Ilmenite-rutile intergrowth (Nigrine) is present in association 2.

Ilmenite contains variable proportion of oriented /irregular patches of rutile (Fig. 7.4i). The feature of the ilmenite rutile intergrowth resembles the similar intergrowth in Nigrine (Dill et al., 2007; Dill and Melcher, 2009).

7.2.3. Petrography of Type I and Type II veins

Type I vein consists of large bladed crystal of sillimanites (0.5 mm to 3 mm in length and upto 0.3 mm in width), coarse-grained quartz and variable amount of massive garnet (Fig. 7.5a). Unlike the host-rock garnet, the garnet in the vein ($garnet_v$) is massive and does not show any fibrolite veins. The bladed sillimanite show two textural types. Commonly the sillimanite blades show wall controlled growth with its sharp tip pointing towards the center of the vein (Fig. 7.5b). In places, sillimanite blades extend from one wall to the other (Fig. 7.5b). In another mode, randomly

oriented bladed sillimanite grain is set in the coarse granular matrix of quartz (Fig. 7.5c, d).

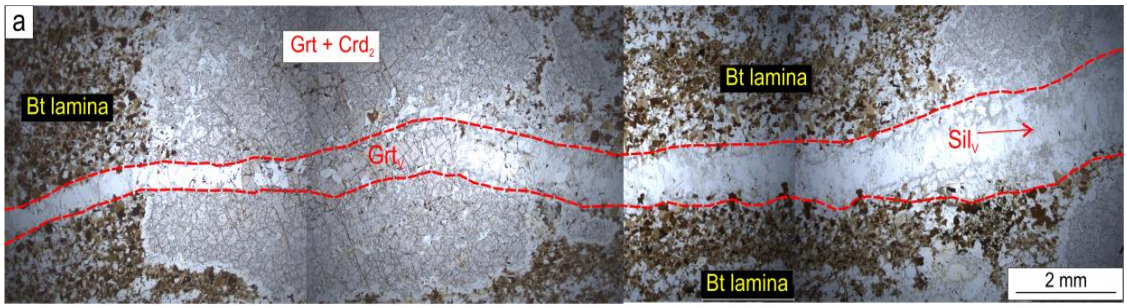

Figure 7.5. (a) Stitched image of type I vein, cutting through the garnet with rim cordierite$_2$ and biotite lamina of the host GCB.

Owing to imposed strain, sillimanite of both textural types are kinked and show undulatory extinction. Quartz grains in the vein show undulatory extinction and grain boundary bulging (Fig. 7.5d, e). The Type I vein cuts the host-rock garnet grains with the rind of cordierite$_2$ as well as thin biotite-fibrolite laminae that develop within the cordierite$_1$ matrix (Fig. 7.5a, f, g). When the Type I cuts the host garnet with a rind of cordierite$_2$ massive garnet$_v$ develops in the vein (Fig. 7.5f, g). In places garnet$_v$ is the dominant mineral in vein I and contains relicts of bladed sillimanite and quartz (Fig. 7.5g). The boundary between host garnet and garnet$_v$ are generally straight. This feature suggests that garnet in the host acted as substrate for the growth of garnet$_v$. Garnet$_v$ is fractured but the fractures are not filled with fibrolite. Some fractures cuts through the boundary between host garnet and garnet$_v$. Biotite rich zone that is proximal to the Type I veins are distinctly depleted in fibrolite relative to its counterpart that developed away from the veins. Quartz is conspicuously absent close to the Type I veins. Aggregates of biotite (with or without fibrolite) protruding into the host-rock garnet are seen close to the vein (Fig. 7.5h). Locally, biotite is replaced with chlorite proximal to the Type I veins (Fig. 7.5i). Prismatic sillimanite in the vein gets bent at the vein boundary and becomes parallel to the vein wall and associated granular garnet margin where the veins are folded or kinked along with biotite rich zone (Fig. 7.5j).

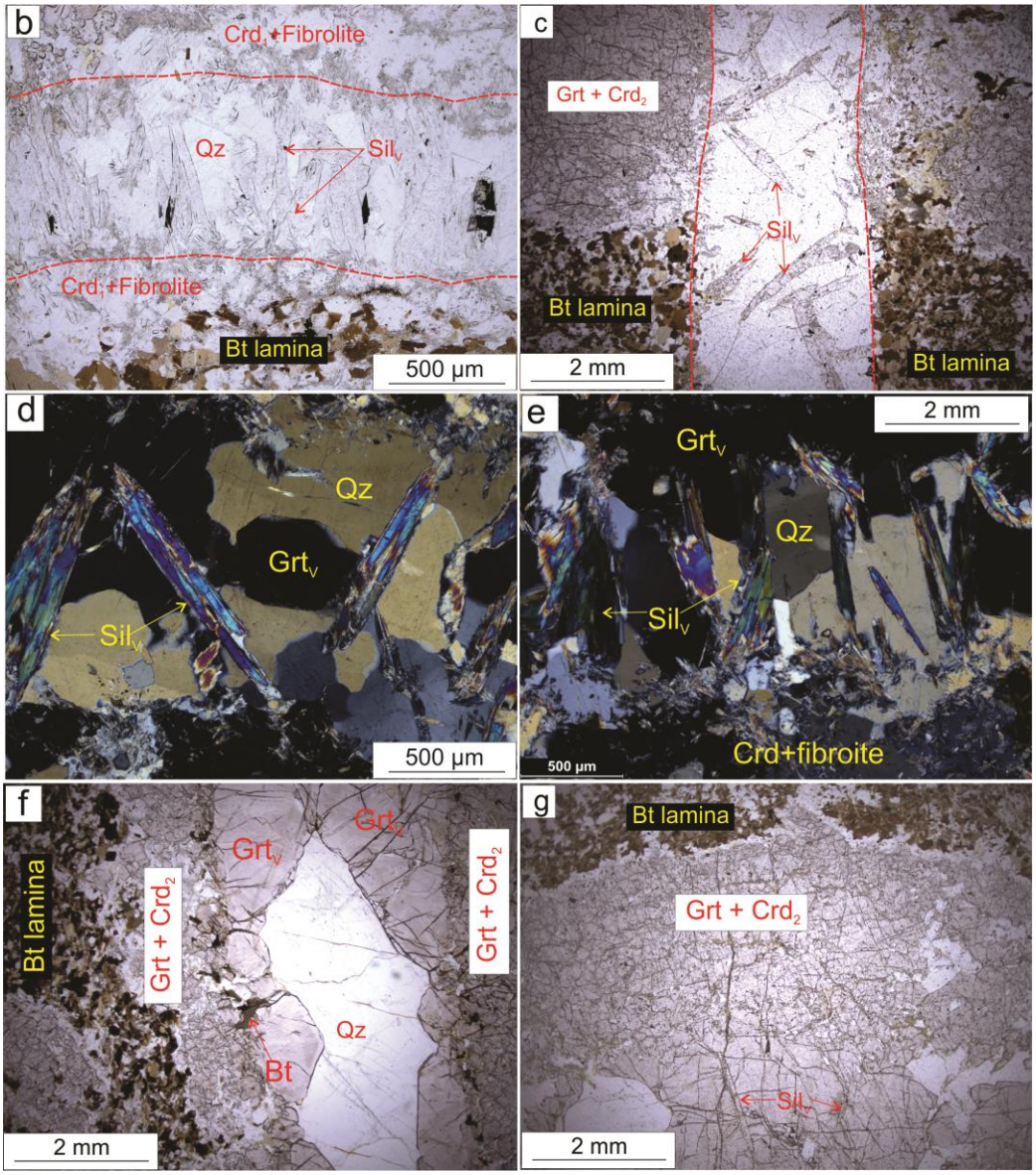

Figure 7.5 contd. (b) Cordierite$_1$+fibrolite define the vein margin where host garnet is absent. Prismatic sillimanite blades extend from wall to wall of the type I vein. (c) Vein sillimanite randomly placed within the vein. d & e) Coarse grained vein quartz show undulose extinction and grain boundary bulging nucleation. f) Massive homogeneous inclusion free garnet develops within the vein at the contact of host garnet at the vein wall. g) Vein garnet growing from host garnet at the vein wall and they include prismatic sillimanite of the vein.

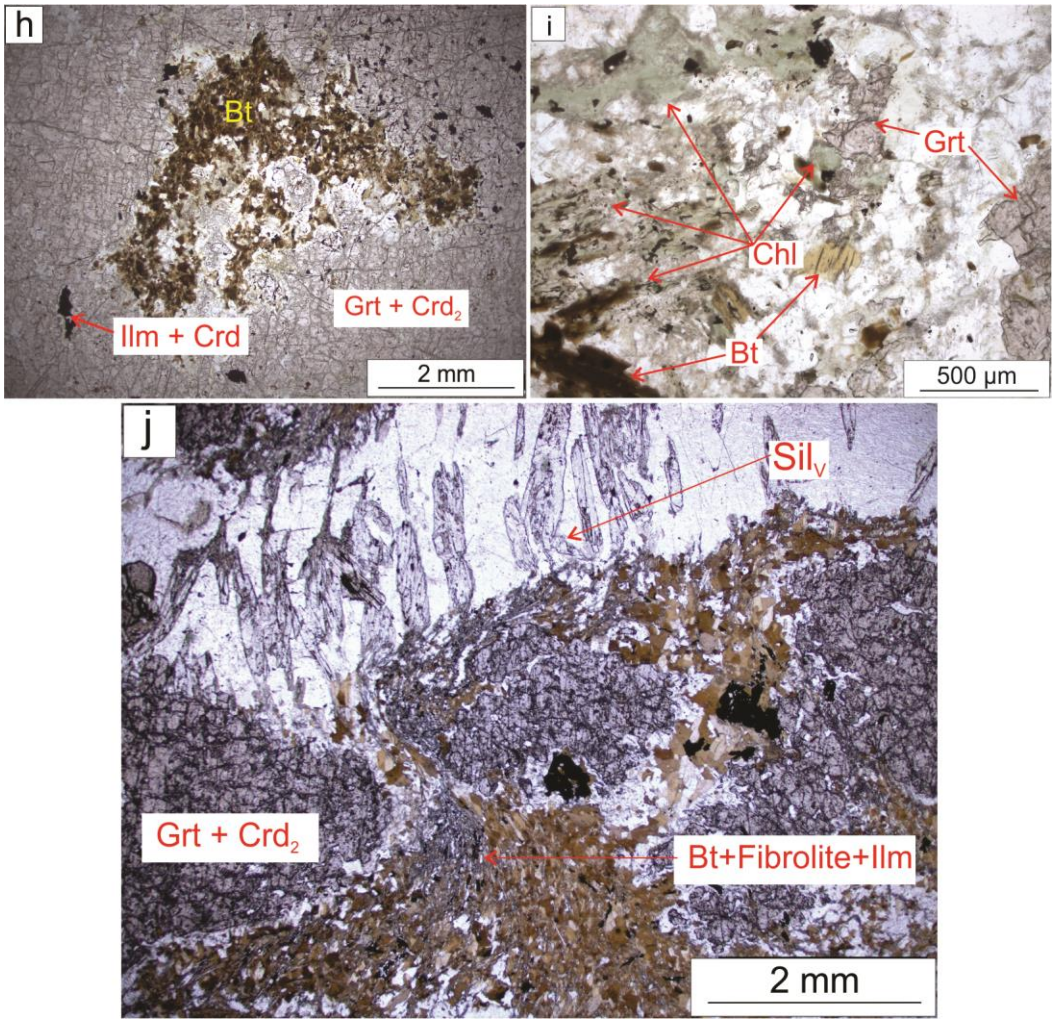

Figure 7.5 contd. (h) Aggregates of biotite (with or without fibrolite) protruding into the host-rock garnet is seen close to the vein. (i) Biotite is replaced with chlorite proximal to the vein I. (j) At places, veins are folded or kinked and together with the biotite lamina, prismatic sillimanites get bent and become parallel to the vein wall.

Type II veins cut across cordierite + biotite + ilmenite matrix in association-2 where the modal abundance of anthophyllite is around 95% (Fig. 7.5k). The vein-margin is demarcated by the fine matrix association. Vein-anthophyllites are haphazardly oriented, do not show any wall-controlled growth and seems to cluster at the central part of the vein (Fig. 7.5l). Numerous cordierite and minor biotite inclusions are present as relic within the vein-anthophyllite (Fig. 7.5l). At few places, biotite is seen to be intergrown with vein-anthophyllite (Fig. 7.5m).

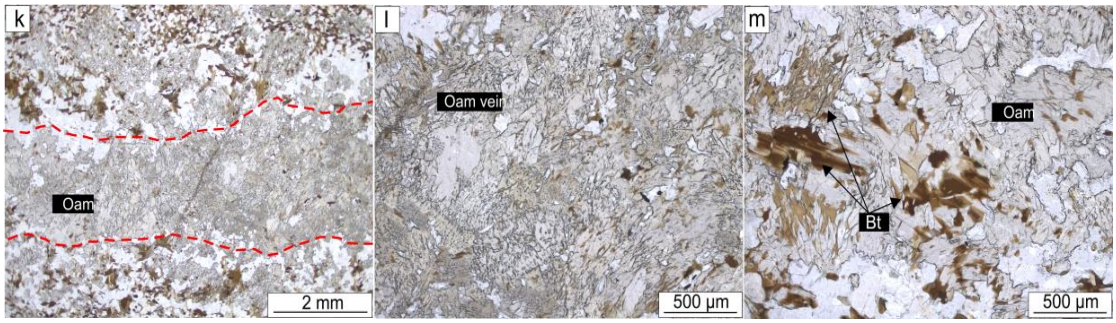

Figure 7.5 contd. (k) Anthophyllite veins cut across cordierite + biotite + ilmenite matrix in association-2. (l) Vein-anthophyllites are haphazardly oriented in the central part of the vein. (m) Cordierite inclusions and biotite patches within vein anthophyllite.

7.2.4. Mineral paragenesis in both the association of GCB

Association-1

1. The earliest association that can be traced back possibly contained granular garnet porphyroblast and cordierite$_1$ with minor amount of sillimanite + ilmenite.

2. In this medium- to fine-grained groundmass, biotite laminae formed due to fluid infiltration and K and Fe-metasomatism through grain-boundary flow as individual biotite grains are haphazardly oriented in the laminae. Fibrolites also developed during this event as well.

3. In the next stage, second generation of cordierite (Cordierite$_2$) is formed and it rimmed and partially pseudomorphed granular garnet porphyroblasts. Cordierite$_2$ also formed rim along biotite + sillimanite and ilmenite at some places. At few places, biotite is replaced by chlorite.

4. At this stage, this rock experienced hydrofracturing and veins were formed. As majority of the prismatic sillimanite in the veins are showing comb-structure, these veins were developed by fracture-fill or crack-seal mechanism. Veins formed later than the biotite laminae and garnet porphyroblasts because they cut across both of them. Massive, inclusion-free garnet developed on host garnet where the veins are cutting across them. This growth of the massive garnet occurred slightly late than vein-sillimanite and quartz as they are included completely within vein-garnet. Hence they

were most probably formed by the fluid activity with the resource from the granular garnet itself.

Association-2

1. In this association garnet and recrystallized cordierite + ilmenite appear to be the earliest phases.

2. Subsequently orthoamphibole develops and includes the garnet grains whereas haphazardly oriented biotite grains develop along the margin of the recrystallized cordierite grains and replace cordierite to variable extent.

3. Direct contact between anthophyllite and gedrite in the host rock of association 2 could not be identified but both of them were possibly formed together after cordierite when the condition was in the two-phase field of orthoamphibole.

4. Anthophyllite veins are possibly formed at this stage by channelized replacement of cordierite by anthophyllite. This is because of the fact that numerous cordierite inclusions are present in anthophyllite veins and the anthophyllite grains are haphazardly oriented. Similar features have been observed in grain boundary fluid flow without any fracture development (Vernon, 2004). So the fluid flow in anthophyllite veins is different from Type I vein.

In the outcrop, the studied GCB does not show any foliation or deformational features but several microstructures indicate that the rock had experienced deformation throughout the metamorphic event.

1. Conjugate fractures were developed within garnet porphyroblasts whereas matrix cordierite got recrystallized and developed straight polygonal grain boundaries.

2. Although biotite laminae have an overall orientation in thin section scale but individual biotite grains within laminae are haphazard.

3. Extension fractures were developed due to external fluid pressure in the GCB and the deformational event continued after these fractures were filled/sealed by mineral precipitation. This is evident from the stretched sillimanite and partially recrystallized quartz within the vein. At some places, Type I veins are folded along with the bounding biotite laminae where prismatic sillimanites get bent and becomes parallel to the vein-wall and biotite + fibrolite lamina gets swerved around the host garnet at vein boundary.

7.2.5. Mineral chemistry

Mineral chemistry of the studied GCB has been analyzed with an Electron Probe Micro-analyser (EPMA) at the University of Cologne, Germany. Detailed analytical technique is given in the Appendix. Representative mineral compositions of the banded psammopelite are presented in Table-7.3.

Garnet: In both the associations of the GCB, garnet is dominated by almandine ($X_{Fe}=Fe^{2+}/Fe^{2+}+Mg=0.74-0.84$) followed by pyrope ($X_{Mg}=Mg/Mg+Fe^{2+}=0.16-0.26$) with minor amount of grossular and spessartine component (<5 mol%, Table-7.3a). No significant compositional difference was noted in garnet in both the association. When in contact with cordierite, the core of the garnet ($Alm_{73-74}Py_{21-23}Grs_{3-4}Sps_1$) is more magnesian than the rim composition ($Alm_{78-82}Py_{15-18}Grs_{2-3}Sps_1$; Table-7.3a) (Fig.

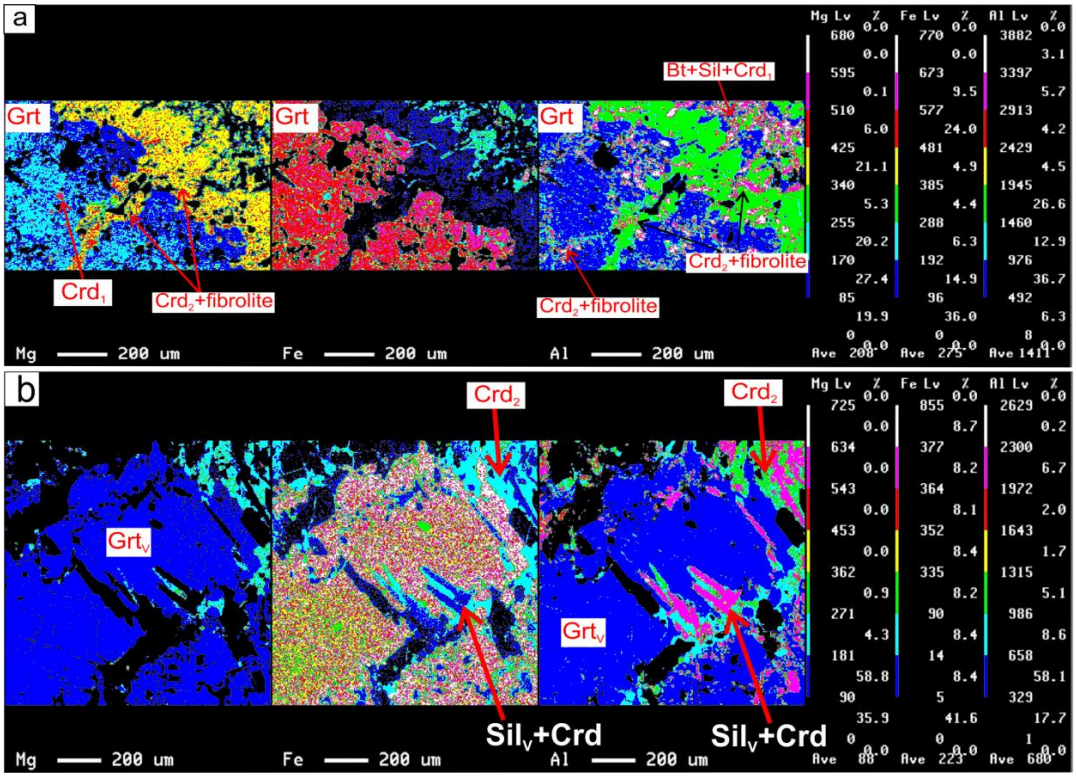

Figure 7.6. a) X-ray elemental map of garnet porphyroblast is association 1. Garnet rim is comparatively less magnesian at the contact of rim cordierite$_2$. b) Vein-garnet is homogeneous in composition.

7.6a). Garnet porphyroblast in association 1 has comparatively more Mg-rich core [X_{Mg} = 0.22-0.24; rim (X_{Mg}=0.16-19) relative to that within association 2 (Table-7.3a). Rim to core compositional profile of a garnet porphyroblast at the contact of secondary biotite in the association 2 show minor Fe-enrichment towards rim (Fig. 7.6c, d). Garnet core has a composition of $Alm_{70}Py_{23}Grs_5Sps_2$ and rim at the contact of biotite shows a composition of $Alm_{76}Py_{17}Grs_5Sps_3$ (Table-7.3b). Garnet relics within host poikiloblastic orthoamphiboles show similar composition to porphyroblastic garnet ($Alm_{70\text{-}72}Py_{20\text{-}23}Grs_5Sps_2$; Table-7.3b). Composition of the massive, inclusion-free garnet in the Type I vein is compositionally homogeneous ($Alm_{75\text{-}76}Py_{19\text{-}20}Grs_{3\text{-}5}Sps_1$).and resembles the composition of the garnet in the host rock (Association 1) (Fig. 7.6a, b; Table-7.3a).

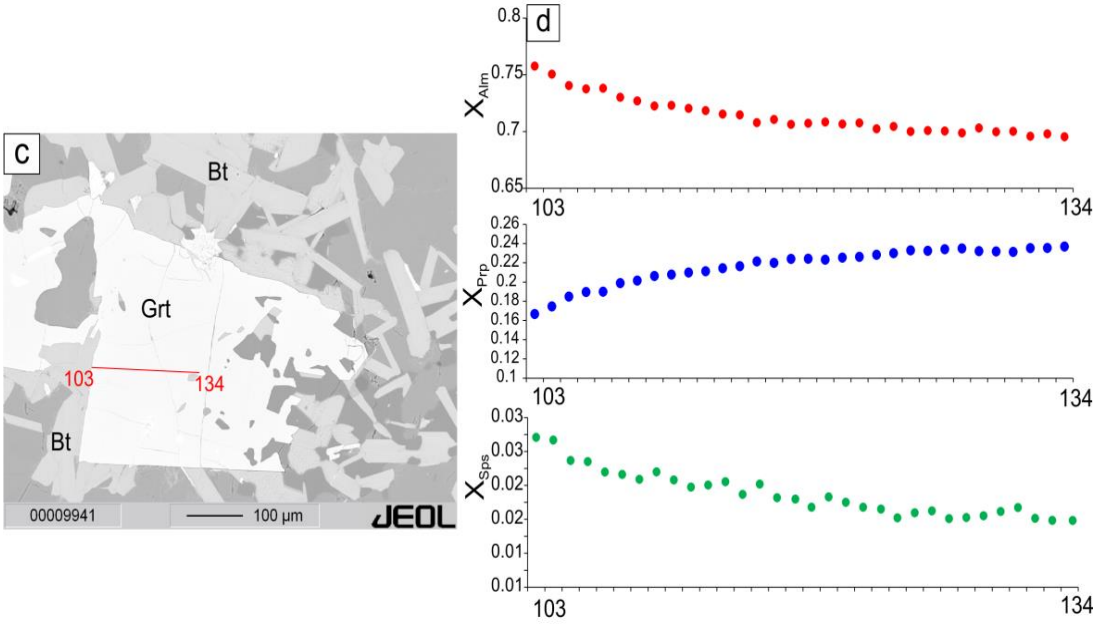

Figure 7.6 contd. c) BSE image of a garnet porphyroblast in association 2 at the contact of secondary ferromagnesian mineral phase (biotite) has been shown. Rim to core compositional profile of the garnet grain along the red line transect (103) to (134). d) Rim to core profile of the garnet porphyroblast within association 2 show a compositionally homogeneous core and minor increase in X_{Alm} , decrease in X_{Prp} and increase in X_{Sps} component towards rim.

Cordierite: Cordierite, in all textural association in association-1 is magnesian without any significant compositional zoning [X_{Mg} ($Mg/Mg+Fe^{2+}$)=0.74-0.82] (Table-7.3c). .In association-2, cordierite grains are more magnesian than the cordierite in association-1 (X_{Mg}=0.82-0.89). Low totals (total=94.11-96.99; Table-7.3c), obtained from the Microprobe analysis suggest significant channel fluids in the structure of cordierite. Similar high fluid content in the cordierite structure has been reported from several pegmatites and fluid-infiltrated high grade terrains in Antarctica and central Australia (Harley and Carrington, 2001).

Biotite: In association-1, biotite, in the initial matrix and laminae shows no significant compositional difference. Biotite grains are homogeneous, Fe-rich in composition (X_{Mg}=0.35-0.43) and contain 0.15-0.23 apfu titanium (TiO_2=2.47-3.57 wt%; Table-7.3d). Relative to association 1, biotite in association-2, is magnesian (X_{Mg}=0.47-0.54) and contain 0.11-0.15 apfu titanium (TiO_2=1.97-2.45wt%; Table-7.3d).

Orthoamphibole: The Si versus $Mg/(Mg+Fe^{2+})$ diagram of Leake et al. (2004) shows that the orthoamphiboles within Type-II vein are anthophyllite and those in the host or association-2 can be categorized as anthophyllite and gedrite (Fig. 7.6e). No significant compositional zoning is observed in the individual orthoamphibole grains within host association-2 and Type-II vein. Range of X_{Mg} is 0.58-0.64, 0.60-0.65 and 0.56-0.61 for the anthophyllite in vein, anthophyllite in the host and gedrite within host respectively (Table-7.3e). Anthophyllite, both within the host and vein has a low amount of Na_2O content (0.05-0.81 wt%) whereas gedrite has comparatively high Na_2O (1.02-1.79 wt%). Al_2O_3 content in all the anthophyllites is in the range of 2.07-7.30 wt% and gedrite has 9.90-14.48 wt% Al_2O_3 (Table-7.3e). In the A-site occupancy vesus Al^{VI} plot of Robinson et al., (1971), the gedrite of the studied rocks shows less amount of Na+K than the 'ideal gedrite' (Fig. 7.6f). The X_{Mg} [$Mg/(Mg+Fe^{2+})$] versus Al^{VI} shows an overall negative compositional trend (Fig. 7.6g). The studied and analyzed orthoamphiboles contain significant degree of edenite and tschermackite substitution as revealed from the systematic negative trend in ($Na+Al^{IV}$) versus Si and Al_{total} versus (Mg+Si) diagrams respectively (Fig. 7.6h, i).

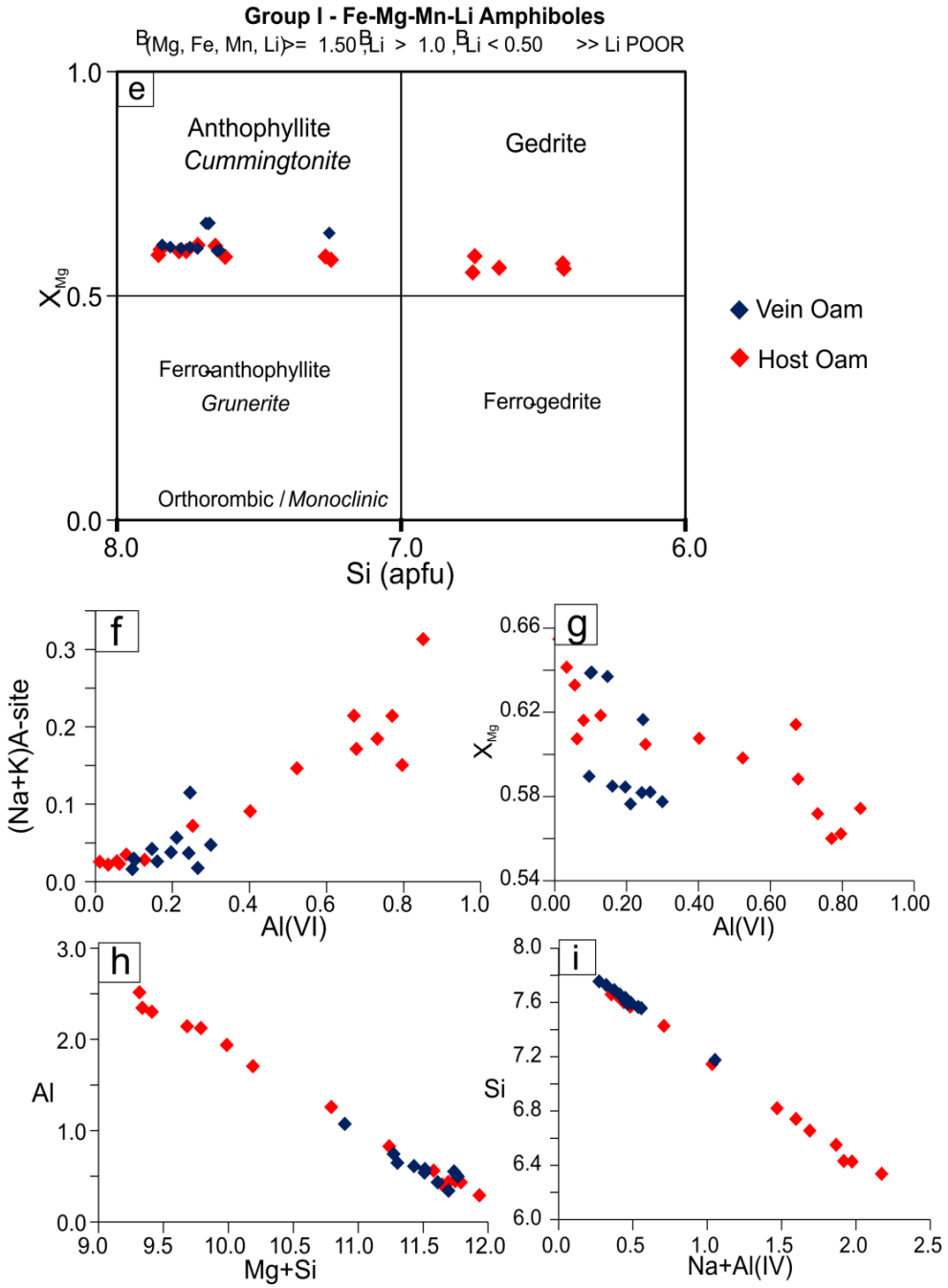

Figure 7.6 contd. (e) Si versus Mg/(Mg+Fe^{2+}) diagram of Leake et al. (2004). (f) A-site occupancy vesus Al^{VI} plot of Robinson et al., (1971). (g) X_{Mg} [Mg/(Mg+Fe^{2+})] versus Al^{VI} shows an overall negative compositional trend. (h) Al_{total} versus (Mg+Si) diagram show consistent negative trend signifies the presence of tschermackite substitution. (i) Systematic negative trend in (Na+Al^{IV}) versus Si plot implies edenite substitution in anthophyllite and gedrite.

Ilmenite-pseudorutile intergrowth: BSE image and electron microprobe analysis show that opaque grains in the association 2 within GCB contain intergrowth of ilmenite and pseudorutile. BSE images reveal that in some of the cases rim part of the opaque grains is ilmenite whereas core portion is either pure rutile or symplectic intergrowth of ilmenite and pseudorutile (Fig. 7.4i). Rutile core contains TiO_2 ~90 wt% and FeO ~7-9 wt% and ilmenite rim contain very minor Fe^{3+} (0.03-0.18 apfu) (Table-7.3f). Compositional profile of an opaque grain with ilmenite-pseudobrookite-pseudorutile symplectite shows a wide compositional variation of pseudorutile and microprobe analyses yield variable analytical totals in the range of 94.5% to 99.6% (Table-7.3f). Symplectic intergrowth of pseudorutile contains large range of TiO_2 (31.89 to 74.55 wt%) and FeO (21.67-60.41 wt%).

Table-7.3a: Representative chemical analyses for garnet (representative oxygen basis are given in tables). Mineral abbreviations are used after Whitney and Evans (2010). Cation calculations have been done following the procedure of Grew (1984).

Sample no	**SR43V**	**SR43V**	**SR43V**	**SR43V**	**SR43V**	**SR43V**	**SR43V**	**SR43V**	**SR43V**	**SR43V**
Mineral	*Grt*	*Grt*	*Grt*	*Grt*	*Grt*	*Grt*	*Grt*	*Grt*	*Grt*	*Grt*
Texture	*Host porphyroblast (Core)*					*Host porphyroblast (Rim)*				
Point no	40*	42*	49*	50*	46*	47*	48*	83*	87*	90*#
SiO_2	37.30	37.95	38.29	38.11	38.33	38.20	38.27	38.78	37.87	37.35
TiO_2	0.01	0.17	0.02	0.00	0.01	0.05	0.02	0.01	0.01	0.02
Al_2O_3	22.42	21.99	21.73	21.38	21.74	21.49	21.71	21.51	20.80	30.44
Cr_2O_3	0.05	0.02	0.01	0.02	0.05	0.06	0.08	0.06	0.00	0.05
CaO	1.21	1.07	1.01	1.02	0.95	1.05	0.98	0.92	0.91	0.77
FeO	33.95	34.50	33.88	34.03	36.36	35.42	34.65	35.68	35.60	28.63
MnO	0.38	0.40	0.30	0.35	0.52	0.51	0.51	0.50	0.42	0.43
MgO	5.75	5.61	5.76	5.71	4.26	4.56	4.28	4.73	4.50	3.81
Na_2O	0.03	0.00	0.03	0.00	0.04	0.00	0.00	0.06	0.06	0.00
K_2O	0.00	0.01	0.00	0.00	0.00	0.00	0.01	0.01	0.01	0.00
Total	101.09	101.73	101.04	100.62	102.25	101.34	100.50	102.26	100.16	101.50
Oxygen basis	**12**	**12**	**12**	**12**	**12**	**12**	**12**	**12**	**12**	**12**
Si	2.91	2.96	3.00	3.00	3.00	3.01	3.04	3.02	3.02	2.87
Ti	0.00	0.01	0.00	0.00	0.00	0.00	0.00	0.00	0.00	0.00
Al	2.06	2.02	2.00	1.98	2.00	1.99	2.03	1.98	1.95	2.76
Ca	0.10	0.09	0.08	0.09	0.08	0.09	0.08	0.08	0.08	0.06
Fe+2	2.11	2.20	2.21	2.22	2.37	2.35	2.41	2.34	2.36	2.34
Fe+3	0.11	0.05	0.01	0.02	0.00	-0.02	-0.11	-0.02	0.01	-0.50
Mg	0.67	0.65	0.67	0.67	0.50	0.54	0.51	0.55	0.53	0.44
Mn	0.03	0.03	0.02	0.02	0.03	0.03	0.03	0.03	0.03	0.03
Na	0.00	0.00	0.00	0.00	0.01	0.00	0.00	0.01	0.01	0.00
K	0.00	0.00	0.00	0.00	0.00	0.00	0.00	0.00	0.00	0.00
Total	8.00	8.00	8.00	8.00	8.00	8.00	8.00	8.00	8.00	8.00
X_{Alm}	*0.73*	*0.74*	*0.74*	*0.74*	*0.80*	*0.78*	*0.79*	*0.78*	*0.79*	*0.82*
X_{Prp}	*0.23*	*0.22*	*0.22*	*0.22*	*0.17*	*0.18*	*0.17*	*0.18*	*0.18*	*0.15*
X_{Grs}	*0.03*	*0.03*	*0.03*	*0.03*	*0.03*	*0.03*	*0.03*	*0.03*	*0.03*	*0.02*
X_{Sps}	*0.01*	*0.01*	*0.01*	*0.01*	*0.01*	*0.01*	*0.01*	*0.01*	*0.01*	*0.01*

*'= mineral composition used in conventional thermobarometry

#'= mineral composition used in reaction modeling

Table-7.3a (continued): Representative chemical analyses for garnet (representative oxygen basis are given in tables). Mineral abbreviations are used after Whitney and Evans (2010). Cation calculations have been done following the procedure of Grew (1984).

Sample no	**SR43V**	**SR43V**	**SR43V**	**SR43V**	**SR43V**	**SR43V**	**SR43V**	**SR43V**	**SR43V**	**SR43V**	**SR43V**	**SR43V**	**SR43V**	**SR43V**
Mineral	*Grt*	*Grt*	*Grt*	*Grt*	*Grt*	*Grt*	*Grt*	*Grt*	*Grt*	*Grt*	*Grt*	*Grt*	*Grt*	*Grt*
Texture	*Granular garnet (resembling host Grt porphyroblast) at the vein-wall*					*Inclusion-free Vein-garnet (Grt $_V$)*								
Point no	43	44	51	52	53	57	58	59	61	62	66	67	71	72
SiO_2	38.20	38.53	38.51	38.38	37.94	38.07	37.90	37.83	38.35	37.65	38.26	37.83	37.26	37.41
TiO_2	0.02	0.02	0.02	0.18	0.01	0.00	0.01	0.28	0.00	0.02	0.00	0.00	0.01	0.03
Al_2O_3	20.64	20.63	20.69	20.72	20.46	20.52	20.64	20.83	20.57	20.29	20.83	20.22	20.44	20.38
Cr_2O_3	0.02	0.01	0.04	0.01	0.03	0.00	0.02	0.01	0.00	0.01	0.05	0.03	0.04	0.02
CaO	1.30	2.37	1.17	1.15	1.07	1.17	1.31	1.69	1.17	1.16	0.99	1.04	1.05	1.13
FeO	34.37	33.69	34.14	34.24	34.20	35.06	34.80	32.60	35.24	35.13	35.67	35.39	35.12	35.55
MnO	0.47	0.52	0.40	0.42	0.46	0.47	0.43	0.40	0.40	0.38	0.43	0.53	0.45	0.49
MgO	5.41	5.12	5.56	5.51	5.81	5.08	5.20	4.82	5.24	4.99	4.66	5.05	4.98	4.58
Na_2O	0.00	0.03	0.00	0.07	0.00	0.04	0.00	0.02	0.00	0.00	0.00	0.01	0.00	0.00
K_2O	0.00	0.00	0.00	0.00	0.02	0.00	0.00	0.00	0.01	0.00	0.02	0.00	0.00	0.01
Total	100.43	100.93	100.52	100.67	99.99	100.41	100.33	98.47	100.98	99.64	100.90	100.10	99.36	99.61
Oxygen basis	**12**	**12**	**12**	**12**	**12**	**12**	**12**	**12**	**12**	**12**	**12**	**12**	**12**	**12**
Si	3.02	3.03	3.04	3.02	3.01	3.02	3.01	3.05	3.02	3.01	3.03	3.01	2.99	3.00
Ti	0.00	0.00	0.00	0.01	0.00	0.00	0.00	0.02	0.00	0.00	0.00	0.00	0.00	0.00
Al	1.92	1.91	1.92	1.92	1.91	1.92	1.93	1.98	1.91	1.91	1.94	1.90	1.93	1.93
Ca	0.11	0.20	0.10	0.10	0.09	0.10	0.11	0.15	0.10	0.10	0.08	0.09	0.09	0.10
Fe+2	2.24	2.19	2.26	2.24	2.20	2.27	2.25	2.31	2.28	2.29	2.36	2.29	2.27	2.32
Fe+3	0.03	0.03	-0.01	0.01	0.07	0.05	0.06	-0.11	0.04	0.06	0.00	0.07	0.08	0.06
Mg	0.64	0.60	0.65	0.65	0.69	0.60	0.61	0.58	0.62	0.60	0.55	0.60	0.60	0.55
Mn	0.03	0.03	0.03	0.03	0.03	0.03	0.03	0.03	0.03	0.03	0.03	0.04	0.03	0.03
Na	0.00	0.00	0.00	0.01	0.00	0.01	0.00	0.00	0.00	0.00	0.00	0.00	0.00	0.00
K	0.00	0.00	0.00	0.00	0.00	0.00	0.00	0.00	0.00	0.00	0.00	0.00	0.00	0.00
Total	8.00	8.00	8.00	8.00	8.00	8.00	8.00	8.00	8.00	8.00	8.00	8.00	8.00	8.00
X_{Alm}	*0.74*	*0.72*	*0.74*	*0.74*	*0.73*	*0.76*	*0.75*	*0.75*	*0.75*	*0.76*	*0.78*	*0.76*	*0.76*	*0.77*
X_{Prp}	*0.21*	*0.20*	*0.22*	*0.21*	*0.23*	*0.20*	*0.20*	*0.19*	*0.20*	*0.20*	*0.18*	*0.20*	*0.20*	*0.18*
X_{Grs}	*0.04*	*0.07*	*0.03*	*0.03*	*0.03*	*0.03*	*0.04*	*0.05*	*0.03*	*0.03*	*0.03*	*0.03*	*0.03*	*0.03*
X_{Sps}	*0.01*	*0.01*	*0.01*	*0.01*	*0.01*	*0.01*	*0.01*	*0.01*	*0.01*	*0.01*	*0.01*	*0.01*	*0.01*	*0.01*

Table-7.3b: Representative chemical analyses for garnet (representative oxygen basis are given in tables). Mineral abbreviations are used after Whitney and Evans (2010). Cation calculations have been done following the procedure of Grew (1984).

Sample no	SR43G	SR43G	SR43G	SR43G	SR43G	SR43G	SR43G	SR43G	SR43G	SR43G	SR43G	SR43G	SR43G	SR43G	SR43G	SR43G	SR43G	SR43G	SR43G	SR43G	SR43G	SR43G	SR43G	SR43G	SR43G	SR43G	SR43G	SR43G	SR43G1	SR43G1	SR43G1
Mineral	*Grt*	*Grt*	*Grt*	*Grt*	*Grt*	*Grt*	*Grt*	*Grt*	*Grt*	*Grt*	*Grt*	*Grt*	*Grt*	*Grt*	*Grt*	*Grt*	*Grt*	*Grt*	*Grt*	*Grt*	*Grt*	*Grt*	*Grt*	*Grt*	*Grt*	*Grt*	*Grt*	*Grt*	*Grt*	*Grt*	*Grt*
Texture	*Porphyroblast: Compositional profile (Rim to Core)*																												*triangular grains*		
Point no	103	104	105	106	107	108	109	110	111	112	113	114	115	116	117	118	119	120	121	122	123	124	125	126	127*	128*	78*#	79*	81*		
SiO_2	37.68	37.57	37.62	37.58	37.70	37.41	37.60	37.42	37.45	37.81	37.51	37.71	37.36	37.47	37.25	37.57	37.57	37.70	37.75	37.43	37.56	37.33	37.54	37.62	37.31	37.70	37.01	37.29	36.30		
TiO_2	0.04	0.03	0.03	0.04	0.02	0.04	0.03	0.03	0.01	0.01	0.05	0.02	0.02	0.02	0.01	0.04	0.02	0.02	0.00	0.02	0.02	0.00	0.02	0.03	0.00	0.00	0.02	0.01	0.04		
Al_2O_3	21.34	21.43	21.39	21.42	21.50	21.52	21.48	21.53	21.40	21.50	21.51	21.29	21.37	21.43	21.35	21.47	21.43	21.53	21.61	21.56	21.32	21.36	21.43	21.25	21.61	21.47	20.59	21.12	20.46		
Cr_2O_3	0.05	0.06	0.05	0.05	0.06	0.04	0.05	0.04	0.04	0.05	0.05	0.05	0.04	0.05	0.04	0.04	0.05	0.05	0.05	0.04	0.04	0.05	0.05	0.05	0.04	0.04	0.03	0.02	0.04		
CaO	1.67	1.75	1.69	1.71	1.69	1.72	1.68	1.64	1.69	1.71	1.67	1.70	1.71	1.72	1.66	1.73	1.69	1.70	1.71	1.66	1.65	1.68	1.68	1.67	1.69	1.64	1.75	1.74	1.72		
FeO	34.25	34.19	34.04	33.83	33.96	33.75	33.51	33.53	33.58	33.38	33.14	33.06	32.90	33.19	32.99	33.13	33.06	32.97	32.54	32.56	32.68	33.01	32.62	32.78	32.77	32.72	32.76	32.82	33.45		
MnO	1.21	1.10	1.10	1.05	1.04	1.00	1.05	1.00	0.96	0.98	0.99	0.93	0.98	0.91	0.97	0.86	0.92	0.89	0.94	0.80	0.86	0.83	0.84	0.80	0.80	0.82	0.94	1.02	0.97		
MgO	4.40	4.65	4.78	4.78	5.02	5.06	5.20	5.21	5.27	5.36	5.36	5.47	5.54	5.52	5.60	5.65	5.62	5.69	5.78	5.77	5.70	5.82	5.85	5.89	5.88	5.87	5.37	5.72	4.95		
Na_2O	0.00	0.00	0.00	0.00	0.00	0.00	0.00	0.00	0.00	0.00	0.06	0.00	0.00	0.00	0.00	0.00	0.00	0.00	0.00	0.00	0.00	0.02	0.00	0.03	0.00	0.00	0.00	0.02	0.01		
K_2O	0.06	0.03	0.02	0.01	0.02	0.00	0.00	0.01	0.00	0.00	0.00	0.00	0.02	0.01	0.00	0.01	0.00	0.01	0.00	0.00	0.00	0.00	0.00	0.00	0.00	0.00	0.02	0.00	0.01		
Total	100.70	100.81	100.72	100.46	101.00	100.53	100.60	100.40	100.39	100.80	100.35	100.23	99.93	100.32	99.87	100.49	100.36	100.56	100.37	99.86	99.82	100.10	100.04	100.11	100.09	100.26	98.49	99.76	97.96		
Oxygen basis	**12**	**12**	**12**	**12**	**12**	**12**	**12**	**12**	**12**	**12**	**12**	**12**	**12**	**12**	**12**	**12**	**12**	**12**	**12**	**12**	**12**	**12**	**12**	**12**	**12**	**12**	**12**	**12**	**12**		
Si	2.98	2.97	2.97	2.98	2.97	2.95	2.97	2.96	2.96	2.97	2.96	2.98	2.96	2.96	2.95	2.96	2.96	2.96	2.97	2.96	2.97	2.95	2.96	2.97	2.94	2.97	2.98	2.96	2.95		
Ti	0.00	0.00	0.00	0.00	0.00	0.00	0.00	0.00	0.00	0.00	0.00	0.00	0.00	0.00	0.00	0.00	0.00	0.00	0.00	0.00	0.00	0.00	0.00	0.00	0.00	0.00	0.00	0.00	0.00		
Al	1.99	2.00	1.99	2.00	1.99	2.00	2.00	2.00	1.99	1.99	2.00	1.98	1.99	1.99	1.99	1.99	1.99	1.99	2.00	2.01	1.99	1.99	1.99	1.97	2.01	1.99	1.95	1.97	1.96		
Fe+2	2.23	2.20	2.19	2.20	2.16	2.15	2.14	2.14	2.13	2.14	2.10	2.13	2.09	2.10	2.08	2.09	2.10	2.09	2.09	2.08	2.10	2.06	2.08	2.07	2.06	2.09	2.12	2.06	2.13		
Fe+3	0.04	0.06	0.06	0.04	0.07	0.08	0.07	0.08	0.09	0.06	0.08	0.06	0.09	0.09	0.10	0.09	0.08	0.07	0.06	0.07	0.06	0.12	0.08	0.09	0.11	0.07	0.09	0.12	0.14		
Mg	0.52	0.55	0.56	0.56	0.59	0.60	0.61	0.61	0.62	0.63	0.63	0.64	0.65	0.65	0.66	0.66	0.66	0.67	0.68	0.68	0.67	0.68	0.69	0.69	0.69	0.69	0.64	0.68	0.60		
Mn	0.08	0.07	0.07	0.07	0.07	0.07	0.07	0.07	0.06	0.07	0.07	0.06	0.07	0.06	0.07	0.06	0.06	0.06	0.06	0.05	0.06	0.06	0.06	0.05	0.05	0.05	0.06	0.07	0.07		
Ca	0.14	0.15	0.14	0.14	0.14	0.15	0.14	0.14	0.14	0.14	0.14	0.14	0.14	0.15	0.14	0.15	0.14	0.14	0.14	0.14	0.14	0.14	0.14	0.14	0.14	0.14	0.15	0.15	0.15		
Na	0.00	0.00	0.00	0.00	0.00	0.00	0.00	0.00	0.00	0.00	0.01	0.00	0.00	0.00	0.00	0.00	0.00	0.00	0.00	0.00	0.00	0.00	0.00	0.00	0.00	0.00	0.00	0.00	0.00		
K	0.01	0.00	0.00	0.00	0.00	0.00	0.00	0.00	0.00	0.00	0.00	0.00	0.00	0.00	0.00	0.00	0.00	0.00	0.00	0.00	0.00	0.00	0.00	0.00	0.00	0.00	0.00	0.00	0.00		
Total	8.00	8.00	8.00	8.00	8.00	8.00	8.00	8.00	8.00	8.00	8.00	8.00	8.00	8.00	8.00	8.00	8.00	8.00	8.00	8.00	8.00	8.00	8.00	8.00	8.00	8.00	8.00	8.00	8.00		
X_{Alm}	*0.76*	*0.75*	*0.74*	*0.74*	*0.74*	*0.73*	*0.73*	*0.72*	*0.72*	*0.72*	*0.72*	*0.72*	*0.71*	*0.71*	*0.71*	*0.71*	*0.71*	*0.71*	*0.71*	*0.71*	*0.70*	*0.70*	*0.70*	*0.70*	*0.70*	*0.70*	*0.71*	*0.70*	*0.72*		
X_{Prp}	*0.17*	*0.17*	*0.18*	*0.19*	*0.19*	*0.20*	*0.20*	*0.21*	*0.21*	*0.21*	*0.21*	*0.21*	*0.22*	*0.22*	*0.22*	*0.22*	*0.22*	*0.22*	*0.23*	*0.23*	*0.23*	*0.23*	*0.23*	*0.23*	*0.23*	*0.23*	*0.22*	*0.23*	*0.20*		
X_{Grs}	*0.05*	*0.05*	*0.05*	*0.05*	*0.05*	*0.05*	*0.05*	*0.05*	*0.05*	*0.05*	*0.05*	*0.05*	*0.05*	*0.05*	*0.05*	*0.05*	*0.05*	*0.05*	*0.05*	*0.05*	*0.05*	*0.05*	*0.05*	*0.05*	*0.05*	*0.05*	*0.05*	*0.05*	*0.05*		
X_{Sps}	*0.03*	*0.03*	*0.02*	*0.02*	*0.02*	*0.02*	*0.02*	*0.02*	*0.02*	*0.02*	*0.02*	*0.02*	*0.02*	*0.02*	*0.02*	*0.02*	*0.02*	*0.02*	*0.02*	*0.02*	*0.02*	*0.02*	*0.02*	*0.02*	*0.02*	*0.02*	*0.02*	*0.02*	*0.02*		

Table-7.3c: Representative chemical analyses for cordierite (representative oxygen basis are given in tables). Mineral abbreviations are used after Whitney and Evans (2010). Cation calculations have been done following the procedure of Grew (1984).

Association	**Association 1**													**Association 2**						
Sample no	**SR43V**	**SR43V**	**SR43V**	**SR43V**	**SR43V**	**SR43V**	**SR43V**	**SR43V**	**SR43V**	**SR43V**	**SR43V**	**SR43V**	**SR43V**	**SR43 G**	**SR43 G**	**SR43 G**	**SR43 G**	**SR43 G**	**SR43 G**	**SR43 G**
Mineral	*Crd*	*Crd*	*Crd*	*Crd*	*Crd*	*Crd*	*Crd*			*Crd*	*Crd*	*Crd*	*Crd*	*Crd*	*Crd*	*Crd*	*Crd*	*Crd*	*Crd*	*Crd*
Texture	*Inclusion within grt*	*Matrix recrystallized grain*						*porphyroblast Grt40*	*porphyroblast Grt42*	*Qz-Sil-Grt vein selvage*	*Qz-Sil-Grt vein selvage*	*Vein-Grt57*	*Vein-Grt62*	*Inclusion within grt*	*Inclusion within Oam*			*Matrix near Oam*		
Point no.	64	33*#	34*	77*	79*	82*	86	41*#	43*	36	40	56	65	97	4*	44#	82*	3*	16*	33*
SiO2	47.35	46.25	47.28	47.64	48.02	47.74	44.90	47.95	48.30	47.20	47.54	47.77	48.00	46.87	47.16	47.78	47.49	47.49	47.40	48.03
TiO2	0.00	0.00	0.00	0.00	0.02	0.00	0.00	0.00	0.00	0.00	0.00	0.01	0.00	0.01	0.00	0.01	0.01	0.02	0.01	0.03
Al2O3	31.96	33.21	33.22	31.25	31.83	31.58	30.53	32.47	32.60	31.80	31.70	31.58	31.81	32.65	33.14	33.35	32.86	33.33	33.14	33.42
Cr2O3	0.01	0.03	0.00	0.00	0.00	0.00	0.01	0.00	0.03	0.00	0.00	0.00	0.00	0.01	0.00	0.00	0.00	0.00	0.00	0.01
FeO	5.26	6.22	6.21	4.24	5.94	6.04	6.23	6.18	5.87	5.69	5.85	4.83	5.62	5.05	5.78	5.60	5.12	5.48	5.42	5.04
MnO	0.02	0.03	0.03	0.01	0.01	0.01	0.05	0.04	0.01	0.04	0.03	0.01	0.02	0.04	0.10	0.04	0.04	0.06	0.03	0.04
MgO	9.25	9.41	9.55	8.19	9.43	9.29	9.56	9.72	9.87	9.07	9.02	9.49	9.70	10.42	10.12	10.16	10.58	10.09	9.93	10.32
CaO	0.25	0.01	0.01	0.06	0.00	0.00	0.03	0.01	0.02	0.02	0.01	0.03	0.01	0.00	0.02	0.00	0.01	0.01	0.02	0.00
Na2O	0.17	0.13	0.07	1.10	0.06	0.20	1.00	0.13	0.12	0.05	0.14	0.26	0.09	0.14	0.07	0.05	0.12	0.01	0.15	0.07
K2O	0.28	0.01	0.00	1.95	0.07	0.30	0.23	0.01	0.00	0.23	0.01	0.43	0.01	0.00	0.00	0.00	0.00	0.02	0.00	0.00
Total	94.56	95.30	96.38	94.44	95.39	95.16	92.54	96.51	96.82	94.11	94.30	94.42	95.26	95.20	96.39	96.99	96.23	96.51	96.09	96.95
Oxygen basis	**18**	**18**	**18**	**18**	**18**	**18**	**18**	**18**	**18**	**18**	**18**	**18**	**18**	**18**	**18**	**18**	**18**	**18**	**18**	**18**
Si	5.00	4.85	4.91	4.99	5.04	5.02	4.81	4.97	4.98	5.02	5.05	5.04	5.03	4.89	4.88	4.91	4.90	4.90	4.91	4.93
Ti	0.00	0.00	0.00	0.00	0.00	0.00	0.00	0.00	0.00	0.00	0.00	0.00	0.00	0.00	0.00	0.00	0.00	0.00	0.00	0.00
Al	3.98	4.10	4.06	3.86	3.94	3.91	3.86	3.96	3.96	3.99	3.97	3.93	3.93	4.01	4.04	4.04	4.00	4.06	4.05	4.04
Fe+3	0.10	0.23	0.14	0.63	0.00	0.13	0.00	0.13	0.09	0.01	-0.04	0.11	0.02	0.23	0.22	0.15	0.22	0.14	0.16	0.11
Fe+2	0.37	0.32	0.40	-0.26	0.52	0.40	0.56	0.41	0.41	0.49	0.56	0.32	0.48	0.21	0.28	0.33	0.22	0.34	0.31	0.32
Mg	1.46	1.47	1.48	1.28	1.48	1.46	1.53	1.50	1.52	1.44	1.43	1.49	1.52	1.62	1.56	1.56	1.63	1.55	1.53	1.58
Mn	0.00	0.00	0.00	0.00	0.00	0.00	0.00	0.00	0.00	0.00	0.00	0.00	0.00	0.00	0.01	0.00	0.00	0.01	0.00	0.00
Ca	0.03	0.00	0.00	0.01	0.00	0.00	0.00	0.00	0.00	0.00	0.00	0.00	0.00	0.00	0.00	0.00	0.00	0.00	0.00	0.00
Na	0.04	0.03	0.01	0.22	0.01	0.04	0.21	0.03	0.02	0.01	0.03	0.05	0.02	0.03	0.01	0.01	0.02	0.00	0.03	0.01
K	0.04	0.00	0.00	0.26	0.01	0.04	0.03	0.00	0.00	0.03	0.00	0.06	0.00	0.00	0.00	0.00	0.00	0.00	0.00	0.00
Total	11.00	11.00	11.00	11.00	11.00	11.00	11.00	11.00	11.00	11.00	11.00	11.00	11.00	11.00	11.00	11.00	11.00	11.00	11.00	11.00
X_{Mg}	*0.80*	*0.82*	*0.79*	*0.78*	*0.74*	*0.79*	*0.73*	*0.79*	*0.79*	*0.74*	*0.72*	*0.82*	*0.76*	*0.89*	*0.85*	*0.83*	*0.88*	*0.82*	*0.83*	*0.83*

*'= mineral composition used in conventional thermobarometry

#'= mineral composition used in reaction modeling

Table-7.3d: Representative chemical analyses for biotite (representative oxygen basis are given in tables). Mineral abbreviations are used after Whitney and Evans (2010). Cation calculations have been done following the procedure of Grew (1984).

Association	**Association 1**																	
Sample no	**SR43V**	**SR43V**	**SR43V**	**SR43V**	**SR43V**	**SR43V**	**SR43V**	**SR43V**	**SR43V**	**SR43V**	**SR43V**	**SR43V**	**SR43V**	**SR43V**	**SR43V**	**SR43V**	**SR43V**	**SR43V**
Mineral	*Bt*	*Bt*	*Bt*	*Bt*	*Bt*	*Bt*	*Bt*	*Bt*	*Bt*	*Bt*	*Bt*	*Bt*	*Bt*	*Bt*	*Bt*	*Bt*	*Bt*	*Bt*
Texture	*Host matrix*						*Selvage or lamina ^ granular h ost Grt*				*Selvage or lamina^Type I vein*					*Matrix*		
Point no	1./6*	1./7*	1./8*	1./17*	1./18*	1./19	1./42#	1./43	1./44	1./45	1./53	1./54	1./55	1./56	1./57	91	92	93
SiO_2	34.81	35.03	35.46	35.75	35.61	35.97	35.26	34.71	35.51	35.04	35.21	35.53	35.29	35.46	35.02	35.88	32.67	36.75
TiO_2	3.07	2.82	3.21	2.99	2.68	2.65	3.34	3.77	3.55	3.57	3.15	2.73	3.24	3.24	2.91	2.47	2.63	2.96
Al_2O_3	17.45	17.77	17.42	17.94	17.68	17.7	17.2	16.76	17.2	18	17.19	17.64	17.4	17.45	17.26	17.64	15.55	18.28
Cr_2O_3	0.12	0.11	0.08	0.14	0.11	0.17	0.02	0.04	0.04	0.11	0.07	0.13	0.09	0.07	0.15	0.06	0.08	0.09
FeO	17.5	18.79	17.9	18.37	18.43	17.79	18.58	17.96	17.81	16.93	18.25	17.87	17.88	17.74	17.3	17.93	16.79	16.58
MnO	-0.08	0.06	0.06	-0.03	0	0.04	-0.04	0.02	0	0.02	0.07	0	0	-0.01	-0.01	0.02	0.02	0.02
MgO	10.5	10.84	10.63	11	10.82	10.98	10.63	10.21	10.42	9.99	10.7	10.91	10.62	10.46	10.8	11.18	9.37	10.18
CaO	-0.01	0.03	-0.01	0.01	0.01	0.03	0.03	0.02	0.02	0.19	0	-0.03	0.01	0.03	0.06	0.03	4.06	0.05
Na_2O	0.21	0.19	0.17	0.24	0.18	0.19	0.25	0.21	0.24	0.34	0.2	0.18	0.22	0.12	0.24	0.27	0.27	0.25
K_2O	8.63	8.08	8.87	8.57	9.08	8.75	8.75	9.06	9.03	7.52	8.7	8.93	9.08	8.86	8.74	8.61	8.11	7.68
Total	92.2	93.72	93.79	94.98	94.6	94.27	94.02	92.76	93.82	91.71	93.54	93.89	93.83	93.42	92.47	94.13	89.61	92.88
Oxygen basis	**11**	**11**	**11**	**11**	**11**	**11**	**11**	**11**	**11**	**11**	**11**	**11**	**11**	**11**	**11**	**11**	**11**	**11**
Si	2.96	2.94	2.97	2.96	2.97	2.99	2.96	2.95	2.98	2.97	2.96	2.97	2.96	2.98	2.97	2.99	2.91	3.05
Al-iv	0.84	0.88	0.83	0.86	0.87	0.84	0.83	0.80	0.80	0.80	0.84	0.85	0.83	0.82	0.84	0.84	0.74	0.80
Al-vi	0.91	0.87	0.89	0.89	0.87	0.89	0.87	0.88	0.90	0.99	0.87	0.88	0.89	0.91	0.89	0.89	0.79	0.99
Al-tot	1.75	1.76	1.72	1.75	1.74	1.73	1.70	1.68	1.70	1.80	1.71	1.74	1.72	1.73	1.73	1.73	1.63	1.79
Ti	0.20	0.18	0.20	0.19	0.17	0.17	0.21	0.24	0.22	0.23	0.20	0.17	0.20	0.20	0.19	0.15	0.18	0.18
Fe+2	1.25	1.32	1.25	1.27	1.28	1.24	1.30	1.28	1.25	1.20	1.28	1.25	1.25	1.25	1.23	1.25	1.25	1.15
Mn	-0.01	0.00	0.00	0.00	0.00	0.00	0.00	0.00	0.00	0.00	0.00	0.00	0.00	0.00	0.00	0.00	0.00	0.00
Mg	1.33	1.36	1.33	1.36	1.34	1.36	1.33	1.30	1.30	1.26	1.34	1.36	1.33	1.31	1.37	1.39	1.25	1.26
Ca	0.00	0.00	0.00	0.00	0.00	0.00	0.00	0.00	0.00	0.02	0.00	0.00	0.00	0.00	0.01	0.00	0.39	0.00
K	0.94	0.86	0.95	0.90	0.97	0.93	0.94	0.98	0.97	0.81	0.93	0.95	0.97	0.95	0.95	0.91	0.92	0.81
Na	0.03	0.03	0.03	0.04	0.03	0.03	0.04	0.03	0.04	0.06	0.03	0.03	0.04	0.02	0.04	0.04	0.05	0.04
P	0.00	0.00	0.00	0.00	0.00	0.00	0.00	0.00	0.00	0.00	0.00	0.00	0.00	0.00	0.00	0.00	0.00	0.00
F	0.00	0.00	0.00	0.00	0.00	0.00	0.00	0.00	0.00	0.00	0.00	0.00	0.00	0.00	0.00	0.00	0.00	0.00
Cl	0.00	0.00	0.00	0.00	0.00	0.00	0.00	0.00	0.00	0.00	0.00	0.00	0.00	0.00	0.00	0.00	0.00	0.00
SUM	8.45	8.45	8.45	8.46	8.49	8.45	8.47	8.47	8.45	8.34	8.47	8.48	8.48	8.44	8.47	8.47	8.58	8.30
X_{Mg}	*0.40*	*0.39*	*0.40*	*0.40*	*0.41*	*0.41*	*0.40*	*0.40*	*0.39*	*0.36*	*0.40*	*0.41*	*0.41*	*0.39*	*0.41*	*0.42*	*0.43*	*0.35*

*'= mineral composition used in conventional thermobarometry

#'= mineral composition used in reaction modeling

Table-7.3d (continued): Representative chemical analyses for biotite (representative oxygen basis are given in tables). Mineral abbreviations are used after Whitney and Evans (2010). Cation calculations have been done following the procedure of Grew (1984).

Association	**Association 2**														
Sample no	**SR43 G**	**SR43 G**	**SR43 G**	**SR43 G**	**SR43 G**	**SR43 G**	**SR43 G**	**SR43 G**	**SR43 G**	**SR43 G**	**SR43 G**	**SR43 G**	**SR43 G**	**SR43 G**	**SR43 G**
Mineral	*Bt*	*Bt*	*Bt*	*Bt*	*Bt*	*Bt*	*Bt*	*Bt*	*Bt*	*Bt*	*Bt*	*Bt*	*Bt*	*Bt*	*Bt*
Texture	*^Oam8*	*^Oam11*				*^Host Gedrite*				*^Grt85*	*^Grt90*	*incl. ^Grt91*		*^Grt103-135*	
Point no	7#	10	26#	27	28	37	38	41	43	88*	89*	93	98*	99*	100*
SiO_2	35.67	36.16	36.70	36.53	35.68	37.20	36.60	36.69	36.73	35.93	35.48	35.95	36.53	36.55	34.59
TiO_2	2.03	2.06	2.45	2.10	2.52	2.25	2.36	2.42	1.98	2.44	2.27	2.30	2.12	2.04	1.97
Al_2O_3	17.15	17.66	17.09	17.25	16.61	17.61	17.51	17.69	17.49	16.89	16.48	17.34	17.30	17.39	17.01
Cr_2O_3	0.12	0.16	0.06	0.06	0.06	0.12	0.11	0.13	0.12	0.12	0.11	0.12	0.11	0.12	0.13
FeO	15.90	15.75	15.27	14.98	15.41	15.87	15.76	15.79	15.86	14.56	15.80	15.32	14.91	15.42	17.16
MnO	0.00	0.00	0.03	0.00	0.05	0.00	0.00	0.02	0.06	0.01	0.00	0.04	0.01	0.01	0.04
MgO	14.01	14.20	14.43	14.36	14.33	14.10	13.87	14.04	14.09	14.67	15.08	14.89	15.09	15.10	15.05
CaO	0.02	0.00	0.00	0.01	0.01	0.01	0.03	0.02	0.02	0.03	0.00	0.03	0.00	0.01	0.03
Na_2O	0.25	0.14	0.32	0.29	0.19	0.22	0.27	0.21	0.16	0.21	0.05	0.25	0.30	0.25	0.17
K_2O	8.32	8.24	8.12	8.55	7.69	7.73	8.08	8.18	8.29	8.84	8.42	8.41	8.10	7.68	6.09
Total	93.47	94.38	94.46	94.13	92.53	95.09	94.59	95.19	94.80	93.71	93.70	94.63	94.47	94.58	92.24
Oxygen basis	**11**	**11**	**11**	**11**	**11**	**11**	**11**	**11**	**11**	**11**	**11**	**11**	**11**	**11**	**11**
Si	2.78	2.79	2.82	2.81	2.81	2.85	2.82	2.81	2.82	2.78	2.75	2.75	2.80	2.80	2.74
Ti	0.12	0.12	0.14	0.12	0.15	0.13	0.14	0.14	0.11	0.14	0.13	0.13	0.12	0.12	0.12
Al	1.57	1.60	1.55	1.57	1.54	1.59	1.59	1.60	1.58	1.54	1.51	1.57	1.56	1.57	1.59
Fe+3	-0.51	-0.60	-0.64	-0.55	-0.66	-0.78	-0.68	-0.67	-0.63	-0.48	-0.43	-0.48	-0.57	-0.63	-0.66
Fe+2	1.54	1.61	1.62	1.52	1.67	1.79	1.69	1.68	1.64	1.42	1.46	1.47	1.52	1.62	1.79
Mn	0.00	0.00	0.00	0.00	0.00	0.00	0.00	0.00	0.00	0.00	0.00	0.00	0.00	0.00	0.00
Mg	1.63	1.63	1.65	1.65	1.68	1.61	1.59	1.60	1.61	1.69	1.74	1.70	1.72	1.72	1.77
Ca	0.00	0.00	0.00	0.00	0.00	0.00	0.00	0.00	0.00	0.00	0.00	0.00	0.00	0.00	0.00
Na	0.04	0.02	0.05	0.04	0.03	0.03	0.04	0.03	0.02	0.03	0.01	0.04	0.04	0.04	0.03
K	0.83	0.81	0.80	0.84	0.77	0.76	0.79	0.80	0.81	0.87	0.83	0.82	0.79	0.75	0.61
Total	8.00	8.00	8.00	8.00	8.00	8.00	8.00	8.00	8.00	8.00	8.00	8.00	8.00	8.00	8.00
X_{Mg}	*0.51*	*0.50*	*0.51*	*0.52*	*0.50*	*0.47*	*0.48*	*0.49*	*0.50*	*0.53*	*0.54*	*0.50*	*0.53*	*0.52*	*0.50*

*' = mineral composition used in conventional thermobarometry

#' = mineral composition used in reaction modeling

Table-7.3e: Representative chemical analyses for orthoamphibole (representative oxygen basis are given in tables). Mineral abbreviations are used after Whitney and Evans (2010). Cation calculations have been done following the procedure of Leake et al. (2004).

Association	**Association 2**																		
Sample no	**SR43G**	**SR43G**	**SR43G**	**SR43G**	**SR43G**	**SR43G**	**SR43G**	**SR43G**	**SR43G**	**SR43G**	**SR43G**	**SR43G**	**SR43G**	**SR43G**	**SR43G**	**SR43G**	**SR43G**	**SR43G**	**SR43G**
Mineral	*Oam*	*Oam*	*Oam*	*Oam*	*Oam*	*Oam*	*Oam*	*Oam*	*Oam*	*Oam*	*Oam*	*Oam*	*Oam*	*Oam*	*Oam*	*Oam*	*Oam*	*Oam*	*Oam*
Texture	*poikiloblastic host Oam*									*Host #Bt37,38,41,43*					*#Grt78,79,81; Bt80*	*Vein Oam*			
Point no	1#	2	8#	9	14					39	40	42	46	47	83	22	24	29	30
SiO2	51.34	51.31	46.71	43.02	45.15	45.54	46.75	44.20	44.53	48.94	50.49	50.59	52.41	52.27	52.85	49.28	52.30	51.88	51.81
TiO2	0.04	0.07	0.27	0.30	0.18	0.34	0.21	0.20	0.23	0.14	0.11	0.05	0.04	0.04	0.05	0.45	0.08	0.25	0.10
Al2O3	3.22	2.48	9.90	14.48	12.40	12.43	11.39	13.67	13.51	7.30	4.76	2.28	2.53	2.60	2.07	6.24	2.90	2.97	3.19
Cr2O3	0.05	0.02	0.06	0.11	0.14	0.26	0.05	0.26	0.10	0.07	0.05	0.02	0.02	0.04	0.02	0.06	0.03	0.03	0.04
FeO	22.42	22.20	23.36	22.95	22.69	23.22	23.22	24.62	24.81	22.67	22.59	22.50	22.23	22.31	21.33	22.90	21.64	21.27	21.15
MnO	0.20	0.26	0.24	0.28	0.27	0.25	0.19	0.28	0.23	0.25	0.24	0.26	0.24	0.20	0.17	0.27	0.21	0.21	0.22
MgO	18.27	18.24	15.50	13.58	14.99	13.91	15.11	13.43	13.85	16.77	17.40	17.70	19.38	19.07	20.08	17.16	19.22	19.12	18.96
CaO	0.21	0.23	0.28	0.41	0.40	0.33	0.36	0.30	0.35	0.24	0.25	0.20	0.16	0.21	0.21	0.26	0.23	0.26	0.21
Na2O	0.18	0.15	1.02	1.79	1.49	1.22	1.21	1.42	1.25	0.63	0.48	0.15	0.14	0.17	0.05	0.81	0.21	0.20	0.30
K2O	0.01	0.07	0.00	0.00	0.01	-0.05	0.00	0.02	0.04	0.00	0.02	0.00	0.01	0.01	0.10	0.00	0.00	0.00	0.00
Total	95.94	95.04	97.34	96.90	97.71	97.43	98.53	98.46	98.98	97.01	96.39	93.76	97.15	96.91	96.93	97.43	96.82	96.17	95.96
Oxygen basis	**23**	**23**	**23**	**23**	**23**	**23**	**23**	**23**	**23**	**23**	**23**	**23**	**23**	**23**	**23**	**23**	**23**	**23**	**23**
Si	7.57	7.65	6.82	6.34	6.55	6.66	6.74	6.43	6.43	7.15	7.43	7.66	7.60	7.61	7.66	7.18	7.60	7.59	7.60
Al (IV)	0.43	0.35	1.18	1.66	1.45	1.34	1.26	1.57	1.57	0.85	0.57	0.34	0.40	0.39	0.34	0.82	0.40	0.41	0.40
Ti	0.00	0.00	0.00	0.00	0.00	0.00	0.00	0.00	0.00	0.00	0.00	0.00	0.00	0.00	0.00	0.00	0.00	0.00	0.00
Sum T	8.00	8.00	8.00	8.00	8.00	8.00	8.00	8.00	8.00	8.00	8.00	8.00	8.00	8.00	8.00	8.00	8.00	8.00	8.00
Al (VI)	0.13	0.08	0.52	0.85	0.67	0.80	0.68	0.77	0.73	0.40	0.25	0.06	0.03	0.06	0.01	0.25	0.10	0.10	0.15
Ti	0.00	0.01	0.03	0.03	0.02	0.04	0.02	0.02	0.02	0.02	0.01	0.01	0.00	0.00	0.01	0.05	0.01	0.03	0.01
Cr +3	0.01	0.00	0.01	0.01	0.02	0.03	0.01	0.03	0.01	0.01	0.01	0.00	0.00	0.00	0.00	0.01	0.00	0.00	0.00
Fe +3	0.29	0.24	0.59	0.62	0.72	0.48	0.53	0.71	0.76	0.41	0.29	0.27	0.35	0.32	0.30	0.47	0.27	0.25	0.23
Mg	4.01	4.05	3.37	2.98	3.24	3.03	3.25	2.91	2.98	3.65	3.81	3.99	4.19	4.14	4.34	3.72	4.16	4.17	4.14
Fe +2	0.56	0.62	0.48	0.51	0.34	0.63	0.52	0.56	0.49	0.51	0.63	0.67	0.42	0.48	0.35	0.50	0.45	0.45	0.46
Mn	0.00	0.00	0.00	0.00	0.00	0.00	0.00	0.00	0.00	0.00	0.00	0.00	0.00	0.00	0.00	0.00	0.00	0.00	0.00
Li	0.00	0.00	0.00	0.00	0.00	0.00	0.00	0.00	0.00	0.00	0.00	0.00	0.00	0.00	0.00	0.00	0.00	0.00	0.00
Sum C	5.00	5.00	5.00	5.00	5.00	5.00	5.00	5.00	5.00	5.00	5.00	5.00	5.00	5.00	5.00	5.00	5.00	5.00	5.00
Mg	0.00	0.00	0.00	0.00	0.00	0.00	0.00	0.00	0.00	0.00	0.00	0.00	0.00	0.00	0.00	0.00	0.00	0.00	0.00
Fe +2	1.92	1.91	1.78	1.70	1.70	1.73	1.75	1.73	1.74	1.84	1.86	1.91	1.93	1.92	1.94	1.81	1.91	1.91	1.90
Mn	0.02	0.03	0.03	0.03	0.03	0.03	0.02	0.03	0.03	0.03	0.03	0.03	0.03	0.02	0.02	0.03	0.03	0.03	0.03
Li	0.00	0.00	0.00	0.00	0.00	0.00	0.00	0.00	0.00	0.00	0.00	0.00	0.00	0.00	0.00	0.00	0.00	0.00	0.00
Ca	0.03	0.04	0.04	0.06	0.06	0.05	0.06	0.05	0.05	0.04	0.04	0.03	0.02	0.03	0.03	0.04	0.04	0.04	0.03
Na	0.03	0.02	0.14	0.20	0.21	0.19	0.17	0.19	0.17	0.09	0.07	0.02	0.02	0.02	0.01	0.11	0.03	0.03	0.04
Sum B	2.00	2.00	2.00	2.00	2.00	2.00	2.00	2.00	2.00	2.00	2.00	2.00	2.00	2.00	2.00	2.00	2.00	2.00	2.00
Ca	0.00	0.00	0.00	0.00	0.00	0.00	0.00	0.00	0.00	0.00	0.00	0.00	0.00	0.00	0.00	0.00	0.00	0.00	0.00
Na	0.03	0.02	0.15	0.31	0.21	0.16	0.17	0.21	0.18	0.09	0.07	0.02	0.02	0.02	0.01	0.11	0.03	0.03	0.04
K	0.00	0.01	0.00	0.00	0.00	-0.01	0.00	0.00	0.01	0.00	0.00	0.00	0.00	0.00	0.02	0.00	0.00	0.00	0.00
Sum A	0.03	0.03	0.15	0.31	0.21	0.15	0.17	0.21	0.18	0.09	0.07	0.02	0.02	0.03	0.03	0.11	0.03	0.03	0.04
TOTAL	15.03	15.03	15.15	15.31	15.21	15.15	15.17	15.21	15.18	15.09	15.07	15.02	15.02	15.03	15.03	15.11	15.03	15.03	15.04
Classification	*anth/cumm*	*anth/cumm*	*Ged*	*Ged*	*Ged*	*Ged*	*Ged*	*Ged*	*Ged*	*anth/cumm*	*anth/cumm*	*anth/cumm*	*anth/cumm*	*anth/cumm*	*anth/cumm*	*anth/cumm*	*anth/cumm*	*anth/cumm*	*anth/cumm*
X_{Mg}	*0.62*	*0.62*	*0.60*	*0.57*	*0.61*	*0.56*	*0.59*	*0.56*	*0.57*	*0.61*	*0.60*	*0.61*	*0.64*	*0.63*	*0.65*	*0.62*	*0.64*	*0.64*	*0.64*

#'= mineral composition used in reaction modeling

Table-7.3f: Representative chemical analyses for opaque minerals (representative oxygen basis are given in tables). Cation calculations have been done following the procedure of Grew (1984).

Association	**Association 2**											
Sample no	**SR43G**	**SR43G**	**SR43G**	**SR43G**	**SR43G**	**SR43G**	**SR43G**	**SR43G**	**SR43G**	**SR43G**	**SR43G**	**SR43G**
Mineral	*Rutile*	*Rutile*	*Ilmenite*	*Ilmenite*	*Ilmenite*	*Pseudobrookite*	*Pseudobrookite*	*Ilmenite*	*Ilmenite*	*Pseudobrookite*	*Pseudobrookite*	*Pseudobrookite*
Texture		*Matrix*					*Opaque symplectite profile*					
Point No.	17	20	5	6	50	51	52	54	56	57	58	60
SiO_2	0.13	0.45	0.11	0.00	2.48	1.13	1.15	0.62	0.92	0.89	0.71	1.06
TiO_2	89.24	90.25	47.42	48.22	42.55	31.89	36.81	49.69	60.47	33.93	22.93	33.43
Al_2O_3	0.05	0.16	0.05	0.03	1.11	0.49	0.47	0.21	0.35	0.46	0.37	0.48
Cr_2O_3	0.07	0.09	0.07	0.05	0.07	0.05	0.05	0.08	0.08	0.08	0.07	0.07
FeO	8.92	7.35	50.23	49.91	41.34	60.33	57.94	46.99	34.07	60.41	73.29	60.02
MnO	0.00	0.04	0.65	0.54	0.55	0.07	0.07	0.00	0.00	0.00	0.01	0.00
MgO	0.04	0.12	0.05	0.00	1.67	0.56	0.24	0.12	0.14	0.33	0.28	0.43
CaO	0.01	0.10	0.00	0.02	3.27	0.93	0.13	0.05	0.05	0.02	0.04	0.03
Na_2O	0.00	0.00	0.01	0.00	0.00	0.00	0.00	0.02	0.00	0.00	0.00	0.00
K_2O	0.01	0.01	0.07	0.01	0.00	0.00	0.02	0.00	0.02	0.03	0.00	0.01
Total	98.45	98.58	98.65	98.78	93.03	95.46	96.87	97.78	96.10	96.14	97.70	95.54
Oxygen basis	**3**	**3**	**3**	**3**	**3**	**5**	**5**	**3**	**3**	**5**	**5**	**5**
Si	0.00	0.01	0.00	0.00	0.06	0.04	0.04	0.02	0.02	0.03	0.03	0.04
Ti	1.79	1.81	0.91	0.92	0.83	0.92	1.06	0.96	0.91	0.98	0.65	0.97
Al	0.00	0.01	0.00	0.00	0.03	0.02	0.02	0.01	0.01	0.02	0.02	0.02
Fe+3	-1.59	-1.65	0.18	0.15	0.17	2.05	1.77	0.04	0.13	1.95	2.64	1.95
Fe+2	1.79	1.81	0.89	0.91	0.73	-0.11	0.08	0.97	0.91	-0.01	-0.35	-0.02
Mn	0.00	0.00	0.01	0.01	0.01	0.00	0.00	0.00	0.00	0.00	0.00	0.00
Mg	0.00	0.00	0.00	0.00	0.06	0.03	0.01	0.00	0.01	0.02	0.02	0.02
Ca	0.00	0.00	0.00	0.00	0.09	0.04	0.01	0.00	0.00	0.00	0.00	0.00
Na	0.00	0.00	0.00	0.00	0.00	0.00	0.00	0.00	0.00	0.00	0.00	0.00
K	0.00	0.00	0.00	0.00	0.00	0.00	0.00	0.00	0.00	0.00	0.00	0.00
Total	2.00	2.00	2.00	2.00	2.00	3.00	3.00	2.00	2.00	3.00	3.00	3.00

Table-7.3f (continued): Representative chemical analyses for opaque minerals (representative oxygen basis are given in tables). Cation calculations have been done following the procedure of Grew (1984).

Association	**Association 2**											
Sample no	**SR43G**	**SR43G**	**SR43G**	**SR43G**	**SR43G**	**SR43G**	**SR43G**	**SR43G**	**SR43G**	**SR43G**	**SR43G**	**SR43G**
Mineral	*Pseudobrookite*	*Pseudobrookite*	*Ilmenite*	*Ilmenite*	*Pseudorutile*	*Pseudorutile*	*Ilmenite*	*Ilmenite*	*Pseudorutile*	*Pseudorutile*	*Pseudorutile*	*Pseudorutile*
Texture	*Opaque symplectite profile*											
Point No.	62	63	65	67	68	69	70	71	72	73	74	75
SiO_2	0.91	0.95	1.37	0.92	0.96	0.70	1.06	1.11	0.79	1.03	1.21	1.02
TiO_2	34.72	39.57	47.13	46.69	57.03	60.27	50.97	46.81	65.74	62.23	57.91	61.38
Al_2O_3	0.51	0.52	0.53	0.42	0.39	0.27	0.45	0.44	0.30	0.44	0.54	0.49
Cr_2O_3	0.06	0.08	0.09	0.08	0.08	0.07	0.07	0.07	0.09	0.10	0.08	0.08
FeO	60.36	54.82	48.07	48.19	38.85	36.22	41.50	43.94	29.86	31.05	35.98	32.84
MnO	0.02	0.00	0.00	0.02	0.00	0.00	0.00	0.04	0.00	0.04	0.05	0.02
MgO	0.37	0.26	0.51	0.38	0.37	0.17	0.40	0.52	0.23	0.30	0.42	0.37
CaO	0.02	0.03	0.02	0.03	0.04	0.04	0.04	0.03	0.08	0.31	0.15	0.02
Na_2O	0.00	0.00	0.00	0.00	0.00	0.00	0.00	0.00	0.00	0.00	0.12	0.06
K_2O	0.00	0.00	0.02	0.00	0.03	0.00	0.00	0.01	0.00	0.01	0.00	0.03
Total	96.98	96.22	97.73	96.73	97.74	97.74	94.50	92.97	97.09	95.50	96.46	96.30
Oxygen basis	**5**	**5**	**3**	**3**	**9**	**9**	**3**	**3**	**9**	**9**	**9**	**9**
Si	0.03	0.04	0.03	0.03	0.06	0.05	0.02	0.03	0.05	0.07	0.08	0.07
Ti	0.99	1.15	1.00	0.90	2.77	2.94	1.18	1.02	3.25	3.11	2.84	3.04
Al	0.02	0.02	0.02	0.02	0.03	0.02	0.01	0.01	0.02	0.03	0.04	0.04
Fe+3	1.92	1.60	-0.08	0.11	2.31	2.00	-0.40	-0.11	1.37	1.60	2.13	1.76
Fe+2	0.01	0.17	1.01	0.92	-0.21	-0.03	1.19	1.03	0.27	0.12	-0.16	0.04
Mn	0.00	0.00	0.00	0.00	0.00	0.00	0.00	0.00	0.00	0.00	0.00	0.00
Mg	0.02	0.01	0.02	0.02	0.04	0.02	0.01	0.02	0.02	0.03	0.04	0.04
Ca	0.00	0.00	0.00	0.00	0.00	0.00	0.00	0.00	0.01	0.02	0.01	0.00
Na	0.00	0.00	0.00	0.00	0.00	0.00	0.00	0.00	0.00	0.00	0.02	0.01
K	0.00	0.00	0.00	0.00	0.00	0.00	0.00	0.00	0.00	0.00	0.00	0.00
Total	3.00	3.00	2.00	2.00	5.00	5.00	2.00	2.00	5.00	5.00	5.00	5.00

7.2.6. Reaction modeling

The textural relations derived from petrographic observation in the studied GCB can be depicted by mass-balanced chemical reactions using algebraic analysis of participating mineral compositions and mobile components in a metasomatic process (Fisher, 1989; Lang et al., 2004). They are inputted as phases in the program C-space, which employs the condition of mass balance and solves linear algebraic equations (Torres-Roldan et al., 2000). Detail of singular value decomposition (SVD) technique and matrix operations of C-space is discussed in several articles (Chowdhury et al., 2013; Karmakar et al., 2017; Lang et al., 2004). Representative mineral compositions used in C-space programming are presented in Table-7.3. In current study we followed the textural relations and mineral paragenesis of association-1 to derive series of mass balanced chemical reactions and examine the output for the following purposes:

a) the reactants and product phases, observed from petrographic study should lie on the opposite side of the equations.

b) the volume changes (ΔV) resulting from the reactions have been inspected. The molar volumes of the required phases are taken from the internally consistent thermodynamic dataset (hp02ver) by Holland and Powell (1998) using the updated version of computer program PERPLE_X (6.9.1) (Connolly, 2009, 2005).

Association-1: Biotite laminae and fibrolite formation

In the earliest granoblastic assemblage of granular garnet porphyroblast and cordierite matrix, biotite + sillimanite laminae can be formed by either of the two following processes:

As the amount of cordierite is the most significant difference between the mineral association inside and outside the laminae, they are formed from matrix cordierite by K and Fe-metasomatism by the following reaction:

1.00 **Cordierite** + 1.69 Fe^{2+} + 1.13 K^{+} = 1.16 **Biotite** + 1.03 **Sillimanite**

On the other hand, fibrolites are also seen to partially replace garnet porphyroblasts. Hence cordierite and garnet can both be involved in biotite laminae and fibrolite formation simultaneously by the following reaction:

5.12 **Garnet** + 4.37 **Cordierite** + 6.87 K^+ + 4.21 H^+ = 7.61 **Sillimanite** + 7.47 **Biotite** + 8.86 SiO_2

Association-1: Rim cordierite (Crd_2) formation

Second generation cordierite, which rims and replaces granular garnet porphyroblasts and biotite in the laminae can be formed by the following reactions with or without the involvement of biotite:

1.00 **Garnet** + 3.42 **Biotite +** 2.97 **Sillimanite** = 3.54 **Cordierite** + 7.34 Fe^{2+} + 3.36 K^+

Association-1: Chlorite formation

Chlorite replaces biotite grains by the following reaction:

1.86 **Biotite +** 2.05 Fe^{2+} + 6.16 H_2O = 1.00 **Chlorite** + 1.90 K^+

Association-2: Anthophyllite/gedrite formation

As poikiloblastic anthophyllite in the association 2 contains numerous cordierite inclusions, anthophyllite was formed via the following reaction:

1.29 **Cordierite** + 1.94 Fe^{2+} + 2.25 Mg^{2+} = 1.00 **Anthophyllite** + 4.83 Al^{3+}

Similarly, gedrites were probably formed via:

1.28 **Cordierite** + 1.46 Fe^{2+} + 1.45 Mg^{2+} = 1.00 **Gedrite** + 3.08 Al^{3+}

Association-2: Biotite formation

Biotite in association 2 replaces garnet and cordierite to variable extent and anthophyllite is observed to be intergrown with biotite. Hence biotite and anthophyllite can be simultaneously formed by the following reaction:

2.06 **Garnet** + 2.30 **Cordierite** + 3 H_2O + 2.09 K^+ + 3.75 Mg^{2+} = 1.36 **Anthophyllite** + 1.99 **Biotite** + 10.38 Al^{3+} + 7.11 SiO_2

From the reaction modeling, it is evident that K^+ and Fe^{2+} are mobilized in most of the balanced chemical reactions in association 1 whereas Al^{3+} is comparatively more mobile in the chemical reactions of association 2. These mobile elements got dissolved in the influxed fluid during metasomatism or chemical alteration of the GCB

and transported to the different reaction sites in both the studied association. Reaction modeling predicts that K^+ and Fe^{2+} are required for the biotite laminae formation whereas second generation rim cordierite ($Cordierite_2$) formation released these mobile elements. On the other hand, anthophyllite/gedrite formation or biotite + anthophyllite formation from the initial garnet + cordierite releases significant amount of Al^{3+} which can facilitate the formation of fibrolite and precipitation of vein prismatic sillimanite in adjacent locale of association 1.

7.2.7. Physical conditions of metamorphism

Conventional thermobarometry

The association garnet-cordierite-sillimanite-quartz has been used to constrain the P-T condition of the earliest granoblastic associations. To obtain equilibrium pressure and temperature, the Fe-Mg exchange garnet-cordierite thermometer (Bhattacharya et al., 1988)and the net garnet-cordierite-sillimanite-quartz barometer (Perchuk et al., 1985) have been employed. The garnet-cordierite-sillimanite barometer is susceptible to H_2O content in the cordierite structure (Bhattacharya et al., 1988; Martignole and Sisi, 1981; Newton, 1972). Depending upon the fluid content in the cordierite channel there can be an upward revision of pressure by 2-4 kbar. The barometric formulation that is used for the association garnet-cordierite-sillimanite-quartz involves anhydrous cordierite. So the estimated pressure value represent the minimum value of the equilibrium pressure as the cordierite in the studied rock contains significant fluid (Table-7.3c). .

Several garnet-cordierite pair concordant with textural studies is used and the results for "average value ± standard deviation" are presented in Table-7.4. For association 1, core garnet and distant matrix cordierite (Crd_1) yield temperature value between 660±10°C (Bhattacharya et al., 1988) and pressure value between 5±0.3 kbar (Perchuk et al. 1985). Rim garnet and coronal cordierite (Crd_2) constrain slightly lower temperature and pressure value [590±10°C (Bhattacharya et al., 1988) and 4±0.3 kbar (Perchuk et al. 1985)]. From association-2, porphyroblastic garnet and matrix cordierite constrain a temperature 610±10°C (Bhattacharya et al., 1988). As

sillimanite is absent in association 2, pressure condition cannot be constrained using conventional barometry for the association.

Temperature constrained from the T-X_{MgO} diagrams

The compatibility of the associations in the isobaric T-X_{MgO} (bulk rock

Table 7.4: P–T estimates of GCB, obtained using various conventional thermobarometers (T: °C, P: kbar).

Thermometer used	Rock type (Sample No.)	Mineral Assemblages (Grt core-matrix Crd1)	P_{ref}* (kbar)	Results		Thermometer used	Rock type (Sample No.)	Mineral Assemblages (Grt rim-Rim Crd2)	P_{ref}* (kbar)	Results	
				T (°C)	Avg					T (°C)	Avg
		Grt (40) - Crd (33)		653				Grt (47) - Crd (36)		596	
	SR43V	Grt (42) - Crd (34)		626			SR43V	Grt (48) - Crd (41)		595	
Grt-Crd[a]	(Association 1)	Grt (46) - Crd (77)	5	681	660±10	Grt-Crd[a]	(Association 1)	Grt (83) - Crd (43)	5	628	590±10
		Grt (49) - Crd (79)		702				Grt (87) - Crd (40)		610	
		Grt (50) - Crd (82)		618				Grt (90) - Crd (56)		574	
				T (°C)	Avg						
		Grt (78) - Crd (3)		584							
	SR43G	Grt (79) - Crd (16)		599							
Grt-Crd[a]	(Association 2)	Grt (81) - Crd (82)	5	627	610±10						
		Grt (127) - Crd (33)		636							
		Grt (128) - Crd (4)		600							

Barometer used			T_{ref}* (°C)	Results		Barometer used			T_{ref}* (°C)	Results	
				P (kbar)	Avg					P (kbar)	Avg
		Grt (40) - Crd (33)		5.1				Grt (47) - Crd (36)		3.8	
	SR43V	Grt (42) - Crd (34)		5.3			SR43V	Grt (48) - Crd (41)		3.9	
Grt-Crd-Sil-Qz[b]	(Association 1)	Grt (46) - Crd (77)	650	5.4	5 ± 0.3	Grt-Crd-Sil-Qz[b]	(Association 1)	Grt (83) - Crd (43)	600	4.4	4 ± 0.3
		Grt (49) - Crd (79)		4.7				Grt (87) - Crd (40)		4.4	
		Grt (50) - Crd (82)		4.8				Grt (90) - Crd (56)		3.9	

Grt: Garnet, Crd: Cordierite, Sil: Sillimanite, Qz: Quartz
Grt-Crd thermometer: [a] Bhattacharya et al. (1988)
Grt-Crd-Sil-Qz barometer: [b] Perchuk et al. (1985),

X_{MgO}=MgO/(MgO+FeO)) provides constraint on the minimum temperature and the bulk rock X_{MgO} that are required to stabilize the association garnet+cordierite$_1$+sillimanite (association 1). Since no trace of K-feldspar or any other K-bearing phases were stabilized with the granoblastic association garnet-cordierite$_1$-sillimanite, the following phases are chosen in the temperature range of 500°-900°C. In the system FeO-MgO-Al_2O_3-SiO_2–H_2O (FMASH) the diagrams are calculated with staurolite, chlorite, orthoamphibole, spinel, garnet, and cordierite along with sillimanite and quartz being excess phases. The T-X_{MgO} diagrams at different pressure sections are calculated using the computer program PERPLEX 6.9.1, working with internally consistent thermodynamic dataset of Holland and Powell (2002). Following solid solution models are used: chlorite, garnet and cordierite (White et al., 2014), orthoamphibole (Diener and Powell, 2012), staurolite and spinel (Holland and Powell, 1998).We chose isobaric (5, 7, 8, 9 kbar) sections for the calculation. The T-X_{MgO} diagrams (Fig. 7.7a) are computed for 'unconstrained bulk composition' (i.e. the diagrams are not dependent on the specific rock composition). Fig. 7.7a show that the mineralogy of the association 1 (garnet-cordierite-sillimanite-quartz) can only stable at temperature >~650°C in the X_{MgO} of the bulk composition between 0.2-0.8. At higher and lower X_{MgO} values of the bulk stabilize only cordierite and garnet respectively in the temperature range of ~650°-900°C. Fe-Mg spinel does not appear in the chosen temperature range except for a very small high temperature window at 5 kbar, neither spinel is observed in the studied rock. The minimum temperature and X_{MgO} of the bulk that is required for the appearance of garnet + cordierite + sillimanite + quartz increase with the pressure. However, the variation in the minimum temperature for the appearance of the association ranges between ~650°-700°C in the pressure range of 5-9 kbar. Within the X_{MgO} range of ~0.2-0.8, orthoamphibole is restricted within a very narrow temperature range that is bounded by garnet+cordierite (higher temperature) and staurolite+chlorite bearing association (lower temperature) at pressure ≥7 kbar. Since sillimanite is not recorded in the association 2, the T-X_{MgO} diagram cannot be applied for the association 2.

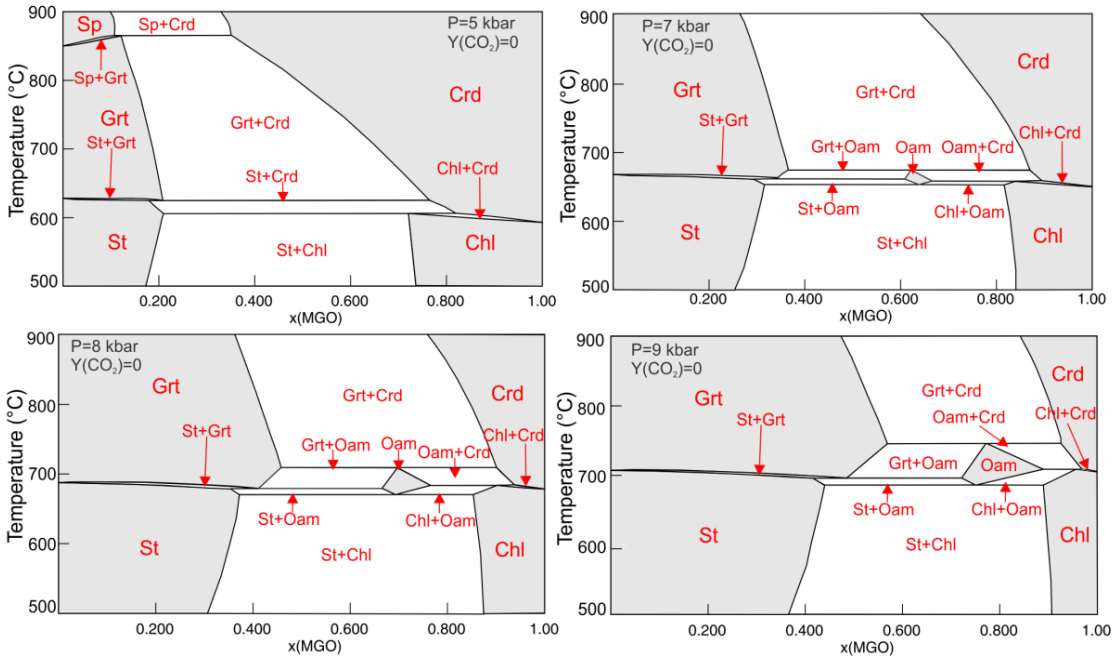

Figure 7.7. (a) Isobaric (5, 7, 8, 9 kbar) T-X_{MgO} diagrams show the compatibility of the associations and provide constraint on the minimum temperature and the bulk rock X_{MgO} that are required to stabilize the association garnet+cordierite$_1$+sillimanite (association 1).

Phase compatibilities in the Al_2O_3-FeO-MgO (AFM) diagram

For the system FMASH, the chosen phases and their solution models used for T-X_{MgO} diagram can also be used to compute phase compatibilities over a range of physical conditions with quartz and H_2O being the excess phases. The phase compatibilities in the AFM planes are calculated for different geothermal gradients (90°C/kbar to 140°C/kbar). The computed AFM compatibility diagrams are presented in Fig. 7.7b. Several points emerge from AFM diagrams. These are:

1. The garnet + cordierite can coexist with sillimanite or orthoamphibole only at temperature above 650°C along a range of geothermal gradients.

2. The association garnet + cordierite + sillimanite (association 1) occurs in more aluminous bulk composition than the association garnet + cordierite + orthoamphibole (association 2). Association 2 is more likely to be stable in magnesian

bulk. Occurrence of two contrasting associations 1 and 2 in the same out crop seems to be related to the local variation of the bulk rock compositions.

3. At temperature >700°C, garnet-cordierite-orthoamphibole is shifted to higher MgO but the stability of the association garnet-cordierite-sillimanite remain only marginally shifted to higher Al_2O_3 value with a prominent zone with only two phases garnet +cordierite (no sillimanite or orthoamphibole.

4. With decreasing geothermal gradient (140°C/kbar to 90°C/kbar) the first appearance or phase compatibility of the association garnet+ cordierite+ sillimanite and garnet+ cordierite+ orthoamphibole occurs at higher pressures.

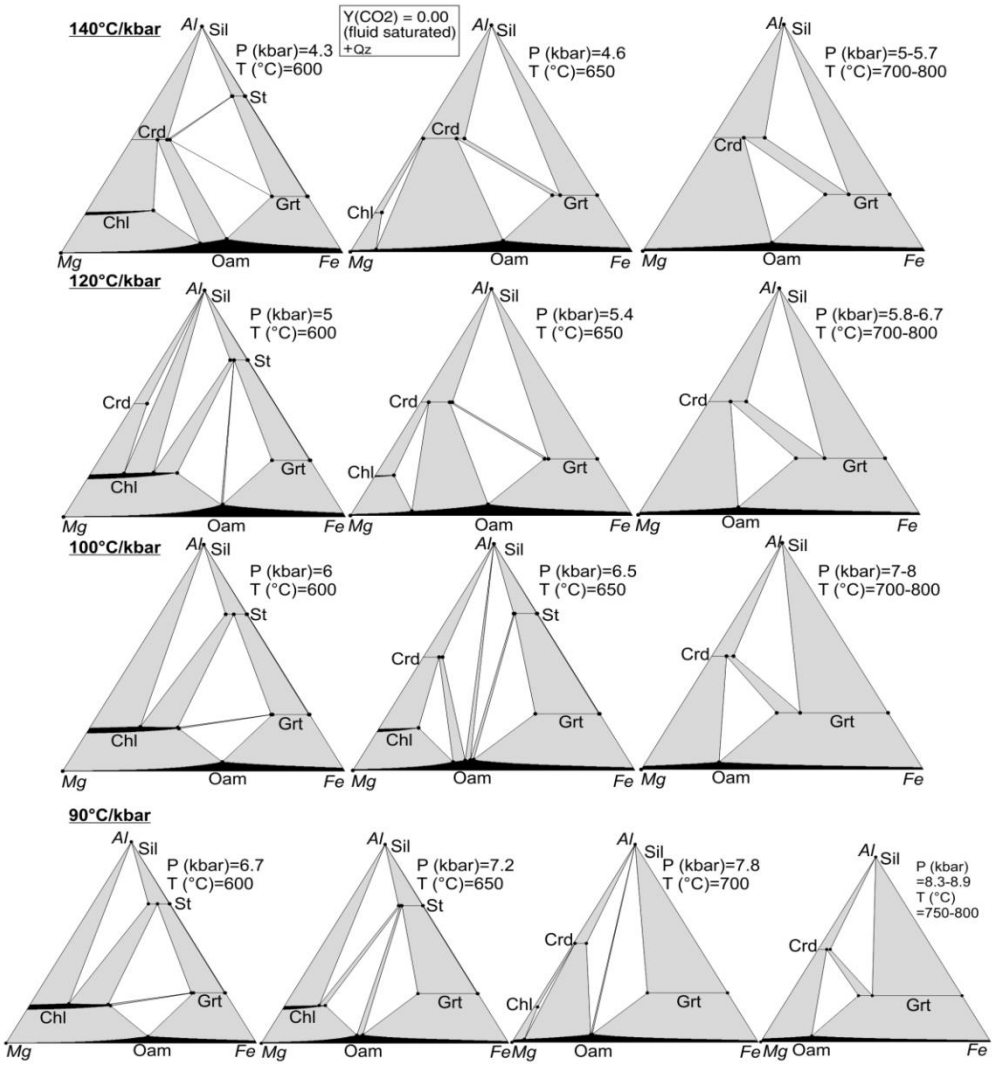

Figure 7.7 contd. (b) Phase compatibilities in the Al_2O_3-FeO-MgO (AFM) diagram, calculated for different geothermal gradients (90°C/kbar to 140°C/kbar).

P-T constrains from the microbulk of Association 1

As inferred earlier, garnet + cordierite + sillimanite represents the initial peak metamorphic association prior to the extensive metasomatism in Association-1. But the physical conditions of the metamorphism could not be constrained from the using the whole-rock bulk because of the high variance of the association resulting from element mobility and this typical granulite grade association has a large P-T stability field (Spear, 1993). Hence we attempted to constrain the physical condition of the final stabilized mineral association from association-1 in NCKFMASTH (Na_2O-CaO-K_2O-FeO-MgO-Al_2O_3-SiO_2-TiO_2-H_2O) system (Fig. 7.7c). As the studied samples contain numerous cross-cutting vein, we considered the modal percentage of only the host mineralogy (garnet + cordierite + biotite + sillimanite) to calculate the 'effective bulk' or 'microbulk' for the pseudosection analysis (Stüwe, 1997). We calculated 'effective bulk composition from the linear combinations of modal proportions of the minerals and respective mineral compositions in domains where low-variance associations are developed. Perple_X 6.9.1 program (Connolly, 2009) has been used along with the internally consistent thermodynamic dataset of Holland and Powell (2002). The following a-X relationships for chlorite, muscovite, biotite, garnet, cordierite, ilmenite and melt are taken from White et al. (2014). Considering the higher amount of hydrous cordierite (approximately 40 wt. %) and biotite (approximately 20 wt. %) in the host, 1 weight% H_2O is added with the calculated effective bulk for the computation.

The results show that the initial low-temperature chlorite + muscovite association terminates at around 620-650°C (Fig. 7.7c). Pseudosection analysis also reveals that garnet has a large P-T stability field but cordierite is restricted below ~7.5 kbar in the computed low-variance effective bulk. The observed mineral assemblage comprising garnet + cordierite + sillimanite + ilmenite + quartz + biotite, in association-1 stabilizes between 3.5-8 kbar and 650-800°C (Fig. 7.7c). Compositional isopleths of garnet rim composition and X_{Mg} of cordierite at immediate contact of garnet yield an intersection at around 4.5 kbar pressure and 650-700°C temperature (Fig. 7.7c).

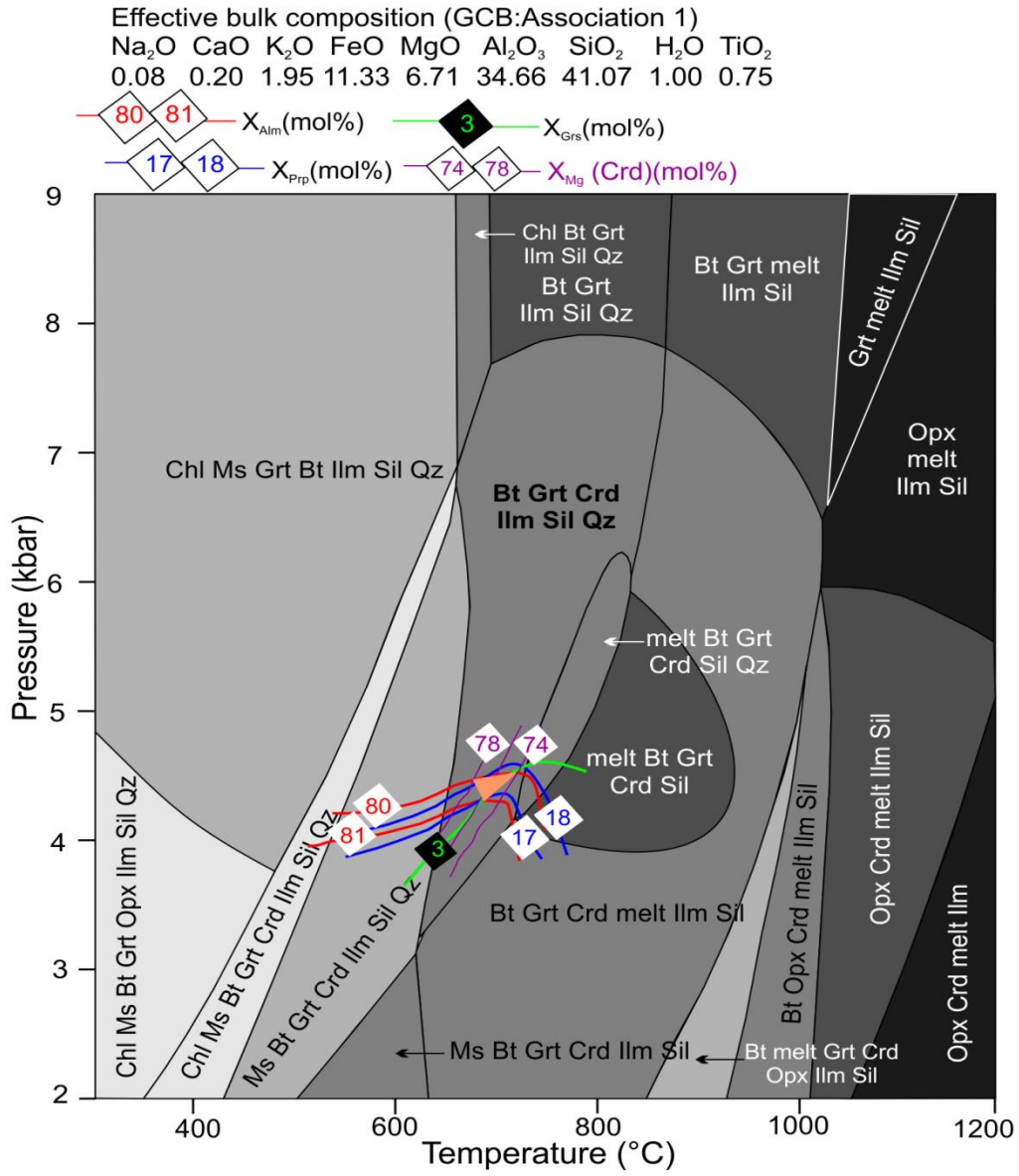

Figure 7.7 contd. (c) P-T pseudosection for the studied GCB (association 1) in NCKFMASTH system. Garnet rim composition ($Alm_{80\text{-}81}Py_{17\text{-}18}Grs_3$) and X_{Mg} of cordierite provide the physical condition of the final stabilized association at 4.5kbar-700℃.

CHAPTER 8

EVOLUTION OF THE META-MAFIC ROCKS

Lithological map and field petrology show that meta-mafic rocks, variable in appearance, grain size and mineralogy are present as one of the most extensive lithounit in the study area (Fig. 3.1). They are mostly present as dykes, cutting across other lithounits in the study area whereas at few places they show isolated boulder type outcrops covering vast fields in the area. The following sections present the salient features of the studied mafic lithounits of the MKGB.

8.1. Petrography of meta-mafic rocks

From the field study meta-mafic rocks are divided into two types: Type-I (coarse grained and devoid of foliation in the outcrop scale) and Type-I (fine grained and weak foliation discernable in the field). These two types are characterized by different mineralogical assemblage and distinctive textures under microscope. Microscopic features of these rocks are described in the following section and detailed modal abundance of the minerals is presented in Table-8.1. Mineral abbreviations used in the following sections are taken from Whitney and Evans (2010). BSE images provided in the petrographic figures are done using SEM-EDS at Department of Geological Sciences, Jadavpur University.

Table 8.1: Comparative modal abundance of the studied meta-mafic rocks. Mineral abbreviations are after Whitney & Evans (2010).

Sample no	Location of the sample	Minerals											
		Ol	Cpx	Opx	Pl	Ilm	Mgt	Grt	Amp	Bt	Qz	Ap	Sp
SR41A	N23°58.31'E82°39.80'	-	-	-	30	5	-	-	45	-	15	-	-
SR44	N23°58.44'E82°35.44'	-	10	30	30	10	-	-	20	-	-	-	-
SR46A	N23°58.96'E82°34.86'	15	10	20	25	10	5	-	5	10	-	-	P
SR46C		-	-	-	30	15	-	-	40	-	10	-	-
SR46D		-	-	-	30	10	-	-	40	-	15	-	-
SR46F		-	-	-	30	15	-	-	40	-	10	-	-
SR64Z	N23°59.63'E82°42.83'	-	-	-	25	10	-	10	35	-	15	-	-
SR76	N23°58.95'E82°34.68'	-	10	20	25	10	10	-	5	10	-	10	P
SR82B	N23°58.77'E82°34.62'	-	-	-	35	15	-	-	45	-	-	-	-
SR87Z	N23°53.28'E82°38.58'	-	-	10	30	10	-	-	30	20	-	-	-
SR93	N23°54.64'E82°34.14'	-	-	15	30	5	-	10	20	15	-	-	-
SR94/2	N23°59.85'E82°40.92'	-	10	15	25	10	-	8	20	12	-	-	-
SR94/7		-					-				-	-	-
SR103A	N23°57.51'E82°34.23'	-	-	25	35	15	-	-	-	25	-	-	-
SR116	N24°0.25'E82°56.45'	-	-	-	35	15	-	-	45	-	-	-	-
SR117C		-	-	-	30	10	-	-	30	20	-	-	-
SR147	N23°55.11'E82°40.44'	15	10	20	25	10	5	-	5	10	-	-	P

8.1.1. Type-I

Types-I meta-mafic rocks are comparatively coarse grained (2-5 mm) and contain olivine + clinopyroxene + orthopyroxene + plagioclase + ilmenite + magnetite + amphibole + biotite ± apatite. Depending upon the presence of apatite and intact olivine grains and difference in texture under microscope type-I rocks are further classified into two types.

Type-IA

Type-IA samples contain olivine + clinopyroxene + orthopyroxene + plagioclase + ilmenite + magnetite + amphibole + biotite + spinel. They dominantly show subophitic to intergranular texture which corroborates the observation depicted in the outcrop and hand specimen scale. Primary plagioclase laths are varied in grain size from 1 mm upto 5 mm and often form triangular interstitial spaces occupied by pyroxenes (Fig. 8.1.1a, b). On the contrary, fine grains plagioclase laths (<1 mm) are partially to completely surrounded by clinopyroxenes forming sub-ophitic to ophitic texture (Fig. 8.1.1a, b).

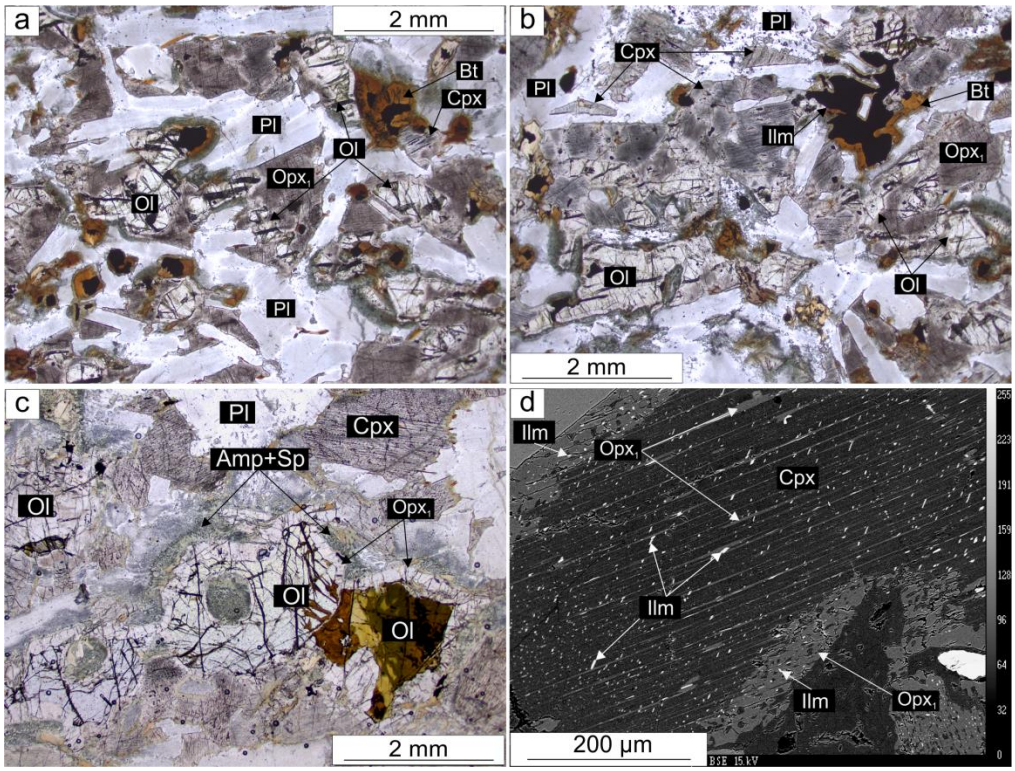

Figure 8.1.1. (a, b) Olivine, clinopyroxene and plagioclase grains are showing sub-ophitic to intergranular texture in Type-IA meta-mafic rocks. Olivine grains are highly fractured and both the pyroxenes and plagioclase grains are clouded. Ilmenite grains are partially rimmed by biotite. (c) Altered olivine grains are observed in few samples. (d) Clinopyroxene contains exsolved orthopyroxene (Opx_1) lamellae, very fine ilmenite inclusions oriented in two different directions and is replaced by orthopyroxene.

Coarse olivine and clinopyroxene grains are showing intergranular texture with large plagioclase laths (Fig. 8.1.1a, b). Olivine grains are highly fractured and mostly unaltered except for a few places where they are partially altered (Fig. 8.1.1c). Primary ilmenite and magnetites form individual grains along with olivine, pyroxenes and plagioclase. Clinopyroxenes contain very fine ilmenite inclusions at two different orientations and exsolved orthopyroxene (Opx_1) lamellae (Fig. 8.1.1d). BSE images depict that plagioclase laths contain very fine ilmenite grains which are the most probable reason of their clouded appearance under plane polarized light (Fig. 8.1.1a, b, f, g). BSE images also confirm that clouded orthopyroxene (Opx_1) grains which engulf and replace olivine and clinopyroxenes (Fig. 8.1.1a, b), contain numerous ilmenite inclusions. Olivine grains are often rimmed by double-layered coronae consisting of multiple mineral associations (Fig. 8.1.1h-m).

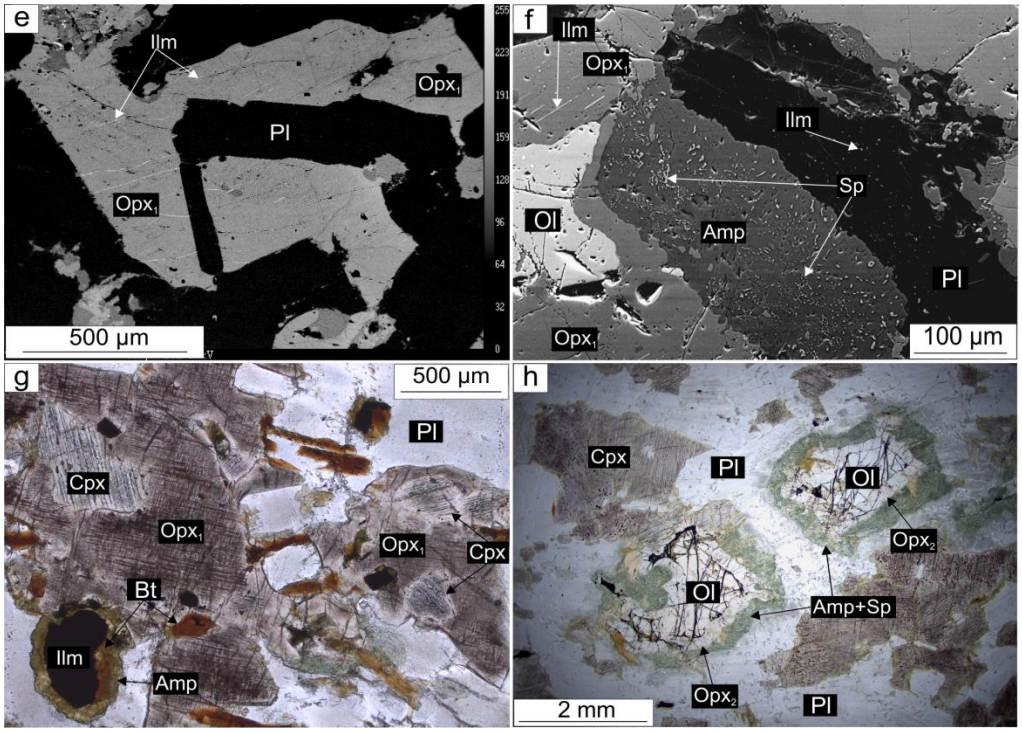

Figure 8.1.1 contd. (e) Intergranular texture depicted by pyroxene and plagioclase. Orthopyroxene (Opx_1) contains very fine ilmenite inclusions. (f) BSE image showing plagioclase grains contain very fine ilmenite inclusions, responsible for their clouded appearance under PPL in Fig. 8.1.1a, b. (g) Both the pyroxenes and plagioclase laths are clouded. Clinopyroxene grains are engulfed and replaced by orthopyroxene (Opx_1). (h) Double corona between olivine and plagioclase. Inner corona consists of orthopyroxene (Opx_2) and outer corona contains symplectic spinel within amphibole.

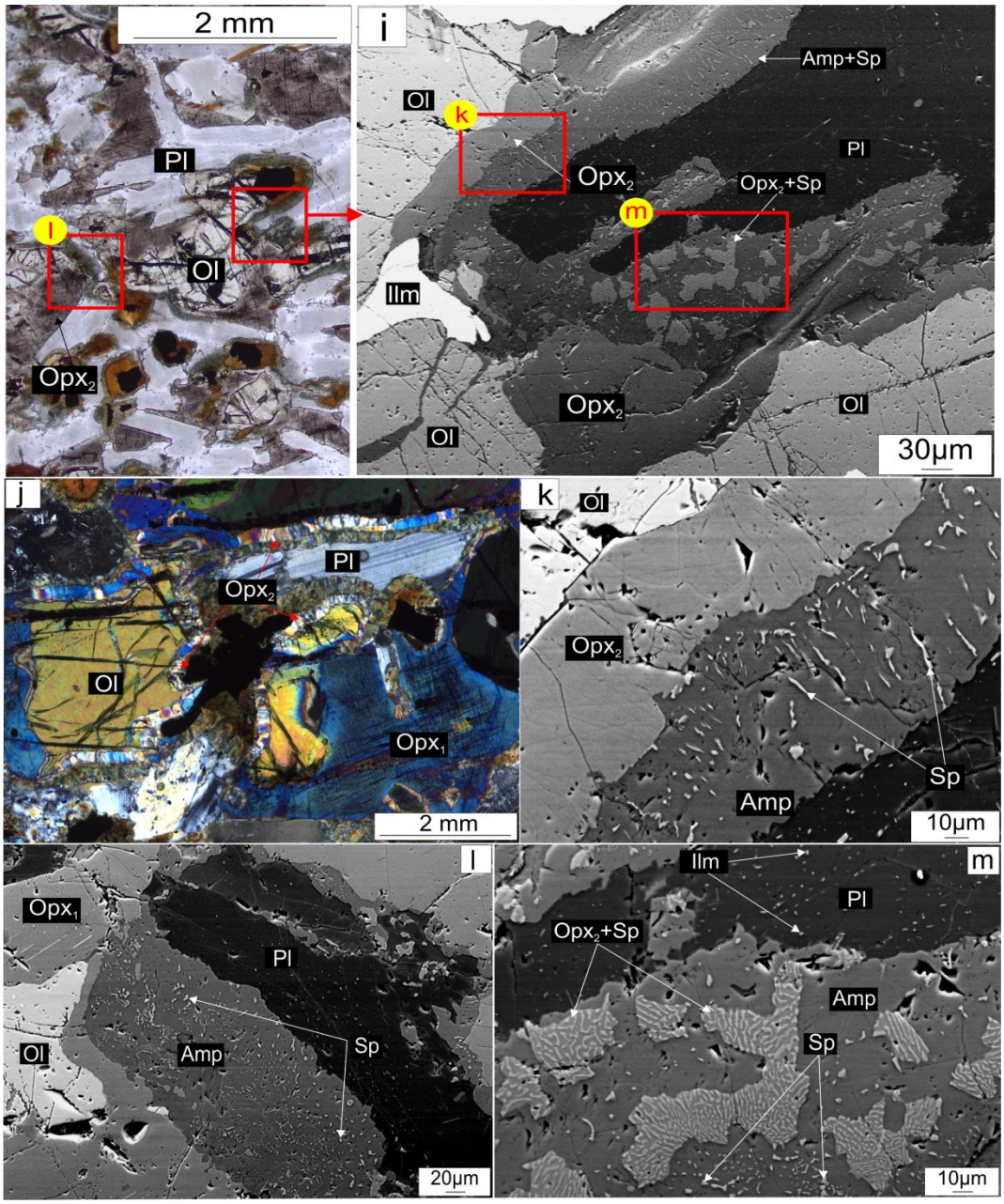

Figure 8.1.1 contd. Red squares in the PPL and BSE image in Fig. 8.1.1i, k, l, m. (i) BSE image of the double corona between olivine and plagioclase. Inner corona is monomineralic and consists of orthopyroxene (Opx_2). Amphibole in the outer corona contains heterogeneously distributed symplectic spinel. This outer corona also contains irregular patches of symplectic orthopyroxene (Opx_2) + spinel association. (j) Orthopyroxenes (Opx_2) in the inner corona are columnar and scale-like. (k) Enlarged BSE of the olivine double corona. (l) Spinel grains are heterogeneously distributed within the amphibole of the outer corona. (m) Enlarged BSE of the symplectic orthopyroxene (Opx_2) + spinel within amphibole of the outer corona.

The layer/corona at the immediate contact (inner corona) of the olivine is monomineralic and consists of orthopyroxene (Opx_2) (devoid of any ilmenite-inclusions) appearing scale-like or columnar perpendicular to the rim wall (Fig. 8.1.1i, j). The outer layer of coronae (outer corona), at the contact of the plagioclase, consists of vermicular spinel (discernable in scanning electron microscope and confirmed from SEM-EDS analysis) with a base of amphibole (Fig. 8.1.1i, k-m). These spinel intergrowths are heterogeneously distributed within the amphibole rims (Fig. 8.1i, k-m). Often irregular patches of orthopyroxene (Opx_2)-spinel symplectites are also observed within the amphibole-spinel coronae (Fig. 8.1.1i, m). Primary ilmenite and magnetite grains are always partially or completely surrounded by double-layered coronae consisting of biotite and amphibole or amphibole-spinel with occasional irregular patches of orthopyroxene (Opx_2)-spinel (Fig. 8.1.1n, o).

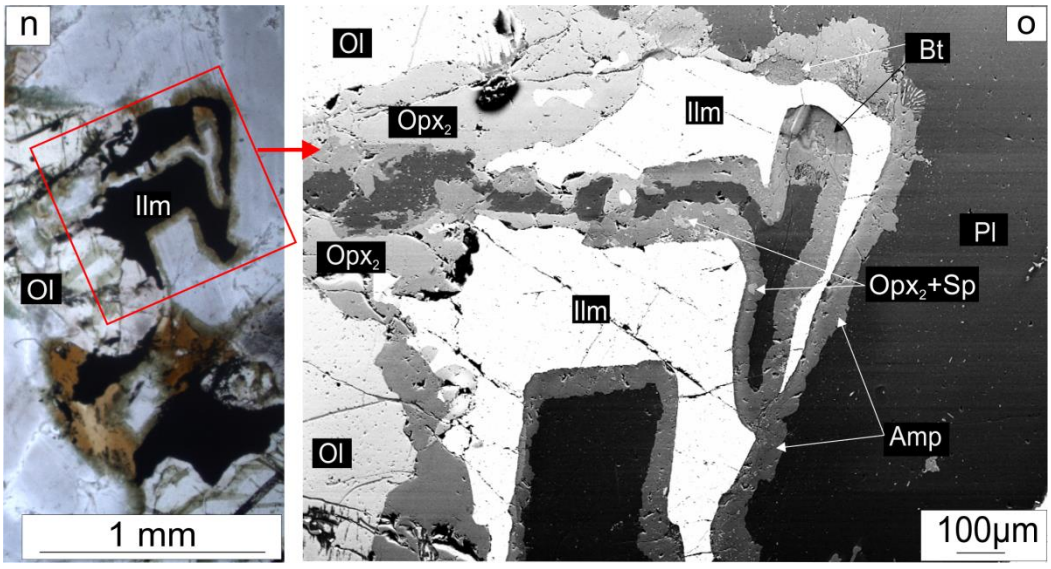

Figure 8.1.1 contd. (n) Ilmenite rimmed by biotite and amphibole. (o) Enlarged BSE image of the red square showing in Fig. 8.1.1n. Double corona between ilmenite and plagioclase. Inner biotite partially rims ilmenite whereas outer corona of amphibole completely rims the grain. Irregular patches of symplectic orthopyroxene (Opx_2) + spinel and very few individual worm-like spinel grains are also present within the amphibole of the outer corona.

Type-IB:

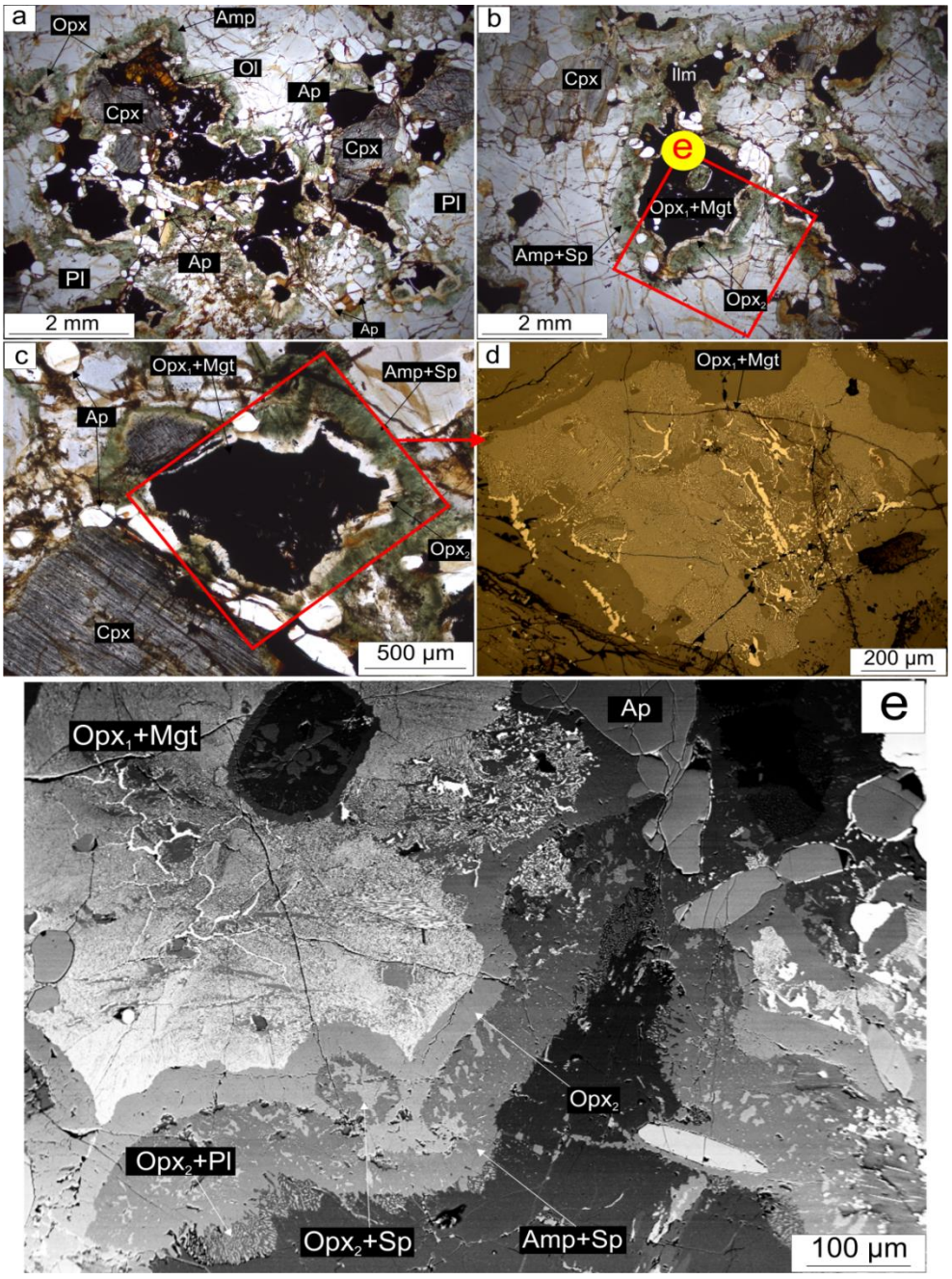

Figure 8.1.2. (a, b) Type-IB samples under PPL consisting of clinopyroxene, orthopyroxene, plagioclase, apatite, ilmenite-magnetite which show interlocking texture. Large opaque grains, rimmed by double corona of orthopyroxene (Opx_2) (inner corona) and amphibole (outer corona) are symplectic association of orthopyroxene-magnetite as revealed by transmitted light and BSE images in Fig. 8.1.2d, e. (c) Orthopyroxene (Opx_1)-magnetite symplectic assemblage pseudomorphs olivine. Orthopyroxene (Opx_1)-magnetite grains are replaced by double coronae. (d) Image under transmitted light Fig. 8.1.2c. Symplectic magnetites are variable in size. (e) Enlarged BSE image of the red square area in Fig. 8.1.2b. Inner corona of orthopyroxene (Opx_1) + magnetite and plagioclase consists of orthopyroxene (Opx_2). Outer corona is made up of amphibole with occasional spinel symplectites and contains irregular patches of symplectic orthopyroxene (Opx_2) + spinel.

Type-IB samples contain Clinopyroxene + orthopyroxene + plagioclase + magnetite + ilmenite + apatite ± olivine + amphibole + biotite and they show interlocking texture and lack of subophitic pattern between clinopyroxene and plagioclase (Fig. 8.1.2a, b). In most of the cases, olivine grains are not intact. They are almost completely pseudomorphed by the intergrowth of orthopyroxene (Opx_1)-magnetite, advocated by the presence of relict of the former mineral within the intergrowth (Fig. 8.1.2b-d). These intergrowths are highly variable in terms of grain size, arrangement and pattern (Fig. 8.1.2c-i). Under transmitted light (Fig. 8.1.2a-c) most of these grains appear opaque due to the presence of disseminated magnetite hence their characteristics are studied under reflected light (Fig. 8.1.2d, h) and scanning electron microscope (Fig. 8.1.2e-g, i). Some of the magnetite grains in the orthopyroxene (Opx_1)-magnetite association are symplectic (worm-like or vermicular; whereas at places magnetite grains are lamellar (Fig. 8.1.2f-i). Both these vermicular and lamellar magnetite grains exist within the same single/individual grain mass of orthopyroxene (Opx_1) (i.e. previously primary olivine) (Fig. 8.1.2f-i). Magnetite grains of different size, arrangement and pattern seem to form different clusters or zones in the same orthopyroxene (Opx_1) base and often coalesce together and forms patches and veins at places (Fig. 8.1.2g-i). Lamellar and vermicular magnetites are either parallel or perpendicular to the veins of same and never cut across them (Fig. 8.1.2g,

h). Few zones of the pseudomorphed olivine grains are devoid of magnetite where only orthopyroxene (Opx_1) is present (Fig. 8.1.2h, i).

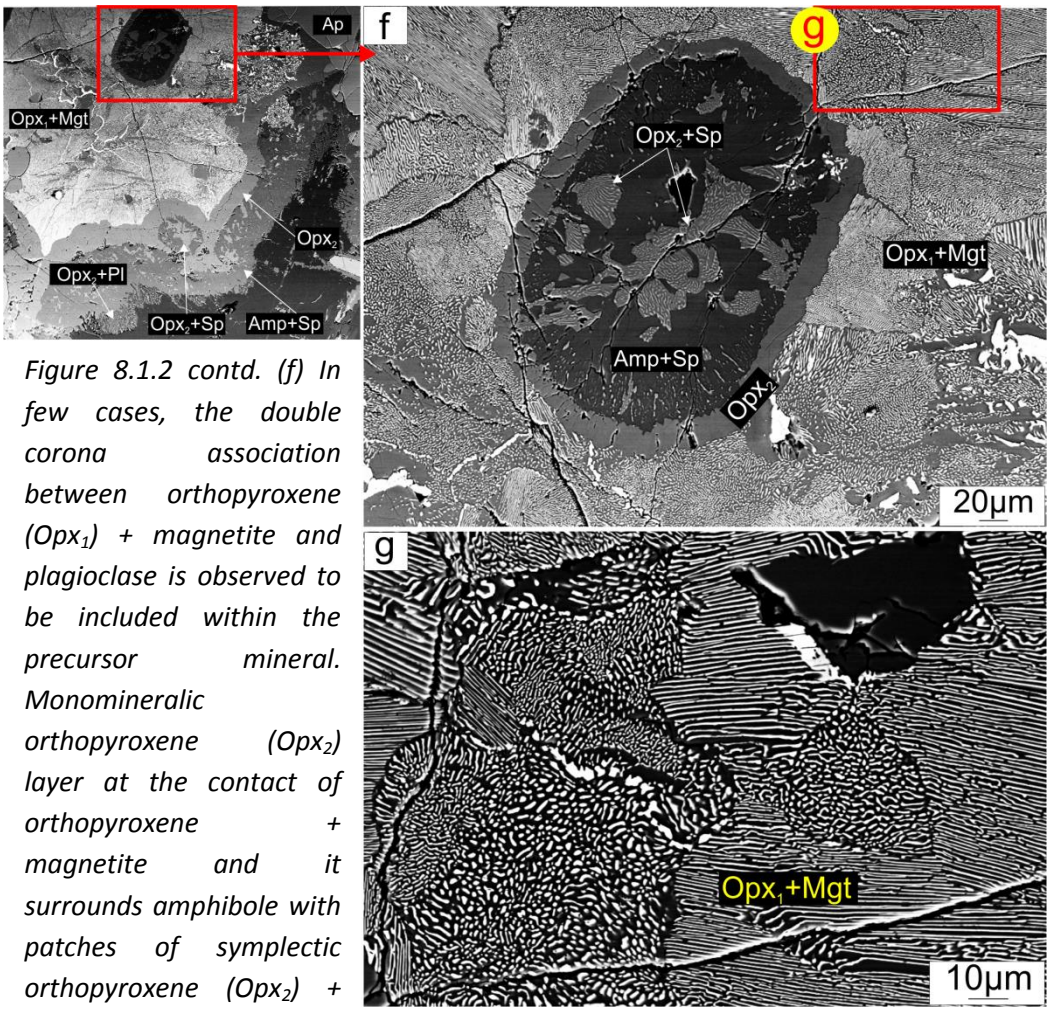

Figure 8.1.2 contd. (f) In few cases, the double corona association between orthopyroxene (Opx_1) + magnetite and plagioclase is observed to be included within the precursor mineral. Monomineralic orthopyroxene (Opx_2) layer at the contact of orthopyroxene + magnetite and it surrounds amphibole with patches of symplectic orthopyroxene (Opx_2) +

(g) Magnetite grains of different size, arrangement and pattern seem to form different clusters or zones in the same orthopyroxene (Opx_1) base and often coalesce together and forms patches and veins at places

Primary plagioclase grains are varied in shape from elongated laths to polygonal. Primary apatite grains of various shape and size are clustered and associated with clinopyroxene, plagioclase, ilmenite-magnetite and orthopyroxene (Opx_1)-magnetite (Fig. 8.1.2a, b). Primary ilmenite and magnetite form individual grains whereas at places magnetite contains band-like or lamellar ilmenite intergrowths (Fig. 8.1.2j). The magnetite and ilmenite grains are partially surrounded by biotite which is again rimmed by amphibole-spinel ± orthopyroxene (Opx_2)-plagioclase corona (Fig.

8.1.2k). Similar to type-IA, primary clinopyroxene and plagioclase grains are clouded due to occurrence of ilmenite intergrowths. Clinopyroxene grains contain exsolved

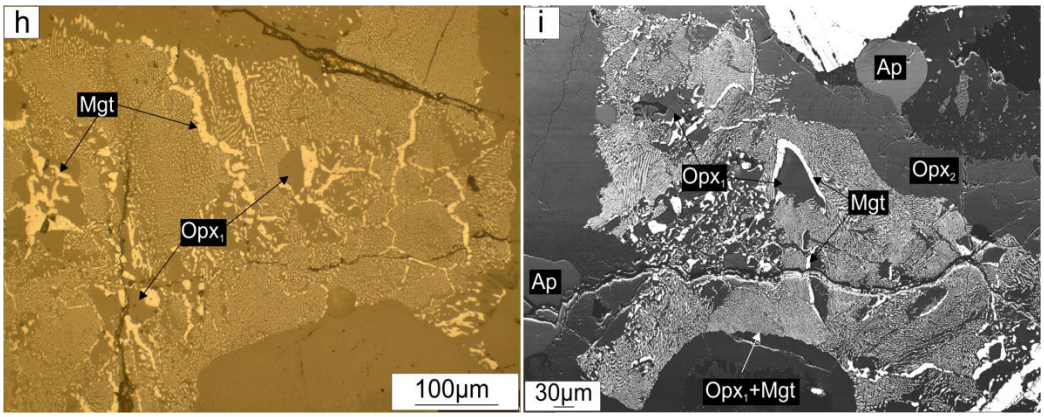

Figure 8.1.2 contd. (h) Transmitted light image of orthopyroxene (Opx_1) + magnetite association. Magnetites form veins and fine globular to worm-like magnetites never cut across these veins. Veins divide this pseudomorphed association in several clusters. (i) BSE image of orthopyroxene (Opx_1) + magnetite association. Some magnetite-free orthopyroxene (Opx_1) grains are present within this pseudomorphed association.

orthopyroxene (Opx_1) lamellae and are partially replaced by orthopyroxene in few occasions. Primary olivine (now pseudomorphed into orthopyroxene (Opx_1)-magnetite) is rimmed by double-layered coronae [orthopyroxene (Opx_2) and amphibole + spinel with irregular patches of orthopyroxene + spinel] and primary ilmenite-magnetite grains are often associated with double-layered coronae [biotite and amphibole + spinel with rare patches of orthopyroxene (Opx_2) + spinel] (Fig. 8.1.2a-c, e, l-n). At places irregular fan-shaped orthopyroxene (Opx_2)-plagioclase symplectites grows at the contact of amphibole+ spinel and primary plagioclase (Fig. 8.1.2l). Occasionally, the same two layered coronae [Orthopyroxene (Opx_2) and amphibole + spinel] are present well within the pseudomorphed olivine grains which possibly indicate presence of early inclusion of plagioclase within olivine (Fig. 8.1.2b, e, f).

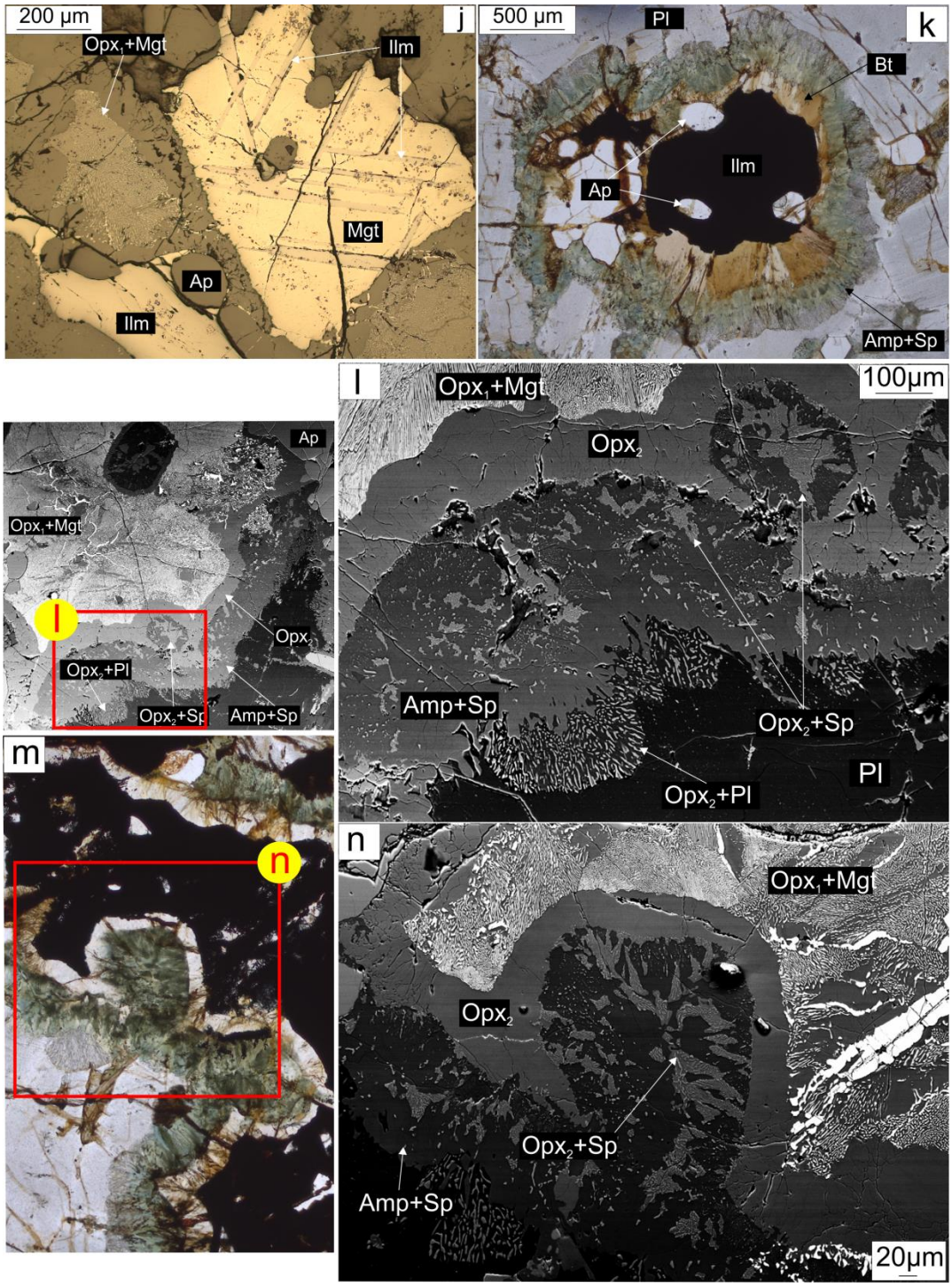
200 µm
j
Opx1+Mgt
Ilm
Mgt
Ap
Ilm
500 µm
Pl
k
Bt
Ilm
Ap
Amp+Sp
l
Opx1+Mgt
100µm
Opx2
Amp+Sp
Opx2+Sp
Pl
Opx2+Pl
Ap
Opx1+Mgt
l
Opx2
Opx2+Pl
Opx2+Sp
Amp+Sp
m
n
n
Opx1+Mgt
Opx2
Opx2+Sp
Amp+Sp
20µm

Figure 8.1.2 contd. (j) Primary ilmenite and magnetite grains are shown under transmitted light. Apart from individual grains magnetites often contain ilmenite lamellae. (k) Ilmenite-apatite association. Ilmenites are rimmed by orthopyroxene (Opx_2) and amphibole + spinel double corona at the contact of plagioclase. (l) Enlarged BSE image of the double corona between orthopyroxene (Opx_1) + magnetite and plagioclase. Boundary between outer and inner coronae is convex towards orthopyroxene of the inner corona. Patches of orthopyroxene (Opx_2) + spinel symplectite are partially surrounded by this convex-inward margin of outer amphibole corona. (m) Convex-inward margin of the amphibole + spinel outer corona. (n) Enlarged BSE image of Fig. 8.1.2m. Orthopyroxene (Opx_2) + spinel symplectic patches within appear as early relics within outer corona consisting of amphibole. String-like portions of these patches are connected with the inner corona consisting of orthopyroxene (Opx_2) alone.

8.1.2. Type-II

Type-II meta-mafic rocks are dominant in the study area. They are medium to fine grained (<1 mm grain size) and contain clinopyroxene ± orthopyroxene + plagioclase + ilmenite ± garnet + amphibole + biotite ± quartz. They show a wide variety in texture under microscope from intergranular to granoblastic. Depending on the presence of primary pyroxenes type-II rocks are further divided into two groups.

Type-IIA

Type-IIA meta-mafic samples contain clinopyroxene ± orthopyroxene + plagioclase + ilmenite ± garnet + amphibole + biotite. They show variable texture from intergranular to granoblastic under microscope.

The garnet-absent samples are contain primary clinopyroxene, plagioclase and ilmenite grains that show either overall intergranular (SR87Z, SR117C) or granoblastic (SR44, SR103A) texture (Fig. 8.1.3a, b). Clinopyroxenes are replaced by biotite and amphibole and ilmenite grains are rimmed by amphibole at some places (Fig. 8.1.3c, d). In most of the places, pyroxenes are completely replaced by amphibole with no relics of primary pyroxenes within them. Secondary amphiboles are often recrystallized and numerous fine amoeboid quartz and/or plagioclase

inclusions within them define a poikiloblastic or sieve-like texture (Fig. 8.1.3e). Plagioclase grains are sericitized in some cases (Fig. 8.1.3f).

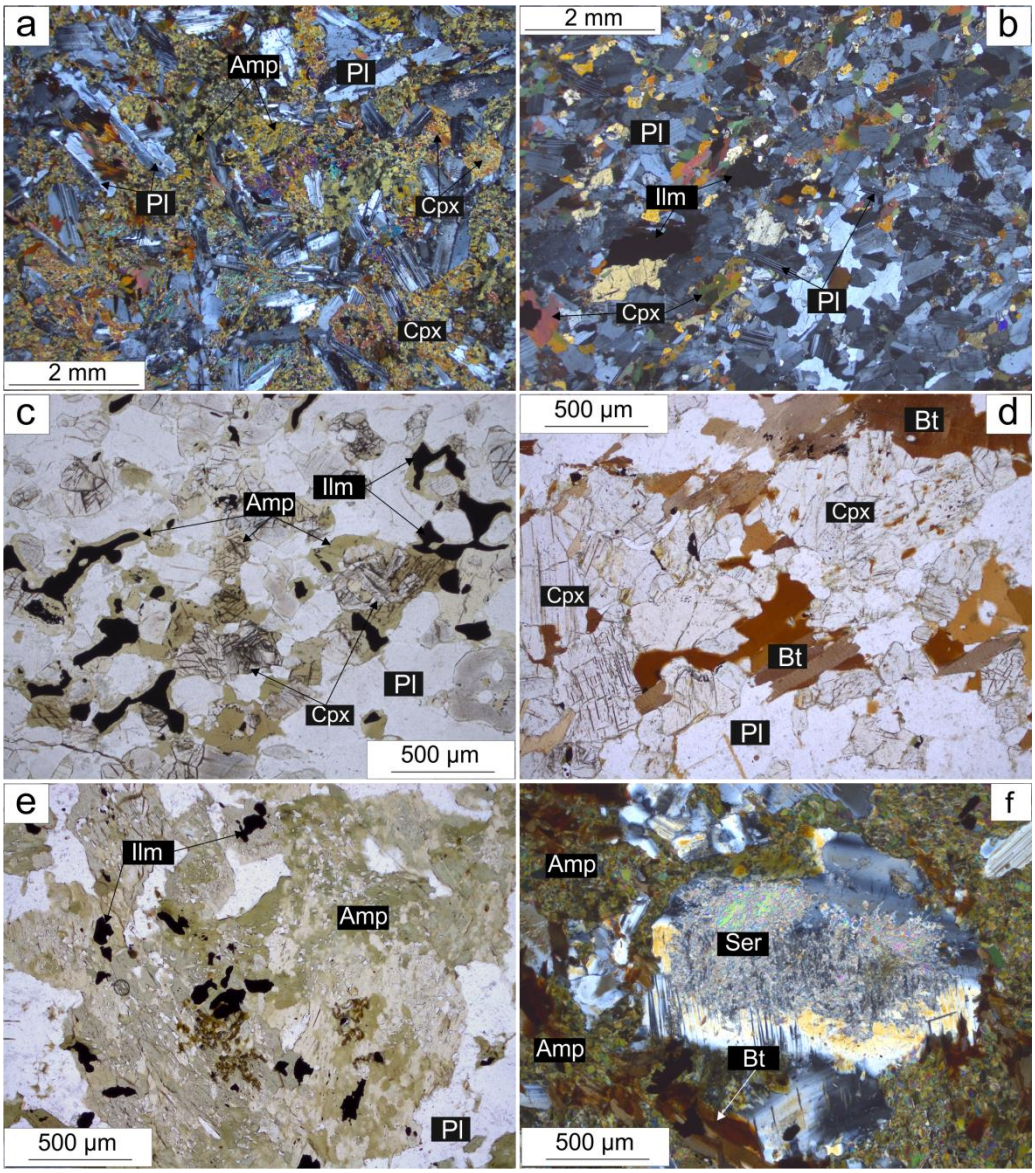

Figure 8.1.3. (a) Type-IIA samples under CPL showing intergranular texture between primary clinopyroxene and plagioclase. Clinopyroxenes are partially replaced by amphibole. (b) Type-IIA samples under CPL showing overall granoblastic texture. (c) Clinopyroxenes are partially replaced by amphiboles. Ilmenites are rimmed by thin amphibole coronae. (d) Clinopyroxene replaced by biotite. (e) Amphibole completely replaces clinopyroxene. Very fine quartz ± plagioclase and ilmenite inclusions within secondary amphibole give them sieve-like texture. (f) Plagioclase altered to sericite.

On the other hand, garnet-present samples are either medium grained (1-2 mm grain size) with intergranular texture (SR94/2, SR94/7) or fine grained (< 500 µm

grain size) with overall granoblastic texture (SR93, SR116). In the medium grained samples, large plagioclase laths (<2 mm) form triangular interstices which are filled

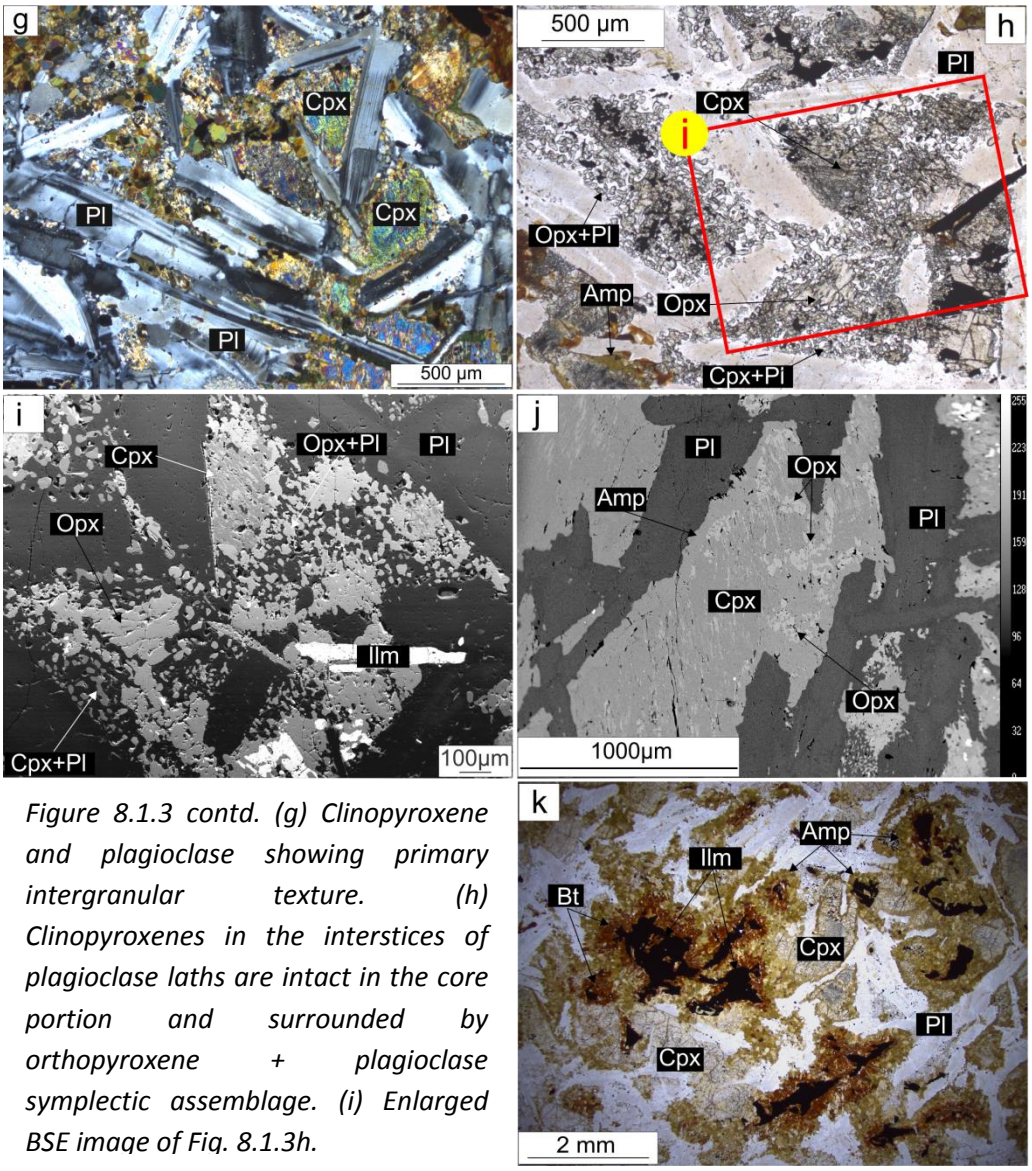

Figure 8.1.3 contd. (g) Clinopyroxene and plagioclase showing primary intergranular texture. (h) Clinopyroxenes in the interstices of plagioclase laths are intact in the core portion and surrounded by orthopyroxene + plagioclase symplectic assemblage. (i) Enlarged BSE image of Fig. 8.1.3h. Clinopyroxenes are replaced by symplectic orthopyroxene + plagioclase and vice versa. (j) Exsolved lamellae of orthopyroxene within clinopyroxenes often become granular towards the grain margin. Amphibole rims clinopyroxene. (k) Ilmenite is rimmed by double corona comprising of biotite (inner corona) and amphibole (outer corona).

with primary orthopyroxene and clinopyroxene (Fig. 8.1.3g). Interstitial clinopyroxene grains are preserved at the central part and replaced by symplectic intergrowth clinopyroxene + plagioclase along straight grain margins (Fig. 8.1.3h, i). Similar to the type-I samples, clinopyroxene grains contain exsolved orthopyroxene lamellae and are replaced by orthopyroxene to some extent along the grain margins (Fig. 8.1.3j). Recrystallized amphibole partially replaces and rims the pyroxene grains

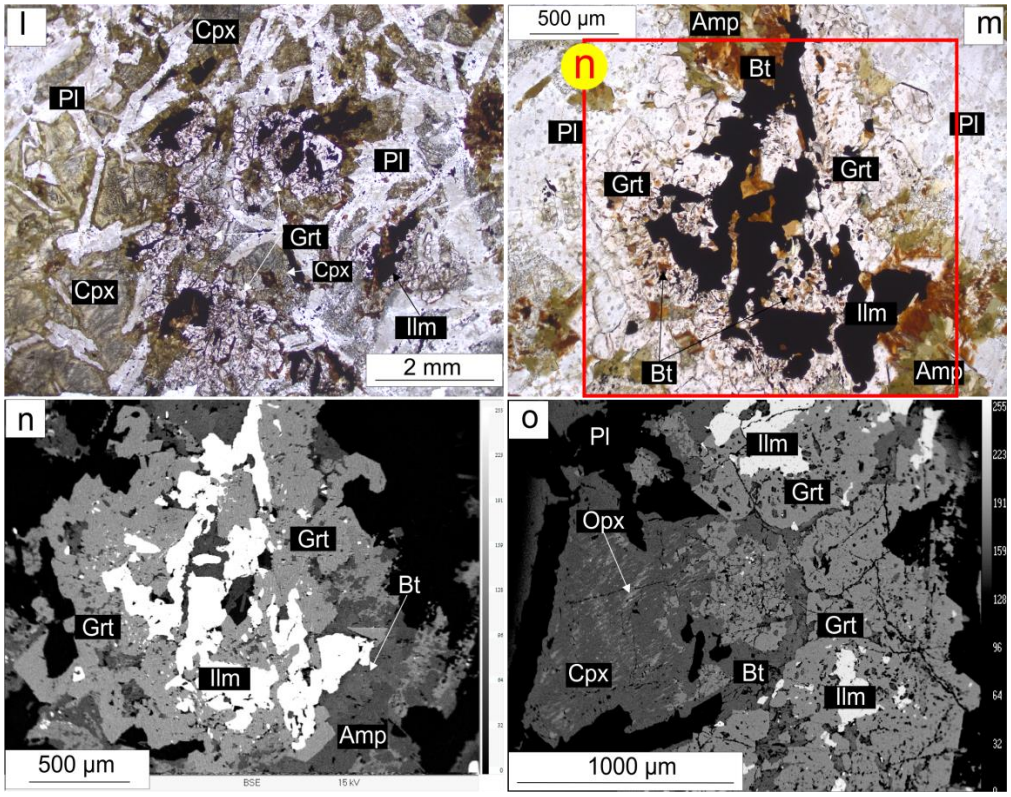

Figure 8.1.3 contd. (l) Fractured block-shaped garnet grains with partial straight grain margin are present in association with ilmenites and clinopyroxenes. (m) Garnet partially rims ilmenite and contains numerous biotite inclusions. Garnets are replaced by both amphibole and biotite. (n) BSE image of Fig. 8.1.3m. (o) Garnet shares straight, non-interfering grain contact with clinopyroxene.

(Fig. 8.1.3j, k). Ilmenite grains are rimmed by recrystallized biotite and amphibole similar to the type-I samples (Fig. 8.1.3k). Highly fractured block-shaped garnet grains with partial straight grain margin are present in association with ilmenites (Fig. 8.1.3l-n). At places, garnet blocks partially rim ilmenite (Fig. 4l-n) and contain numerous biotite and ilmenite inclusions (Fig. 8.1.3m). Garnet shares straight, non-

interfering grain contact with clinopyroxene and is partially replaced by biotite at places (Fig. 8.1.3l, o).

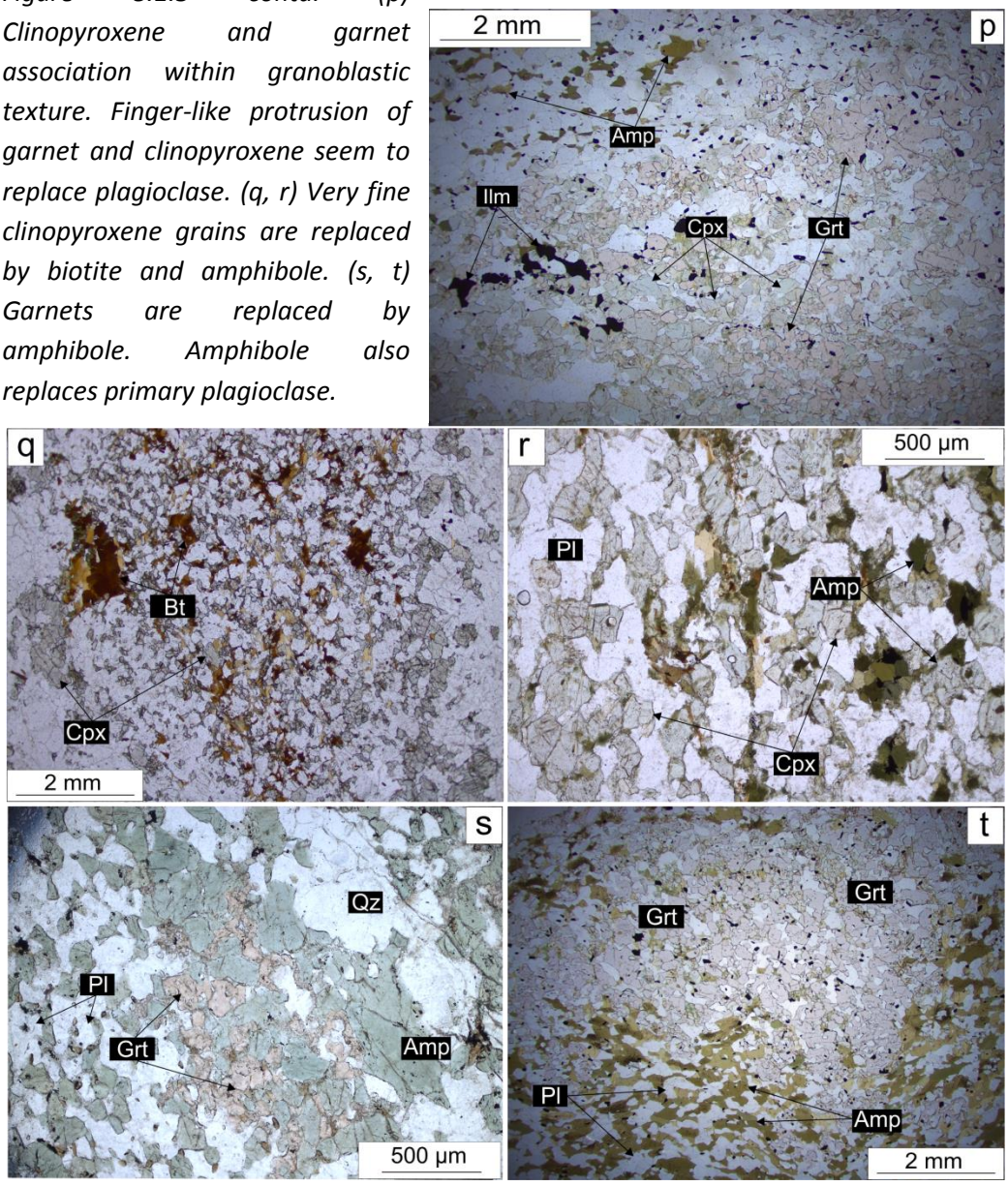

Figure 8.1.3 contd. (p) Clinopyroxene and garnet association within granoblastic texture. Finger-like protrusion of garnet and clinopyroxene seem to replace plagioclase. (q, r) Very fine clinopyroxene grains are replaced by biotite and amphibole. (s, t) Garnets are replaced by amphibole. Amphibole also replaces primary plagioclase.

The fine grained samples with granoblastic texture contain clinopyroxene, plagioclase, ilmenite, garnet, amphibole, biotite and quartz. Fine anhedral clinopyroxene grains share non-interfering grain contact with garnets (Fig. 8.1.3p) and are partially replaced by amphibole and biotite along corroded grain margins (Fig. 8.1.3q, r) whereas garnet grains are always associated and replaced by amphibole (Fig.

8.1.3s). Anhedral garnet and amphibole grains individually or in few cases collectively replace primary plagioclase (Fig. 8.1.3s, t).

Type-IIB

Type-IIB meta-mafic rocks of the study area are devoid of any primary pyroxene. Garnet porphyroblasts are nodule shaped and contain numerous rounded to amoeboid quartz and ilmenite inclusions which give them sieve texture (Fig. 8.1.4a). Porphyroblastic garnets have a rind of quartz which separate them from the granoblastic matrix association of amphibole + ilmenite + plagioclase + quartz (Fig. 8.1.4b). Anhedral amphibole aggregates replace plagioclase grains which are mostly sericitized and scapolite is present in some of the samples (Fig. 8.1.4c, d).

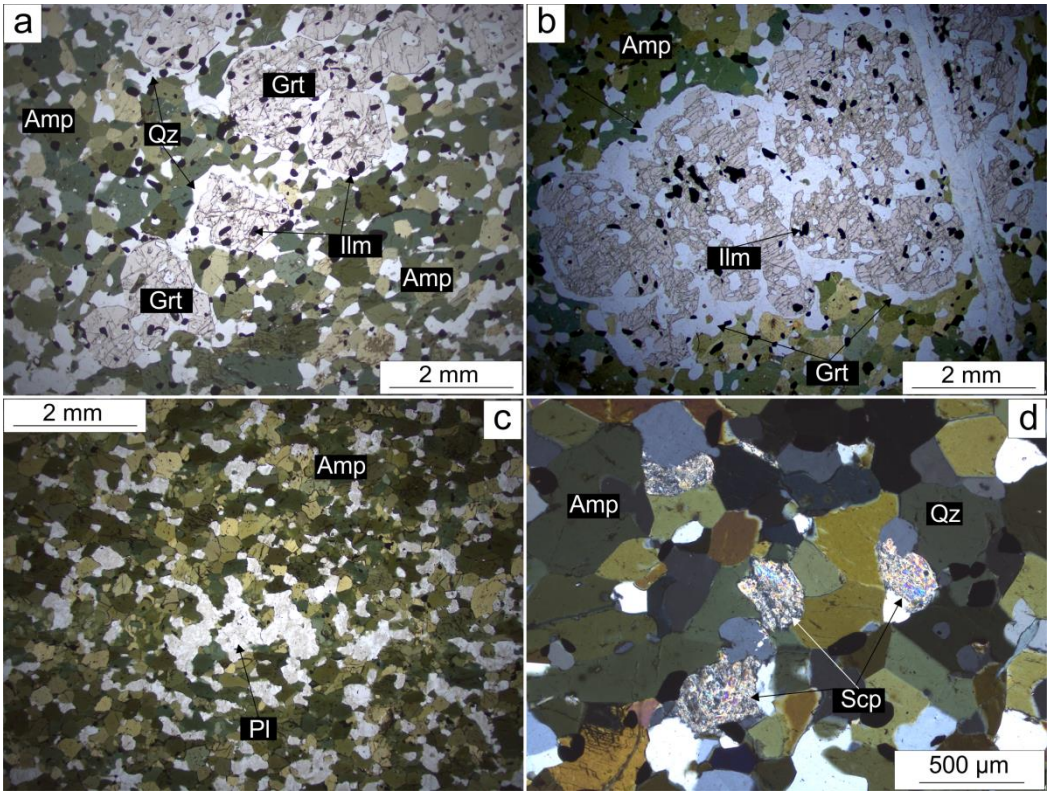

Figure 8.1.4. (a) Garnet porphyroblasts are nodule shaped and contain numerous rounded to amoeboid quartz and ilmenite inclusions which give them sieve texture. (b) Porphyroblastic garnets have a rind of quartz which separate them from the granoblastic matrix association of amphibole + biotite + ilmenite + plagioclase + quartz. (c, d) Anhedral amphibole replaces plagioclase grains which are mostly sericitized and scapolite is present.

8.1.3. Mineral paragenesis and multiple coronae in the meta-mafic rocks

Based on petrographic observation the magmatic mineralogy of type-I rocks is olivine + clinopyroxene + plagioclase + orthopyroxene (Opx_1) + ilmenite + magnetite ± apatite whereas orthopyroxene (Opx_2) + amphibole + biotite + spinel constitutes the metamorphic mineralogy. On the contrary, the magmatic mineralogy of type-II rocks is clinopyroxene + Plagioclase ± orthopyroxene + ilmenite whereas garnet + amphibole + biotite + quartz constitute the metamorphic mineral association.

Significant variation in the grain size of the plagioclase laths and resulting subophitic to intergranular texture between magmatic clinopyroxene and plagioclase indicates a change in the crustal depth during magmatic crystallization of the studied type-I rocks. Regardless the chronology of magmatic crystallization of clinopyroxene + plagioclase olivine + ilmenite + magnetite ± apatite is always the earliest cumulous assemblage in the crystallizing mafic magma of type-I. In the subsolidus stage the double coronae between olivine and plagioclase were formed via the following qualitative reactions based on petrographic study:

Olivine + Plagioclase ➔ Orthopyroxene (Opx_2) ± Spinel + Ca^{2+} (R1)

Orthopyroxene (Opx_2) + Spinel + Ca^{2+} + H_2O ➔ Amphibole (R2)

In high grade metagabbros, multi-layered coronae between olivine and plagioclase are reported and analyzed by several researchers worldwide (Ashworth et al., 2001; Claeson, 1998; Gallien et al., 2012; Joesten, 1986; Lang et al., 2004; Mongkoltip and Ashworth, 1986). The anhydrous coronae (orthopyroxene and clinopyroxene+spinel) are widely argued to be formed via diffusion controlled metamorphic solid-state replacement at <840°C (Gallien et al., 2012). The authors suggested that the hydrous coronae (orthopyroxene and amphibole + spinel) are formed by production of peritectic orthopyroxene from trapped interstitial liquid between olivine and plagioclase in the magmatic stage. Regardless the magmatic or metamorphic origin of these multi-mineral coronae and their growth requires diffusion at the reaction zone/interface (White and McGrail, 2008). As aluminum is known to be largely immobile under most natural situations, spinel crystallizes in close proximity to the plagioclase. Textural features support that orthopyroxene (Opx_2) + spinel is formed from olivine and plagioclase. As the reaction front progressed towards olivine, the rim

becomes monomineralic (Opx_2) and is devoid of spinel. Later, amphibole is crystallized at the expense of orthopyroxene (Opx_2) + spinel. Multi-layered coronae between adjacent olivine and plagioclase at constant or variable P-T condition can be formed by chemical potential gradients and different diffusivities of involved chemical elements (Mg, Al, Ca and Si) (Gallien et al., 2012).

In type IB samples, the orthopyroxene (Opx_1)-magnetite symplectite, completely replaces/pseudomorphs olivine which can be formed via oxidation (Gallien et al., 2012). The FMQ (Fayalite-Magnetite-Quartz) redox buffer states that fayalite reacts with oxygen to form magnetite + quartz and the excess quartz subsequently reacts with the forsterite component to produce orthopyroxene by the following reaction (Goode, 1974):

Olivine + O_2 ➔ Orthopyroxene + Magnetite (R3)

In a contrasting opinion, several workers suggest that olivine is non-isochemically replaced by orthopyroxene-magnetite symplectites and this process is governed by grain-boundary diffusion (Barton and Van Gaans, 1988; Barton, 1991) whereas others advocate for development of this eutectic-like texture during late magmatic crystallization (Ambler and Ashley, 1977).

8.2. Mineral chemistry

Representative mineral compositions in the meta-mafic rocks are analyzed with an Electron Probe Micro-analyser (EPMA) at the Department of Geology and Geophysics, IIT Kharagpur and Department of Applied Geology IIT (ISM), Dhanbad. Detailed analytical technique is given in the Appendix. Data are presented in Table-8.2. In the following section salient compositional features of the different minerals are presented. .

Olivine: Within type-IA meta-mafic samples, olivine grains are compositionally homogeneous with its composition varying between Fo_{48} to Fo_{54} (Table-8.2a). As mentioned in the petrographic description, olivine grains are mostly pseudomorphed by orthopyroxene-magnetite in type-IB samples. Rarely preserved olivine grains are compositionally similar with those of the type-IA samples and their composition is Fo_{51-59} (Table-8.2a).

Clinopyroxene: In type-I samples, clinopyroxene grains are compositionally similar and the most magnesian mineral in these rocks (X_{Mg}=Mg/Mg+Fe^{2+}=0.70-0.73). Clinopyroxenes in the type-IA samples contain slightly more wollastonite component whereas those in the type-IB samples show composition along diopside-hedenburgite (Fig. 8.2a). In type-I meta-mafic rocks Al_2O_3 and TiO_2 contents are low in the clinopyroxene grains (Al_2O_3=1.69-2.73 wt%; TiO_2=0.54-1.64 wt%) (Table-8.2b). In the garnet-present type-IIA samples, clinopyroxene grains are comparatively less magnesian (X_{Mg}=Mg/Mg+Fe^{2+}=0.58-0.67) than those in the type-I rocks (Table-8.2b). They show slight variation in CaO content (17.92-22.36 wt%) (Table-8.2b). Al_2O_3 content in clinopyroxene within the garnet-present type-IIA meta-mafic rocks are comparatively high with respect to type-I samples and show significant variation (Al_2O_3=0.91-5.07 wt%) (Table-8.2b). TiO_2 contents in these clinopyroxenes also show significant variation (TiO_2=0.09-0.74 wt%) and TiO_2 content increases with an increase in the Al_2O_3 content in these samples (Table-

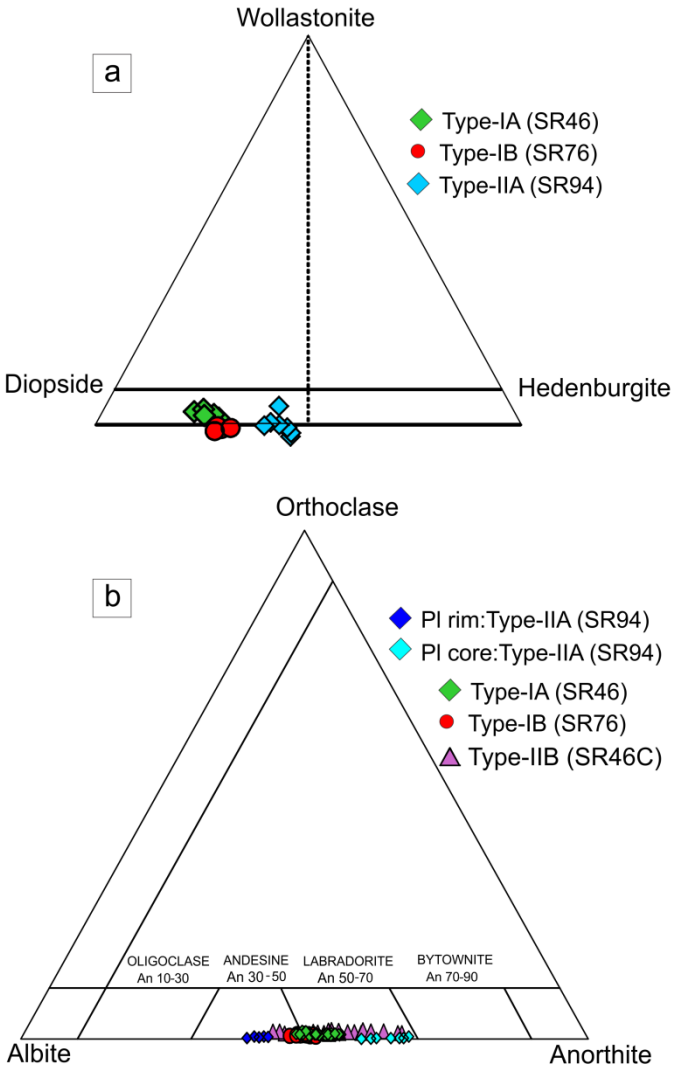

Figure 8.2. (a) Pyroxene compositions in En-Fs-Wo triangular plot in two types of meta-mafic rocks in the study area. (b) Plagioclase compositions plotted in Or-Ab-An triangle for all types of meta-mafic samples analyzed from the study area.

8.2b). No systematic textural connotation for these variations in terms of TiO_2 and Al_2O_3 within the clinopyroxenes is noticed.

Orthopyroxene*:* Orthopyroxene within all the meta-mafic rocks are less magnesian than clinopyroxenes. In type-IA meta-mafic samples, individual orthopyroxene grains interlocked with olivines and corona surrounding olivines have similar X_{Mg} content (0.60-0.66) (Table-8.2c). X_{Mg} values of the orthopyroxenes are lower than the clinopyroxene grains but higher than olivine grains in these rocks. CaO, Al_2O_3 and TiO_2 contents of the orthopyroxene grains as the coronae are lower than individual grains within interlocking texture in type-IA samples (Table-8.2c). Orthopyroxenes as coronae contain 0.11-0.94 wt% CaO, 0.70-1.25 wt% Al_2O_3 and 0.03-0.23 wt% TiO_2 whereas those as individual matrix grains in association with olivine and clinopyroxenes contain 0.42-3.97 wt% CaO, 0.88-2.73 wt% Al_2O_3, 0.11-1.83 wt% TiO_2 (Table-8.2c). In type-IB meta-mafic samples, orthopyroxenes in association with symplectic and lamellar magnetite that pseudomorphs olivine grains have lower X_{Mg} content (0.45-0.49) than those as coronae (0.55-0.56) and lamellae within clinopyroxenes (0.53-0.56) (Table-8.2c). Grains within orthopyroxene-magnetite association also show slightly lower value of the Al_2O_3 content (0.52-0.66 wt%) than those in the coronae (0.93-1.45 wt%) and within clinopyroxenes (0.95-1.66 wt%) (Table-8.2c). In these type-IB rocks, orthopyroxene grains in all the textural association have similar CaO and TiO_2 contents. The garnet-present type-IIA samples, orthopyroxene grains have the lowest X_{Mg} values (0.41-0.43) among all the analyzed meta-mafic rocks in the study area. Orthoproxenes as the individual grains and lamellae within clinopyroxenes are compositionally similar. They have low value of CaO (0.44-1.51 wt%), Al_2O_3 (0.36-0.54 wt%) and TiO_2 (0.02-0.45 wt%) (Table-8.2c).

Plagioclase*:* No compositional zoning is noted in the cumulous and lath-shaped plagioclase within type-I samples. Cloudy plagioclase laths of type-IA meta-mafic rocks have a composition of $Ab_{42.7\text{-}49.4}An_{50.1\text{-}56.9}Or_{0.2\text{-}0.9}$ (Fig. 8.2b; Table-8.2d). Cumulous plagioclase grains of type-IB meta-mafic rocks have a composition of $Ab_{46.9\text{-}51.0}An_{48.8\text{-}53.1}Or_{0.1\text{-}0.5}$ (Fig. 8.2b; Table-8.2d). In the garnet-present type-IIA samples, plagioclase laths in the intergranular texture show significant compositional zoning for the core and rim of an individual grain. Plagioclase core is comparatively

anorthite rich (X_{An}=0.58-0.66) and has a composition of $Ab_{33.8-41.8}An_{57.7-65.8}Or_{0.3-0.7}$ (Fig. 8.2b). Plagioclase rim in these samples shows albitic composition ($Ab_{53.3-57.5}An_{41.7-45.7}Or_{0.8-1.0}$) (Fig. 8.2b; Table-8.2d). In the type-IIB samples, fine plagioclase grains in the matrix granoblastic texture do not show any compositional zoning in an individual grain but they overall show a compositional variation with respect to albitic to anorthitic component ($Ab_{40.3-54.0}An_{45.8-59.5}Or_{0.1-0.6}$) (Table-8.2d).

Garnet*:* Garnet grains within type-IIA meta-mafic samples, are compositionally homogeneous from core to rim and chiefly constituted of almandine and grossular in composition (X_{Alm}=0.62-0.65; X_{Grs}=0.21-0.22) with minor pyrope (X_{Prp}=0.11-0.12) and spessartine (X_{Sps}=0.03-0.04) (Table-8.2e). No compositional zoning was recorded in the garnets. The garnet within type-IIB meta-mafic rocks are also compositionally homogeneous and has slightly low X_{Mg} content (0.10-0.13) than those in type-IIA samples (0.15-0.17) (Table-8.2e). Similar to type-IIA samples, garnets within these completely altered type-IIB rocks are mainly composed of almandine and grossular (X_{Alm}=0.66-0.71; X_{Grs}=0.15-0.19) with minor pyrope (X_{Prp}=0.08-0.10) and spessartine (X_{Sps}=0.5-0.06) (Table-8.2e).

Ilmenite-Magnetite*:* In type-IA meta-mafic rocks ilmenite grains interlocked with primary olivine, pyroxenes and plagioclase have very low amount of Fe^{3+} (0.003-0.016 apfu) and Mn (0.009-0.016 apfu) in their structures (Table-8.2f). For type-IB samples, ilmenites which are present as lamellar intergrowth within orthopyroxene have slightly higher Fe^{3+} (0.022-0.059 apfu) than individual grains in the cumulate texture (0-0.026 apfu) (Table-8.2f). Ilmenite grains within the garnet-present type-IIA samples contain low amount (0.004-0.032 apfu) of Fe^{3+} whereas those in the type-IIB have 0.021-0.059 apfu Fe^{3+} in their structure (Table-8.2f).

Magnetites in type-IA and symplectic magnetite within orthopyroxene-magnetite association and individual grains in the cumulate texture of the type-IB rocks are compositionally similar. They contain 0.994-1.066 apfu Fe^{2+}, 1.797-1.959 apfu Fe^{3+}, 0.007-0.078 apfu Ti and no detectable amount of Mn in their structures (Table-8.2f).

Apatite*:* Apatite grains in type-IB meta-mafic samples contain significant amount of F and low amount of Cl in their mineral structures (1.97-3.58 wt% F_2O_3; 0.01-0.33 wt% Cl) (Table-8.2f).

Amphibole: In type-IA meta-mafic rocks, amphibole as coronae with symplectic spinel around olivine-orthopyroxene and amphibole as coronae around ilmenite are compositionally similar and can be classified as pargasite (Fig. 8.2c; Leake et al., 2004). Amphiboles in these samples have comparatively higher X_{Mg} content (0.68-0.75) than those of other meta-mafic samples in the study area. In type-IB samples, amphibole grains as outer coronae of the ilmenite are pargasitic to ferro-pargasitic in composition and show a significant range in X_{Mg} value (0.45-0.66) (Fig. 8.2c; Table-8.2g). Amphiboles as outer coronae surrounding olivine-orthopyroxene-magnetite and as replacement phases of the clinopyroxene with orthopyroxene lamellae are pargasitic in composition and have a narrow range of X_{Mg} value (0.60-0.64) (Table-8.2g). In the garnet-present type-IIA samples, amphibole grains replacing garnet and clinopyroxene and those as outer coronae of the primary ilmenite, are compositionally similar and majorly ferropargasitic (Fig. 8.2c; Table-8.2g) and they have X_{Mg} value of 0.44-0.49. In a garnet-present type-IIB sample, amphibole grains in contact with the garnets have the

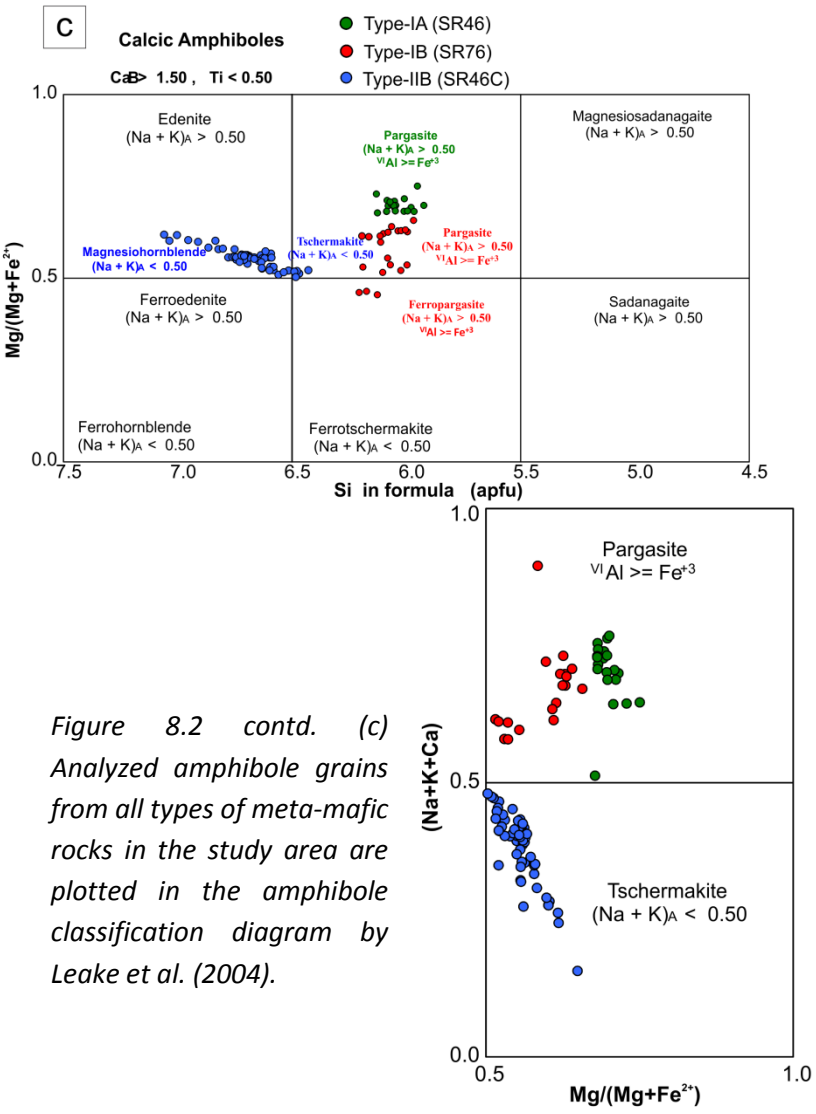

Figure 8.2 contd. (c) Analyzed amphibole grains from all types of meta-mafic rocks in the study area are plotted in the amphibole classification diagram by Leake et al. (2004).

lowest X_{Mg} content (0.37-0.39) among all the analyzed meta-mafic rocks and these amphiboles are ferro-tschermakitic in composition (Fig. 8.2c; Table-8.2g). In the garnet-absent type-IIB sample, amphiboles, both the coarse and fine-grained ones can be classified as magnesio-hornblende (Fig. 8.2c) and their X_{Mg} varies between 0.54-0.65 (Table-8.2g).

Biotite*:* Biotite, present as patch that forms partial rim around ilmenite in type-IA samples is the most magnesian among all the analyzed biotite grains in the studied meta-mafic rocks. In these samples, biotites have X_{Mg} value of 0.73-0.76 and contain 2.55-3.17 wt% TiO_2 (Table-8.2h). Within type-IB, biotite grains as inner coronae around ilmenite and magnetite have X_{Mg} value of 0.50-0.58 and contain 2.35-3.64 wt% TiO_2 (Table-8.2h). In the garnet-present type-IIA meta-mafic rocks, biotite grains which are present as inner coronae around ilmenites and those replacing garnet grains are compositionally similar. They have the lowest X_{Mg} values (0.36-0.40) and they contain 4.40-5.07 wt% TiO_2 (Table-8.2h). Biotites within the garnet-present type-IIA samples contain the lowest (almost negligible; 0.009-0.015 wt% F_2O_3) fluorine than those within type-IA (0.09-0.25 wt% F_2O_3) and type-IB 28-0.56 wt% F_2O_3) (Table-8.2h). Biotites within type-IB also show some amount of Cl (0.08-0.18 wt%) in their structures.

Table 8.2a: Representative chemical analyses for olivine (representative oxygen basis is given). Mineral abbreviation is used after Whitney and Evans (2010). Cation calculations have been done following the procedure of Grew (1984).

Rock type	**Type IA**								**Type IB**	
Sample no	**SR46A**	**SR46A**	**SR46A**	**SR46A**	**SR46A**	**SR46A**	**SR46A**	**SR46A**	**SR76A**	**SR76A**
Mineral	*Ol*	*Ol*	*Ol*	*Ol*	*Ol*	*Ol*	*Ol*	*Ol*	*Ol*	*Ol*
Texture	*Fractured individual grains (surronded by double coronae)*					*Relics within Opx $_1$*			*Relics within Opx $_1$ +Mgt*	
Point no	20	50	51	53	107	108	111	127	83	84
SiO_2	34.56	35.20	35.23	34.82	34.87	34.91	34.66	35.17	41.28	44.90
TiO_2	-0.02	0.00	0.03	0.00	0.02	0.03	-0.03	0.02	0.23	4.53
Al_2O_3	-0.03	-0.01	-0.03	-0.01	-0.02	0.00	0.01	0.01	1.06	1.55
Cr_2O_3	0.01	0.00	0.01	-0.01	0.01	0.00	0.01	-0.01	0.07	0.01
FeO	41.52	40.39	42.78	42.45	43.64	44.23	43.53	40.17	45.28	33.52
MnO	0.41	0.38	0.26	0.61	0.61	0.46	0.66	0.52	0.36	0.56
MgO	22.49	23.24	23.47	22.49	21.30	20.87	21.05	23.73	17.54	17.79
CaO	0.03	0.06	0.02	0.03	-0.01	0.03	0.00	0.04	0.15	0.17
Na_2O	0.00	0.00	0.02	0.09	0.00	0.00	-0.02	0.01	-0.01	-0.01
K_2O	-0.04	-0.01	-0.03	0.02	-0.02	-0.01	-0.04	-0.02	0.00	-0.01
Total	98.93	99.25	101.76	100.49	100.40	100.52	99.83	99.64	105.96	103.01
Oxygen basis	**4**	**4**	**4**	**4**	**4**	**4**	**4**	**4**	**4**	**4**
Si	1.00	1.01	1.00	1.00	1.01	1.01	1.01	1.01	1.11	1.16
Ti	0.00	0.00	0.00	0.00	0.00	0.00	0.00	0.00	0.00	0.09
Al	0.00	0.00	0.00	0.00	0.00	0.00	0.00	0.00	0.03	0.05
Al-iv	1.00	0.99	1.00	1.00	0.99	0.99	0.99	0.99	0.89	0.84
Al-vi	-1.00	-0.99	-1.00	-1.00	-0.99	-0.99	-0.99	-0.99	-0.86	-0.79
Cr	0.00	0.00	0.00	0.00	0.00	0.00	0.00	0.00	0.00	0.00
Fe^{+2}	1.01	0.97	1.01	1.02	1.05	1.07	1.06	0.96	1.01	0.73
Mn	0.01	0.01	0.01	0.01	0.01	0.01	0.02	0.01	0.01	0.01
Mg	0.97	1.00	0.99	0.96	0.92	0.90	0.91	1.01	0.70	0.69
Ca	0.00	0.00	0.00	0.00	0.00	0.00	0.00	0.00	0.00	0.00
Na	0.00	0.00	0.00	0.01	0.00	0.00	0.00	0.00	0.00	0.00
K	0.00	0.00	0.00	0.00	0.00	0.00	0.00	0.00	0.00	0.00
Sum	3.00	2.99	3.00	3.00	2.99	2.99	2.99	2.99	2.87	2.73
Fa	*48.87*	*50.40*	*49.29*	*48.21*	*46.18*	*45.42*	*45.92*	*50.97*	*40.65*	*48.19*
Fo	*50.62*	*49.14*	*50.40*	*51.05*	*53.07*	*54.01*	*53.27*	*48.40*	*58.87*	*50.94*
X_{Mg}	*0.49*	*0.51*	*0.49*	*0.49*	*0.47*	*0.46*	*0.46*	*0.51*	*0.41*	*0.49*

Table 8.2b: Representative chemical analyses for clinopyroxene (representative oxygen basis is given). Mineral abbreviation is used after Whitney and Evans (2010). Cation calculations have been done following the procedure of Grew (1984).

Rock type	**Tyoe IA**				**Type IB**			**Type IIA**					
Sample no	**SR46A**	**SR46A**	**SR46A**	**SR46A**	**SR76A**	**SR76A**	**SR76A**	**SR94**	**SR94**	**SR94**	**SR94**	**SR94**	**SR94**
Mineral	*Cpx*	*Cpx*	*Cpx*	*Cpx*	*Cpx*	*Cpx*	*Cpx*	*Cpx*	*Cpx*	*Cpx*	*Cpx*	*Cpx*	*Cpx*
Texture	*Relics in Opx $_1$*		*Clouded grains with Opx $_1$*		*Clouded grains with Opx $_1$ lamellae*			*Clouded grains in straight boundary contact with Grt*					
Point no	128	130	47	48	88	89	101	17 / 1 . *	19 / 1 .*	25 / 1 . *	26 / 1 .*	16 / 1 . *	18 / 1 .
SiO_2	52.03	52.34	51.60	51.76	51.43	51.74	51.63	49.53	50.90	48.48	49.51	49.75	51.38
TiO_2	1.64	0.71	0.74	0.73	0.66	0.56	0.54	0.32	0.09	0.61	0.50	0.74	0.36
Al_2O_3	1.69	2.54	2.73	2.64	2.53	2.33	2.23	2.57	0.91	4.12	3.56	5.07	2.64
Cr_2O_3	0.07	0.13	0.19	0.17	0.00	-0.01	0.02	0.04	0.00	0.05	0.08	0.28	0.14
FeO	12.03	8.15	8.64	8.65	9.91	9.43	9.25	15.53	13.38	15.19	14.66	14.30	12.83
MnO	0.28	0.16	0.20	0.40	0.23	0.21	0.25	0.15	0.31	0.15	0.09	0.19	0.23
MgO	16.59	14.04	13.54	13.44	13.32	13.46	13.45	10.66	10.76	10.38	10.44	10.49	11.05
CaO	20.28	21.96	21.44	21.86	21.13	21.31	20.61	19.38	22.36	19.36	19.76	17.92	20.05
Na_2O	0.25	0.34	0.28	0.30	0.29	0.29	0.26	0.41	0.23	0.69	0.63	0.82	0.46
K_2O	0.01	-0.03	-0.01	-0.01	0.00	-0.01	-0.02	0.11	0.00	0.25	0.20	0.37	0.13
Total	104.87	100.34	99.35	99.94	99.50	99.31	98.22	98.71	98.96	99.28	99.47	99.93	99.29
Oxygen basis	**6**	**6**	**6**	**6**	**6**	**6**	**6**	**6**	**6**	**6**	**6**	**6**	**6**
Si	1.87	1.93	1.92	1.92	1.93	1.94	1.96	1.91	1.96	1.86	1.89	1.89	1.96
Ti	0.04	0.02	0.02	0.02	0.02	0.02	0.02	0.01	0.00	0.02	0.01	0.02	0.01
Al	0.07	0.11	0.12	0.12	0.11	0.10	0.10	0.12	0.04	0.19	0.16	0.23	0.12
Al-iv	0.13	0.07	0.08	0.08	0.07	0.06	0.04	0.00	0.00	0.00	0.00	0.00	0.00
Al-vi	-0.05	0.04	0.04	0.04	0.05	0.05	0.06	0.00	0.00	0.00	0.00	0.00	0.00
Cr	0.00	0.00	0.01	0.00	0.00	0.00	0.00	0.00	0.00	0.00	0.00	0.00	0.00
Fe^{+2}	0.78	0.87	0.86	0.87	0.85	0.86	0.84	0.43	0.38	0.36	0.39	0.42	0.43
Mg	0.36	0.28	0.30	0.30	0.31	0.30	0.29	0.61	0.62	0.59	0.59	0.59	0.63
Mn	0.01	0.00	0.01	0.01	0.01	0.01	0.01	0.01	0.01	0.00	0.00	0.01	0.01
Ca	0.89	0.77	0.75	0.74	0.75	0.75	0.76	0.80	0.92	0.79	0.81	0.73	0.82
Na	0.02	0.02	0.02	0.02	0.02	0.02	0.02	0.03	0.02	0.05	0.05	0.06	0.03
K	0.00	0.00	0.00	0.00	0.00	0.00	0.00	0.01	0.00	0.01	0.01	0.02	0.01
Sum	4.05	4.01	4.00	4.01	4.00	4.00	3.99	4.00	4.00	4.00	4.00	4.00	4.00

**' denotes the mineral compositions used in conventional thermobarometry*

Table 8.2c: Representative chemical analyses for orthopyroxene (representative oxygen basis is given). Mineral abbreviation is used after Whitney and Evans (2010). Cation calculations have been done following the procedure of Grew (1984).

Rock type	**Type IA**																					
Sample no	SR46A	SR46A	SR46A	SR46A	SR46A	SR46A	SR46A	SR46A	SR46A	SR46A	SR46A	SR46A	SR46A	SR46A	SR46A	SR46A	SR46A	SR46A	SR46A	SR46A	SR46A	SR46A
Mineral	Opx_1	Opx_1	Opx_1	Opx_1	Opx_1	Opx_1	Opx_1	Opx_1	Opx_1	Opx_1	Opx_1	Opx_1	Opx_1	Opx_2	Opx_2	Opx_2	Opx_2	Opx_2	Opx_2	Opx_2	Opx_2	Opx_2
Texture	*Matrix interlocking texture*													*Inner corona between Olv and Pl*								
Point no	136	137	138	139	141	142	143	144	147	148	150	151	152	55	56	87	88	89	90	9	10	74
SiO_2	53.73	53.18	53.15	53.36	52.54	53.32	53.56	51.80	52.70	53.36	53.13	51.39	52.92	52.65	53.11	52.54	53.38	52.68	53.24	52.04	52.15	52.62
TiO_2	0.11	0.13	0.15	0.23	0.82	0.10	0.13	1.83	0.62	0.18	0.09	2.72	0.17	0.22	0.16	0.03	0.03	0.00	0.05	0.33	0.10	0.13
Al_2O_3	0.88	1.07	0.77	0.83	0.84	1.11	1.16	1.38	1.13	1.04	0.97	0.91	1.41	1.03	1.05	1.52	0.91	1.21	1.02	1.13	0.90	1.21
Cr_2O_3	0.04	0.04	0.03	0.03	0.04	0.08	0.08	0.03	0.06	0.04	0.06	0.08	0.08	0.06	0.06	0.02	0.00	-0.01	0.00	0.08	0.04	0.03
FeO	22.26	22.35	22.42	23.11	22.30	22.19	22.63	23.10	21.76	19.15	24.22	24.07	21.21	23.67	23.11	22.79	24.48	24.49	23.98	22.69	23.22	23.93
MnO	0.63	0.38	0.50	0.64	0.40	0.57	0.50	0.60	0.46	0.49	0.55	0.61	0.26	0.40	0.69	0.43	0.49	0.50	0.58	0.56	0.47	0.61
MgO	21.38	21.89	21.90	21.90	21.44	21.95	21.99	21.23	21.40	21.00	21.49	21.94	21.07	20.96	21.47	21.24	21.69	21.31	21.81	20.97	21.38	21.83
CaO	1.59	0.48	0.69	0.54	1.39	0.50	1.26	0.41	1.67	3.97	0.74	0.42	3.26	0.94	0.54	0.66	0.11	0.20	0.25	1.87	0.27	0.72
Na_2O	0.04	0.01	-0.01	-0.03	0.00	0.00	0.03	0.06	0.01	0.05	-0.01	0.01	0.06	0.01	0.00	-0.01	-0.02	0.00	0.03	0.02	0.01	0.02
K_2O	0.00	0.00	-0.01	0.01	-0.01	0.00	-0.02	0.01	0.00	0.02	-0.02	0.00	0.02	0.01	-0.01	0.02	-0.02	-0.02	0.03	-0.02	0.01	-0.02
Total	100.66	99.53	99.59	100.62	99.76	99.82	101.32	100.45	99.81	99.30	101.22	102.15	100.46	99.95	100.18	99.24	101.05	100.36	100.99	99.67	98.55	101.08
Oxygen basis	**6**	**6**	**6**	**6**	**6**	**6**	**6**	**6**	**6**	**6**	**6**	**6**	**6**	**6**	**6**	**6**	**6**	**6**	**6**	**6**	**6**	**6**
Si	1.99	1.99	1.99	1.98	1.97	1.99	1.97	1.93	1.97	1.99	1.97	1.90	1.96	1.98	1.98	1.97	1.98	1.97	1.98	1.96	1.98	1.96
Ti	0.00	0.00	0.00	0.01	0.02	0.00	0.00	0.05	0.02	0.01	0.00	0.08	0.00	0.01	0.00	0.00	0.00	0.00	0.00	0.01	0.00	0.00
Al	0.04	0.05	0.03	0.04	0.04	0.05	0.05	0.06	0.05	0.05	0.04	0.04	0.06	0.05	0.05	0.07	0.04	0.05	0.04	0.05	0.04	0.05
Al-iv	0.01	0.01	0.01	0.02	0.03	0.01	0.03	0.07	0.03	0.01	0.03	0.10	0.04	0.02	0.02	0.03	0.02	0.03	0.02	0.04	0.02	0.04
Al-vi	0.03	0.03	0.02	0.02	0.00	0.03	0.02	-0.01	0.02	0.04	0.01	-0.06	0.03	0.02	0.03	0.04	0.02	0.02	0.02	0.01	0.02	0.01
Cr	0.00	0.00	0.00	0.00	0.00	0.00	0.00	0.00	0.00	0.00	0.00	0.00	0.00	0.00	0.00	0.00	0.00	0.00	0.00	0.00	0.00	0.00
Fe^{+2}	0.69	0.70	0.70	0.72	0.70	0.69	0.70	0.72	0.68	0.60	0.75	0.74	0.66	0.74	0.72	0.72	0.76	0.77	0.74	0.71	0.74	0.74
Mg	1.18	1.22	1.22	1.21	1.20	1.22	1.21	1.18	1.19	1.17	1.19	1.21	1.17	1.17	1.19	1.19	1.20	1.19	1.21	1.18	1.21	1.21
Mn	0.02	0.01	0.02	0.02	0.01	0.02	0.02	0.02	0.01	0.02	0.02	0.02	0.01	0.01	0.02	0.01	0.02	0.02	0.02	0.02	0.02	0.02
Ca	0.06	0.02	0.03	0.02	0.06	0.02	0.05	0.02	0.07	0.16	0.03	0.02	0.13	0.04	0.02	0.03	0.00	0.01	0.01	0.08	0.01	0.03
Na	0.00	0.00	0.00	0.00	0.00	0.00	0.00	0.00	0.00	0.00	0.00	0.00	0.00	0.00	0.00	0.00	0.00	0.00	0.00	0.00	0.00	0.00
K	0.00	0.00	0.00	0.00	0.00	0.00	0.00	0.00	0.00	0.00	0.00	0.00	0.00	0.00	0.00	0.00	0.00	0.00	0.00	0.00	0.00	0.00
Sum	3.99	3.99	3.99	3.99	3.99	3.99	4.00	3.99	3.99	3.98	4.00	4.01	4.00	4.00	3.99	3.99	4.00	4.00	4.00	4.01	4.00	4.01

Table 8.2c (continued): Representative chemical analyses for orthopyroxene (representative oxygen basis is given). Mineral abbreviation is used after Whitney and Evans (2010). Cation calculations have been done following the procedure of Grew (1984).

Rock type	**Type IB**												**Type IIA**						
Sample no	SR76A	SR76A	SR76A	SR76A	SR76A	SR76A	SR76A	SR76A	SR76A	SR76A	SR76A	SR76A	SR94	SR94	SR94	SR94	SR94	SR94	SR94
Mineral	Opx_1	Opx_1	Opx_1	Opx_1	Opx_1	Opx_1	Opx_2	Opx_2	Opx_2	Opx_1	Opx_1	Opx_1	Opx	Opx	Opx	Opx	Opx	Opx	Opx
Texture	*Opx_1 with Mgt intergrowth pseudomorphing Olv*						*Inner corona between Opx_1 +Mgt and Pl*			*Lamellae within Cpx*			*Matrix interlocking texture*					*Lamellae within Cpx*	
Point no	86	90	91	97	98	100	77	78	79	3	4	20	15 / 1 .	18 / 1 .	20 / 1 .	21 / 1 .	22 / 1 .	27 / 1 .	19 / 1 .
SiO_2	52.03	52.03	52.06	51.43	51.38	51.56	51.85	51.55	51.83	50.90	50.97	51.41	49.36	49.34	49.18	50.83	50.83	49.92	51.04
TiO_2	0.05	0.06	0.13	0.07	0.06	0.12	0.04	0.01	0.01	0.10	0.12	0.05	0.04	0.45	0.03	0.02	0.02	0.05	0.08
Al_2O_3	0.93	0.95	1.07	1.37	1.66	1.37	0.94	1.41	1.45	0.52	0.55	0.55	0.36	0.38	0.43	0.54	0.46	0.49	0.43
Cr_2O_3	-0.01	-0.02	0.00	-0.01	0.00	0.02	0.03	-0.02	-0.01	0.01	0.02	0.00	0.00	0.01	0.00	0.00	0.00	0.18	0.17
FeO	26.63	27.14	25.96	25.99	26.61	26.72	26.58	26.77	27.60	31.98	31.56	30.86	33.50	34.83	34.77	30.98	31.80	34.69	31.26
MnO	0.39	0.68	0.58	0.58	0.34	0.69	0.61	0.35	0.37	0.77	0.72	0.70	0.46	0.55	0.52	0.58	0.81	0.42	0.73
MgO	19.02	18.78	18.44	18.73	18.35	18.47	18.98	18.80	19.02	15.02	15.34	16.30	13.69	13.25	13.28	14.21	14.21	13.65	14.21
CaO	0.23	0.27	0.85	0.30	0.34	0.61	0.35	0.15	0.18	0.33	0.37	0.28	0.50	0.55	1.51	0.49	0.44	0.56	0.61
Na_2O	0.02	-0.02	-0.02	-0.02	0.01	0.01	0.05	0.01	0.02	0.02	0.02	0.00	0.00	0.02	0.00	0.03	0.00	0.01	0.04
K_2O	-0.02	0.02	0.01	-0.01	0.00	-0.02	0.01	0.02	0.03	0.00	0.01	-0.01	0.00	0.01	0.01	0.00	0.00	0.01	0.01
Total	99.27	99.89	99.08	98.43	98.75	99.55	99.44	99.05	100.50	99.65	99.68	100.14	97.93	99.39	99.73	97.68	98.59	99.99	98.59
Oxygen basis	**6**	**6**	**6**	**6**	**6**	**6**	**6**	**6**	**6**	**6**	**6**	**6**	**6**	**6**	**6**	**6**	**6**	**6**	**6**
Si	1.99	1.98	1.99	1.98	1.98	1.97	1.98	1.98	1.97	2.00	1.99	1.99	1.99	1.97	1.95	2.04	2.03	1.98	2.03
Ti	0.00	0.00	0.00	0.00	0.00	0.00	0.00	0.00	0.00	0.00	0.00	0.00	0.00	0.01	0.00	0.00	0.00	0.00	0.00
Al	0.04	0.04	0.05	0.06	0.08	0.06	0.04	0.06	0.06	0.02	0.03	0.03	0.02	0.02	0.02	0.03	0.02	0.02	0.02
Al-iv	0.01	0.02	0.01	0.02	0.02	0.03	0.02	0.02	0.03	0.00	0.01	0.01	0.00	0.00	0.00	0.00	0.00	0.00	0.00
Al-vi	0.03	0.03	0.04	0.04	0.05	0.03	0.02	0.04	0.03	0.02	0.02	0.02	0.00	0.00	0.00	0.00	0.00	0.00	0.00
Cr	0.00	0.00	0.00	0.00	0.00	0.00	0.00	0.00	0.00	0.00	0.00	0.00	0.00	0.02	0.00	0.00	0.00	0.01	0.01
Fe^{+2}	0.85	0.87	0.83	0.84	0.86	0.85	0.85	0.86	0.88	1.05	1.03	1.00	1.13	1.15	1.09	1.14	1.14	1.13	1.13
Mg	1.08	1.07	1.05	1.08	1.05	1.05	1.08	1.07	1.08	0.88	0.89	0.94	0.82	0.79	0.79	0.85	0.84	0.81	0.84
Mn	0.01	0.02	0.02	0.02	0.01	0.02	0.02	0.01	0.01	0.03	0.02	0.02	0.02	0.02	0.02	0.02	0.03	0.01	0.02
Ca	0.01	0.01	0.03	0.01	0.01	0.02	0.01	0.01	0.01	0.01	0.02	0.01	0.02	0.02	0.06	0.02	0.02	0.02	0.03
Na	0.00	0.00	0.00	0.00	0.00	0.00	0.00	0.00	0.00	0.00	0.00	0.00	0.00	0.00	0.00	0.00	0.00	0.00	0.00
K	0.00	0.00	0.00	0.00	0.00	0.00	0.00	0.00	0.00	0.00	0.00	0.00	0.00	0.00	0.00	0.00	0.00	0.00	0.00
Sum	3.99	3.99	3.98	3.99	3.99	3.99	4.00	3.99	4.00	3.99	3.99	3.99	4.00	4.00	4.00	4.00	4.00	4.00	4.00

Table 8.2d: Representative chemical analyses for plagioclase (representative oxygen basis is given). Mineral abbreviation is used after Whitney and Evans (2010). Cation calculations have been done following the procedure of Grew (1984).

Rock type	**Type IA**														**Type IB**							
Sample no	SR46A	SR46A	SR46A	SR46A	SR46A	SR46A	SR46A	SR46A	SR46A	SR46A	SR46A	SR46A	SR46A	SR46A	SR76A	SR76A	SR76A	SR76A	SR76A	SR76A	SR76A	SR76A
Mineral	*Pl*	*Pl*	*Pl*	*Pl*	*Pl*	*Pl*	*Pl*	*Pl*	*Pl*	*Pl*	*Pl*	*Pl*	*Pl*	*Pl*	*Pl*	*Pl*	*Pl*	*Pl*	*Pl*	*Pl*	*Pl*	*Pl*
Texture	*Laths within matrix interlocing texture with Cpx*														*Laths within matrix interlocing texture with Cpx*							
Point no	29	30	43	65	66	67	68	98	99	102	115	119	126	135	44	45	46	47	94	95	109	110
SiO_2	53.45	53.96	54.86	53.85	54.15	54.35	54.06	53.53	51.37	54.46	54.85	54.63	54.03	54.39	55.14	55.44	54.73	55.26	54.88	55.10	54.74	55.35
TiO_2	0.03	0.02	0.04	0.11	0.04	0.03	0.03	0.32	0.04	-0.01	0.02	0.03	0.02	0.03	0.02	-0.01	0.05	0.11	0.04	0.02	0.01	0.02
Al_2O_3	29.12	28.98	28.40	28.99	29.18	29.31	29.04	28.84	30.48	28.86	29.14	28.95	29.17	29.39	28.09	28.21	28.39	28.06	28.42	28.24	28.46	28.02
Cr_2O_3	-0.01	0.02	0.00	0.01	0.01	0.01	0.00	-0.01	0.00	-0.02	-0.01	0.00	0.00	0.00	0.02	-0.02	-0.02	0.01	-0.01	0.00	0.00	0.00
FeO	-0.03	0.03	0.15	0.22	0.07	0.12	0.08	0.08	0.33	0.16	0.05	0.32	0.04	-0.10	0.22	0.16	0.07	0.21	0.06	0.34	0.16	0.18
MnO	0.05	-0.09	0.03	-0.14	-0.03	0.07	0.01	-0.02	0.05	-0.07	-0.06	-0.03	0.04	-0.16	-0.05	0.11	0.10	-0.12	0.18	0.05	0.12	-0.01
MgO	0.02	0.01	-0.02	-0.02	0.00	0.02	0.00	0.01	0.54	0.00	0.00	0.09	-0.01	0.04	0.01	0.00	0.01	0.00	0.02	0.01	-0.01	0.01
CaO	11.56	11.39	10.11	11.43	11.59	11.45	11.36	11.31	13.60	11.30	11.13	11.24	11.37	11.08	10.42	10.22	10.50	10.26	10.75	10.46	10.53	10.11
Na_2O	4.79	4.72	5.51	4.92	4.85	4.94	4.89	4.75	3.82	5.01	4.98	4.96	4.78	4.91	5.42	5.63	5.32	5.53	5.25	5.42	5.51	5.60
K_2O	0.07	0.06	0.08	0.03	0.04	0.06	0.04	0.07	0.04	0.05	0.07	0.10	0.07	0.03	0.08	0.08	0.02	0.05	0.01	0.04	0.09	0.04
Total	99.05	99.10	99.16	99.40	99.90	100.36	99.51	98.88	100.27	99.74	100.17	100.29	99.51	99.61	99.37	99.82	99.17	99.37	99.60	99.68	99.61	99.32
Oxygen basis	**8**	**8**	**8**	**8**	**8**	**8**	**8**	**8**	**8**	**8**	**8**	**8**	**8**	**8**	**8**	**8**	**8**	**8**	**8**	**8**	**8**	**8**
Si	2.44	2.45	2.49	2.44	2.45	2.44	2.45	2.44	2.33	2.46	2.46	2.46	2.45	2.45	2.50	2.50	2.48	2.50	2.48	2.49	2.48	2.51
Ti	0.00	0.00	0.00	0.00	0.00	0.00	0.00	0.01	0.00	0.00	0.00	0.00	0.00	0.00	0.00	0.00	0.00	0.00	0.00	0.00	0.00	0.00
Al	1.56	1.55	1.52	1.55	1.55	1.55	1.55	1.55	1.63	1.54	1.54	1.54	1.56	1.56	1.50	1.50	1.52	1.50	1.51	1.50	1.52	1.50
Cr	0.00	0.00	0.00	0.00	0.00	0.00	0.00	0.00	0.00	0.00	0.00	0.00	0.00	0.00	0.00	0.00	0.00	0.00	0.00	0.00	0.00	0.00
Fe^{+2}	0.00	0.00	0.01	0.01	0.00	0.00	0.00	0.00	0.01	0.01	0.00	0.01	0.00	0.00	0.01	0.01	0.00	0.01	0.00	0.01	0.01	0.01
Mn	0.00	0.00	0.00	-0.01	0.00	0.00	0.00	0.00	0.00	0.00	0.00	0.00	0.00	-0.01	0.00	0.00	0.00	0.00	0.01	0.00	0.00	0.00
Mg	0.00	0.00	0.00	0.00	0.00	0.00	0.00	0.00	0.04	0.00	0.00	0.01	0.00	0.00	0.00	0.00	0.00	0.00	0.00	0.00	0.00	0.00
Ca	0.56	0.55	0.49	0.56	0.56	0.55	0.55	0.55	0.66	0.55	0.54	0.54	0.55	0.54	0.51	0.49	0.51	0.50	0.52	0.51	0.51	0.49
Na	0.42	0.42	0.48	0.43	0.42	0.43	0.43	0.42	0.34	0.44	0.43	0.43	0.42	0.43	0.48	0.49	0.47	0.49	0.46	0.48	0.48	0.49
K	0.00	0.00	0.00	0.00	0.00	0.00	0.00	0.00	0.00	0.00	0.00	0.01	0.00	0.00	0.00	0.00	0.00	0.00	0.00	0.00	0.01	0.00
Sum	4.99	4.98	5.00	4.99	4.99	4.99	4.99	4.98	5.02	4.99	4.98	4.99	4.98	4.98	4.99	5.00	4.99	4.99	4.99	5.00	5.01	4.99
XOr	*0.00*	*0.00*	*0.00*	*0.00*	*0.00*	*0.00*	*0.00*	*0.00*	*0.00*	*0.00*	*0.00*	*0.01*	*0.00*	*0.00*	*0.00*	*0.00*	*0.00*	*0.00*	*0.00*	*0.00*	*0.01*	*0.00*
XAb	*0.43*	*0.43*	*0.49*	*0.44*	*0.43*	*0.44*	*0.44*	*0.43*	*0.34*	*0.44*	*0.45*	*0.44*	*0.43*	*0.44*	*0.48*	*0.50*	*0.48*	*0.49*	*0.47*	*0.48*	*0.48*	*0.50*
XAn	*0.57*	*0.57*	*0.50*	*0.56*	*0.57*	*0.56*	*0.56*	*0.57*	*0.66*	*0.55*	*0.55*	*0.55*	*0.57*	*0.55*	*0.51*	*0.50*	*0.52*	*0.50*	*0.53*	*0.51*	*0.51*	*0.50*

Table 8.2d (continued): Representative chemical analyses for plagioclase (representative oxygen basis is given). Mineral abbreviation is used after Whitney and Evans (2010). Cation calculations have been done following the procedure of Grew (1984).

Rock type	**Type IIA**													**Type IIB**									
Sample no	SR94	SR94	SR94	SR94	SR94	SR94	SR94	SR94	SR94	SR94	SR94	SR94	SR94	SR46C	SR46C	SR46C	SR46C	SR46C	SR46C	SR46C	SR46C	SR46C	SR46C
Mineral	*Pl*	*Pl*	*Pl*	*Pl*	*Pl*	*Pl*	*Pl*	*Pl*	*Pl*	*Pl*	*Pl*	*Pl*	*Pl*										
Texture	*Pl core (laths in the matrix interlocking texture)*							*Pl rim (laths in the matrix interlocking texture)*															
Point no	11 / 1 . *	30 / 1 .*	22 / 1 . *	19	2	44*	45*	10 / 1 . *	8 / 1 . *	13 / 1 . *	10	47*	51*	128	130	132	136	140	153	154	165	166	167
SiO_2	50.91	50.25	53.44	54.10	50.76	53.74	53.45	56.04	55.66	55.91	57.05	58.04	56.88	56.00	55.11	57.00	57.05	55.50	56.05	54.53	57.27	58.25	57.73
TiO_2	0.04	0.29	0.01	0.03	0.06	0.01	-0.03	0.05	0.00	0.00	0.19	0.08	0.04	0.02	0.03	0.02	0.04	0.01	0.01	0.01	-0.01	-0.01	0.02
Al_2O_3	29.88	29.87	29.62	28.66	29.71	29.20	29.85	27.05	26.88	28.01	27.11	26.31	26.86	28.87	29.33	28.31	28.26	29.21	28.76	29.89	27.82	27.57	27.77
Cr_2O_3	0.00	0.00	0.00	0.01	0.00	-0.01	-0.01	0.00	0.00	0.11	0.01	0.00	0.00	0.04	0.01	0.00	-0.01	0.02	0.01	-0.01	0.01	0.00	0.01
FeO	0.09	0.41	0.06	0.16	0.09	0.23	0.03	0.24	0.00	0.05	0.29	0.29	0.09	0.05	0.16	0.20	0.10	-0.01	-0.04	0.13	0.10	0.09	0.15
MnO	0.00	0.00	0.04	0.05	0.00	-0.08	0.08	0.06	0.00	0.06	0.02	-0.15	-0.05	-0.15	0.07	0.13	-0.03	0.06	-0.14	0.03	-0.06	0.10	0.02
MgO	0.00	0.00	0.00	-0.01	-0.02	0.00	-0.01	0.00	0.00	0.00	0.00	0.00	-0.01	0.00	0.00	0.02	0.00	0.01	-0.01	-0.02	0.01	0.02	0.00
CaO	13.35	13.45	11.96	12.07	13.26	12.15	12.87	9.37	9.44	10.22	9.53	8.54	9.46	11.28	11.77	10.16	10.22	11.45	11.00	12.33	9.91	9.43	9.89
Na_2O	4.09	4.00	4.66	4.83	3.77	4.88	4.39	6.39	6.08	5.80	6.18	6.51	6.13	5.43	5.00	5.71	5.93	5.22	5.15	4.62	6.00	6.15	6.16
K_2O	0.06	0.09	0.13	0.08	0.07	0.08	0.05	0.15	0.17	0.11	0.13	0.13	0.09	-0.01	-0.01	0.00	0.06	0.01	0.05	0.04	0.06	0.03	0.00
Total	98.45	98.36	99.90	100.05	97.82	100.24	100.67	99.34	98.23	100.28	100.51	99.74	99.57	101.53	101.47	101.55	101.62	101.48	100.84	101.55	101.11	101.63	101.75
Oxygen basis	**8**	**8**	**8**	**8**	**8**	**8**	**8**	**8**	**8**	**8**	**8**	**8**	**8**	**8**	**8**	**8**	**8**	**8**	**8**	**8**	**8**	**8**	**8**
Si	2.34	2.32	2.42	2.45	2.36	2.42	2.41	2.53	2.54	2.51	2.55	2.61	2.57	2.48	2.45	2.52	2.52	2.47	2.50	2.43	2.54	2.57	2.55
Ti	0.00	0.01	0.00	0.00	0.00	0.00	0.00	0.00	0.00	0.00	0.01	0.00	0.00	0.00	0.00	0.00	0.00	0.00	0.00	0.00	0.00	0.00	0.00
Al	1.62	1.63	1.58	1.53	1.63	1.55	1.58	1.44	1.45	1.48	1.43	1.39	1.43	1.51	1.54	1.48	1.47	1.53	1.51	1.57	1.46	1.43	1.44
Cr	0.00	0.00	0.00	0.00	0.00	0.00	0.00	0.00	0.00	0.00	0.00	0.00	0.00	0.00	0.00	0.00	0.00	0.00	0.00	0.00	0.00	0.00	0.00
Fe^{+2}	-0.05	-0.06	0.01	0.01	0.02	-0.02	0.01	-0.06	-0.02	-0.01	0.01	0.06	0.03	0.00	0.01	0.01	0.00	0.00	0.00	0.00	0.00	0.00	0.01
Mn	0.00	0.00	0.00	0.00	0.00	0.00	0.00	0.00	0.00	0.00	0.00	-0.01	0.00	-0.01	0.00	0.00	0.00	0.00	-0.01	0.00	0.00	0.00	0.00
Mg	0.00	0.00	0.00	0.00	0.00	0.00	0.00	0.00	0.00	0.00	0.00	0.00	0.00	0.00	0.00	0.00	0.00	0.00	0.00	0.00	0.00	0.00	0.00
Ca	0.66	0.67	0.58	0.59	0.66	0.59	0.62	0.45	0.46	0.49	0.46	0.41	0.46	0.54	0.56	0.48	0.48	0.55	0.52	0.59	0.47	0.45	0.47
Na	0.37	0.36	0.41	0.42	0.34	0.43	0.38	0.56	0.54	0.50	0.54	0.57	0.54	0.47	0.43	0.49	0.51	0.45	0.44	0.40	0.52	0.53	0.53
K	0.00	0.01	0.01	0.00	0.00	0.00	0.00	0.01	0.01	0.01	0.01	0.01	0.01	0.00	0.00	0.00	0.00	0.00	0.00	0.00	0.00	0.00	0.00
Sum	5.00	5.00	5.00	5.00	5.00	5.00	5.00	5.00	5.00	5.00	5.00	5.00	5.00	4.99	4.99	4.98	5.00	4.99	4.97	4.99	4.99	4.98	4.99
Or	*0.00*	*0.01*	*0.01*	*0.00*	*0.00*	*0.00*	*0.00*	*0.01*	*0.01*	*0.01*	*0.01*	*0.01*	*0.01*	*0.00*	*0.00*	*0.00*	*0.00*	*0.00*	*0.00*	*0.00*	*0.00*	*0.00*	*0.00*
Ab	*0.36*	*0.35*	*0.41*	*0.41*	*0.34*	*0.41*	*0.38*	*0.55*	*0.53*	*0.52*	*0.54*	*0.58*	*0.54*	*0.47*	*0.43*	*0.50*	*0.51*	*0.45*	*0.46*	*0.40*	*0.52*	*0.54*	*0.53*
An	*0.64*	*0.65*	*0.58*	*0.58*	*0.66*	*0.58*	*0.62*	*0.44*	*0.46*	*0.49*	*0.46*	*0.42*	*0.46*	*0.53*	*0.57*	*0.50*	*0.49*	*0.55*	*0.54*	*0.59*	*0.48*	*0.46*	*0.47*

**' denotes the mineral compositions used in conventional thermobarometry*

Table 8.2e: Representative chemical analyses for garnet (representative oxygen basis is given). Mineral abbreviation is used after Whitney and Evans (2010). Cation calculations have been done following the procedure of Grew (1984).

Rock type	**Type IIA**											**Type IIB**								
Sample no	**SR94**	**SR94**	**SR94**	**SR94**	**SR94**	**SR94**	**SR94**	**SR94**	**SR94**	**SR94**	**SR94**	**SR64Z**	**SR64Z**	**SR64Z**	**SR64Z**	**SR64Z**	**SR64Z**	**SR64Z**	**SR64Z**	**SR64Z**
Mineral	*Grt*	*Grt*	*Grt*	*Grt*	*Grt*	*Grt*	*Grt*	*Grt*	*Grt*	*Grt*	*Grt*	*Grt*	*Grt*	*Grt*	*Grt*	*Grt*	*Grt*	*Grt*	*Grt*	*Grt*
Texture	*Block shaped Grt rim around Ilm*											*Grt rim^Am*	*Grt ~core*			*Grt rim*	*Grt ~core*	*Grt rim*	*Grt ~core*	
	Core	*Rim*	*Core*	*Rim*	*Core*	*Rim*	*Rim*	*Rim*	*Core*	*Core*	*Core*									
Point no	1 / 1 . *	2 / 1 .*	4 / 1 . *	7 / 1 .*	14 / 1 .*	22 / 1 .*	24 / 1 .*	31 / 1 .*	5 / 1 .*	6 / 1 . *	7 / 1 .	27	30	31	34	35	38	39	42	43
SiO_2	35.29	36.17	35.97	36.04	37.66	37.30	37.36	36.25	36.39	36.83	36.96	37.24	37.51	37.58	37.91	37.70	37.59	37.81	37.92	37.80
TiO_2	0.04	0.01	0.00	0.00	0.00	0.02	0.05	0.05	0.02	0.21	0.01	0.02	0.02	0.01	0.05	0.01	0.04	0.05	0.01	0.01
Al_2O_3	20.74	21.06	20.86	20.61	21.22	21.28	21.46	21.20	21.01	21.26	21.21	20.04	19.82	20.03	19.83	19.93	20.04	20.00	20.29	20.06
Cr_2O_3	0.01	0.02	0.00	0.02	0.00	0.04	0.00	0.02	0.00	0.04	0.00	0.01	0.03	0.00	-0.01	0.02	-0.03	0.00	0.02	0.01
FeO	29.67	29.21	29.77	31.03	29.73	29.53	29.82	29.90	30.24	29.54	28.55	31.65	31.93	28.77	30.25	29.80	30.08	30.76	30.02	30.84
MnO	1.35	1.33	1.29	1.50	1.46	1.71	1.24	1.71	1.81	1.89	1.69	2.74	2.70	2.25	2.18	2.50	2.39	2.52	2.34	2.51
MgO	2.73	2.87	2.98	2.55	2.80	2.70	2.76	2.73	3.12	3.20	3.33	1.95	2.36	2.35	2.27	2.10	2.43	1.86	2.40	2.31
CaO	7.34	7.32	7.43	7.39	7.41	7.55	7.42	7.48	6.26	6.46	7.39	5.32	5.15	6.32	5.95	5.40	6.43	5.65	6.43	6.35
Na_2O	0.00	0.01	0.01	0.00	0.00	0.01	0.00	0.06	0.00	0.03	0.02	0.00	0.02	0.05	0.04	0.02	0.00	0.03	0.07	0.03
K_2O	0.00	0.00	0.00	0.00	0.01	0.00	0.00	0.00	0.00	0.00	0.00	-0.02	-0.01	0.01	0.01	0.00	-0.01	0.00	-0.01	0.00
Total	98.19	98.00	98.33	99.14	100.29	100.16	100.12	99.40	98.86	99.45	99.17	98.95	99.57	97.33	98.49	97.65	98.95	98.68	99.49	99.92
Oxygen basis	**12**	**12**	**12**	**12**	**12**	**12**	**12**	**12**	**12**	**12**	**12**	**12**	**12**	**12**	**12**	**12**	**12**	**12**	**12**	**12**
Si	2.89	2.93	2.91	2.90	2.99	2.96	2.97	2.90	2.93	2.94	2.95	3.03	3.04	3.07	3.08	3.08	3.04	3.07	3.05	3.04
Ti	0.00	0.00	0.00	0.00	0.00	0.00	0.00	0.00	0.00	0.01	0.00	0.00	0.00	0.00	0.00	0.00	0.00	0.00	0.00	0.00
Al	2.00	2.01	1.99	1.96	1.98	1.99	2.01	2.00	1.99	2.00	2.00	1.92	1.89	1.93	1.90	1.92	1.91	1.91	1.92	1.90
Cr	0.00	0.00	0.00	0.00	0.00	0.00	0.00	0.00	0.00	0.00	0.00	0.00	0.00	0.00	0.00	0.00	0.00	0.00	0.00	0.00
Fe^{+2}	1.82	1.86	1.81	1.86	1.93	1.88	1.93	1.80	1.89	1.89	1.80	2.16	2.16	1.97	2.05	2.04	2.04	2.09	2.02	2.07
Mn	0.09	0.09	0.09	0.10	0.10	0.12	0.08	0.12	0.12	0.13	0.11	0.19	0.19	0.16	0.15	0.17	0.16	0.17	0.16	0.17
Mg	0.33	0.35	0.36	0.31	0.33	0.32	0.33	0.33	0.37	0.38	0.40	0.24	0.28	0.29	0.27	0.26	0.29	0.23	0.29	0.28
Ca	0.64	0.64	0.64	0.64	0.63	0.64	0.63	0.64	0.54	0.55	0.63	0.46	0.45	0.55	0.52	0.47	0.56	0.49	0.55	0.55
Na	0.00	0.00	0.00	0.00	0.00	0.00	0.00	0.01	0.00	0.00	0.00	0.00	0.00	0.01	0.01	0.00	0.00	0.00	0.01	0.00
K	0.00	0.00	0.00	0.00	0.00	0.00	0.00	0.00	0.00	0.00	0.00	0.00	0.00	0.00	0.00	0.00	0.00	0.00	0.00	0.00
Sum	8.00	8.00	8.00	8.00	8.00	8.00	8.00	8.00	8.00	8.00	8.00	8.00	8.01	7.97	7.98	7.95	8.00	7.97	8.00	8.01
XAlm	*0.63*	*0.63*	*0.62*	*0.64*	*0.65*	*0.64*	*0.65*	*0.62*	*0.65*	*0.64*	*0.61*	*0.71*	*0.70*	*0.66*	*0.69*	*0.69*	*0.67*	*0.70*	*0.67*	*0.68*
XPrp	*0.12*	*0.12*	*0.12*	*0.11*	*0.11*	*0.11*	*0.11*	*0.11*	*0.13*	*0.13*	*0.13*	*0.08*	*0.09*	*0.10*	*0.09*	*0.09*	*0.10*	*0.08*	*0.10*	*0.09*
XGrs	*0.22*	*0.22*	*0.22*	*0.22*	*0.21*	*0.22*	*0.21*	*0.22*	*0.18*	*0.19*	*0.21*	*0.15*	*0.15*	*0.19*	*0.17*	*0.16*	*0.18*	*0.17*	*0.18*	*0.18*
XSp	*0.03*	*0.03*	*0.03*	*0.04*	*0.03*	*0.04*	*0.03*	*0.04*	*0.04*	*0.04*	*0.04*	*0.06*	*0.06*	*0.05*	*0.05*	*0.06*	*0.05*	*0.06*	*0.05*	*0.06*

**' denotes the mineral compositions used in conventional thermobarometry*

Table 8.2f: Representative chemical analyses for ilmenite (representative oxygen basis is given). Mineral abbreviation is used after Whitney and Evans (2010). Cation calculations have been done following the procedure of Grew (1984).

Rock type	**Type IA**			**Type IB**					**Type IIA**		**Type IIB**					
Sample no	SR46A	SR46A	SR46A	SR76A	SR76A	SR76A	SR76A	SR76A	SR94	SR94	SR46C	SR46C	SR46C	SR64Z	SR64Z	SR64Z
Mineral	*Ilm*	*Ilm*	*Ilm*	*Ilm*	*Ilm*	*Ilm*	*Ilm*	*Ilm*	*Ilm*	*Ilm*	*Ilm*	*Ilm*	*Ilm*	*Ilm*	*Ilm*	*Ilm*
Texture	*Matrix interlocking texture, grains rimmed by double*			*Matrix in association with Ap*					*Rimmed by Grt*					*Ilm in Grt*	*Ilm in Grt*	*Ilm^ Amp*
Point no	6	7	8	14	15	22	25	26	12 / 1 .	3 / 1 .	149	150	179	28	33	41
SiO_2	0.03	0.00	0.02	0.03	-0.01	0.00	-0.02	-0.02	0.00	0.00	0.02	0.05	-0.01	0.08	0.05	0.04
TiO_2	52.46	52.91	53.10	50.97	51.14	52.29	51.45	51.87	51.92	51.75	51.81	52.16	51.84	50.40	49.87	51.29
Al_2O_3	-0.04	0.02	-0.03	0.02	0.02	-0.03	0.02	0.01	0.36	0.31	0.01	0.01	-0.03	-0.02	0.01	-0.01
Cr_2O_3	0.06	0.07	0.06	-0.01	0.02	0.00	0.01	0.02	0.04	0.10	0.16	0.17	0.11	0.04	0.02	0.00
FeO	44.91	45.09	44.79	47.70	46.12	46.40	46.17	45.95	47.46	45.95	45.87	46.86	46.50	46.84	45.60	45.41
MnO	0.66	0.70	0.55	0.38	0.42	0.62	0.46	0.74	0.43	0.40	1.28	1.06	1.39	1.22	1.44	1.22
MgO	1.29	1.33	1.29	0.41	0.37	0.41	0.42	0.31	0.14	0.16	0.29	0.29	0.13	0.01	-0.01	0.02
CaO	0.00	0.01	0.03	-0.02	-0.03	0.00	0.02	-0.02	0.00	0.00	-0.01	0.00	0.04	0.09	0.05	0.05
Na_2O	0.03	0.02	0.05	0.00	0.01	-0.01	0.01	-0.02	0.02	0.03	0.02	-0.02	-0.01	0.00	-0.01	0.01
K_2O	-0.01	-0.02	0.00	-0.03	-0.02	-0.01	0.00	0.00	0.00	0.00	-0.02	0.00	0.02	0.00	-0.01	0.00
Total	99.39	100.13	99.86	99.45	98.04	99.67	98.54	98.84	100.37	98.69	99.43	100.58	99.98	98.67	96.97	98.02
Oxygen basis	**3**	**3**	**3**	**3**	**3**	**3**	**3**	**3**	**3**	**3**	**3**	**3**	**3**	**3**	**3**	**3**
Si	0.00	0.00	0.00	0.00	0.00	0.00	0.00	0.00	0.00	0.00	0.00	0.00	0.00	0.00	0.00	0.00
Ti	0.99	0.99	1.00	0.97	0.99	0.99	0.99	0.99	0.98	0.99	0.99	0.98	0.98	0.97	0.98	0.99
Al	0.00	0.00	0.00	0.00	0.00	0.00	0.00	0.00	0.01	0.01	0.00	0.00	0.00	0.00	0.00	0.00
Cr	0.00	0.00	0.00	0.00	0.00	0.00	0.00	0.00	0.00	0.00	0.00	0.00	0.00	0.00	0.00	0.00
Fe^{+2}	0.93	0.93	0.93	0.95	0.96	0.97	0.96	0.97	0.96	0.98	0.95	0.95	0.95	0.94	0.95	0.96
Mn	0.01	0.01	0.01	0.01	0.01	0.01	0.01	0.02	0.01	0.01	0.03	0.02	0.03	0.03	0.03	0.03
Mg	0.05	0.05	0.05	0.02	0.01	0.02	0.02	0.01	0.01	0.01	0.01	0.01	0.00	0.00	0.00	0.00
Ca	0.00	0.00	0.00	0.00	0.00	0.00	0.00	0.00	0.00	0.00	0.00	0.00	0.00	0.00	0.00	0.00
Na	0.00	0.00	0.00	0.00	0.00	0.00	0.00	0.00	0.00	0.00	0.00	0.00	0.00	0.00	0.00	0.00
K	0.00	0.00	0.00	0.00	0.00	0.00	0.00	0.00	0.00	0.00	0.00	0.00	0.00	0.00	0.00	0.00
Sum	2.00	2.00	2.00	2.00	2.00	2.00	2.00	2.00	2.00	2.00	2.00	2.00	2.00	2.00	2.00	2.00

Table 8.2f (continued): Representative chemical analyses for magnetite and apatite (representative oxygen basis is given). Mineral abbreviation is used after Whitney and Evans (2010). Cation calculations have been done following the procedure of Grew (1984).

Rock type	**Type IA**		**Type IB**																	
Sample no	SR46A	SR46A	SR76A	SR76A	SR76A	SR76A	SR76A	SR76A	SR76A	SR76A	SR76A	SR76A	SR76A	SR76A	SR76A	SR76A	SR76A	SR76A	SR76A	SR76A
Mineral	*Mgt*	*Mgt*	*Mgt*	*Mgt*	*Mgt*	*Mgt*	*Mgt*	*Mgt*	*Mgt*	*Mgt*	*Ap*	*Ap*	*Ap*	*Ap*	*Ap*	*Ap*	*Ap*	*Ap*	*Ap*	*Ap*
Texture	*Matrix*		*Ilm-Ap association*				*Olv-Opx-Mgt intergrowth*													
Point no	154	155	57	58	68	70	73	75	85	87	13	27	28	29	30	31	32	33	59	60
SiO_2	0.07	0.08	0.07	0.05	0.08	0.07	0.13	0.11	0.14	0.13	0.05	0.09	1.70	0.09	0.05	0.08	0.13	0.11	0.07	0.06
TiO_2	0.29	0.89	0.33	0.39	0.54	1.02	0.46	0.32	2.59	0.61	0.01	0.05	0.01	-0.01	0.01	0.03	0.03	0.02	-0.01	0.03
Al_2O_3	0.45	0.25	0.42	0.63	0.34	1.20	0.38	1.08	0.82	0.57	0.01	-0.05	2.33	0.00	-0.04	0.00	0.01	-0.01	-0.04	-0.02
Cr_2O_3	0.15	0.09	0.13	0.13	0.12	0.12	0.12	0.08	0.10	0.12	0.01	-0.01	-0.01	-0.01	0.00	0.02	-0.01	-0.03	0.01	0.01
FeO	90.06	92.11	89.97	89.55	89.31	88.97	89.79	87.87	85.92	89.20	0.11	0.16	2.00	0.22	0.05	0.07	0.37	0.21	0.08	0.22
MnO	-0.02	0.15	-0.14	0.01	-0.15	-0.13	0.11	0.14	0.14	-0.10	0.08	0.01	-0.01	0.02	-0.07	0.06	0.09	0.10	-0.02	0.14
MgO	0.00	0.02	0.00	0.08	0.05	0.08	0.02	0.13	0.05	0.04	0.03	0.03	1.19	0.02	0.00	0.01	0.01	0.03	0.01	0.00
CaO	0.05	0.03	0.03	0.02	0.03	0.02	0.00	0.01	0.01	0.04	53.18	54.61	48.78	53.79	54.33	54.53	54.81	53.75	54.77	53.78
Na_2O	0.04	-0.02	0.05	-0.01	0.02	-0.02	0.06	0.05	0.04	0.03	-0.02	-0.01	-0.01	0.00	0.00	-0.03	0.01	-0.01	0.02	0.02
K_2O	-0.01	0.02	-0.03	0.00	-0.01	0.00	0.03	-0.01	0.03	0.00	-0.01	0.00	0.00	0.00	-0.02	-0.02	-0.03	0.01	-0.01	-0.02
P_2O_5	-	-	-	-	-	-	-	-	-	-	40.46	41.32	37.59	40.43	41.02	40.91	40.96	40.11	41.13	40.47
F	-	-	-	-	-	-	-	-	-	-	2.80	3.58	2.98	3.01	2.99	3.42	3.44	3.10	2.87	2.27
Cl	-	-	-	-	-	-	-	-	-	-	0.20	0.12	0.15	0.15	0.08	0.07	0.10	0.15	0.05	0.04
Total	91.08	93.62	90.83	90.85	90.33	91.33	91.10	89.78	89.84	90.64	96.91	99.90	96.70	97.71	98.40	99.15	99.92	97.54	98.93	97.00
Oxygen basis	**4**	**4**	**4**	**4**	**4**	**4**	**4**	**4**	**4**	**4**	**12**	**12**	**12**	**12**	**12**	**12**	**12**	**12**	**12**	**12**
Si	0.00	0.00	0.00	0.00	0.00	0.00	0.01	0.00	0.01	0.01	0.00	0.01	0.14	0.01	0.00	0.01	0.01	0.01	0.01	0.00
Ti	0.01	0.03	0.01	0.01	0.02	0.03	0.01	0.01	0.08	0.02	0.00	0.00	0.00	0.00	0.00	0.00	0.00	0.00	0.00	0.00
Al	0.02	0.01	0.02	0.03	0.02	0.06	0.02	0.05	0.04	0.03	0.00	0.00	0.22	0.00	0.00	0.00	0.00	0.00	0.00	0.00
Cr	0.00	0.00	0.00	0.00	0.00	0.00	0.00	0.00	0.00	0.00	0.00	0.00	0.00	0.00	0.00	0.00	0.00	0.00	0.00	0.00
Fe^{+2}	1.00	1.02	1.01	1.01	1.02	1.03	1.00	0.99	1.07	1.02	0.01	0.01	0.14	0.01	0.00	0.00	0.02	0.01	0.01	0.01
Mn	0.00	0.00	0.00	0.00	-0.01	0.00	0.00	0.00	0.00	0.00	0.01	0.00	0.00	0.00	0.00	0.00	0.01	0.01	0.00	0.01
Mg	0.00	0.00	0.00	0.00	0.00	0.00	0.00	0.01	0.00	0.00	0.00	0.00	0.14	0.00	0.00	0.00	0.00	0.00	0.00	0.00
Ca	0.00	0.00	0.00	0.00	0.00	0.00	0.00	0.00	0.00	0.00	4.64	4.62	4.25	4.66	4.66	4.65	4.65	4.67	4.68	4.69
Na	0.00	0.00	0.00	0.00	0.00	0.00	0.00	0.00	0.00	0.00	0.00	0.00	0.00	0.00	0.00	0.00	0.00	0.00	0.00	0.00
K	0.00	0.00	0.00	0.00	0.00	0.00	0.00	0.00	0.00	0.00	0.00	0.00	0.00	0.00	0.00	0.00	0.00	0.00	0.00	0.00
P	-	-	-	-	-	-	-	-	-	-	2.79	2.76	2.59	2.77	2.78	2.76	2.74	2.75	2.78	2.79
F	-	-	-	-	-	-	-	-	-	-	0.72	0.89	0.77	0.77	0.76	0.86	0.86	0.79	0.72	0.58
Cl	-	-	-	-	-	-	-	-	-	-	0.03	0.02	0.02	0.02	0.01	0.01	0.01	0.02	0.01	0.01
Sum	1.05	1.07	1.05	1.06	1.06	1.13	1.05	1.08	1.20	1.07	8.19	8.31	8.26	8.24	8.21	8.29	8.31	8.27	8.20	8.10
Fe^{+3}	1.95	1.93	1.95	1.94	1.94	1.87	1.95	1.92	1.80	1.93										

Table 8.2g: Representative chemical analyses for amphibole (representative oxygen basis is given). Mineral abbreviation is used after Whitney and Evans (2010). Cation calculations have been done following the procedure of Leake et al. (2004).

Rock type	**Type IA**												**Type IB**									
Sample no	**SR46A**	**SR46A**	**SR46A**	**SR46A**	**SR46A**	**SR46A**	**SR46A**	**SR46A**	**SR46A**	**SR46A**	**SR46A**	**SR46A**	**SR76A**	**SR76A**	**SR76A**	**SR76A**	**SR76A**	**SR76A**	**SR76A**	**SR76A**	**SR76A**	**SR76A**
Mineral	*Amp*	*Amp*	*Amp*	*Amp*	*Amp*	*Amp*	*Amp*	*Amp*	*Amp*	*Amp*	*Amp*	*Amp*	*Amp*	*Amp*	*Amp*	*Amp*	*Amp*	*Amp*	*Amp*	*Amp*	*Amp*	*Amp*
Texture	*Cor^Opq*	*Cor^Opq*	*Cor^Opx^ Olv*	*Cor^Opx^ Olv*	*Cor^Opx^ Olv*	*Sym Cor ^Opq*	*Sym Cor ^Opq*	*Cor^Bt^ Opq*	*Cor^Bt^ Opq*	*Sym Cor ^Opx^ Olv*	*Sym Cor ^Opx^ Olv*	*Sym Cor ^Opx^ Olv*	*Outer Cor^Ilm-Ap*					*Outer Cor^ Olv-Opx-Mgt intergrowth*				
Point no	4	5	23	24	25	31	32	41	42	92	93	94	43	48	53	62	63	80	81	82	92	93
SiO_2	39.79	39.85	41.03	40.48	41.08	41.09	40.78	40.16	41.81	40.82	41.30	40.27	39.78	39.44	40.49	40.34	40.49	40.82	40.43	40.48	40.72	40.28
TiO_2	1.27	1.41	3.18	0.26	0.35	0.86	1.18	1.42	1.20	0.10	0.33	0.11	0.95	1.06	1.00	0.62	0.89	0.48	0.70	1.04	1.05	1.08
Al_2O_3	16.18	16.11	13.85	16.63	16.66	16.20	15.93	16.06	14.64	16.83	16.60	17.32	15.46	15.85	15.89	16.22	15.89	15.93	16.52	15.70	15.59	15.70
Cr_2O_3	0.03	0.11	0.05	0.01	0.03	0.02	0.04	0.14	0.06	0.00	0.01	0.00	0.00	0.01	0.02	0.00	0.00	-0.01	0.01	0.01	0.01	0.02
FeO	11.18	11.46	11.31	12.08	11.70	11.55	11.89	11.62	12.58	11.23	12.03	11.83	16.75	17.03	14.12	14.71	14.71	14.14	14.32	13.24	13.76	14.41
MnO	0.23	-0.03	0.21	0.08	0.17	0.09	0.21	0.11	-0.02	-0.03	0.22	0.18	0.14	0.02	0.13	0.22	0.24	0.08	0.18	0.16	0.22	0.07
MgO	11.46	11.81	12.02	12.01	12.08	11.96	11.90	11.72	12.83	12.01	12.05	12.16	8.78	8.77	10.72	10.92	10.64	10.99	10.62	10.54	10.75	10.79
CaO	11.03	11.11	11.87	11.04	11.16	11.10	10.92	11.26	10.50	11.32	11.40	10.70	10.78	10.76	11.00	10.99	10.83	11.13	11.03	11.08	11.38	11.35
Na_2O	2.60	2.57	1.72	2.50	2.52	2.58	2.53	2.54	2.54	2.58	2.51	2.40	1.87	1.94	2.47	2.35	2.39	2.41	2.53	2.40	2.28	2.37
K_2O	0.77	0.66	0.40	0.58	0.65	0.64	0.68	0.73	0.67	0.76	0.71	0.64	0.78	0.87	0.66	0.71	0.71	0.71	0.76	0.75	0.61	0.57
Total	94.67	95.08	96.06	95.77	96.48	96.06	96.14	95.98	96.92	95.66	97.39	95.82	95.99	96.07	96.42	97.26	97.15	97.09	97.30	95.63	96.45	96.99
Oxygen basis	**23**	**23**	**23**	**23**	**23**	**23**	**23**	**23**	**23**	**23**	**23**	**23**	**23**	**23**	**23**	**23**	**23**	**23**	**23**	**23**	**23**	**23**
Si	6.01	5.98	6.13	6.01	6.05	6.08	6.05	5.99	6.13	6.06	6.05	5.95	6.07	6.00	6.04	5.97	6.02	6.06	5.99	6.10	6.08	6.00
Al (IV)	1.99	2.02	1.87	1.99	1.95	1.92	1.95	2.01	1.87	1.94	1.95	2.05	1.93	2.00	1.96	2.03	1.98	1.94	2.01	1.90	1.92	2.00
Ti	0.00	0.00	0.00	0.00	0.00	0.00	0.00	0.00	0.00	0.00	0.00	0.00	0.00	0.00	0.00	0.00	0.00	0.00	0.00	0.00	0.00	0.00
Sum T	8.00	8.00	8.00	8.00	8.00	8.00	8.00	8.00	8.00	8.00	8.00	8.00	8.00	8.00	8.00	8.00	8.00	8.00	8.00	8.00	8.00	8.00
Al (VI)	0.89	0.83	0.56	0.92	0.94	0.90	0.83	0.82	0.66	1.01	0.92	0.97	0.85	0.84	0.83	0.80	0.81	0.85	0.88	0.89	0.82	0.76
Ti	0.14	0.16	0.36	0.03	0.04	0.10	0.13	0.16	0.13	0.01	0.04	0.01	0.11	0.12	0.11	0.07	0.10	0.05	0.08	0.12	0.12	0.12
Cr +3	0.00	0.01	0.01	0.00	0.00	0.00	0.00	0.02	0.01	0.00	0.00	0.00	0.00	0.00	0.00	0.00	0.00	0.00	0.00	0.00	0.00	0.00
Fe +3	0.21	0.26	0.14	0.44	0.35	0.28	0.34	0.24	0.50	0.26	0.33	0.57	0.41	0.44	0.35	0.56	0.44	0.39	0.37	0.22	0.28	0.40
Mg	2.58	2.64	2.67	2.66	2.65	2.64	2.63	2.61	2.80	2.66	2.63	2.68	2.00	1.99	2.38	2.41	2.36	2.43	2.35	2.37	2.39	2.40
Fe +2	1.17	1.09	1.26	0.95	1.01	1.08	1.07	1.16	0.90	1.06	1.08	0.77	1.63	1.61	1.32	1.16	1.29	1.27	1.32	1.40	1.38	1.32
Mn	0.00	0.00	0.00	0.00	0.00	0.00	0.00	0.00	0.00	0.00	0.00	0.00	0.00	0.00	0.00	0.00	0.00	0.00	0.00	0.00	0.00	0.00
Li	0.00	0.00	0.00	0.00	0.00	0.00	0.00	0.00	0.00	0.00	0.00	0.00	0.00	0.00	0.00	0.00	0.00	0.00	0.00	0.00	0.00	0.00
Sum C	5.00	5.00	5.00	5.00	5.00	5.00	5.00	5.00	5.00	5.00	5.00	5.00	5.00	5.00	5.00	5.00	5.00	5.00	5.00	5.00	5.00	5.00
Mg	0.00	0.00	0.00	0.00	0.00	0.00	0.00	0.00	0.00	0.00	0.00	0.00	0.00	0.00	0.00	0.00	0.00	0.00	0.00	0.00	0.00	0.00
Fe +2	0.03	0.08	0.01	0.10	0.08	0.07	0.07	0.05	0.15	0.08	0.07	0.12	0.09	0.11	0.08	0.09	0.10	0.10	0.08	0.04	0.05	0.08
Mn	0.03	0.00	0.03	0.01	0.02	0.01	0.03	0.01	0.00	0.00	0.03	0.02	0.02	0.00	0.02	0.03	0.03	0.01	0.02	0.02	0.03	0.01
Li	0.00	0.00	0.00	0.00	0.00	0.00	0.00	0.00	0.00	0.00	0.00	0.00	0.00	0.00	0.00	0.00	0.00	0.00	0.00	0.00	0.00	0.00
Ca	1.79	1.79	1.90	1.76	1.76	1.76	1.73	1.80	1.65	1.80	1.79	1.69	1.76	1.75	1.76	1.74	1.73	1.77	1.75	1.79	1.82	1.81
Na	0.16	0.13	0.06	0.13	0.14	0.16	0.17	0.13	0.20	0.12	0.11	0.16	0.13	0.13	0.14	0.14	0.15	0.12	0.14	0.15	0.10	0.10
Sum B	2.00	2.00	2.00	2.00	2.00	2.00	2.00	2.00	2.00	2.00	2.00	2.00	2.00	2.00	2.00	2.00	2.00	2.00	2.00	2.00	2.00	2.00
Ca	0.00	0.00	0.00	0.00	0.00	0.00	0.00	0.00	0.00	0.00	0.00	0.00	0.00	0.00	0.00	0.00	0.00	0.00	0.00	0.00	0.00	0.00
Na	0.61	0.61	0.44	0.59	0.58	0.58	0.56	0.60	0.52	0.62	0.60	0.53	0.43	0.44	0.57	0.54	0.54	0.57	0.59	0.55	0.56	0.59
K	0.15	0.13	0.08	0.11	0.12	0.12	0.13	0.14	0.13	0.14	0.13	0.12	0.15	0.17	0.13	0.13	0.13	0.13	0.14	0.14	0.12	0.11
Sum A	0.75	0.74	0.51	0.70	0.71	0.70	0.69	0.74	0.64	0.77	0.73	0.65	0.58	0.61	0.70	0.67	0.68	0.71	0.73	0.70	0.68	0.69
TOTAL	15.75	15.74	15.51	15.70	15.71	15.70	15.69	15.74	15.64	15.76	15.73	15.65	15.58	15.61	15.70	15.67	15.68	15.71	15.73	15.70	15.68	15.69
X-Mg	*0.68*	*0.69*	*0.68*	*0.72*	*0.71*	*0.70*	*0.70*	*0.68*	*0.73*	*0.70*	*0.70*	*0.75*	*0.54*	*0.54*	*0.63*	*0.66*	*0.63*	*0.64*	*0.63*	*0.62*	*0.62*	*0.63*
Classification	*Pargasite*																					

Table 8.2g (continued): Representative chemical analyses for amphibole (representative oxygen basis is given). Mineral abbreviation is used after Whitney and Evans (2010). Cation calculations have been done following the procedure of Leake et al. (2004).

Rock type	**Type IIA**								**Type IIB**															
Sample no	**SR94**	**SR94**	**SR94**	**SR94**	**SR94**	**SR94**	**SR94**	**SR94**	**SR46C**	**SR46C**	**SR46C**	**SR46C**	**SR46C**	**SR46C**	**SR46C**	**SR46C**	**SR46C**	**SR46C**	**SR46C**	**SR64Z**	**SR64Z**	**SR64Z**	**SR64Z**	**SR64Z**
Mineral	*Amp*	*Amp*	*Amp*	*Amp*	*Amp*	*Amp*	*Amp*	*Amp*	*Amp*	*Amp*	*Amp*	*Amp*	*Amp*	*Amp*	*Amp*	*Amp*	*Amp*	*Amp*	*Amp*	*Amp*	*Amp*	*Amp*	*Amp*	*Amp*
Texture	*ᵃGrt*	*ᵃGrt*	*ᵃGrt*	*ᵃGrt*	*ᵃCpx*	*ᵃGrt*	*ᵃCpx*	*ᵃCpx*						*Matrix ᵃPl*									*Matrix ᵃPl*	
Point no	8 / 1 .*	9 / 1 .*	23 / 1 .*	28 / 1 .*	29 / 1 .	1 / 1 .*	14 / 1 .	17 / 1 .	112	113	114	115	116	117	120	122	125	126	127	*26*	*36*	*37*	*40*	*47*
SiO_2	40.81	41.02	41.49	40.00	40.14	40.43	41.55	42.52	45.53	44.89	46.64	47.36	46.33	46.35	45.55	44.76	45.97	46.01	45.67	40.87	40.9	40.71	41.21	40.04
TiO_2	2.10	1.97	2.00	2.18	1.99	1.81	2.02	1.81	0.92	0.92	0.80	0.73	0.78	0.79	0.82	0.86	0.79	0.78	0.78	0.82	0.72	0.71	0.71	0.86
Al_2O_3	11.61	11.79	12.01	12.62	12.00	12.06	12.30	12.08	10.71	11.28	10.04	9.65	10.39	10.71	10.81	11.82	10.87	11.04	10.79	13.30	12.99	13.30	12.91	13.21
Cr_2O_3	0.00	0.00	0.04	0.06	0.11	0.00	0.13	0.23	0.05	0.01	0.01	0.03	0.00	0.04	0.02	0.04	0.01	0.03	0.02	0.00	0.02	0.04	0.04	0.01
FeO	19.28	19.33	19.55	18.70	19.12	17.26	17.63	17.07	16.85	16.75	16.34	16.45	16.75	16.81	16.52	17.17	16.15	16.32	16.44	21.11	21.85	22.24	21.62	21.82
MnO	8.35	8.20	8.07	7.80	8.30	8.87	8.48	8.51	0.25	0.32	0.11	0.39	0.30	0.11	0.17	0.45	0.27	0.21	0.03	0.26	0.29	0.07	0.27	0.13
MgO	0.18	0.19	0.15	0.15	0.15	0.16	0.14	0.03	10.54	10.29	11.23	11.56	10.57	10.60	10.58	9.76	10.54	10.55	10.49	6.29	6.47	6.30	6.43	6.05
CaO	11.64	11.73	11.48	11.44	11.65	11.74	11.47	11.26	11.88	11.62	11.83	11.84	12.09	11.87	11.99	11.68	11.94	11.98	11.78	10.70	10.91	10.66	10.88	10.45
Na_2O	1.73	1.76	1.86	1.82	1.71	1.61	1.66	1.59	1.19	1.25	1.10	0.94	0.85	0.93	0.93	1.25	1.00	1.07	1.00	1.53	1.52	1.49	1.47	1.47
K_2O	1.23	1.30	1.29	1.35	1.27	1.29	1.40	1.30	0.70	0.80	0.68	0.56	0.73	0.74	0.78	0.89	0.78	0.81	0.75	0.59	0.54	0.61	0.52	0.65
Total	96.96	97.32	97.97	96.12	96.44	95.24	96.82	96.41	98.94	98.28	98.97	99.64	99.01	99.06	98.28	98.87	98.56	98.95	98.00	95.66	96.45	96.25	96.20	94.87
Oxygen basis	**23**	**23**	**23**	**23**	**23**	**23**	**23**	**23**	**23**	**23**	**23**	**23**	**23**	**23**	**23**	**23**	**23**	**23**	**23**	**23**	**23**	**23**	**23**	**23**
Si	6.27	6.29	6.31	6.21	6.20	6.28	6.35	6.48	6.69	6.63	6.80	6.83	6.78	6.76	6.71	6.60	6.75	6.73	6.74	6.34	6.30	6.28	6.36	6.28
Al (IV)	1.73	1.71	1.69	1.79	1.80	1.72	1.65	1.52	1.31	1.37	1.20	1.17	1.22	1.24	1.29	1.40	1.25	1.27	1.26	1.66	1.70	1.72	1.64	1.72
Ti	0.00	0.00	0.00	0.00	0.00	0.00	0.00	0.00	0.00	0.00	0.00	0.00	0.00	0.00	0.00	0.00	0.00	0.00	0.00	0.00	0.00	0.00	0.00	0.00
Sum T	8.00	8.00	8.00	8.00	8.00	8.00	8.00	8.00	8.00	8.00	8.00	8.00	8.00	8.00	8.00	8.00	8.00	8.00	8.00	8.00	8.00	8.00	8.00	8.00
Al (VI)	0.38	0.43	0.47	0.52	0.39	0.49	0.56	0.65	0.54	0.59	0.53	0.48	0.57	0.60	0.58	0.65	0.63	0.63	0.62	0.78	0.67	0.70	0.70	0.72
Ti	0.24	0.23	0.23	0.25	0.23	0.21	0.23	0.21	0.10	0.10	0.09	0.08	0.09	0.09	0.09	0.10	0.09	0.09	0.09	0.10	0.08	0.08	0.08	0.10
Cr +3	0.00	0.00	0.01	0.01	0.01	0.00	0.02	0.03	0.01	0.00	0.00	0.00	0.00	0.00	0.00	0.00	0.00	0.00	0.00	0.00	0.00	0.00	0.00	0.00
Fe +3	0.19	0.12	0.14	0.09	0.25	0.11	0.05	0.01	0.23	0.25	0.23	0.34	0.21	0.22	0.23	0.22	0.16	0.16	0.19	0.35	0.51	0.54	0.44	0.48
Mg	1.91	1.88	1.83	1.80	1.91	2.05	1.93	1.93	2.31	2.26	2.44	2.49	2.30	2.30	2.32	2.14	2.31	2.30	2.31	1.45	1.49	1.45	1.48	1.41
Fe +2	2.27	2.35	2.33	2.33	2.21	2.13	2.20	2.16	1.81	1.79	1.71	1.61	1.83	1.78	1.77	1.89	1.81	1.82	1.79	2.32	2.25	2.23	2.29	2.28
Mn	0.00	0.00	0.00	0.00	0.00	0.00	0.00	0.00	0.00	0.00	0.00	0.00	0.00	0.00	0.00	0.00	0.00	0.00	0.00	0.00	0.00	0.00	0.00	0.00
Li	0.00	0.00	0.00	0.00	0.00	0.00	0.00	0.00	0.00	0.00	0.00	0.00	0.00	0.00	0.00	0.00	0.00	0.00	0.00	0.00	0.00	0.00	0.00	0.00
Sum C	5.00	5.00	5.00	5.00	5.00	5.00	5.00	5.00	5.00	5.00	5.00	5.00	5.00	5.00	5.00	5.00	5.00	5.00	5.00	5.00	5.00	5.00	5.00	5.00
Mg	0.00	0.00	0.00	0.00	0.00	0.00	0.00	0.00	0.00	0.00	0.00	0.00	0.00	0.00	0.00	0.00	0.00	0.00	0.00	0.00	0.00	0.00	0.00	0.00
Fe +2	0.01	0.01	0.02	0.01	0.01	0.00	0.00	0.00	0.03	0.03	0.05	0.03	0.01	0.05	0.03	0.01	0.01	0.02	0.05	0.07	0.05	0.10	0.06	0.10
Mn	0.02	0.03	0.02	0.02	0.02	0.02	0.02	0.00	0.03	0.04	0.01	0.05	0.04	0.01	0.02	0.06	0.03	0.03	0.00	0.03	0.04	0.01	0.04	0.02
Li	0.00	0.00	0.00	0.00	0.00	0.00	0.00	0.00	0.00	0.00	0.00	0.00	0.00	0.00	0.00	0.00	0.00	0.00	0.00	0.00	0.00	0.00	0.00	0.00
Ca	1.92	1.93	1.87	1.90	1.93	1.95	1.88	1.84	1.87	1.84	1.85	1.83	1.90	1.86	1.89	1.84	1.88	1.88	1.86	1.78	1.80	1.76	1.80	1.76
Na	0.04	0.04	0.09	0.07	0.04	0.02	0.11	0.16	0.07	0.09	0.09	0.09	0.06	0.08	0.06	0.09	0.08	0.08	0.08	0.12	0.11	0.13	0.11	0.13
Sum B	2.00	2.00	2.00	2.00	2.00	2.00	2.00	2.00	2.00	2.00	2.00	2.00	2.00	2.00	2.00	2.00	2.00	2.00	2.00	2.00	2.00	2.00	2.00	2.00
Ca	0.00	0.00	0.00	0.00	0.00	0.00	0.00	0.00	0.00	0.00	0.00	0.00	0.00	0.00	0.00	0.00	0.00	0.00	0.00	0.00	0.00	0.00	0.00	0.00
Na	0.47	0.49	0.46	0.48	0.47	0.46	0.39	0.31	0.27	0.27	0.22	0.17	0.19	0.18	0.21	0.26	0.21	0.23	0.21	0.34	0.35	0.32	0.33	0.32
K	0.24	0.25	0.25	0.27	0.25	0.26	0.27	0.25	0.13	0.15	0.13	0.10	0.14	0.14	0.15	0.17	0.15	0.15	0.14	0.12	0.11	0.12	0.10	0.13
Sum A	0.71	0.74	0.71	0.74	0.72	0.72	0.66	0.56	0.40	0.42	0.35	0.28	0.32	0.32	0.35	0.43	0.36	0.38	0.35	0.46	0.46	0.44	0.43	0.45
TOTAL	15.71	15.74	15.71	15.74	15.72	15.72	15.66	15.56	15.40	15.42	15.35	15.28	15.32	15.32	15.35	15.43	15.36	15.38	15.35	15.46	15.46	15.44	15.43	15.45
X-Mg	*0.46*	*0.44*	*0.44*	*0.44*	*0.46*	*0.49*	*0.47*	*0.47*	*0.56*	*0.55*	*0.58*	*0.60*	*0.56*	*0.56*	*0.56*	*0.53*	*0.56*	*0.56*	*0.56*	*0.38*	*0.39*	*0.38*	*0.39*	*0.37*
Classification				*Ferropargasite*									*Magnesio-Hornblende*									*Ferro-tschermakite*		

**' denotes the mineral compositions used in conventional thermobarometry*

Table 8.2h: Representative chemical analyses for biotite (representative oxygen basis is given). Mineral abbreviation is used after Whitney and Evans (2010). Cation calculations have been done following the procedure of Grew (1984).

Rock type	**Type IA**							**Type IB**									**Type IIA**							
Sample no	**SR46A**	**SR46A**	**SR46A**	**SR46A**	**SR46A**	**SR46A**	**SR46A**	**SR76A**	**SR76A**	**SR76A**	**SR76A**	**SR76A**	**SR76A**	**SR76A**	**SR76A**	**SR76A**	**SR94**	**SR94**	**SR94**	**SR94**	**SR94**	**SR94**	**SR94**	**SR94**
Mineral	Bt	Bt	Bt	Bt	Bt	Bt	Bt	Bt	Bt	Bt	Bt	Bt	Bt	Bt	Bt	Bt	Bt	Bt	Bt	Bt	Bt	Bt	Bt	Bt
Texture	*Cor^Opq*							*Inner Cor^Ilm-Ap*									*Incl. ^Grt*	*Incl. ^Grt*	*^Ilm*			*^Grt*		
Point no	11	12	13	34	35	38	39	11	16	17	34	35	36	37	38	39	5 / 1 .	6 / 1 .	16 / 1 .	2 / 1 .	9 / 1 .	10 / 1 .	11 / 1 .	12 / 1 .
SiO_2	36.49	36.12	36.75	36.45	36.81	36.27	35.91	34.42	36.10	34.99	35.32	35.48	36.19	35.64	34.79	35.53	33.71	33.68	34.42	34.28	34.86	34.95	35.61	35.47
TiO_2	3.02	3.17	2.85	2.55	2.55	2.82	2.92	3.64	2.88	2.81	2.85	2.57	2.40	2.70	2.35	2.73	4.92	4.74	5.07	4.64	4.87	4.40	4.99	4.64
Al_2O_3	16.41	15.98	16.01	16.39	16.39	15.77	16.30	15.05	15.64	15.75	16.76	16.41	16.26	16.36	17.07	16.18	13.69	13.95	14.35	14.09	14.38	14.10	14.24	14.37
Cr_2O_3	0.18	0.18	0.19	0.18	0.17	0.19	0.18	0.01	0.01	0.01	0.01	0.02	0.00	0.03	0.06	0.01	0.00	0.02	0.02	0.04	0.00	0.01	0.05	0.06
FeO	11.17	10.53	10.67	10.47	9.94	9.74	10.61	18.77	16.59	17.73	16.96	16.87	15.71	16.66	17.75	17.12	20.69	19.68	21.06	19.11	20.03	19.81	20.09	20.66
MnO	0.08	0.00	0.05	0.00	-0.03	-0.15	0.10	-0.02	-0.02	0.17	0.13	0.16	-0.03	0.00	-0.02	0.14	0.14	0.10	0.07	0.10	0.06	0.00	0.06	0.01
MgO	17.14	16.49	16.88	17.13	17.87	17.23	16.86	10.73	12.78	12.57	12.89	13.21	13.34	13.15	12.97	13.05	9.69	9.90	9.32	10.64	10.48	10.42	9.95	10.25
CaO	0.00	0.01	0.03	0.02	0.01	-0.02	-0.01	0.03	-0.01	0.04	0.01	0.04	-0.01	0.03	0.09	0.04	0.00	0.01	0.00	0.00	0.00	0.00	0.00	0.00
Na_2O	0.52	0.41	0.47	0.53	0.51	0.47	0.49	0.12	0.25	0.30	0.28	0.34	0.36	0.33	0.31	0.26	0.14	0.08	0.08	0.25	0.12	0.10	0.33	0.09
K_2O	8.88	9.23	8.84	8.70	8.71	9.15	8.74	8.70	8.78	8.97	9.08	8.81	8.80	8.79	7.86	8.66	9.13	9.14	9.27	8.95	9.44	9.08	9.38	8.71
F	0.23	0.09	0.24	0.15	0.15	0.25	0.16	0.22	0.37	0.45	0.4	0.28	0.56	0.33	0.31	0.34								
Cl	0.01	0.01	0.01	0.01	0.02	0.01	0.02	0.18	0.15	0.16	0.1	0.08	0.11	0.09	0.07	0.08								
Total	94.13	92.26	92.97	92.59	93.11	91.74	92.26	91.85	93.53	93.98	94.80	94.27	93.72	94.14	93.61	94.14	92.12	91.35	93.69	92.15	94.28	92.89	94.73	94.29
Oxygen basis	**11**	**11**	**11**	**11**	**11**	**11**	**11**	**11**	**11**	**11**	**11**	**11**	**11**	**11**	**11**	**11**	**11**	**11**	**11**	**11**	**11**	**11**	**11**	**11**
Si	2.71	2.74	2.76	2.74	2.74	2.75	2.72	2.74	2.78	2.71	2.70	2.71	2.77	2.73	2.68	2.72	2.77	2.78	2.79	2.79	2.78	2.83	2.84	2.84
Ti	0.17	0.18	0.16	0.14	0.14	0.16	0.17	0.22	0.17	0.16	0.16	0.15	0.14	0.16	0.14	0.16	0.30	0.29	0.31	0.28	0.29	0.27	0.30	0.28
Al	1.44	1.43	1.42	1.45	1.44	1.41	1.45	1.41	1.42	1.44	1.51	1.48	1.47	1.47	1.55	1.46	1.33	1.36	1.37	1.35	1.35	1.35	1.34	1.36
Cr	0.01	0.01	0.01	0.01	0.01	0.01	0.01	0.00	0.00	0.00	0.00	0.00	0.00	0.00	0.00	0.00	0.00	0.00	0.00	0.00	0.00	0.00	0.00	0.00
Fe^{+2}	0.69	0.67	0.67	0.66	0.62	0.62	0.67	1.25	1.07	1.15	1.08	1.08	1.01	1.07	1.14	1.10	1.92	1.90	2.03	1.84	1.87	1.93	1.94	2.09
Mn	0.01	0.00	0.00	0.00	0.00	-0.01	0.01	0.00	0.00	0.01	0.01	0.01	0.00	0.00	0.00	0.01	0.01	0.01	0.00	0.01	0.00	0.00	0.00	0.00
Mg	1.90	1.86	1.89	1.92	1.99	1.95	1.90	1.27	1.47	1.45	1.47	1.51	1.52	1.50	1.49	1.49	1.19	1.22	1.13	1.29	1.25	1.26	1.18	1.22
Ca	0.00	0.00	0.00	0.00	0.00	0.00	0.00	0.00	0.00	0.00	0.00	0.00	0.00	0.00	0.01	0.00	0.00	0.00	0.00	0.00	0.00	0.00	0.00	0.00
Na	0.07	0.06	0.07	0.08	0.07	0.07	0.07	0.02	0.04	0.05	0.04	0.05	0.05	0.05	0.05	0.04	0.02	0.01	0.01	0.04	0.02	0.01	0.05	0.01
K	0.84	0.89	0.85	0.83	0.83	0.89	0.84	0.88	0.86	0.89	0.88	0.86	0.86	0.86	0.77	0.85	0.96	0.96	0.96	0.93	0.96	0.94	0.95	0.89
Sum	7.85	7.84	7.82	7.84	7.84	7.85	7.84	7.79	7.80	7.87	7.85	7.85	7.81	7.83	7.82	7.83	8.00	8.00	8.00	8.00	8.00	8.00	8.00	8.00
X_{Mg}	*0.73*	*0.74*	*0.74*	*0.74*	*0.76*	*0.76*	*0.74*	*0.50*	*0.58*	*0.56*	*0.58*	*0.58*	*0.60*	*0.58*	*0.57*	*0.58*	*0.38*	*0.39*	*0.36*	*0.41*	*0.40*	*0.39*	*0.38*	*0.37*

8.3. Physical condition of metamorphism

Physical conditions of metamorphism, experienced by the meta-mafic rocks in the study area are calculated from the garnetiferous samples using: a) Conventional geothermobarometry and b) Pseudosection analysis.

8.3.1. Conventional geothermobarometry

The garnetiferous type-IIA samples are used for conventional thermobarometry for the suitable metamorphic mineral association. Metamorphic assemblages that are developed in the studied meta-mafic rocks present the opportunity to implement garnet-clinopyroxene (Ganguly, 1979), garnet-amphibole (Perchuk, 1991) and amphibole-plagioclase thermometers (Holland and Blundy, 1994) garnet-clinopyroxene-plagioclase-quartz (Eckert et al., 1991)and garnet-amphibole-plagioclase-quartz (Kohn and Spear, 1990) barometers. The results are presented in Table-8.3. Different mineral pairs have been used and the results presented below represent the "average values ± standard deviation" associated with these permutations. For estimation of temperature, an independent pressure is required. 8 kbar pressure was input based on our observation from the P-T pseudosection study (discussed below).

Garnet in type IIA assemblage, shows homogeneous composition and pair of garnet and clinopyroxene that shares straight grain-contact in the immediate vicinity is used to constrain peak metamorphic condition when garnet and clinopyroxene were in equilibrium. Applications of the garnet-clinopyroxene geothermometer to type IIA mineral assemblage yield tightly clustered temperature value of 770±15°C (Ganguly, 1979) (Table-8.3). For the garnet-clinopyroxene-plagioclase-quartz barometer (Eckert, 1991), this mean temperature 770°C is used and the estimated peak pressure clustered within 8.5±0.5 kbar (Table-8.3). Petrographic study confirms that garnet and clinopyroxene both are always partly replaced by amphibole. Several pairs of garnet from type IIA rocks and secondary amphibole yield 620 ±20°C temperature (Graham and Powell, 1984) and using the same pair garnet-amphibole-plagioclase-quartz barometer (Kohn and Spear, 1990) constrains the pressure condition at 6±0.5 kbar (Table-8.3). Garnet-clinopyroxene-plagioclase mineral pairs most likely constrain the

peak metamorphic condition that was experienced by mafic dykes whereas garnet-amphibole-plagioclase yields the physical condition of subsequent cooling and

Table 8.3: P–T estimates of garnetiferous Type-IIA meta-mafic sample, obtained using various conventional thermobarometers (T: °C, P: kbar).

	Conventional Thermometry						Conventional Barometry					
	Thermometers used	Rock type (Sample No.)	Mineral Assemblages	P_{ref} (kbar)	Results			Barometers used	Rock type (Sample No.)	Mineral Assemblages	T_{ref} (°C)	Results
					T (°C)	Avg						P (kbar) Avg
Peak	Grt-Cpx[a]	Type-IIA (SR94)	Grt (1/1.) - Cpx (19/1.)	8	784	770±15	Peak	Grt-Cpx-Pl-Qz[b]	Type-IIA (SR94)	Grt (1/1.) - Cpx (19/1.)-Pl (11/1.)	770	9.1 8.2 8.5± 0.5
			Grt (4/1.) - Cpx (25/1.)		756					Grt (4/1.) - Cpx (25/1.)-Pl (30/1.)		8.5
			Grt (14/1.) - Cpx (26/1.)		753					Grt (14/1.) - Cpx (26/1.)-Pl (22/1.)		
			Grt (5/1.) - Cpx (16/1.)		789					Grt (5/1.) - Cpx (16/1.)-Pl (44)		6.3
			Grt (6/1.) - Cpx (18/1.)		782					Grt (6/1.) - Cpx (18/1.)-Pl (45)		6.0
					T (°C)	Avg						P (kbar) Avg
Retrogression	Grt-Amp[c]	Type-IIA (SR94)	Grt (2/1.) - Amp (1/1.)	6	642	620 ± 20	Retrogression	Grt-Amp-Pl-Qz[d]	Type-IIA (SR94)	Grt (2/1.) - Amp (1/1.) - Pl (8/1.)	620	5.7 5.8 6.0± 0.5
			Grt (7/1.) - Amp (9/1.)		628					Grt (7/1.) - Amp (9/1.) - Pl (10/1.)		5.3
			Grt (22/1.) - Amp (8/1.)		633					Grt (22/1.) - Amp (8/1.) - Pl (13/1.)		
			Grt (24/1.) - Amp (23/1.)		595					Grt (24/1.) - Amp (23/1.) - Pl (47)		6.4
			Grt (31/1.) - Amp (28/1.)		599					Grt (31/1.) - Amp (28/1.) - Pl (51)		6.5

Grt: Garnet, Amp:Amphibole, Pl: Plagioclase, Cpx: Clinopyroxene, Qz: Quartz

Grt-Cpx thermometer: [a] Ganguly, 1979

Grt-Cpx-Pl-Qz barometer: [b] Eckert (1991),

Grt-Amp thermometers: [c] Graham and Powell (1984)

Grt-Amp-Pl-Qz barometer: [d] Kohn and Spear, 1990

decompression event.

8.3.2. Pseudosection analysis

Petrographic study suggests that the garnetiferous mafic dykes developed garnet + clinopyroxene + orthopyroxene + plagioclase + ilmenite + quartz at the culmination of metamorphism and represented in type IIA assemblage. Subsequently, amphibole and biotite developed during retrogression. Formation of significant biotite in the mafic requires influx of K^+ from the external source and a change in bulk composition. For this reason, two pseudosections are computed, one for anhydrous and other for the amphibole–biotite bearing association. The anhydrous association was modeled in the system Na_2O-CaO-FeO-MgO-Al_2O_3-SiO_2-TiO_2 (NCFMAST) using the micro/local bulk compositions (obtained from modal mineralogy and measured phase compositions; Table-8.2). The calculated pseudosection is presented in Fig. 8.3. The activity models of the observed minerals that are used for the calculations are: garnet, clinopyroxene, orthopyroxene, olivine, biotite and melt (Holland and Powell, 1998), ilmenite (White et al., 2000), amphibole (Dale et al., 2005) and plagioclase (Newton et al., 1980).

The diagram shows that olivine becomes unstable above 5 kbar pressure whereas rutile is stable in high pressure low temperature assemblage within the pseudosection with specified bulk composition (Fig. 8.3a). Within the pressure range of 4-12 kbar the solidus temperature for the representative bulk composition is around 1120°C. The empirically determined and numerically calculated basaltic magma solidus temperature coincides with this temperature (Green and Ringwood, 1967). Textural features suggest that olivine + clinopyroxene + orthopyroxene + plagioclase + ilmenite were crystallized during the magmatic stage and this association is stable below 5 kbar at temperature range between 600-1100°C (Fig. 8.3a).The association garnet+ clinopyroxene+ orthopyroxene+ plagioclase+ ilmenite+ quartz occurs over a large range of P-T and is bounded by rutile-in reaction and garnet-out reactions at high pressure and temperature respectively (Fig. 8.3a). However, the array of the compositional isopleths of the solid solution phases provide restricted P-T range of 7.5-9 kbar and 750-800°C (Fig. 8.3a).

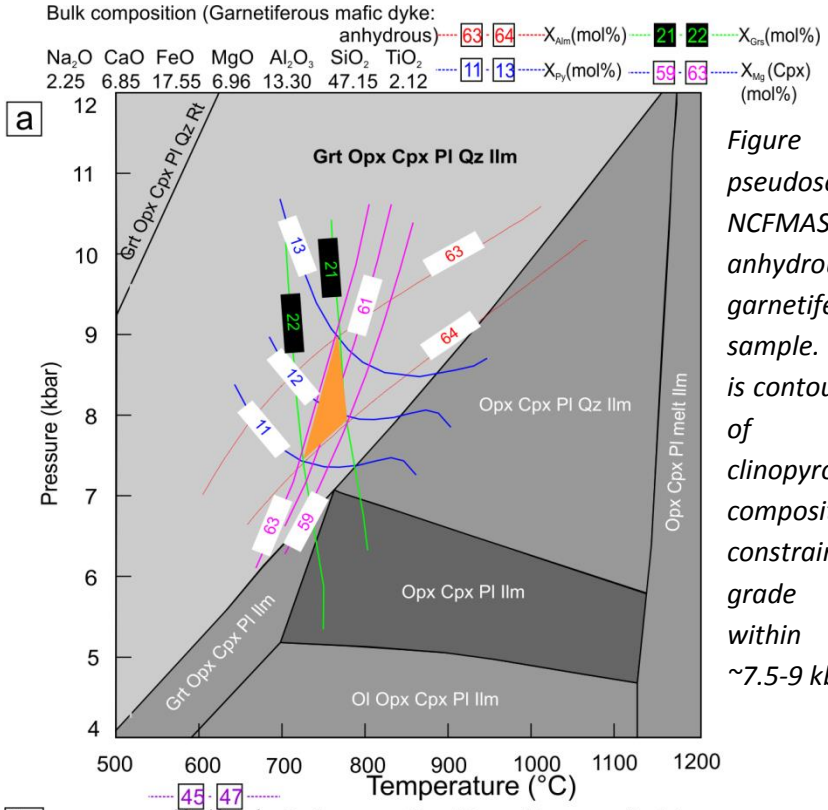

Figure 8.3. (a). P–T pseudosection in a NCFMAST system for anhydrous microbulk of garnetiferous type-IIA sample. The pseudosection is contoured with isopleths of garnet and clinopyroxene compositions. SR94 constrains the P-T of high grade metamorphism within ~750-800ºC and ~7.5-9 kbar (orange box).

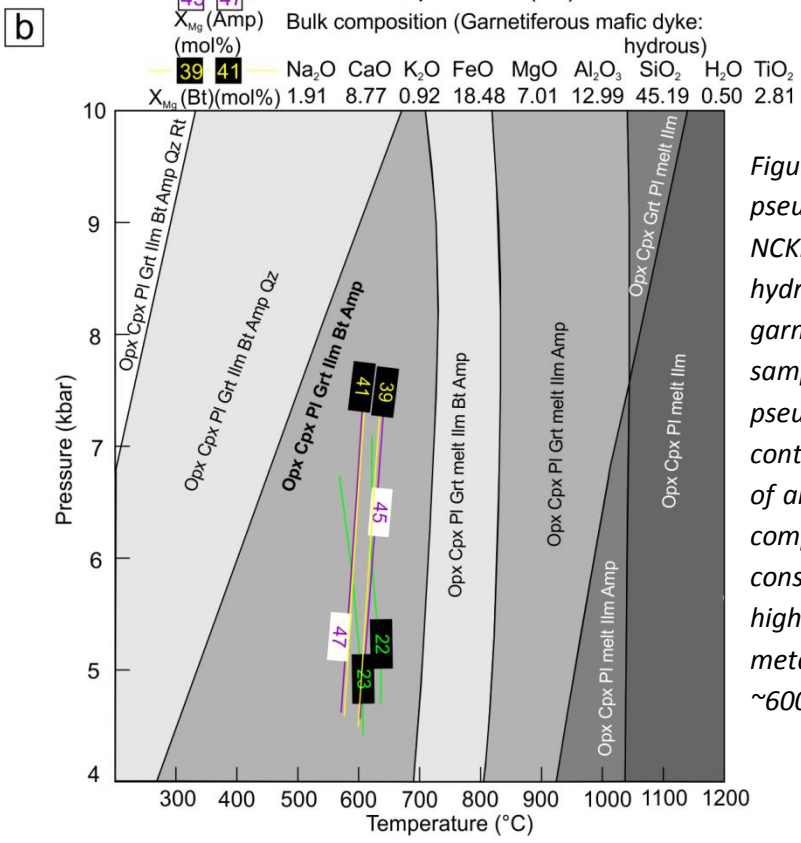

Figure 8.3. (b). P–T pseudosection in a NCKFMASTH system for hydrous microbulk of garnetiferous type-IIA sample. The pseudosection is contoured with isopleths of amphibole and biotite compositions. SR94 constrains the P-T of high grade metamorphism within ~600ºC and ~6 kbar.

For the amphibole–biotite bearing association, pseudosection is calculated for micro/local bulk composition in the system NCKFMASTH (Na_2O-CaO-K_2O-FeO-MgO-Al_2O_3-SiO_2-TiO_2-H_2O) (Fig. 8.3b). Input H_2O is considered in such an amount so that melt and H_2O must not occur together at >5 kbar. The porosity of metamorphic rocks under high pressure conditions is essentially very low (0.1 vol%; Etheridge et al., 1984), corresponding to a very small amount of H_2O (0.03 wt%; Clemens and Vielzeuf, 1987). H_2O is locked within the hydrous mineral structures in these conditions and the studied metagabbros contain 15-20 vol% amphibole + biotite which equates to around 0.5-0.8 wt% of H_2O. Similar to the pseudosection illustrated for the peak metamorphic condition, rutile is restricted to high pressure assemblage. Biotite is stable upto 800°C whereas amphibole is stable upto 1000°C. Melt-in reaction occurs at much lower temperature than that for the anhydrous condition and melt appears at 700°C (Fig. 8.3b). The assemblage that was stable during retrogression (amphibole + biotite + orthopyroxene + clinopyroxene + garnet + ilmenite) occurred at 300-700°C for the entire range of considered pressure (4-10 kbar) (Fig. 8.3b). X_{Mg} values of amphibole and biotite are plotted to narrow down the pressure-temperature condition of retrogression and Mg isopleths yield an average P-T value at around 6 kbar and 600°C (Fig. 8.3b).

8.3.3. Emplacement depth and subsequent metamorphism

Detail geochemical analyses of the meta-mafic rocks are beyond the purview of this study. Moreover, presence of predominant cumulous texture indicates extensive fractional crystallization from the magma which perturbs the original whole rock geochemistry of the mafic rocks and hence does not provide the reliable information about petrogenetic processes (Pearce 1984; 1996). Petrographic study further reveals majority of the samples have experienced extensive metamorphism and hydration and this further inhibits the application of the trace elements to comprehend the tectonic process.

Pseudosection analysis showing anhydrous basaltic bulk composition implies that the mafic magma crystallized at shallow depth (≤5 kbar) which corresponds to less than ~17 km. Intergranular texture where pyroxene crystallizes in the interstitial

spaces of early precipitated plagioclase laths signifies shallow depth of emplacement of the mafic rocks in the study area. Moreover, ophitic and sub-ophitic textures developing from rapid nucleation of plagioclase and clinopyroxene with the higher growth rate of the later one attest shallow depth of emplacement. Similar approach to infer about the depth of emplacement of mafic dykes has been taken by Mukherjee et al. (2018)) and Bhui et al. (2007). The formation of Fe-Ti oxide (ilmenite-magnetite) and apatite (Nelsonite) as cumulate phases with olivine and clinopyroxene in type-IB samples is beyond the scope of current study. Hydrothermal replacement of pre-existing rock (Ross, 1941), liquid immiscibility (Philpotts, 1967), magmatic and sedimentary origin are some of the discussed hypotheses regarding the formation of such association (He et al., 2016; Kolker, 1982).

The amphibole and biotite grains in the fine-grained meta-mafic dykes that define a weak foliation are parallel with the regional S_2 fabric in the study area. The detached bodies of the meta-mafic dykes are oriented parallel with the same pervasive fabric. No evidence of melting (development of leucosome, thin quartzofeldspathic segregation around the grains) is preserved in the mafic dykes. On the other hand, the tightness of D_2 folds, evident from felsic orthogneiss, banded psammopelite and calc-silicate in the study area made S_1, S_2 and the lithocontacts to be virtually parallel. These evidences suggest that the structures in the study area were formed in one progressive deformation which is coeval to early Neoproterozoic tectonothermal event. Garnetiferous samples are used to constrain the physical conditions of metamorphism experienced by these rocks. Garnetiferous meta-mafic dykes having a metamorphic mineralogy of garnet + clinopyroxene + orthopyroxene + plagioclase + ilmenite + quartz yield 750-800°C and 7-9 kbar as the physical condition of peak metamorphism. This was followed by a drop in pressure-temperature condition at 600°C and 6 kbar which results into a clockwise P-T path.

CHAPTER 9
DISCUSSION

Synthesizing the inputs from the preceding chapters this chapter illustrates the magmatic and metamorphic events that shaped the rocks of the MKGB. The magmato-metamorphic sequences in the MKGB then compared with the extant information from the CITZ in the contexts of the architecture of the Greater Indian Landmass and the Proterozoic supercontinental cycles. A viable mechanism of the formation of myrmekite in weakly deformed rocks is also presented in this section.

9.1.Magmatic history of the MKGB

The study area experienced repeated magmatism with distinct geochemical characteristics over a protracted time period ranging from Paleo- to Mesoproterozoic (1750-1350 Ma; Chakrabarty et al., 2023, 2022). Each phase of these magmatic events is discussed which unravel the Proterozoic tectonic scenarios in the study area.

9.1.1. Paleoproterozoic magmatism in MKGB

Detailed scrutiny (field, petrography, geochemistry, phase equilibria modeling and geochronology) of the country rock of the MKGB presents evidence of Paleoproterozoic arc magmatism in the MKGB (Chakrabarty et al. 2023). LILE enrichment, depletion of HFSEs, low value of Ga/Al and low Sr/Y along with the absence of HREE depletion signify melting of crustal rock at shallow depth (not

exceeding 25 km) in a convergent margin or arc setting (Chakrabarty et al., 2023). Geochemical data also suggest that there is a chemical variation in the porphyritic metagranitoid (Fig. 9.1) and to comprehend the probable magmatic processes (fractional crystallization vs. assimilation fractional crystallization) that may lead to such variation, phase equilibrium modeling has been done in open system.

Chemical variation in the Paleoproterozoic granitic magma of MKGB

Fig. 9.1 shows the comparison between the bulk composition of the studied porphyritic metagranitoids and that of modeled extracted bulk of an evolving mafic magma that underwent fractional crystallization all along the isobaric cooling path and crustal contamination at one particular point along the liquid line of descent. In both the cases for added 20% and 40 wt% of assimilant (upper continental crust) the extracted solid system shows an overall negative trend in the Harker diagrams for FeO_t, MgO,

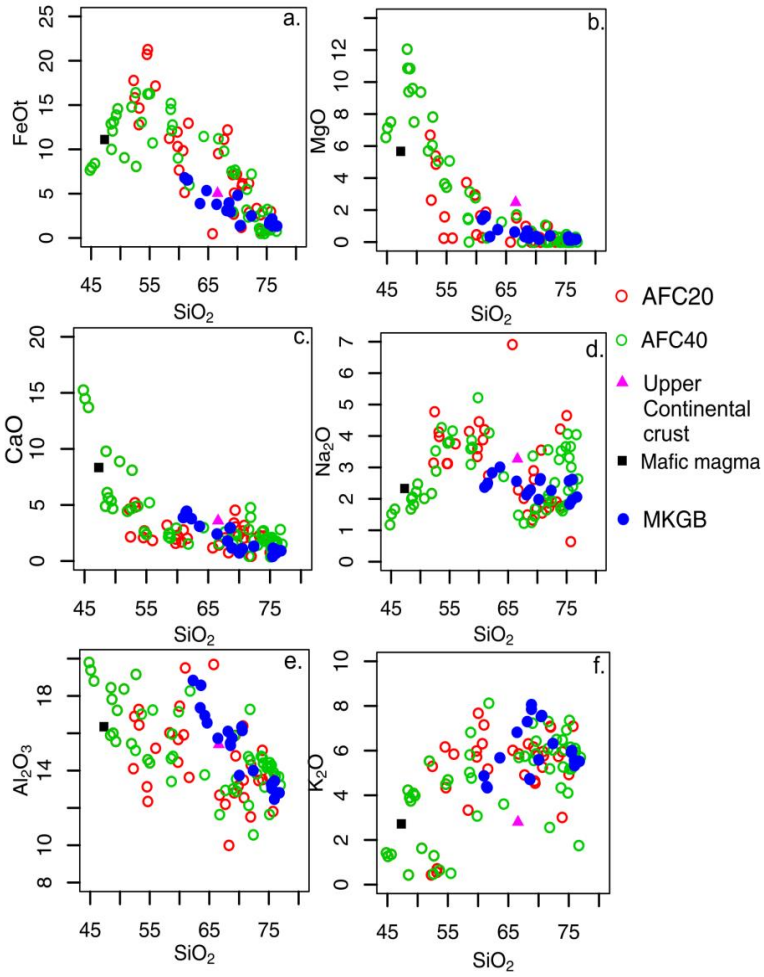

Figure 9.1. (a-f) Harker diagrams i.e., bivariate plots of the major element oxides against SiO_2 illustrating the comparison between the studied porphyritic granitoids and the modeled extracted bulk of the combined assimilation and fractional crystallization (AFC20=Fractional crystallization + 20 wt% crustal assimilant; AFC40=Fractional crystallization + 40 wt% crustal assimilant).

CaO and Al_2O_3 versus SiO_2 content that overlaps with the patterns for the studied metagranitoids (Fig. 9.1a-f). However, these modeled solids have a large range of SiO_2 content (45-76 wt. %) which can lead to a variety of mafic, intermediate and felsic rocks. A large proportion of the extracted solids (Table-4.4a) are more mafic and less siliceous (FeOt + MgO> 10 wt. % and SiO_2< 60 wt. % than the studied porphyritic metagranitoid (SiO_2= 60-76 wt. %). >80% of the modeled extracted bulks are ferroan and metaluminous (Fig. 9.1g-i) in the geochemical classification diagram for granitoids by Frost et al (2001). This solid system shows a significant scatter from calcic to highly alkalic and an overall weak sub-horizontal trend in the MALI versus SiO_2 diagram (Fig. 9.1h). The felsic part of the extracted solid (60-75 wt. % SiO_2) shows similar geochemical variation and magmatic differentiation trends in the bivariate plots of the studied porphyritic metagranitoids.

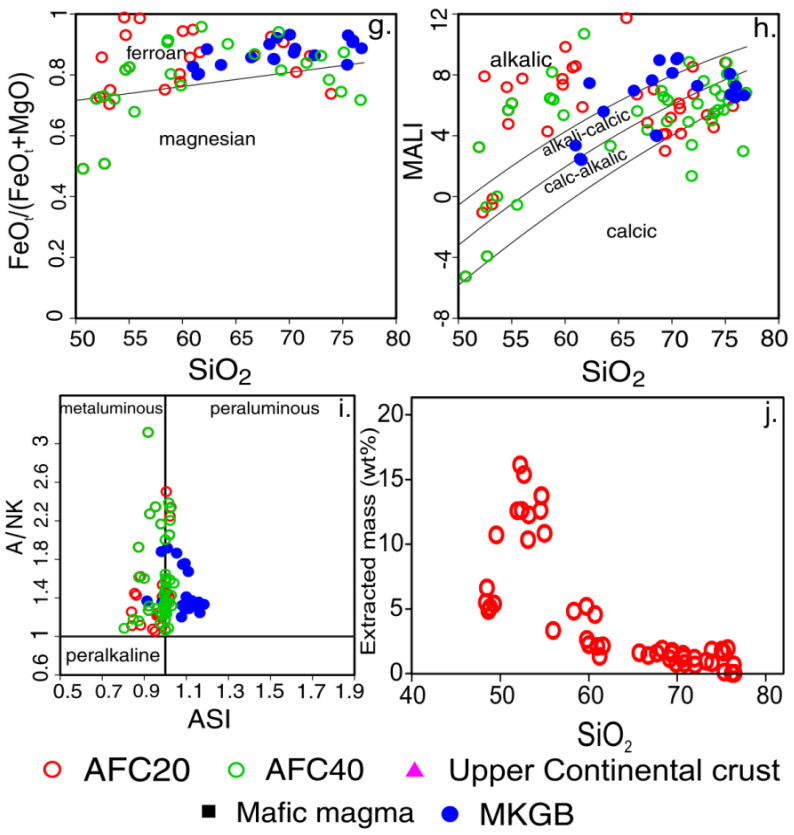

Figure 9.1 contd. (g-i) Modeled extracted bulk or separated crystal fraction and the porphyritic granitoids of the MKGB are plotted in the geochemical classification diagram for granitoids by Frost et al., (2001). (j) Extracted mass (wt%) versus SiO_2 plot shows that combined crustal assimilation-fractional crystallization of a mafic magma would produce significantly small amount of granitic/felsic rock (>60 wt% SiO_2).

Assimilation of a significant amount of older felsic crustal material in fractionating arc basalt commonly manifests with an abundance of inherited zircon

grains, entrapment of older microgranular enclaves, late crystallized plagioclase microcrysts and magmatic pyroxene and amphibole from the original mafic magma (Chiaradia et al., 2011). Careful field and petrographic scrutiny of 17 samples of the studied metagranitoids, spreading over an area of approximately 100 km^2 did not reveal any such evidences. Additionally, the model reveals that formation of granitoids via assimilation and fractionation would produce mafic to intermediate rock types, occupying 3 to 5 times more in volume compared to the felsic rocks (Fig. 9.1j). No such coeval magmatism has been reported so far from the study area. Therefore, we infer that assimilation-

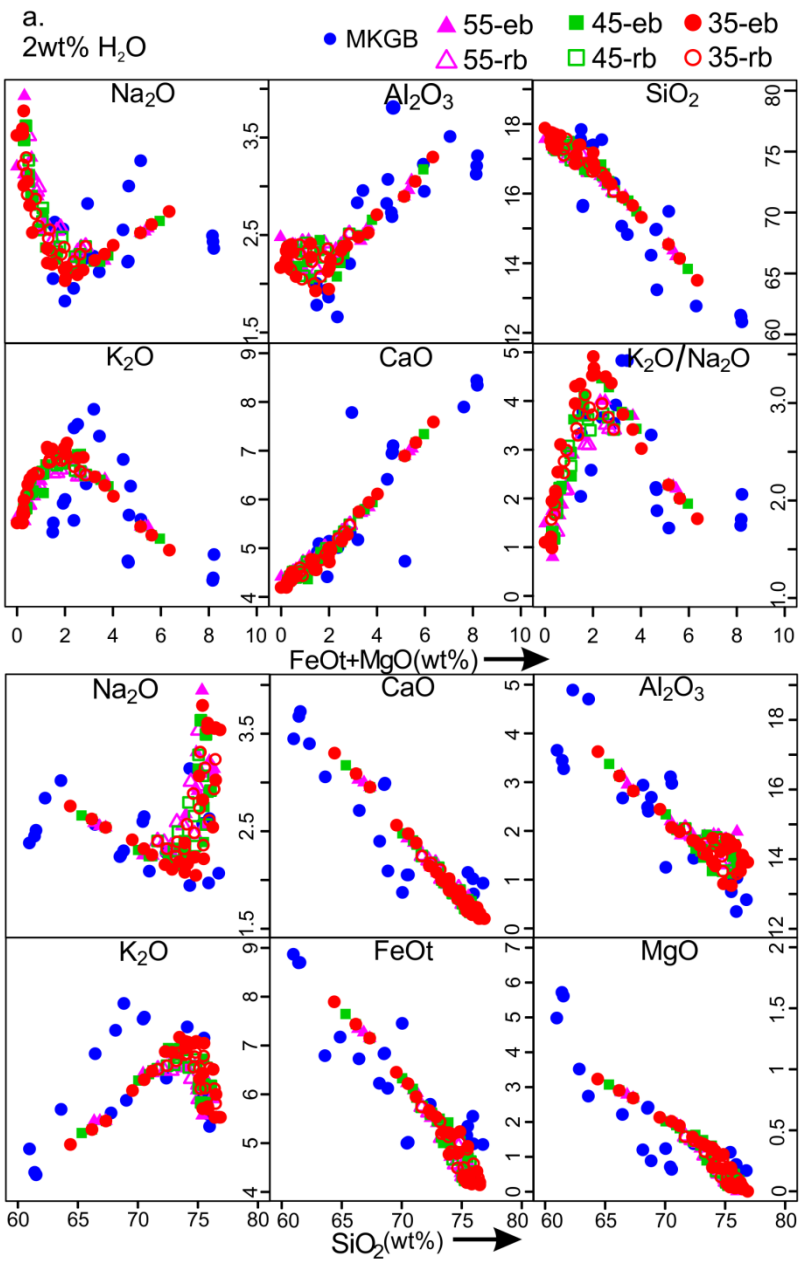

Figure 9.2. (a) Comparison between the major element compositions of the studied porphyritic metagranitoids and the modeled solid and liquid system, acquired from the phase equilibrium modeling with three different CCF (critical crystal fraction) thresholds and the initial magma composition of the studied metagranitoids added with 2 wt% of water.

fractional crystallization of intermediate to basic magma can produce the geochemical trend observed in the studied granitoid, albeit field and petrographic observation suggest this to be an unlikely scenario.

Fig. 9.2 (a, b) illustrates the similarity between the studied porphyritic metagranitoids and solid system or extracted bulk of the modeled felsic magma experiencing post-emplacement crystal-melt separation. Dominance of plagioclase along with orthopyroxene or biotite results in high FeO_t + MgO, CaO and relatively low SiO_2 and Na_2O + K_2O in the modeled early crystallized fraction than the corresponding melt fraction (Table-4.4c, d; Fig. 9.2a, b). Composition and mineralogy of these modeled bulks are similar to those granitoids that are dominated by plagioclase phenocrysts. Plagioclase : K-feldspar ratio (At 5-3 kbar,

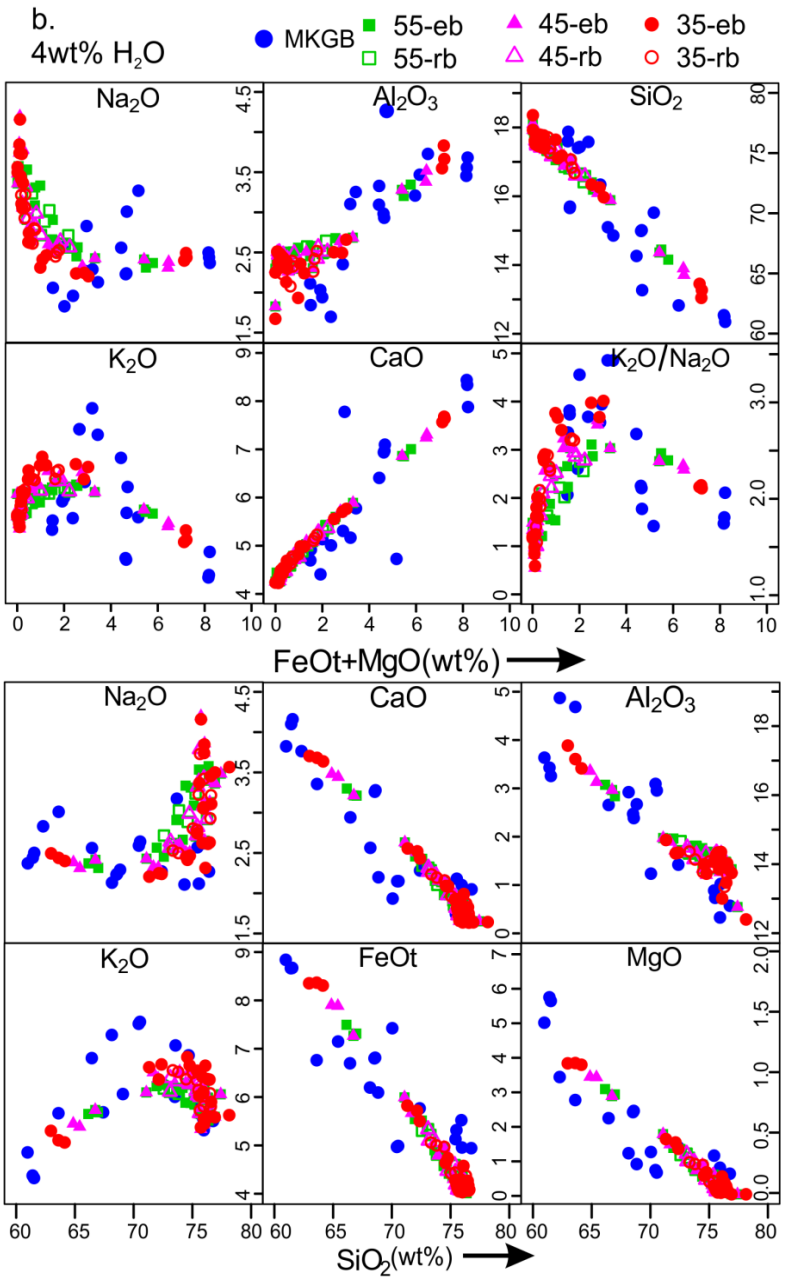

Figure 9.2 contd. (b) Comparison between the major element compositions of the studied porphyritic metagranitoids and the modeled solid and liquid system, acquired from the phase equilibrium modeling with three different CCF (critical crystal fraction) thresholds and the initial magma composition of the studied metagranitoids added with 4 wt% of water.

1.54:1 for 35 wt. % CCF, 1.25:1 for 45 wt. % CCF, 1:1 for 55 wt. % CCF) of the modeled first crystal dominated extracted phase with 2 wt% H_2O matches well with the plagioclase phenocrysts dominated granitoid having the observed plagioclase : K-feldspar phenocrysts ratio of 1.5:1 to 1.22:1 (Table-4.1 and Table-4.4e). With the progressive crystallization/cooling of the magma, the solid fraction contains higher amounts of K-feldspar which lead to the highest K_2O, SiO_2 and lowest FeO_t + MgO in the succeeding fractionation episode. Modeling predicted that in these events plagioclase: K-feldspar ratio varies from 1:1.6 to 1:6 which broadly corroborates with studied granitoids having plagioclase: K-feldspar phenocrysts ratio of 1.5:1 to 1:4 (Table-4.1 and Table-4.4e). Similar to the K-feldspar dominated samples these modeled bulks are also silicic and have higher K_2O/Na_2O (Fig. 9.2a-c). In a few cases, at the lowest pressure crystal separation occurring close to the solidus is devoid of any plagioclase and contains only K-feldspar and quartz similar to the granitoids having only K-feldspar phenocrysts. These bulk compositions also show the highest SiO_2, K_2O and lowest FeO_t + MgO similar to that of the metagranitoids having dominantly K-feldspar.

At lower pressures, biotite is the sole ferromagnesian mineral that controls the decreasing maficity (FeO_t+ MgO) with increasing SiO_2 or vice-versa. It is noteworthy that with low H_2O small amount of garnet and orthopyroxene occurs at 5 kbar. However, orthopyroxene is not observed in any of the samples and garnet, having biotite ± amphibole + ilmenite inclusions, is of metamorphic origin. Therefore, the fractionation presumably occurred at lower pressure and/or with higher water contents (4 wt. %). A decrease in TiO_2 content with decreasing maficity but increasing SiO_2 is revealed from whole-rock geochemistry and points towards fractionation of biotite along with the ilmenite. Positive patterns of CaO and Al_2O_3 with respect to maficity, but the negative trends of the same with increasing SiO_2 can be attributed to plagioclase fractionation during post-emplacement crystallization and progressively increasing albitic component in the matrix plagioclase compared to the plagioclase phenocrysts (Fig. 9.2a, b). K_2O content, controlled by both biotite and orthoclase feldspar, displays positive trend in the variation diagram up to 70 wt% of SiO_2 above which the samples show a steep decline in K_2O whereas Na_2O behaves in the exact

opposite way (Fig. 9.2a-c). The significant role of feldspar fractionation which is portrayed by the patterns in the bivariate plots in the studied granitoids is evident from the phase equilibrium study (Fig. 9.2a, b). Phase abundances, predicted from the fractionation model suggest that both plagioclase and K-feldspar occur as early crystallizing phases and the crystal-melt separation presumably occurred with 45 to 55 % CCF threshold conditions at ≤5 kbar pressure.

Trace elements do not show a strong correlation with SiO_2. Since garnet acts as a sink for Y, HREEs and La/Lu and Y contents do not vary with SiO_2 or maficity i.e., FeO_t + MgO, garnet fractionation can be ruled out. Amphibole fractionation is commonly depicted by decreasing MREE (Gd, Dy) with maficity which is also not evident in the current study. Sr contents show a strong positive correlation with CaO suggesting the role of plagioclase in fractionating Sr.

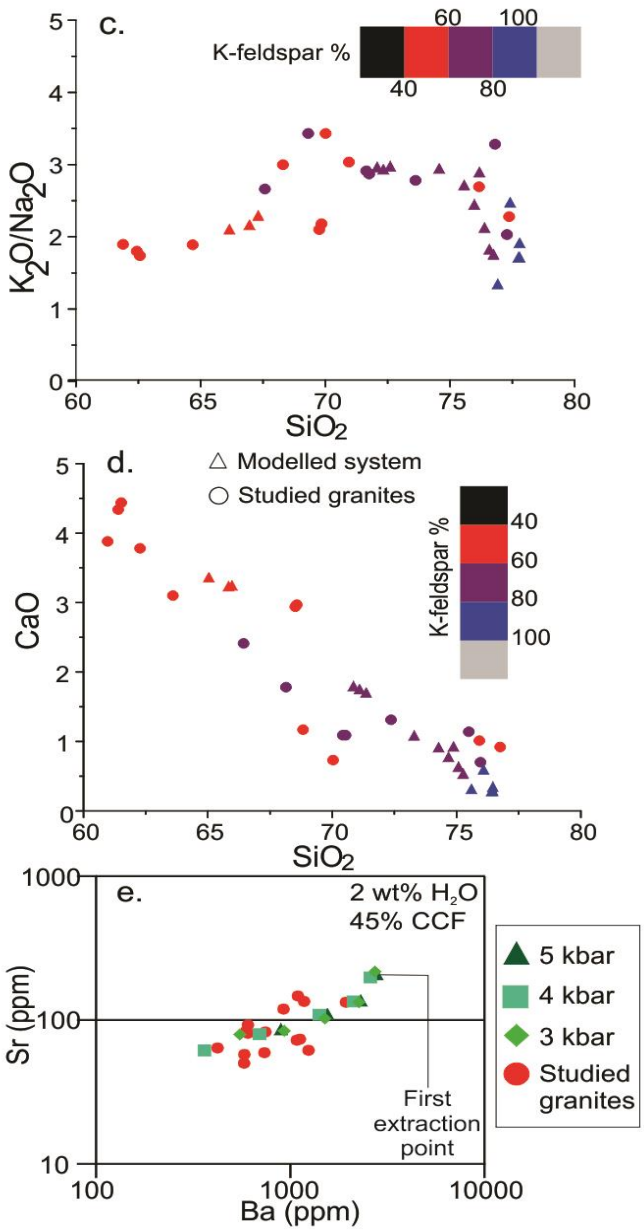

Figure 9.2 contd. (c, d) Major element compositions (K_2O, Na_2O and CaO) show systematic variation with the K-feldspar percentage (K-feldspar/total feldspar), both in case of studied granitoids and the modeled melts. (e) Trace element contents of the studied granitoids and in the modeled solid system, calculated using the amounts predicted from phase equilibrium modeling. Partition coefficients are collected from GERM website.

However, Eu, commonly believed to be preferred by plagioclase, do not show any correlation with CaO and Sr. Rather Eu show a distinct positive correlation with Ba, an element commonly preferred by K-feldspar. This presumably points towards the prominent role of K-feldspar in controlling Eu budget in the magma (cf. Keller et al., 2015). Ba and Sr show a positive trend among the studied samples which attests to the dominance of both plagioclase and K-feldspar crystals in the solids. Using the phase assemblages predicted from the phase equilibrium modeling and the partition coefficients, Ba and Sr contents have been calculated via trace element modeling (Fig. 9.2e). The results show a similar positive trend and matches with the Ba and Sr contents observed in the natural studied metagranitoids as well.

9.1.2. Mesoproterozoic magmatism in MKGB

Middle Mesoproterozoic thermotectonic events in the CITZ are manifested by weak thermal imprints of metamorphic event at ca. 1470-1420 Ma from monazite grains from rocks in the parts of south-west (SW) sector (BBGB) (Bhandari et al., 2011; Bhowmik et al., 2011) and emplacement of A-type granitoids by dehydration melting of shallow granitoid crust at ca. 1322 Ma in the SW sector (Sausar Mobile Belt) (Bose et al., 2023). Coeval granite magmatism has been abundantly recorded from several parts of the CGGC which show typical A-type granitoid compositions (Mukherjee et al., 2018, 2017; Sequeira et al., 2021). On the contrary, the magmatic protolith of the felsic orthogneisses of the MKGB was emplaced within the basement of Paleoproterozoic arc granites at 1377-1352 Ma in a continental arc setting (Chakrabarty et al. 2022). This ca. 1400 Ma arc related felsic magmatism in the MKGB is hitherto unreported from any part of the CITZ.

Chemical variation in the Mesoproterozoic granitic magma of MKGB

Charnockitic orthogneisses (COG) samples show wide compositional variation, scattering in most of the classification and/or discrimination diagrams and considerable enrichment of Fe+ Mg and Ca, relative to the experimentally derived melts (Fig. 9.3a-i). Despite the restricted chemical composition of the garnet orthogneiss (GOG) samples, COG shows chemical variation with a negative trend in

Si, K, ASI, Rb and a positive trend in Ca, Ti, Y, total HREE against maficity (molar Fe+Mg) (Fig. 9.3a-i). Globally, the geochemistry of the S-type granites show considerable compositional variation and their compositions deviate from those determined in the experimentally derived melts from metasedimentary protolith (Stevens et al., 2007; Villaros et al., 2009) (Fig. 9.3j-m). Such variation has been ascribed to source heterogeneity, fractional crystallization, magma mixing and the crystal entrainment from parent rock (non-peritectic component) or product of melting reaction (peritectic component) with the extracted melt (Clemens, 2003; Garcia-Arias and Stevens,2017a). As postulated by several authors, fractionation

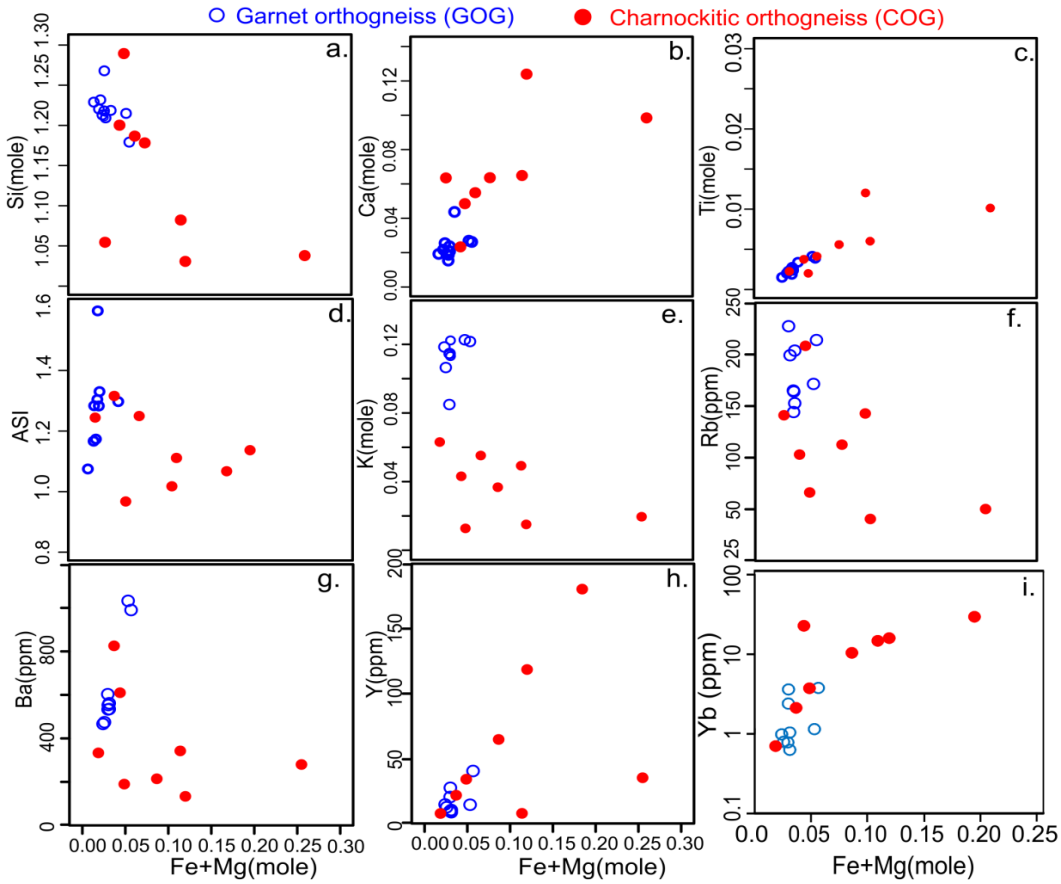

Figure 9.3. (a-i) Major and trace element chemical variation in the studied felsic orthogneisses show that compositions of GOG are restricted (correspond with the melt compositions derived from the partial melting experiments with sedimentary sources; Garcia-Arias and Stevens, 2017). COG shows considerable variations.

and entrainment of mafic minerals (residing as the peritectic entity) leads to considerable compositional variation in felsic magmas that have high viscosity and

low ferromagnesian content (Clemens and Stevens, 2012; Garcia-Arias and Stevens, 2017b, 2017a). However, phase equilibrium studies involving the anatexis of sedimentary sources predicted that crystal fractionation or entrainment cannot be considered as the sole cause for chemical variation in granitoids, because compositional range and the trend within the magma is also largely controlled by the initial melt composition (Garcia-Arias and Stevens, 2017b). Though detailed phase equilibria modeling in path dependent open system scenario for the protolith granite magma of the felsic orthogneisses is beyond the purview of the current study, a preliminary discussion is presented in the following section explaining the probable causes of the observed trends in the bivariate plots.

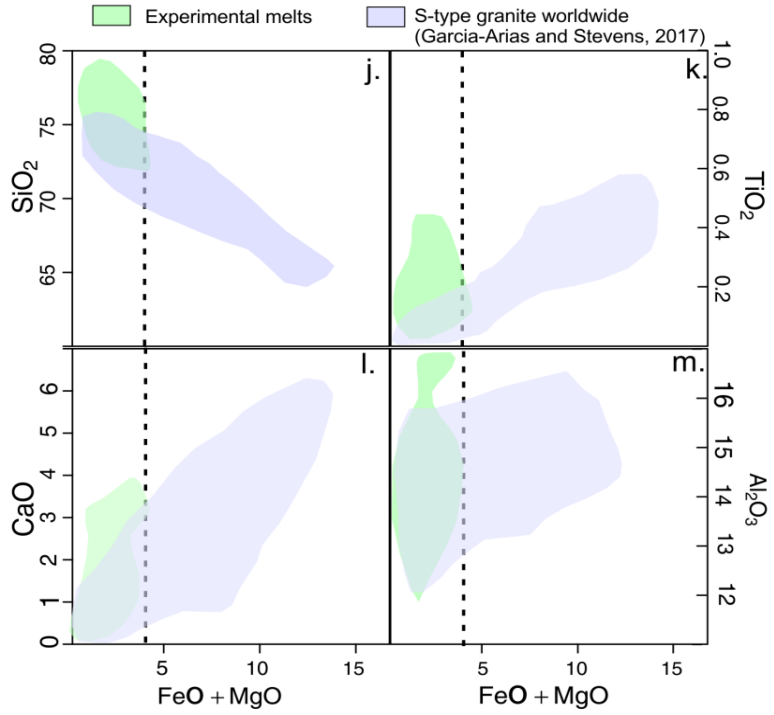

Figure 9.3 contd. (j-m) Major element composition of natural S-type granites worldwide deviate from pure felsic melts derived experimentally from sedimentary protolith (modified after Garcia-Arias and Stevens, 2017).

It is noteworthy that the studied granitoids have experienced high grades of metamorphism which might have resulted in melt loss and hence, extensive change in the pristine magmatic condition. However, the volume and arrangement of leucosomes (the presumed melt phase) indicates that the studied felsic orthogneisses are similar to metatexitic migmatite that are described by Zhang et al. (2019). This observation and the absence of a network of leucosomes that dissect the gneissic fabric are consistent with the view that significant melt loss did not occur during the high grade

metamorphism in the studied area. Moreover, (a) high silica and alkali in the studied rock (SiO_2>70 wt%, alkali ≥8 wt%); (b) small amount (<20 %) of common residual (peritectic) minerals (orthopyroxene+ garnet+ cordierite) in the rock; (c) the restricted range of compositional variation and (b) coherent trace element and LILE contents in the granitic rocks contradicts with the evidence of melt loss suggested by Sawyer and Brown (2008). The whole rock geochemistry of the studied rocks, therefore, has not been extensively altered by the metamorphic process.

Model of the post-emplacement crystal fractionation

For the post-emplacement crystal fractionation scenario in an open system path-dependent phase equilibria modeling study (Rcrust program by Mayne et al., 2016), average major oxide composition of the studied arc granitoids is used as starting material with added 2 wt% of H_2O (Garcia-Arias and Stevens, 2017a, 2017b). In this study, the updated version of Perple_X (v. 6.8.6) has been used with the updated hp633ver dataset (Holland and Powell, 2011). This granitic melt followed an isobaric cooling path (1000-660 °C at 3-9 kbar) and a crystal-laden mush gets separated after each 50% crystal is produced (crystallinity threshold or Critical Crystal Fraction is 50%). Fig. 9.3n-q shows the comparison between major element bulk composition of the studied felsic orthogneisses (COG and GOG) and modeled extracted solid or crystal system produced by post-emplacement crystal fractionation. In spite of the presence of prominent trends or patterns in the Harker diagrams, these modeled solids have comparatively low maficity (FeO_t + MgO), low Ca and high SiO_2 content than the COG samples and hence the entire range of measured compositions of the studied samples cannot be produced only by fractional crystallization.

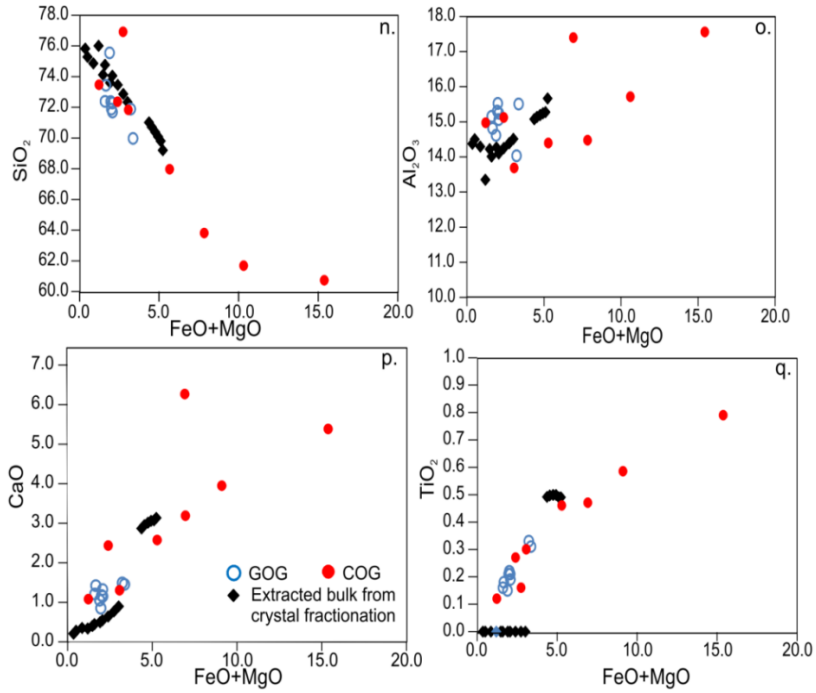

Figure 9.3 contd. (n-q) Harker diagrams of the modeled extracted bulk produced by post-emplacement crystal fractionation and studied felsic orthogneisses plotted with respect to maficity i.e. ferromagnesian content in the bulk.

Model of the peritectic crystal entrainment during magma ascent

In order to comprehend the effect of peritectic (mineral produced in reaction during melting), non-peritectic or residuum (part of source mineralogy) phase entrainment in the melt, a thermodynamic model has been constrained in NCKFMASHTO (Na_2O-CaO-K_2O-FeO-MgO-Al_2O_3-SiO_2-H_2O-TiO_2-O_2) system using the software program Rcrust (Mayne et al., 2016). In this model, the melting of two metasedimentary source rocks [metagreywacke (#CEVP of Vielzeuf and Montel, 1994) and biotite gneiss (#SBG of Patiño Douce and Beard, 1995)] is modeled via the isobaric heating process at a temperature range of 600^0-900^0C and 5-11 kbar pressure with 1 kbar intervals. In order to simulate the fluid-saturated but free fluid-absent partial melting conditions, excess H_2O (2 wt%) has been added to the source and melting has been modeled in such a way that with increasing temperature free H_2O (not accommodated in hydrous phases) will be fractionated from the system leaving 0.1wt% H_2O behind which corresponds to the pore space fluid in the source. Modeling has been done with the threshold for melt extraction, set at 20 vol% with 1vol% melt retention in the system. Earlier workers (Clemens et al., 2011; Clemens and Stevens, 2012; Garcia-Arias and Stevens, 2017a, 2017b; Stevens et al., 2007; Villaros et al.,

2012) have suggested that the proportion of entrained crystal may vary from 0 to 30 vol%. Furthermore, Garcia-Arias and Stevens (2017a) showed that higher CaO contents in the mafic members of the S-type granite plutons often warrants the entrainment of Ca-rich plagioclase in the melt owing to its spatially restricted equilibration behavior that often leads to zoned plagioclase in the restites. In the current modeling we construct both the limiting scenarios with pure melts having no entrained phases and melts with 30% crystal entrainment modeled in such a way that with each melt extraction episodes 30% of the increased mass of any phases between the current point and last melt extraction event or the last melt absent point will be extracted (cf. Mayne et al., 2020). With each extraction events (except for the no entrainment conditions), 10% anorthite has been added to the melt to understand the effect of dissolution of calcic plagioclase as suggested by Garcia-Arias and Stevens (2017a).

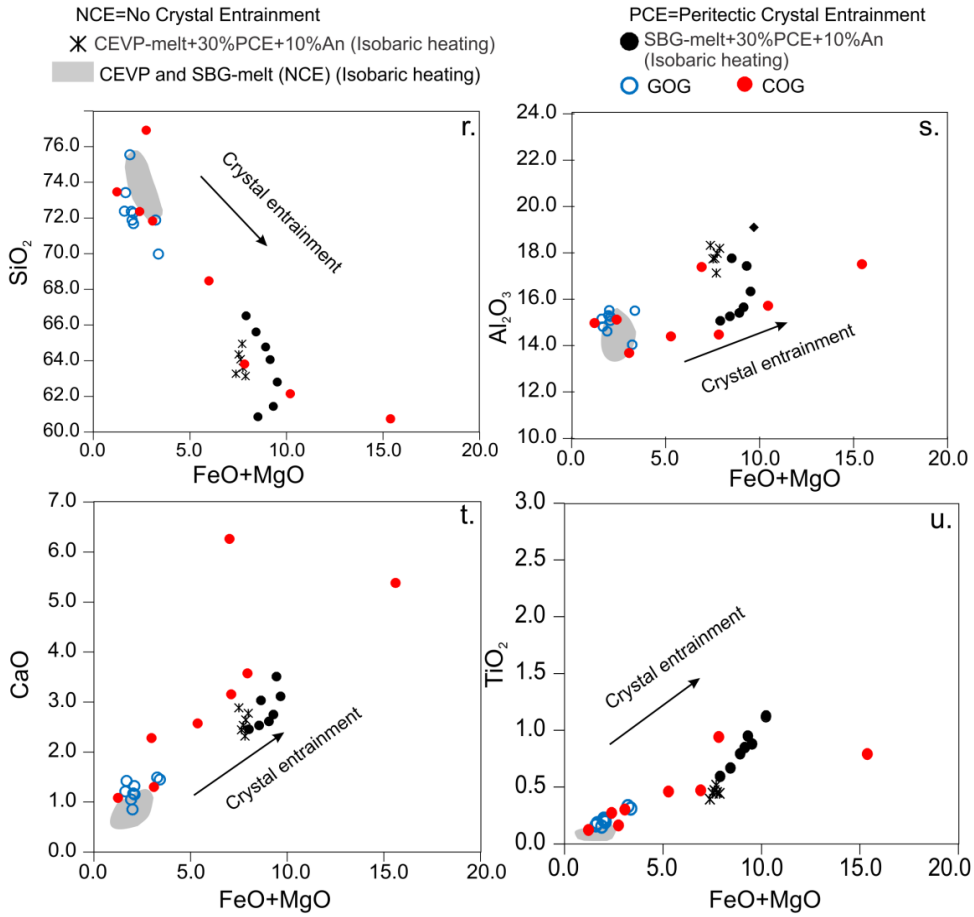

Figure 9.3 contd. (r-u) Comparison of the composition of the studied felsic orthogneisses with modeled melt under the simulated conditions plotted with respect to maficity in the Harker diagrams.

Fig. 9.3r-u shows the comparison of the composition of the studied felsic orthogneisses with modeled melt. Melting of both the sources used for the modeling in the current study shows that the composition of the pure melts (without entrained phases) has a restricted range (similar to the whole rock chemistry of the GOG) whereas crystal entrainment leads to wider compositional variability (similar to the bulk of the COG). The whole compositional range observed in this Mesoproterozoic arc granitoid can be explained by composition of the pure melts via melting of commonly perceived metasedimentary sources with variable amount of entrained phases, dominantly K-feldspar and garnet and/or orthopyroxene. The mineral phases (orthopyroxene, garnet etc), now observed in the studied felsic orthogneisses are evidently the products of metamorphism and not to be confused with the modeled entrained phases within the magma. Current study, in accordance with recent works of Garcia-Arias and Stevens (2017a), shows that multiple phases can be entrained since the melting reactions, envisaged in the current study and the experimental studies produce multiple peritectic phases. Low pressure high temperature extractions frequently entrain orthopyroxene, especially for the less aluminous and less ferroan source (i.e. #SBG used in the modeling), whereas high pressure melts entrain garnet as the dominant ferromagnesian phase. Although both the phases provide significant enrichment of Fe-Mg, a significant amount of Al and Ca in the garnet is supposed to make the melt aluminous and calcic. Further, the elevated CaO contents of the S-type granitoids cannot be explained only by the entrainment of garnet and warrants the limited dissolution of residual anorthite suggesting that both peritectic entrainment and residual unmixing are imp erative in producing the observed chemical variations.

9.2. Metamorphic history of the MKGB

9.2.1. Metamorphic evolution of the felsic orthogneisses

The granoblastic assemblage (garnet ± orthopyroxene + plagioclase + K-feldspar + quartz + ilmenite) in the COG is formed, presumably by amphibole and biotite melting reactions (Fig. 6.4c). Stabilization of orthopyroxene, albeit sporadically, in COG, absence of hydrous phases in peak assemblage and presence of leucosome, presumed to be the quenched melt phase, are consistent with high-grade

metamorphism that was accompanied by the dehydration melting of amphibole and biotite bearing assemblages. In the GOG, dehydration melting produced the assemblage garnet + K-feldspar + quartz ± plagioclase during the granulite facies metamorphism. The P-T estimates for the granoblastic assemblage record 825-850°C and 7.5-7.0 kbar (Fig. 6.4d). The recorded pressure and temperature of the granulite facies metamorphism suggest a transient geothermal gradient of ~35^{o}C/km. From the petrological information of the studied rocks it is not possible to understand if the P_{max} was significantly higher than the recorded pressure of metamorphism (7-7.5 kbar) in the studied rocks. Figure 6.4c shows the P-T pseudosection for COG on which the P-T values calculated from the conventional geothermobarometry are plotted. The felsic orthogneisses were metamorphosed during a progressive deformational event (superposed F_1 and F_2 folding). For this reason the plotted P-T values are joined by a line to reconstruct the retrograde P-T path of metamorphism. The retrograde P-T path has "clockwise" geometry having an initial steeply decompressive segment that was followed by a relatively gently decompressive segment that can be traced up to 4 kbar and 500ºC. In the absence of the diagnostic mineral assemblages and prograde zoning in garnet, the prograde P-T path is shown as schematic line (Fig. 6.4c). Th-U-total Pb monazite geochronology constrains the age of the peak (granulite) to retrograde metamorphism at 974-913 Ma, which overlaps, within the uncertainty of calculation, with two concordant zircon spot dates of (1048±37 and 962±23 Ma) and the lower intercept age in discordia diagram (ca. 986-956 Ma) (Chakrabarty et al. 2022).

9.2.2. Metamorphic evolution of the metasedimentary and meta-mafic rocks

The peak metamorphic assemblage garnet+ plagioclase + K-feldspar + quartz+ ilmenite as observed from thin section of the banded psammopelite, is inferred to be stabilized at 800°C -7 kbar using the phase equilibria modeling. The presence of biotite + muscovite (-chlorite) constrains a probable range of P-T condition (500-600 °C, 4-6 kbar) for retrograde metamorphism which is refined by the conventional thermobarometry (500 °C-5.5 kbar) (Fig. 7.2). Textural evidences suggest that the garnet + cordierite ± sillimanite association stabilized before the metasomatism or chemical alteration in the in the garnet-cordierite-biotite (GCB) rock. This inference,

coupled with the fact that the rock is observed in strike continuity and intercalated with banded psammopelite, indicate towards a pelitic protolith of the GCB. Further evidence of GCB having pelitic protolith stems from the fact that the bulk composition of rock is extremely poor in Ca and alkalis but very high Al, Fe and moderate Mg. Though the peak metamorphic condition could not be preserved in this highly metasomatised lithounit, final assemblage (garnet + cordierite + sillimanite + biotite + ilmenite + quartz) within association 1 is recorded to stabilize at 650 °C and 4.5 kbar (Fig. 7.8). T-X_{MgO} and phase compatibility diagram provide a minimum temperature range of 650°-700°C at around 5-9 kbar pressure for the stability of garnet + cordierite + sillimanite or garnet + cordierite + orthoamphibole in a rock with a certain range of bulk composition (FMASH system). On the other hand, conventional thermobarometry applied to the GCB yield 630 °C and 610 °C for the initial garnet-cordierite equilibration for association 1 and 2 respectively. This lower temperature range can be represented as closure temperature, since Fe-Mg exchange equilibria are controlled by diffusion between the minerals (Frost and Chacko, 1989). Though the timing of the metamorphic event was unclear, Solanki et al. (2003) recorded granulite-grade metamorphism from the garnet-cordierite bearing metapelite in MKGB at ~800° C and 9 kbar followed by isothermal decompression through 740° C at 6.5 kbar and a final re-equilibration at ~685° C (Solanki et al., 2003). The calc-silicate rocks in the study area are also affected by this late stage hydration event and they recorded a slightly higher P-T range of 650-700 °C, 5-6 kbar (Karmakar, 2021). As meta-mafic rocks of the study area are extremely diverse in terms of petrology, garnetiferous type-II samples (fine grained variety that is dominant in the field) are used to constrain the physical conditions of metamorphism experienced by these rocks. Garnetiferous meta-mafic dykes having a metamorphic mineralogy of garnet + clinopyroxene + orthopyroxene + plagioclase + ilmenite + quartz yield 750-800 °C and 7-9 kbar as the peak metamorphic condition which was followed by a drop in pressure-temperature condition at 600°C and 6 kbar (Fig. 8.6a, b).

9.2.3. Tectonic implication of the Neoproterozoic metamorphic imprint in MKGB

Field study, petrology and phase equilibrium modeling for the porphyritic metagranitoids, felsic orthogneisses, metapelites (banded psammopelite and GCB) and garnetiferous meta-mafic rocks of the study area show that all the lithounits share the regional deformation and metamorphism during Neoproterozoic era corresponding with Grenvillian orogeny in the Indian subcontinent. The likely sedimentary protoliths of the metasedimentary rocks of the MKGB are shale-limestone-sandstone sequence that is found in the stable shelf environments. Transport of the felsic rocks and the sedimentary sequences at 22-25 km depth (corresponds to the 7.5-7.0 kbar) or beyond can only be explained by burial in a continent continent-collision zone (cf. Harley, 1989). The transient geothermal gradient of 35ºC/km inferred from the peak metamorphic condition from all the studied lithounits has been reported from many metamorphic terrene that evolved in a continent-continent collision zone (reviewed in Brown, 2014; Chowdhury et al., 2021). The P-T path that the rocks of the studied area followed during the burial (prograde history) is difficult to ascertain. The high temperature (>800ºC) of metamorphism within felsic orthogneiss and banded psammopelites homogenized the garnet composition (barring the retrograde zoning). Therefore, it is now practically impossible to know if the porphyroblastic garnet inherited any component that formed on the prograde path. Lack of suitable mineral inclusions in the porphyroblastic garnet add to the difficulties in tracing the prograde P-T path. Similar observations were noted in many studies (Gapais et al., 2009; Harley, 1989). Several studies have demonstrated that the dehydration melting of rocks in the continent-continent collision zone occurs during the thermal maxima and at pressures that is significantly lower than the maximum pressure (P_{max}) attained by the rocks (reviewed in Chowdhury et al., 2021; Harley, 2016). Depending upon the protolith compositions and the steepness of the retrograde P-T path, dehydration melting can occur at different crustal depths. Melting can also occur at different depths in the same collisional orogen (Chowdhury et al., 2021). Although the evidences of the peak granulite metamorphism are not recorded or preserved in the metagranitoid country rock of the study area conventional thermobarometry and theoretical considerations convey that physical condition of the retrograde metamorphism

(secondary biotite and extensive myrmekite formation) is 500-600 °C, 4-5 kbar (Chakrabarty et al. 2023). Peak to retrograde conditions for all the lithounits of the MKGB illustrates a clockwise geometry. Similar clockwise retrograde P-T path has been documented from several collisional orogens from elsewhere in the world (cf. Bhowmik and Roy, 2003; Brown, 2014; Dasgupta et al., 2009; Dey et al., 2019; Goswami-Banerjee et al., 2014; Goswami et al., 2009; Harley, 1989; Karmakar et al., 2011; Mukherjee et al., 2017; Searle et al., 1992).

9.2.4. Retrograde metamorphism and fluid-induced structures in the lithounits of MKGB

Porphyritic metagranitoid, felsic granulite or orthogneiss, metasupracrustal and meta-mafic rocks are the four major lithounits in the study area. All the lithounits are intensely deformed and metamorphosed at ca. 950 Ma and extensively retrogressed during the terminal phase of this tectonothermal event (Chakrabarty et al., 2022). This infiltration driven metamorphism caused variable extent of hydration of the granulite facies assemblage in the felsic granulites (formation of secondary amphibole and biotite after orthopyroxene), marble and calc-silicate rocks (development of clinohumite), porphyritic metagranitoid (development of biotite folia and myrmekite) and meta-mafic rocks (amphibole, biotite after olivine, clinopyroxene and plagioclase).

Extensive myrmekitisation within porphyritic metagranitoid

Role of deformation and physical conditions on the myrmekite growth:

Microscopic studies suggest two stages of myrmekite formation which has resemblance with the myrmekite described from a Pofadder shear zone, Namibia (Cisneros-Lazaro et al.2019). However, unlike this and many other studies (Menegon et al., 2006; Simpson and Wintsch, 1989; Vernon, 1991), the microstructural features of the studied rock do not support myrmekite formation in shear zone though impress of deformation of various intensities are observed from field and petrographic observation. The polygonal aggregates of Myr2 that presumably formed early, clearly indicate strain induced recrystallization that minimized the interfacial energy among

the grains (Vernon 2004, Cisneros-Lazaro et al. 2019). Microtextural information remains inconclusive regarding the origin of the coarse, locally polygonal, aggregates of Myr2. There exist two possibilities as argued in Cisneros-Lazaro et al. (2019). One possibility is that the Myr2 initially had a vermicular morphology and subsequent recrystallization and grain growth at high temperature led to the larger aggregates with planar to gently curved grain contacts (relative to Myr1). The other option is that the coarser grained in Myr2 did not drive from a vermicular intergrowth. The coarse aggregates of Myr2 formed directly from alkali feldspar at high temperature and fluid pressure. Both these factors contributed to the large length of transport of chemical species so that the product grains have planar contacts with minimum surface energy (Philpotts and Ague, 2009). Irrespective of the two options, role of deformation in the formation of Myr2 seems to be well founded in the studied rock. Unlike Myr2, control of stress on the formation of Myr1 is not straightforward. Growth of vermicular myrmekite on alkali feldspar is a subject of debate. Asymmetric concentration of vermicular myrmekite on surface of alkali feldspar porphyroclast that is at high angles to the direction of compression led Simpson and Wintsch (1989) to conclude that high concentration of tangled dislocation/elastic strain energy on alkali feldspar surface promoted the growth of myrmekite. On the other hand, Vernon (1991) argued that stress is a required but not essential condition for the growth of vermicular myrmekite on alkali feldspar. Ambient stress regime, in most cases, only facilitated the access of fluid that triggered the replacement of alkali feldspar by vermicular intergrowth of plagioclase +quartz. Corroborating other studies (Simpson and Wintsch, 1989), the stoichiometrically balanced reaction in this study suggest ~10% shrink in solid volume during formation of the two generations of myrmekite. This then follows that pressure increase or temperature decrease facilitates the myrmekite forming reaction. Studies have shown that myrmekite starts forming at the interface of plagioclase and alkali feldspar and moves into the alkali feldspar as the process continues. A decrease in temperature, therefore, is consistent with smaller thickness and interlamellar spaces between quartz vermiculae at the frontal part of the myrmekite interface and progressively thicker and widely spaced quartz vermiculae in the distal part of the Myr1 (Harlov and Writh 2000, Abart et al. 2014). The regional P-T path and the

estimated temperature in this study also corroborate the growth of myrmekite during a phase of cooling at 500-600°C and 4-5 kbar pressure. Since a drop in pressure increases the rock volume, it is unlikely that the myrmekite in the studied area that requires ~10 % volume change was formed during a steeply decompressive P-T path. Indeed, tangled dislocations/elastic strain energy concentrates on surface that is at high angle to the direction of shortening. The accrued elastic energy on the surface increases the Gibbs Free energy (or chemical potential) locally, thereby making the surface of high strain energy of alkali feldspar prone to replacement by myrmekite (discussed in Vernon, 2004, Philpotts and Ague, 2009). A number of features in the studied rocks suggest minimal contribution of stress, if any, during the growth of Myr1. The features are:

- Pervasive development of Myr1 all along the periphery of the alkali feldspar (in both megacrystic as well as in the matrix grains) and at the interface of plagioclase inclusions in alkali feldspar. This feature suggests that growth of Myr1 was likely to be unrelated to local kinematic axes (Cesare et al. 2002, Menegon et al. 2006).
- Delicate intergrowth of quartz and plagioclase in Myr1 are not expected to sustain high deviatoric stress (Vernon 1991).
- Intimate association of Myr1 and secondary biotite showing static growth.

The optical continuity of plagioclase porphyroclast and the base plagioclase of Myr 1 suggest heterogeneous nucleation and consequent epitaxial growth of the latter on the former (Vernon 1991). This feature is inconsistent with the preferential growth of Myr1 on the high strain surface of alkali feldspar. Integrating all the evidences it seems reasonable to conclude that deformation did not have a major control on the formation of Myr1.

Role of fluid in the formation of myrmekite

Several textural features including highly irregular myrmekite front and preservation of small rafts of alkali feldspar within the myrmekite colony suggest that myrmekite in this study formed by replacement of alkali feldspar (Becke 1908, Phillips 1974, Simpson and Wintsch, 1989, Vernon 2004, Abart et al. 2014, Menegon

et al. 2006, Ceccato et al.2018, Cisneros-Lazaro et al. 2019). Together with the original work of Becke (1908) and the references cited above, the balanced chemical reactions derived in current study provide additional support for the replacement theory. Replacement of alkali feldspar by myrmekite is a metasomatic process in the sense that composition of the precursor alkali feldspar is grossly different from the product myrmekite that replaces it. Ever since the work of Becke (1908), several studies and this work argue that to accomplish "myrmekitization', Ca and Na need to be added to and K (and Ba) be removed from the alkali feldspar (Collins, 2013). Al and Si remain immobile during the myrmekite formation. Deformation may have a role in determining the site of nucleation and the morphology of the myrmekite as in the case of Myr2. However, mass transport along the chemical potential gradients of the chemical species (Ca and Na towards and K away from the myrmekite front) is a prerequisite condition for chemical transformation of alkali feldspar to myrmekite (cf. Philpotts and Ague 2009). Owing to slow kinetics, purely thermally driven grain boundary diffusion of Ca, Na and K without any fluid mediation cannot explain the extensive growth of myrmekite to the length scale as seen in the studied rock (e.g. Philpotts and Ague, 2009). A fluid mediated transport of Ca+ Na and K (in reverse direction) seems to be the triggering force for formation of myrmekite (Becke 1908, Simpson and Wintsch, 1989, Vernon 1991, Cisneros-Lazaro et al.2019). Intimate association of secondary biotite and myrmekite further corroborates the fluid mediated material transport during the formation of myrmekite in the studied rock. Similar fluid-induced metasomatic changes have also been reported from Jalore and Siwana granites of India, where K-feldspar porphyroclasts were mantled by plagioclase (Mondal et al., 2017). The authors infer that presence of sharp and corroded boundaries between the mantle and the core, protrusion of apophyges into the megacryst interiors, stranded inclusions of K-feldspar within oligoclase mantle and preservation of original megacrystic grain boundary advocates for pseudomorphic replacement through coupled dissolution–reprecipitation replacement process.

The textural features that support the intimate association of myrmekite and secondary biotite can be explained from the isothermal-isobaric $\mu_{CaO} - \mu_{K2O}$ diagrams. The topology of the chemical potential diagrams (Fig. 5.4) suggests that fluid that is in

equilibrium with the myrmekite has higher μ_{K2O} than the fluid in equilibrium with the biotite forming reaction, a sink of K_2O (Fig. 5.4a-d). Consequently, K_2O that is generated at the myrmekite front will move towards garnet and plagioclase porphyroclasts along its chemical potential gradient and trigger the growth of biotite (brown arrow in Fig. 5.4a). The process, in turn, releases CaO and hence increases μ_{CaO} of the fluid at this end (green arrow in Fig. 5.4a). Myrmekite formation consumes CaO and hence, creates a local low μ_{CaO} environment. This allows CaO to move from secondary biotite domain to myrmekite front. This coupled mass transfer, marked by undergoing reactions, continues till (1) sufficient fluids that could dissolve and transport K_2O and CaO (also Na_2O) are available and (2) the fluid gets access to the reactant phases of secondary biotite and myrmekite forming reactions. Since, grain contacts act as fluid conduits (Putnis and Austrheim, 2010), pervasive development of myrmekite and secondary biotite all along the grain contacts can be linked to pervasive fluid flow (Cesare et al., 2002; Dempster et al., 2021; Menegon et al., 2006).

This observation does not follow that the formation of pervasive secondary biotite in the entire volume of the studied rock are produced by local reorganization of elements. Rather, pervasive infiltration driven process that caused secondary biotite (and the accompanying albite rim on plagioclase porphyroclasts) possibly triggered the growth of myrmekite after alkali-feldspar. This observation is corroborated by the inference of Chakrabarty et al. (2022). All rocks of the MKGB were extensively retrogressed during the terminal phase of the ca. 950 Ma tectonothermal event. In a recent communication, Touret et al. (2022) argued that myrmekite on alkali feldspar marks the pathways along which mantle derived brines traversed the rocks. Low dihedral angle that the brine molecules make with silicate minerals allow the brines to move fast and pervasively through the rock (Plümper and Putnis, 2009; Touret et al., 2022). Albitization of plagioclase and K-metasomatism are considered to be a common phenomenon in brine induced metasomatic rocks (Plumper and Putnis 2009). Pervasive development of secondary biotite and the accompanying albite-rich rim on plagioclase porphyroclasts and myrmekite seem to support the postulation of Touret et al. (2022).

~10% volume reduction during the formation created "reaction enhanced secondary porosity" that helped fluid movement toward the alkali-feldspar and triggered the growth of myrmekite (Putnis and Austrheim, 2010). On the other hand, large positive volume change (~46.5%) of the secondary biotite forming reaction expected to create fluid overpressure led to microfractures along which the fluid could move (reviewed in Dempster et al. 2021). Regional deformation also provided access to the infiltrating fluid that is consistent with the formation of biotite folia with one mode of secondary biotite being syntectonic to the regional deformation. Development of secondary biotite and Myr1 on all sides of plagioclase porphyroclasts and alkali-feldspar respectively suggest a feedback mechanism driven by pervasive fluid flow.

Vein formation within metapelites (GCB) and aluminium mobility

Garnet-cordierite-sillimanite-quartz association is observed in widespread high grade metamorphosed pelitic rocks worldwide (Aranovich and Podlesskii, 1983; Chinner and Fox, 2009; Tsunogae and Santosh, 2010; Singh and Dwivedi, 2015; Kumar et al., 2022) albeit the petrogenesis of the cordierite-anthophyllite rock of unusual bulk composition remained ambiguous. Several processes have been proposed for the formation of such association: Several authors (Eskola, 1948) have argued that syn-metamorphic Mg or Fe-metasomatism, extraction of lime and alkalis can produce the observed mineralogy in a variety of protolith whereas others (Vallance, 1967) opined for isochemical metamorphism of mafic volcanic rocks.

At lower metamorphic grades, fractures filled with minerals precipitated from fluid are common in deformed metamorphic rocks (Vernon, 2018). The fluid that infiltrates in the hydrofractures carries dissolved chemical components either from external distant sources or from internal local origin(Cartwright and Buick, 1996; Ferry, 1994; Ferry and Dipple, 1991; Oliver, 1996). In case of aluminosilicate veins, the relative role of infiltration-driven metasomatism versus formation of closed-system vein-producing fluids has been largely debated (Bohlen et al., 1991). According to the infiltration model, aluminosilicate-bearing veins develop as a result of metamorphic fluid moving Al and Si into cracks after reacting with an aluminous host rock such as metapelites (Whitney and Dilek, 2000). If the vein and host rock contain the same

Al_2SiO_5 polymorph, it is possible that the host rock and the veins interacted chemically, physically, or both during the formation of the veins (Sepahi et al., 2004). In GCB, type-I vein comprises of the same minerals as that of the host or wall-rock i.e. association 1 and prismatic vein-sillimanite grows perpendicular to the vein-wall. In most places, sillimanite needles are stretched and continue up to the opposite vein-wall which is a characteristic of stretched-crystal veins. In stretched crystal veins, vein-minerals are similar to those of the wall rock and they grow across the vein nucleating from either of the walls (Durney & Ramsay, 1973). Contrary to the widely investigated quartz-aluminosilicate veins (Ague, 1995; Sepahi et al., 2004; Whitney and Dilek, 2000), the studied GCB contains only sillimanite (mostly prismatic coarse-grained and few late fibrolites) as Al_2SiO_5 polymorph along with quartz within the veins. Despite the variation of thermodynamic properties and kinetic behavior of prismatic coarse sillimanite and fibrolites (Hollaway and Mukhopadhyay, 1993), it can be concluded that the temperature during the vein formation in the GCB was >550°C though the pressure condition can be as low as 2 kbar depending on the existing temperature.

The formation of coarse grained sillimanite (Al_2SiO_5) as a vein forming mineral clearly indicates that Al was mobile/ soluble during the vein formation. This is in contradiction to the general notion that Al is one of the least soluble and hence immobile major elements in metamorphic fluids. However, experimental studies have shown that the combined effect of pressure, temperature, dissolved SiO_2 and halides (NaCl, KCl) significantly increases Al solubility by the formation of Na/K-Al-Si-O clusters and/or polymers (Hayden and Manning, 2011; Manning et al., 2008; Tropper and Manning, 2005). Since both quartz and sillimanite occur as vein forming minerals in the studied rocks, following the results of the high P experiments, it can be inferred that Al mobility in this case was at least enhanced due to the presence of dissolved SiO_2 in the fluids and if not halides. The question still remains as to the source of Al or scale of Al transport. Aluminous veins may form by removal of mobile components (Na, Si, Ca, Fe, Mg), thereby leaving behind a refractory residue enriched in Al. Alternately, if the host rocks are aluminous (e.g. metapelites), it has been proposed that metamorphic fluids may react with the host rock and transport Al and Si into

fractures where a drop in pressure precipitates quartz and an Al_2SiO_5 polymorph (Whitney et al., 2000). As already described, it is inferred that the veins formed through crack and seal mechanism, indicating the involvement of infiltrating fluids. Aluminium transport via the infiltration fluid resulted in two major processes in the GCB: fibrolite formation by base leaching and solution reprecipitation of elements within the veins. Following the approach of Hemley and Jones (1964), Veron (1979) suggested hydrogen metasomatism (base-cation leaching) as a probable cause for the growth of fibrolite at grain-scale. Abundant fibrolite growth with all the mineral associations in the studied rocks advocates for chemical instability with the minerals that are being replaced (Vernon, 1979). In the studied GCB the biotite and fibrolitic sillimanite were formed simultaneously by the following reaction:

4.37 **Cordierite** + 5.12 **Garnet** + 6.87 K^+ + 4.21 H^+

= 7.61 **Sillimanite** + 7.47 **Biotite** + 8.86 SiO_2

No new quartz grains are evident to be formed with fibrolitic sillimanite in the GCB hence this SiO_2 can form a hydrous complex by dissolving in the infiltrated fluid which is explained by previous workers (Morey, 1957; Vernon, 1979). Moreover, no quartz grain is observed at the immediate contact of the type-I vein and host rock which affirms that coarse vein quartz grains were formed by solution reprecipitation and leaching from the host GCB. Host of these veins contains abundant aluminosilicate but petrography and reaction modeling of association 2 reveal that anthophyllite formation from cordierite or anthophyllite + biotite formation from garnet + cordierite releases a significant amount of Al^{3+} which is a possible source for the sillimanite in type-I vein in the nearby regime.

9.3. Proterozoic evolution of MKGB in the context of the CITZ

Following section briefly describes the Proterozoic tectonic scenario of MKGB and entire CITZ based on the available information from the preexisting literature and current study (Fig. 9.4; 9.5).

I. Late Paleoproterozoic (Statherian period):

Till date the 2200-1800 Ma sedimentation history (Roy and Prasad, 2003), accompanied by 1894 Ma acidic magmatism in a continental arc setting (Sharma et al., 2022) and subsequent deformation-metamorphism of the MSB sediments at ca. 1800-1600 Ma (Deshmukh et al., 2017) mark the oldest events in the CITZ (Fig. 9.4). Voluminous calc-alkaline magmatism in the northern and southern margin of the MSB during late Paleoproterozoic (1758-1753 Ma; Bora et al., 2013), coeval with ongoing low-pressure, high-temperature metamorphism of supracrustals suggest the presence of a compressional regime in the north CITZ. Late collisional widespread I- and S-type magmatism of slightly younger age (1736-1610 Ma) has been reported from eastern parts of MSB (Bora and Kumar, 2015; Yadav et al., 2015) (Fig. 9.4). The post-collisional (A-type) granite emplacement in the central and western part of the MSB at similar time period during late Paleoproterozoic (1796, 1695, 1645 Ma) is explained by the partial

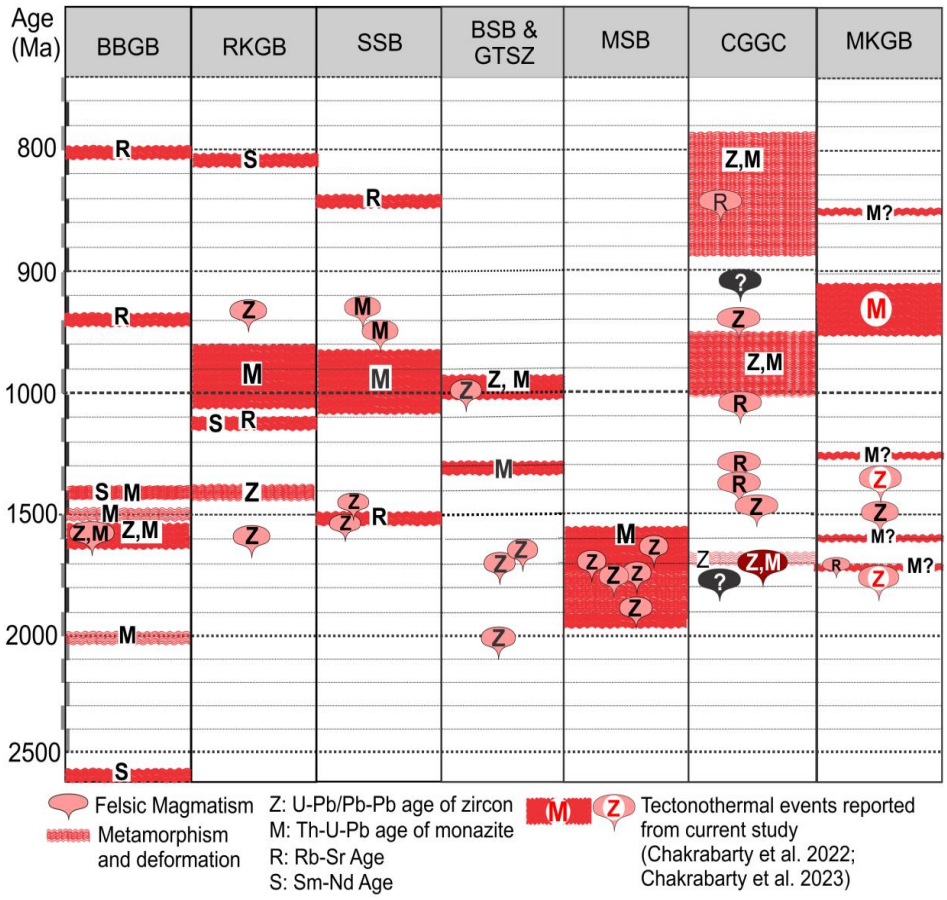

Figure 9.4. Diagram portraying the magmatic and metamorphic tectonothermal events in CITZ and CGGC composite. Apart from the current study the references of the magmato-metamorphic events are given in Table-2.1.

melting of the same source (Bundelkhand tonalitic-granodioritic crust) under different petrogenetic conditions (Yadav et al., 2020, 2015) (Fig. 9.4). From the south of the Son-Narmada South Fault, current study from the MKGB documents a late Paleoproterozoic (ca. 1750 Ma) arc magmatism suggesting that MSB and MKGB represented a coherent block at least up to 1750 Ma. This further implies that Son-Narmada South Fault did not exist as a prominent shear zone at least at ca. 1750 Ma and that MSB and MKGB are both part of the Bundelkhand craton i.e. the northern crustal component of the Indian subcontinent. The axial spine of the CITZ, the major geological formations between MKGB and BSB is covered by Mesozoic Deccan volcanics and Permo-carboniferous Gondwana sediments. Hence tectonic framework amid the northern and southern sector is poorly constructed. Recent petrology, geochemistry and robust geochronological information from BSB reveal that the protolith of the Betul Gneiss emplaced at ca. 2167 Ma in a continental arc setting by intracrustal melting of the overriding plate supposedly Bundelkhand cratonic block (Dora et al., 2023). Information from the pillow basalts (parts of Bargaon Formation, BSB) suggests development of a volcano-sedimentary unit in a subduction accretionary orogeny at ca. 2050-1800 Ma (Dora et al., 2023). All these tectonothermal events indicate the northward subduction of the Bastar craton beneath the northern cratonic block i.e. Bundelkhand craton (Bhowmik et al., 2012; Chattopadhyay et al., 2017; Roy and Prasad, 2003; Yadav et al., 2020) that initiated at around 2200 Ma and ended with the closure of the back-arc basin, low-pressure/ high temperature metamorphism of Mahakoshal sediments and syn-tectonic I-type granite emplacement up to around 1750 Ma (Fig. 9.5a). Slightly younger late collisional (ca. 1736-1610 Ma) and anorogenic granite emplacement in MSB (ca. 1695, 1645 Ma) and in BSB (ca. 1715±10, 1671±29 Ma) could be the effect of a local rifting event which can potentially create an opening between MSB and southern parts of the CITZ along the Son-Narmada South Fault (Fig. 9.5b).

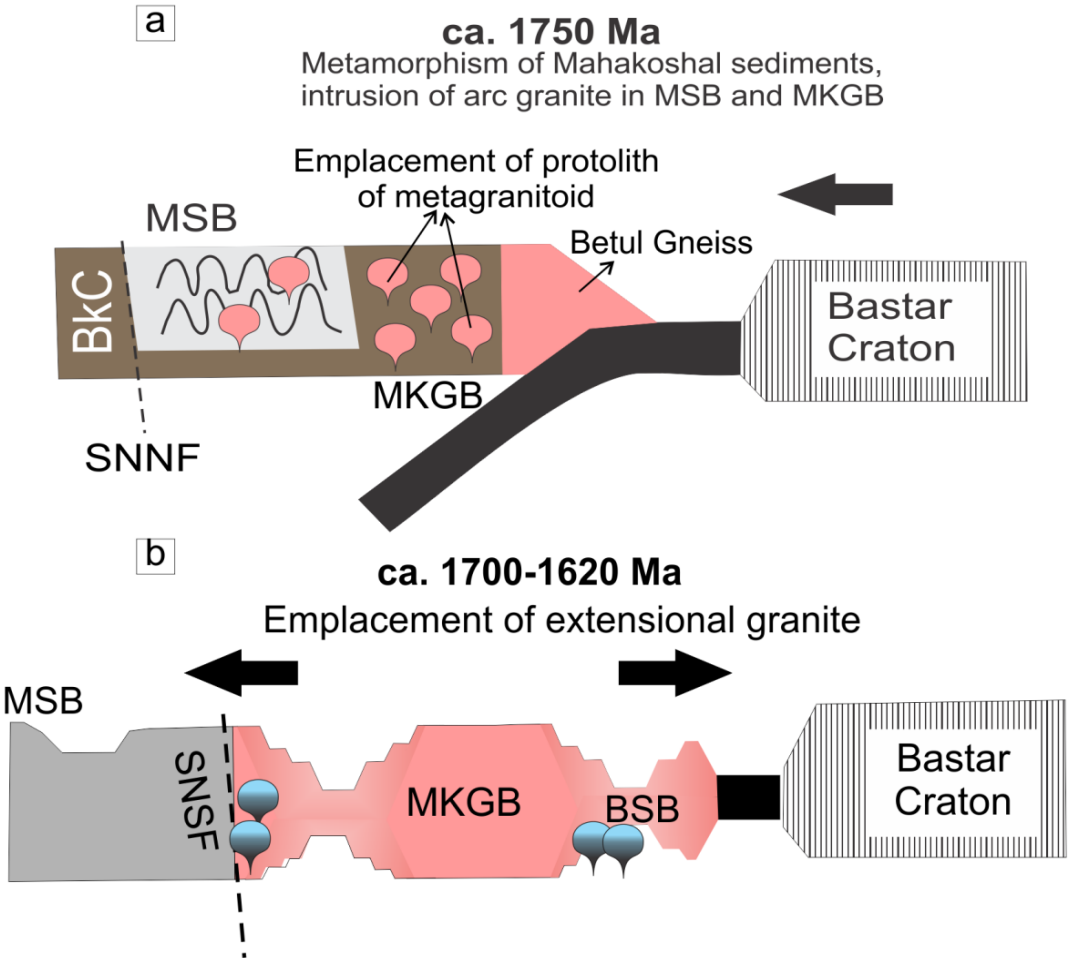

Figure 9.5. (a) Paleoproterozoic northward subduction of Bastar craton beneath Bundelkhand craton ended with back-arc basin (MSB) closure manifested by low pressure/high temperature metamorphism of MSB sediments and I-type granite emplacement in MSB and MKGB (protolith of the studied porphyritic metagranitoids) at ca. 1750 Ma. (b) Late collisional and anorogenic granite emplacement in MSB and in BSB could be the effect of a local rifting event which can potentially create opening between MSB and southern parts of the CITZ along the Son-Narmada South Fault.

II. Early Mesoproterozoic (early Calymmian period):

Existing study suggests that during 1620-1540 Ma, MSB, MKGB and BSB do not record any thermotectonic events and hence were quiescent and the orogenic front is perceived to exist along the southern margin of the CITZ (Bhowmik, 2019; Chattopadhyay et al., 2020). Extensive magmatic arc (Tirodi Biotite Gneiss) with

Paleoproterozoic ancestry (Model age: 2379 Ma) formed at the beginning of Mesoproterozoic era (1618 Ma: Bhowmik et al., 2011; 1534-1454 Ma: Ahmad et al., 2009) (Fig. 9.4, 9.5c). Subsequent slab-rollback, back-arc extension and resultant mantle upwelling caused multi-cyclic UHT metamorphism (counterclockwise P-T path: 1600-1540 Ma from psammopelitic granulite) in the Balaghat-Bhandara Granulite Belt of Paleoarchean ancestry (Model age: 3630-3051 Ma from anatectic granite) (reviewed in Bhowmik, 2019) (Fig. 9.4, 9.5c). In contrast to the older arc setting in the north CITZ, the early Mesoproterozoic arc magmatism in the southern CITZ is inferred to have resulted from southward subduction of the Bundelkhand craton below the Bastar craton (Fig. 9.5c; Bhowmik, 2019; Deshmukh and Prabhakar, 2020).

III. Mesoproterozoic (late Calymmian and Ectasian period):

From a suite of mafic-felsic magmatism it has been inferred that early Mesoproterozoic (~1500 Ma) continental arc setting supposedly prevailed in the Betul Supracrustal Belt (Roy et al., 2004; Yousuf et al., 2019). From the south CITZ, a weak thermal imprint of extension-related metamorphic event at 1470-1420 Ma is recorded from the Balaghat-Bhandara Granulite Belt (Bhowmik, 2019). On the contrary, the MKGB preserves felsic magmatism with arc affinity of 1400-1350 Ma (Chakrabarty et al., 2022). Although the connotation of ca. 1500 Ma arc magma in the Betul Supracrustal Belt (BSB) is ambiguous, while explaining the arc magmatism in the MKGB, Chakrabarty et al. (2022) suggested that crustal extension in the easterly located CGGC (ferroan granite magmatism at ca. 1450 Ma; Mukherjee et al., 2018), opening of southerly lying Sausar basin (after 1540 Ma) and emplacement of anorogenic granitic magma within Sausar Supracrustal Belt (SSB) at ca. 1322 Ma (Bose et al., 2023) presumably resulted in a compressional setting and arc magmatism in the northern blocks of the CITZ (Fig. 9.5d).

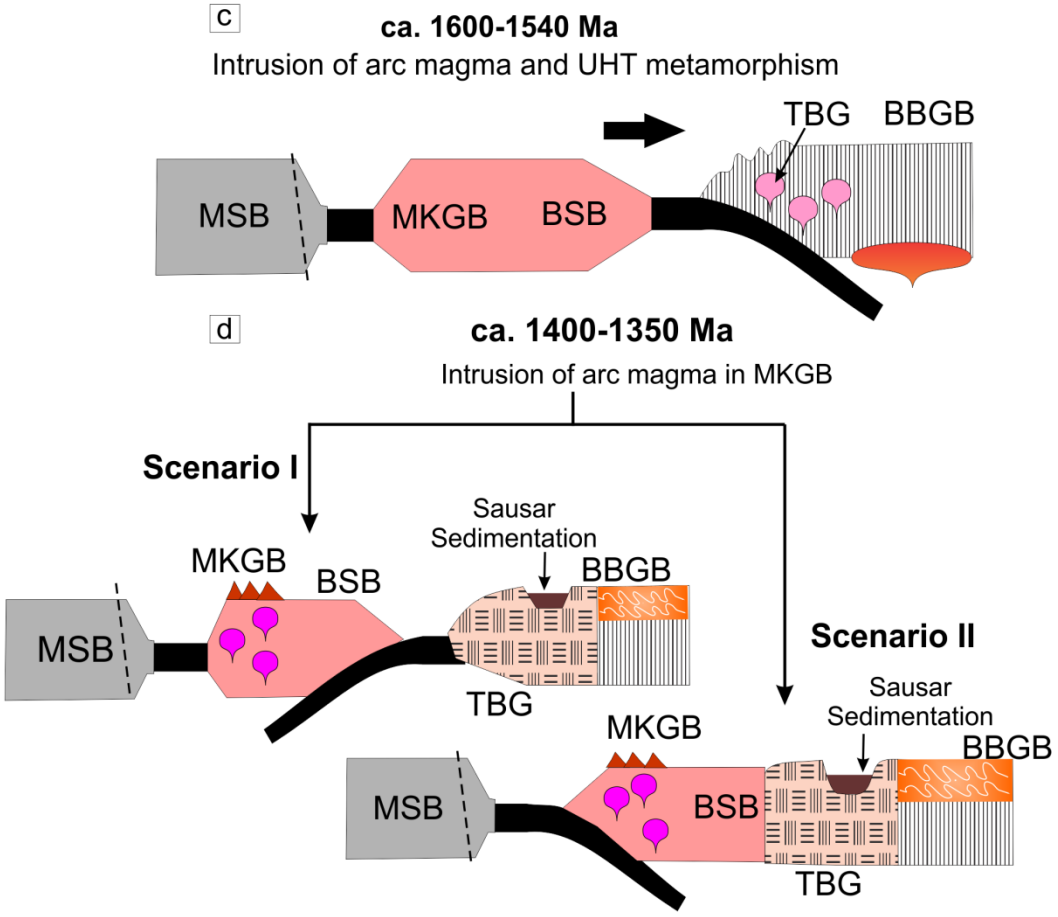

Figure 9.5 contd. (c) The orogenic front of the CITZ is present in the southern part during early Mesoproterozoic. Southward subduction resulted in large scale arc magmatism in the non-subducting northern margin of the Bastar craton (Tirodi Biotite Gneiss) (Bhowmik, 2019 and references therein) and subsequent UHT metamorphism in BBGB. (d) Bimodal volcanism in an arc setting in BSB during ca. 1500 Ma and emplacement of arc granite (protolith magmas of studied felsic orthogneisses) during ca. 1400-1350 Ma demand the central block (comprising MKGB and BSB) of CITZ to act as the overriding plate during a probable northward subduction of the oceanic slab between TBG and BSB. A possibility of southward subduction of the oceanic crust at the south of MSB below the Paleoproterozoic crust of the MKGB cannot be ruled out yet.

IV. Early Neoproterozoic (Tonian period):

Neoproterozoic collisional event recorded from different granulite belts in the southern parts of the CITZ is believed to be the manifestation of the closure of the Sausar basin and final amalgamation of different blocks of the CITZ (Bhowmik,

2019). While the high pressure granulite grade metamorphism of the RKGB (Bhowmik and Roy, 2003; Bhowmik and Spiering, 2004) marks a thick collisional orogen SSB records middle to upper amphibolite facies metamorphism (Bhowmik et al., 1999; Bhowmik et al., 2012). Early Neoproterozoic ages (1050-950 Ma) of the deformation-metamorphism in RKGB and SSB, marking the closure of Sausar basin, transpressional deformation and granite magmatism in GTSZ (Chattopadhyay et al., 2017; Chattopadhyay and Khasdeo, 2011), magmatic crystallization and a thermal (possibly metamorphic) imprint at ca. 1079 and 954 Ma respectively from Navegaon granite, BSB (Dora et al., 2023) advocate for the final collisional orogeny during this time. While MKGB distinctly experienced this Grenvillian high grade metamorphic event, MSB (in the north) does not record any coeval event. Drawing analogy from prolonged subduction-accretion during middle Mesoproterozoic, closure of Sausar basin and subsequent Neoproterozoic collisional orogeny in the SSB and RKGB (reviewed in Bhowmik, 2019; Chattopadhyay et al., 2020) it is most likely that MKGB got thrusted below MSB (Fig. 9.5e).

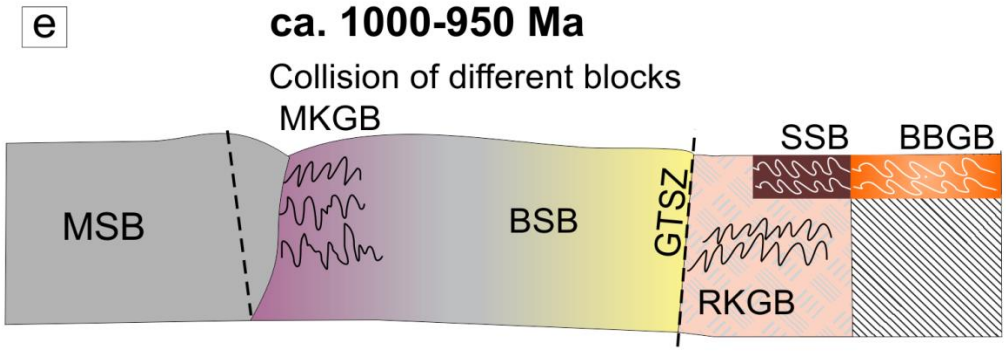

Figure 9.5 contd. (e) Neoproterozoic ages (1050-950 Ma) are recovered from the MKGB (current study), Gavilgarh-Tan Shear Zone (Chattopadhyay et al. 2017), BSB (Dora et al. 2023), RKGB and SSB (Bhowmik et al. 2012). As MSB did not experience any tectonothermal event during this Grenvillian orogeny, it can be inferred that MKGB got thrusted below MSB which resulted into the final amalgamation of north and south Indian blocks.

9.4. Linking the Proterozoic scenario of CITZ with India

9.4.1. Late Paleoproterozoic magmatic and metamorphic events in India

Prolonged late Paleoproterozoic (ca. 1900-1600 Ma) arc-magmatism and metamorphism have been reported from different parts of the peninsular as well as the extra-peninsular India (Table-9.1, Fig. 9.6a-c). While the older phase (ca. 1900-1800 Ma) of arc magmatism is mostly restricted to the lower lesser Himalayas and parts of the Aravalli Delhi Fold Belts, the younger phase of the arc magmatism (~1750-1600 Ma) has been recorded from the CITZ, CGGC and SMGC (Bhowmik et al., 2011;

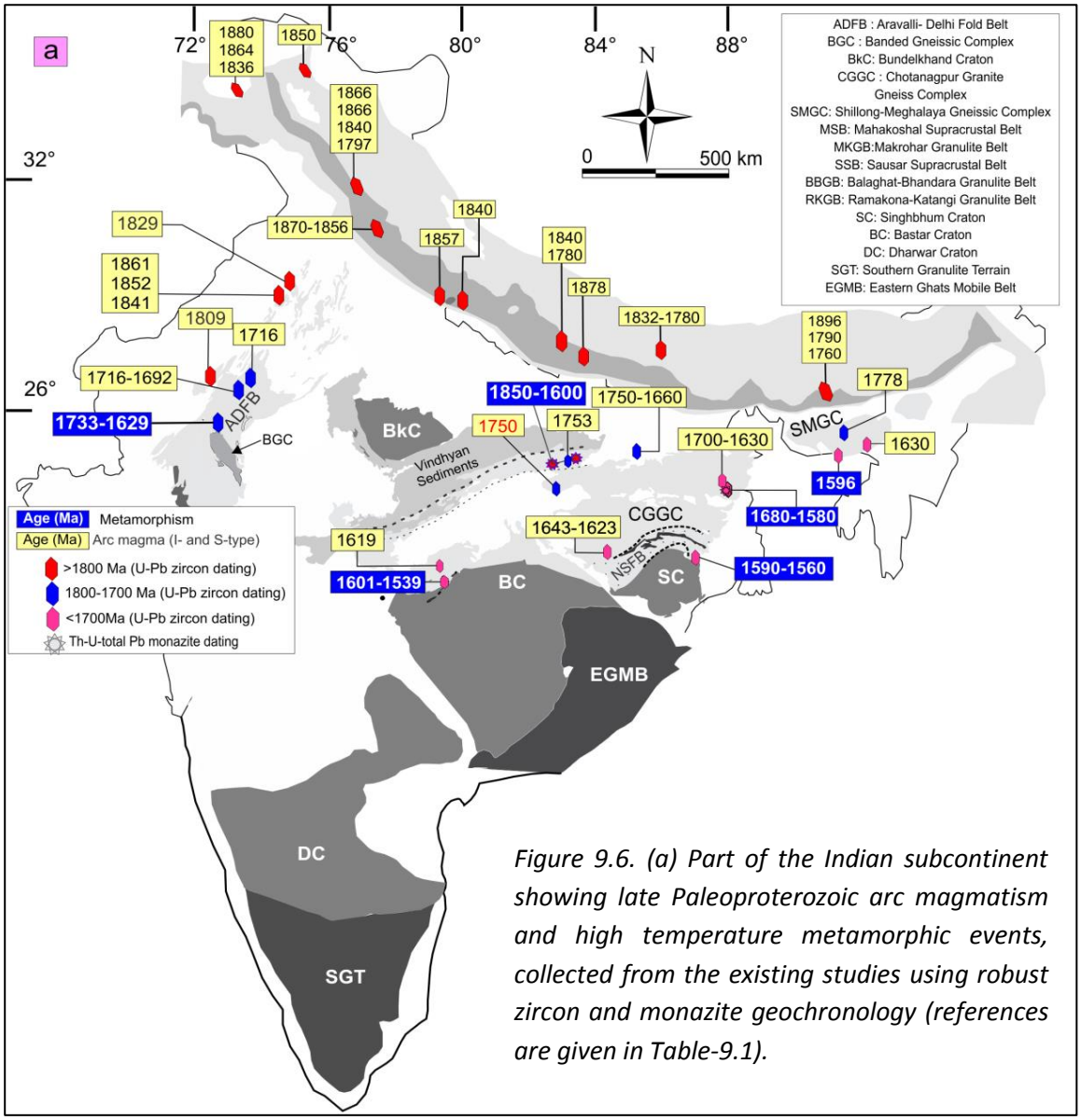

Figure 9.6. (a) Part of the Indian subcontinent showing late Paleoproterozoic arc magmatism and high temperature metamorphic events, collected from the existing studies using robust zircon and monazite geochronology (references are given in Table-9.1).

Ahmad et al., 2009; Mukherjee et al., 2019; Saikia et al., 2017) (Fig. 9.6a-c). Most of the areas between these orogenic belts are covered by younger sedimentary and igneous rocks (e.g., Gondwana basin sediments, Gangetic alluvium and Deccan trap volcanics) which hinder the proper correlation between these grossly coeval arc magmas. Concerning the present-day location of the Bundelkhand craton, northern (lower lesser Himalayas) and western (Aravalli Delhi Fold belt) orogenic as a ca. 1730-1660 Ma (Kaur et al., 2017) inferred to have formed in a late/post-orogenic extensional settings (Fig. 9.6a, b). Coeval UHT metamorphism (ca. 1720 Ma) has been reported from the ADFB as well (Bhowmik and Dasgupta, 2012) (Fig. 9.6b, c).

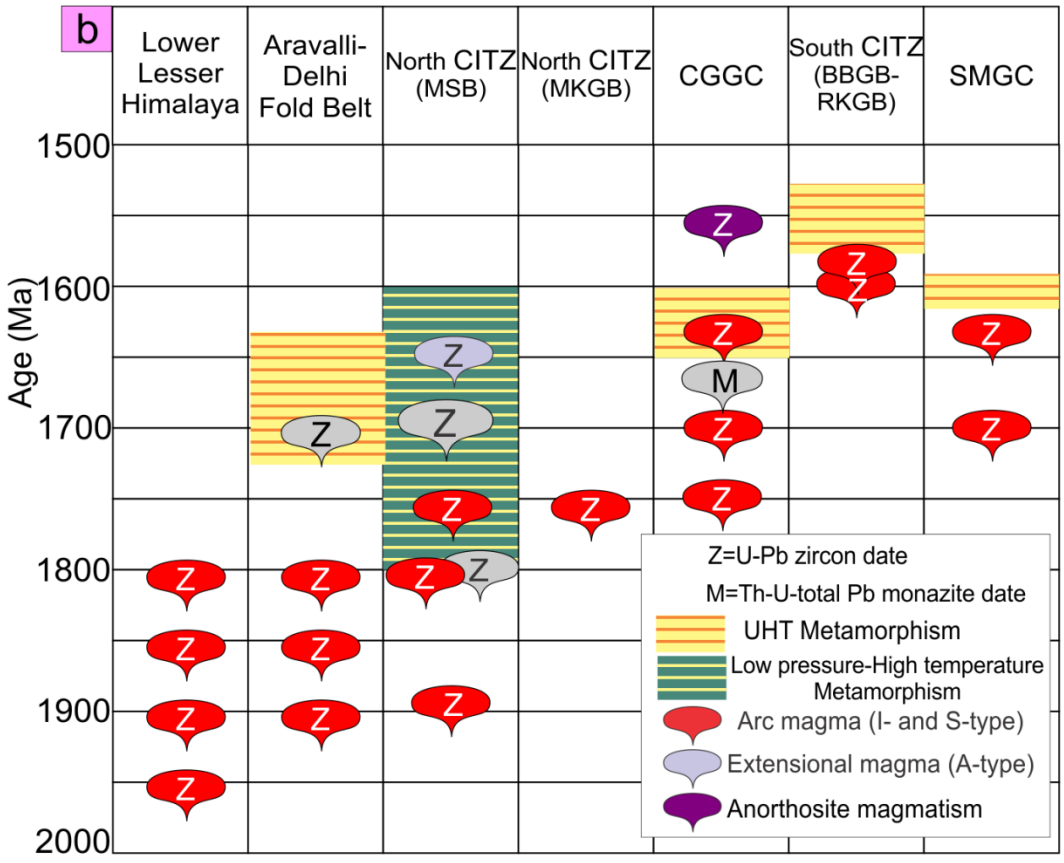

Figure 9.6 contd. (b) Balloon diagram showing Paleoproterozoic arc and extensional magmatism in north and central part of the Indian subcontinent (references are in Table-9.1)

Table 9.1: Events of the arc and extensional magma emplacement and HT-UHT metamorhism in the Lower Lesser Himalayas, Aravalli-Delhi Fold Belt, Central Indian Tectonic Zone, Chotanagpur Granite Gneissic Complex and Shillong-Meghalaya Gneissic Complex.

	Age	*Rock/Area*	*Event*	*Source*
Lower Lesser Himalayas	1880±24	Beham Gneiss	Magmatism (arc)	Treloar and Rex (1990)
	1864±4	Shang orthogneiss	Magmatism (arc)	DiPietro and Isachsen (2001)
	1836 ± 1	Kotla Complex	Magmatism (arc)	DiPietro and Isachsen (2001)
	1850 ± 14	Iskere gneiss	Magmatism (arc)	Zeitler et al. (1989)
	1840 ± 16	Rampur orthogneiss	Magmatism (arc)	Miller et al. (2000)
	1866 ± 10	Wangtu orthogneiss	Magmatism (arc)	Singh et al. (1994)
	1866 ± 6		Magmatism (arc)	Richards et al. (2005)
	1797 ± 19	Jutogh leucogranites	Magmatism (arc)	Chambers et al. (2008)
	1870-1856	Ramgarh Complex	Magmatism (arc)	Célérier et al.(2009)
	1840 ± 30	Ulleri augen gneiss	Magmatism (arc)	DeCelles et al. (2000)
	1840 ± 40		Magmatism (arc)	Célérier et al.(2009)
	1780 ± 23		Magmatism (arc)	Kohn et al. (2010)
	1878 ± 11		Magmatism (arc)	Kohn et al. (2010)
	1780 ± 23	Granitic orthogneiss	Magmatism (arc)	Kohn et al. (2010)
	1791 ± 12		Magmatism (arc)	Kohn et al. (2010)
	1832 ± 23		Magmatism (arc)	Kohn et al. (2010)
	1760 ± 70	Felsic gneiss	Magmatism (arc)	Daniel et al. (2003)
	1790 ± 30	Metarhyollite	Magmatism (arc)	Richards et al. (2005)
	1896 ± 16	Orthogneiss, Daling	Magmatism (arc)	Long et al. (2008)
	1743 ± 4	Bomdila augen gneiss	Magmatism (arc)	Yin et al. (2010)
	1747 ± 7	Augen gneiss	Magmatism (arc)	Yin et al. (2010)
	1857± 19	Askot granodiorite	Magmatism (arc)	Mandal et al. (2016)
Aravalli-Delhi Fold Belt	1861 ± 5	Rajota gneiss	Magmatism (arc)	Kaur et al. (2017a)
	1852 ± 5	Jhujhapur gneiss	Magmatism (arc)	Kaur et al. (2017a)
	1841 ± 10	Jarsapur gneiss	Magmatism (arc)	Kaur et al. (2017a)
	1809 ± 9	Anasagar gneiss	Magmatism (arc)	Kaur et al. (2017a)
	1821 ± 0.4	Jarsapur gneiss	Magmatism (arc)	Kaur et al. (2009)
	1716±6	Enderbite, Sandmata Complex	Magmatism (arc)	Buick et al. (2006)
	1716-1692	Mangalwar Complex	Magmatism (arc)	Buick et al. (2006)
	1730-1700	Granite, Khetri and Alwar	Magmatism (extensional)	Kaur et al. (2017b)
	1733-1629	Banded Gneissic Complex	Metamorphism	Bhowmik et al. (2012)
Central CITZ	1894±9	Pyroclastics, Parsoi Formation,	Magmatism (arc)	Sharma et al. (2022)
	1800-1600	Andalusite schist, Mahakoshal	Metamorphism	Deshmukh et al. (2017)
	1796±17	Porphyritic grey granite, Sidhi,	Magmatism (extensional)	Yadav et al. (2020)
	1753±9	Jhirgadandi granitoid pluton,	Magmatism (arc)	Bora et al. (2013)
	1750-1747	Porphyritic granite, Makrohar	Magmatism (arc)	Current study
	1695±9	Madanmahal granite,	Magmatism (extensional)	Yadav et al. (2020)
	1645±25	Pink granite, Sidhi	Magmatism (extensional)	Yadav et al. (2020)
	1619 ± 7	Tirodi Gneiss	Magmatism (arc)	Bhowmik et al. (2011)
	1612-1574	Balaghat Bhandara Gneiss	Metamorphism	Bhandari et al. (2011)
	1400-1350	Felsic orthogneiss, Makrohar	Magmatism (arc)	Chakrabarty et al. (2022)
CGGC	1750-1660	Bathani Volcanics, CGGC	Magmatism (arc)	Saikia et al. (2017)
	1697±17	Granite at Gaya, CGGC	Magmatism (extensional)	Chatterjee and Ghose (2011)
	1710-1630	Jasidih-Deoghar, CGGC	Magmatism (arc)	Mukherjee et al. (2019)
	1670-1640	Jasidih-Deoghar, CGGC	Metamorphism	Dey et al. (2019)
	1648 ±9	Ekma Granite	Magmatism (arc)	Chakrabarty et al. (2019)
	1643-1623	Southwest CGGC	Magmatism (arc)	Chakrabarty et al. (2019)
	1590-1560	North Singhbhum Fold Belt	Metamorphism	Rekha et al. (2011)
	1550±12	Anorthosite	Magmatism (extensional)	Chatterjee et al. (2008)
	1469-1446	Charnockite and migmatitic felsic	Magmatism (extensional)	Mukherjee et al. (2018)
SMGC	1778 ± 37	Rongjeng granite gneiss	Magmatism	Kumar et al. (2017)
	1630 ± 16	Guwahati granite gneiss	Magmatism	Kumar et al. (2017)
	1596±15	Garo-Goalpara Hills	Metamorphism	Chatterjee et al. (2007)

Subsequent arc magmatism at ca. 1750 Ma is mostly recorded from the MSB (Bora et al., 2013; Bora and Kumar, 2015), MKGB (this study) and Bathani Volcanic Suite (north CGGC) (Saikia et al., 2017) which occur as roughly NE-SW trending zones (Fig. 9.6a-c). Saikia et al. (2017) suggested that the Bathani Volcanic Suite (north CGGC) is essentially equivalent to the MSB of the central CITZ. Geochemical similarities of the studied porphyritic granite near Makrohar with coeval arc granitoids from the MSB, north and eastern CGGC attest that MSB + north CGGC along with the MKGB formed a coherent crust that experienced profuse arc magmatism at ca. 1750 Ma.

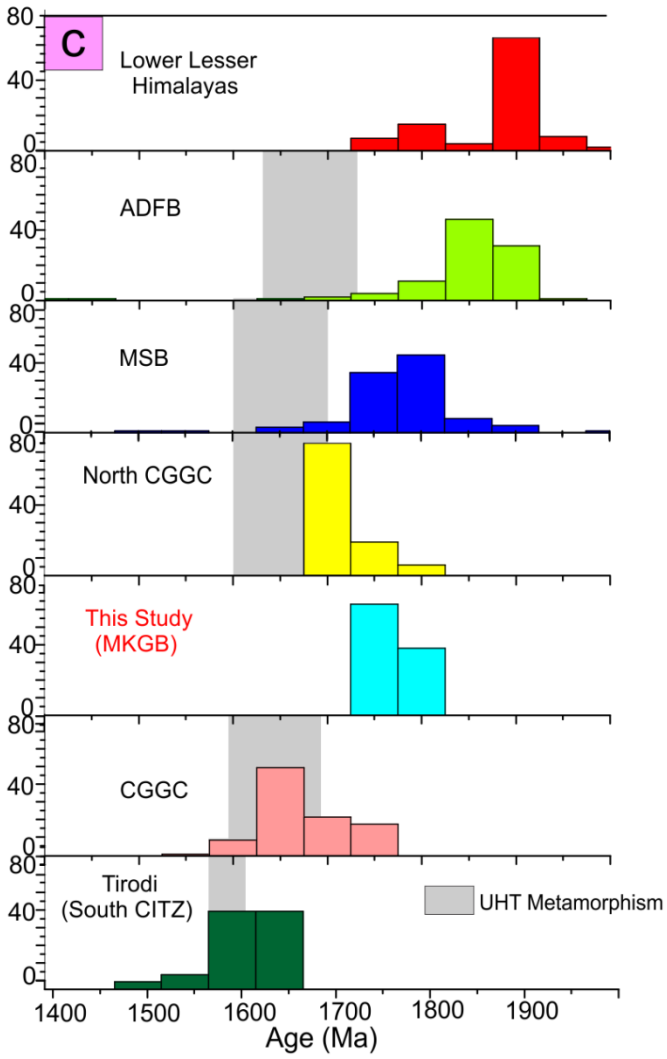

Figure 9.6 contd. (c) Comparative study shows the relative timing of the arc and extensional magma emplacement and subsequent HT-UHT metamorphism in the north and central India.

This zone is located towards the south and east of the orogenic belts with older arc magmas. Subsequent post-orogenic extension at ca. 1700-1650 Ma has been inferred from the ferroan A-type granites located in the southern parts of both the MSB (Yadav et al. 2020) and the Bathani Volcanic Suite (Chatterjee and Ghose, 2011; Yadav et al., 2014). The calculated Sm-Nd model ages (Model age: 2496-2266 Ma) of the Bathani granitoid hints towards the involvement of older crustal rocks (Saikia et al., 2017), presumably coeval with the intrusives in the Bundelkhand craton. Inferred Neoarchean

ancestry (Model age: 3140-2481 Ma) of these A-type granitoids from the MSB and Bathani Volcanic Suite led the workers (Yadav et al., 2020, 2015) to suggest that both the arc and extensional granites in this belt formed predominantly via the partial melting of same source (Bundelkhand tonalitic-granodioritic crust) under different petrogenetic conditions.

Extension-related granite magmatism in the MSB + Bathani Volcanic Suite (north CGGC) overlaps with the arc magmatism of 1700-1630 Ma reported from further south of the Bathani (central and eastern CGGC) (Chakraborty et al., 2019; Mukherjee et al., 2019). Metapelitic enclaves within the country rocks of the CGGC preserved imprints of HT metamorphism of 1680-1580 Ma (Dey et al., 2019a; Rekha et al., 2011). Slightly younger (1620-1580 Ma) arc magmas (Tirodi Biotite Gneiss) and UHT metamorphism (ca. 1600 Ma) have been reported from the southern margin of the CITZ (Bhandari et al., 2011; Bhowmik et al., 2011).

HT/UHT metamorphism and extensional magmatism immediately succeeded the compressional setting in each block indicating cessation of compression at that particular terrane. The precise tectonic setting responsible for the HT/UHT conditions is highly debated (Harley, 2016; Kelsey and Hand, 2015). Long-lived HT/UHT metamorphism is inferred to be formed in 'Large Hot Orogens' (LHO) during continent-continent collision and HT/UHT rocks formed through these processes commonly record higher pressure (>10 kbar) and clockwise P-T path (Harley, 2016). Short-lived (5-10 Myr) HT/UHT metamorphism forms during the arc-back-arc accretion or subduction roll back where the heat flux is supplied by upwelled mantle melts underplated below the thin crust. While explaining the prevailing tectonic conditions, Dey et al. (2019a) suggested a possible collisional setting followed by slab delamination. From the southern parts of the CITZ, Bhowmik and Chakraborty (2017) studied different pulses of metamorphism between 1620 to 1540 Ma and revealed a series of slab-roll back, back-arc extension and slab advancement that eventually resulted in continent-continent collision.

Spatial and temporal shift of arc magmatism towards the southern and eastern direction and extensional magmatism following the arc magma possibly points towards an arc migration, commonly envisaged in modern-day plate tectonics such as

in Andes (Gianni and Luján, 2021). Existing study shows that the volcanic activity became gradually younger towards south and south-eastern blocks in the Indian subcontinent. Combining these events of arc magmatism and the younger HT/UHT metamorphism (Fig. 9.6c), it can be inferred that prolonged compressional setting (ca. 1900 to ca. 1550 Ma) involved subduction and slab-rollback mechanism and migration of arc that eventually fused the Greater Indian Landmass.

9.4.2. Mesoproterozoic magmatic events in India

Table 9.2: Events of arc and extensional magma emplacement during Mesoproterozoic in India.

Age (Ma)	Rock/Area	Event	Source
1618±8	Tirodi Biotite Gneiss, SSB, CITZ	Magmatic (arc)	Bhowmik et al. 2011
1605±3	Monzodiorite (Bopudi region, EGMB)	Magmatic (arc)	Rao et al. 2013
1599 ± 17	Granitoids, Mesoproterozoic Kaziranga magmato-sedimentary domain, Shillong Plateau	Magmatic (extensional)	Majumdar and Gogoi (2020)
1588.4 ± 7.1 and 1589.7 ± 5.7	Vinuonda granite, EGMB	Magmatic (extensional)	Dobmeier et al. 2006
ca. 1582	Rapaivi granite (Bopudi region, EGMB)	Magmatic (arc)	Rao et al. 2013
1581±24	Felsic orthogneiss, Beawar gneiss unit within the central Aravalli orogen	Magmatic (arc)	Kaur et al. 2020
1550±12	Bengal anorthosite, CGGC	Magmatic (extensional)	Chatterjee et al. 2008
1534±13	Tirodi Biotite Gneiss, SSB, CITZ	Magmatic (arc)	Ahmad et al. 2009
1442±30	Elchuru alkaline rocks, EGMB	Magmatic (extensional)	Upadhyay et al. 2006
1377-1352	Felsic orthogneiss, MKGB, CITZ	Magmatic (arc)	Chakrabarty et al. 2022
1352±2	Errakonda and Uppalapadu alkaline rocks, EGMB	Magmatic (extensional)	Vijaya Kumar et al. 2007
1334 ± 15, 1338 ± 27 and 1251.2 ± 9.4	Purimetla, Kanigiri and P C Palle gabbro plutons (Prakasam Igneous Province, Nellore Schist Belt)	Magmatic (arc)	Subramanyam et al. 2016
ca. 1263	Nephline syenite, Jojuru (Kondapalle, EGMB)	Magmatic (extensional)	Upadhyay and Raith, 2006

Globally the Mesoproterozoic magmatic activities are dominated by anorthosite and ferroan A-type granites which corresponds to the extensional settings owing to the breakdown of Columbia supercontinent (Frost and Frost, 2013; Goodge et al., 2008). In India, early Mesoproterozoic anorthosites have been reported from eastern parts of the CGGC (Bangal Anorthosite with emplacement age of 1550 Ma; Chatterjee et al. 2008) and Southern parts of the EGMB (Kondapalli anorthosite with an emplacement age of 1634 Ma; Dharma Rao et al., 2011). Mesoproterozoic (1450 to 1350 Ma) ferroan A-type granites have been identified in different parts of the CGGC (Mukherjee et al., 2022; Sequeira et al., 2021) which lies east of the current study area. Recently, ferroan A-type granites of ca. 1350 Ma (Bose et al., 2023) have been documented form the southern parts of the CITZ. Mesoproterozoic extensional granite magmatism at ca. 1500 Ma has also been recently reported from the northern part of the CITZ (MKGB; Yadav et al., 2022). Mesoproterozoic magmatic events in the Indian subcontinent, reported till date are presented in Table-9.2.

9.4.3. Neoproterozoic high grade metamorphic event in India

Evolutionary P-T path for the early Neoproterozoic high grade metamorphism experienced by all the lithounits of the MKGB illustrate a clockwise geometry (Fig. 9.7). The signature of this early Neoproterozoic high grade metamorphism characterized by clockwise P-T path and hence continent-continent collision event, have been documented extensively from the SW part of the CITZ [Gavilgarh-Tan Shear Zone-Chattopadhyay et al., 2017; RKGB-Bhowmik et al., 2012; SSB-Bhowmik et al., 2012; Chattopadhyay et al., 2015; Mohanty, 2015), albeit MKGB (where it has been reported for the first time), and the CGGC lying to the ENE of the MKGB (Roy Choudhury et al. 2023; Dey et al., 2019a; Karmakar et al., 2011; Kumar and Dwivedi, 2019; Mukherjee et al., 2017; Rekha et al., 2011) (Fig. 9.7). In the RKGB the peak metamorphism culminated at ~9 kbar ~800°C, followed by a decompression to ~7 kbar pressure and 700-750°C (Bhowmik and Roy, 2003), whereas metamorphism in the central domain of the Sausar belt corresponds to amphibolite grade conditions (~7 kbar and ~675°C) associated with a clockwise P-T path (Bhowmik et al., 1999).

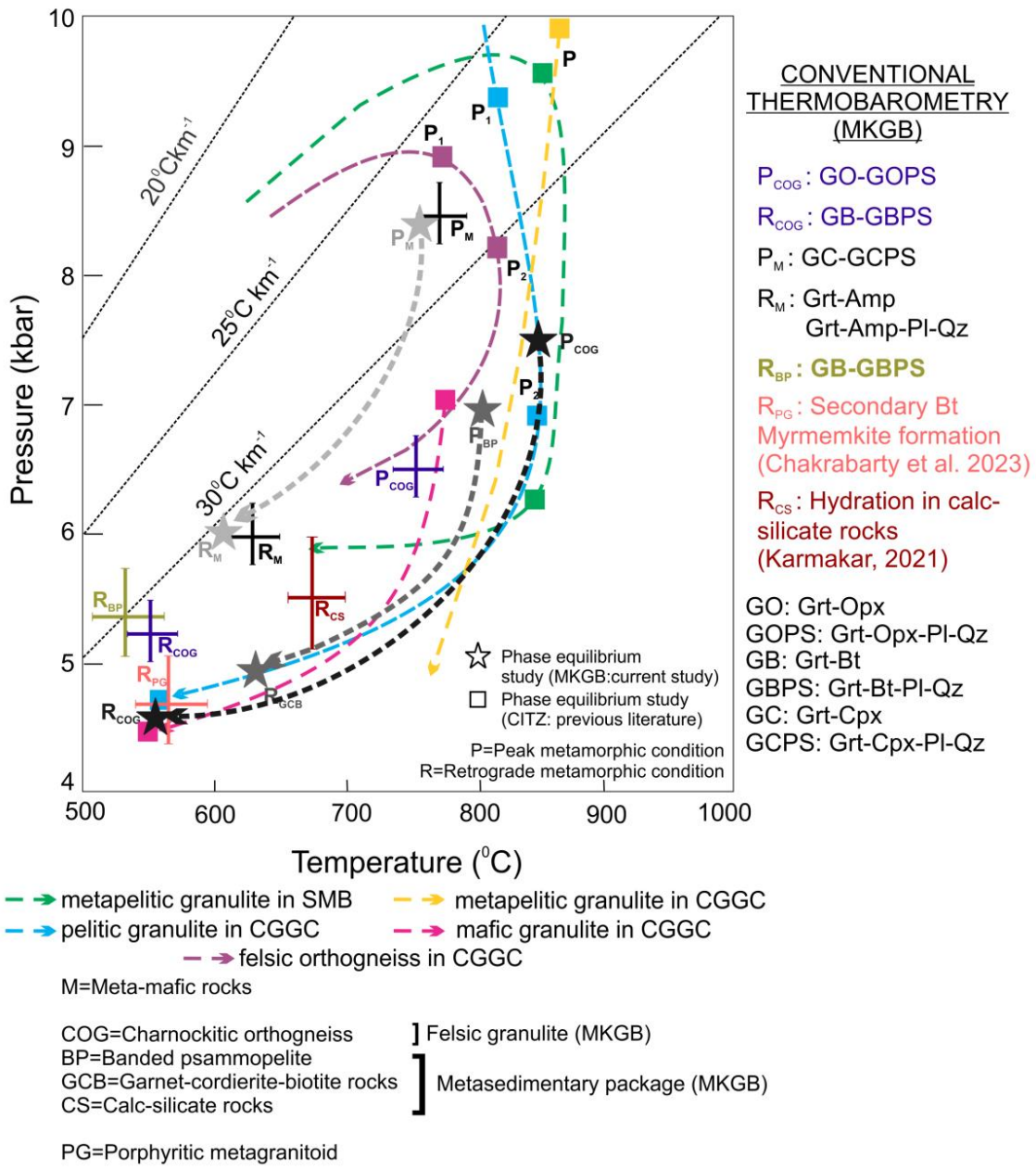

Figure 9.7. Comparison of coeval (early Neoproterozoic) CW P-T-t paths from different parts of CITZ [SMB (Sausar Mobile Belt) after Bhowmik and Spiering, 2004; CGGC after Dey et al., 2019; Karmakar et al., 2011; Kumar and Dwivedi, 2021; Mukherjee et al., 2017; MKGB from this study].

Petrology, combined with geochronology of metapelitic rocks from Daltonganj (western part of CGGC), located at the east of current study area suggests Neoproterozoic (972-962 Ma) granulite grade metamorphism that recorded a high geothermal gradient (>30°C/km; Kumar and Dwivedi, 2021, 2019). From further east

of CGGC, a Stenian-Tonian (ca. 1050-950 Ma) high grade tectonothermal event with an average geothermal gradient of 25-30ºC/km, associated with a clockwise P-T-t path, has been documented, confirming a continent-continent collisional setting (Roy Choudhury et al. 2023; Dey et al., 2019a, 2019b; Karmakar et al., 2011; Mukherjee et al., 2017). The style and timing of these metamorphic events from other parts of the CITZ and adjoining areas from CGGC corroborate well with the P-T-t path recovered from the lithounits of the study area (Fig. 9.7).

Similar tectonothermal episodes, typified by Neoproterozoic high-to-intermediate pressure granulite facies metamorphism on a clockwise P-T path have occurred in EGMB (mostly in the Eastern Ghats Province) (Rengali: Chattopadhyay et al. 2015; Anakapalli: Dasgupta et al., 1994; Arakku: Das et al., 2011 G. Madugula: Mohan et al., 1997). Ca. 1000-950 Ma granulite grade metamorphism and late thermal imprints are also reported from migmatitic metapelites and felsic orthogneisses from Aravalli Supergroup and Delhi Supergroup equivalent (ADFB) (Buick et al., 2010, 2006; Ghosh et al., 2023; Kaur et al., 2017; Ozha et al., 2016).

9.5.CITZ in the context of Proterozoic supercontinental cycle

Late Paleoproterozoic tectonothermal events are commonly associated with the assembly of the Columbia supercontinent (Meert and Santosh, 2017; Zhang et al., 2012; Zhao et al., 2004). However, the timing of the amalgamation and the architecture is debated. Pioneer workers suggested that Columbia supercontinent assembled and accreted for a protracted interval of 1900-1400 Ma and their disintegration commenced at 1400 Ma (Meert and Santosh, 2017; Zhang et al., 2012). As most of the cratonic nuclei record paleomagnetic data in around 1500-1400 Ma, the phase of accretion/coalescence of the Archean continental blocks reached its utmost condition during this period (Meert and Santosh, 2017). Archean basements are mostly exposed in present-day North China, India, Australia, North America and parts of Baltica, South Africa which are merged/connected through Paleoproterozoic (ca. 2000-1800 Ma) orogenic belts (such as Trans-North China Orogen, Central Indian Tectonic Zone, Capricorn and Halls Creek Orogen, Trans-Hudson and Taltson-Thelon Orogen etc.) (Zhao et al., 2004).In the configuration of Zhao et al. (2004), India is

placed at the east of North China from the analogy of the resemblance of the Trans-North China Orogen, Eastern and Western cratons of North China with CITZ, South and North Indian Block of the peninsular India (Zhao et al., 2004). In this scenario, East Antarctica is positioned adjacent to India and the late Paleoproterozoic arc magmatism and metamorphism in the EGMB is believed to be the manifestation of Indo-Antarctic fusion. Although the arc magmatism is conspicuously reported from the lower lesser Himalayas and Aravalli Delhi Fold Belt, the antiquity of the subduction could not be comprehended. However, the arc magmatism in the CITZ and CGGC resulted from the subduction and final collision of the north Indian blocks and south Indian blocks in response to a prolonged compressional orogeny during the formation of the Columbia supercontinent.

Extensive petrological, geochronological and paleomagnetic studies on the Paleoproterozoic mobile belts have identified a large supercontinent, named Columbia (Rogers and Santosh, 2002; Zhao et al., 2002). After the initial integration of older continental fragments between 2100-1800Ma, (Hou et al., 2008; Rogers and Santosh, 2002; Zhao et al., 2002), Columbia supercontinent experienced a protracted episodic growth till ca. 1300 Ma by a series of subduction-accretion events along the continental margins (Fig. 12a; Meert and Santosh, 2017; Sarkar and Schenk, 2016). The maximum packing of Columbia is considered to have formed during the time period between 1500-1400 Ma (Meert and Santosh, 2017). The major configurations of the Columbia supercontinent have been published (Zhao et al. 2011, 2004 and Rogers and Santosh, 2002; later modified by Meert and Santosh, 2017, Fig. 9.8a, b). In both the configurations, a unified Indian shield including north and south Indian blocks and CITZ in between has been considered to be a part of a peripheral unit of the Columbia supercontinent (Fig. 9.8a, b). Subsequent studies, however, favored the opinion that the juxtaposition of north and south Indian blocks did not occur before the onset of the Grenvillian orogenesis (ca. 1000-900 Ma). (Bhowmik, 2019; Chattopadhyay et al., 2020; Meert and Santosh, 2017).

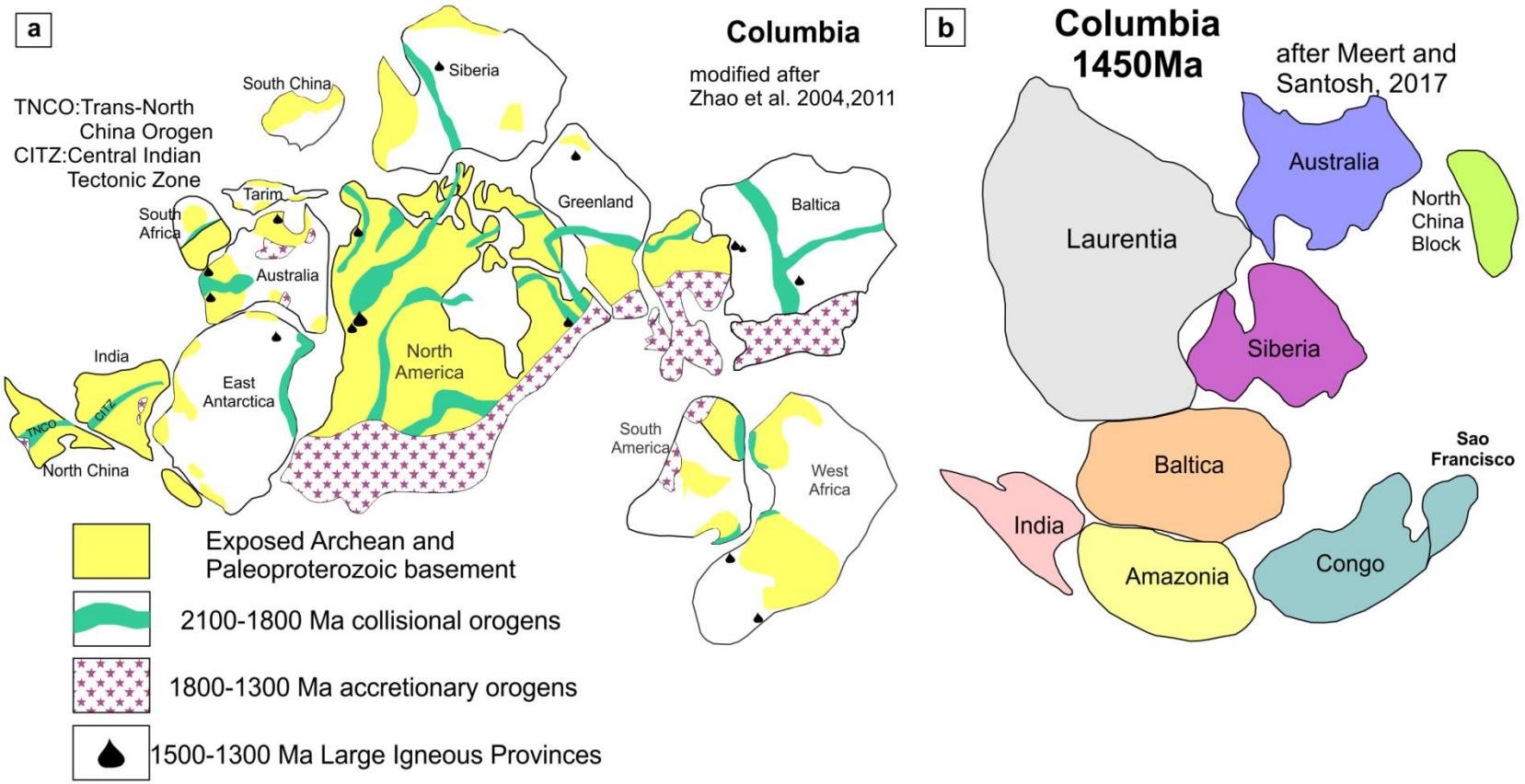

Figure 9.8. (a) Configuration of Paleo-Mesoproterozoic supercontinent Columbia marked with collisional, accretionary orogeny and voluminous magmatic activity (LIPs) during that time period (Zhao et al. 2004; Ernst et al. 2008). (b) Configuration of Columbia during 1450 Ma (after Meert and Santosh 2017) derived from paleomagnetic studies of different continental blocks.

Evidence in support of ca. 1700-1500Ma old arc magmatism has been documented from several parts of the eastern margin of the Indian shield (CGGC: Mukherjee et al., 2019b, Ongole domain of the Eastern Ghats: reviewed in Sarkar and Schenk, 2016, Nellore Schist Belt: Subramanyam et al., 2016). 1780-1300 Ma arc magmatism is also documented along the periphery of the different parts of the Columbia supercontinent including the cratons of North China, North America, Greenland, Baltica, Amazonia and north Australia (reviewed in Zhao et al., 2011). These observations are consistent with the participation of a unified Indian shield in the Columbia Supercontinent. Studies have shown that Columbia supercontinents started disintegrating from 1600 Ma and the fragmentation became complete by 1200 Ma (reviewed in Meert and Santosh, 2017; Zhao et al., 2011). The disintegration of Columbia supercontinent is manifested by rift related magmatism and formation of sedimentary basins along the margin and at the heart of the supercontinent (reviewed in Meert and Santosh, 2017; Zhao et al., 2011, 2004, 2002).In the Indian shield, extensive rift related magmatism has been recorded during ca. 1500-1300 Ma from the western part of the Eastern Ghats Belt (Upadhyay and Raith, 2006; Ranjan et al. 2018), from the CGGC that is considered to be the eastern extension of CITZ (ca. 1550 Ma old anorthosite: Chatterjee et al., 2008 and ca. 1450 Ma old A-type granitoids: Mukherjee et al., 2018) and from the CITZ (ca. 1498 Ma A-type granitoids in MKGB: Yadav et al. 2022; ca. 1322 Ma A-type granitoid emplacement within SSB: Bose et al. 2023) . Imprints of ca.1470-1420 Ma crustal extension related magmatism and metamorphism have also been recorded, though sporadically, from SW part of the CITZ (Balaghat Bhandara Granulite Belt, Bhowmik 2019). The published information supports the view that the Indian shield behaved as a coherent landmass, which existed atleast before 1450 Ma. This is consistent with the view of Zhao et al. (2004), Meert and Santosh, (2017) that Indian shield including the CITZ participated in the long lived Columbia supercontinent. The MKGB is situated in the NE part of CITZ that is located at the heart of the Indian shield. Formation of the 1400-1350 Ma old magmatic arc in the MKGB (Chakrabarty et al. 2022) must be linked to an open ocean basin. This is possible if the >1450 Ma old coherent Indian shield is again fragmented to develop an open ocean basin in the CITZ. It is not clear if the ca. 1498-1420 Ma crustal extension eventually evolved into an ocean basin or the latter is the product of an unrelated crustal extension. Subduction of the oceanic crust led to ca. 1400-1350

Ma old arc magma in the MKGB. The compression that is required for the partial closure of the open ocean basin and formation of the ca. 1400-1350 Ma old arc magma in the MKGB could be a consequence of the contemporaneous rifting along the eastern margin of the Indian Shield (Nance and Murphy 2013).

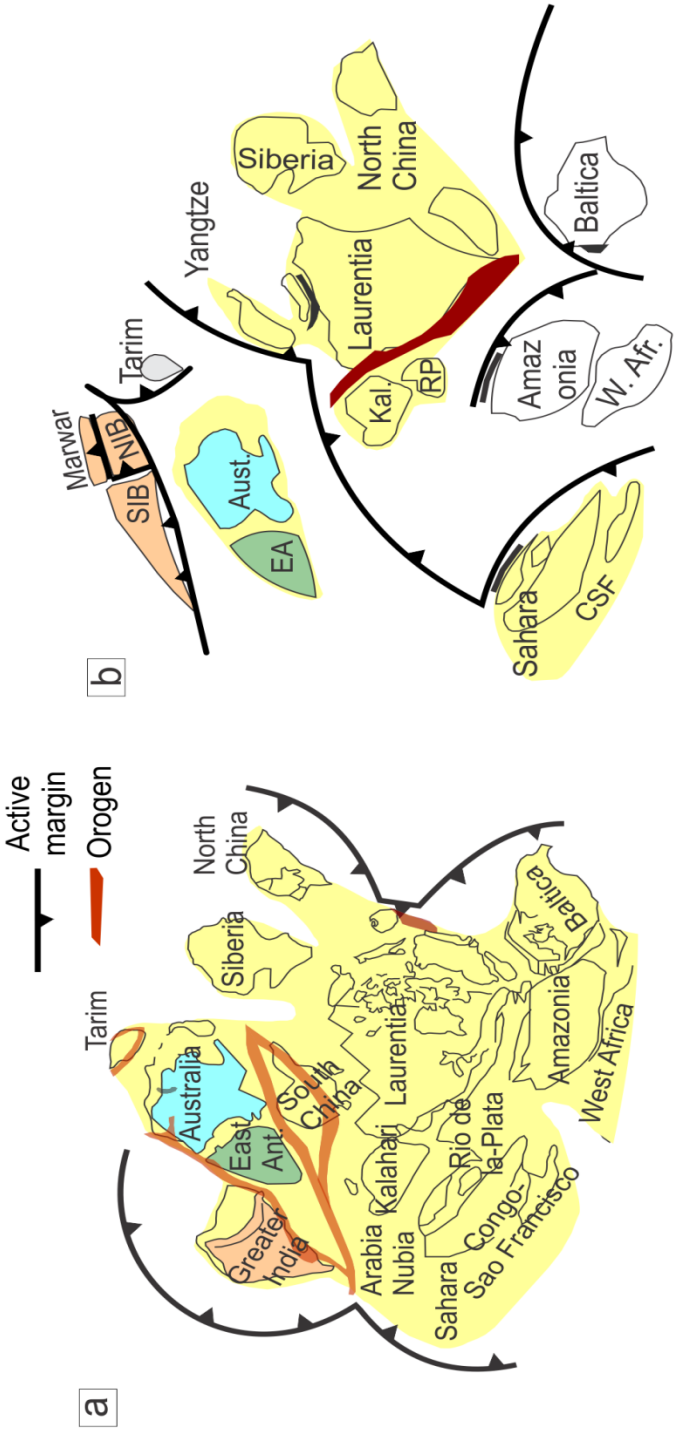

Figure 9.9. (a) Rodinia at 900 Ma placing India at western fringe of the supercontinent attached to Australia and east Antarctica. (b) Different blocks of Greater Indian Landmass which are separated by active margins.

The ca. 1000-950 Ma collisional events that reworked all the lithounits of the MKGB have also been recorded from the different parts of the Indian shield including the CITZ (SW CITZ: Bhowmik, 2019; Chattopadhyay et al., 2020, CGGC: Mukherjee et al., 2017, Eastern Ghats Mobile Belt: Dasgupta et al., 2017, Aravalli-Delhi Mobile Belt: Bhowmik et al. 2012). These early Neoproterozoic collisional events as recorded by the rocks of the Indian shield form part of the globally extensive Grenvillian orogeny that was instrumental in the formation of the Rodinia supercontinent (Li et al., 2008). Previous studies considered India to be attached with Australia and East Antarctica along the fringe of this early Neoproterozoic supercontinent (Fig. 9.9a; Dasgupta and Sengupta, 2003; Li et al., 2008; Torsvik et al., 2001) whereas few recent geophysical investigations obtain paleomagnetic pole positioned between India and Australia+ Antarctica atleast from 1050 Ma and opposes the earlier insight (Fig. 9.9b; Bhowmik et al., 2010; Fitzsimons, 2000; Powell and Pisarevsky, 2002). According to Bhowmik et al. (2010), there might have been more than one nucleus of continental expansion between around 1000 and 900 Ma, and it is improbable that the Greater Indian Landmass was entirely built and a part of the equatorial Rodinia supercontinent (Fig. 9.9b).

CHAPTER 10
CONCLUSIONS

Conclusions of the current study are as follows:

1) The Makrohar Granulite Belt (MKGB), located in the northeastern parts of the CITZ, represents an ensemble of different types of meta-igneous (felsic and mafic) and metasedimentary rocks. Lithological distribution points towards repeated magmatic intrusions while structural features are indicative of multiple phases of deformation and metamorphism that shaped the terrain.
2) As identified in the current study, the oldest lithounit of the area also happens to be the country rock, is represented by a Paleoproterozoic porphyritic granitoid that has been deformed and metamorphosed, and currently occurs as metagranitoid in the study area. U-Pb zircon geochronology and the major and trace element geochemistry suggest that the granitoids were emplaced at ca. 1750 Ma in an arc setting. Coeval arc magmatism in the Mahakoshal Supracrustal Belt (MSB), northern parts of the MKGB suggests that MSB and MKGB acted as a coherent block at least up to ca. 1750 Ma.
3) The porphyritic metagranitoids show considerable variation in terms of mineralogy and composition. Open system phase equilibrium modeling suggests that such variation can occur during post-emplacement fractional crystallization or assimilation of crustal material with a mafic magma and subsequent fractionation. However, the modeling predicts the latter process would produce higher amount of residual mafic rocks. Absence of such rocks in the field area rules out the assimilation-fractional crystallization process and favors the notion of post-emplacement crystal fractionation. The modeling further predicts that early crystallization events were dominated by presence of plagioclase feldspar and orthopyroxene/biotite culminating in a less siliceous more calcic whole rock compositions, while the late crystallization products are dominated by alkali

feldspar and quartz, and are more siliceous and alkali rich. These compositional variations corroborate well with the observed variations in the natural samples.

4) Compositionally the late Paleoproterozoic arc granites of the study area are similar to the coeval arc granitoids reported from different parts of India. While granitoids from northern India (lower lesser Himalayas and Aravalli Delhi Fold Belt) are slightly older (ca. 1950 to 1800 Ma), granitoids towards the southern parts [Central India; MSB, MKGB, Chotanagpur Granite Gneissic Complex (CGGC)] are considerably younger (ca. 1750 to 1650 Ma) and experienced HT/UHT metamorphism. This probably indicates the southward progression of the Paleoproterozoic arc front in the peninsular India.
5) Paleoproterozoic arc magmatism was followed by the intrusion of Mesoproterozoic S-type granite that was inferred to have been formed by partial melting of older sedimentary rocks in an arc setting. Although coeval extensional magmatism has been reported from different parts of India, presence of arc magma in the CITZ is reported for the first time. Preliminary phase equilibrium modeling suggests that the compositional variation observed in the suite can be attributed to the entrainment of up to 30% of peritectic minerals along with 10% anorthite. The arc magmatism was presumably triggered by the development of a local convergent margin at the northern CITZ in response to crustal extension in the Eastern Ghats Mobile Belt, southern parts of the CITZ and in eastern CGGC.
6) Development of a significant amount of leucosome and presence of garnet ± orthopyroxene as the peak metamorphic assemblage indicate that the granitoids have been metamorphosed under granulite facies conditions converting them into charnockite. Conventional geothermobarometry and the pseudosection analyses also corroborate the notion that the estimated P-T recovered from the assemblage is around 800-850 °C and 7-7.5 kbar. Zircon and monazite geochronology suggest that the metamorphism occurred around 1000 to 950 Ma. High T-P metamorphism combined with the deformational imprints suggests that the event resulted from a continent-continent collisional zone which resulted from the final amalgamation of Indian blocks.

7) Combined field relations and phase equilibria modeling study on the banded psammopelites identify an early granulite facies metamorphism, manifested by the garnetiferous leucosomes that define a regional planar fabric formed at ~800°C, 7 kbar. Phase equilibrium modeling of the garnetiferous (olivine-absent) meta-mafic rocks suggests that metamorphism culminated at 750-800 °C and 7-9 kbar stabilizing the peak metamorphic mineralogy.
8) High-grade metamorphic assemblages have been extensively replaced by retrogressed mineral assemblages in all the lithounits. Alkali feldspar porphyroclasts have been replaced by vermicular intergrowth of plagioclase and quartz. Textural modeling, mass balance and the phase equilibrium modeling suggest that infiltration of brine-rich fluid produced a chemical potential gradient of CaO and K_2O which resulted in a feedback mechanism, operated between reaction sites in the natural system. Variation of chemical potentials of chemical species at nearly constant P-T was responsible for the stability of anthophyllite in a domain of the garnet-cordierite-biotite rock. The garnet-aluminosilicate veins that dissect the garnet-cordierite-biotite rock are interpreted by infiltration-driven metasomatism where the infiltrated fluid interacted with aluminous host rock causing hydrofractures and deposited prismatic sillimanite, coarse vein quartz and garnet (crack-seal mechanism).
9) MKGB experienced a protracted period of magmatism, both and mafic compositions, sedimentation (protoliths of metasedimentary rocks) and deformation that can be tracked from ca.1750 Ma to 913 Ma. Late Paleoproterozoic and mid-Mesoproterozoic arc magmatism in the MKGB can be correlated with the formation and prolonged accretion of the Columbia supercontinent. Early Neoproterozoic deformation and high grade metamorphism, characterized by a clockwise P-T path, is attributed to global Grenvillian orogeny and major part of the Indian shield behaved as a coherent block during the assembly of the Rodinia supercontinent.

List of publications:

Chakrabarty Arimita, Mukherjee Subham, Karmakar Shreya, Sanyal Sanjoy, Sengupta Pulak (2023). Petrogenesis and in situ U-Pb zircon dates of a suite of granitoid in the northern part of the Central Indian tectonic Zone: Implications for prolonged arc magmatism during the formation of the Columbia supercontinent. **Precambrian Research**, 387, https://doi.org/10.1016/j.precamres.2023.106990

Chakrabarty Arimita, Karmakar Shreya, Mukherjee Subham, Roy Choudhury, Sirina, Maiti Prithwiraj, Sanyal Sanjoy, Sengupta Pulak (2022). Neoproterozoic reworking of a Mesoproterozoic magmatic arc from the north-eastern part of the Central Indian Tectonic Zone: Implication for the growth and disintegration of the Indian shield in the Proterozoic supercontinental cycles. **Precambrian Research**, 378, 1-22. https://doi.org/10.1016/j.precamres.2022.106758

Chakrabarty Arimita, Karmakar Shreya, Dutta Upama, Sanyal Sanjoy, Sengupta Pulak. Evidence of fluid-induced myrmekite formation after K-feldspar megacryst: example from metaporphyritic granite in Makrohar, Madhya Pradesh, India. **Mineralogical Magazine**, *DOI: https://doi.org/10.1180/mgm.2023.90*

List of Abstracts:

Chakrabarty, Arimita, Mukherjee, Subham (2023). Role of crystal entrainment in producing chemical variation in S-type granite: a case study from Central Indian Tectonic Zone. **Goldschmidt 2023 Conference**.

Chakrabarty, Arimita, Karmakar, Shreya, Sanyal, Sanjoy, Sengupta, Pulak. (2020). Fluid induced origin of myrmekite in a porphyritic granitoid from parts of the Makrohar Granulite Belt of Central India. **36th International Geological Congress**, India. Abs no. 4124-3498

Chakrabarty, Arimita, Karmakar, Shreya, Mukherjee, Subham, Sanyal, Sanjoy, Sengupta, Pulak. (2020). Petrology and Th-U-total Pb Monazite dating of a suite of felsic orthogneisses from Makrohar area, Central India: Evidence of Neoproterozoic reworking of Mesoproterzoic crust. **International Symposium on Food, Livelyhood, Opportunity & Wood (FLOW)**, Raichak, India. Pg 46-47

Chakrabarty, Arimita, Karmakar, Shreya, Sanyal, Sanjoy, Sengupta, Pulak (2017). Petrology of quartz-sillimanite veins and host garnet-cordierite granulite of unknown origin from Makrohar Granulite Belt, Central India: Evidence for Al-mobility. **International Symposium on 'Earth and Material Sciences for Sustainable Societal Developments**', Raichak, India. Pg 40

APPENDIX

A1. ANALYTICAL TECHNIQUES FOR BSE IMAGES USED FOR PETROGRAPHIC DESCRIPTION OF STUDIED ROCKS

Back-scattered electron (BSE) images are taken using ZEISS EVO-18 scanning electron microscope at Jadavpur University, Kolkata, India, equipped with an energy dispersive spectrometer (EDS), operating at an accelerating voltage of 20 kV and a beam current of 1.0 nA.

A2. ANALYTICAL TECHNIQUE FOR MINERAL CHEMISTRY

Composition of different mineral phases has been done at the Department of Geology and Geophysics, Indian Institute of Technology, Kharagpur, Central Research Facility of the Indian Institute of Technology (IIT-ISM), Dhanbad and Institute of Geology and Mineralogy, University of Cologne, Germany.

Department of Geology and Geophysics, IIT, Kharagpur uses a Cameca SX100 Electron Probe Micro Analyser, equipped with four wavelength dispersive spectrometers. Analyses were done using acceleration voltage of 15 KV and a beam current of 20 nA with a beam size of 1 μm. Dwell times for all the measured elements were set as 10 sec at peak and 5 sec at background. The standards (and emission lines) used are: jadeite (Na-Kα, Si-Kα), diopside (Ca-Kα, Mg-Kα), orthoclase (K-Kα, Al-Kα), NaCl (Cl-Kα), Fe2O3 (Fe-Kα), rhodonite (Mn-Kα), TiO_2 (Ti-Kα). TAP crystal was used to analyse F, Na, Al, Si and Mg; PET for Ca, Ti, K and Cl; LPET for P; LIF for Mn and Fe.

Central Research Facility of the IIT-ISM, Dhanbad, analyzed the mineral compositions with a CAMECA SX5 microprobe with 5 WDS. Operating conditions were 15kV accelerating voltage and 15nA beam current, with a beam diameter 2-3μm.

Natural standards were used for most major elements (Si, Al, Cr, Fe, Mg, Ca, Na, K) except for Mn and Ti, for which synthetic standards were used.

A JEOL JXA-8900RL electron microprobe equipped with five-WDS was used for analysis at the University of Cologne. The operation conditions were set to set to 12 kV accelerating voltage, 6 nA beam current and 5-10 μm beam diameter. The internal reference materials (Lipari glass ID3506, a scapolite from the Smithsonian National Museum of Natural History) were used to calibrate the machine. All other minerals from the P&H Geostandard Block), the analytical crystals and counting times: Lipari glass ID3506 (SI, AL; TAP; 20 SEC), almandine (Fe, LIF; 30 sec), rutile (Ti; PETH; 30 sec), rhodenite (Mn; LIF; 30 sec), clinopyroxene (Mg; TAP; 30 sec), orthoclase (K; TAP; 10 sec), apatite (P; PETH; 40 sec), scapolite NMNH R6600 (Cl; PETH; 40 sec), fluorite (F; TAP; 40 sec) and baryte (S; PETJ; 40 sec).

A3. ANALYTICAL TECHNIQUE FOR WHOLE-ROCK GEOCHEMISTRY

Owing to the banded nature of the rock, observed in the field and petrography, considerably large samples were used for powdering and analyses to minimize the effects of the compositional heterogeneity, often imparted by the gneissic banding in various lithounits of the study area.

The major element composition of the whole rock has been analyzed in X-ray Fluorescence Laboratory of National Centre for Earth Science Studies (NCESS), Trivandrum, India using a Bruker S4 Pioneer sequential wavelength-dispersive X-ray spectrometer and resulting data were calibrated by geochemical reference materials of felsic compositions like G2, GSP2, STM1, SARM1, SARM2, SY3, RGM, GA, GH, GS-N, AC-E, MDOG, ISHG, VS-N, JG-1, JG-2, JG-3, JR-3, and JSY-1, used as standards. Detailed procedure, followed in the XRF lab is discussed by Ravindra Kumar and Sreejith (2016).

Trace elements were determined using Agilent Triple Quadrupole Inductively Coupled Plasma Mass Spectrometer (QQQ-ICP-MS), also known as ICP-MS/MS and their concentrations were measured at the Department of Earth Sciences in Indian Institute of Technology, Kanpur by using acid solution of powdered samples. Detailed methodology of the solution preparation and calibration of the data is discussed in

Mukherjee et al. (Mukherjee et al., 2019b). Trace-element concentrations were determined at 500 ppm total dissolved solid solutions, whereas REEs were determined at~2000 ppm. Solutions of reference materials, SBC-1 (Shale standard, USGS) and AGV-2 (Andesite, USGS) were analyzed to assess precision of the measured data. Uranium and Thorium concentration could not be measured due to analytical uncertainty.

The geochemical data were plotted using the R software package GCDkit (Janoušek et al., 2006).

A4. ANALYTICAL TECHNIQUE FOR U-PB ZIRCON GEOCHRONOLOGY

Uranium-lead (U-Pb) isotope dating of in-situ zircon was done at the Radiogenic Isotope Facility of the Department of Geology and Geophysics, Indian Institute of Technology (IIT), Kharagpur. BSE and CL images have been used to assort necessary and viable spots for dating. Zircon grains were identified and their Cathodo-luminescence (CL) images have been taken to understand zoning and grain interiors using JEOL JSA 6490 Scanning Electron Microscope at the Department of Geology and Geophysics, IIT Kharagpur. Detailed methodology and handling of the analyzed data are discussed in Chakraborty et al., 2019. Uncertainties of the analyzed data are reported in 2σ and the standard deviation of isotopic ratios and U content have been calculated using GJ-1 reference zircon.

The U–Pb isotopes were measured using a Thermo-Fisher Scientific iCAP-Q quadrupole ICP-MS attached to a New Wave 193 ArF Excimer laser ablation system. The laser was operated with ~5 J/cm^2 beam energy density at 5 Hz repetition rate. Depending on the thickness of the zones within the zircon grains the spot sizes has been fixed at 25–40 μm. For maximum sensitivity on Pb, Th, and U, the ICPMS was optimized using the NIST 612 reference glass. The oxide production rate monitored on $^{232}Th_{16}O$ was varying between 0.6–0.8%. The data were analyzed in time-resolved mode with each analysis having 30s background measurement and 40s peak signal measurement. External standardization was done by bracketing ten measurements of unknowns with three measurements of the GJ-1 reference zircons (Jackson et al., 2004). To monitor the quality of the data, the 91500 reference zircon (Wiedenbeck et

al., 1996) were analysed as unknowns. The measured $^{206}Pb/^{238}U$ ratios (0.1795±2.4 %, 2σ) and $^{207}Pb/^{206}Pb$ ratios (0.0748± 3%, 2σ) ratios for the 91500 overlap with the recommended values [$^{206}Pb/^{238}U$ = 0.1792 (±8%, 2σ) and $^{207}Pb/^{206}Pb$ = 0.0749 (±1%, 2σ)] within the analytical uncertainties. The weighted mean values were calculated and diagrams were plotted using the IsoplotR tool box (Vermeesch, 2018).

A5. ANALYTICAL TECHNIQUE FOR TH-U-TOTAL PB MONAZITE GEOCHRONOLOGY

Compositions of the Monazite grains were analyzed using the same Cameca SX100 Electron Probe Micro Analyzer at the Department of Geology and Geophysics, Indian Institute of Technology, Kharagpur. Analyses were done using an acceleration voltage of 20 KV, a beam current of 150 nA and a beam size of 1μm. Specific standards used for monazite calibration are: pyromorphite for Pb; UO_2 for U; ThO_2 for Th; synthetic REE-glass for La, Ce, Nd, Pr, Sm, Ho, Dy, Gd; apatite for Ca and P; yttrium aluminium garnet (YAG) for Y; hematite for Fe; corundum for Al and Th-glass for Si. Dates on each analyzed spot is calculated with the calibration of Montel et al.(1996) using in built age quant software of CAMECA SX-100. Details of the analytical methods have been presented in Bhandari et al.(2011). Probability diagrams have been constructed using the isoplot program of Ludwig (2003).

REFERENCES

Abart, R., Heuser, D., Habler, G., 2014. Mechanisms of myrmekite formation : case study from the Weinsberg granite , Moldanubian zone , Upper Austria. Contrib. to Mineral. Petrol. 168:1074. https://doi.org/10.1007/s00410-014-1074-7

Abart, R., Petrishcheva, E., Joachim, B., 2012. Thermodynamic model for growth of reaction rims with lamellar microstructure. Am. Mineral. 97, 231–240.

Acharyya, S.K., 2003. The Nature of Mesoproterozoic Central Indian Tectonic Zone with Exhumed and Reworked Older Granulites. Gondwana Res. 6, 197–214. https://doi.org/10.1016/S1342-937X(05)70970-9

Ague, J.J., 1995. Deep crustal growth of quartz, kyanite and garnet into large-aperture, fluid-filled fractures, north-eastern Connecticut, USA. J. Metamorph. Geol. 13, 299–314.

Ague, J.J., 2003. Fluid infiltration and transport of major, minor, and trace elements during regional metamorphism of carbonate rocks, Wepawaug Schist, Connecticut, USA. Am. J. Sci. 303, 753–816. https://doi.org/10.2475/ajs.303.9.753

Ahmad, T., Kaulina, T. V, Wanjari, N., Mishra, M.K., Nitkina, E.A., 2009. U–Pb zircon chronology and Sm–Nd isotopic characteristics of the Amgaon and Tirodi Gneissic Complex, Central Indian Shield: constraints on Precambrian crustal evolution, in: Precambrian Continental Growth and Tectonism. pp. 137–138.

Alonso-perez, R., Muntener, O., Ulmer, P., 2009. Igneous garnet and amphibole fractionation in the roots of island arcs : experimental constraints on andesitic liquids. Contrib. to Mineral. Petrol. 157, 541–558. https://doi.org/10.1007/s00410-008-0351-8

Ambler, E.P., Ashley, P.M., 1977. Vermicular orthopyroxene-magnetite symplectites from the Wateranga layered mafic intrusion, Queensland, Australia. Lithos 10, 163–172.

Aranovich, L.Y., Berman, R.G., 1997. A new garnet-orthopyroxene thermometer based on reversed Al2O3 solubility in FeO-Al2O3-SiO orthopyroxene. Am. Mineral. 82, 345–353. https://doi.org/10.2138/am-1997-3-413

Aranovich, L.Y., Podlesskii, K.K., 1983. The cordierite-garnet-sillimanite-quartz equilibrium: experiments and applications. Kinet. Equilib. Miner. React. 173–198.

Arzi, A.A., 1978. Critical phenomena in the rheology of partially melted rocks. Tectonophysics 44, 173–184.

Ashworth, J.R., 1972. Myrmekites of Exsolution and Replacement Origins. Geol. Mag. 109, 45–62. https://doi.org/10.1017/S0016756800042266

Ashworth, J.R., Sheplev, V.S., Khlestov, V. V, Ananyev, V.A., 2001. Geothermobarometry using minerals at non-equilibrium: a corona example. Eur. J. Mineral. 13, 1153–1161.

Banerjee, A., Sequeira, N., Bhattacharya, A., 2021. Tectonics of the Greater India Proterozoic Fold Belt, with emphasis on the nature of curvature of the belt in west-central India. Earth-Science Rev. 221, 103758.

Barton, M., Van Gaans, C., 1988. Formation of orthopyroxene-Fe-Ti oxide symplectites in Precambrian intrusives, Rogaland, southwestern Norway. Am. Mineral. 73, 1046–1059.

Barton, P.B., 1991. Ore textures: problems and opportunities. Mineral. Mag. 55, 303–315.

Baswani, S.R., Mishra, B.P., Mahapatro, S.N., Meshram, T., Pati, P., Shareef, M., Korakoppa, M., Mishra, M., Raza, M.A., Roy, S., 2022. Petrochemical evaluation of gahnite from volcanogenic massive sulfide deposits in Betul belt, Central India: Insight from petrography and in-situ trace element geochemistry. Geol. J. 57, 4508–4528.

Baxter, S., 2003. Field and petrographic evidence for magma mixing and mingling in Granitoids: Examples from the Galway Granite , Connemara. Mineral. Petrol. 76, 63–74. https://doi.org/10.1007/s00710-001-0178-8

Baxter, S., Feely, M., 2002. Magma mixing and mingling textures in granitoids: Examples from the Galway Granite, Connemara, Ireland. Mineral. Petrol. 76, 63–74. https://doi.org/10.1007/s007100200032

Bea, F., Montero, P., González-Lodeiro, F., Talavera, C., 2007. Zircon Inheritance Reveals Exceptionally Fast Crustal Magma Generation Processes in Central Iberia during the Cambro-Ordovician. J. Petrol. 48, 2327–2339. https://doi.org/10.1093/petrology/egm061

Becke, F., 1908. Uber myrmekit. Min. Pet. Mitt 27, 377–391.

Bhandari, A., Pant, N.C., Bhowmik, S.K., Goswami-Banerjee, S., 2011. 1.6 Ga ultrahigh-temperature granulite metamorphism in the Central Indian Tectonic Zone_ insights from metamorphic reaction history, geothermobarometry and monazite chemical ages. Geol. J. 46, 198–2016. https://doi.org/10.1002/gj.1221 ?1.6Ga

Bhattacharya, A., Krishnakumar, K.R., Raith, M., 1991. An Improved Set of a-X Parameters for Fe-Mg-Ca Garnets and Refinements of the Orthopyroxene-Garnet Thermometer and the Orthopyroxene-Garnet-Plagioclase-Quartz Barometer. J. Petrol. 32, 629–656.

Bhattacharya, A., Mazumdar, A.C., Sen, S.K., 1988. Fe-Mg mixing in cordierite; constraints from natural data and implications for cordierite-garnet geothermometry in granulites. Am. Mineral. 73, 338–344.

Bhattacharya, A., Mohanty, L., Maji, A., Sen, S.K., Raith, M., 1992. Non-ideal mixing in the phlogopite-annite binary: constraints from experimental data on Mg-Fe partitioning and a reformulation of the biotite-garnet geothermometer. Contrib. to Mineral. Petrol. 111, 87–93. https://doi.org/10.1007/BF00296580

Bhowmik, S.K., 2006. Ultra high temperature-metamorphism and its significance in the Central Indian Tectonic Zone. LITHOS 92, 484–505. https://doi.org/10.1016/j.lithos.2006.03.061

Bhowmik, S.K., 2019. The current status of orogenesis in the Central Indian Tectonic Zone: A view from its Southern Margin. Geol. J. 1–23. https://doi.org/10.1002/gj.3456

Bhowmik, S.K., Alexanderwilde, S., Bhandari, A., Sarbadhikari, A.B., 2014. Zoned monazite and zircon as monitors for the thermal history of granuliteterranes: An example from the Central Indian Tectonic Zone. J. Petrol. 55, 585–621. https://doi.org/10.1093/petrology/egt078

Bhowmik, S.K., Bernhardt, H.-J., Dasgupta, S., 2010. Grenvillian age high-pressure upper amphibolite-granulite metamorphism in the Aravalli-Delhi Mobile Belt, Northwestern India: New evidence from monazite chemical age and its implication. Precambrian Res. 178, 168–184. https://doi.org/10.1016/j.precamres.2010.02.015

Bhowmik, S.K., Chakraborty, S., 2017. Sequential kinetic modelling: A new tool decodes pulsed tectonic patterns in early hot orogens of Earth. Earth Planet. Sci. Lett. 460, 171–179. https://doi.org/10.1016/j.epsl.2016.12.018

Bhowmik, S.K., Dasgupta, S., 2012. Tectonothermal evolution of the Banded Gneissic Complex in central Rajasthan, NW India: Present status and correlation. J. Asian Earth Sci. 49, 339–348. https://doi.org/10.1016/j.jseaes.2011.07.025

Bhowmik, S.K., Pal, T., Roy, A., Pant, N.C., 1999. Evidence for Pre-Grenvillian high-pressure granulite metamorphism from the northern margin of the Sausar mobile belt in Central India. J. Geol. Soc. India. 53, 385–399.

Bhowmik, S.K., Roy, a, 2003. Garnetiferous metabasites from the Sausar Mobile Belt: Petrology, P-T path and implications for the tectonothermal evolution of the Central Indian Tectonic Zone. J. Petrol. 44, 387–420. https://doi.org/10.1093/petrology/44.3.387

Bhowmik, S.K., Sarbadhikari, A.B., Spiering, B., Raith, M.M., 2005. Mesoproterozoic reworking of palaeoproterozoic ultrahigh-temperature granulites in the Central Indian Tectonic Zone and its implications. J. Petrol. 46, 1085–1119. https://doi.org/10.1093/petrology/egi011

Bhowmik, S.K., Spiering, B., 2004. Constraining the prograde and retrograde P-T paths of granulites using decomposition of initially zoned garnets: An example from the Central Indian Tectonic Zone. Contrib. to Mineral. Petrol. 147, 581–603. https://doi.org/10.1007/s00410-004-0573-3

Bhowmik, S.K., Wilde, S.A., Bhandari, A., 2011. Zircon U-Pb/Lu-Hf and monazite chemical dating of the Tirodi biotite gneiss: Implication for latest Palaeoproterozoic to Early Mesoproterozoic orogenesis in the Central Indian Tectonic Zone. Geol. J. 46, 574–596. https://doi.org/10.1002/gj.1299

Bhowmik, S.K., Wilde, S.A., Bhandari, A., Pal, T., Pant, N.C., 2012. Growth of the Greater Indian Landmass and its assembly in Rodinia: Geochronological evidence from the Central Indian Tectonic Zone. Gondwana Res. 22, 54–72. https://doi.org/10.1016/j.gr.2011.09.008

Bhui, U.K., Sengupta, Pulak, Sengupta, Pranesh, 2007. Phase relations in mafic dykes and their host rocks from Kondapalle , Andhra Pradesh , India : Implications for the time – depth trajectory of the Palaeoproterozoic (late Archaean ?) granulites from southern Eastern Ghats Belt. Precambrian Res. 156, 153–174. https://doi.org/10.1016/j.precamres.2007.03.005

Boehnke, P., Watson, E.B., Trail, D., Harrison, T.M., Schmitt, A.K., 2013. Zircon saturation re-revisited. Chem. Geol. 351, 324–334. https://doi.org/10.1016/j.chemgeo.2013.05.028

Bohlen, S.R., Montana, A., Kerrick, D.M., 1991. Precise determinations of the equilibria kyanite⇌ sillimanite and kyanite⇌ andalusite and a revised triple point for Al2SiO5 polymorphs. Am. Mineral. 76, 677–680.

Bora, S., 2015. Mineralogy Geochemistry and Geochronology of Granitoid Plutons of Dudhi Gneissic Complex Mahakoshal Belt Central India. Nainital.

Bora, S., Kumar, S., 2015. Geochemistry of biotites and host granitoid plutons from the Proterozoic Mahakoshal Belt, central India tectonic zone: implication for nature and tectonic setting of magmatism. Int. Geol. Rev. 57, 1686–1706. https://doi.org/10.1080/00206814.2015.1032372

Bora, S., Kumar, S., Yi, K., Kim, N., Lee, T.H., 2013. Geochemistry and U-Pb SHRIMP zircon chronology of granitoids and microgranular enclaves from Jhirgadandi Pluton of Mahakoshal Belt, Central India Tectonic Zone, India. J. Asian Earth Sci. 70–71, 99–114. https://doi.org/10.1016/j.jseaes.2013.03.006

Bose, S., Anand, R., D'Souza, J., Hartnady, M., Kirkland, C., Kooijman, E., 2023. Zircon UPb and Hf isotope insights into the Mesoproterozoic breakup of supercontinent Columbia from the Sausar Belt, Central Indian Tectonic Zone. Geochemistry.

Brown, M., 2013. Granite: From genesis to emplacement. Bull. Geol. Soc. Am. 125, 1079–1113. https://doi.org/10.1130/B30877.1

Brown, M., 2014. The contribution of metamorphic petrology to understanding lithosphere evolution and geodynamics. Geosci. Front. 5, 553–569. https://doi.org/10.1016/j.gsf.2014.02.005

Buick, I.S., Allen, C., Pandit, M., Rubatto, D., Hermann, J., 2006. The Proterozoic magmatic and metamorphic history of the Banded Gneiss Complex, central Rajasthan, India: LA-ICP-MS U-Pb zircon constraints. Precambrian Res. 151, 119–142. https://doi.org/10.1016/j.precamres.2006.08.006

Buick, I.S., Clark, C., Rubatto, D., Hermann, J., Pandit, M., Hand, M., 2010. Constraints on the Proterozoic evolution of the Aravalli–Delhi Orogenic belt (NW India) from monazite geochronology and mineral trace element geochemistry. Lithos 120, 511–528.

Cartwright, I., Buick, I.S., 1996. Determining the direction of contact metamorphic fluid flow: an assessment of mineralogical and stable isotope criteria. J. Metamorph. Geol. 14, 289–305.

Castro, A., 2014. The off-crust origin of granite batholiths. Geosci. Front. 5, 63–75. https://doi.org/10.1016/j.gsf.2013.06.006

Ceccato, A., Menegon, L., Pennacchioni, G., Morales, L.F.G., 2018. Myrmekite and strain weakening in granitoid mylonites. Solid Earth 9, 1399–1419.

Cesare, B., Marchesi, C., Connolly, J.A.D., 2002. Growth of myrmekite coronas by contact metamorphism of granitic mylonites in the aureole of Cima di Vila, Eastern Alps, Italy. J. Metamorph. Geol. 20, 203–213. https://doi.org/10.1046/j.0263-4929.2001.00351.x

Cesare, B., Marchesi, C., Connolly, J.A.D., 2002. Growth of myrmekite coronas by contact metamorphism of granitic mylonites in the aureole of Cima di Vila, Eastern Alps, Italy. J. Metamorph. Geol. 20, 203–213. https://doi.org/10.1046/j.0263-4929.2001.00351.x

Chakrabarty, A., Karmakar, S., Mukherjee, S., Roy Choudhury, S., Maiti, P., Sanyal, S., Sengupta, P., 2022. Neoproterozoic reworking of a Mesoproterozoic magmatic arc from the north-eastern part of the Central Indian Tectonic Zone: Implication for the growth and disintegration of the Indian shield in the Proterozoic supercontinental cycles. Precambrian Res. 378. https://doi.org/10.1016/j.precamres.2022.106758

Chakrabarty, A., Karmakar, S., Mukherjee, S., Roy, S., 2022. Neoproterozoic reworking of a Mesoproterozoic magmatic arc from the north-eastern part of the Central Indian Tectonic Zone : Implication for the growth and disintegration of the Indian shield in the Proterozoic supercontinental cycles. Precambrian Res. 378, 106758. https://doi.org/10.1016/j.precamres.2022.106758

Chakrabarty, A., Mukherjee, S., Karmakar, S., Sanyal, S., Sengupta, P., 2023. Petrogenesis and in situ U-Pb zircon dates of a suite of granitoid in the northern part of the Central Indian tectonic Zone: Implications for prolonged arc magmatism during the formation of the Columbia supercontinent. Precambrian Res. 387, 106990. https://doi.org/10.1016/j.precamres.2023.106990

Chakraborty, S., 2008. Diffusion in solid silicates: A tool to track timescales of processes comes of age. Annu. Rev. Earth Planet. Sci. 36, 153–190. https://doi.org/10.1146/annurev.earth.36.031207.124125

Chakraborty, T., Upadhyay, D., Ranjan, S., Pruseth, K.L., Nanda, J.K., 2019. The geological evolution of the Gangpur Schist Belt , eastern India : Constraints on the formation of the Greater Indian Landmass in the Proterozoic. J. Metamorph. Geol. 37, 113–151. https://doi.org/10.1111/jmg.12452

Chappell, B.W., 1996. Magma Mixing and the Production of Compositional Variation within Granite Suites: Evidence from the Granites of Southeastern Australia. J. Petrol. 37, 449–470. https://doi.org/10.1093/petrology/37.3.449

Chappell, B.W., White, A.J.R., 1974. Two contrasting granite types. Pacific Geol. 8, 173–174.

Chappell, B.W., White, A.J.R., 2001. Two contrasting granite types : 25 years later. Aust. J. Earth Sci. 48, 489–499.

Chappell, B.W., White, A.J.R., Williams, I.S., Wyborn, D., 2004. Low- and high-temperature granites. Trans. R. Soc. Edinb. Earth Sci. 95, 125–140.

Chatterjee, N., Banerjee, M., Bhattacharya, A., Maji, A.K., 2010. Monazite chronology, metamorphism–anatexis and tectonic relevance of the mid-Neoproterozoic Eastern Indian Tectonic Zone. Precambrian Res. 179, 99–120. https://doi.org/10.1016/j.precamres.2010.02.013

Chatterjee, N., Crowley, J.L., Ghose, N.C., 2008. Geochronology of the 1.55Ga Bengal anorthosite and Grenvillian metamorphism in the Chotanagpur gneissic complex, eastern India. Precambrian Res. 161, 303–316. https://doi.org/10.1016/j.precamres.2007.09.005

Chatterjee, N., Ghose, N.C., 2011. Extensive Early Neoproterozoic high-grade metamorphism in North Chotanagpur Gneissic Complex of the Central Indian Tectonic Zone. Gondwana Res. 20, 362–379. https://doi.org/10.1016/j.gr.2010.12.003

Chattopadhyay, A., Bhowmik, S.K., Roy, A., 2020. Tectonothermal evolution of the Central Indian Tectonic Zone and its implications for Proterozoic supercontinent assembly: The current status. Episodes 43, 132–144. https://doi.org/10.18814/epiiugs/2020/020008

Chattopadhyay, A., Chatterjee, A., Das, K., Sarkar, A., 2017. Neoproterozoic transpression and granite magmatism in the Gavilgarh-Tan Shear Zone, central India: Tectonic significance of U-Pb zircon and U-Th-total Pb monazite ages. J. Asian Earth Sci. 147, 485–501. https://doi.org/10.1016/j.jseaes.2017.08.018

Chattopadhyay, A., Das, K., Hayasaka, Y., Sarkar, A., 2015. Syn- and post-tectonic granite plutonism in the Sausar Fold Belt, central India: Age constraints and tectonic implications. J. Asian Earth Sci. 107, 110–121. https://doi.org/10.1016/j.jseaes.2015.04.006

Chattopadhyay, A., Khasdeo, L., 2011. Structural evolution of Gavilgarh-Tan Shear Zone, central India: A possible case of partitioned transpression during Mesoproterozoic oblique collision within Central Indian Tectonic Zone. Precambrian Res. 186, 70–88.

Chiaradia, M., Müntener, O., Beate, B., 2011. Enriched basaltic andesites from mid-crustal fractional crystallization, recharge, and assimilation (Pilavo volcano, Western Cordillera of Ecuador). J. Petrol. 52, 1107–1141. https://doi.org/10.1093/petrology/egr020

Chowdhury, P., Chakraborty, S., Gerya, T. V., 2021. Time will tell: Secular change in metamorphic timescales and the tectonic implications. Gondwana Res. 93, 291–310. https://doi.org/10.1016/j.gr.2021.02.003

Chowdhury, P., Talukdar, M., Sengupta, P., Sanyal, S., Mukhopadhyay, D., 2013. Controls of P-T path and element mobility on the formation of corundum pseudomorphs in Paleoproterozoic high-pressure anorthosite from Sittampundi , Tamil Nadu , India. Am. Mineral. 98, 1725–1737.

Cisneros-Lazaro, D.G., Miller, J.A., Baumgartner, L.P., 2019. Role of myrmekite and associated deformation fabrics in controlling development of granitic mylonites in the Pofadder Shear Zone of southern Namibia. Contrib. to Mineral. Petrol. 174, 1–20.

Claeson, D.T., 1998. Coronas, reaction rims, symplectites and emplacement depth of the Rymmen gabbro, Transscandinavian Igneous Belt, southern Sweden. Mineral. Mag. 62, 743–757.

Clemens, J.D., 1990. The granulite—Granite connexion., in: Vielzeuf, D., Vidal, P. (Eds.), Granulites and Crustal Differentiation. Springer, Dordrecht, pp. 25–36.

Clemens, J.D., 2003. S-type granitic magmas - petrogenetic issues, models and evidence. Earth-Science Rev. 61, 1–18. https://doi.org/10.1016/S0012-8252(02)00107-1

Clemens, J.D., Stevens, G., 2012. What controls chemical variation in granitic magmas? Lithos 134–135, 317–329. https://doi.org/10.1016/j.lithos.2012.01.001

Clemens, J.D., Stevens, G., Bryan, S.E., 2020. Conditions during the formation of granitic magmas by crustal melting – Hot or cold; drenched, damp or dry? Earth-Science Rev. 200. https://doi.org/10.1016/j.earscirev.2019.102982

Clemens, J.D., Stevens, G., Farina, F., 2011. The enigmatic sources of I-type granites: The peritectic connexion. Lithos 126, 174–181. https://doi.org/10.1016/j.lithos.2011.07.004

Clemens, J.D., Vielzeuf, D., 1987. Constraints on melting and magma production in the crust. Earth Planet. Sci. Lett. 86, 287–306.

Clemens, J.D., Watkins, J.M., 2001. The fluid regime of high-temperature metamorphism during granitoid magma genesis. Contrib. to Mineral. Petrol. 140, 600–606. https://doi.org/10.1007/s004100000205

Collins, L.G., 2013. Origin of myrmekite as it relates to K- , Na- , and Ca-metasomatism and the metasomatic origin of some granite masses where myrmekite occurs . 1–137.

Condie, K.C., 2013. Plate tectonics & crustal evolution. Elsevier.

Condie, K.C., Kröner, A., 2013. The building blocks of continental crust: Evidence for a major change in the tectonic setting of continental growth at the end of the Archean. Gondwana Res. 23, 394–402. https://doi.org/10.1016/j.gr.2011.09.011

Connolly, J.A.D., 2005. Computation of phase equilibria by linear programming: A tool for geodynamic modeling and its application to subduction zone decarbonation. Earth Planet. Sci. Lett. 236, 524–541. https://doi.org/10.1016/j.epsl.2005.04.033

Connolly, J.A.D., 2009. The geodynamic equation of state: What and how. Geochemistry, Geophys. Geosystems 10. https://doi.org/10.1029/2009GC002540

Connolly, J.A.D., 2009. The geodynamic equation of state: What and how. Geochemistry, Geophys. Geosystems 10. https://doi.org/10.1029/2009GC002540

Corfu, F., Hanchar, J.M., Hoskin, P.W.O., Kinny, P., 2003. Atlas of Zircon Textures. Rev. Mineral. Geochemistry 53, 469–500. https://doi.org/10.2113/0530469

Dale, J., Powell, R., White, R.W., Elmer, F.L., Holland, T.J.B., 2005. A thermodynamic model for Ca-Na clinoamphiboles in Na2O–CaO–FeO–MgO–Al2O3– SiO2–H2O–O for petrological calculations. J. Metamorph. Geol. 23, 771–791.

Das, K., Bose, S., Karmakar, S., 2011. Multiple tectonometamorphic imprints in the lower crust : first evidence of ca . 950 Ma (zircon U-Pb SHRIMP) compressional reworking of UHT aluminous granulites from the Eastern Ghats Belt , India. Geol. J. 239, 217–239. https://doi.org/10.1002/gj.1246

Dasgupta, S., Bose, S., Bhowmik, S.K., Sengupta, P., 2017. The Eastern Ghats Belt, India , in the context of supercontinent assembly. Crustal Evol. India Antarct. Supercontinent Connect. Geol. Soc. London, Spec. Publ. 457. https://doi.org/doi.org/10.1144/SP457.5

Dasgupta, S., Chakraborty, S., Neogi, S., 2009. PETROLOGY OF AN INVERTED BARROVIAN SEQUENCE OF METAPELITES IN SIKKIM HIMALAYA , INDIA : CONSTRAINTS ON THE TECTONICS OF INVERSION. Am. J. Sci. 309, 43–84. https://doi.org/10.2475/01.2009.02

Dasgupta, S., Sanyal, S., Sengupta, P., Fukuoka, M., 1994. Petrology of granulites from anakapalle-evidence for proterozoic decompression in the Eastern Ghats, India. J. Petrol. 35, 433–459. https://doi.org/10.1093/petrology/35.2.433

Dasgupta, S., Sengupta, P., 2003. Indo-Antarctic Correlation: a perspective from the Eastern Ghats Granulite Belt, India. Geol. Soc. London, Spec. Publ. 206, 131–143. https://doi.org/10.1144/GSL.SP.2003.206.01.08

Deering, C.D., Bachmann, O., 2010. Trace element indicators of crystal accumulation in silicic igneous rocks. Earth Planet. Sci. Lett. 297, 324–331. https://doi.org/10.1016/j.epsl.2010.06.034

Dempster, T.J., Hollinsworth, A.D., McIntosh, E., Edgar, S., Faithfull, J.W., Koehn, D., 2021. Deformation-induced and reaction-enhanced permeability in Metabasic Gneisses, Iona, Scotland: controls and scales of retrograde fluid movement. Geofluids 2021, 1–18.

Deshmukh, T., Prabhakar, N., 2020. Linking collision, slab break-off and subduction polarity reversal in the evolution of the Central Indian Tectonic Zone. Geol. Mag. 157, 340–350. https://doi.org/10.1017/S0016756819001419

Deshmukh, T., Prabhakar, N., Bhattacharya, A., Madhavan, K., 2017. Late Paleoproterozoic clockwise P – T history in the Mahakoshal Belt, Central Indian Tectonic Zone: Implications for Columbia supercontinent assembly. Precambrian Res. 298, 56–78. https://doi.org/10.1016/j.precamres.2017.05.020

Dey, A., Karmakar, S., Ibanez-Mejia, M., Mukherjee, S., Sanyal, S., Sengupta, P., 2019. Petrology and geochronology of a suite of pelitic granulites from parts of the Chotanagpur Granite Gneiss Complex, eastern India: Evidence for Stenian-Tonian reworking of a late Paleoproterozoic crust. Geol. Journal. 1–30.

Dey, A., Karmakar, S., Ibanez-Mejia, M., Mukherjee, S., Sanyal, S., Sengupta, P., 2019a. Petrology and geochronology of a suite of pelitic granulites from parts of the Chotanagpur Granite Gneiss Complex, eastern India: Evidence for Stenian-Tonian reworking of a late Paleoproterozoic crust. Geol. Journal. 1–30.

Dey, A., Karmakar, S., Mukherjee, S., Sanyal, S., Dutta, U., Sengupta, P., 2019b. High Pressure metamorphism of mafic granulites from the Chotanagpur Granite Gneissic Complex, India: Evidence for collisional tectonics during assembly of Rodinia. J. Geodyn. in press. https://doi.org/10.1016/j.jog.2019.03.005

Dharma Rao, C. V., Santosh, M., Purohit, R., Wang, J., Jiang, X., Kusky, T., 2011. LA-ICP-MS U-Pb zircon age constraints on the Paleoproterozoic and Neoarchean history of the Sandmata Complex in Rajasthan within the NW Indian Plate. J. Asian Earth Sci. 42, 286–305. https://doi.org/10.1016/j.jseaes.2011.01.018

Diener, J.F.A., Powell, R., 2012. Revised activity-composition models for clinopyroxene and amphibole. J. Metamorph. Geol. 30, 131-142.

Dill, H.G., Melcher, F., 2009. Nigrine-a heavy mineral aggregate indicative of pegmatites and their siliceous root zones. Zeitschrift der Dtsch. Gesellschaft fur Geowissenschaften 160, 191.

Dill, H.G., Melcher, F., Fuessl, M., Weber, B., 2007. The origin of rutile-ilmenite aggregates ("nigrine") in alluvial-fluvial placers of the Hagendorf pegmatite province, NE Bavaria, Germany. Mineral. Petrol. 89, 133–158.

Dora, M.L., Meshram, T., Rao Baswani, S., Malviya, V.P., Upadhyay, D., Shareef, M., Atif Raza, M., Ranjan, S., Meshram, R., Kumar Patnaik, M., Randive, K., 2023. Geological evolution of the Proterozoic Betul belt (~2.16–0.95 Ga) of the Central Indian tectonic Zone: Its linkage to the assembly and dispersal of Columbia and Rodinia supercontinents. Gondwana Res. 116, 168–197. https://doi.org/10.1016/j.gr.2022.11.017

Eckert, J.O., Newton, R.C., Kleppa, O.J., 1991. The deltaH of reactions and recalibration of garnet-pyroxene-plagioclase- quartz geobarometers in the CMAS system by solution calorimetry. Am. Mineral. 76, 148–160.

Eskola, P.E., 1948. The problem of mantled gneiss domes. Q. J. Geol. Soc. 104, 461–476.

Etzel, T.M., Catlos, E.J., 2021. Garnet Chemical Zoning Based Thermobarometry: Method Evaluation and Applications in the Menderes Massif, Western Turkey. Geosciences 11, 505.

Etzel, T.M., Catlos, E.J., 2021. Garnet Chemical Zoning Based Thermobarometry: Method Evaluation and Applications in the Menderes Massif, Western Turkey. Geosciences 11, 505.

Evans, T.P., 2004. A method for calculating effective bulk composition modification due to crystal fractionation in garnet-bearing schist: Implications for isopleth thermobarometry. J. Metamorph. Geol. 22, 547–557. https://doi.org/10.1111/j.1525-1314.2004.00532.x

Farina, F., Mayne, M.J., Stevens, G., Soorajlal, R., Frei, D., Gerdes, A., 2020. Phase equilibria constraints on crystallization differentiation: Insights into the petrogenesis of the normally zoned Buddusò pluton in north-central Sardinia. Geol. Soc. Spec. Publ. 491, 243–265. https://doi.org/10.1144/SP491-2019-37

Ferry, J.M. t, Spear, F.S., 1978. Experimental calibration of the partitioning of Fe and Mg between biotite and garnet. Contrib. to Mineral. Petrol. 66, 113–117.

Ferry, J.M., 1994. A historical review of metamorphic fluid flow. J. Geophys. Res. Solid Earth 99, 15487–15498.

Ferry, J.M., Dipple, G.M., 1991. Fluid flow, mineral reactions, and metasomatism. Geology 19, 211–214.

Fisher, G.W., 1989. Matrix analysis of metamorphic mineral assemblages and reactions. Contrib. to Mineral. Petrol. 102, 69–77.

Fitzsimons, I.C.W., 2000. Grenville-age basement provinces in East Antarctica: Evidence for three separate collisional orogens. Geology 28, 879–882. https://doi.org/10.1130/0091-7613(2000)28<879:GBPIEA>2.0.CO;2

Fitzsimons, I.C.W., Harley, S.L., 1994. The influence of retrograde cation exchange on granulite P-T estimates and a convergence technique for the recovery of peak metamorphic conditions. J. Petrol. 35, 543–576. https://doi.org/10.1093/petrology/35.2.543

Fouqué, F., Lévy, A.M., 1879. Minéralogie micrographique roches éruptives françaises. A. Quantin.

Frost, B.R., Barnes, C.G., Collins, W.J., Arculus, R.J., Ellis, D.J., Frost, C.D., 2001. A geochemical classification for granitic rocks. J. Petrol. 42, 2033–2048. https://doi.org/10.1093/petrology/42.11.2033

Frost, B.R., Barnes, C.G., Collins, W.J., Arculus, R.J., Ellis, D.J., Frost, C.D., 2001. A geochemical classification for granitic rocks. J. Petrol. 42, 2033–2048. https://doi.org/10.1093/petrology/42.11.2033

Frost, B.R., Barnes, C.G., Collins, W.J., Arculus, R.J., Ellis, D.J., Frost, C.D., 2001. A geochemical classification for granitic rocks. J. Petrol. 42, 2033–2048. https://doi.org/10.1093/petrology/42.11.2033

Frost, B.R., Chacko, T., 1989. The Granulite Uncertainty Principle: Limitations on Thermobarometry in Granulites. J. Geol. 97, 435–450.

Frost, C.D., Frost, B.R., 2013. Proterozoic ferroan feldspathic magmatism. Precambrian Res. 228, 151–163. https://doi.org/10.1016/j.precamres.2013.01.016

Gallien, F., Mogessie, A., Hauzenberger, C.A., Bjerg, E., Delpino, S., Castro de Machuca, B., 2012. On the origin of multi-layer coronas between olivine and plagioclase at the gabbro–granulite transition, Valle Fértil–La Huerta Ranges, San Juan Province, Argentina. J. Metamorph. Geol. 30, 281–302.

Ganguly, J., 1979. Garnet and clinopyroxene solid solutions, and geothermometry based on Fe-Mg distribution coefficient. Geochim. Cosmochim. Acta 43, 1021–1029. https://doi.org/10.1016/0016-7037(79)90091-7

Ganguly, J., Saxena, S.K., 2012. Mixtures and mineral reactions. Springer Science & Business Media.

Gao, P., Zheng, Y.F., Yakymchuk, C., Zhao, Z.F., Meng, Z.Y., 2021. The Effects of Source Mixing and Fractional Crystallization on the Composition of Eocene Granites in the Himalayan Orogen. J. Petrol. 62, 1–23. https://doi.org/10.1093/petrology/egab037

Gapais, D., Cagnard, F., Gueydan, F., Barbey, P., Ballevre, M., 2009. Mountain building and exhumation processes through time: inferences from nature and models. Terra Nov. 21, 188–194.

Garcia-Arias, M., Stevens, G., 2017. Phase equilibrium modelling of granite magma petrogenesis: A. An evaluation of the magma compositions produced by crystal entrainment in the source. Lithos 277, 131–153. https://doi.org/10.1016/j.lithos.2016.09.028

Garcia-Arias, M., Stevens, G., 2017a. Phase equilibrium modelling of granite magma petrogenesis: B. An evaluation of the magma compositions that result from fractional crystallization. Lithos 277, 109–130.

Garcia-Arias, M., Stevens, G., 2017b. Phase equilibrium modelling of granite magma petrogenesis: A. An evaluation of the magma compositions produced by crystal entrainment in the source. Lithos 277, 131–153. https://doi.org/10.1016/j.lithos.2016.09.028

Gehrels, G.E., Valencia, V.A., Ruiz, J., 2008. Enhanced precision, accuracy, efficiency, and spatial resolution of U-Pb ages by laser ablation-multicollector-inductively coupled plasma-mass spectrometry. Geochemistry, Geophys. Geosystems 9, 1–13. https://doi.org/10.1029/2007GC001805

Ghosh, S., Tomson, J.K., Prabhakar, N., Sheth, H., 2023. An extended Neoarchaean to Neoproterozoic history of the Sandmata Complex (Aravalli Craton, northwestern India): Insights from metamorphic evolution and zircon-monazite geochronology of high-grade quartzofeldspathic gneisses. Precambrian Res. 394, 107107.

Gianni, G.M., Luján, S.P., 2021. Geodynamic controls on magmatic arc migration and quiescence. Earth-Science Rev. 218. https://doi.org/10.1016/j.earscirev.2021.103676

Gogoi, B., Hazarika, G., Chauhan, H., 2021. Origin of porphyritic texture by magma mixing in the andesitic rocks of Ghansura Rhyolite Dome from the Bathani volcano-sedimentary sequence, Eastern India. Geochem. J. 55, 11–25.

Goode, A.D.T., 1974. Oxidation of natural olivines. Nature 248, 500–501.

Goodge, J.W., Vervoort, J.D., Fanning, C.M., Brecke, D.M., Farmer, G.L., Williams, I.S., Myrow, P.M., Depaolo, D.J., 2008. A Positive Test of East Antarctica–Laurentia Juxtaposition Within the Rodinia Supercontinent. Science (80-.). 321, 235–240.

Goswami, B., Bhattacharyya, C., 2010. Tectonothermal Evolution of Chhotanagpur Granite Gneiss Complex From Northeastern Part of Puruliya District, West Bengal, Eastern India. Indian J. Geol. 80, 41–54.

Goswami, S., Bhowmik, S.K., Dasgupta, S., 2009. Petrology of a non-classical Barrovian inverted metamorphic sequence from the western Arunachal Himalaya, India. J. Asian Earth Sci. 36, 390–406. https://doi.org/10.1016/j.jseaes.2009.07.006

Goswami-Banerjee, S., Bhowmik, S.K., Dasgupta, S., Pant, N.C., 2014. Burial of thermally perturbed Lesser Himalayan mid-crust: Evidence from petrochemistry and P-T estimation of the western Arunachal Himalaya, India. Lithos 208, 298–311. https://doi.org/10.1016/j.lithos.2014.09.015

Graham, C.M., Powell, R., 1984. A garnet–amphibole geothermometer: calibration, testing, and application to the Pelona Schist, Southern California. J. Metamorph. Geol. 2, 13–31.

Green, D.H., Ringwood, a E., 1967. An experimental investigation of the gabbro to eclogite transformation and its petrological applications. Geochim. Cosmochim. 31, 767–833. https://doi.org/10.1016/S0016-7037(67)80031-0

Green, E.C.R., White, R.W., Diener, J.F.A., Powell, R., Holland, T.J.B., Palin, R.M., 2016. Activity–composition relations for the calculation of partial melting equilibria in metabasic rocks. J. Metamorph. Geol. 34, 845–869. https://doi.org/10.1111/jmg.12211

Guo, Z., Zou, H., 2023. Temperature and Hf-O isotope correlations of young erupted zircons from Tengchong (SE Tibet): Assimilation fractional crystallization during monotonic cooling. Geosci. Front. 14, 101497. https://doi.org/10.1016/j.gsf.2022.101497

Harley, S.L., 1989. The origins of granulites: a metamorphic perspective. Geol. Mag. 126, 215–247. https://doi.org/10.1017/S0016756800022330

Harley, S.L., 2016. A matter of time: The importance of the duration of UHT metamorphism. J. Mineral. Petrol. Sci. 111, 50–72. https://doi.org/10.2465/jmps.160128

Harley, S.L., Carrington, D.P., 2001. The distribution of H2O between cordierite and granitic melt: H2O incorporation in cordierite and its application to high-grade metamorphism and crustal anatexis. J. Petrol. 42, 1595–1620.

Harley, S.L., Kelly, N.M., Möller, A., 2007. Zircon Behaviour and the Thermal Histories of Mountain Chains. Elements 3, 25–30.

Harlov, D.E., Wirth, R., 2000. K-feldspar–quartz and K-feldspar–plagioclase phase boundary interactions in garnet–orthopyroxene gneiss's from the Val Strona di Omegna, Ivrea–Verbano Zone, northern Italy. Contrib. to Mineral. Petrol. 140, 148–162.

Harlov, D.E., Wirth, R., Hetherington, C.J., 2011. Fluid-mediated partial alteration in monazite : the role of coupled dissolution – reprecipitation in element redistribution and mass transfer. Contrib. to Mineral. Petrol. 162, 329–348. https://doi.org/10.1007/s00410-010-0599-7

Harris, L.B., 1993. Correlations between the Central Indian Tectonic Zone and the Albany Mobile Belt of Western Australia: evidence for a continuous Proterozoic orogenic belt, in: Gondwana 8: Assembly, Evolution and Dispersal. CRC Press/Balkema, pp. 165–180.

Hayden, L.A., Manning, C.E., 2011. Rutile solubility in supercritical NaAlSi3O8-H2O fluids. Chem. Geol. 284, 74–81. https://doi.org/10.1016/j.chemgeo.2011.02.008

He, D., Dong, Y., Liu, X., Yang, Z., Sun, S., Cheng, B., Li, W., 2016. Tectono-thermal events in East Kunlun, Northern Tibetan Plateau: evidence from zircon U–Pb geochronology. Gondwana Res. 30, 179–190.

Hinchey, A.M., 2021. Lithogeochemical and Nd isotopic constraints on felsic magmatism in the Makkovik Orogen, Labrador, Canada: Implications for assembly of the supercontinent Nuna. Lithos 382–383, 105917. https://doi.org/10.1016/j.lithos.2020.105917

Hoisch, T.D., 1990. Empirical calibration of six geobarometers for the mineral assemblage quartz+ muscovite+ biotite+ plagioclase+ garnet. Contrib. to Mineral. Petrol. 104, 225–234.

Holland, T., Blundy, J., 1994. Non-ideal interactions in calcic amphiboles and their bearing on amphibole-plagioclase thermometry. Contrib. to Mineral. Petrol. 116, 433–447.

Holland, T.J.B., Green, E.C.R., Powell, R., 2018. Melting of peridotites through to granites: a simple thermodynamic model in the system KNCFMASHTOCr. J. Petrol. 59, 881–900.

Holland, T.J.B., Powell, R., 1998. An internally consistent thermodynamic data set for phases of petrological interest. J. Metamorph. Geol. 16, 309–343. https://doi.org/10.1111/j.1525-1314.1998.00140.x

Holland, T.J.B., Powell, R., 2003. Activity-composition relations for phases in petrological calculations: an asymmetric multicomponent formulation. Contrib. to Mineral. Petrol. 145, 492-501.

Holland, T.J.B., Powell, R., 2011. An improved and extended internally consistent thermodynamic dataset for phases of petrological interest, involving a new equation of state for solids. J. Metamorph. Geol. 29, 333–383. https://doi.org/10.1111/j.1525-1314.2010.00923.x

Hollaway, M.J., Mukhopadhyay, B., 1993. Geothermobarometry in pelitic schists: a rapidly evolving field. Am. Mineral. 78, 681–693.

Hou, G., Santosh, M., Qian, X., Lister, G.S., Li, J., 2008. Configuration of the Late Paleoproterozoic supercontinent Columbia: Insights from radiating mafic dyke swarms. Gondwana Res. 14, 395–409. https://doi.org/10.1016/j.gr.2008.01.010

Indares, A., Martignole, J., 1985. Biotite–garnet geothermometry in the granulite facies: the influence of Ti and Al in biotite. Am. Mineral. 70, 272–278.

Jagoutz, O.E., 2010. Construction of the granitoid crust of an island arc. Part II: A quantitative petrogenetic model. Contrib. to Mineral. Petrol. 160, 359–381. https://doi.org/10.1007/s00410-009-0482-6

Jain, S.C., Yedekar, D.B., Nair, K.K.K., 1991. Central Indian Shear Zone- A Major Precam,brian Crustal Boundary. J. Geol. Soc. India 37, 521–531.

Joesten, R., 1986. The role of magmatic reaction, diffusion and annealing in the evolution of coronitic microstructure in troctolitic gabbro from Risör, Norway. Mineral. Mag. 50, 441–467.

Karmakar, S., 2021. Formation of clinohumite ± spinel in dolomitic marbles from the Makrohar Granulite Belt, Central India: Evidence for Ti mobility during regional metamorphism. Am. Mineral. 106, 1818–1827. https://doi.org/10.2138/am-2021-7755

Karmakar, S., Bose, S., Sarbadhikari, A.B., Das, K., 2011. Evolution of granulite enclaves and associated gneisses from Purulia, Chhotanagpur Granite Gneiss Complex, India: Evidence for 990-940Ma tectonothermal event(s) at the eastern India cratonic fringe zone. J. Asian Earth Sci. 41, 69–88. https://doi.org/10.1016/j.jseaes.2010.12.006

Karmakar, S., Mukherjee, S., Sanyal, S., Sengupta, P., 2017. Origin of peraluminous minerals (corundum , spinel , and sapphirine) in a highly calcic anorthosite from the. Contrib. to Mineral. Petrol. 172:67. https://doi.org/10.1007/s00410-017-1383-8

Katz, M.B., Premoli, C., 1979. India and Madagascar in Gondwanaland based on matching Precambrian lineaments. Nature 279, 312–315.

Kaur, P., Zeh, A., Chaudhri, N., Eliyas, N., 2017. Two distinct sources of 1.73–1.70Ga A-type granites from the northern Aravalli orogen, NW India: Constraints from in situ zircon U-Pb ages and Lu-Hf isotopes. Gondwana Res. 49, 164–181. https://doi.org/10.1016/j.gr.2017.05.012

Keller, C.B., Schoene, B., Barboni, M., Samperton, K.M., Husson, J.M., 2015. Volcanic-plutonic parity and the differentiation of the continental crust. Nature 523, 301–307. https://doi.org/10.1038/nature14584

Kelsey, D.E., Hand, M., 2015. On ultrahigh temperature crustal metamorphism: Phase equilibria, trace element thermometry, bulk composition, heat sources, timescales and tectonic settings. Geosci. Front. 6, 311–356. https://doi.org/10.1016/j.gsf.2014.09.006

Khanna, T.C., Rao, D.V.S., Sai, V.V.S., Satyanarayanan, M., 2020. ca. 2.1 Ga Mahakoshal Supracrustal Belt: An allochthonous terrain in Central India Tectonic Zone. Lithos 374, 105705.

Kirkland, C.L., Smithies, R.H., Taylor, R.J.M., Evans, N., McDonald, B., 2015. Zircon Th/U ratios in magmatic environs. Lithos 212–215, 397–414. https://doi.org/10.1016/j.lithos.2014.11.021

Kohn, M.J., Spear, F., 2000. Retrograde net transfer reaction insurance for pressure-temperature estimates. Geology 28, 1127–1130.

Kohn, M.J., Spear, F.S., 1990. Two new barometers for garnet amphibolites with applications to eastern Vermont. Am. Mineral. 75, 89–96. https://doi.org/scopus/2-s2.0-0025205495

Kolker, A., 1982. Mineralogy and geochemistry of Fe-Ti oxide and apatite (nelsonite) deposits and evaluation of the liquid immiscibility hypothesis. Econ. Geol. 77, 1146–1158.

Kumar, R.R., Dwivedi, S.B., 2019. EPMA monazite geochronology of the granulites from Daltonganj, eastern India and its correlation with the Rodinia supercontinent. J. Earth Syst. Sci. 128. https://doi.org/10.1007/s12040-019-1254-y

Kumar, R.R., Dwivedi, S.B., 2021. Exsolution intergrowth of cpx-opx and pseudosection modelling of two-pyroxene mafic granulite from Daltonganj of Chhotanagpur Granite Gneiss Complex, Eastern India. Arab. J. Geosci. 14. https://doi.org/10.1007/s12517-021-07093-4

Kumar, R.R., Kawaguchi, K., Dwivedi, S.B., Das, K., 2022. Metamorphic evolution of the pelitic and mafic granulites from Daltonganj, Chhotanagpur Granite Gneiss Complex, India: Constraints from zircon U–Pb age and phase equilibria modelling. Geol. J. 57, 1284–1310. https://doi.org/https://doi.org/10.1002/gj.4340

Lake, E.T., 2013. Crystallization and saturation front propagation in silicic magma chambers. Earth Planet. Sci. Lett. 383, 182–193. https://doi.org/10.1016/j.epsl.2013.09.039

Lang, H.M., Watcher, A.J., Peterson, V.L., Ryan, J.G., 2004. Coexisting clinopyroxene/spinel and amphibole/spinel symplectites in metatroctolite from the Buck Creek ultramafic body, North Carolina Blue Ridge. Am. Mineral. 89, 20–30.

Lang, H.M., Watcher, A.J., Peterson, V.L., Ryan, J.G., 2004. Coexisting clinopyroxene/spinel and amphibole/spinel symplectites in metatroctolite from the Buck Creek ultramafic body, North Carolina Blue Ridge. Am. Mineral. 89, 20–30.

Lazaro, D.G.C., Baumgartner, J.A.M.L.P., 2019. Role of myrmekite and associated deformation fabrics in controlling development of granitic mylonites in the Pofadder Shear Zone of southern Namibia. Contrib. to Mineral. Petrol. 174:22. https://doi.org/10.1007/s00410-019-1555-9

Le Maitre, R.W., Streckeisen, A., Zanettin, B., Le Bas, M.J., Bonin, B., Bateman, P., Bellieni, G., Dudek, A., Efremova, S., Keller, J., Lameyre, J., Sabine, P.A., Schmid, R., Sørensen, H., Woolley, A.R., 2002. Igneous Rocks. A Classification and Glossary of Terms. Recommendations of the International Union of Geological Sciences Subcommission on the Systematics of Igneous Rocks, 2nd Edition., 2nd Editio. ed. Cambridge University Press.

Leake, B.E.E., Hairman, C., Ecretary, A.L.A.N.R.W.O.S., Irch, W.I.D.B., Urke, E.R.A.J.B., Erraris, G.I.F., Rice, J.O.E.L.D.G., Awthorne, F.R.C.H., Isch, H.A.J.K., Rivovichev, V.L.G.K., Chumacher, J.O.H.N.C.S., Tephenson,

N.I.C.N.S., Hittaker, E.R.I.C.J.W.W., Leake, B.E., Woolley, A.R., Birch, W.D., Burke, E.A.J., Ferraris, G., Grice, J.D., Hawthorne, F.C., Kisch, H.J., Krivovichev, V.G., Schumacher, J.C., Stephenson, N.C.N., Whittaker, E.J.W., Eake, B.E.E.L., Hairman, C., Ecretary, A.L.A.N.R.W.O.S., Irch, W.I.D.B., Urke, E.R.A.J.B., Erraris, G.I.F., Rice, J.O.E.L.D.G., Awthorne, F.R.C.H., Isch, H.A.J.K., Rivovichev, V.L.G.K., Chumacher, J.O.H.N.C.S., Tephenson, N.I.C.N.S., Hittaker, E.R.I.C.J.W.W., Leake, B.E., Woolley, A.R., Birch, W.D., Burke, E.A.J., Ferraris, G., Grice, J.D., Hawthorne, F.C., Kisch, H.J., Krivovichev, V.G., Schumacher, J.C., Stephenson, N.C.N., Whittaker, E.J.W., 2004. Nomenclature of amphiboles : Additions and revisions to the International Mineralogical Association's amphibole nomenclature. Am. Mineral. 89, 883–887.

Lee, H.Y., Ganguly, J., 1988. Equilibrium Compositions of Coexisting Garnet and Orthopyroxene: Experimental Determinations in the System FeO-MgO-Al2O3-SiO2, and Applications. J. Petrol. 29, 93–113.

Li, Z.X., Bogdanova, S. V., Collins, A.S., Davidson, A., De Waele, B., Ernst, R.E., Fitzsimons, I.C.W., Fuck, R.A., Gladkochub, D.P., Jacobs, J., Karlstrom, K.E., Lu, S., Natapov, L.M., Pease, V., Pisarevsky, S.A., Thrane, K., Vernikovsky, V., 2008. Assembly, configuration, and break-up history of Rodinia: A synthesis. Precambrian Res. 160, 179–210. https://doi.org/10.1016/j.precamres.2007.04.021

Mahadevan, T.M., 2002. Geology of Bihar & Jharkhand. Geological Society of India, Bangalore.

Mahakud, S.P., Raut, P.K., Hansda, C., Ramteke, P., Chakraborty, U., Sisodiya, D., 2001. Sulphide mineralisation in the central part of Betul Belt around Ghisl-Muanya-Koparpan~ area, Betul dlstrlct, Madhya Pradesh Geol Sum India. Geol. Surv. India Spec. Publ. 64, 377–385.

Maji, A.K., Goon, S., Bhattacharya, A., Mishra, B., Mahato, S., Bernhardt, H.J., 2008. Proterozoic polyphase metamorphism in the Chhotanagpur Gneissic Complex (India), and implication for trans-continental Gondwanaland correlation. Precambrian Res. 162, 385–402. https://doi.org/10.1016/j.precamres.2007.10.002

Manning, C.E., Wilke, M., Schmidt, C., Cauzid, J., 2008. Rutile solubility in albite-H2O and Na2Si3O7-H2O at high temperatures and pressures by in-situ synchrotron radiation micro-XRF. Earth Planet. Sci. Lett. 272, 730–737. https://doi.org/10.1016/j.epsl.2008.06.004

Martignole, J., Sisi, J.-C., 1981. Cordierite-garnet-H2O equilibrium: a geological thermometer, barometer and water fugacity indicator. Contrib. to Mineral. Petrol. 77, 38–46.

Mayne, M.J., Moyen, J.F., Stevens, G., Kaislaniemi, L., 2016. Rcrust: a tool for calculating path-dependent open system processes and application to melt loss. J. Metamorph. Geol. 34, 663–682. https://doi.org/10.1111/jmg.12199

Mayne, M.J., Stevens, G., Moyen, J.-F., 2020. A phase equilibrium investigation of selected source controls on the composition of melt batches generated by sequential melting of an average metapelite. Geol. Soc. London, Spec. Publ. 491, 223–241. https://doi.org/10.1144/sp491-2018-121

Mayne, M.J., Stevens, G., Moyen, J.-F., Johnson, T., 2020. Performing process-oriented investigations involving mass transfer using Rcrust: a new phase equilibrium modelling tool. Geol. Soc. London, Spec. Publ. 491, 209–221. https://doi.org/10.1144/sp491-2018-85

McDonough, W.F., Sun, S.S., 1995. The composition of the Earth. Chem. Geol. 120, 223–253.

Meert, J.G., Santosh, M., 2017. The Columbia supercontinent revisited. Gondwana Res. 50, 67–83. https://doi.org/10.1016/j.gr.2017.04.011

Menegon, L., Pennacchioni, G., Stünitz, H., 2006. Nucleation and growth of myrmekite during ductile shear deformation in metagranites. J. Metamorph. Geol. 24, 553–568.

Menegon, L., Pennacchioni, G., Stünitz, H., 2006. Nucleation and growth of myrmekite during ductile shear deformation in metagranites. J. Metamorph. Geol. 24, 553–568.

Middlemost, E.A.K., 1994. Naming materials in the magma/igneous rock system. Earth-Science Rev. 37, 215–224.

Miller, C.F., McDowell, S.M., Mapes, R.W., 2003. Hot and cold granites: Implications of zircon saturation temperatures and preservation of inheritance. Geology 31, 529–532. https://doi.org/10.1130/0091-7613(2003)031<0529:HACGIO>2.0.CO;2

Mohan, A., Tripathi, P., Motoyoshi, Y., 1997. Reaction history of sapphirine granulites and a decompressional P-T path in a granulite complex from the Eastern Ghats., in: Earth and Planetary Sciences. pp. 115-129.

Mohanty, S.P., 2015. Palaeoproterozoic supracrustals of the Bastar Craton: Dongargarh Supergroup and Sausar Group. Geol. Soc. Mem. 43, 151–164. https://doi.org/10.1144/M43.11

Mondal, S., Upadhyay, D., Banerjee, A., 2017. The origin of rapakivi feldspar by a fluid-induced coupled dissolution- reprecipitation process. J. Petrol. 58, 1393–1418. https://doi.org/10.1093/petrology/egx058

Mongkoltip, P., Ashworth, J.R., 1986. Amphibolitization of metagabbros in the Scottish Highlands. J. Metamorph. Geol. 4, 261–283.

Morey, G.W., 1957. The solubility of solids in gases. Econ. Geol. 52, 225–251.

Moyen, J.F., Laurent, O., Chelle-Michou, C., Couzinié, S., Vanderhaeghe, O., Zeh, A., Villaros, A., Gardien, V., 2017. Collision vs. subduction-related magmatism: Two contrasting ways of granite formation and implications for crustal growth. Lithos 277, 154–177. https://doi.org/10.1016/j.lithos.2016.09.018

Mukherjee, S., Dey, A., Ibanez-Mejia, M., Sanyal, S., Sengupta, P., 2018. Geochemistry, U-Pb geochronology and Lu-Hf isotope systematics of a suite of ferroan (A-type) granitoids from the CGGC: Evidence for Mesoproterozoic crustal extension in the east Indian shield. Precambrian Res. 305, 40–63. https://doi.org/https://doi.org/10.1016/j.precamres.2017.11.018

Mukherjee, S., Dey, A., Roy, S., Mayne, M.J., 2022. Effect of source heterogeneity , melt extraction and crystal separation on the composition of a suite of ferroan (A-type) granites from parts of the Chotanagpur Granite Gneissic Complex (CGGC), India. LITHOS 430–431, 106875. https://doi.org/10.1016/j.lithos.2022.106875

Mukherjee, S., Dey, A., Sanyal, S., Ibanez-Mejia, M., Dutta, U., Sengupta, P., 2017. Petrology and U–Pb geochronology of zircon in a suite of charnockitic gneisses from parts of the Chotanagpur Granite Gneiss Complex (CGGC): evidence for the reworking of a Mesoproterozoic basement during the formation of the Rodinia supercontinent. Crustal Evol. India Antarct. Supercontinent Connect. Geol. Soc. London, Spec. Publ. 457, 197–232. https://doi.org/org/10.1144/SP457.6

Mukherjee, S., Dey, A., Sanyal, S., Ibanez-Mejia, M., Sengupta, P., 2019a. Bulk rock and zircon geochemistry of granitoids from the Chotanagpur Granite Gneissic Complex (CGGC): implications for the late Paleoproterozoic continental arc magmatism in the East Indian Shield. Contrib. to Mineral. Petrol. 1–17. https://doi.org/10.1007/s00410-019-1601-7

Mukherjee, S., Dey, A., Sanyal, S., Ibanez-Mejia, M., Sengupta, P., 2019. Bulk rock and zircon geochemistry of granitoids from the Chotanagpur Granite Gneissic Complex (CGGC): implications for the late Paleoproterozoic continental arc magmatism in the East Indian Shield. Contrib. to Mineral. Petrol. 1–17. https://doi.org/10.1007/s00410-019-1601-7

Mukherjee, S., Dey, A., Sanyal, S., Sengupta, P., 2018. Tectonothermal imprints sin a suite of mafic dykes from the Chotanagpur Granite Gneissic complex (CGGC), Jharkhand, India: Evidence for late Tonian reworking of an early Tonian continental crust. Lithos. https://doi.org/10.1016/j.lithos.2018.09.01

Mukherjee, S., Dey, A., Sanyal, S., Sengupta, P., 2019b. Proterozoic Crustal Evolution of the Chotanagpur Granite Gneissic Complex, Jharkhand-Bihar-West Bengal, India: Current Status and Future Prospect, in: Mukherjee, Soumyajit (Ed.), Tectonics and Structural Geology : Indian Context. Springer Nature Switzerland, pp. 7–54.

Mukherjee, Subham, Dey, A., Sanyal, S., Sengupta, P., 2019. Proterozoic Crustal Evolution of the Chotanagpur Granite Gneissic Complex, Jharkhand-Bihar-West Bengal, India: Current Status and Future Prospect, in: Mukherjee, Soumyajit (Ed.), Tectonics and Structural Geology : Indian Context. Springer Nature Switzerland, pp. 7–54.

Nance, R.D., Murphy, J.B., 2013. Origins of the supercontinent cycle. Geosci. Front. 4, 439–448. https://doi.org/10.1016/j.gsf.2012.12.007

Nandedkar, R.H., Ulmer, P., Müntener, O., 2014. Fractional crystallization of primitive, hydrous arc magmas: An experimental study at 0.7 GPa. Contrib. to Mineral. Petrol. 167, 1–27. https://doi.org/10.1007/s00410-014-1015-5

Nandedkar, R.H., Ulmer, P., Müntener, O., 2014. Fractional crystallization of primitive, hydrous arc magmas: An experimental study at 0.7 GPa. Contrib. to Mineral. Petrol. 167, 1–27. https://doi.org/10.1007/s00410-014-1015-5

Naqvi, S.M., Rogers, J.J.W., 1987. Precambrian geology of India. (No Title).

Nebel, O., Nebel-Jacobsen, Y., Mezger, K., Berndt, J., 2007. Initial Hf isotope compositions in magmatic zircon from early Proterozoic rocks from the Gawler Craton, Australia: A test for zircon model ages. Chem. Geol. 241, 23–37. https://doi.org/10.1016/j.chemgeo.2007.02.008

Newton, R.C., 1972. An experimental determination of the high-pressure stability limits of magnesian cordierite under wet and dry conditions. J. Geol. 80, 398–420.

Newton, R.C., Charlu, T.V., Kleppa, O.J., 1980. Thermochemistry of the high structural state plagioclases. Geochemica Cosmochim. Acta 44, 933–941.

Newton, R.C., Manning, C.E., 2000. Quartz solubility in H2O-NaCl and H2O-CO2 solutions at deep crust-upper mantle pressures and temperatures: 2–15 kbar and 500–900°C. Geochemica Cosmochim. Acta 64, 2993–3005.

Ohta, T., Arai, H., 2007. Statistical empirical index of chemical weathering in igneous rocks: A new tool for evaluating the degree of weathering. Chem. Geol. 240, 280–297.

Oliver, N.H.S., 1996. Review and classification of structural controls on fluid flow during regional metamorphism. J. Metamorph. Geol. 14, 477–492.

Ozha, M.K., Mishra, B., Hazarika, P., Jeyagopal, A. V, Yadav, G.S., 2016. EPMA monazite geochronology of the basement and supracrustal rocks within the Pur-Banera basin, Rajasthan: Evidence of Columbia breakup in Northwestern India. J. Asian Earth Sci. 117, 284–303.

Pal, T., Bhowmik, S., 1998. Metamorphic history of Sausar Group of rocks.

Patiño Douce, A.E., Beard, J.S., 1995. Dehydrations-melting of Biotite Gneiss and Quartz Amphibolite from 3 to 15 kbar. J. Petrol. 36, 707–738.

Pearce, J. a, Harris, N.B.W., Tindle, A.G., 1984. Trace element distribution diagrams for the tectonic interpretation of granitic rocks. J. Petrol. 25, 956–983. https://doi.org/10.1093/petrology/25.4.956

Perchuk, L.L., 1991. Studies in magmatism, metamorphism, and geodynamics. Int. Geol. Rev. 33, 311–374.

Perchuk, L.L., Aranovich, L.Y., Podlesskii, K.K., Lavrant'eva, I., Gerasimov, V.Y., Fed'Kin, V. V, Kitsul, V.I., Karsakov, L.P., Berdnikov, N. V, 1985. Precambrian granulites of the Aldan shield, eastern Siberia, USSR. J. Metamorph. Geol. 3, 265–310.

Phillips, E.R., 1980. On polygenetic myrmekite. Geol. Mag. 117, 29–36. https://doi.org/10.1017/S0016756800033070

Philpotts, A.R., 1967. Origin of certain iron-titanium oxide and apatite rocks. Econ. Geol. 62, 303–315.

Philpotts, A.R., Ague, J.J., 2009. Principles of igneous and metamorphic petrology. Cambridge University Press.

Plümper, O., Putnis, A., 2009. The complex hydrothermal history of granitic rocks: multiple feldspar replacement reactions under subsolidus conditions. J. Petrol. 50, 967–987.

Plunder, A., Le Pourhiet, L., Räss, L., Gloaguen, E., Pichavant, M., Gumiaux, C., 2022. Pegmatites as geological expressions of spontaneous crustal flow localisation. Lithos 416, 106652.

Powell, C.M., Pisarevsky, S.A., 2002. Late neoproterozoic assembly of East Gondwana. Geology 30, 3–6. https://doi.org/10.1130/0091-7613(2002)030<0003:LNAOEG>2.0.CO;2

Powell, R., Holland, T.J.B., 2008. On thermobarometry. J. Metamorph. Geol. 26, 155–179.

Praveen, M.N., Nambiar, C.G., Huston, D.L., 2021. Geochemistry and petrogenesis of Paleoproterozoic rhyolite-hosted zinc-rich metamorphosed volcanogenic massive sulfide deposits in the eastern Betul Belt, central India. Ore Geol. Rev. 131, 103918.

Putnis, A., 2002. Mineral replacement reactions: from macroscopic observations to microscopic mechanisms. Mineral. Mag. 66, 689–708.

Putnis, A., Austrheim, H., 2010. Fluid-induced processes: metasomatism and metamorphism. Geofluids 10, 254–269.

Radhakrishna, B.P., Naqvi, S.M., 1986. Precambrian continental crust of India and its evolution. J. Geol. 94, 145–166.

Ramachandra, H.M., Nanda, J.K., Sarkar, A., Chakrabarti, C., Mallick, S.B., Guha, D., Chakraborty, K., 2020. Central Indian tectonic zone. A manual of the Geology of India: Central Part of the Peninsula. Geol. Surv. India Spec. Publ. 77, 121–138.

Raut, P.K., Mahakud, S.P., 2004. Geology, geochemistry and tectonic setting of volcanosedimentary sequence of Betul belt, Madhya Pradesh and genesis of zinc and copper sulphide mineralisation. Geol. Surv. India, Spl. Pub 72, 133–146.

Ray Barman, T.K., Bishui, P.K., 1994. Dating of Chotanagpur gneissic complex of eastern Indian Precambrian shield. Rec. Geol. Surv. India 127, 25–27.

Rekha, S., Upadhyay, D., Bhattacharya, A., Kooijman, E., Goon, S., Mahato, S., Pant, N.C., 2011. Lithostructural and chronological constraints for tectonic restoration of Proterozoic accretion in the Eastern Indian Precambrian shield. Precambrian Res. 187, 313–333. https://doi.org/10.1016/j.precamres.2011.03.015

Remmert, P., Heinrich, W., Wunder, B., Morales, L., Wirth, R., Rhede, D., Abart, R., 2018. Synthesis of monticellite–forsterite and merwinite–forsterite symplectites in the CaO–MgO–SiO 2 model system: influence of temperature and water content on microstructure evolution. Contrib. to Mineral. Petrol. 173, 1–17.

Renner, J., Evans, B., Hirth, G., 2000. On the rheologically critical melt fraction. Earth Planet. Sci. Lett. 181, 585–594.

Rogers, J.J.W., Santosh, M., 2002. Configuration of Columbia, a Mesoproterozoic Supercontinent. Gondwana Res. 5, 5–22. https://doi.org/10.1016/S1342-937X(05)70883-2

Rosenberg, C.L., Handy, M.R., 2005. Experimental deformation of partially melted granite revisited: Implications for the continental crust. J. Metamorph. Geol. 23, 19–28. https://doi.org/10.1111/j.1525-1314.2005.00555.x

Ross, C.P., 1941. The quicksilver deposits of the Terlingua region, Texas. Econ. Geol. 36, 115–142.

Roy Choudhury, S., Dey, A., Mukherjee, S., Sanyal, S., Karmakar, S., Sengupta, P., 2023. On the factors controlling the incorporation of aluminium within titanites: a case study from medium pressure calc-silicate granulites in parts of the East Indian shield. Mineral. Petrol. https://doi.org/10.1007/s00710-023-00826-1

Roy, A., Chore, S.A., Viswakarma, L.L., Chakraborty, K., 2004. Geology and petrochemistry of Padhar mafic-ultramafic complex from Betul Belt: A study on arc type magmatism in Central Indian Tectonic Zone. Geol. Surv. India. Spec. Publ 84, 297–318.

Roy, A., Devarajan, M.K., 2000. A reappraisal of the stratigraphy and tectonics of the Palaeoproterozoic Mahakoshal supracrustal belt, Central India. Geol. Surv. India Spec. Publ 57, 79–97.

Roy, A., Prasad, M.H., 2003. Tectonothermal events in Central Indian Tectonic Zone (CITZ) and its implications in Rodinian crustal assembly. J. Asian Earth Sci. 22, 115–129. https://doi.org/10.1016/S1367-9120(02)00180-3

Roy, Abhijit, Kagami, H., Yoshida, M., Roy, Abhinaba, Bandyopadhyay, B.K., Chattopadhyay, A., Khan, A.S., Huin, A.K., Pal, T., 2006. Rb – Sr and Sm – Nd dating of different metamorphic events from the Sausar Mobile Belt , central India : implications for Proterozoic crustal evolution. J. Asian Earth Sci. 26, 61–76. https://doi.org/10.1016/j.jseaes.2004.09.010

Rudnick, R.L., Gao, S., 2003. Composition of the Continental Crust, in: Holland, H.D., Turekian, K.K. (Eds.), Treatise on Geochemistry. Elsevier, pp. 1–64. https://doi.org/10.1016/B0-08-043751-6/03016-4

Saikia, A., Gogoi, B., Kaulina, T., Lialina, L., Bayanova, T., Ahmad, M., 2017. Geochemical and U – Pb zircon age characterization of granites of the Bathani Volcano Sedimentary sequence , Chotanagpur Granite Gneiss Complex , eastern India : vestiges of the Nuna supercontinent in the Central Indian Tectonic Zone, in: Pant, N.C., Dsgupta, S. (Eds.), Crustal Evolution of India and Antarctica: The Supercontinent Connection. Geological Society, London, Special Publications, 457.

Sanyal, S., Sengupta, P., 2012. Metamorphic evolution of the Chotanagpur Granite Gneiss Complex of the East Indian Shield: current status. Geol. Soc. London, Spec. Publ. 365, 117–145. https://doi.org/10.1144/SP365.7

Sarbadhikari, A.B., Bhowmik, S.K., 2008. Constraining the metamorphic evolution of a cryptic hot Mesoproterozoic orogen in the Central Indian Tectonic Zone, using P–T pseudosection modelling of mafic intrusions and host reworked granulites. Precambrian Res. 162, 128–149.

Sarkar, A., Boda, M.S., Kundu, H.K., Mamgain, V.V., Ravishankar, 1998. Geochronology and geochemistry of Mesoproterozoic intrusive plutonites from the eastern segment of the Mahakoshal greenstone belt, Central India., in: IGCP-368 Seminar on Precambrian Crust.

Sarkar, T., Schenk, V., 2016. Early Mesoproterozoic (1.6–1.5 Ga) granulite facies events in the Ongole domain: geodynamic significance and global correlation. J. Metamorph. Geol. 34, 765–784. https://doi.org/10.1111/jmg.12207

Sawyer, E.W., Brown, M., 2008. Working with migmatites. Mineralogical Assn of Canada.

Schandl, E.S., Gorton, M.P., 2002. Application of high field strength elements to discriminate tectonic settings in VMS environments. Econ. Geol. 97, 629–642.

Schwantke, A., 1909. Die Beimischung von Ca in Kalifeldspat und die myrmekitbildung. Zentblatt fur Mineral. 1, 311.

Searle, M.P., Waters, D.J., Rex, D.C., Wilson, R.N., 1992. Pressure, temperature and time constraints on Himalayan metamorphism from eastern Kashmir and western Zanskar. J. Geol. Soc. London. 149, 753–773. https://doi.org/10.1144/gsjgs.149.5.0753

Sederholm, J.J., 1899. Über eine archäische Sedimentformation im südwestlichen Finland und ihre Bedeutung für die Erklärung der Entstehungsweise des Grundgebirges. Kuopio.

Sepahi, A.A., Whitney, D.L., Baharifar, A.A., 2004. Petrogenesis of andalusite–kyanite–sillimanite veins and host rocks, Sanandaj-Sirjan metamorphic belt, Hamadan, Iran. J. Metamorph. Geol. 22, 119–134.

Sequeira, N., Bhattacharya, A., Bell, E., 2021. The ~1.4 Ga A-type granitoids in the “Chottanagpur crustal block” (India), and its relocation from Columbia to Rodinia? Geosci. Front. 1138. https://doi.org/10.1016/j.gsf.2020.12.017

Shafaii Moghadam, H., Li, X.H., Ling, X.X., Santos, J.F., Stern, R.J., Li, Q.L., Ghorbani, G., 2015. Eocene Kashmar granitoids (NE Iran): Petrogenetic constraints from U-Pb zircon geochronology and isotope geochemistry. Lithos 216–217, 118–135. https://doi.org/10.1016/j.lithos.2014.12.012

Sharma, A., Das, K., Chakraborty, P.P., Shiraishi, F., Kayama, M., 2022. U–Pb zircon geochronology of a pyroclastic rock from the Parsoi Formation, Mahakoshal Group: Implications towards age and tectonics of the Basin in Central Indian Tectonic Zone. Geol. J.

Siégel, C., Bryan, S.E., Allen, C.M., Gust, D.A., 2018. Use and abuse of zircon-based thermometers: A critical review and a recommended approach to identify antecrystic zircons. Earth-Science Rev. 176, 87–116. https://doi.org/10.1016/j.earscirev.2017.08.011

Simpson, C., Wintsch, R.P., 1989. Evidence for deformation-induced K-feldspar replacement by myrmekite. J. Metamorph. Geol. 7, 261–275. https://doi.org/10.1111/j.1525-1314.1989.tb00588.x

Singh, S.P., Dwivedi, S.B., 2015. High grade metamorphism in the Bundelkhand massif and its implications on Mesoarchean crustal evolution in central India. J. Earth Syst. Sci. 124, 197–211. https://doi.org/10.1007/s12040-014-0516-y

Solanki, J.N., Sen, B., Soni, M.K., Tomar, N.S., Pant, N.C., 2003. Granulites from southeast of Wardha, Sidhi district, Madhya Pradesh in NW extension of Chhotanagpur Gneissic Complex: Petrography and geothermobarometric Estimation. Gondwana Geol. Mag. 7, 297–311.

Spear, F.S., 1993. Metamorphic Phase Equilibria and Pressure-Temperature-Time Paths.Monograph 1. Mineralogical Society of America.

Spencer, C.J., Kirkland, C.L., Taylor, R.J.M., 2016. Strategies towards statistically robust interpretations of in situ U-Pb zircon geochronology. Geosci. Front. 7, 581–589. https://doi.org/10.1016/j.gsf.2015.11.006

Stevens, G., Villaros, A., Moyen, J.F., 2007. Selective peritectic garnet entertainment as the origin of geochemical diversity in S-type granites. Geology 35, 9–12. https://doi.org/10.1130/G22959A.1

Stüwe, K., 1997. Effective bulk composition changes due to cooling: a model predicting complexities in retrograde reaction textures. Contrib. to Mineral. Petrol. 129, 43–52. https://doi.org/10.1007/s004100050322

Subramanyam, K.S.V., Santosh, M., Yang, Q.Y., Zhang, Z. ming, Balaram, V., Reddy, U.V.B., 2016. Mesoproterozoic island arc magmatism along the south-eastern margin of the Indian Plate: Evidence from geochemistry and zircon U-Pb ages of mafic plutonic complexes. J. Asian Earth Sci. 130, 116–138. https://doi.org/10.1016/j.jseaes.2016.07.027

Takeda, Y.-T., Obata, M., 2003. Some comments on the rheologically critical melt percentage. J. Struct. Geol. 25, 813–818.

Torres-Roldan, R.L., Garcia-Casco, A., Garcia-Sanchez, P.A., 2000. CSpace: An integrated workplace for the graphical and algebraic analysis of phase assemblages on 32-bit wintel platforms. Comput. Geosci. 26, 779–793. https://doi.org/10.1016/S0098-3004(00)00006-6

Torsvik, T.H., Carter, L.M., Ashwal, L.D., Bhushan, S.K., 2001. Rodinia refined or obscured : palaeomagnetism of the Malani igneous suite (NW India). Precambrian Res. 108, 319–333.

Touret, J.L.R., Santosh, M., Huizenga, J.M., 2022. Composition and evolution of the continental crust: Retrospect and prospect. Geosci. Front. 101428.

Tropper, P., Manning, C., 2005. Very low solubility of rutile in H 2 O at high pressure and temperature , and its implications for Ti mobility in subduction zones. Am. Mineral. 90, 502–505. https://doi.org/10.2138/am.2005.1806

Tsunogae, T., Santosh, M., 2010. Ultrahigh-temperature metamorphism and decompression history of sapphirine granulites from Rajapalaiyam, southern India: Implications for the formation of hot orogens during Gondwana assembly. Geol. Mag. 147, 42–58. https://doi.org/10.1017/S0016756809990100

Tsurumi, J., Hosonuma, H., Kanagawa, K., 2002. Strain localization due to a positive feedback of deformation and myrmekite-forming reaction in granite and aplite mylonites along the Hatagawa Shear Zone of NE Japan. J. Struct. Geol. 25, 557–574. https://doi.org/10.1016/S0191-8141(02)00048-2

Upadhyay, D., Raith, M.M., 2006. Petrogenesis of the Kunavaram alkaline complex and the tectonothermal evolution of the neighboring Eastern Ghats Belt granulites, SE India. Precambrian Res. 150, 73–94. https://doi.org/10.1016/j.precamres.2006.07.006

Vallance, T.G., 1967. Palaeozoic low-pressure regional metamorphism in southeastern Australia. Meddelelser fra Dansk Geol. Foren. 17, 494–503.

Vernon, R.H., 1979. Formation of late sillimanite by hydrogen metasomatism (base-leaching) in some high-grade gneisses. Lithos 12, 143–152. https://doi.org/10.1016/0024-4937(79)90045-8

Vernon, R.H., 1991. Questions about myrmekite in deformed rocks. J. Struct. Geol. 13, 979–985.

Vernon, R.H., 2004. A Practical Guide To Rock Microstructure - Ron H . Vernon. https://doi.org/10.1017/CBO9780511807206

Vernon, R.H., 2018. A practical guide to rock microstructure. Cambridge university press.

Vernon, R.H., Paterson, S.R., 2008. How late are K-feldspar megacrysts in granites? Lithos 104, 327–336. https://doi.org/10.1016/j.lithos.2008.01.001

Vernon, R.H., Williams, V.A., D'arcy, W.F., 1983. Grain-size reduction and foliation development in a deformed granitoid batholith. Tectonophysics 92, 123–145.

Vielzeuf, D., Montel, J.M., 1994. Partial melting of metagreywackes. Part I. Fluid-absent experiments and phase relationships. Contrib. to Mineral. Petrol. 117, 375–393. https://doi.org/10.1007/BF00307272

Villaros, A., Buick, I.S., Stevens, G., 2012. Isotopic variations in S-type granites: An inheritance from a heterogeneous source? Contrib. to Mineral. Petrol. 163, 243–257. https://doi.org/10.1007/s00410-011-0673-9

Villaros, A., Stevens, G., Buick, I.S., 2009. Tracking S-type granite from source to emplacement: Clues from garnet in the Cape Granite Suite. Lithos 112, 217–235. https://doi.org/10.1016/j.lithos.2009.02.011

Wanjari, N.R., Chaturvedi, R., Mahanta, D.N., 2012. Specialised thematic mapping in Munger–Rajgir Group of rocks to examine structural and stratigraphic set up in and around Gaya–Rajgir areas in parts of Gaya, Nawada and Jahanabad districts of Bihar. Unpubl. report, GSI (FS 2008-09, 2009-10).

Watkins, J.M., Clemens, J.D., Treloar, P.J., 2007. Archaean TTGs as sources of younger granitic magmas: Melting of sodic metatonalites at 0.6-1.2 GPa. Contrib. to Mineral. Petrol. 154, 91–110. https://doi.org/10.1007/s00410-007-0181-0

Watson, E., Harrison, T.M., 1983. Zircon saturation reviseted: temperature and composition effects in a variety of crustal magmas types. Earth Planet. Sci. Lett. 64, 295–304.

Whalen, J.B., Currie, K.L., Chappell, B.W., 1987. A-type granites: geochemical characteristics, discrimination and petrogenesis. Contrib. to Mineral. Petrol. 95, 407–419. https://doi.org/10.1007/BF00402202

White, M.D., McGrail, B.P., 2008. Numerical simulation of methane hydrate production from geologic formations via carbon dioxide injection, in: Offshore Technology Conference. OTC, p. OTC-19458.

White, R.W., Powell, R., Clarke, G.L., 2002. The interpretation of reaction textures in Fe-rich metapelitic granulites of the Musgrave Block, Central Australia: Constraints from mineral equilibria calculations in the system. J. Metamorph. Geol. 20, 41–55. https://doi.org/10.1046/j.0263-4929.2001.00349.x

White, R.W., Powell, R., Holland, T.J.B., Johnson, T.E., Green, E.C.R., 2014. New mineral activity-composition relations for thermodynamic calculations in metapelitic systems. J. Metamorph. Geol. 32, 261–286. https://doi.org/10.1111/jmg.12071

White, R.W., Powell, R., Holland, T.J.B., Worley, B.A., 2000. The effect of TiO2 and Fe2O3 on metapelitic assemblages at greenshist and amphibolite facies conditions: mineral equilibria calculations in the system K2O-FeO-MgO-Al2O3-SiO2- H2O-TiO2-Fe2O3. J. Metamorph. Geol. 18, 497-512.

Whitney, Dilek, 2000. Andalusite–sillimanite–quartz veins as indicators of low-pressure–high-temperature deformation during late-stage unroofing of a metamorphic core complex, Turkey. J. Metamorph. Geol. 18, 59–66.

Worley, B., Powell, R., 2000. High-precision relative thermobarometry: theory and a worked example. J. Metamorph. Geol. 18, 91–102.

Wyllie, P.J., Wolf, M.B., 1993. Amphibolite dehydration-melting: sorting out the solidus. Geol. Soc. London, Spec. Publ. 76, 405–416. https://doi.org/10.1144/GSL.SP.1993.076.01.20

Yadav, B.S., Ahmad, T., Bhutani, R., Kaulina, T., Bayanova, T., 2023. Geochronological and geochemical constraints on the petrogenesis of alkali granites from the Makrohar Granulite Belt: Evidence for Mesoproterozoic extensional regime in the eastern Central Indian Shield. Geol. J. 58, 563–582.

Yadav, B.S., Ahmad, T., Kaulina, T., Bayanova, T., 2015. Geochemistry and petrogenesis of Paleo-Proterozoic granitoids from Mahakoshal Supracrustal Belt (MSB), CITZ, in: EGU General Assembly Conference Abstracts.

Yadav, B.S., Ahmad, T., Kaulina, T., Bayanova, T., Bhutani, R., 2020. Origin of post-collisional A-type granites in the Mahakoshal Supracrustal Belt, Central Indian Tectonic Zone, India: Zircon U-Pb ages and geochemical evidences. J. Asian Earth Sci. 191, 104247. https://doi.org/10.1016/j.jseaes.2020.104247

Yadav, B.S., Wanjari, N., Ahmad, T., Chaturvedi, R., 2014. Geochemistry and petrogenesis of proterozoic granitic rocks from northern margin of the chotanagpur gneissic complex (CGC). J. Earth Syst. Sci. 125, 1041–1060. https://doi.org/10.1007/s12040-016-0709-7

Yakymchuk, C., Brown, M., 2014. Consequences of open-system melting in tectonics. J. Geol. Soc. London. 171, 21–40. https://doi.org/10.1144/jgs2013-039

Yedekar, D.B., Jain, S.C., Nair, K.K.K., Dutta, K.K., 1990. The Central Indian collision suture. Precambrian of Central India. Geol. Surv. India Spec. Publ. 28, 1–37.

Yousuf, I., Subba Rao, D. V., Balakrishnan, S., Ahmad, T., 2019. Geochemistry and petrogenesis of acidic volcanics from Betul–Chhindwara Belt, Central Indian Tectonic Zone (CITZ), central India. J. Earth Syst. Sci. 128. https://doi.org/10.1007/s12040-019-1255-x

Zhang, J., Liu, W., Yakymchuk, C., Sa, R., Zeng, Z., Ding, R., Tang, G., Liu, H., Xu, Q., Wang, Y., 2019. Partial Melting and Crustal Deformation during the Early Paleozoic Wuyi–Yunkai Orogeny: Insights from Zircon U-Pb Geochronology and Structural Analysis of the Fuhuling Migmatites in the Yunkai Region, South China. Minerals 9, 621.

Zhang, S., Li, Z.X., Evans, D.A.D., Wu, H., Li, H., Dong, J., 2012. Pre-Rodinia supercontinent Nuna shaping up: A global synthesis with new paleomagnetic results from North China. Earth Planet. Sci. Lett. 353–354, 145–155. https://doi.org/10.1016/j.epsl.2012.07.034

Zhao, G., Cawood, P.A., 2012. Precambrian geology of China. Precambrian Res. 222, 13–54.

Zhao, G., Cawood, P.A., Wilde A., S., Sun, M., 2002. Review of global 2.1-1.8 Ga orogens: inplications for a pre-Rhodinia supercontinent. Earth-Science Rev. 59, 125–162. https://doi.org/10.1016/B978-0-08-087780-8.00052-8

Zhao, G., Li, S., Sun, M., Wilde, S. a., 2011. Assembly, accretion, and break-up of the Palaeo-Mesoproterozoic Columbia supercontinent: record in the North China Craton revisited. Int. Geol. Rev. 53, 1331–1356. https://doi.org/10.1080/00206814.2010.527631

Zhao, G., Sun, M., Wilde, S.A., Li, S., 2004. A Paleo-Mesoproterozoic supercontinent: Assembly, growth and breakup. Earth-Science Rev. 67, 91–123. https://doi.org/10.1016/j.earscirev.2004.02.003

Zheng, Y.F., Gao, P., 2021. The production of granitic magmas through crustal anatexis at convergent plate boundaries. Lithos 402–403, 106232. https://doi.org/10.1016/j.lithos.2021.106232